The Origin and Evolution of Heavy Rare Earth Element Mineralisation in the Browns Range Area, Northern Australia

Thesis submitted by

Teimoor Nazari Dehkordi

November 2018

For the Degree of Doctor of Philosophy in the

College of Science and Engineering of

James Cook University

This thesis is dedicated to:

The Aboriginal and Torres Strait Islander People:
The First Inhabitants, Traditional Owners and
The Forgotten People of Australia

Acknowledgments

I would like to greatly thank my advisory panel: Carl Spandler, Nickolas Oliver and Paul Dirks, for their help and support. In particular, I am forever in debt to Carl who provided continuous encouragement and thorough feedback throughout the project.

I appreciate all faculty (Jan Marten Huizenga, Eric Roberts, Mike Rubenach, Rob Holm, Zhaoshan Chang and Cassian Pirard) and staff (Judy Botting, Kaylene Camuti, Mark Stokes and Huiqing Huang) members of the Economic Geology Research Centre (EGRU). Special thanks to Rebecca Steele (College's academic services officer) for her assistance during my study. Advanced Analytical Centre (Kevin Blake, Yi Hu and Shane Askew) and Northern Minerals Ltd (Robin Wilson and Jaqueline Chapman) are also acknowledged for helping with sample preparation, laboratorial and field works. I also thank my fellow doctoral students, Stephanie Mrozek, Fredrik Sahlstrom, Ibrahim Mohamed and Joao Babo for their feedback and cooperation.

Lastly, I would like to thank my parents and siblings, two brothers and one sister, for their love and support throughout my life.

Statement of Contribution by Others

Nature of assistance	Contribution	Name	Affiliation
Intellectual support	**Proposal writing**	Carl Spandler	James Cook University
	Data analysis	Carl Spandler	James Cook University
		Nickolas Oliver	James Cook University
		Jan Marten Huizenga	James Cook University
		Mike Rubenach	James Cook University
Financial support	**Stipend and tuition fees**	JCU-PRS	James Cook University
		CSE Write-up Grant	James Cook University
	Field work		James Cook University
			Northern Minerals
	Conference attendance		James Cook University
			Economic Geology Research Centre
	Analytical cost	Carl Spandler	James Cook University
			Economic Geology Research Centre
		CSE and GRS	James Cook University
Data Collection	**Whole-rock geochemistry**		Bureau Veritas Laboratories
	WDS and EDS	Kevin Blake	James Cook University
		Shane Askew	James Cook University
	LA-ICP-MS	Yi Hu	James Cook University
	Ar-Ar	Chris Hall	University of Michigan
	Stable isotope	Chris Harris	Univeristy of Cape Town
	Fluid inclusion	Jan Marten Huizenga	James Cook University
	Sample collection	Carl Spandler	James Cook University
		Nickolas Oliver	James Cook University
		Jacqueline Chapman	Northern Minerals
		Robin Wilson	Northern Minerals

Statement of Contribution of Co-authors

Chapter	Paper	Authorship	Roles
2	Provenance, tectonic setting and source of Archean metasedimentary rocks of the Browns Range Metamorphics, Tanami Region, Western Australia Published in *Australian Journal of Earth Sciences*	Teimoor Nazari Dehkordi Carl Spandler Nickolas Oliver Jacqueline Chapman Robin Wilson	Major research concepts were developed by the authors. Nazari, Spandler, Chapman and Wilson collected the samples. BVL carried out whole-rock geochemistry analysis. Nazari and Spandler conducted and analysed U-Pb and Lu-Hf analyses. Nazari wrote the first draft and prepared figures and tables. Spandler, Oliver, Chapman and Wilson provided extensive editorial feedback.
3	Age, geological setting and paragenesis of heavy rare earth element mineralisation of the Tanami and Halls Creek Regions, Western Australia	Teimoor Nazari Dehkordi Carl Spandler Nickolas Oliver Robin Wilson	Major research concepts were developed by the authors. Nazari, Spandler, Oliver and Wilson collected the samples. Nazari and Spandler conducted and analysed WDS, EDS, U-Pb and Lu-Hf analyses. Nazari wrote the first draft and prepared figures and tables. Spandler, Oliver and Wilson provided extensive editorial feedback.
4	Unconformity-Related Rare Earth Element deposits: A regional-scale hydrothermal mineralization type of northern Australia Published in *Economic Geology*	Teimoor Nazari Dehkordi Carl Spandler Nickolas Oliver Robin Wilson	Major research concepts were developed by the authors. Nazari, Spandler, Oliver and Wilson collected the samples. Nazari and Spandler conducted and analysed WDS, EDS and LA-ICP-MS analyses. Nazari wrote the first draft and prepared figures and tables. Spandler, Oliver and Wilson provided extensive editorial feedback.
5	Paragenesis and chemistry of the xenotime and florencite from the heavy rare earth element mineralisation of the Browns Range, Western Australia	Teimoor Nazari Dehkordi Carl Spandler Nickolas Oliver Robin Wilson	Major research concepts were developed by the authors. Nazari, Spandler, Oliver and Wilson collected the samples. Nazari and Spandler conducted and analysed WDS, EDS and LA-ICP-MS analyses. Nazari wrote the first draft and prepared figures and tables. Spandler, Oliver and Wilson provided extensive editorial feedback.
6	Fluid inclusion and stable isotope constraints on the heavy rare earth element mineralisation in the Browns Range Dome, Tanami Region, Western Australia	Teimoor Nazari Dehkordi Jan Marten Huizenga Carl Spandler Nickolas Oliver	Major research concepts were developed by the authors. Nazari and Spandler collected the samples. Nazari and Marten Huizenga performed microthermometry analysis. Nazari and Spandler conducted LA-ICP-MS analyses. UCT carried out stable isotope analysis, and Nazari and Spandler analysed the results. Nazari wrote the first draft and prepared figures and tables. Marten Huizenga, Spandler and Oliver provided extensive editorial feedback.

Abstract

This thesis investigates a regional-scale heavy rare earth element (HREE) mineralisation style that appears as several structurally-controlled orebodies distributed from the Halls Creek Orogen to the Tanami Region, in an area labelled the North Australian HREE+Y (NAHREY) mineral field. The ore minerals consist only of xenotime [(Y,HREE)PO_4] and minor florencite [$LREEAl_3(PO_4)_2(OH)_6$], and occur mainly near a regional unconformity between the Archean metasedimentary rocks of the Browns Range Metamorphics (BRM) and overlying Paleoproterozoic Birrindudu Group sandstones in northwest of the Tanami Region.

The BRM are medium- to coarse-grained arkosic metasandstones that host the bulk of the HREE mineralisation in the NAHREY mineral field. The BRM consists mainly of detrital quartz and feldspars with minor granitic lithic fragments. Isotopic data acquired from detrital zircons from the BRM and intruding felsic igneous rocks yielded a well-defined age of ca. 3.2 to ca. 3.0 Ga, with relatively radiogenic εHf values (εHf = –1.7 to +5.1), indicating derivation from a Mesoarchean granitic basement of juvenile origin, and deposition in a continental rift basin setting. The sedimentation is constrained to between the ca. 3.0 Ga age of the source rocks and ca. 2.5 Ga age of the felsic igneous bodies that cross-cut the BRM. The ca. 2.5 Ga zircons from the felsic igneous rocks have εHf model ages comparable to those of the ca 3.2 to ca. 3.0 Ga detrital and inherited zircons (ca. 3.4 to ca. 3.1 Ga), consistent with formation via partial melting of the BRM, or the Mesoarchean granitic basement. The unconformably-overlying Gardiner Sandstone of the Birrindudu Group contains detrital zircons of ca 2.6 to ca 1.8 Ga age with no trace of Mesoarchean age, which discounts a significant contribution from the underlying BRM.

A detailed paragenetic study of the mineralisation revealed; (1) a pre-ore stage displaying mostly a greenschist-facies overprint, with the detrital/metamorphic minerals including quartz (several generations), alkali feldspar, plagioclase, and coarse-grained muscovite aligned in the pre-mineralisation foliation; (2) syn-ore quartz and white mica alteration associated with a complex multi-stage mineralisation of the ore minerals, primarily in breccias and veins; (3) a post-ore stage characterised by several generations of quartz, hematite, barite, anhydrite and pyrite veining and brecciation. Isotopic dating of xenotime ore from across the NAHREY mineral field constrained the main stage of ore formation to between ca. 1.65 Ga and ca. 1.60

Ga, which is significantly younger that the pre-ore muscovite $^{40}Ar/^{39}Ar$ age of ca. 1.72 Ga that corresponds to a regional metamorphism. The ca. 1.65-1.60 Ga timeframe does not correlate to any local magmatism or orogeny but was coincident with the collision of the North Australian Craton with the Arunta Inlier and Laurentia and subsequent initiation of the Isan and Liebig Orogenies. Far field stresses from these craton-scale events potentially acted as drivers of large-scale fluid flow and fault (re)activation that led to the HREE ore formation.

Ore petrography indicates multiple stages of xenotime and florencite crystallisation and re-crystallisation. Early xenotime (up to 1 mm), coexisting with early florencite, appears in breccias (breccia-hosted) and mineralised quartz veins (vein-type). Late xenotime (<100 µm) occurs largely as pyramid-shaped overgrowths on the pre-existing xenotime and coexists with late florencite that mainly replaces early xenotime and also appears as narrow rims on early florencite. Compared with early xenotime, the late xenotime overgrowths are richer in the HREE and more depleted in P and LREE, owing to crystallisation of late florencite. Moreover, early florencite has a nearly pure florencite composition whereas the late florencite is defined by a broad chemistry including components of svanbergite, goyazite and woodhouseite. Both xenotime and florencite incorporated quantities of trace elements via a number of substitution mechanisms. High U content of xenotime and composition of early florencite potentially support a genetic association between the HREE mineralisation and the coeval U deposits of northern Australia that formed across the same basin.

Samples of the BRM are variably depleted in HREE compared to sedimentary protoliths, and also have unradiogenic Nd isotope compositions that are comparable to the orebodies, but quite distinct from the igneous rocks or other sedimentary rocks (Birrindudu Group) from across the North Australian Craton. These observations demonstrated that the ore metals were derived directly from the BRM. Moreover, investigation of a large number (ca. 550) of primary fluid inclusions from both mineralised and barren quartz veins, revealed three types of hydrothermal fluids available only in the mineralised samples including type I low salinity H_2O-NaCl (largely <5 wt.% salinity; consistent with meteoric water), type II medium salinity H_2O-NaCl (12-18 wt.% salinity) and type III high salinity H_2O-$CaCl_2$-NaCl (up to 25 wt.% salinity). The trapping temperature and pressure during the ore formation was between 100 to 250 °C and between 0.4 and 1.6 Kbar, respectively. Trace element analysis detected Y, Ce and Cl only in the type III fluid inclusions, which indicates that transportation of ore metals was (at least partly) by Cl complexes in the type III fluid. The P required for phosphate ore mineral formation was likely

transported by the type I fluid. Moreover, mineralised quartz samples returned $\delta^{18}O_{fluid}$ values in the range defined by the BRM ($\delta^{18}O_{fluid}$ = +1.8 to +5.2‰) and the Birrindudu Group sandstones ($\delta^{18}O_{fluid}$ = +8‰).

Combining whole-rock, fluid inclusion and isotopic data, an ore genesis model is developed that suggests mixing of at least two hydrothermal fluids, one (type III) leached HREE+Y from the BRM and moved upward along fault structures in the vicinity of the regional unconformity, and there mixed with another down-flowing P-bearing fluid (represented potentially by the type I fluid inclusions) originated from the Birrindudu Group sandstones. Leaching of ore metals was greatly enhanced by halogen (Cl, F) complexes. Introduction of P during fluid mixing/dilution and an increase in pH as recorded by the syn-ore muscovite alteration, resulted in HREE deposition.

Globally, the closest analogue to the NAHREY ore deposits is the Maw Zone, which formed in a very similar geological setting in the Athabasca Basin, Canada. Collectively, this style of REE mineralisation is unlike any other known REE ore style, and is herein labelled "Unconformity-Related REE deposit". There is great potential for further unconformity-related REE deposits to be found in intercontinental basins in close proximity to regional unconformities between Archean basement rocks and overlying Proterozoic sedimentary sequences.

Table of Content

List of Figures

List of Tables

Chapter 1

Introduction

Thesis subject

This thesis investigates the poorly-understood, recently-discovered heavy rare earth element (HREE) mineralisation distributed within a vast area of ~300 km in length, from the Halls Creek Orogen to the Tanami Region of north-western Australia (Fig. 1-1). The HREE mineralisation occurs as numerous structurally-controlled deposits/prospects of variable grade and tonnage, consisting exclusively of xenotime [(YHREE)PO_4] and minor florencite [LREE$Al_3(PO_4)_2(OH)_6$], hosted by the metasedimentary/sedimentary rocks of the Browns Range Metamorphics (BRM) and Birrindudu Group sandstones of the Tanami Region, and the Red Rock Basin of the Halls Creek Orogen.

The primary focus of the research work is on the HREE deposits/prospects hosted by the BRM, and particularly on the Wolverine, being the largest deposit with a total mineral resource of 4.97 Mt @ 0.86% total rare earth oxide. Compared with the major known REE orebodies worldwide (Smith et al., 2016 and the references therein, Fig. 1-2), Wolverine can be considered to be of low grade (e.g., ca. 5-6 wt. % REE_2O_3 at Bayan Obo; ca. 9 wt. % REE_2O_3 at Mountain Pass; Mariano and Mariano, 2012) and low tonnage (e.g., Mountain Pass, with ca. 16.7 Mt of resources, Mt. Weld, with ca. 23.9 Mt of resources; Weng et al., 2013, 2015), following the classification outlined in Laznicka (1999). Nonetheless, Wolverine is significantly enriched in HREE (84 % of the total resource); which are of high value and high demand (Goodenough et al., 2017).

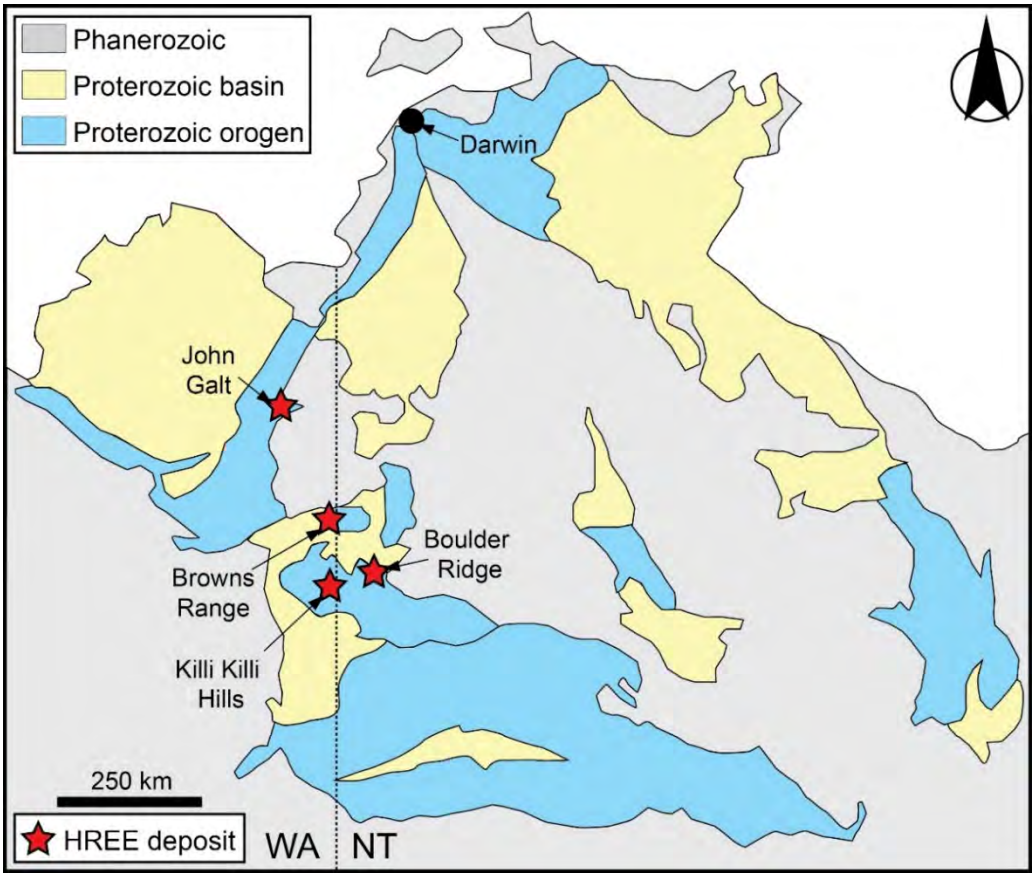

Fig. 1-1: Simplified geological map of northern Australia showing the distribution of the HREE mineralisation in northern Australia.

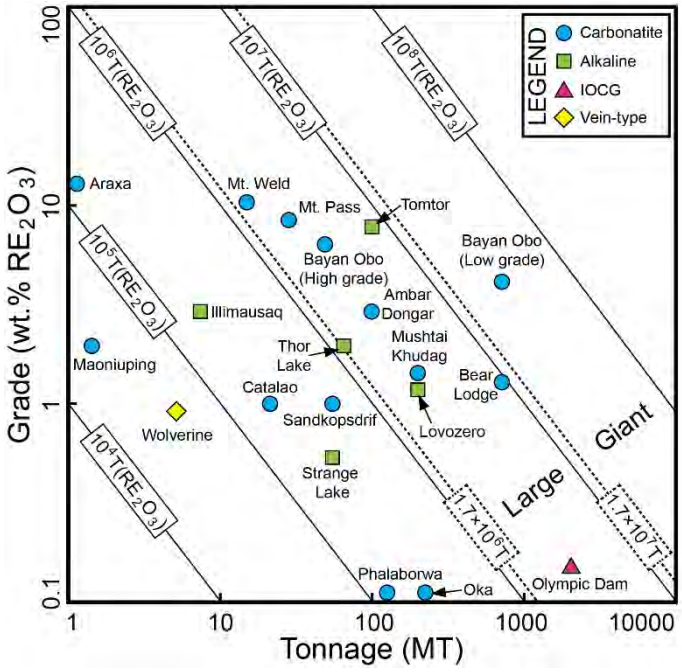

Fig. 1-2: Grade versus tonnage of major REE deposits (Jaireth et al., 2014).Note that Wolverine orebody has a comparably low grade and tonnage.

Significance

The rare earth elements (REE), also known as the lanthanides (Ln), are commonly divided into light and heavy REEs (LREE and HREE, respectively). Classification of these elements into light and heavy is somewhat inconsistent, but the most commonly-used approach, employed in this thesis, considers La to Gd, whose orthophosphates assume a monoclinic structure, as LREE. Subsequently, Tb to Lu characterised with orthophosphates that display a tetragonal zircon-type structure, are considered as HREE (Ni et al., 1995). Furthermore, yttrium (Y) is also often regarded as one of the HREE, due to its very similar geochemical characteristics to Ho (Connelly et al., 2005).

Owing to their unusual physical and chemical properties such as unique magnetic and optical properties (Table 1-1), the REE are used in a wide range of applications ranging from everyday household items to cutting-edge technologies. Also branded as the “green elements”, the REE are a major component of the green energy technologies such as hybrid electric vehicles, wind power, low energy light bulbs and biofuels. Reportedly, battery alloys, magnets, polishing powder, auto-catalysts, phosphors, fluid cracking catalysts and metallurgy are the major applications that require REE. Despite this enormous economic and political interest, the bulk of the REE production derives from a single deposit (Bayan Obo REE-Nb-Fe deposit, China), causing geopolitical insecurity in the global REE market. Moreover, overwhelming majority of the known REE occurrences are enriched in LREE (La-Gd), resulting in a marked increase in the price of the HREE (Tb-Lu plus Y) compared with their light counterparts. In particular, dysprosium (Dy) faces the highest supply risk in the near future (e.g., Hatch et al., 2012; Goodenough et al., 2017). To ensure a steady production of REE, further understanding of REE mineralisation in different geological settings is essential.

Table 1-1: Major physical and chemical properties of the REE as well as scandium and yttrium

Element	Symbol	Atomic number	Atomic weight	Density (gr/cm^3)	Melting point (°C)	Boiling point (°C)	Crustal abundance	Vicker's hardness	Crystal structure
Scandium	Sc	21	44.9	2.98	1541	2832	8	85	Hexagonal
Yttrium	Y	39	88.9	4.46	1522	3337	30	38	Hexagonal
Lanthanium	La	57	138.9	6.14	918	3469	30	37	Hexagonal
Cerium	Ce	58	140.1	8.16	789	3257	60	24	Cubic
Praseodymium	Pr	59	140.9	6.77	931	3127	7	37	Hexagonal
Neodymium	Nd	60	144.2	7	1021	3127	25	35	Hexagonal
Promethium	Pm	61	145	7.26	1042	3000	$4.5*10^{-20}$	n.a.	Hexagonal
Samarium	Sm	62	150.3	7.52	1074	1900	5	45	Rhombohedral
Europium	Eu	63	151.9	5.24	822	1597	1	17	Cubic
Gadolinium	Gd	64	157.2	7.9	1313	3233	4	57	Hexagonal
Terbium	Tb	65	158.9	8.23	1356	3041	0.7	46	Hexagonal
Dysprosium	Dy	66	162.5	8.55	1412	2562	3.5	42	Hexagonal
Holmium	Ho	67	164.9	8.79	1474	2720	0.8	42	Hexagonal
Erbium	Er	68	167.2	9.06	1529	2510	2.3	44	Hexagonal
Thulium	Tm	69	168.9	9.32	1545	1727	0.3	48	Hexagonal
Ytterbium	Yb	70	173	6.96	819	1466	2.2	21	Cubic
Lutetium	Lu	71	174.9	9.84	1663	3315	4.4	77	Hexagonal

Data are from Gupta and Krishnamurthy (2005).

Comprehensive reviews on the characteristics of the major US, European and Australian REE occurrences are provided in Long et al. (2010), Goodenough et al. (2016) and Jaireth et al. (2014), respectively. Briefly, a commonly-used approach divides natural REE occurrences into "primary" deposits occurred mainly through magmatic processes and hydrothermal fluid mobilisation and precipitation, and "secondary" deposits formed chiefly by processes that move or concentrate REE from, or in, the original place of formation via sedimentary concentration or weathering (Walters et al., 2010).

Globally, the great majority of the well-studied REE deposits (e.g., Bayan Obo, China, Yang et al., 2009; Maoniuping, China, Xie et al., 2009; Mountain Pass, United States, Castor, 2008; Mount Weld, Australia, Lottermoser, 1990; Strange Lake, Canada, Gysi and Williams-Jones, 2013; Nechalacho, Canada, Sheard et al., 2012), are genetically and spatially associated with magmatic rocks, particularly carbonatites and alkaline/peralkaline rocks (Figs. 1-3, 1-4). Moreover, many so-called "vein-type" REE deposits are suggested to be linked to magmatic activity (e.g., Nolans Bore, Australia, Anenburg et al., 2018; Snowbird, USA, Samson et al., 2004). Hence, REE deposits of indisputable hydrothermal origin, with no links to magmatism, appear to be very rare in geological record (e.g., Maw Zone HREE prospect, Athabasca Basin, Rabiei et al., 2017), although experimental studies demonstrated that aqueous transportation and deposition of REE to economically significant levels is feasible under specific hydrothermal conditions (Migdisov et al., 2009, 2011; Loges et al., 2013; Migdisov and Williams-Jones, 2014; Timofeev et al., 2015, 2017). Moreover, a vast majority of the currently-

exploited REE deposits are LREE-enriched with only few small occurrences enriched in HREE minerals (Lofdal Carbonatite, Namibia, Wall et al., 2008; Songwe Hill Carbonatite, Malawi, Broom-Fendley, 2017; Music Valley Gneiss, USA, McKinney, 2015). As documented in this thesis, the REE mineralisation in northern Australia is remarkably rich in the HREE and also displays evidence for an exclusively hydrothermal origin with no apparent relationship with magmatism of any type. Thus, this thesis can provide implications for further discovery of the economically significant HREE enriched orebodies formed under hydrothermal conditions using approaches unlike those currently employed for exploration of REE deposits associated with magmatism.

This thesis aims primarily to:

(1) Delineate the depositional timing and origin of the BRM (prime host to the ore)
(2) Detail the mineral paragenesis and alterations associated with the ore and host rocks
(3) Determine the age of mineralisation in context of local and regional geological history
(4) Investigate ore mineral chemistry
(5) Provide constraints on the conditions (P-T) of ore deposition
(6) Define the geological processes responsible for mineralisation
(7) Describe the ore style
(8) Develop implications for exploration purposes

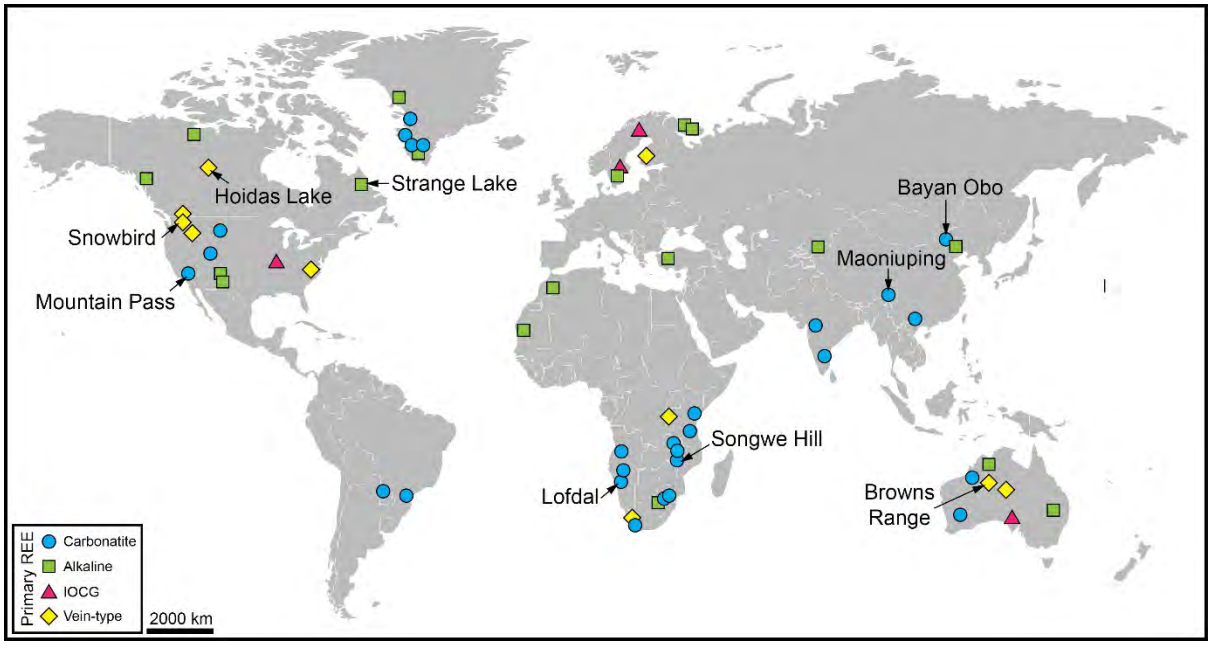

Fig. 1-3: Global distribution of major primary REE deposits (Walters et al., 2010).

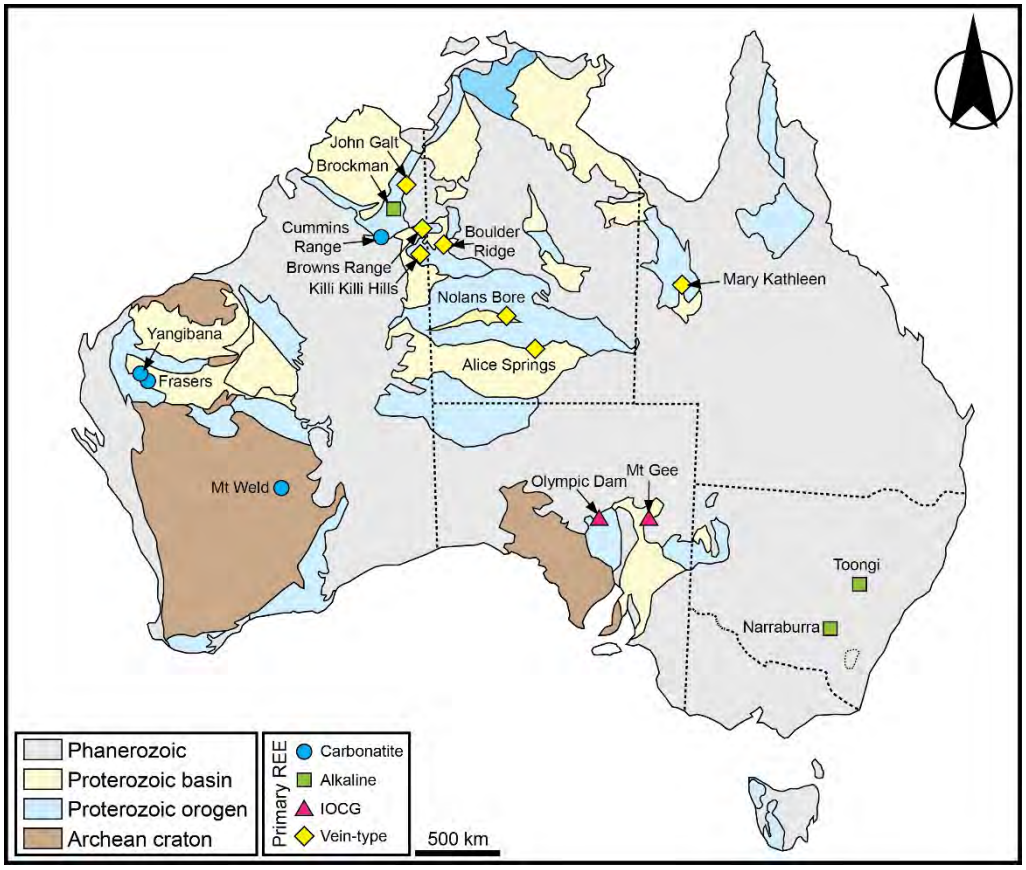

Fig. 1-4: Distribution of major primary REE deposits in Australia (Jaireth et al., 2014).

Previous study of the Browns Range

Exploration and mining

Uranium and HREE anomalies were first identified in the Browns Range in the 1970s, when a number of companies, including Esso Australia, Peachiney Australia, Alcoa, Cultus Pacific Uranex JV and Denison, searched the area primarily for unconformity-related uranium mineralisation. These HREE anomalies were, however, considered economically insignificant. Later, PNC Exploration (Power Reactor and Nuclear Fuel Development Corporation) explored the Browns Range between 1987 and 1991, and conducted geophysical surveys, geological mapping, rock chip assays, petrological analysis and drilling. Despite finding traces of xenotime veins in the outcrops, exploration ceased and again the Browns Range was concluded to be infertile for mineralisation. Limited outcrop exposure and difficulty of access meant that very limited subsequent exploration was conducted in the area until mid-2000s, when Northern

Minerals Ltd recognised the potential for HREE mineralisation and embarked on regional-scale exploration work including geophysical surveys, geological mapping and drilling. Northern Minerals Ltd have since identified and named numerous HREE deposits and prospects and now hold exploration and mining leases in and outside of the Browns Range. Northern Minerals Ltd commenced mining operations for HREE at Wolverine and the nearby Gambit deposits in 2017, aiming for a full scale production of 585,000 tons per annum through a combination of open pit and underground mining operations.

Research

Very little geological research has been conducted on the Browns Range area to date. The first stratigraphic column that considered the Browns Range as part of the Tanami Region was published by Blake et al. (1979); this stratigraphy has since been refined on the basis of new observations and geochronological data (Page et al., 1995; Cross and Crispe, 2007). The term Browns Range Metamorphics (BRM), used in this thesis to describe the Archean metasedimentary rocks lying exclusively on the western margin of the Browns Range Dome (BRD), was adopted from Blake et al. (2000). Geochronological data for the Browns Range Dome are limited to U-Pb zircon dating from a sample of the BRD granite collected from the southern margin of the Dome within the Northern Territory (Page et al., 1995; Cross and Crispe, 2007). These papers identified zircon age populations of ca. 3.15 to ca. 3.04 Ga, ca. 2.67 to ca. 2.44 Ga and ca. 1.99 to ca. 1.87 Ga. Cross and Crispe (2007) interpreted the youngest age to be the crystallisation age of the BRD granite, and the Archean-aged zircons to be inherited material from the basement. This has led to the conclusion that the BRD includes rock units of both Archean and Paleoproterozoic age. In more recent years, the regional geology of the Browns Range was broadly discussed in reports published by Northern Territory Geological Survey (NTGS) and Geological Survey of Western Australia (GSWA) (e.g., Blake et al., 2000; Hendrickx et al., 2000; Crispe and Vandenberg, 2004), but little new data was presented in these publications.

Vallini et al. (2007) studied xenotime occurrence at Boulder Ridge, about 40 km south of the BRD, and reported a wide range of ages from 1639 Ma to 1564 Ma. The first and yet the only thesis, an honours thesis, on the Browns Range was produced by O'Reilly in 2012 from the University of Adelaide. This thesis mainly investigated the mineralogy and petrography of the

HREE mineralisation. The major results of this thesis were published in a paper in "Lithos" in 2013 by Cook et al. (2013). Moreover, Morin-Ka et al. (2016) published results of U-Pb dating of xenotime ore from Wolverine (1646 ± 5 Ma) and also from John Galt (1619 ± 9 Ma) hosted in the Halls Creek Orogen. Most recently, Richter et al. (2018) presented fluid inclusion assemblages of the mineralised hydrothermal quartz veins, and suggested a low P environment for the ore formation.

Thesis structure

This thesis presents a series of five independent result chapters (Chapters 2-6), bracketed by an "Introduction" (Chapter 1) and a "Conclusion" (Chapter 7), with the intention that each result chapter will be published in an internationally well-recognised Earth Science journal. Subsequently, each result chapter is presented in a format similar to a published paper, causing some inevitable repetition, particularly in text sections such as Introduction and Geological Setting and Analytical techniques. Nonetheless, each chapter presents a separate body of work that discusses new geological aspects using a variety of analytical techniques and approaches. At the time to submission, Chapters 2 and 4 had already been published in "*Australian Journal of Earth Sciences*" and "*Economic Geology*", respectively. The remaining chapters (Chapters 3, 5 and 6) will also be submitted shortly. These paper-based result chapters are followed by a "Conclusion" that combines and summarises major findings presented in the five result chapters (Chapters 2-6). The final section of this thesis is the "Appendices" which includes a complete list of datasets as well as accessory information and documents.

Chapter outlines

A brief outline of the content of each of the "result" chapters is provided below:

Chapter 2: Provenance, tectonic setting and source of Archean metasedimentary rocks of the Browns Range Metamorphics, Tanami Region, Western Australia.

This chapter characterises the Archean metasedimentary rocks of the BRM that host bulk of the HREE mineralisation, using whole-rock geochemical and petrological data combined with U-Pb age and Lu-Hf isotope data derived from the BRM and cross-cutting felsic igneous rocks.

These data are used to evaluate the age and nature of the sediment source rock, the timing and tectonic setting of deposition, and post-depositional alteration and weathering.

Chapter 3: Age, geological setting and paragenesis of heavy rare earth element mineralisation of the Tanami and Halls Creek Regions, Western Australia.

This chapter documents the mineral assemblage, paragenetic relationships and geological setting of the HREE mineralisation, complimented with a comprehensive U-Pb age dataset of xenotime ore from a number of HREE deposits/prospects. These data are then employed to evaluate possible driving forces of the HREE mineralisation, and potential genetic associations with other ore deposits of northern Australia.

Chapter 4: Unconformity-Related Rare Earth Element deposits: A regional-scale hydrothermal mineralization type of northern Australia.

Combining ore petrology, mineral chemistry, geochronology, and Sm-Nd isotope analysis of a number of HREE deposits/prospects, this chapter defines a comprehensive ore genesis model that describes the source/s of the ore metals and the mechanisms whereby the HREE were leached, transported and deposited. These information are also used to determine vectors for further exploration of this type of ore mineralisation.

Chapter 5: Paragenesis and chemistry of the xenotime and florencite from heavy rare earth element mineralisation of the Browns Range, Western Australia.

This chapter details petrographic studies and geochemical data for different generations of xenotime and florencite from a number of the HREE deposits/prospects. These data are used to investigate the composition and distribution of trace elements between xenotime and florencite formed under hydrothermal conditions, and to provide constraints on the physico-chemical conditions of formation of different generations of these REE phosphate minerals.

Chapter 6: Fluid inclusion and stable isotope constraints on the heavy rare earth element mineralisation in the Browns Range Dome, Tanami Region, Western Australia.

To gain further insights into the P-T conditions and nature of ore-forming hydrothermal fluids responsible for HREE mineralisation, this chapter presents a detailed fluid inclusion study incorporating fluid inclusion petrography, microthermometry, laser Raman spectroscopy analysis and trace element microanalysis. Furthermore, oxygen isotope compositions of ore-related minerals and surrounding host rocks are discussed to define the origin of the ore-bearing hydrothermal fluids.

References

Anenburg, M., and Mavrogenes, J., 2018. Carbonatitic versus hydrothermal origin for fluorapatite REE-Th deposits: Experimental study of REE transport and crustal "antiskarn" metasomatism. American Journal of Science, v. 318, p. 335–366.

Blake, D.H., Hodgson I.M., and Muhling, P.C., 1979. Geology of the Granites–Tanami Region. Canberra ACT: Bureau of Mineral Resources, 91 p.

Blake, D.H., Tyler, I.M., and Warren, R.G., 2000. Gordon Downs (Second edition) 1:250000 geological series, explanatory notes. Canberra ACT: Australian Geological Survey Organisation, and Perth WA: Geological Survey of Western Australia (National Geoscience Mapping Accord).

Broom-Fendley, S., Wall, F., Spiro, B., and Ullmann, C.V., 2017. Deducing the source and composition of rare earth mineralising fluids in carbonatites: insights from isotopic (C, O, $^{87}Sr/^{86}Sr$) data from Kangankunde, Malawi. Contributions to Mineralogy and Petrology, 172, p. 96. DOI 10.1007/s00410-017-1412-7.

Castor, S.B., 2008. The Mountain Pass rare-earth carbonatite and associated ultrapotassic rocks, California. The Canadian Mineralogist, v. 46, p. 779–806.

Connelly, N.G., Damhus, T., Hartsborn, R.M., and Hutton, A.T., 2005. Nomenclature of Inorganic Chemistry. IUPAC Recommendations 2005. RSC Publishing. Cambridge UK: 377 p.

Cook, N.J., Ciobanu, C.L., O'Rielly, D., Wilson, R., Das, K., and Wade, B., 2013. Mineral chemistry of Rare Earth Element (REE) mineralization, Browns Ranges, Western Australia. Lithos, v. 172–173, p. 192–213.

Crispe, A.J., and Vandenberg, L.C., 2004. Northern Tanami: findings from reconnaissance mapping 2003. Annual Geoscience Exploration Seminar (AGES) Record of abstracts, Northern Territory Geological Survey Record 2004–001.

Cross, A., and Crispe, A., 2007. SHRIMP U–Pb analyses of detrital zircon: a window to understanding the Paleoproterozoic development of the Tanami Region, northern Australia. Mineralium Deposita, v. 42, p. 27–50.

Goodenough, K.M, Wall, F., and Merriman, D., 2017. The Rare Earth Elements: Demand, Global Resources, and Challenges for Resourcing Future Generations. Natural Resources Research. DOI: 10.1007/s11053-017-9336-5.

Goodenough, K.M., Schilling, J., Jonsson, E., Kalvig, P., Charles, N., Tuduri, J., Deady, E.A., Sadeghi, M., Schiellerup, H., Müller, A., Bertrand, G., Arvanitidis, N., Eliopoulos, D.G., Shaw, R.A., Thrane, K., and Keulen, N., 2016. Europe's rare earth element resource potential: An overview of REE metallogenetic provinces and their geodynamic setting. Ore Geology Reviews, v. 72, p. 838–856.

Gysi, A.P., and Williams-Jones, A.E., 2013. Hydrothermal mobilization of pegmatite-hosted REE and Zr at Strange Lake, Canada: A reaction path model. Geochimica et Cosmochimica Acta, v. 122, p. 324–352.

Gupta, C.K., and Krishnamurthy, N., 2005. Extractive metallurgy of rare Earths. CRC Press: Boca Raton.

Hatch, G.P., 2012. Dynamics in the global market for rare earths. Elements, v. 8, p. 341–346.

Hendrickx, M.A., Slater, K., Crispe, A.J., Dean, A.A., Vandenberg, L.C., and Smith, J.B., 2000. Paleoproterozoic stratigraphy of the Tanami Region: regional correlations realisation preliminary results. Darwin NT: Northern Territory Geological Survey Record, 71 pp.

Huston, D.L., Maas, R., Cross, A., Hussey, K.J., Mernagh, T.P., Fraser, G., and Champion, D.C., 2016. The Nolans Bore rareearth element-phosphorus-uranium mineral system: geology, origin and post depositional modifications. Mineralium Deposita, v. 51, p. 797–822.

Jaireth, S., Hoatson, D.M., and Miezitis, Y., 2014. Geological setting and resources of the major rare-earth-element deposits in Australia. Ore Geology Reviews, v. 62, p. 72–128.

Laznicka, P., 1999. Quantitative relationships among giant deposits of metals. Economic Geology, v. 94, p. 455–473.

Loges, A., Migdisov, A.A., Wagner, T., Williams-Jones, A.E., and Markl, G., 2013. An experimental study of the aqueous solubility and speciation of Y(III) fluoride at temperatures up to 250 °C. Geochimica et Cosmochimica Acta, v. 123, p. 403–415.

Long, K.R., Van Gosen, B.S., Foley, N.K., and Cordier, D., 2010. The principal rare earth elements deposits of the United States - a summary of domestic deposits and a global perspective. U.S. Geological Survey Scientific Investigations Report 2010–5220.

Lottermoser, B.G., 1990. Rare earth element mineralisation within the Mt. Weld carbonatite laterite, Western Australia. Lithos, v. 24, p. 151–167.

Mariano, A.N., and Mariano, J.A., 2012. Rare earth mining and exploration in North America. Elements, v. 8, p. 369–376.

McKinney, S.T., Cottle, J.M., and Lederer, G.W., 2015. Evaluating rare earth element (REE) mineralization mechanisms in Proterozoic gneiss, Music Valley, California. Geological Society of America Bulletin, v. 12, p. 1135–1152.

Migdisov, A.A., and Williams-Jones, A.E., 2014. Hydrothermal transport and deposition of the rare earth elements by fluorine bearing aqueous liquids. Mineralium Deposita, v. 49, p. 987–997.

Migdisov, A.A., Williams-Jones, A.E., and Wagner, T., 2009. An experimental study of the solubility and speciation of the Rare Earth Elements (III) in fluoride- and chloride-bearing aqueous solutions at temperatures up to 300°C. Geochimica et Cosmochimica Acta, v. 73, p. 7087–7109.

Migdisov, A.A., Williams-Jones, A.E., van Hinsberg, V., and Salvi, S., 2011. An experimental study of the solubility of baddeleyite (ZrO_2) in fluoride-bearing solutions at elevated temperature. Geochimica et Cosmochimica Acta, v. 75, p. 7426–7434.

Morin-Ka, S., Beardsmore, T.J., Hancock, E.A., Rasmussen, B., Dunkley, D., Muhling, J., Zi, J., Wilson, R., and Champion, J., 2016. Alteration and Age of the Browns Range Rare Earth Element Deposits. Western Australian Department of Mines and Petroleum.

Ni, Y., Hughes J.M., and Mariano A.N., 1995. Crystal chemistry of the monazite and xenotime structures. American Mineralogist, v. 80, p. 21–26.

O'Rielly, D., 2012. Mineralogy and Petrography of Rare Earth Element (REE) mineralisation, Browns Ranges, W.A. (Honours Dissertation). University of Adelaide. 83 p.

Page, R., Sun, S.S., Blake, D., Edgecombe, D., and Pearcey, D., 1995. Geochronology of an exposed late Archean basement terrane in the Granites–Tanami region. Australian Geological Survey Organisation Research Newsletter, v. 22, p. 21–22.

Rabiei, M., Chi, G., Normand, C., Davis, W.J., Fayek, M., and Blamey, N.J.F., 2017. Hydrothermal Rare Earth Element (Xenotime) Mineralization at Maw Zone, Athabasca Basin, Canada, and Its Relationship to Unconformity-Related Uranium Deposits. Economic Geology, v. 112, p. 1483–1507.

Richter, L., Diamond, L.W., Atanasova, P., Banks, D.A., and Gutzmer, J., 2018. Hydrothermal formation of heavy rare earth element (HREE)-xenotime deposits at 100 °C in a sedimentary basin. Geology, DOI: https://doi.org/10.1130/G39871.1.

Samson, I.M., Wood, S.A., and Finucane, K., 2004. Fluid Inclusion Characteristics and Genesis of the Fluorite-Parisite Mineralization in the Snowbird Deposit, Montana. Economic Geology, v. 99, p. 1727–1744.

Schoneveld, L., Spandler, C., and Hussey, K., 2015. Genesis of the Central Zone of the Nolans Bore rare earth element deposit, Northern Territory, Australia. Contributions to Mineralogy and Petrology, v. 170, p. 1–22.

Sheard, E.R., Williams-Jones, A.E., Heiligman, M., Pederson, C., and Trueman, D.L., 2012. Controls on the concentration of zirconium, niobium and the rare earth elements in the Thor Lake rare metal deposit, Northwest Territories, Canada. Economic Geology, v. 107, p. 81–104.

Smith, M., Moore, K., Kavecsanszki, D., Finch, A., Kynicky, J., and Wall, F., 2016. From mantle to critical zone: a review of large and giant sized deposits of the rare earth elements. Geoscience Frontiers, v. 7, p. 315–334.

Timofeev, A., Migdisov, A.A., and Williams-Jones, A.E., 2017. An experimental study of the solubility and speciation of tantalum in fluoride-bearing aqueous solutions at elevated temperature. Geochimica et Cosmochimica Acta, v. 197, p. 294–304.

Timofeev, A., Migdisov, A.A., and Williams-Jones, A.E., 2015. An experimental study of the solubility and speciation of niobium in fluoride-bearing aqueous solutions at elevated temperature. Geochimica et Cosmochimica Acta, v. 158, p. 103–111.

Vallini, D.A., Groves, D.I., McNaughton, N.J., and Fletcher, I.R., 2007. Uraniferous diagenetic xenotime in northern Australia and its relationship to unconformity-associated uranium mineralisation. Mineralium Deposita, v. 42, p. 51–64.

Wall, F., Niku-Paavola, V.N., Storey, C., Muller, A., and Jeffries, T., 2008. Xenotime-(Y) from carbonatite dykes at Lofdal, Nambia: Unusually low LREE:HREE ratio in carbonatite, and the first dating of xenotime overgrowths on zircon. The Canadian Mineralogist, v. 46, p. 861–877.

Walters, A., Lusty, P., Chetwyn, C., and Hill, A., 2010. Rare Earth Elements. Mineral Profile Series. British Geological Survey UK, 45 pp.

Weng, W., Jowitt, S.M., Mudd, G.M., and Haque, N., 2015. A Detailed Assessment of Global Rare Earth Element Resources: Opportunities and Challenges. Economic Geology, v. 110, p. 1925–1952.

Weng, Z.H., Jowitt, S.M., Mudd, G.M., and Hague, N., 2013. Assessing rare earth element mineral deposit types and links to environmental impacts: Transactions of the Institute of Mining and Metallurgy B. Applied Earth Science, v. 122, p. 83–96.

Xie, Y.L., Hou, Z.Q., Yin, S.P., Dominy, S.C., Tian, S.H., and Xu, W.Y., 2009. Continuous Carbonatitic Melt-Fluid Evolution for REE Mineralization System: Evidence from

Inclusions in the Maoniuping REE Deposit in the western Sichuan, China. Ore Geology Reviews, v. 36, p. 90–105.

Yang, X.Y., Sun, W.D., Zhang, Y.X., and Zheng, Y-Z., 2009. Geochemical constraints on the genesis of the Bayan Obo Fe-Nb-REE deposit in Inner Mongolia, China. Geochimica et Cosmochimica Acta, v. 73, p. 1417–1435.

Chapter 2

Provenance, tectonic setting and source of Archean metasedimentary rocks of the Browns Range Metamorphics, Tanami Region, Western Australia

Teimoor Nazari-Dehkordi[1*], Carl Spandler[1], Nicholas H.S. Oliver[1, 2], Jacqueline Chapman[3], Robin Wilson[3]

[1]Economic Geology Research Centre, James Cook University, Townsville, QLD 4811, Australia

[2]HCOVGlobal Consultants, PO Box 3533, Hermit Park, QLD 4812, Australia

[3]Northern Minerals, PO Box 669, West Perth, WA 6872, Australia

Published in *Australian Journal of Earth Sciences*
https://doi.org/10.1080/08120099.2017.1355844

Abstract

This study combines U–Pb age and Lu–Hf isotope data for magmatic and detrital zircons, with whole-rock geochemistry of the Browns Range Metamorphics (BRM), Western Australia. The BRM are medium- to coarse-grained metasandstones that consist of angular to sub-rounded detrital quartz and feldspars with minor granitic lithic fragments. The sequence has undergone partial to extensive quartz-muscovite alteration, and has been intruded by mafic/ultramafic, syenitic and pegmatitic intrusive rock units.

Uranium–Pb and Lu–Hf isotopic data on detrital zircons from the metasandstones and intruding granitic rocks yield a well-defined age of ca. 3.2 to ca. 3.0 Ga for all samples, with relatively radiogenic εHf values (εHf = –1.7 to 5.1) indicating derivation from Mesoarchean granite basement of juvenile origin. This is consistent with geochemical and petrological data that support deposition from a granitic source in a continental rift basin setting. The timing of sediment deposition is constrained between the ca. 3.0 Ga age of the source rocks and ca. 2.5 Ga age of the granitic intrusive bodies that cross-cut the metasedimentary rocks. The ca. 2.5 Ga zircons from the intrusive rocks have εHf model ages of ca. 3.4 to ca. 3.1 Ga, which is consistent with formation via partial melting of the BRM, or the Mesoarchean granite basement. Zircons of the Gardiner Sandstone that unconformably overlies the BRM return detrital ages of ca. 2.6 to ca. 1.8 Ga with no trace of ca. 3.1 Ga zircons, which discounts a significant contribution from the underlying BRM.

The Mesoarchean age and isotopic signatures of the BRM zircons are shared by some zircon records from the Pine Creek Orogen, and the Pilbara, Yilgarn and Gawler cratons. Collectively, these records indicate that juvenile Mesoarchean crust is a more significant component of Australian cratons than is currently recognised. This work also further demonstrates that detrital minerals in Paleoproterozoic/Archean sedimentary rocks are archives to study the early crustal record of Earth.

Keywords: U–Pb dating, Lu–Hf isotope, Mesoarchean, Browns Range Metamorphics, Western Australia, Tanami, zircon, arkose, North Australia Craton, HREE

Introduction

Archean cratons are of interest to understanding the formation and evolution of the earliest crust on Earth. The West Australian Craton, comprising Yilgarn and Pilbara cratons, has a well-established and extensively studied Archean rock record (e.g., Nebel-Jacobsen et al., 2010; Kemp et al., 2015). By contrast, the neighbouring North Australian Craton contains only rare and spatially disconnected exposures of Archean rocks. Metasedimentary rocks of the Browns Range Metamorphics (as per Blake et al., 2000), herein abbreviated as BRM, represent one of these rare Archean cratonic nuclei within the North Australian Craton. Although these metasedimentary rocks host several recently discovered heavy rare earth element (HREE) deposits (Cook et al., 2013), they have received little previous study due to their geographic isolation.

Detrital minerals from ancient sedimentary sequences can preserve isotopic and geochemical signatures of their primary source rock, despite concealment or destruction of the source rocks over geological time. This is particularly relevant for understanding the early Earth, as studies of Archean and Hadean detrital zircons from the Jack Hills meta-conglomerate of the Yilgarn Craton demonstrate (Kemp et al., 2010). Accordingly, analysis of the BRM provides important insights into the early geological history of the North Australian Craton, as well as informing on the possible source and genesis of the HREE mineralisation (Cook et al., 2013; Nazari-Dehkordi et al., 2016).

This paper combines bulk-rock geochemical and petrographic analysis, with U–Pb age and Lu–Hf isotope data for zircons from the BRM and the cross-cutting intrusive rocks. These data are used to evaluate the age and nature of the sediment source rock, the timing and tectonic setting of deposition, and post-depositional alteration and weathering (e.g., Cullers, 2000; Griffin et al., 2004; Thomas, 2011). We show that the BRM were sourced from juvenile Mesoarchean crust, and therefore provide new insights into a poorly understood period of evolution of the Northern Australian Craton.

Geological setting

The Browns Range Dome (BRD) is an east-west trending ovoid-shaped structure measuring ~60 km by ~30 km, situated in the northwest of the Tanami Region of the North Australian Craton (Fig. 2-1). Geological understanding of the BRD is lacking due to limited previous study, which in part is due to the remoteness of the area and difficulty of access. Interpretations of large-scale geological and geophysical surveys suggest that the core of the BRD is a 1-3 km thick, largely granitic body (herein labelled BRD granite; Fig. 2-1) that has been cut by numerous mainly east-west trending faults. Variable magnetic anomalies within this granitic unit were interpreted to represent multiple intrusions of varying composition (Hendrickx et al., 2000), although there have been few field studies to substantiate these interpretations. Enveloping the BRD granite and occupying the outer margins of the dome are Paleoproterozoic sedimentary rocks of the Pargee Sandstone and the Birrindudu Group to the east and north, a package of undifferentiated sedimentary rocks of unknown age to the south, and the metasedimentary rocks of the BRM to the west (Fig. 2-1).

Geochronological data for the Browns Range Dome is limited to U–Pb zircon dating from a sample of the BRD granite collected from the southern margin of the dome within the Northern Territory (Page et al., 1995; Cross and Crispe, 2007). These authors found zircon age populations of ca. 3.15 to 3.04 Ga, ca. 2.67 to 2.44 Ga and ca. 1.99 to 1.87 Ga. Cross and Crispe (2007) interpreted the youngest age to be the crystallisation age of the BRD granite, and the Archean-aged zircons to be inherited material from the basement. This has led to the conclusion that the BRD includes rock units of both Archean and Paleoproterozoic age. Nevertheless, the timing of deposition of the BRM has remained poorly resolved prior to the present study.

The metasedimentary rocks that occupy the Western Australian segment of the BRD (Fig. 2-1), are the focus of this paper. The BRM outcrop over an area of ~100 km^2 (Fig. 2-1) within Western Australia and consist mainly of metasedimentary rocks that experienced regional metamorphism, mostly of greenschist facies, but locally up to amphibolite grade. The metasedimentary rocks are mainly metasandstones occasionally containing interbedded medium- to coarse-grained conglomerates, and less common calc-silicate rocks and banded iron formations, although the limited field exposure and metamorphism preclude detailed stratigraphic descriptions of the sequence. The BRM have been cut by numerous granitic,

syenitic and pegmatitic intrusions measuring 10s to 100s of metres in dimension, and mafic-ultramafic intrusions (Blake et al., 1979; Page et al., 1995; Hendrickx et al., 2000). The occurrence of the mafic-ultramafic intrusions is inferred mainly from geophysics, but has been confirmed by limited exploration drilling. These rocks are dominated by a secondary alteration assemblage including tremolite, chlorite, ± sericite, ± titanite, which is consistent with metamorphism of mid- to upper-greenschist facies.

The BRM are unconformably overlain by a thick sequence of low-grade Paleoproterozoic marine sedimentary rocks with rare volcanic units (Fig. 2-1; Crispe et al., 2007; Bagas et al., 2008). These include the ca. 1864 Ma Dead Bullock Formation, and overlying turbiditic rocks of the Killi Killi Formation, both of which form the Tanami Group (Crispe et al., 2007). Crispe et al. (2007) infers that the Tanami Group is unconformably overlain by the coarse-grained sandstones and felsic volcanic rocks of the 1825 and 1815 Ma Ware Group, although the contact is not exposed. Both the Tanami Group and Ware Group were intruded by extensive granitic magmatism (Birthday, Frederick and Grimwade suites, indicated in Fig. 2-1B as "undifferentiated granites") spanning the period ca. 1825 to ca. 1790 Ma (Smith, 2001). This age range also corresponds to the ca. 1790 Ma gold mineralisation within the Tanami Region (Bagas et al., 2007). These granite suites have been suggested to be derived from melting of upper continental crust in a syn-collisional tectonic setting that resulted from collision between the Tanami Region to the north and the Arunta Orogen to the south (Bagas et al., 2010). The Mount Charles Formation (ca. 1800 Ma; Crispe et al., 2007), which consists of basalts and intercalated clastic sedimentary rocks, post-dates Ware Group sedimentation. All of these rock sequences are overlain by relatively flat-lying sedimentary rocks of the Pargee Sandstone and Birrindudu Group, probably deposited in the interval of 1.78 to 1.64 Ga (Crispe et al., 2007). The Birrindudu Group consists of three units including the basal Gardiner Sandstone, the fine-grained and calcareous Talbot Well Formation, and Coomarie Sandstone (Blake et al., 1975). The broadly domed and unconformable contact between the Gardiner Sandstone and the BRM is well exposed, and forms a prominent topographic feature at the western margin of the Dome.

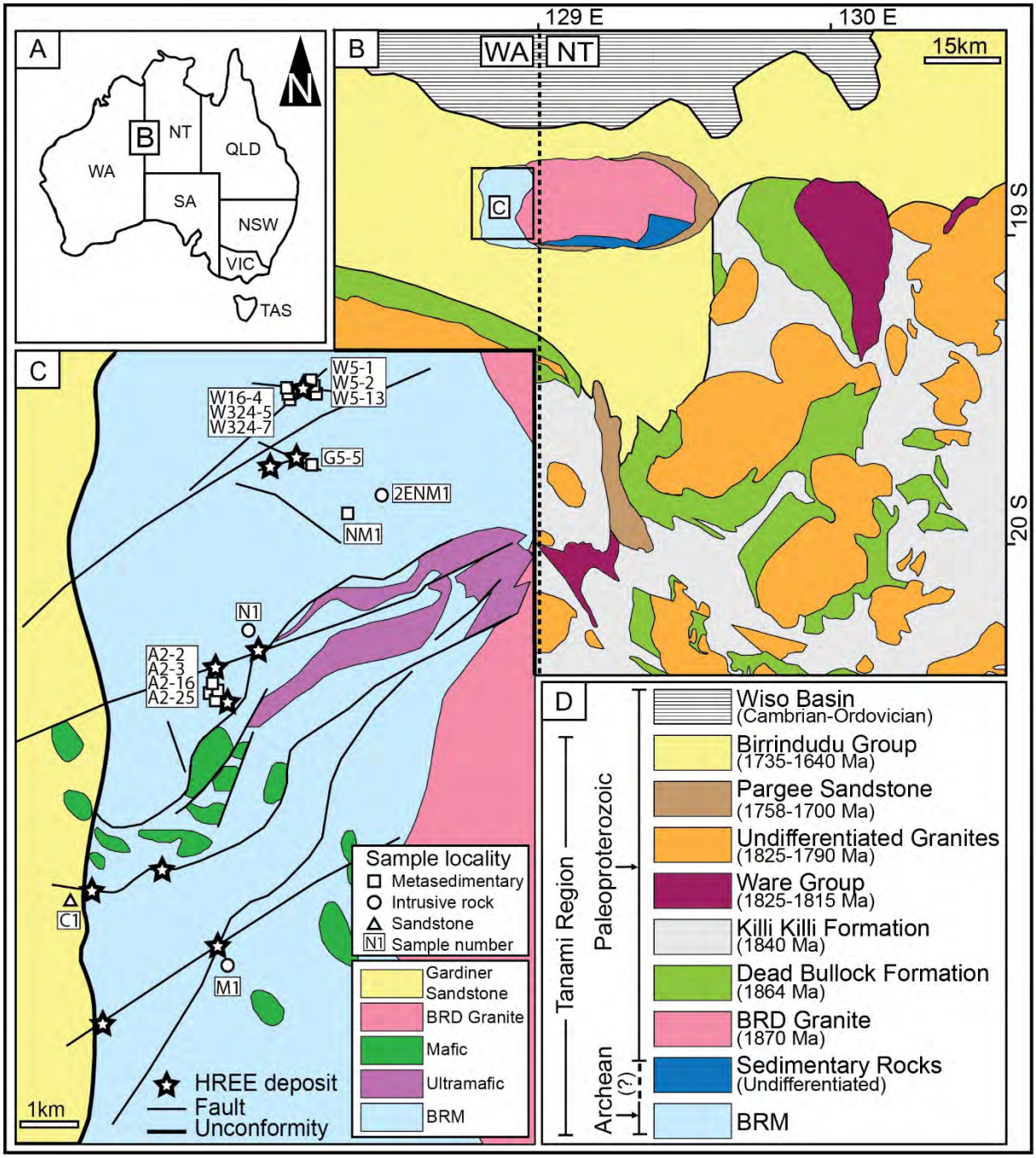

Fig. 2-1: Geological maps of the Tanami Region and Browns Range. (A) The location of the Tanami Region and the Browns Range Dome in Northern Australia; (B) simplified geological map of the Tanami Region (modified after Bagas et al., 2008); (C) simplified geological map of the western margin of the Browns Range Dome within Western Australia (after Hendrickx et al., 2000) showing the location of analysed samples; and (D) simplified stratigraphic column of the Tanami Region (after Crispe et al., 2007). Note that the undifferentiated granites shown in Fig. 2-1B have been divided into three suites including Birthday, Frederick and Grimwade suites. BRM, Browns Range Metamorphics; BRD, Browns Range Dome.

The BRM host a number of economically-significant HREE deposits (Cook et al., 2013). The largest of these deposits, the Wolverine deposit, contains xenotime and minor florencite mineralisation in hydrothermal lodes within massive arkosic metasedimentary rocks. Steeply dipping mineralisation is associated with silicification at major fault junctions, and occurs mostly as: (1) high grade, low tonnage lodes with large (>10 m long and 1 m wide) veins and chaotic breccias of massive xenotime (± quartz, ± hematite, ± sericite); and (2) low grade, probably higher tonnage disseminated mm-scale xenotime–quartz veins and crackle breccias in which xenotime grains occur in a number of morphological types (Nazari-Dehkordi et al., 2016). Cook et al. (2013) reports that xenotime hosted by the BRM is more enriched by 3-7% total REE than other occurrences in the world.

Sampling and analytical techniques

Sampling

The location of the samples analysed in this study is shown in Fig. 2-1C with details in Table 2-1. Sampling was focussed in the northern portion of the field area, although from field observations it appears that the general sedimentary characteristics of the metasedimentary rocks do not vary significantly throughout the district. To best avoid surface weathering, the majority of the samples were taken from core samples drilled in the vicinity of REE orebodies. The cores were carefully described for petrographic, structural and sedimentary features, as well as occurrence of cross-cutting intrusive rocks and veins. To evaluate the nature and intensity of the alteration associated with the mineralisation, the samples were taken both proximal to and distal from the mineralisation.

Twelve samples of BRM that are least affected by weathering and hydrothermal alteration were analysed for bulk rock geochemistry, and nine samples, including five BRM samples, three felsic intrusive rocks and one sample of the Gardiner Sandstone, were processed for zircon U–Pb dating and Lu–Hf isotope analysis. All zircon analysis was conducted at the Advanced Analytical Centre at James Cook University, Townsville.

Table 2-1: Sample locations

No.	Rock type	Drill core	Depth (m)	Easting	Northing	Analysis
A2-2	BRM	BRAD0002	46.9	492231.3	7909977	WR
A2-3	BRM	BRAD0002	51.3	492231.3	7909977	WR
A2-16	BRM	BRAD0002	138.2	492231.3	7909977	WR
A2-25	BRM	BRAD0002	187.5	492231.3	7909977	WR
W5-1	BRM	BRWT0332W5	441.2	493508.1	7915069	WR, Zircon U-Pb
W5-2	BRM	BRWT0332W5	487.6	493508.1	7915069	WR
W5-13	BRM	BRWT0332W5	550.7	493508.1	7915069	WR
W324-5	BRM	BRWT0324	409.5	493541.2	7914984	WR
W324-7	BRM	BRWT0324	441.6	493541.2	7914984	WR, Zircon U-Pb and Lu-Hf
NM1	BRM	Outcrop	Surface	494489	7912111	WR, Zircon U-Pb and Lu-Hf
W16-4	BRM	BRWD0016	103.5	493599.5	7914773	WR, Zircon U-Pb and Lu-Hf
G5-5	BRM	BRGD0005	98.1	493098.1	7913652	WR, Zircon U-Pb and Lu-Hf
2ENM1	Intrusive	Outcrop	Surface	496643	7912590	Zircon U-Pb and Lu-Hf
M1	Intrusive	Outcrop	Surface	493458	7903099	Zircon U-Pb and Lu-Hf
N1	Intrusive	Outcrop	Surface	492576	7910925	Zircon U-Pb and Lu-Hf
C1	Sedimentary	Outcrop	Surface	489642	7904606	Zircon U-Pb

WR: Whole-rock geochemistry

Analytical techniques

All of the collected samples were lightly brushed and washed in an ultrasonic bath to remove any contamination from drilling mud. Thin sections of representative samples were prepared for textural characterisation and mineralogical identification using petrographic and scanning electron microscopy (SEM) techniques. The modal composition of the samples was determined using the classic Gazzi-Dickinson point-counting method on a petrographic microscope (Dickinson, 1970).

Whole-rock geochemistry

Twelve samples of the least altered metasedimentary rocks with no trace of HREE mineralisation were analysed for major and trace element composition by Bureau Veritas Laboratories in Vancouver, Canada. Approximately 100 mg of finely milled powder of each sample was fused to glass using lithium metaborate/tetraborate flux. The fused discs were then digested in nitric acid and analysed for major elements by ICP-OES. A full suite of trace elements were analysed using the 1:1:1 Aqua Regia Ultratrace ICP-MS procedure, which utilises 1:1:1 $HCl:HNO_3:H_2O$ combination to achieve ultra-low detection limits. Sample preparation and analytical procedures are as outlined in Jarvis and Jarvis (1995) and Pearce et

al. (1999). Briefly, the procedure starts with the addition of 4 ml HF and 1 ml HNO_3 (SPA, ROMIL Cambridge) to 100 mg of powdered sample within a Teflon vial which is then sealed and left on a hot plate at 150 °C for 48 h. Followed by a two-step addition of 1 ml HNO_3 into the moist residue, the insoluble fluoride species convert into soluble nitrate species. Moreover, an internal standard combined with 2.5 ml HNO_3 are supplemented, following which the mixture is diluted to 50 ml, generating a final concentration of 20 ppb Re and Rh. The internal standard is, then, used to compensate for any analytical drift and matrix suppression effects. The relative analytical uncertainty on these data is <1% for elements that are substantially above their detection limits, including 0.005 wt.% for most major elements, ~4 ppm for transition metals and <1 ppm for most lithophile trace elements.

Uranium-Pb zircon dating

Nine samples, including five metasedimentary samples from the BRM, three felsic intrusive rocks and one sample of the Gardiner Sandstone, were processed for zircon dating. The samples were crushed and milled down to a <500 µm grain size, washed to remove the clay fraction and separated by combination of heavy liquid density separation and magnetic separation. All the zircon grains were handpicked and mounted in epoxy along with GJ-1, FC-1 and Temora-2 zircon standards. Epoxy mounts were polished and carbon-coated. Cathodoluminescence (CL) images of zircon grains were obtained by a JEOL-JSM5410LV scanning electron microprobe equipped with a Robinson CL detector at Advanced Analytical Centre (AAC) at James Cook University (JCU). Uranium-Pb dating of zircon was conducted by laser ablation ICP-MS using the setup described by Tucker et al. (2013). The setup couples a GeoLas pro 193 nm ArF laser ablation system with a Bruker (formally Varian) 820-MS ICP-MS. The ICP-MS was tuned to ensure approximately equal sensitivity of U, Th and Pb to minimize isotope fractionation due to matrix effect. Analytes collected were ^{29}Si, ^{90}Zr, ^{202}Hg, ^{204}Pb, ^{206}Pb, ^{207}Pb, ^{208}Pb, ^{232}Th, ^{235}U and ^{238}U. For quantification of U and Th concentration in zircon samples, NIST-SRM-612 reference glass was analysed at the beginning, middle and end of every analytical session, with ^{29}Si used as the internal standard assuming perfect zircon stoichiometry. Zircon analysis was carried out with a beam diameter of 32 µm and beam energy density on the sample of 6 J/cm^2. Selection of analytical sample spots was guided by CL images. All data reduction was carried out using the GLITTER software (Van Achterbergh et al., 2001). All time-resolved single isotope signals from standards and samples were filtered for signal spikes or perturbations related to inclusions and fractures. Subsequently, the most

stable and representative ratios were selected taking into account possible mixing of different age domains and zoning. Zircon standard GJ-1 was used as the primary reference standard (Jackson et al., 2004). Secondary zircon standards FC-1 and Temora-2 returned ages of 1098 ± 11 Ma, (MSWD: 1.01) and 416 ± 7 Ma, (MSWD: 1.0), which compare well with the published values of 1111 Ma for FC-1 (Orihashi et al., 2008) and 416.8 Ma for Temora-2 (Black et al., 2004). A conservative 20 % discordance threshold was used for the populations containing more than two concordant or near concordant ages, as the cut-off limit. For the populations with less than two concordant or near concordant ages, the upper intercept age of the entire array of Pb loss was considered.

Zircon Hf isotopic analyses

In situ Hf isotope analyses of zircons were conducted at the Advanced Analytical Centre at James Cook University, using a GeoLas 193-nm ArF Excimer laser ablation system connected to a Thermo-Scientific Neptune multicollector ICP-MS, following the set-up outlined in Naeraa et al. (2012) and Kemp et al. (2009). Most analyses were obtained using a beam diameter of 32 μm and a 5 Hz repetition rate. The isotope ratios were derived from a 60s ablation period, comprising 60 cycles of 1s integration time. Data were normalised to $^{179}Hf/^{177}Hf = 0.7325$, using an exponential correction for mass bias. Interference of ^{176}Lu on ^{176}Hf is corrected using the Hf mass bias factor and by measuring the intensity of the interference-free ^{175}Lu isotope and using $^{176}Lu/^{175}Lu = 0.02669$ (De Bievre and Taylor, 1993; Griffin et al., 2004) to calculate $^{176}Lu/^{177}Hf$. The accuracy and external reproducibility were verified by repeated analyses of the standard zircons FC-1 and Mud Tank Zircon, which yielded $^{176}Hf/^{177}Hf$ ratios of 0.282159 ± 10 (2σ) (n = 19) and 0.282505 ± 9 (2σ) (n = 26), respectively. These ratios are in good agreement with published data of 0.282174 ± 12 (2σ) (FC-1) and 0.282499 ± 18 (2σ) (Mud Tank Zircon). The measured $^{176}Lu/^{177}Hf$ ratios of the zircons were used to calculate initial $^{176}Hf/^{177}Hf$ ratios. These age corrections are very small, and the typical uncertainty on a single analysis of $^{176}Lu/^{177}Hf$ (+1%) contributes an uncertainty of <0.05 εHf units. $^{176}Hf/^{177}Hf$ initial values were calculated using the ^{176}Lu decay constant of Soderlund et al. (2004). DM ($^{176}Lu/^{177}Hf = 0.0384$, $^{176}Hf/^{177}Hf = 0.28325$; Griffin et al., 2004) parameters were used for model age calculations. CHUR isotopic ratios of $^{176}Lu/^{177}Hf = 0.0336$ and $^{176}Hf/^{177}Hf = 0.282785$ were used (Bouvier et al., 2008).

Petrography

Metasedimentary rocks of the BRM

The BRM are mainly composed of light-coloured weakly to strongly foliated metasedimentary rocks (Fig. 2-2A) with fine hematite-stained reddish interlayers (Fig. 2-2B). The metasedimentary rocks are mainly coarse-grained (>1.5 mm grains) with intermittent fine-grained intervals (usually <0.5 mm grains, Fig. 2-2C) and local conglomerate layers (Fig. 2-2D). The coarse-grained samples tend to be mineralogically and texturally immature to sub-mature, being composed primarily of angular to sub-angular monocrystalline and polycrystalline detrital quartz (40–80 vol%) and angular alkali feldspar (20–60 vol%; mostly orthoclase) grains, with accessory zircon and rutile. The finer grained units have a similar mineralogy and grain morphology to the coarse samples, but tend to be dominated by monocrystalline quartz. The samples are deficient in Ca–Fe–Mg phases, such as amphibole, chlorite or epidote.

Lithic fragments that comprise a minor (<10 vol%) component of some samples (Fig. 2-2E) tend to be rounded to sub-rounded granitic clasts that range from a few mm to several cm in size. These granitic clasts are composed mainly of interlocking quartz and alkali feldspar, and also contain rare small (<50 μm) grains of fractured zircon. No sedimentary, metamorphic and volcanic fragments were observed. Isotopic analysis of zircons from the granite clasts was not attempted here, due to the small size of the clasts (Fig. 2-2E) and their zircons.

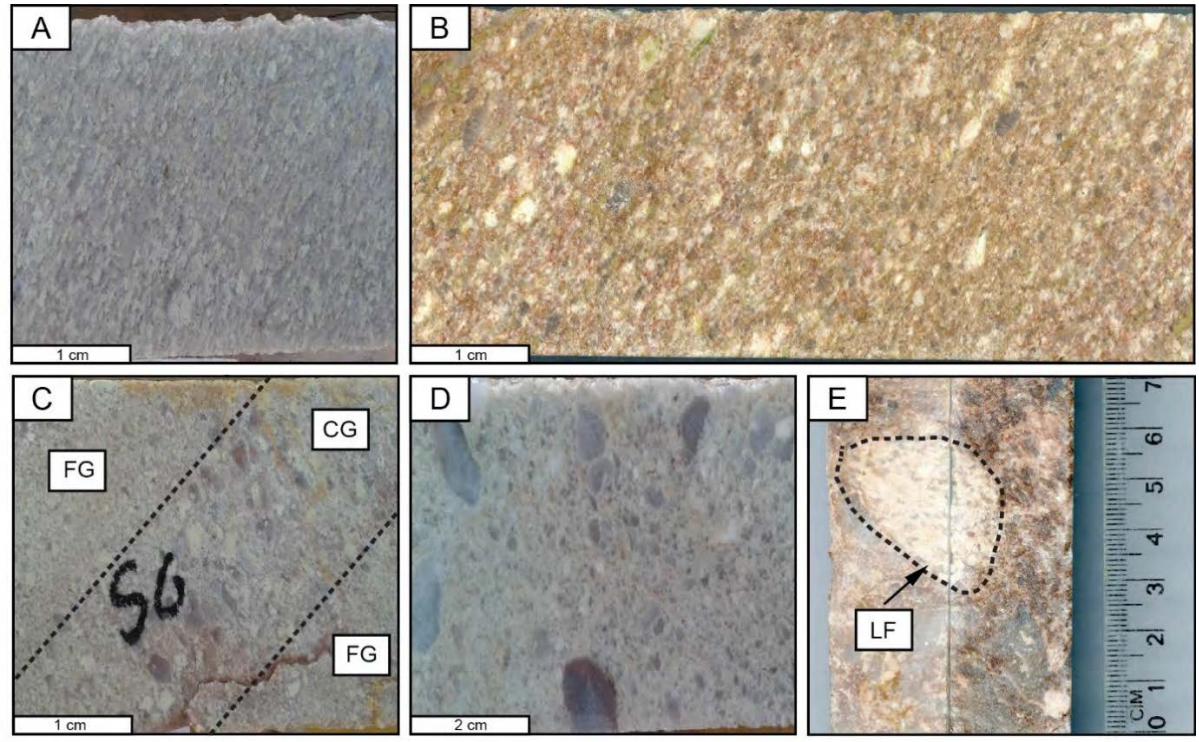

Fig. 2-2: Drill core photographs of the BRM. (A) White metasandstone displaying well-developed foliation; (B) foliated red metasandstone containing detrital quartz and feldspar (white) partially replaced by clay minerals and sericite (green); (C) medium-grained metasandstone with coarse-grained interlayers (black pen markings); (D) conglomerate, and; (E) granitic lithic fragment within arkosic metasediment. CG, coarse-grained; FG, fine-grained; LF, lithic fragment.

Occasional thin (~30 cm thickness) and discontinuous conglomeritic units occur throughout the sequence. The conglomerates are poorly sorted and are predominantly composed of angular to sub-angular pebbles of quartz and granite clasts (~5 cm in size), which are supported by a matrix of fine- to coarse-grained metasandstone. These granite clasts have a similar texture and mineralogy to the lithic fragments. The conglomerates constitute a minor lithofacies, and are not further discussed here.

Considering the lithological and mineralogical variations observed, the suggested average (sedimentary) modal composition of the BRM is 65 vol% quartz, 30 vol% feldspar and 5 vol% lithic fragments, which is consistent with a classification of feldspathoquartzose arkose to sub-arkose (Pettijohn, 1975; Fig. 2-3).

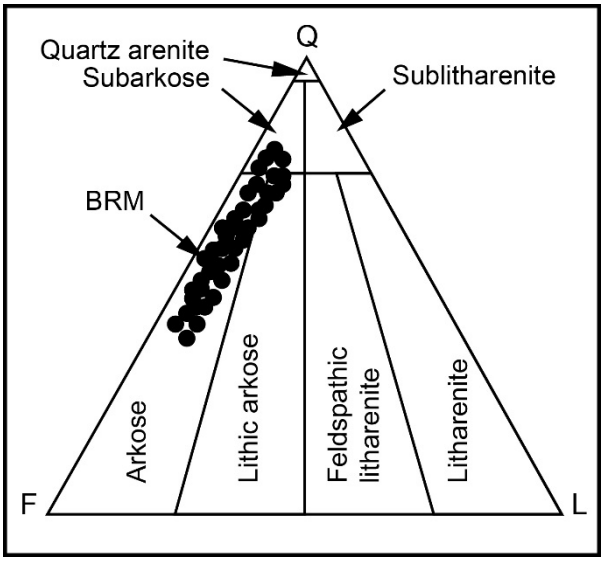

Fig. 2-3: Quartz–Feldspar–Lithic (QFL) ternary diagram for the BRM (after Pettijohn, 1975).

Secondary alteration minerals include clays (illite-sericite and minor kaolinite), muscovite, and occasionally albite, hematite, and pyrite. The clay and muscovite are observed to replace alkali feldspar (Figs. 2-4A-B); this alteration style is pervasive throughout the region, but tends to be most intense in close proximity to zones of HREE mineralisation. In addition, trace quantities of authigenic florencite [$REEAl_3(PO_4)_2(OH)_6$] were identified as clusters of tiny (<5 µm) grains enclosed within the clay minerals (Fig. 2-4C) in some samples. The florencite tends to form cubic shaped grains with a skeletal texture in which a narrow rim of the original grain remains (Fig. 2-4D). The nature of this alteration is partly due to weathering (e.g., clay formation), and partly due to hydrothermal alteration related to HREE mineralisation (quartz-muscovite alteration).

The mineral assemblage of the metasedimentary rocks is stable over a wide range of pressure and temperature conditions, and is not a good indicator of the metamorphic grade. However, the well-developed schistose foliation combined with tangential, concavo convex and sutured contacts between the grains (Fig. 2-4E) and deformation features observed in the grains (e.g., undulose extinction in quartz; Fig. 2-4F) are interpreted to have formed during greenschist-facies metamorphism (Harwood and Miller, 1990). This metamorphism is tentatively correlated to the Tanami Event that caused a regional greenschist-facies metamorphism (ca. 1830 Ma; Crispe et al., 2007).

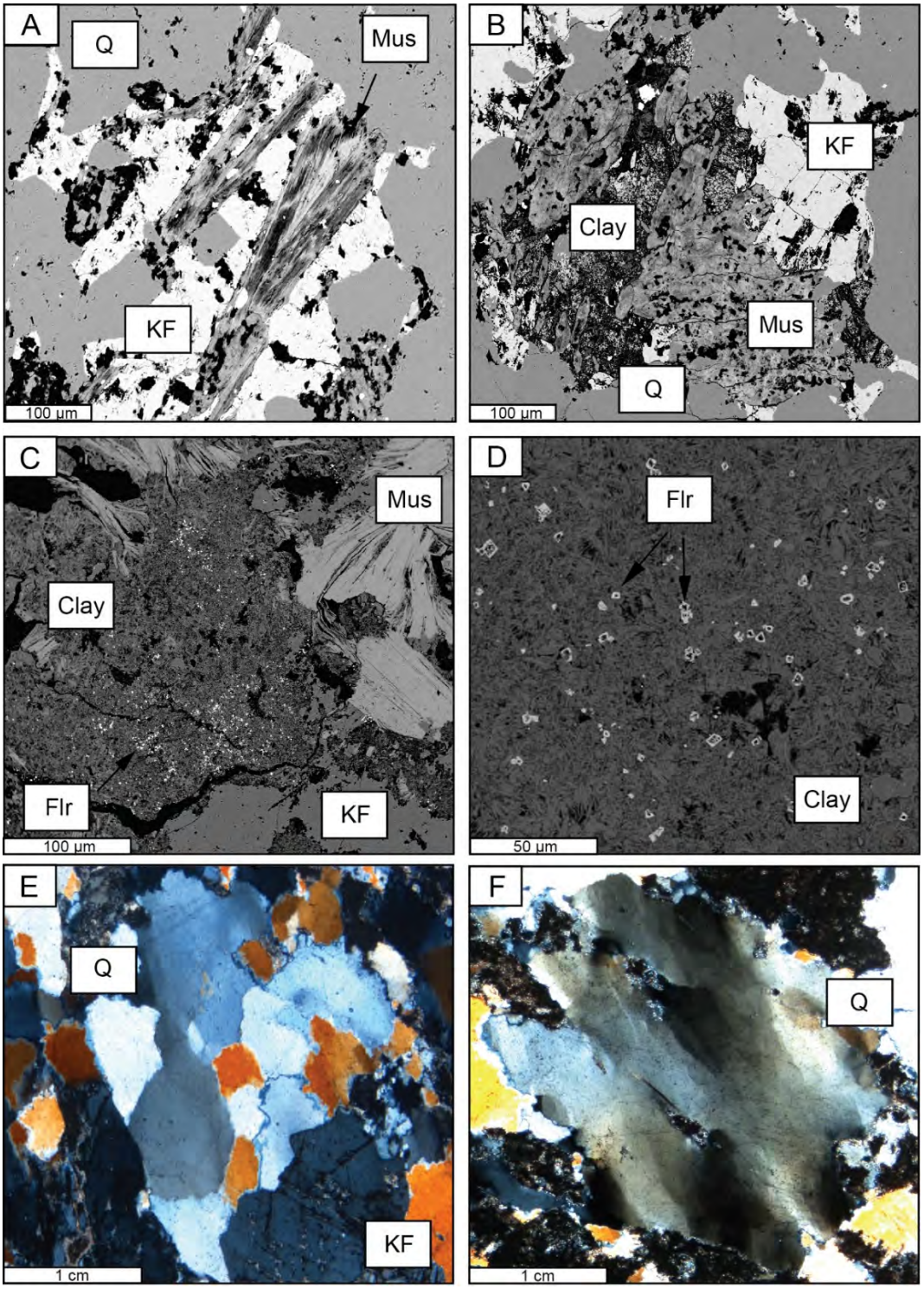

Fig. 2-4: Petrography of the BRM. Back-scattered electron (A–D) and cross-polarised transmitted-light microscopic (E–F) images of samples of the BRM. (A) Alkali feldspar partly replaced by muscovite; (B) alkali feldspar altered to clay and muscovite; (C) fine authigenic florencite enclosed in clay; (D) fine skeletal florencite within clay; (E) sutured contacts between quartz grains; and (F) undulose extinction in quartz grain. Mus = muscovite; KF = alkali feldspar; Q = quartz; Flr = florencite.

Intrusive rocks cutting the BRM

Intrusive rocks cutting the BRM are variable in dimension, ranging from a few centimetres in thickness as observed in the drill core, to large exposure measuring 100s of metres across. These rocks are mainly equigranular weakly-foliated granite, syenite and pegmatite bodies. The samples analysed here are syenitic with a dominant mineral assemblage of quartz, alkali feldspar (microcline and orthoclase), albitic plagioclase, muscovite, minor pyroxene (augite) and/or amphibole (actinolite), and accessory zircon.

Gardiner Sandstone of the Birrindudu Group

The Gardiner Sandstone unconformably overlies the BRM, and is characterised by medium-grained sub-lithic to lithic arenite and quartz arenite, with subordinate shale and siltstone units. A thin conglomerate unit is commonly found at the base of the sequence (Blake et al., 1979). The sample analysed here is a red, moderately well-sorted sandstone that was collected from a massive outcrop in the southwest of the field area near the unconformity with the underlying BRM (Fig. 2-1). This sample largely consists of fine- to medium-grained sub-angular to sub-rounded quartz grains and minor sedimentary and metasedimentary lithic fragments.

Results

Major and trace element geochemistry

The major and trace element compositions of unmineralised BRM samples are given in Table 2-2. The metasedimentary rocks are rich in SiO_2 (72–94 wt%), have variable Al_2O_3 (4.1–19.6 wt%) and K_2O (1.3–7.5 wt%) and have low content of MgO (0.05–0.77 wt%), CaO (<0.07 wt%), Fe_2O_3 (<1.4 wt%), Na_2O (<0.21 wt%) and TiO_2 (<0.22 wt%). Therefore, the metasedimentary rocks are characterised by very high K_2O/Na_2O and Al_2O_3/TiO_2. Most major elements are positively correlated with Al_2O_3 and negatively correlated with SiO_2 (Fig. 2-5). The LOI (0.7–3 wt%) is positively correlated to Al_2O_3, but shows no trend against K_2O/N_2O and Al_2O_3/TiO_2.

Table 2-2: Major (wt.%) and trace element (ppm) concentrations of the BRM

	A2-2	A2-3	A2-16	A2-25	W5-1	W5-2	W5-13	W324-5	W324-7	NM1	W16-4	G5-5
SiO_2	88	83	86	88	88	91	87	94	90	72	77	78
Al_2O_3	8.5	11.5	7.4	6	8.2	5.5	7.1	4.1	6.7	19.6	16.6	13.6
TiO_2	0.06	0.16	0.15	0.04	0.10	0.07	0.06	0.06	0.06	0.22	0.11	0.15
Fe_2O_3	0.7	0.8	0.4	1.4	0.9	0.8	0.5	0.5	0.5	1.4	0.8	0.3
MnO	0.02	0.02	0.02	0.02	0.02	0.02	0.02	0.02	0.02	0.02	0.02	0.02
MgO	0.40	0.77	0.05	0.08	0.37	0.40	0.19	0.25	0.26	0.34	0.31	0.26
CaO	0.02	0.02	0.01	0.03	0.02	0.03	0.02	0.02	0.02	0.07	0.04	0.05
Na_2O	0.02	0.02	0.15	0.10	0.04	0.02	0.09	0.01	0.01	0.04	0.11	0.21
K_2O	2.2	3.8	5.9	4.3	2.6	1.7	4.4	1.3	2.1	5.7	4.9	7.5
P_2O_5	0.02	0.04	0.04	0.02	0.02	0.05	0.03	0.04	0.02	0.12	0.08	0.10
LOI	2.2	2.1	0.7	1	1.7	1.4	1	0.9	1.3	3.0	2.6	1.5
K_2O/Na_2O	112	189	39	43	66	86	49	127	207	143	44	36
Al_2O_3/TiO_2	142	72	49	150	82	79	118	68	112	89	151	91
CIA	0.4	0.5	0.9	1	0.5	0.5	0.7	0.5	0.4	0.4	0.4	0.6
ICV	77	73	53	55	73	74	59	74	75	75	75	61
Ba	21	61	465	655	84	645	459	37	25	158	78	855
Sc	1.0	2.0	2.0	0.5	2.0	5.0	0.5	2.0	1.0	5.0	1.5	3.0
Cs	1.5	1.9	0.8	1.2	1.3	0.5	0.9	0.4	0.3	2.5	2.2	1.8
Ga	9.7	17.1	3.7	3.3	9.7	7.1	6.1	5.4	7.1	22.6	20	19
Hf	2.7	3.6	2.4	2.2	2.6	1.9	2.5	1.4	2.6	5.2	6.2	5.5
Nb	1.9	5.4	2.6	1.8	3.3	2.3	1.7	1.7	2.0	6.1	5.2	4.9
Rb	56	102	143	109	69	27	95	24	27	170	176	160
Sr	17	87	61	70	28	145	53	54	55	175	147	197
Ta	0.3	0.5	0.3	0.3	0.4	0.3	0.2	0.2	0.2	1.0	0.5	0.6
Th	25	41	24	19	25	22	25	12	27	103	87	47
U	2.1	2.1	2.2	2.5	1.3	2.0	0.7	1.6	1.0	1.0	1.8	4.5
V	14	19	6.0	6.0	9.0	16	6.0	13	6.0	20	17	14
Mo	0.08	0.03	0.06	0.07	0.06	0.07	0.08	0.09	0.05	1.6	5.7	5.4
Cu	1.6	1.2	1.1	5.5	0.6	139	0.8	18.5	0.5	15.6	5.0	20.5
Pb	0.8	1.2	1.5	3.2	1.3	1.3	1.3	0.9	1.0	42	6.5	40
Zn	2.4	2.0	0.9	3.0	1.0	0.8	0.4	0.5	0.4	13.4	7.6	13
Ni	2.7	1.7	0.7	0.9	0.8	2.9	1.9	2.6	0.6	3.2	2.9	4.5
Co	2.0	0.6	0.3	0.8	0.3	1.5	1.2	3.1	0.2	5.7	5.8	3.1
Mn	25	13	38	60	26	21	28	28	23	34	25	31
As	0.1	1.0	3.2	1.1	0.4	6.4	2.3	2.5	1.3	9.5	10	9.6
Cr	2.4	2.6	2.5	5.7	2.6	2.0	2.0	2.8	2.5	5.6	3.7	2.8
Li	0.4	0.2	0.3	0.2	0.6	0.3	0.1	0.3	0.2	0.2	0.3	0.4
F	343	202	46	50	129	174	87	122	126	101	95	125
Zr	93	123	85	73	92	81	82	40	84	151	180	170
Y	15	23.3	10.3	8.4	12	6.8	17.3	20.1	5.4	3.11	14.1	16.03
La	27.3	85.0	32.2	36.2	25.3	42.8	29.8	51.9	32.8	70.1	51.4	51.4
Ce	47.9	152.1	55.0	61.0	42.9	81.8	50.3	103	58.8	130.1	107.7	103.7
Pr	4.33	15.9	5.51	6.61	4.03	8.41	4.77	10.7	6.41	12.8	9.87	9.88
Nd	14.1	57.7	18.9	21.9	12.4	30.6	15.9	35.1	24.6	45.5	33.1	34.6
Sm	2.50	8.96	2.78	2.88	2.39	4.44	2.61	5.37	3.44	5.59	4.81	5.58
Eu	0.34	0.62	0.30	0.25	0.24	0.30	0.42	0.43	0.25	0.28	0.38	0.37
Gd	2.42	4.00	1.91	1.90	2.02	1.60	2.86	3.12	1.32	1.55	2.26	2.62
Tb	0.38	0.63	0.30	0.26	0.34	0.21	0.49	0.53	0.16	0.11	0.36	0.43
Dy	2.29	3.65	1.50	1.20	1.80	1.00	2.61	3.15	0.88	0.50	1.90	2.41
Ho	0.50	0.77	0.35	0.29	0.40	0.24	0.59	0.67	0.19	0.11	0.48	0.54
Er	1.52	2.15	1.07	0.87	1.10	0.75	1.75	2.01	0.59	0.33	1.41	1.61
Tm	0.24	0.30	0.17	0.15	0.17	0.13	0.27	0.29	0.11	0.07	0.20	0.25
Yb	1.45	2.08	1.16	1.06	1.17	1.00	1.69	1.90	0.90	0.50	1.30	1.56
Lu	0.22	0.31	0.17	0.15	0.17	0.14	0.25	0.28	0.13	0.06	0.19	0.23
$(Gd/Yb)_N$	1.3	1.6	1.3	1.4	1.4	1.3	1.4	1.3	1.2	2.5	1.4	1.4
$(La/Sm)_N$	6.9	6	7.3	7.9	6.6	6	7.2	6.1	6	7.9	6.7	5.8

Major elements are normalised to 100% on a LOI-free basis. CIA: Chemical Index of Alteration = 100[mol. $Al_2O_3/(Al_2O_3+CaO^*+Na_2O+K_2O]$ where CaO* is the silicate fraction of CaO (Nesbitt and Young, 1982). ICV: Index of Compositional Variability = [mol. $(CaO+K_2O+Na_2O+Fe_2O_3+MgO+MnO+TiO_2)/Al_2O_3$] (Cox et al., 1995).

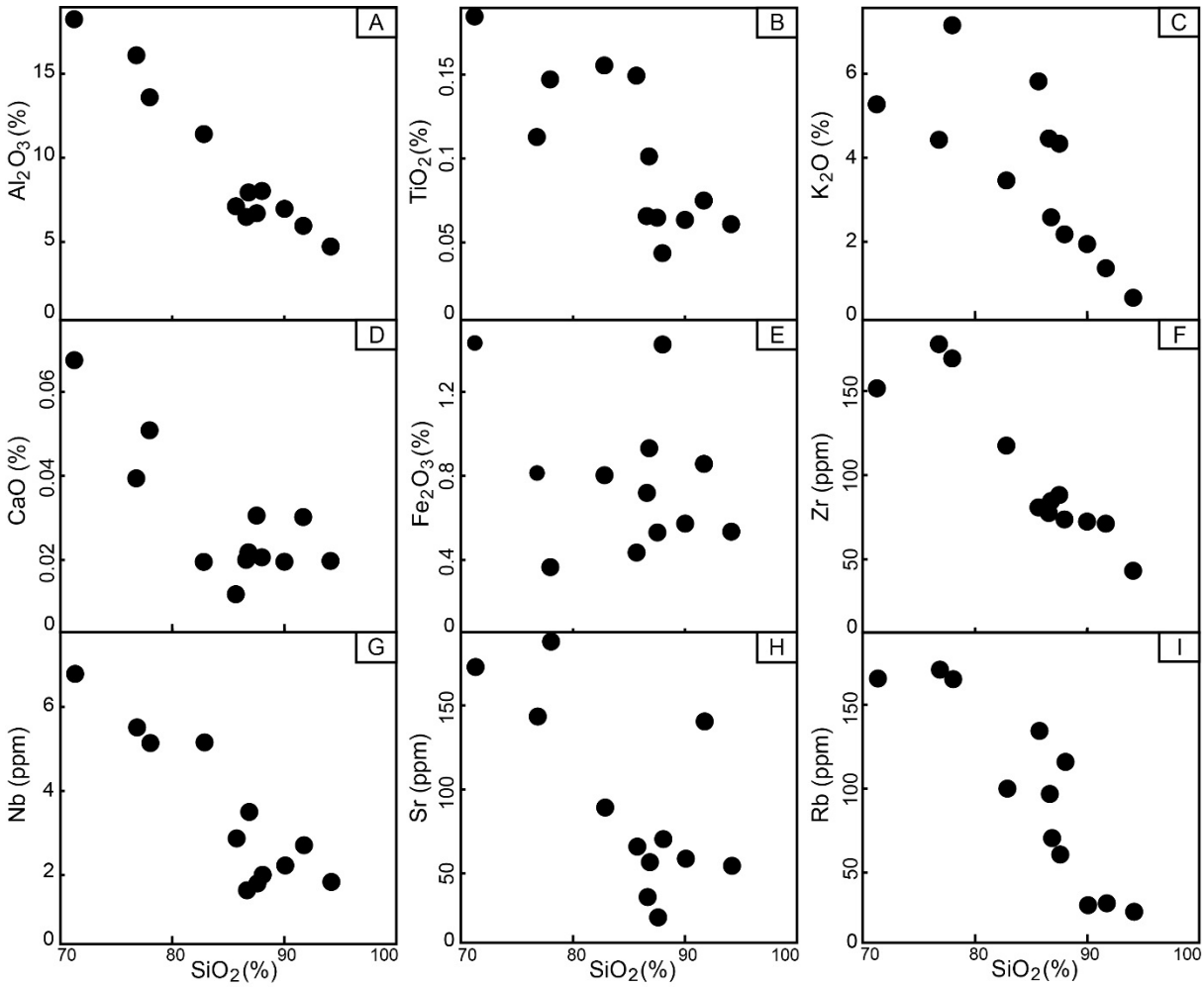

Fig. 2-5: Scatterplots of selected major and trace elements against SiO_2 (wt%) for the BRM.

Most trace elements are negatively correlated with SiO_2 (Fig. 2-5), indicating a degree of elemental dilution with increasing quartz content. Rubidium and Ba positively correlate to K_2O, whereas the concentrations of the transition elements (e.g., Cr, Co, Ni, V) are low in all samples. Chondrite-normalised REE patterns have relative enrichment in LREE and variable depletions in HREE (Fig. 2-6) that are broadly comparable to PAAS (Taylor and McLennan, 1985). The samples have strong negative europium anomalies with Eu/Eu* ranging from 0.32 to 0.46. The HREE vary by approximately an order of magnitude and extend to very low concentrations, which may be related to the HREE mineralisation hosted by the BRM.

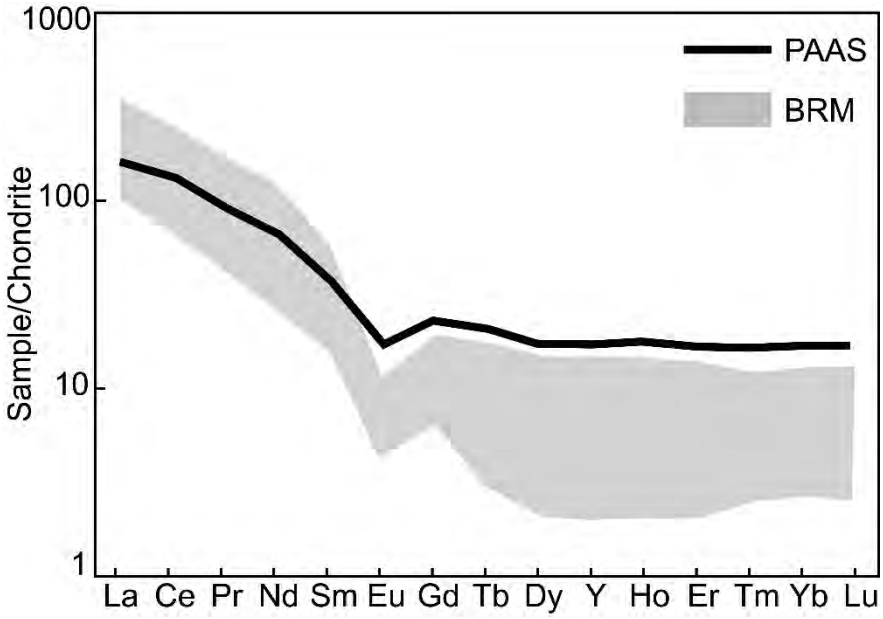

Fig. 2-6: Chondrite-normalised REE patterns for samples of the BRM compared to PAAS (post-Archean Australian shale). Data for chondrite and PAAS are from McDonough and Sun (1995) and Taylor and McLennan (1985), respectively.

Zircon geochronology

All U–Pb isotope data and calculated ages are presented in the Appendix 2-1.

Detrital zircons of the Browns Range Metamorphics

Zircon grains recovered from five arkosic metasedimentary samples (NM1, W5-1, W324-7, W16-4, G5-5) that all share similar petrographical features. The zircons are generally euhedral to subhedral and range from 50 to 200 µm in length with length/width ratios of about 1:1 to 1:3. In cathodoluminescence (CL) images, most grains exhibit well-defined concentric oscillatory zoning (Fig. 2-7A) with some grains showing dark internal zoning (Fig. 2-7B). Several zircon grains have narrow bright or dark discontinuous rims (typically <10 µm) that truncate internal zones (Figs. 2-7C-D). The samples also contain highly fractured, CL dark metamict grains that were not used for subsequent analysis. Instead, inclusion- and fracture-free zircon domains were targeted for U-Pb dating. Most of the zircon analyses produced discordant ages; these were characterised by relatively high Th and Th/U (0.8 to 3.8) compared to those of concordant or near concordant ages (Th/U = 0.4 to 1.5) (Fig. 2-8). Nonetheless, the

upper intercept ages obtained from all samples fall within the same broad range. However, due to the rarity of concordant analyses of similar age combined with a poorly-defined concordia trend, these upper-intercept ages tend to have relatively large MSWD values.

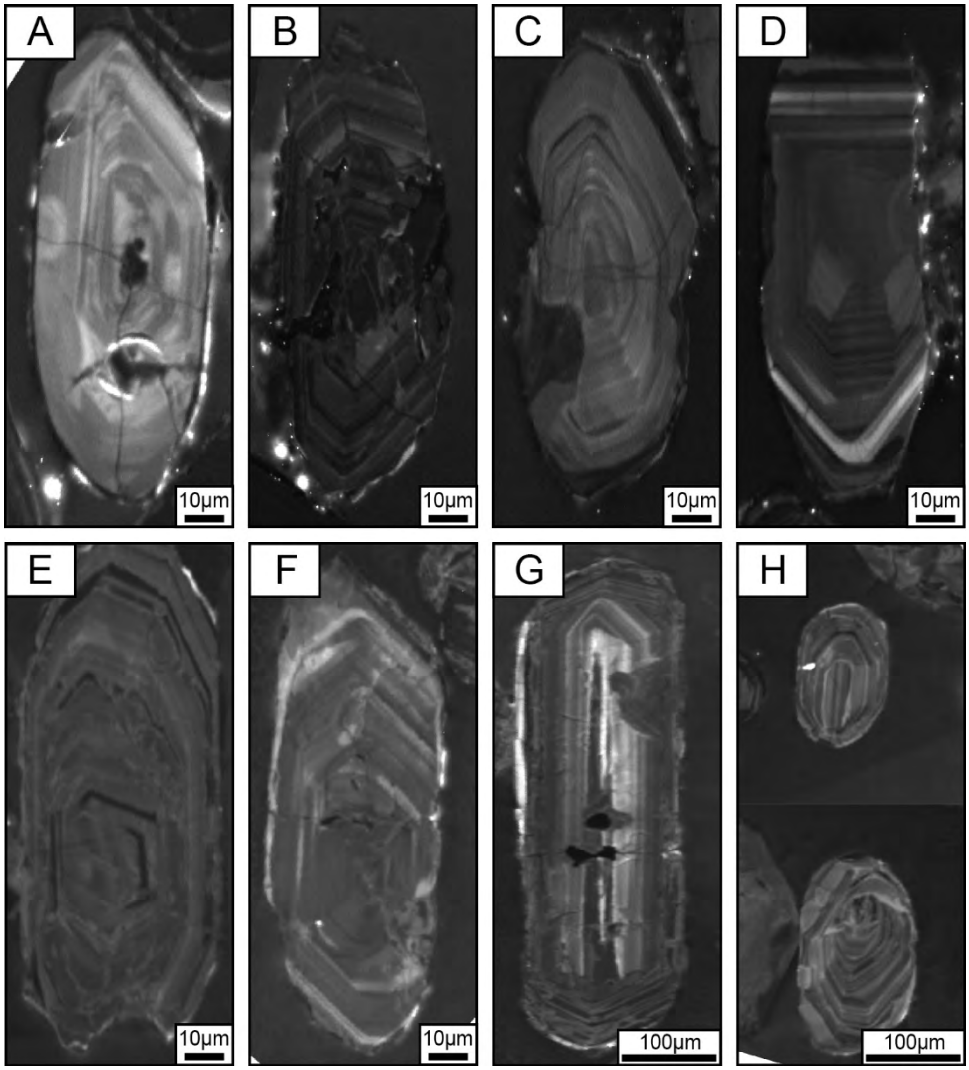

Fig. 2-7: Cathodoluminescence images of the zircons from samples of the BRM (A–B), intrusive rocks (E–G), and the Gardiner Sandstone (H). (A) Zircon with bright oscillatory zoning; (B) zircon with dark oscillatory zoning; (C) zircon with an oscillatory zoned core surrounded by narrow dark rim; (D) zircon with an oscillatory zoned core with bright rim; (E, F) zircon grains with bright oscillatory zoning; (G) elongate zircon grain with oscillatory zoning; and (H) rounded zircons with bright oscillatory zoning. Note that the intrusive rocks contain zircons of two age populations including ca. 3.2 to ca. 3.0 Ga zircons (E, F), which are of similar size to the ca. 3.2 to ca. 3.0 Ga detrital zircons recovered from the metasedimentary rocks (A–D), and the ca. 2.5 Ga zircons (G), which are comparatively elongate.

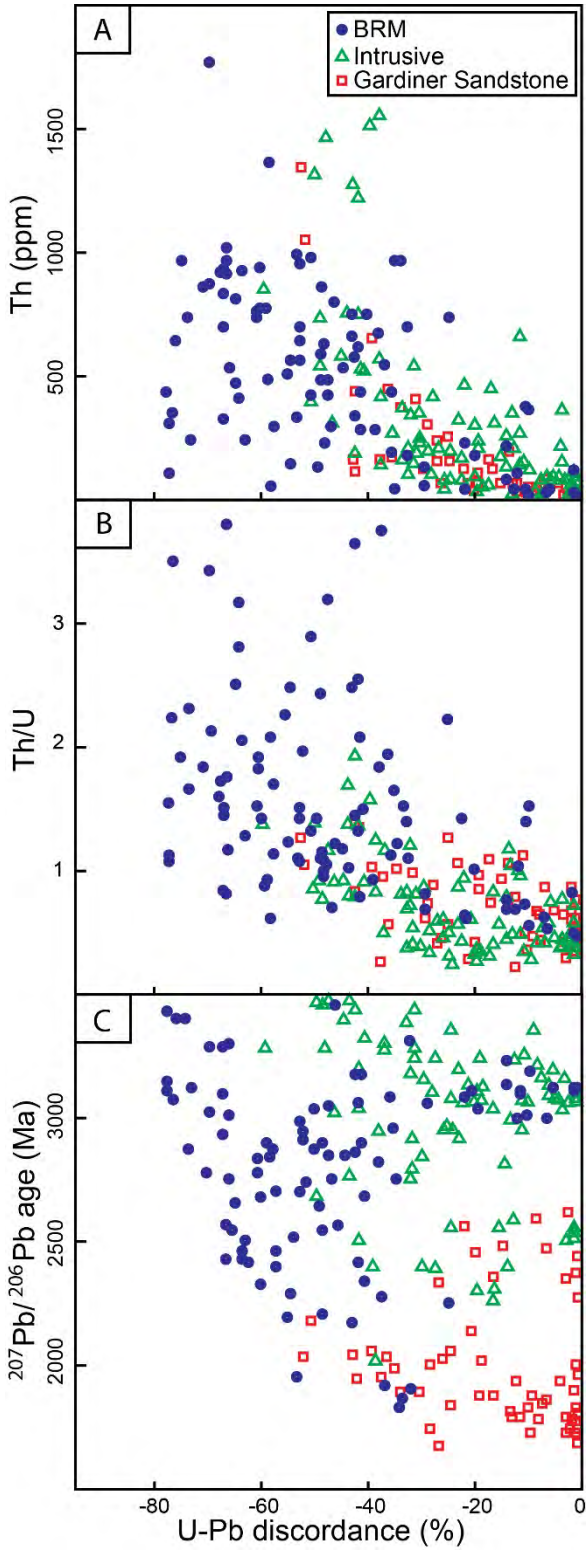

Fig. 2-8: Uranium–Pb discordance versus (A) Th, (B) Th/U ratio, and (C) $^{207}Pb/^{206}Pb$ age (Ma) for the zircon grains from the BRM, intrusive rocks and the Gardiner Sandstone. Note the broad increase of Th content and Th/U ratio with discordance for all samples. See Appendix 2-1 for discordance calculation methods.

Zircon grains of concordant and near concordant ages from sample NM1 define a single coherent upper intercept age of 3123 ± 10 Ma (MSWD = 0.9; Fig. 2-9A). The datasets for samples W5-1, W324-7, W16-4, and G5-5 yielded poorly constrained upper intercept ages of 3090 ± 10 Ma (MSWD = 3.1), 3146 ± 16 Ma (MSWD = 3.7), 3026 ± 11 Ma (MSWD = 3.3), and 3061 ± 10 Ma (MSWD = 4.4), respectively (Figs. 2-9B-E). These ages are also consistent with most of the calculated $^{207}Pb/^{206}Pb$ ages (Fig. 2-8; see Appendix 2-1). Collectively, the detrital zircons from all samples returned ages within a relatively restricted range of ca. 3.2 to ca. 3.0 Ga. The lower intercept ages calculated for the metasedimentary rocks vary from ca. 450 to ca. 40 Ma.

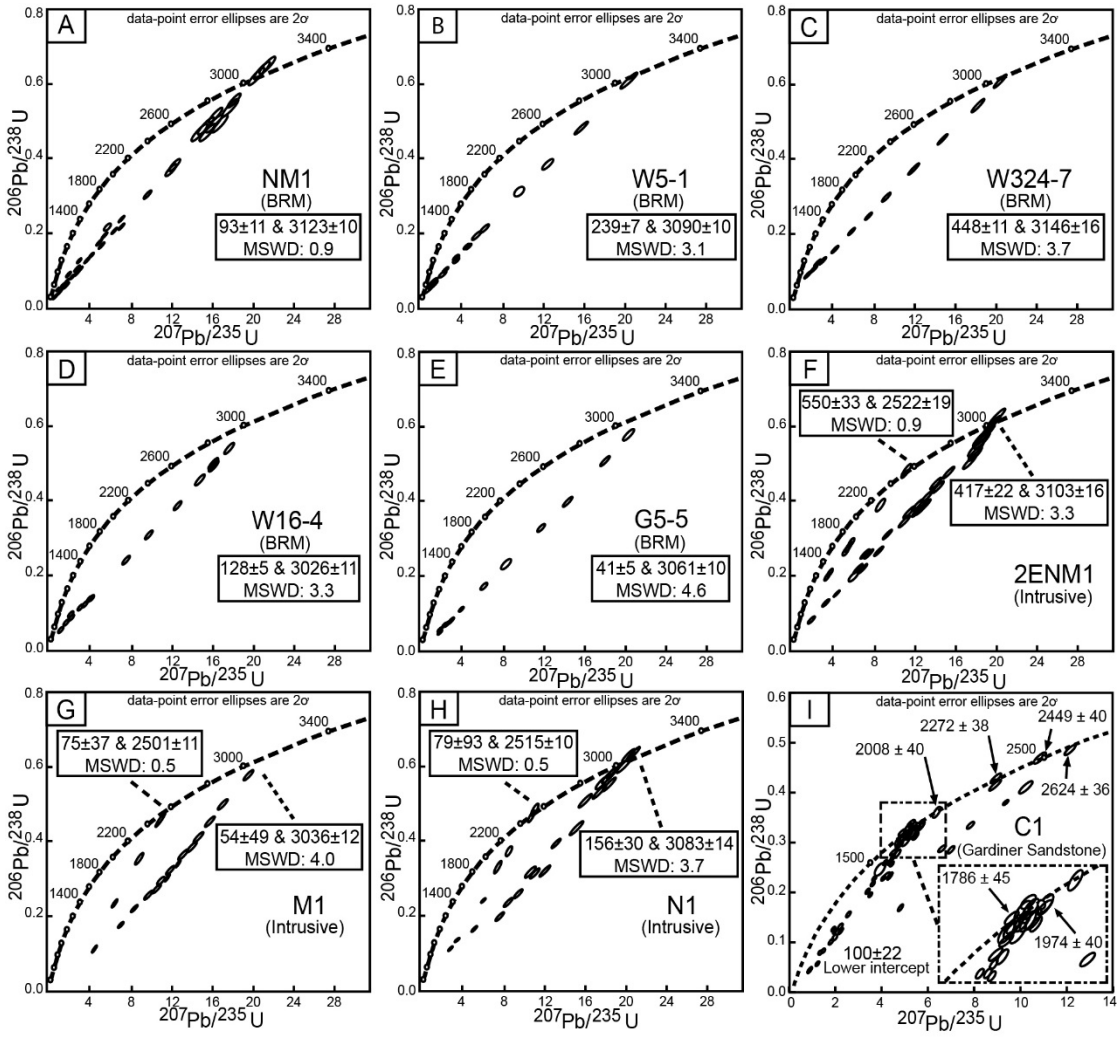

Fig. 2-9: Uranium–Pb concordia diagrams for zircon analyses from five BRM samples: (A) sample NM1, (B) sample W5-1, (C) sample W324-2, (D) sample W16-4, and (E) sample G5-5. Three intrusive rock samples: (F) sample 2ENM1, (G) sample M1, (H) sample N1) and one sample of the Gardiner Sandstone (I) sample C1. Ages provided are upper and lower intercept ages.

Zircons from felsic intrusive rock samples

High zircon yields were recovered from all three of the processed felsic intrusive samples. Most grains share similar morphology, size and internal zoning characteristics, including a subhedral tabular habit of ~100 µm length, with a typical length/width ratio of about 1:3. All of these grains have oscillatory internal zoning in CL images (Figs. 2-7E-F), which is typical of magmatic zircons (Grant et al., 2009). Some of the zircon grains exhibit narrow bright or dark discontinuous rims that are usually <5 µm width (Figs. 2-7F-G). A few grains are notably larger (>400 µm in length) than the bulk of the grains with a typical length/width ratio of about 1:5 (Fig. 2-7G). These large grains display oscillatory zoning, and have a subhedral habit. As with the metasedimentary samples, we targeted the most pristine and inclusion free zircon domains for U–Pb isotopic dating.

Uranium–Pb data for 38 zircon grains analysed from sample 2ENM1 define two distinct arrays on a conventional concordia plot (Fig. 2-9F), again with discordant analysis generally extending to higher Th, U and Th/U (Fig. 2-8). The concordant and near concordant analyses of the steepest array project to an upper concordia intercept at 3103 ± 16 Ma (MSWD = 3.3). These zircons have Th/U ratios from 0.3 to 1.1 (mean = 0.5). The second array intercepts concordia at a younger age of 2522 ± 19 Ma (MSWD = 0.9), and have Th/U ratio ranges from 0.4 to 0.8. The ca. 3.1 Ga and ca. 2.5 Ga zircon can be distinguished based on morphological characteristics, as the ca. 2.5 Ga zircons tend to be larger (>400 µm in length) and more elongate (width/length ratio of 1:4 and 1:5) compared to the ca. 3.1 Ga zircons (width/length ratio of 1:1 to 1:3).

As with sample 2ENM1, zircon analyses from granite samples M1 (n = 23) and N1 (n = 24) each define two age arrays with variable Pb loss, with upper intercepts ages of 3036 ± 12 Ma (MSWD = 4.0) and 2501 ± 11 Ma (MSWD = 0.52) for M1 (Fig. 2-9G), and 3083 ± 14 Ma (MSWD = 3.7) and 2515 ± 10 Ma (MSWD = 0.57) for N1 (Fig. 2-9H). In both samples, the ca. 2.5 Ga zircons tend to be relatively large and elongate compared to the ca. 3.1 Ga zircons. Th/U ratios of all zircons range from 0.3 to 1.6. Lower intercept ages for age populations from both intrusive rock samples intersect concordia at between ca. 550 and ca. 50 Ma.

Detrital zircon of Gardiner Sandstone

Zircon grains separated from the Gardiner Sandstone sample (C1) are clear and colourless, approx. 100 μm in size, and tend to be rounded to sub-rounded in form (Fig. 2-7H). CL imaging shows oscillatory internal zoning typical of magmatic zircon. Some of the grains were identified to be metamict and highly fractured, and contain micro-inclusions, all of which were accordingly avoided during subsequent analysis.

Most of the 59 zircon analyses returned discordant ages that are consistent with Pb loss (Fig. 2-9I; see Appendix 2-1). The ages range between ca. 2.6 Ga to ca. 1.8 Ga, with a major cluster at ca. 2.0–ca. 1.8 Ga, and individual concordant ages at ca. 2.6 Ga, ca. 2.5 Ga, and ca. 2.2 Ga (Fig. 2-9I). The ca. 2.6 Ga, ca. 2.5 Ga, and ca. 2.2 Ga zircons are present in minor quantities, however these zircons seem to have relatively lower U and Th contents compared to those of the ca. 2.0–ca. 1.8 Ga zircons. Nonetheless, the Th/U ratio is within the same range for all the populations, varying from 0.3 to 0.9.

Zircon Lu-Hf isotopes

Most zircon grains recovered from the metasedimentary and intrusive rocks produced highly discordant ages, which may not provide reliable information on the Hf isotope compositions (Zeh et al., 2010; Guitreau and Blichert-Toft, 2014). Hafnium isotope analyses were, therefore, targeted to zircon grains that produced concordant or near concordant (<20% discordance) ages. In total, 31 zircons from 3 metasedimentary rocks and 3 intrusive samples were analysed for their Hf isotope composition with results presented in Fig. 2-10 and Table 2-3. The initial $^{176}Hf/^{177}Hf$ and $^{176}Lu/^{177}Hf$ ratios for zircon from the metasedimentary rocks are between 0.280755–0.280836, and 0.000692–0.004748, respectively. These values are in the same range as the ca. 3.2 to ca. 3.0 Ga zircons from the intrusive samples (initial $^{176}Hf/^{177}Hf$ = 0.280742–0.280941, $^{176}Lu/^{177}Hf$ = 0.000561–0.001992). Collectively, the ca. 3.2 to ca. 3.0 Ga zircons give initial εHf of -7.1 to 5.1, although this range of values is largely an artefact of the input $^{207}Pb/^{206}Pb$ ages used for each zircon, which are – to varying extents – affected by Pb loss (Fig. 2-10). The zircon grains that produced concordant ages returned εHf values of –1.7 to 5.1, which are interpreted to be the primary values for the ca. 3.2 to ca. 3.0 Ga zircon grains prior to Pb loss. The ca. 2.5 Ga zircons of the intrusive rocks generated initial $^{176}Hf/^{177}Hf$ ratios of

0.280793–0.280984 and $^{176}Lu/^{177}Hf$ of 0.000574–0.001512, with the concordant zircons giving εHf of –13.7 to –5.8.

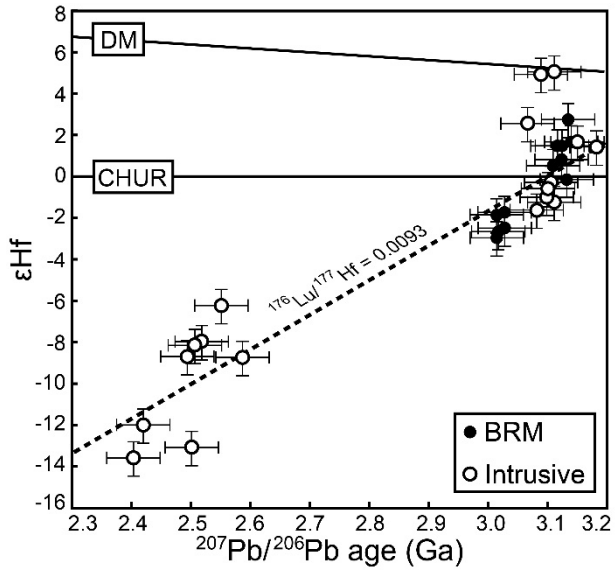

Fig. 2-10: εHf versus $^{207}Pb/^{206}Pb$ age (Ga) of zircon from the BRM and cross-cutting intrusive rocks. Note the influence of Pb loss on apparent εHf, which is broadly consistent with isotopic evolution of upper crustal rocks with $^{176}Lu/^{177}Hf$ ratio of 0.0093 (Amelin et al., 1999).

Table 2-3: Zircon Lu-Hf isotopic data for the BRM and intrusive rocks

	Rock type	$^{207}Pb/^{206}Pb$ age (Ma)	$^{176}Hf/^{177}Hf$	2σ	$^{176}Lu/^{177}Hf$	2σ	$^{176}Hf/^{177}Hf$ (i)	εHf	2σ	T_{DM}
NM1_1	BRM	3129	0.280803	0.000019	0.000797	0.000319	0.280755	-0.3	0.7	3377
NM1_2	BRM	3025	0.280826	0.000015	0.000726	0.000173	0.280783	-1.8	0.5	3341
NM1_3	BRM	3123	0.280828	0.000017	0.000819	0.000047	0.280779	0.4	0.6	3346
NM1_5	BRM	3121	0.280839	0.000015	0.000841	0.000058	0.280788	0.7	0.5	3333
NM1_12	BRM	3107	0.280836	0.000019	0.000822	0.000233	0.280787	0.3	0.7	3334
NM1_14	BRM	3012	0.280835	0.000017	0.000823	0.000184	0.280787	-1.9	0.6	3336
NM1_18	BRM	3112	0.280866	0.000019	0.000818	0.000112	0.280817	1.5	0.7	3295
NM1_28	BRM	3122	0.280861	0.000021	0.000869	0.000211	0.280809	1.4	0.7	3306
NM1_32	BRM	3010	0.280803	0.000021	0.000692	0.000161	0.280762	-2.8	0.7	3368
NM1_44	BRM	3133	0.280888	0.000019	0.000870	0.000542	0.280836	2.7	0.7	3269
W324-7_2	BRM	3120	0.280871	0.000022	0.000870	0.000211	0.280809	1.4	0.7	3306
W16-4_15	BRM	3024	0.280910	0.000024	0.002535	0.000826	0.280763	-2.5	0.9	3385
W16-4_19	BRM	3011	0.281031	0.000025	0.004748	0.000776	0.280756	-3.1	0.9	3421
2ENM1_14	Intrusive	3202	0.280881	0.000024	0.001992	0.000834	0.280758	1.5	0.9	3377
2ENM1_18	Intrusive	3094	0.280829	0.000024	0.001008	0.000867	0.280769	-0.6	0.9	3360
2ENM1_27	Intrusive	3102	0.280863	0.000023	0.001512	0.000850	0.280773	-0.3	0.8	3359
2ENM1_38	Intrusive	2413	0.280952	0.000025	0.001172	0.000868	0.280898	-12.0	0.9	3208
M1_07	Intrusive	3058	0.280939	0.000024	0.000991	0.000867	0.280881	2.5	0.9	3211
M1_09	Intrusive	3141	0.280884	0.000024	0.001379	0.000855	0.280800	1.6	0.9	3319
M1_12	Intrusive	3106	0.280957	0.000021	0.000574	0.000883	0.280922	5.1	0.8	3153
M1_13	Intrusive	2552	0.281020	0.000024	0.000765	0.000890	0.280983	-5.8	0.9	3083
M1_20	Intrusive	3082	0.280968	0.000024	0.000606	0.000881	0.280932	4.9	0.9	3141
M1_21	Intrusive	3077	0.280805	0.000022	0.000944	0.000869	0.280749	-1.7	0.8	3387
M1_24	Intrusive	2514	0.280966	0.000024	0.000679	0.000878	0.280933	-8.4	0.9	3149
N1_06	Intrusive	2403	0.280920	0.000024	0.001362	0.000888	0.280858	-13.7	0.9	3267
N1_07	Intrusive	3090	0.280857	0.000022	0.001635	0.000846	0.280760	-1.1	0.8	3378
N1_16	Intrusive	2515	0.280985	0.000024	0.000836	0.000873	0.280945	-8.0	0.9	3136
N1_17	Intrusive	3083	0.281006	0.000024	0.001265	0.000858	0.280931	4.9	0.9	3142
N1_24	Intrusive	2586	0.280905	0.000021	0.000657	0.000879	0.280872	-8.9	0.8	3229
N1_27	Intrusive	2499	0.280881	0.000024	0.001410	0.000854	0.280813	-13.0	0.9	3325
N1_29	Intrusive	3105	0.280784	0.000022	0.000696	0.000877	0.280743	-1.3	0.8	3393

Discussion

The original volume of the sedimentary package now preserved as the BRM remains unknown due, in part, to blanketing by younger cover sequences, incomplete drill core coverage, and the presence of intervening crustal-scale faults. Nonetheless, given the outcropping surface area of at least 100 km^2 (Fig. 2-1C) and an estimated thickness of 0.5–3 km (Hendrickx et al., 2000), a minimum volume for the BRM of 50 to 300 km^3 is calculated. Given this substantial volume, the BRM may provide crucial insights into the early geological history of the poorly understood North Australian Craton. However, to apply our petrographic, geochemical and geochronological data to accurately understand the geological origins of the BRM, we first need to distinguish the role that post depositional processes, such as hydrothermal activity, may have had on altering rock compositions.

Effect of post-depositional alteration

Petrographic analysis of the BRM reveals a relatively simple mineralogy dominated by detrital quartz and K-feldspar, with the latter being altered to muscovite and clay to variable extents (Fig. 2-4A-B). Our geochemical data can be employed to further evaluate the effects of this alteration. Our samples define two distinct trends in bulk-rock SiO_2–K_2O–Al_2O_3 compositions on a ternary diagram (Fig. 2-11), which are consistent with the mineralogy of quartz plus mainly K-feldspar (four samples), and quartz plus muscovite (8 samples). These trends are consistent with mineral modal analysis from thin section observations. Fig. 2-11 is also useful for demonstrating the variable quartz contents of the rocks, as is also evident from the variable bulk-rock SiO_2 contents (Fig. 2-5), particularly for the muscovite-bearing rocks. Based on geochemical and textural observations, we interpret the quartz–muscovite assemblage with variable degrees of associated silicification to be a result of post-depositional hydrothermal alteration of the metasedimentary rocks. This is consistent with the core-logging observations that silicification tends to be most intense adjacent to the HREE orebodies and major fault structures that cut the metasedimentary rocks.

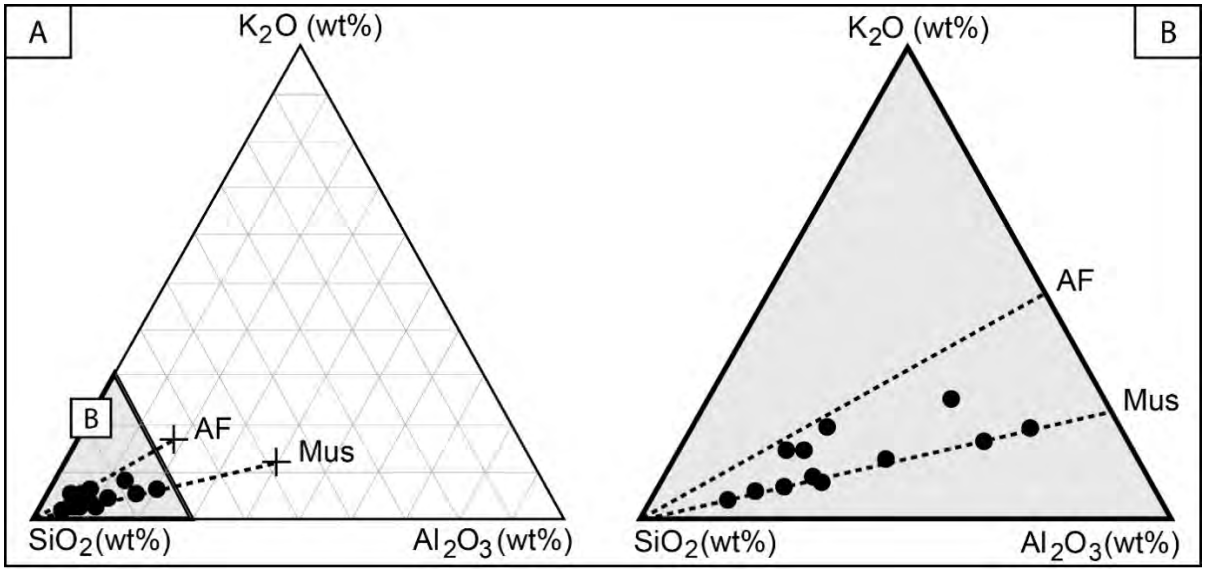

Fig. 2-11: BRM bulk-rock ternary diagrams: (A) SiO_2–K_2O–Al_2O_3 diagram showing the data locating near SiO_2 apex, (B) SiO_2–K_2O–Al_2O_3 (>70%–>30%–>30%) diagram with most data points falling along two broad arrays corresponding to quartz–muscovite and quartz–alkali feldspar assemblages. AF, alkali feldspar; Mus, muscovite.

Uranium–Pb discordia in zircon

Most of the zircons analysed in this study produced highly discordant ages, with lower intercept ages mainly falling between ca. 150 and 40 Ma, and from ca. 550 to ca. 400 Ma. Similar lower intercept ages reported from zircons of the Tanami Region (Bagas et el., 2010), have been interpreted to be due to isotopic disturbance related to Alice Springs Orogeny (450-300 Ma; Raimondo et al., 2011), or modern weathering (e.g., Cross and Crispe, 2007). Likewise, radiogenic Pb loss reported from hydrothermal xenotime of the Kimberley Basin (Lan and Chen, 2012), and zircon and monazite of the Arunta Inlier (Harts Range; Hand et al., 1999; Mount Peake Gabbro; Beyer et al., 2016) have also been attributed to the Alice Springs Orogeny. Accordingly, we regard our lower intercept ages to be due to the combined effects of the Alice Springs Orogeny and/or modern weathering. Our upper intercept ages are interpreted to be representative of the crystallisation age of the zircons, as discussed below.

Uranium–Pb discordance in zircon is commonly attributed to Pb loss during alteration of zircon, although Pidgeon et al. (2017) suggest that in some cases zircons may undergo Th and/or U uptake during weathering or alteration, leading to elevated Th/U. Our analyses show

a broad correlation between Th, U, Th/U and degree of discordance (Figs. 2-8A-B), although values for Th, U and Th/U are all within the range reported for igneous zircon (Hoskin and Schaltegger, 2003). We also observe that $^{207}Pb/^{206}Pb$ ages remain undisturbed up to about 30% of U–Pb discordance (Fig. 2-8C), but then become disturbed at greater discordance levels. Based on these observations, we suggest that the discordance observed in the zircons is due both to Th and U uptake during weathering (as per Pidgeon et al., 2017), and Pb loss, with zircon domains with the highest Th and U experiencing greater Pb loss (and hence greater discordance) due to higher levels of radiation damage.

Provenance characteristics

Despite the hydrothermal overprint, the mineralogy and petrography of the metasedimentary rocks can be used to determine the nature of the depositional environment and source of the sediments. Application of the Quartz–Feldspar–Lithic (QFL) triangular diagram scheme of Dickinson et al. (1983) indicates that the BRM were likely derived from cratonic interiors and/or transitional continental blocks (Fig. 2-12A). Petrographic features such as the medium to coarse grain size, poor sorting and immature nature of the detritus indicate a short transport distance and relatively rapid burial for the metasedimentary rocks (Nesbitt and Young, 1982).

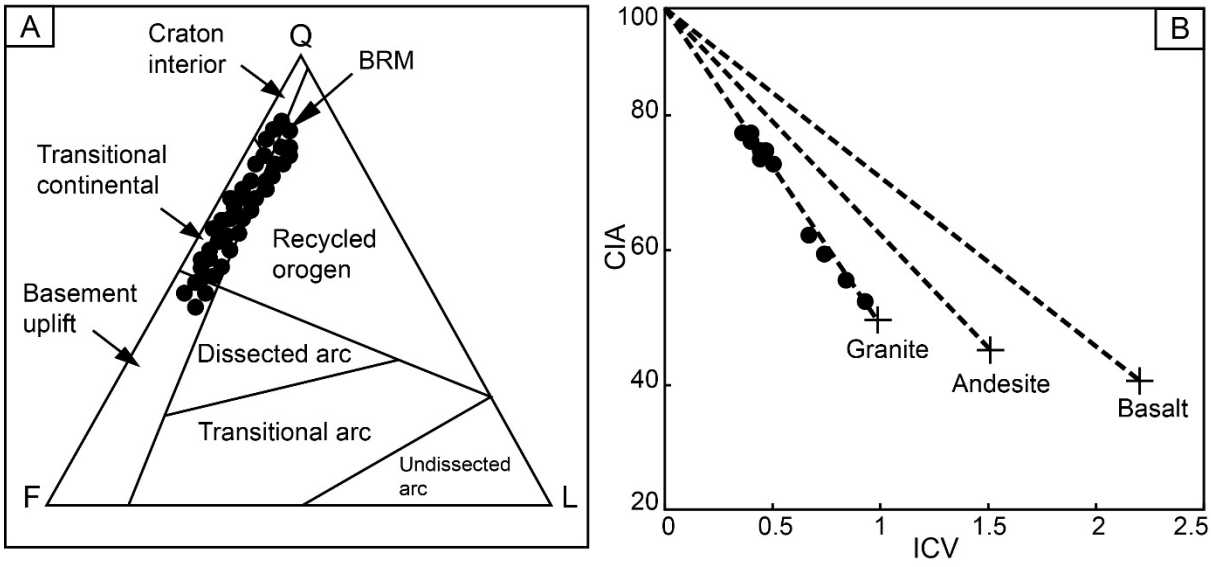

Fig. 2-12: Provenance characteristics of the BRM: (A) QFL diagram after Dickinson et al. (1983); and (B) correlation between CIA and ICV weathering indices, suggesting a granite source terrane for the BRM (after Cox et al., 1995; Potter et al., 2005).

The index of compositional variability (ICV; see Cox et al., 1995; Potter et al., 2005) and the chemical index of alteration (CIA; see Nesbitt and Young, 1982), are both useful measures of sediment source compositions, while also incorporating the degree of weathering/alteration. On a plot of CIA versus ICV (Fig. 2-12B) all BRM samples fall on the weathering/alteration trend of granite (or direct erosional products such as arkose), suggesting a felsic source of granitic composition. The most altered samples of quartz–muscovite assemblage tend to plot towards high CIA and low ICV, but still lie on the granite array. We regard this array of compositions to be due to hydrothermal alteration of the samples, rather than weathering, as outlined above. Moreover, the general REE characteristics (e.g., LREE enrichment and negative Eu anomalies; Taylor and McLennan, 1985; Fig. 2-6), and the low content of the transition elements (e.g., Cr, Co and Ni) of the BRM are typical of continental-derived silicic rocks, such as granite. These geochemical criteria are also consistent with the predominance of coarse alkali feldspar as a major detrital phase and the common occurrence of granitic clasts (Fig. 2-2E) in the metasedimentary rocks.

Emplacement age and origin of the intrusive rocks

The three felsic intrusive bodies analysed returned two age populations of ca. 3.2 to ca. 3.0 Ga, and ca. 2.5 Ga. Although all zircons have oscillatory internal zoning characteristic of a magmatic source (Grant et al., 2009), the ca. 2.5 Ga zircon grains tend to be markedly larger (Fig. 2-7G) than the ca. 3.2 to ca. 3.0 Ga zircons (Figs. 2-7E-F). We interpret the ca. 2.5 Ga (the weighted mean age: 2511 ± 24 Ma, MSWD: 2.7) zircons to record the igneous crystallisation of the intrusive rocks cutting the BRM. This age broadly corresponds to the ca. 2.67 Ga to ca. 2.44 Ga age determined for a sample of the BRD granite collected from the Northern Territory (Cross and Crispe, 2007), and may indicate that there is a regional-scale magmatic activity at ca. 2.5 Ga. More broadly, this age also corresponds to emplacement of granitic plutons within the Tanami Region (2514 ± 3 Ma Billabong Complex; Page et al., 1995) and the Pine Creek Orogen (2527-2510 Ma Kukalak Gneiss, 2520 Ma Nanambu Complex, and the 2545-2521 Ma Rum Jungle Complex; Hollis et al., 2009).

The ca. 3.2 to ca. 3.0 Ga zircons of the intrusive rocks share very similar morphology and size to those recovered from the BRM (Fig. 2-7). Moreover, they have comparable T_{DM} ages (T_{DM} = ca. 3.4–ca. 3.1 Ga) and initial $^{176}Hf/^{177}Hf$ and $^{176}Lu/^{177}Hf$ ratios to the ca. 3.2 to ca. 3.0 Ga

detrital zircons of the BRM (Table 2-3). Such similarities suggest that the ca. 3.2 to ca. 3.0 Ga zircons of the intrusive rocks are detrital, and derive from the BRM. Additionally, similar T_{DM} model ages calculated for the ca. 2.5 Ga zircons of the intrusive rocks to the ca. 3.2 to ca. 3.0 Ga detrital zircons demonstrate that the intrusive rocks formed during the partial melting of the BRM or the Mesoarchean granite basement from which the BRM were derived.

Timing of deposition of the metasedimentary rocks

The similarity in size, shape and internal structure, suggests a common source for all the ca. 3.2 to ca. 3.0 Ga zircons analysed from the metasedimentary and intrusive rocks. This age is consistent with the ca. 3.15 to ca. 3.04 Ga age reported by Cross and Crispe (2007) for inherited zircons from a sample of the BRD granite from the southern margin of the Browns Range Dome. Most of the ca. 3.2 to ca. 3.0 Ga zircons have oscillatory or planar zoning features consistent with a magmatic origin (Grant et al., 2009).

Owing to the effects of Pb loss for many of the analysed zircons, our zircon crystallisation ages for individual samples were obtained by upper intercepts to concordia and, hence, are relatively poorly constrained. Nevertheless, we can assume our youngest detrital age of 3026 ± 11 Ma for sample W16-4 to be the maximum depositional age of the metasedimentary rocks of the BRM. The minimum depositional age of the BRM can be constrained by the age of the intrusive rocks (ca. 2.5 Ga) that cross-cut the metasedimentary rocks. The common emplacement of ca. 2.5 Ga magmatic rocks suggests a major shift in the tectonics of the region, which may have been responsible for termination of sedimentation forming the BRM. Regardless, the geochronological data confirm that these metasedimentary rocks were deposited in the time period between ca. 3.0 Ga and ca. 2.5 Ga. Based on global geological events during this time period, we speculate that the sedimentation may have been synchronous with the rifting of the Pilbara Craton leading to the deposition of the Fortescue Group (e.g., Blake et al., 2004) and major global magmatism (Jia et al., 2016, and the references therein) that occurred at ca. 2.8 to ca. 2.7 Ga.

Dating of zircons from Gardiner Sandstone, which unconformable overlies the BRM, produced a wide range of detrital ages from ca. 2.6 to ca. 1.8 Ga (Fig. 2-9I). These ages are comparable to the zircon ages reported from another sample of the Gardiner Sandstone analysed by Cross

and Crispe (2007). Although these detrital zircons are likely to derive from the recycling of the underlying Tanami Group (Cross and Crispe, 2007), the ultimate source of the zircons is interpreted to be linked to extensive granite magmatism in the Tanami Region at ca. 1.8 Ga (Smith, 2001) and ca. 2.5 Ga (e.g., Billabong Complex; Page et al., 1995). The minimum depositional age of the Gardiner Sandstone can be inferred from diagenetic xenotime growth (ca. 1.63 Ga; Vallini et al., 2007) in the west of the Tanami Group. In this case, the unconformity between the BRM and Gardiner Sandstone represents a hiatus of at least 800 Ma.

Of note is the lack of the 3.2 to 3.0 Ga zircons in the Gardiner Sandstone, which rules out any source contribution from the BRM. This suggests that the drainage systems supplying sediment for the Gardiner Sandstone did not drain from exposures of the BRM, or that the BRM were not exposed at the time of deposition of the Gardiner Sandstone.

Tectonic setting of deposition of the BRM

Inferences on tectonic settings based solely on whole-rock geochemistry of the sedimentary rocks have been shown to be inconsistent with the known geology of the ancient terrains, and hence cannot be reliably applied to Archean-derived sedimentary rocks (Armstrong-Altrin and Verma, 2005; Ryan and Williams, 2007). Instead we use analysis of detrital zircon populations, which has been successfully used to constrain the tectonic setting of the sedimentary rocks (e.g., Cawood et al., 2012). This approach discriminates three major tectonic settings (convergent, collisional, and extensional), and is more effective when the depositional age of the sedimentary rocks is well constrained. The convergent and collisional settings include sedimentary rocks indicated by a wide spectrum of detrital ages due to syn-depositional magmatism and variability of the source rocks. By contrast, sedimentary rocks of the extensional settings (e.g., rift basins) are characterised by limited age populations, a lack of a syn-depositional magmatic activity, and proximity to the source rocks (Cawood et al., 2003).

The observation that the BRM contain detrital zircons all of ca. 3.2 to ca. 3.0 Ga age suggests derivation from – and deposition close to – a single source terrain. The proximal deposition to the source can also be inferred from the immature and poorly sorted nature of the metasedimentary rocks. Based on these data, we suggest that the metasedimentary rocks were likely deposited within a continental rift basin with uplifted rift flanks of Mesoarchean granite

basement that restricted the sediment source region to the rift flanks. This is consistent with current models for other Archean sedimentary sequences that propose that locally derived sediments were deposited in rift basins (e.g., the Barren Basin, Yilgarn Craton, Spaggiari et al., 2014; Fortescue Group, Pilbara Craton, Blake et al., 2004).

Comparison with Australian Archean cratons

The time-period ca. 3.2 to ca. 3.0 Ga is not recognised as a major crust-forming episode in Australia (Huston et al., 2012), yet zircons (mostly of detrital origin) of this age have been reported from most of the Australian's Archean cratons (Fig. 2-13). Detrital zircons of ca. 3.1 Ga age form components of sedimentary rocks of the Tanami Region (e.g., Killi Killi Formation, Mount Charles Formation and Pargee Sandstone; Cross and Crispe, 2007), and the Pine Creek Orogen (e.g., Cahill Formation, Nourlangie Schist, Crater Formation; Hollis et al., 2010, 2014). Together with our newly-identified ca. 3.2 to ca. 3.0 Ga granitic source for the BRM, these records indicate that there were significant volumes of Mesoarchean continental crust within the North Australian Craton that has since been eroded and/or buried, and/or dismembered by tectonism. The similarity in εHf of the ca. 3.1 Ga zircons of the Crater Formation (εHf = –3 to +1; Hollis et al., 2010) and those of the BRM (εHf = –1.7 to 5.1), further supports a common crustal origin (Fig. 2-13). The ca. 2.5 Ga magmatic zircons from intrusive rocks cross-cutting the BRM have similar T_{DM} ages to the ca. 3.2 to ca. 3.0 Ga detrital zircons of the BRM (T_{DM} = ca. 3.4–ca. 3.1 Ga). Likewise, Hf and O isotopic data reported from several ca. 2.5 Ga intrusive units of the Pine Creek Orogen (e.g., Kukalak Gneiss, Nanambu Complex and Rum Jungle Complex) are characterised by non-radiogenic Hf and enriched $\delta^{18}O$ zircon values (εHf of up to ~–7 and $\delta^{18}O$ > 6.5‰; Beyer et al., 2013). Collectively, these records are consistent with derivation of the ca. 2.5 Ga magmatism in North Australian Craton via partial melting of the Mesoarchean crust, or the sediments sourced from this crust (e.g., BRM).

The oldest detrital zircons (ca. 4.4 to ca. 3.3 Ga) from the Mt Narryer and Jack Hills metasedimentary sequences of the Yilgarn Craton predate the age of the BRM source and are not considered further here. Younger detrital zircons (ca. 2.6 Ga) from Jack Hills (Fig. 2-13) have relatively non-radiogenic Hf (εHf = –8 to –16) and are explained by an evolution line of ca. 4.5 Ga mafic crust with $^{176}Lu/^{177}Hf$ ratio of 0.025 (Kemp et al., 2010). Collectively, these

isotopic data do not support a common history or origin for the Mt Narryer and Jack Hills metasedimentary rocks, and the BRM. The Murchison Domain of the Yilgarn Craton comprises ca. 2.9–ca. 2.6 Ga volcano-sedimentary rocks whose Hf isotopic data indicate input from both depleted mantle and older crust. The ca. 2.9 Ga zircons (εHf values = –5 to +2), have T_{DM} ages of ca. 3.3 to ca. 3.1 Ga, whereas the ca. 2.8 to ca. 2.6 Ga zircons vary in εHf from –13 to +4, giving T_{DM} ages of ca. 3.8 to 3.7 Ga, ca. 3.1 Ga and ca. 2.9 Ga (Ivanic et al., 2012). The isotopic data from the Murchison Domain, therefore, are consistent with the involvement of an early Archean (ca. 3.8 to ca. 3.7 Ga) felsic source, as well as recycling of the Mesoarchean (ca. 3.3 to ca. 3.1 Ga) felsic crust. Juvenile Mesoarchean magmatism (ca. 3.2 to ca. 3.1 Ga) was also inferred from the detrital zircon record of the northern portion of the Eastern Goldfields Province (Griffin et al., 2004). These data indicate the occurrence of significant, but poorly recognised, Mesoarchean mantle-derived magmatism within the Yilgarn Craton, which may be genetically related to that of the BRM.

Major crust forming events of the Pilbara Craton at ca. 3.6 Ga and ca. 3.4 Ga (Kemp et al., 2015) both predate the age of the source rocks to the BRM. Nevertheless, the Pilbara also experienced a major ca. 3.2 Ga rifting event that divided the Pilbara Supergroup (Hickman and Van Kranendonk, 2012) into the Karratha, Kurrana and the East Pilbara terranes (Van Kranendonk et al., 2010), all of which were reassembled during the ca. 3.07 Ga Prinsep Orogeny and ca. 2.9 Ga Mosquito Creek Orogeny (Smithies et al., 2005). The ca. 3.2 Ga rifting event led to the deposition of extensive sedimentary (Croydon Group and Dixon Island Formation; Kiyokawa et al., 2002; Smithies et al., 2001), and volcanic sequences, such as the Regal Formation basalts with εNd values of +1.4 to +3.6 (Smithies et al., 2007). Similar results (εNd = +2 to +3; Smithies et al., 2005) were reported from the ca. 3.1 Ga Whundo Group and coeval granitic rocks of the Railway Supersuite of the Sholl Terrane. These data indicate extensive mantle-derived magmatism and sedimentation occurred within the Pilbara Craton from ca. 3.2 to ca. 3.1 Ga.

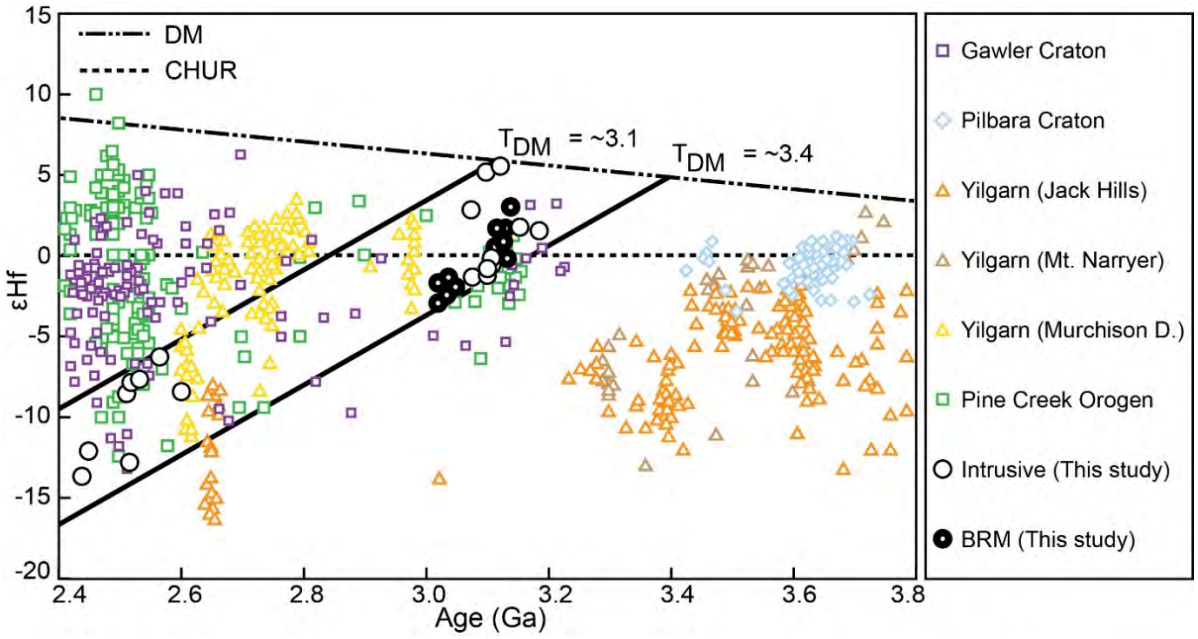

Fig. 2-13: Compilation of the Hf isotope compositions versus age (Ga) of zircons from Australian Archean cratons, as well as the dataset from the BRM (this study). The data are from Belousova et al. (2009; Gawler Craton), Kemp et al. (2015; Pilbara Craton), Amelin et al. (1999), Kemp et al. (2010), Bell et al. (2011) (Jack Hills, Yilgarn Craton), Nebel-Jacobsen et al. (2010; Mt Narryer, Yilgarn Craton), Ivanic et al. (2012; Murchison Domain, Yilgarn Craton), Hollis et al. (2010, 2014) and Beyer et al. (2013) (Pine Creek Orogen). DM, CHUR and ^{176}Lu decay constant values are from Griffin et al. (2004), Bouvier et al., (2008), and Soderlund et al. (2004), respectively. Note that the black lines indicate the isotopic evolutionary trends, showing the maximum and minimum T_{DM} model ages calculated for the ca. 2.5 Ga magmatic and ca. 3.2 to ca. 3.0 Ga detrital zircons, using an upper crustal ^{176}Lu/^{177}Hf ratio of 0.0093 (Amelin et al., 1999).

Within the Gawler Craton of South Australia lies the ca. 3.1 Ga Cooyerdoo Granite that has whole-rock εNd values of –1 to +1, and T_{DM} model ages of ca. 3.4 Ga to ca. 3.2 Ga (Fraser et al., 2010). Comparable isotopic results were obtained from ca. 3.2 Ga detrital zircons of the Olympic Domain (εHf values of up to +4, T_{DM} = ca. 3.5 Ga to ca. 3.1 Ga; Belousova et al., 2009), which also fall within the εHf evolution band defined by the BRM zircons (Fig. 2-13). Like the BRM, the Gawler Craton also experienced widespread magmatism at ca. 2.5 Ga, at least some of which (Lake Gilles leucogranite) was generated from melting of a ca. 3.2 Ga source (Fraser et al., 2010).

Collectively, there are significant records of ca. 3.2 to ca. 3.0 Ga crust formation in all four of Australia's Archean cratonic blocks. In some cases, these records are only preserved as detrital

zircons in relatively mature sediments, but magmatic rocks of this age are preserved, and the BRM represents erosional products of significant volumes of Mesoarchean granite. The Mesoarchean magmatic record in all cratons includes a significant juvenile mantle-derived component. The commonality of these records does tempt correlation between the cratons, however, we are currently unable to further evaluate the relationships between these crustal blocks in the absence of Mesoarchean plate reconstructions.

Implications for the Archean crustal evolution

Recent studies based on a global compilation of isotopic data from detrital and magmatic zircons indicate major episodes of continental crust formation at ca. 4.2, ca. 3.6, ca. 2.7 and ca. 1.8 Ga (Belousova et al., 2010; Hawkesworth et al., 2010). Early Archean (>3.4 Ga) zircons tend to have chondritic to sub-chondritic Hf isotope compositions (Naeraa et al., 2012; Kemp et al., 2015), suggesting a limited contribution from a depleted mantle source. In contrast, a major portion of the younger (>3.0 Ga) zircon record has radiogenic Hf isotopic signatures (Hawkesworth and Kemp, 2006; Griffin et al., 2014), consistent with at least partial derivation from a depleted mantle source. These results, combined with a significant increase in the $\delta^{18}O$ values of some >3.2 Ga zircons (Dhuime et al., 2012; Van Kranendonk et al., 2015) are interpreted to be indicative of the onset of the plate tectonic regime at around 3.0 Ga. Thus, the Mesoarchean period represents a transition in the tectonic style from crustal growth dominated by the formation (and remelting) of volcanic plateaus over hot, upwelling and/or overturning mantle to tectonics driven by subduction-related arc magmatism and horizontal terrane accretion (Naeraa et al., 2012; Griffin et al., 2014; Kemp et al., 2015; Van Kranendonk et al., 2015).

Our new data, combined with other records of Mesoarchean crustal evolution in Australia (outlined above) and elsewhere (South Africa; Zeh et al., 2009; Zeh et al., 2011; Greenland; Naeraa et al., 2012; Szilas et al., 2016; India; Lancaster et al., 2014; Santosh et al., 2014) point to a significant episode of juvenile magmatism during the Mesoarchean that in part appears to be tapping depleted mantle domains. This observation is contrary to the suggestion of Griffin et al. (2014) that there was limited juvenile magmatism at ca. 3.0 Ga, but is consistent with proposal that this time period marks the onset of subduction-driven plate tectonics (Dhuime et al., 2012).

Conclusions

The major findings of this study include:

(1) The BRM are mineralogically and texturally immature to sub-mature, meta-arkosic rocks with minor quantities of granitic lithic fragments. These rocks are consistent with derivation from a proximal granitic source in a continental rift basin setting.
(2) Five BRM samples and three granitic intrusive samples yielded a dominant detrital and inherited zircon component age of ca. 3.2 to 3.0 Ga, indicating the presence (or former presence) of Mesoarchean crystalline basement in the North Australian Craton. The age of emplacement of the granites is interpreted to be ca. 2.5 Ga, which constrains the depositional age of the BRM to between ca. 3.0 Ga and ca. 2.5 Ga.
(3) The T_{DM} model ages calculated for the ca. 3.1 Ga ($\varepsilon Hf = -1.7$ to 5.1) and ca. 2.5 Ga ($\varepsilon Hf = -13.7$ to -5.8) zircon grains suggest derivation from juvenile crust between ca. 3.4 Ga to ca. 3.1 Ga. We suggest that Mesoarchean crust may have been a more significant component of the North Australian Craton than is currently recognised.

Acknowledgements

This work was supported by an ARC Future Fellowship (FT 120100198) to Spandler. The authors would like to acknowledge Northern Minerals Ltd for financial and logistical support of this research, and their assistance with fieldwork. We thank Geoff Fraser and Bob Pidgeon for insightful reviews.

References

Amelin, Y., Lee, D.C., Halliday, A.N., and Pidgeon, R.T., 1999. Nature of the Earth's earliest crust from hafnium isotopes in single detrital zircons. Nature, v. 399, p. 252–255.

Armstrong-Altrin, J.S., and Verma, S.P., 2005. Critical evaluation of six tectonic setting discrimination diagrams using geochemical data of Neogene sediments from known tectonic setting. Sedimentary Geology, v. 177 (1–2), p. 115–129.

Bagas, L., Bierlein, F.P., Anderson, J.A.C., and Maas, R., 2010. Collision-related granitic magmatism in the Granites–Tanami Orogen, Western Australia. Precambrian Research, v. 177, p. 212–226.

Bagas, L., Bierlein, F.P., English, L., Anderson, J.A.C., Maidment, D., and Huston, D.L., 2008. An example of a Palaeoproterozoic back-arc basin: Petrology and geochemistry of the ca. 1864 Ma Stubbins Formation as an aid towards an improved understanding of the Granites–Tanami Orogen, Western Australia. Precambrian Research, v. 166, p. 168–184.

Bagas, L., Huston, D.L., Anderson, J., and Mernagh, T.P., 2007. Paleoproterozoic gold deposits in the Bald Hill and Coyote areas, Western Tanami, Western Australia. Mineralium Deposita, v. 42, p. 127–144.

Bell, E.A., Harrison, T.M., McCulloch, M.T., and Young, E.D., 2011. Early Archean crustal evolution of the Jack Hills zircon source terrain inferred from Lu–Hf, $^{207}Pb/^{206}Pb$, and $\delta^{18}O$ systematics of Jack Hills zircons. Geochimica et Cosmochimica Acta, v. 17, p. 4816–4829.

Belousova, E.A., Kostitsyn, Y.A., Griffin, W.L., Begg, G.C., O'Reilly, S.Y., and Pearson, N.J., 2010. The growth of the continental crust: constraints from zircon Hf-isotope data. Lithos, v. 119, p. 457–466.

Belousova, E.A., Reid, A.J., Griffin, W.L. and O'Reilly, S.Y., 2009. Rejuvenation vs. recycling of Archean crust in the Gawler Craton, South Australia. Evidence from U–Pb and Hf-isotopes in Detrital Zircon. Lithos, v. 113, p. 570–582.

Beyer, E.E., Donnellan, N., Meffre, S., and Thompson, J.M., 2016. Summary of results. NTGS laser ablation ICP-MS in situ zircon and baddeleyite geochronology project: Mount Peake Gabbro, Arunta Region, Northern Territory. Darwin NT: Northern Territory Geological Survey, Record 002–2016.

Beyer, E.E., Hollis, J.A., Whelan, J.A., Glass, L.M., Donnellan, N., Yaxley, G., Armstrong, R., and Allen, C., 2013. Summary of results. NTGS laser and SHRIMP U–Pb, Hf and O geochronology project: Pine Creek Orogen, Arunta Region and Murphy Inlier. Darwin NT. Northern Territory Geological Survey, Record 007–2012.

Black, L.P., Kamo, S.L., Allen, C.M., Davis, D.W., Aleinikoff, J.N., Valley, J.W., Mundil, R., Campbell, I.H., Korsch, R.J., Williams, I.S., and Foudoulis, C., 2004. Improved $^{206}Pb/^{238}U$ microprobe geochronology by the monitoring of a trace-element-related matrix effect: SHRIMP, ID-TIMS, ELA-ICP-MS and oxygen isotope documentation for a series of zircon standards. Chemical Geology, v. 205, p. 115-140.

Blake, D.H., Hodgson I.M., and Muhling P.C., 1979. Geology of the Granites–Tanami Region. Canberra ACT. Bureau of Mineral Resources, 91 p.

Blake, D.H, Hodgson, I.M., and Smith, P.A., 1975. Geology of the Birrindudu and Tanami 1:2500000 Sheet Areas, Northern Territory. Canberra ACT. Bureau of Mineral Resources, Australia, Report 174.

Blake, D.H., Tyler, I.M., and Warren, R.G., 2000. Gordon Downs (Second edition) 1:250000 geological series, explanatory notes. Canberra ACT: Australian Geological Survey Organisation, and Perth WA: Geological Survey of Western Australia (National Geoscience Mapping Accord).

Blake, T.S., Buick, R., Brown, J.A., and Barley, M.E., 2004. Geochronology of a Late Archaean flood basalt province in the Pilbara Craton, Australia: constraints on basin evolution, volcanic and sedimentary accumulation, and continental drift rates. Precambrian Research, v. 133, p. 143–173.

Bouvier, A., Vervoort, J.D., and Patchett, P.J., 2008. The Lu–Hf and Sm–Nd isotopic composition of CHUR: constraints from unequilibrated chondrites and implications for the bulk composition of terrestrial planets. Earth and Planetary Science Letters, v. 273, p. 48–57.

Cawood, P.A., Hawkesworth, C.J., and Dhuime, B., 2012. Detrital zircon record and tectonic setting. Geology, v. 40, p. 875–878.

Cawood, P.A., Nemchin, A.A., Freeman, M., and Sircombe, K., 2003. Linking source and sedimentary basin: detrital zircon record of sediment flux along a modern river system and implications for provenance studies. Earth and Planetary Science Letters, v. 210, p. 259–268.

Cook, N.J., Ciobanu, C.L., O'Rielly, D., Wilson, R., Das, K., and Wade, B., 2013. Mineral chemistry of Rare Earth Element (REE) mineralization, Browns Ranges, Western Australia. Lithos, v. 172–173, p. 192–213.

Cox, R., Lowe, D.R., and Cullers, R.L., 1995. The influence of sediment recycling and basement composition of evolution of mudrock geochemistry in the southwestern United States. Geochimica et Cosmochimica Acta, v. 59, p. 2919–2940.

Crispe, A., Vandenberg, L., and Scrimgeour, I., 2007. Geological framework of the Archean and Paleoproterozoic Tanami Region, Northern Territory. Mineralium Deposita, v. 42, p. 3–26.

Cross, A., and Crispe, A., 2007. SHRIMP U–Pb analyses of detrital zircon: a window to understanding the Paleoproterozoic development of the Tanami Region, northern Australia. Mineralium Deposita, v. 42, p. 27–50.

Cullers, R.L., 2000. The geochemistry of shales, siltstones and sandstones of Pennsylvanian–Permian age, Colorado, USA: implications for provenance and metamorphic studies. Lithos, v. 51, p. 181–203.

De Bievre, P., and Taylor, P.D.P., 1993. Table of the isotopic composition of the elements. International Journal of Mass Spectrometry and Ion Processes, v. 123, p. 149–166.

Dickinson, W.R., 1970. Interpreting detrital modes of graywacke and arkose. Journal of Sedimentary Petrology, v. 40, p. 695–707.

Dickinson, W.R., Beard, S., Brakenbridge, F., Erjavec, J., Ferguson, R., Inman, K., Knepp, R., Lindberg, P., and Ryberg, P., 1983. Provenance of North American Phanerozoic sandstones in relation to tectonic setting. Geological Society of America Bulletin, v. 64, p. 233–235.

Dhuime, B., Hawkesworth, C.J., Cawood, P.A., and Storey, C.D., 2012. A change in the geodynamics of continental growth 3 billion years ago. Science, v. 335, p. 1334–1336.

Fraser, G., McAvaney, S., Neumann, N., Szpunar, M., and Reid, N., 2010. Discovery of early Mesoarchean crust in the eastern Gawler Craton, South Australia. Precambrian Research, v. 179, p. 1–21.

Grant, M.L., Wilde, S.A., Wu, F.Y., and Yang, J.H., 2009. The application of zircon cathodoluminescence imaging, Th–U–Pb chemistry and U–Pb ages in interpreting discrete magmatic and high-grade metamorphic events in the North China Craton at the Archean/Proterozoic boundary. Chemical Geology, v. 261, p. 155–171.

Griffin, W.L., Belousova, E.A., O'Neill, O'Reilly, S.Y., Malkovets, V., Pearson, N.J., Spetsius, S., and Wilde, S.A., 2014. The world turns over: Hadean–Archean crust–mantle evolution. Lithos, v. 189, p. 2–15.

Griffin, W.L., Belousova, E.A., Shee, S.R., Pearson, N.J., and O'Reilly, S.Y., 2004. Archaean crustal evolution in the northern Yilgarn Craton: U–Pb and Hf-isotope evidence from detrital zircons. Precambrian Research, v. 131, p. 231–282.

Guitreau, M., and Blichert-Toft, J., 2014. Implications of discordant U–Pb ages on Hf isotope studies of detrital zircons. Chemical Geology, v. 385, p. 17–25.

Hand, M., Mawby, J., Kinny, P., and Foden, J., 1999. U–Pb ages from the Harts Range, central Australia: evidence for early Ordovician extension and constraints on Carboniferous metamorphism. Journal of the Geological Society of London, v. 156, p. 715–730.

Harwood, D.S., and Miller, M.M., 1990. Palaeozoic and early Mesozoic paleogeographic relations: Sierra Nevada, Klamath Mountains, and related terranes. Boulder Co: Geological Society of America Special Papers, 255.

Hawkesworth, C.J., and Kemp, A.I.S., 2006. Using hafnium and oxygen isotopes in zircons to unravel the record of crustal evolution. Chemical Geology, 226, 144–162.

Hawkesworth, C.J., Dhuime, B., Pietranik, A.B., Cawood, P.A., Kemp, A.I.S., and Storey, C.D., 2010. The generation and evolution of the continental crust. Journal of the Geological Society of London, v. 167, p. 229–248.

Hendrickx, M.A., Slater, K., Crispe, A.J., Dean, A.A., Vandenberg, L.C., and Smith, J.B., 2000. Paleoproterozoic stratigraphy of the Tanami Region: regional correlations realisation preliminary results. Darwin NT: Northern Territory Geological Survey Record, 71 pp.

Hickman, A.H., and Van Kranendonk, M.J., 2012. Early Earth evolution: Evidence from the 3.5–1.8 Ga geological history of the Pilbara region of Western Australia. Episodes, v. 35, p. 283–297.

Hollis, J.A., Beyer, E.E., Whelan, J.A., Kemp, A.I.S., Schersten, A., and Greig, A., 2010. Summary of results. NTGS laser U–Pb and Hf geochronology project: Pine Creek Orogen, Murphy Inlier, McArthur Basin and Arunta Region. Darwin NT: Northern Territory Geological Survey, Record 2010–001.

Hollis, J.A., Carson, C.J., and Glass, L.M., 2009. SHRIMP U–Pb zircon geochronological evidence for Neoarchean basement in western Arnhem Land, northern Australia. Precambrian Research, v. 174 (3–4), p. 364–380.

Hollis, J.A., Carson, C.J., Glass, L.M., Kositcin, N., Schersten, A., Worden, K.E., Armstrong, R.A., Yaxley, G.M., and Kemp, A.I.S., 2014. Detrital zircon U–Pb–Hf and O isotope character of the Cahill Formation and Nourlangie Schist, Pine Creek Orogen: implications for the tectonic correlation and evolution of the North Australian Craton. Precambrian Research, v. 246, p. 35–53.

Hoskin, P.W., and Schaltegger, U., 2003. The composition of zircon and igneous and metamorphic petrogenesis. Reviews in Mineralogy and Geochemistry, v. 53, p. 27–62.

Huston, D.L., Blewett, R.S., and Champion, D.C., 2012. The evolution of the Australian continent. Episodes, v. 35, p. 23–44.

Ivanic, T.J., Van Kranendonk, M.J., Kirkland, C.L., Wyche, S., Wingate, M.T.D., and Belousova, E.A., 2012. Zircon Lu–Hf isotopes and granite geochemistry of the Murchison Domain of the Yilgarn Craton: evidence for reworking of Eoarchean crust during Meso-Neoarchean plume-driven magmatism. Lithos, v. 148, p. 112–127.

Jackson, S.E., Pearson, N.J., Griffin, W.L., and Belousova, E.A., 2004. The application of laser ablation-inductively coupled plasma-mass spectrometry to in situ U-Pb zircon geochronology. Chemical Geology, v. 211, p. 47-69.

Jarvis, I., and Jarvis, K.E., 1995. Plasma spectrometry in earth sciences: techniques, applications and future trends. Chemical Geology, v. 95, p. 1-33.

Jia, X., Zhu, X., Zhai, M., Zhao, Y., Zhang, H., Wu, J., and Liu, T., 2016. Late Mesoarchean crust growth event: evidence from the ca. 2.8 Ga granodioritic gneisses of the Xiaoqinling area, southern North China Craton. Science Bulletin, v. 61 (12), p. 974–990.

Kemp, A.I.S., Hawkesworth, C.J., Collins, W.J., Gray, C.M., Blevin, P.L., and Edinburgh Ion Microprobe Facility, 2009. Isotopic evidence for rapid continental growth in an extensional accretionary orogeny: The Tasmanides, eastern Australia. Earth and Planetary Science Letters, v. 284, p. 455–466.

Kemp, A.I.S., Hickman, A.H., Kirkland, C.L., and Vervoort, J.D., 2015. Hf isotopes in detrital and inherited zircons of the Pilbara Craton provide no evidence for Hadean continents. Precambrian Research, v. 261, p. 112–126.

Kemp, A.I.S., Wilde, S.A., Hawkesworth, C.J., Coath, C., Nemchin, A.A., Pidgeon, R.T., Vervoort, J.D., and DuFrane, S.A., 2010. Hadean crustal evolution revisited: new constraints from Pb–Hf isotope systematics of the Jack Hills zircons. Earth and Planetary Science Letters, v. 296, p. 45–56.

Kiyokawa, S., Taira, A., Byrne, T., Bowring, S., and Sano, Y., 2002. Structural evolution of the middle Archaean coastal Pilbara terrane, Western Australia. Tectonics, v. 21, p. 1–24.

Lancaster, P.J., Dey, S., Storey, C., Mitra, A., and Bhunia, R.K., 2014. Contrasting crustal evolution processes in the Dharwar craton: insights from detrital zircon U–Pb and Hf isotopes. Gondwana Research, v. 23, p. 1361–1372.

Lan, Z-W., and Chen, Z-Q., 2012. New xenotime ages obtained from the Paleoproterozoic Kimberley Group, NW Australia: implications for regional hydrothermal events. Australian Journal of Earth Sciences, v. 59, p. 119–133.

McDonough, W.F., and Sun, S.S., 1995. Composition of the Earth. Chemical Geology, v. 120, p. 223–253.

Naeraa, T., Schersten, A., Rosing, M.T., Kemp, A.I.S., Hoffmann, J.E., Kokfelt, T.F., and Whitehouse, M.J., 2012. Hafnium isotope evidence for a transition in the dynamics of continental growth 3.2 Gyr ago. Nature, v. 485, p. 627–631.

Nazari-Dehkordi, T., Spandler, C., Oliver, N.H.S., and Chapman, J., 2016. The unique Wolverine HREE deposit, Browns Range area, Western Australia. In: Abstracts from the Goldschmidt Conference, p. 2258, 26 June - 1 July 2017, Yokohama, Japan.

Nebel-Jacobsen, Y.J., Munker, C., Nebel, O., Gerdes, A., Mezger, K., and Nelson, D.R., 2010. Reworking of Earth's first crust: constraints from Hf isotopes in Archean zircons from Mt. Narryer, Australia. Precambrian Research, v. 182, p. 175–186.

Nesbitt, H.W., and Young, G.M., 1982. Early Proterozoic climates and plate motions inferred from major element chemistry of lutites. Nature, v. 299, p. 715–717.

Orihashi, Y., Nakai, S., and Hirata, T., 2008. U-Pb age determination for seven standard zircons using Inductively Coupled Plasma-Mass Spectrometry Coupled with frequency quintupled Nd-YAG (λ = 213 nm) laser ablation system: Comparison with LA-ICP-MS zircon analyses with a NIST glass reference material. Resource Geology, v. 58, p. 101–123.

Page, R., Sun, S.S., Blake, D., Edgecombe, D., and Pearcey, D., 1995. Geochronology of an exposed late Archean basement terrane in the Granites–Tanami region. Australian Geological Survey Organisation Research Newsletter, v. 22, p. 21–22.

Pearce, T.J., Besly, B.M., Wray, D.S., and Wright, D.K., 1999. Chemostratigraphy: a method to improve interwell correlation in barren sequences, a case study using onshore Duckmantian/Stephanian sequences (West Midlands, U.K.). Sedimentary Geology, v. 124, p. 197–220.

Pettijohn, F.J., 1975. Sedimentary Rocks. Harper and Row, New York, 628 p.

Pidgeon, R.T., Nemchin, A.A., and Whitehouse, M.J., 2017. The effect of weathering on U–Th–Pb and oxygen isotope systems of ancient zircons from the Jack Hills, Western Australia. Geochimica et Cosmochimica Acta, v. 197, p. 142–166.

Potter, P.E., Maynard, J.B., and Depetris, P.J., 2005. Mud and Mudstones: Introduction and Overview. Heidelberg, Germany: Springer-Verlag, 297 p.

Raimondo, T., Clark, C., Hand, M., and Faure, K., 2011. Assessing the geochemical and tectonic impacts of fluid–rock interaction in mid-crustal shear zones: a case study from the intracontinental Alice Springs Orogen, central Australia. Journal of Metamorphic Geology, v. 29, p. 821–850.

Ryan, K.M., and Williams, D.M., 2007. Testing the reliability of discrimination diagrams for determining the tectonic depositional environment of ancient sedimentary basins. Chemical Geology, v. 242, p. 103–125.

Santosh, M., Yang, Q.Y., Shaji, E., Mohan, M.R., Tsunogae, T., and Satyanarayanan, M., 2014. Oldest rocks from Peninsular India: evidence for Hadean to Neoarchean crustal evolution. Gondwana Research, v. 65, p. 357–367.

Smith, J.B., 2001. Summary of results, joint NTGS–AGSO age determination program 1999–2001. Darwin NT: Northern Territory Geological Survey, Record 2001–007.

Smithies, R.H., Champion, D.C., Van Kranendonk, M.J., and Hickman, A.H., 2007. Geochemistry of Volcanic Rocks of the Northern Pilbara Craton, Western Australia. Perth WA: Western Australia Geological Survey, Report 104, 47 pp.

Smithies, R.H., Champion, D.C., Van Kranendonk, M.J., Howard, H.M., and Hickman, A.H., 2005. Modern-style subduction processes in the Mesoarchaean: geochemical evidence from the 3.12 Ga Whundo intra-oceanic arc. Earth and Planetary Science Letters, v. 231, p. 221–237.

Smithies, R.H., Nelson, D.R., and Pike, G., 2001. Development of the Archaean Mallina Basin, Pilbara Craton, north-western Australia; a study of detrital and inherited zircon ages. Sedimentary Geology, v. 141–142, p. 79–94.

Soderlund, U., Patchett, J.P., Vervoort, J.D., and Isachsen, C.E., 2004. The ^{176}Lu decay constant determined by Lu–Hf and U–Pb isotope systematics of Precambrian mafic intrusions. Earth and Planetary Science Letters, v. 219, p. 311–324.

Spaggiari, C.V., Kirkland, C.L., Smithies, R.H., and Wingate, M.T.D., 2014. Tectonic links between Proterozoic sedimentary cycles, basin formation and magmatism in the

Albany–Fraser Orogen. Perth WA: Western Australia Geological Survey, Report 133, 63 pp.

Szilas, K., Tusch, J., Hoffmann, J.E., Garde, A.D., and Munker, C., 2016. Hafnium isotope constraints on the origin of Mesoarchaean andesites in southern West Greenland, North Atlantic Craton. London UK: Geological Society, London, Special Publications 449.

Taylor, S.R., and McLennan, S.M., 1985. The Continental Crust: Its Composition and Evolution. Oxford UK: Blackwell.

Thomas, W.A., 2011. Detrital-zircon geochronology and sedimentary provenance. Lithosphere, v. 3, p. 304–308.

Tucker, R.T., Roberts, E.M., and Salisbury, S.W., 2013. U-Pb detrital zircon constraints on the depositional age of the Winton Formation, western Queensland, Australia: contextualizing Australia's Late Cretaceous dinosaur faunas. Gondwana Research, v. 24, p. 767–779.

Vallini, D.A., Groves, D.I., McNaughton, N.J., and Fletcher, I.R., 2007. Uraniferous diagenetic xenotime in northern Australia and its relationship to unconformity-associated uranium mineralisation. Mineralium Deposita, v. 42, p. 51–64.

Van Achterbergh, E., Ryan, C.G., Jackson, S.E., and Griffin, W.L., 2001. Data reduction software for LA-ICP-MS, in: Sylvester, P.J., (Ed.), Laser Ablation-ICP Mass Spectrometry in the Earth Sciences: Principles and Applications. Mineralogical Association of Canada, v. 29, p. 239–243.

Van Kranendonk, M.J., Kirkland, C.L., and Cliff, J., 2015. Oxygen isotope in Pilbara Craton zircons support a global increase in crustal recycling at 3.2 Ga. Lithos, v. 228–229, p 90–98.

Van Kranendonk, M.J., Smithies, R.H., Hickman, A.H., Wingate, M.T.D., and Bodorkos, S., 2010. Evidence for Mesoarchean (~3.2 Ga) rifting of the Pilbara Craton: The missing link in an early Precambrian Wilson cycle. Precambrian Research, v. 177, p, 145–161.

Zeh, A., Gerdes, A., and Barton, Jr.J.M., 2009. Archean accretion and crustal evolution of the Kalahari Craton-the zircon age and Hf isotope record of granitic rocks from Barberton/Swaziland to the Francistown Arc. Journal of Petrology, v. 50, p. 933–966.

Zeh, A., Gerdes, A., Barton, Jr.J.M., and Klemd, R., 2010. U–Th–Pb and Lu–Hf systematics of zircon from TTG's, leucosomes, meta-anorthosites and quartzites of the Limpopo Belt (South Africa): constraints for the formation, recycling and metamorphism of Palaeoarchaean crust. Precambrian Research, v. 179, p. 50–69.

Zeh, A., Gerdes, A., and Millonig, L., 2011. Hafnium isotope record of the Ancient Gneiss Complex, Swaziland, southern Africa: evidence for Archaean crust–mantle formation and crust reworking between 3.66 and 2.73 Ga. Journal of the Geological Society, v. 168, p. 953–963.

Chapter 3

Age, geological setting and paragenesis of heavy rare earth element mineralisation of the Tanami and Halls Creek Regions, Western Australia

Teimoor Nazari-Dehkordi[1*], Carl Spandler[1], Nicholas H.S. Oliver[1, 2], Robin Wilson[3]

[1]Economic Geology Research Centre, Department of Geoscience, James Cook University, Townsville, QLD 4811, Australia

[2]HCOVGlobal Consultants, PO Box 3533, Hermit Park, QLD 4812, Australia

[3]Northern Minerals, PO Box 669, West Perth, WA 6872, Australia

Abstract

Metasedimentary-rock hosted heavy rare earth element (HREE) mineralisation occurs as numerous orebodies distributed across a large district of the northern Australia. Most orebodies are located in the northwest Tanami Region close to a regional unconformity between Archean metasedimentary rocks of the Browns Range Metamorphics (BRM) and overlying Proterozoic Birrindudu Group sandstones. The orebodies consist predominantly of quartz, xenotime and minor florencite, and occur along steeply-dipping structures within a stockwork of hydrothermal veins and breccias.

Paragenetic stages of the mineralisation include: (1) a pre-ore stage of a greenschist-facies overprint of detrital minerals including quartz (several generations), alkali feldspar, plagioclase, and muscovite aligned in the pre-mineralisation foliation; (2) syn-ore quartz and white mica alteration associated with a multi-stage mineralisation of the ore minerals, primarily in breccias and veins; (3) a post-ore stage of veining and brecciation forming several generations of quartz, plus hematite, barite, anhydrite and pyrite.

In-situ U-Pb dating of xenotime from several deposits/prospects yielded an age range for mineralisation of 1.65 to 1.60 Ga; this timeframe lacks local magmatism or orogeny, and is significantly younger that the ca. 1.72 Ga $^{40}Ar/^{39}Ar$ age of the pre-ore muscovite. The HREE mineralisation, however, coincided with distal continental collision events including the initiation of the Isan Orogeny and Liebig Orogeny along eastern and southern margins of the Craton. Far field stresses from these events are invoked as drivers of large-scale fluid flow and fault (re)activation in the region. We propose that ore formation was achieved via fluid leaching of REE from the BRM, followed by fluid mixing in fault zones, especially in the vicinity of the unconformity between the BRM and overlying Birrindudu Group sandstones. There is significant potential for discovery of further orebodies of this style, especially in the vicinity of regional unconformities, in intercontinental sedimentary basins.

Keywords: Rare earth elements, xenotime, unconformity, isotopic dating, Tanami Region, Halls Creek Orogen

Introduction

Rapid development in high-technology applications such as permanent magnets and renewable energy technologies has promptly increased the demand for rare earth elements (REE). Currently, most of the world's REE supplies come from a single orebody, the Bayan Obo REE-Nb-Fe deposit, China; this restricted source represents a potential geopolitical instability in ongoing global REE supply. Furthermore, both heavy (H) and light (L) REE are sought after commodities, yet most known REE resources across the world, including at Bayan Obo, are rich in LREE. These issues have led to much higher price for HREE relative to LREE. The HREE, particularly Dy, are anticipated to have the highest supply risk in the near future (e.g., Goodenough et al., 2018). Accordingly, there is a strong incentive for discovery and understanding of REE orebodies, particularly those rich in HREE.

Elevated concentrations of the REE have been documented from a variety of geological settings (e.g., magmatic, sedimentary, metamorphic). However, the production of REE has traditionally been dominated by deposits associated with peralkaline silicate magmas and carbonatite-associated complexes (e.g., Chakhmouradian and Zaitsev, 2012; Goodenough et al., 2018), or supergene enrichment environments. Although reported from across the globe, these unusual alkaline or peralkaline rocks are rather minor in the geological rock record, and so to address the current shortage in the REE production, a range of other geological environments where REE can be concentrated into exploitable orebodies are being examined. Newly discovered HREE mineralisation in north-western Australia defines a poorly understood vein and breccia ore style with ore metals contained predominantly in xenotime [(Y,HREE)PO_4] and minor florencite [LREE$Al_3(PO_4)_2(OH)_6$] (Cook et al., 2013; Nazari-Dehkordi et al., 2018). The mineralisation is hosted by the metasedimentary rocks in the Tanami Region, and the Halls Creek Orogen (Fig. 3-1), in an area known as the North Australian HREE+Y (NAHREY) mineral field (Nazari-Dehkordi et al., 2018). Currently defined mineral resources for the NAHREY mineral field are ca. 9 Mt at 0.63% total rare earth oxides (TREO). Wolverine is the largest known deposit, with a total mineral resource of 4.97 Mt at 0.86% TREO (Northern Mineral, 2015). The recognition and characterisation of this style of mineralisation has significant implications for further discovery of HREE, particularly in the North Australian Craton, with widespread Precambrian metasedimentary rocks of potentially suitable age and geochemistry.

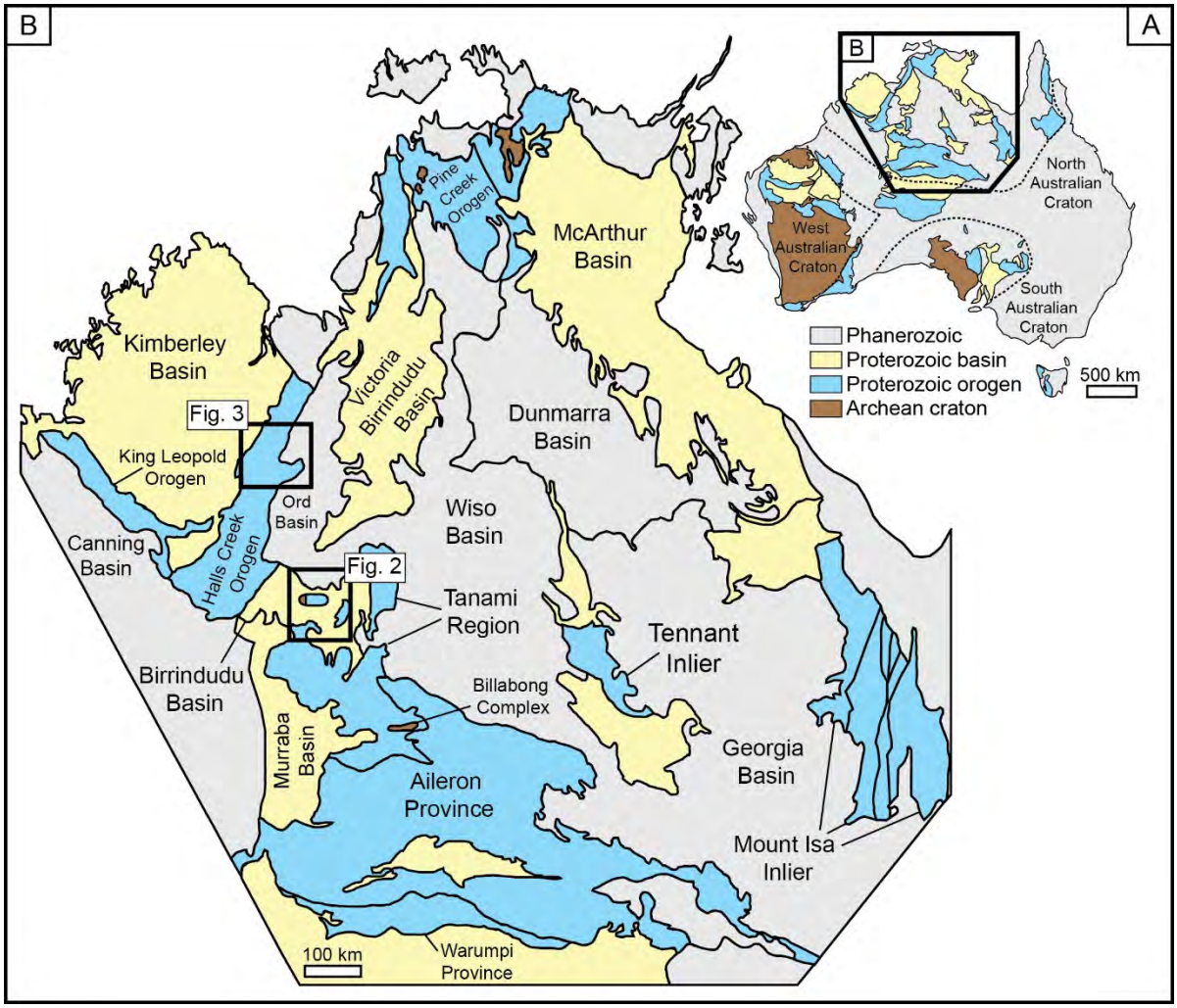

Fig. 3-1: Simplified geological map of Australia showing the three major Australian Cratons (A); (B) Simplified geological map of the North Australian Craton.

In such remote locations where geological relationships are only broadly known, knowledge of the temporal development of mineralisation can greatly aid understanding of the geological history of the district and the processes responsible for ore deposit formation. Xenotime can form over a broad range of geological conditions and is a very useful U-Pb chronometer for dating geological processes ranging from diagenesis (e.g., Vallini et al., 2002), low-grade through to high-grade metamorphism (e.g., Dawson et al., 2003; Sheppard et al., 2007), to hydrothermal mineralisation (e.g., Brown et al., 2002; Aleinikoff et al., 2016). In this paper, we present U-Pb geochronology of ore-related xenotime together with paragenetic relationships from a number of HREE deposits/prospects to understand the genesis and temporal evolution of the NAHREY mineral field. We show that the HREE mineralisation has typical vein-type geometries with a spatial relationship with sub-vertical faults and regional

unconformities. Mineralisation across the field developed in the same time period, and possibly due to similar geological processes, to the unconformity-related uranium deposits of the Pine Creek Orogen in the Northern Territory.

Geological setting

The HREE deposits/prospects of the NAHREY mineral field occur within two domains, the Tanami Region and the Halls Creek Orogen (Fig. 3-1). A summary of the characteristics and location of all the deposits and prospects is provided in Table 3-1, and Figs. 3-2 and 3-3. Most of the deposits/prospects are named after fictional characters of the iconic "X-Men" comic book series of Marvel Comics. Wolverine, Area 5, Banshee, Cyclops, Gambit and West Gambit are classified as deposits, as they each have >0.1 Mt of ore grading at greater than 0.2% TREO, and all are located within the Browns Range Dome (BRD) of the Tanami Region, as described below. Numerous other prospects have been identified within both the Tanami and the Halls Creek Orogen; many of these have potential to be significant HREE resources, but are currently awaiting further exploration work. This study investigates four of the known deposits (Wolverine, Area 5, Banshee and Cyclops) as well as the Dazzler, Longshot, Boulder Ridge and John Galt prospects, although the Wolverine deposit is the main focus of study.

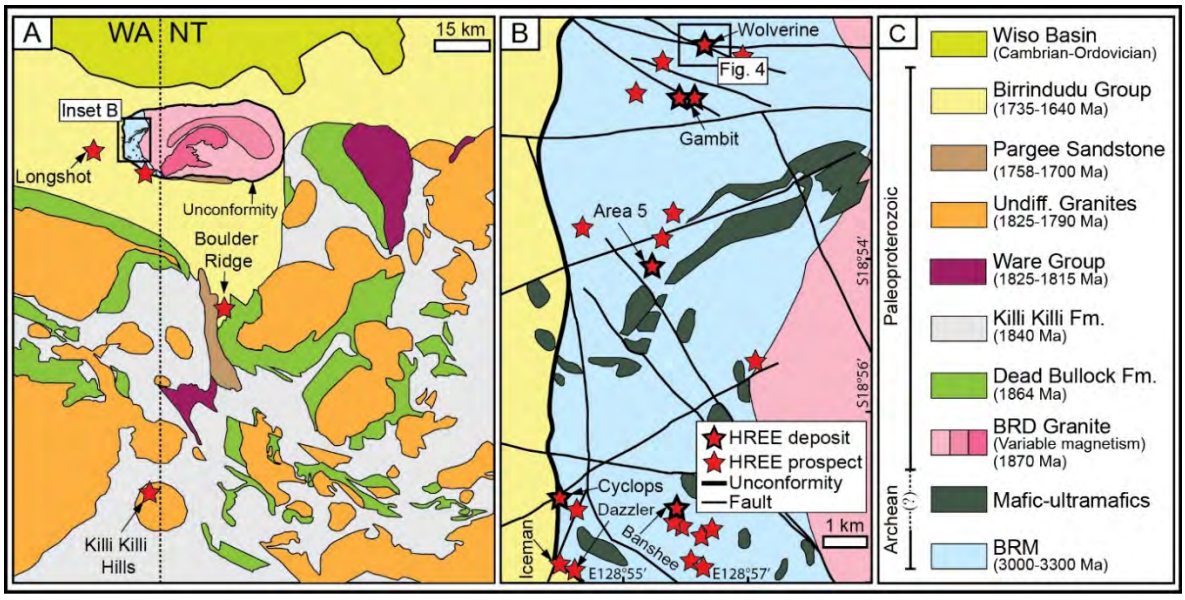

Fig. 3-2: Simplified geological map of the Tanami Region (A) (modified after Bagas et al., 2008); (B) Geological map of the western margin of the Browns Range Dome (after Hendrickx et al., 2000) showing the location of the HREE deposits/prospects; (C) Simplified stratigraphic column of the Tanami Region (after Crispe et al., 2007).

Table 3-1: Characteristics of the main HREE deposits/prospects in northern Australia

	Longitude	Latitude	Host	Proximity to unconformity	Resource (Mt)	TREO (%)	HREE (%)	Ore strike	Age (Ga)	Other
Deposit										
Wolverine	128.9403	-18.8595	BRM	Distal	4.97	0.86	89	WNW	1.65-1.50	
Area 5	128.9249	-18.9024	BRM	Distal	1.52	0.29	69	260°-320°	1.60	Florencite-rich
Cyclops	128.903	-18.9518	BRM	Proximal	0.33	0.27	70	WSW	1.63	
Banshee	128.9289	-18.9552	BRM	Distal	1.66	0.21	87	90°-110°	1.82-1.70	U-rich
Gambit	128.9442	-18.8681	BRM	Distal	0.11	1.13	96	85°-115°	n.a.	
West Gambit	128.9355	-18.8692	BRM	Distal	0.39	1.07	89	80°-90°	n.a.	
Prospect										
Dazzler	128.9082	-18.9741	BRM	Proximal	n.a.	n.a.	n.a.	WSW	1.65-1.62	
Iceman	128.9122	-18.9775	BRM	Proximal	n.a.	n.a.	n.a.	WSW	1.65-1.62	
Longshot	128.8198	-18.9424	BG	Distal	n.a.	n.a.	n.a.	NNW	1.64	
Boulder Ridge	129.2552	-19.8283	BG	Distal	n.a.	n.a.	n.a.	NNW	1.62-1.55	
John Galt	128.2252	-17.2962	RRB	Distal	n.a.	n.a.	94	NNW	1.62-1.57	
Area 5 North	128.9276	-18.8978	BRM	Distal	n.a.	n.a.	n.a.	n.a.	n.a.	Florencite-rich
Banshee South	128.9292	-18.9582	BRM	Distal	n.a.	n.a.	n.a.	NNW	n.a.	
Nightcrawler	128.9295	-18.8926	BRM	Distal	n.a.	n.a.	n.a.	E-W	n.a.	
Mystique	128.9373	-18.9648	BRM	Distal	n.a.	n.a.	n.a.	n.a.	n.a.	
Rogue	128.9618	-19.0095	BRM	Proximal	n.a.	n.a.	n.a.	WNW	n.a.	
Havok	128.9288	-18.8607	BRM	Distal	n.a.	n.a.	n.a.	n.a.	n.a.	
Polaris	128.923	-18.8719	BRM	Distal	n.a.	n.a.	n.a.	n.a.	n.a.	
Rockslider	128.935	-18.9708	BRM	Distal	n.a.	n.a.	n.a.	WNW	n.a.	
Sabretooth	128.9512	-18.9201	BRM	Distal	n.a.	n.a.	n.a.	E-W	n.a.	
Sway	128.9415	-18.964	BRM	Distal	n.a.	n.a.	n.a.	E-W	n.a	

BRM = Browns Range Metamorphics, BG = Birrindudu Group sandstones, RRB = Red Rock Basin, n.a. = Not available. Based on the lateral distance to the regional unconformity, the deposits/prospects are classified as "proximal" (within 50 m of the unconformity) and "distal". Coordinate system WGS84.

Tanami Region

The Browns Range Dome (BRD) is an east-west trending ovoid-shaped structure measuring ca. 60 km by ca. 30 km, situated in the northwest of the Tanami Region (Fig. 3-2). It is cored by a 1 to 3 km thick, largely granitic body, herein named the BRD granite (Hendrickx et al., 2000), of ca. 1.87 Ga age that also includes abundant detrital zircons of ages peaking at ca. 3.1 Ga and ca. 2.5 Ga (Page et al., 1995; Cross and Crispe, 2007). Archean metasedimentary and minor mafic rocks of the Browns Range Metamorphics (BRM) occupy the western section of the dome (Nazari-Dehkordi et al., 2017), and are overlain by Paleoproterozoic sedimentary rocks of the Pargee Sandstone to the south, and the Birrindudu Group to the north, west and south-west (Fig. 3-2).

The BRM crops out over an area of ca. 100 km^2 (Fig. 3-2) and consists mainly of a sequence of greenschist facies (but locally up to amphibolite grade) arkosic metasandstones locally interbedded with medium- to coarse-grained conglomerates and semi-pelitic schists, and less common calc-silicate rocks and banded iron formations. Limited field exposure and deformation have so far precluded detailed stratigraphic descriptions of the sequence. Nazari-

Dehkordi et al. (2017) constrained the timing of deposition of the BRM to between ca. 3.0 Ga and ca. 2.5 Ga, based on the age of the detrital zircons in the BRM, and the emplacement timing of the small (10s to 100s of m) cross-cutting granitic, syenitic and pegmatitic intrusions.

Unconformably overlying the BRM are a thick sequence of Paleoproterozoic sedimentary rocks with rare volcanic units (Fig. 3-2), which have been described in detail by Bagas et al. (2008) and Crispe et al. (2007). The oldest Paleoproterozoic unit of the Tanami Region is the ca. 1.86 to ca. 1.84 Ga Tanami Group, which is unconformably overlain by the ca. 1.83 to ca. 1.81 Ga Ware Group, and then the Mount Charles Formation (ca. 1.80 Ga; Crispe et al., 2007). These units were deformed, domed and then intruded by extensive ca. 1.83 to ca. 1.79 Ga granitoids (Smith, 2001), which was also synchronous with gold mineralisation of the region (Bagas et al., 2007). These rock sequences are in turn unconformably overlain by shallow-dipping sedimentary rocks of the Pargee Sandstone and Birrindudu Group, which were deposited between ca. 1.78 to ca. 1.64 Ga (Crispe et al., 2007). The ca. 6 km thick Birrindudu Group consists of three conformable units including the basal Gardiner Sandstone, the fine-grained calcareous Talbot Well Formation, and Coomarie Sandstone (Blake et al., 1975).

The Gardiner Sandstone, occupying a vast area of the Tanami Region (Fig. 3-2), was deposited within a shallow marine to intertidal environments on a stable continental margin (Clark and Blockley, 1960). The Gardiner Sandstone is weakly metamorphosed and mildly deformed, and unconformably rests on the underlying deeply weathered and metamorphosed rocks of the BRM, Tanami Group, Ware Group and Pargee Sandstone (Crispe and Vandenberg, 2005). It forms the outer margins of the BRD, with gentle (5 to 25º) westerly dips in the west in the vicinity of the HREE mineralisation, and easterly dips in the east of the dome. The depositional age of the Gardiner Sandstone, and generally the Birrindudu Group, is constrained by the youngest detrital zircon age of ca. 1.7 Ga (Crispe and Vandenberg, 2005; Nazari-Dehkordi et al., 2017) and the ca. 1.64 Ga age of the xenotime overgrowing detrital zircons of the Gardiner Sandstone of the Birrindudu Group at the Killi Killi Hills (Vallini et al., 2007, see Fig. 3-2). In the study area, the Gardiner Sandstone directly lies on the Mesoarchean-derived BRM, leaving a sedimentation hiatus of ca. 800 m.y. (Nazari-Dehkordi et al., 2017).

Halls Creek Orogen

The Halls Creek Orogen (Fig. 3-3), located immediately west of the Tanami Region, is a north-northeast trending orogenic belt unconformably overlain by the Kimberley, Speewah and Carr-Boyd Basins to the west and northwest, by the Victoria, Birrindudu, Ord and Osmond Basins to the east and southeast, and by the Canning and Louisa Basins to the south. The Halls Creek Orogen records ca. 130 m.y. of sedimentation, deformation, metamorphism and magmatism, from ca. 1.92 Ga to ca. 1.79 Ga that culminated in the collision of the Kimberley Craton with the North Australian Craton (Page et al., 2001).

The Orogen consists of three distinct metamorphic zones including Eastern, Central and Western Zones, of which the Western and Central Zones correspond to proximal and distal parts of the Kimberley Craton, respectively. The Eastern Zone reflects the passive margin of the North Australian Craton. Different aspects of these zones are discussed in detail in Tyler et al. (1995) and Page et al. (2001). During the ca. 1.87-1.85 Ga Hooper Orogeny, metamorphic sequences of the Western Zone were deformed, and the Central Zone (an island arc) was accreted onto the eastern margin of the Kimberley Craton (Sheppard et al., 1999). These rock units were intruded by syn-orogenic intrusions associated with the ca. 1.84-1.81 Ga Halls Creek Orogeny, during which the North Australian Craton (Halls Creek Group of the Eastern Zone) collided with the Kimberley Craton (Sheppard et al., 1999). The orogenic rocks were subsequently unconformably overlain by rocks of the ca. 1.83 to 1.79 Ga Speewah Group and Kimberley Basin, which are broadly equivalent to the ca.1.80 Ga Red Rock Basin (Tyler et al., 1995; Page et al., 2001) that hosts the John Galt HREE prospect. The poorly-studied Red Rock Basin largely comprises fine- to coarse-grained quartz-rich sandstones with interlayers of pebbly sandstone and conglomerate (Blake et al., 2000). The Red Rock Basin shows, possibly structurally-controlled, rapid lateral variation and fining to the east, and is bounded by the prominent Angelo–Halls Creek–Osmond Fault System (Sheppard et al., 1999). To the east the Red Rock Basin is unconformably overlain by Paleoproterozoic Osmond Basin and the poorly-exposed Birrindudu Group sandstones (Hancock and Rutland, 1984).

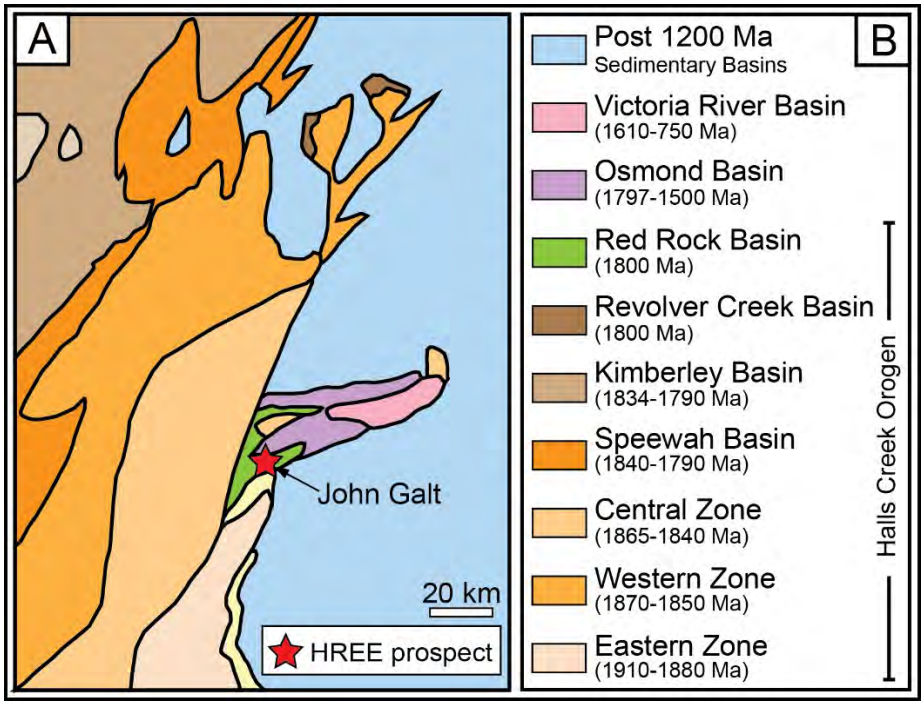

Fig. 3-3: (A) Simplified geological map and (B) stratigraphic column of the Halls Creek Orogen with the location of the John Galt HREE prospect (modified after Tyler et al., 1995, and Page et al., 2001).

Analytical methods

Sampling and petrography

During a program of fieldwork, ore samples were collected from surface outcrops and drill cores acquired by Northern Minerals Ltd. Although sampling focussed in and around the Wolverine deposit, representative samples of most of the deposits/prospects were collected. The samples were lightly brushed and washed in an ultrasonic bath to remove any contamination from drilling mud or soil. Representative samples were then prepared as thin sections for petrographic studies using conventional optical microscopy and scanning electron microscopy.

Whole rock geochemistry analyses

On the order of 12,000 diamond core and drill chip samples were analysed for REE and selected major and minor elements as part of mineral exploration and resource definition work by

Northern Minerals Ltd. All analytical work was completed by Intertek-Genalysis Mineral Services. The samples were dried, crushed, split and pulverised. To ensure complete dissolution of refractory minerals (e.g., xenotime), a 0.25 g aliquot of each sample was fused with 2 g of Na_2O_2 within a nickel crucible by heating to 700 °C for at least 30 minutes. Once cooled, the quenched glass was dissolved with 2 ml of HCl. The final solution, containing no solid deposits indicating a complete dissolution of the sample, was then diluted to 500 ml with deionised water. The final solution was then analysed by inductively coupled plasma mass spectrometry (ICP-MS). Further analytical information are provided in Meisel et al. (2002). The assay data can be provided by the authors on request.

Three dimensional orebody modelling

The Leapfrog Geo three-dimensional modelling software was used to visualize the ore geometry and the grade distribution at Wolverine deposit. Assay data from core samples of approx. 300 individual drill holes were imported and projected into the 3D model. The ore grade (wt.% TREO) was modelled as four shells of >0.25 (high grade), 0.25-0.15, 0.15-0.10 and <0.10 (low grade). To avoid artificial oscillations, the reconstructed shape of each shell was considered the best-fit smooth pattern connecting the corresponding grades through the drill cores. The distribution of the ore grades was used to aid the structural interpretations.

Electron probe microanalysis

Backscattered electron (BSE) imaging and mineral identification and characterisation of samples was undertaken using a JEOL-JXA8200 super probe, housed at the Advanced Analytical Centre (AAC), James Cook University (JCU). Quantitative major element analysis of pre- and syn-ore white mica was conducted by wavelength dispersive spectrometry (WDS) from carbon-coated polished thin sections using a 20 nA beam defocused to 5 µm, and accelerating voltage of 15 kV. The elements measured were Na, Fe, Ca, Si, K, Al, Mn, Cl, Mg, Ti and F. Natural and synthetic standards were used for calibration and the Armstrong-CITZAF (phi-rho-Z) matrix correction procedure (Armstrong, 1991) was applied to all analyses. Further information on the analytical conditions are presented in Appendix 3-1.

In-situ xenotime U-Pb isotope geochronology

In-situ laser ablation (LA) ICP-MS U-Pb dating of xenotime was conducted at the AAC, JCU, using a GeoLas Pro 193 nm excimer laser, and a Bruker (formally Varian) 820-MS ICP-MS. The ICP-MS was tuned to ensure approximately equal sensitivity of U, Th and Pb (e.g., see Pettke et al., 2012) to minimize isotope fractionation due to matrix effects. Further details of the instrumental and analytical set-up are available in Spandler et al. (2016). Analytes collected were ^{31}P, ^{89}Y, ^{204}Pb, ^{206}Pb, ^{207}Pb, ^{208}Pb, ^{232}Th, ^{235}U and ^{238}U. The standards used for calibration include z6413 (primary), MG-1 (secondary) and BS-1 (secondary) xenotime (Fletcher et al., 2004). All analyses were undertaken using a 24 µm beam diameter, and laser energy density on the sample of 6 J/cm^2, and data reduction was carried out using the GLITTER software (Van Achterbergh et al., 2001). All time-resolved single isotope signals from standards and samples were filtered for signal spikes or perturbations related to inclusions and fractures. Subsequently, the most stable and representative ratios were selected taking into account possible mixing of different age domains and zoning. The accuracy of the technique is demonstrated via analysis of secondary standards MG-1 and BS-1; these returned ages of 492 ± 3 Ma, and 506 ± 5 Ma, respectively, which compare well with the published values of 490.1 ± 0.6 Ma for MG-1 and 508.8 ± 0.6 Ma for BS-1 (Fletcher et al., 2004).

^{40}Ar-^{39}Ar geochronology

Five samples of foliation-aligned pre-ore muscovite were selected from both well-mineralised and weakly-mineralised samples of metasedimentary rocks of the Wolverine and Area 5 deposits. Further information on the source locations of these samples are provided in Appendix 3-2. The samples were crushed and sieved to 60 to 80 mesh (0.25 to 0.17 mm) and then white mica flakes were carefully hand-picked to achieve about 95% purity. After cleaning in an ultrasonic ethanol bath, the grain separate underwent subsequent handpicking under a binocular microscope to achieve >99% purity mineral separate. $^{40}Ar/^{39}Ar$ analyses were performed at the Argon Geochronology Laboratory of the University of Michigan using a continuous laser for step-heating and a VG 1200S noble gas mass spectrometer equipped with a Daly detector operated in analog mode using the methods outlined in Streepey et al. (2000) and Keane et al. (2006). Samples were wrapped in aluminium foil, loaded into an aluminium tube, then sealed into a quartz bottle and irradiated for 10.83 h at the McMaster Nuclear reactor.

Neutron flux gradients were monitored with the MMhb-1 standard using an age of 520.4 Ma (Samson and Alexander, 1987). Following irradiation, 1 to 4 grains from each packet were loaded onto a copper disc that was placed into a gas extraction line. An Ar-ion laser, defocused to allow uniform heating, was used to heat the grains on the sample disc. Heating steps were performed for 30 to 60 s with a minimum power of 40 mW for the first step and a maximum power of 2000 mW for the last step. Isotopic ratios were measured on a MAP-215 mass spectrometer following the procedure described by Meert et al. (1994) and Busch et al. (1996). More details of the $^{40}Ar/^{39}Ar$ step-heating measurements are reported in Appendix 3-3.

Results

Geometry and geological setting of the Wolverine deposit

All of the examined HREE deposits/prospects have a spatial and an apparent kinematic relationship with faults and, in many cases, lithological boundaries. The structural relationships with mineralisation is best expressed by the Wolverine deposit, which lies along a WNW-striking fault at an intersection with a cross-cutting W-E trending fault (Fig. 3-4A). Long and cross sections (Figs. 3-4B-C) reveal Wolverine to be a typical vein-type orebody sitting within the steeply (~75° N) dipping WNW-striking fault. The orebody has a strike length of over 400 m and remains open to a depth of ca. 550 metres, and has no significant lateral or vertical ore metal zonation. The orebody appears to have developed either by dilation at this fault junction or by dilation due to bending along the WNW-striking fault, and the tabular, steep-plunging nature of the main ore zone suggests a strike-slip fault movement component contributed to the dilatancy. The displacement on the fault is as yet unknown, as there are few markers in the wall rocks. High-grade ore is defined by a stockwork of thick (up to 1 m) veins and breccia, surrounded by a halo of lower grade rock with thinner, broader spaced veins and less developed brecciation. A significant feature is the occurrence of discontinuities in the orebody, potentially recording post-ore multi-stage doming of the BRD, accompanied by the development of low-grade ore into the host rock. These low-grade zones are inferred to represent minor post-ore remobilisation, either as a product of supergene processes, or as silica-rich fault zones infilled by HREE-poor veins late in the overall hydrothermal history.

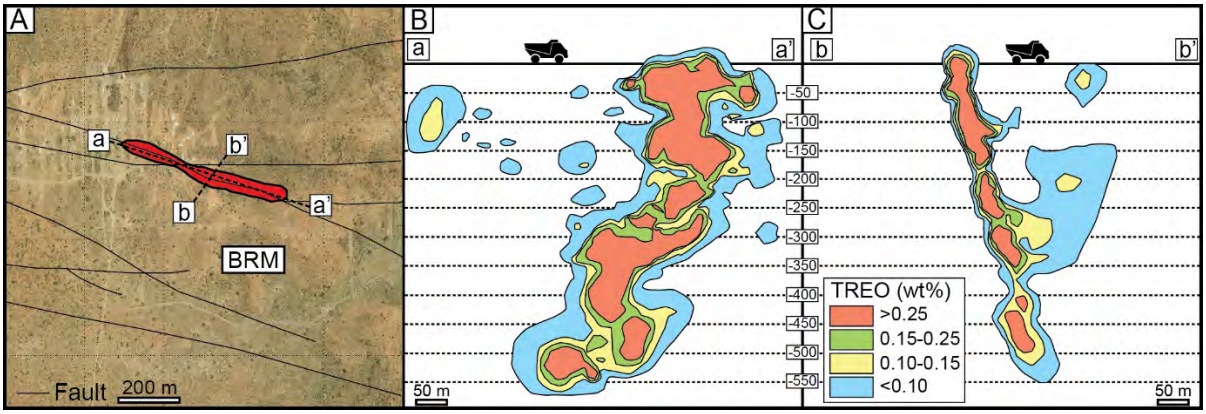

Fig. 3-4: Plan view (A) and long (B) and cross (C) sections of the Wolverine orebody represented by TREO grade shells. See Figure 2B for location of the Wolverine deposit. Note that plane view (A) displays the surface expression of the orebody that reaches the surface only in one area (see B, C).

Geological setting of the other HREE deposits/prospects

Despite their wide distribution, other BRM-hosted deposits/prospects predominantly occur near, or on, the unconformity with the overlying Gardiner Sandstone (e.g., Iceman, Dazzler, and Cyclops). These other deposits/prospects are dominated by hydrothermal mineralised veins and breccias that developed alongside major faults (Fig. 3-2); hence, they have many structural similarities with Wolverine. Mineralisation tends to be developed along steeply-dipping W- to SW-striking structures, or along the unconformity surface itself. The Area 5 deposit is distinguished by its high content of LREE compared to other deposits/prospects, as outlined below. Mineralisation at Area 5 occurs at an intersection of sub-vertical fault zones with prominent W and NW strikes, alongside which the orebody appears as discontinuous pods.

The Banshee deposit (Fig. 3-2) is also distinct from other BRM-hosted deposits/prospects in geochemistry and age (see below), and so is discussed separately here. Banshee lies within a topographic low in the landscape, whereas Wolverine and other deposits/prospects studied here are located along low ridges, or topographic highs. The mineralisation at Banshee is characterised largely by E-W striking hydrothermal breccias and laminated veins that cut the BRM, and dip steeply (65°-85°) to the north. The mineralised zones vary in width from less than one metre up to 10 m, but terminate at depths of 50 to 120 metres where the BRM is underlain by a package of quartz-chlorite schist of possible sedimentary origin. Airborne

magnetic surveys show an approx. 2 km by 1.2 km ovoid-shaped anomaly directly beneath the Banshee deposit. This anomaly is tentatively interpreted to be an igneous intrusion.

Prospects hosted by the Gardiner Sandstone of the Birrindudu Group (Longshot, Boulder Ridge) also demonstrate close association with faults and regional unconformities. Longshot lies to the west of the BRD (Fig. 3-2A) at a location that is between 200 to 1200 m above the unconformity surface with the underlying BRM, as suggested by the available structural and geophysical data. Mineralisation at Longshot occurs within irregular hydrothermal quartz-cemented veins and breccias developed along mostly NNW-striking fault structures that extends outwards and upwards from the BRD, thus showing structural and potentially genetic relationships with the BRM-hosted deposits/prospects. Similarly, xenotime-quartz vein mineralisation at Boulder Ridge, located approx. 40 km south of the BRD, occurs near the unconformity with underlying metasedimentary rocks of the Tanami Group.

John Galt is currently the only recognised xenotime mineralisation outside of the Tanami Region; it is hosted by the metasedimentary rocks of the Red Rock Basin adjacent to an unconformity with older metamorphic rocks of the Halls Creek Orogen (Fig. 3-3). Mineralisation crops out as networks of quartz-xenotime veins along major N-S oriented faults and, most distinctively, along a ca. 100 metre high ENE-trending escarpment. Preliminary drilling results along the escarpment confirm that the main orebody continues to a depth of at least 100 m and likely to much deeper levels, as found in the Brown Range. John Galt is particularly rich in HREE (averaging 94% of TREO; see Table 3-1), which, together with reports of other mineralisation occurrences in the region, suggest this area is especially prospective for further exploration.

Bulk ore geochemistry

Ore minerals at all the deposits/prospects are limited to xenotime and florencite only (see below), yet there are notable variations in the geochemistry of the ore elements (REE+Y), as well as P and U between different deposits/prospects. In particular, we examine the compositional variants from the three largest and most diverse deposits Wolverine, Area 5 and Banshee. Bulk ore geochemistry of Wolverine is characterised by positive correlations between Ce (and LREE), Y (and HREE), U and P (Figs. 3-5A-C), as may be expected for an ore mineral

assemblage consisting of xenotime as the host of HREE, Y (and U), and florencite as the host of LREE. Area 5 and Banshee are comparatively poorer in P (Figs. 3-5A-B). Ore from Banshee extends to high U contents, and shows a broad negative correlation with Ce (Fig. 3-5D), indicating florencite is a relatively minor ore mineral and does not host most of the U. Although there is a poor relationship between U and P (Fig. 3-5E) at Banshee, we have found no other U-bearing minerals (e.g., uraninite), so U is likely primarily hosted in xenotime. Ore from Area 5 also shows an overall positive relationship between Ce, Y, U and P, although less well defined than at Wolverine. However, Area 5 ore extends to higher LREE contents than the other deposits (Fig. 3-5A), which is indicative of the relative dominance of LREE-rich florencite compared with HREE+Y-rich xenotime.

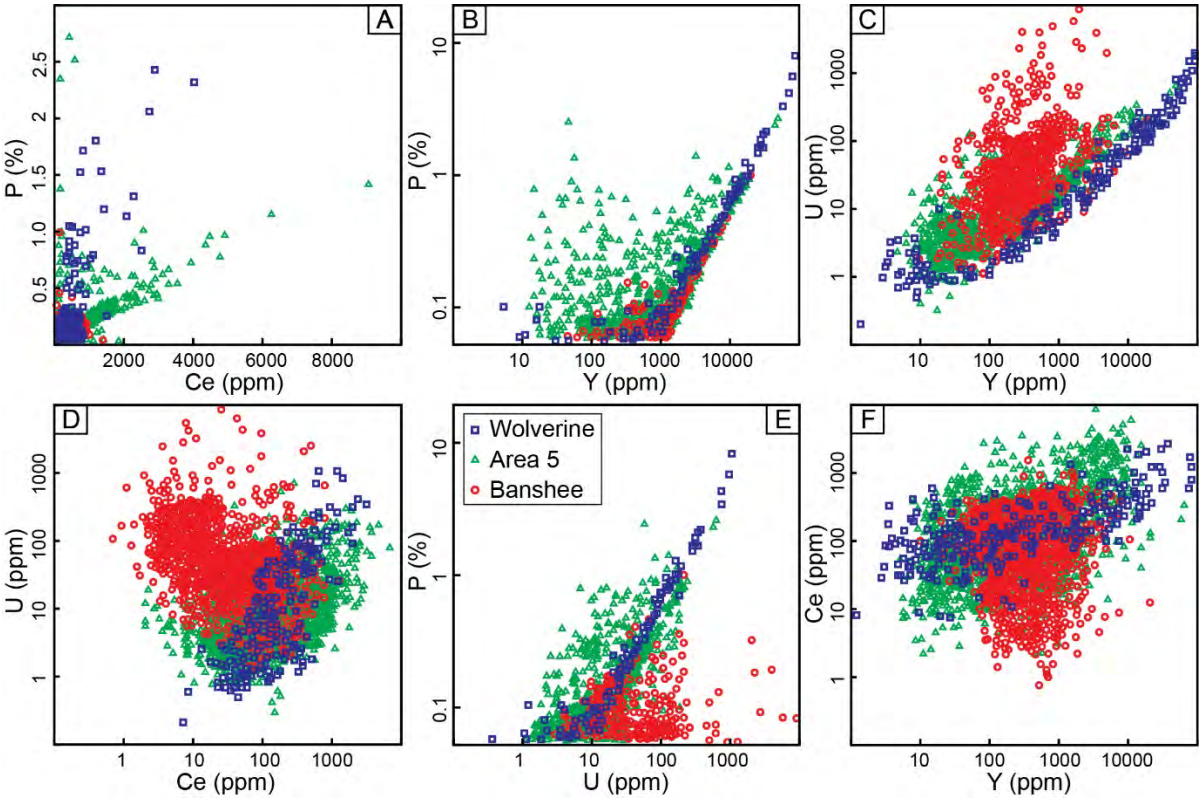

Fig. 3-5: Scatterplots of P, Y, Ce and U for whole-rock assay data from the Wolverine, Area 5 and Banshee deposits.

We also use bulk-rock geochemistry data from the Wolverine deposit to examine alteration of major (i.e., none ore) elements within the host rock during mineralisation. Al-Si-K systematics (Fig. 3-6A) reveals a relatively broad compositional range for the unmineralised BRM, consistent with the occurrence of quartz, alkali feldspar (predominantly K-feldspar) and

muscovite in various proportions, which is in agreement with petrographic observations (Nazari-Dehkordi et al., 2017), and likely represents protolith variations. Some highly aluminous samples represent kaolinite rich alteration zones. Quite distinct from the non-mineralised rocks, almost all the bulk ore samples lie on, or close to, the muscovite (white mica) and quartz tie-line, with much of the quartz as a key vein constituent with the ore minerals. This conversion of a range of original bulk compositions to a very specific muscovite-quartz composition is a typical indicator of large metasomatic fluid fluxes (Korzhinskii, 1970), suggestive of association of the mineralisation with a muscovite alteration. Ore formation is also associated with some Fe enrichment in the form of hematite (Fig. 3-6B) as found in some breccias and veins (see below). Nevertheless, overall most ore samples do not have elevated Fe contents compared to the host BRM samples.

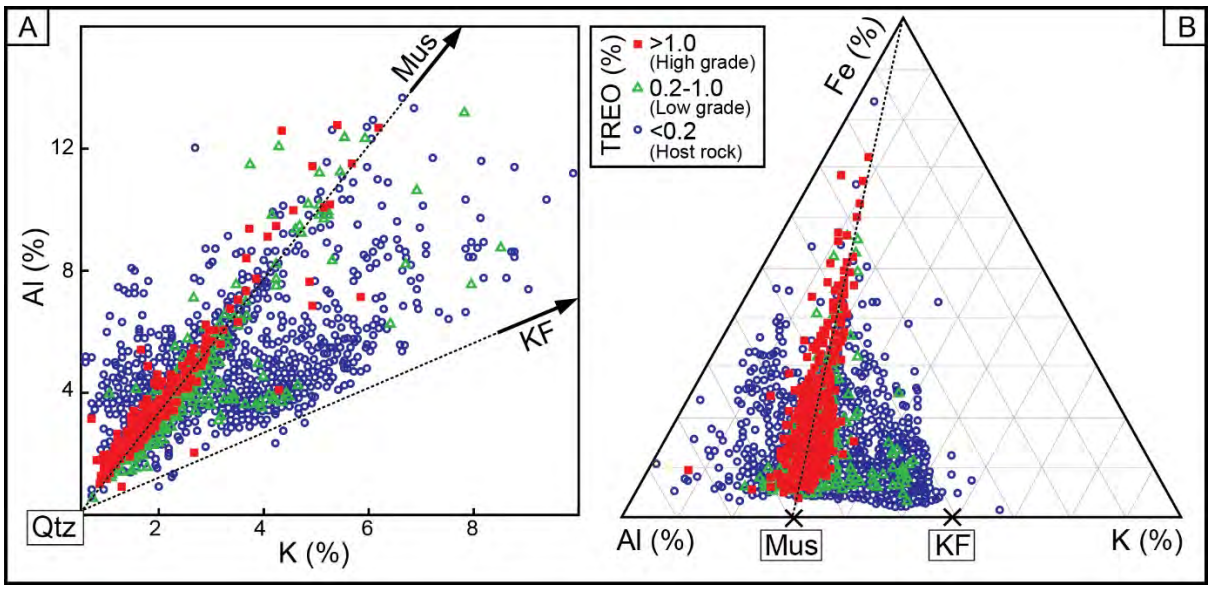

Fig. 3-6: (A) Whole-rock Al versus K; and (B) Al-Fe-K ternary plot for the core samples (n = ca. 8300) from the Wolverine Deposit. Compositions and tie lines between quartz (Qtz) and k-feldspar (KF), and quartz and muscovite-illite (Mus) are shown.

Ore mineral assemblage and paragenesis

A mineral paragenetic sequence was established on the basis of field observations and microscope petrographic studies. Although this paragenetic sequence is based mainly on the samples collected from Wolverine, available field, petrographic, geochemical and isotopic data from across the NAHREY mineral field indicate remarkable consistency among the

mineralisation occurrences. The minerals associated with the orebody and the host metasedimentary rocks can be divided into three general categories: (1) detrital and metamorphic assemblages, which reflect mainly a greenschist-facies overprint on the predominantly meta-arkosic host rocks; (2) hydrothermal minerals related to the mineralisation event(s), and; (3) hydrothermal minerals that formed after the mineralisation event(s) (Fig. 3-7).

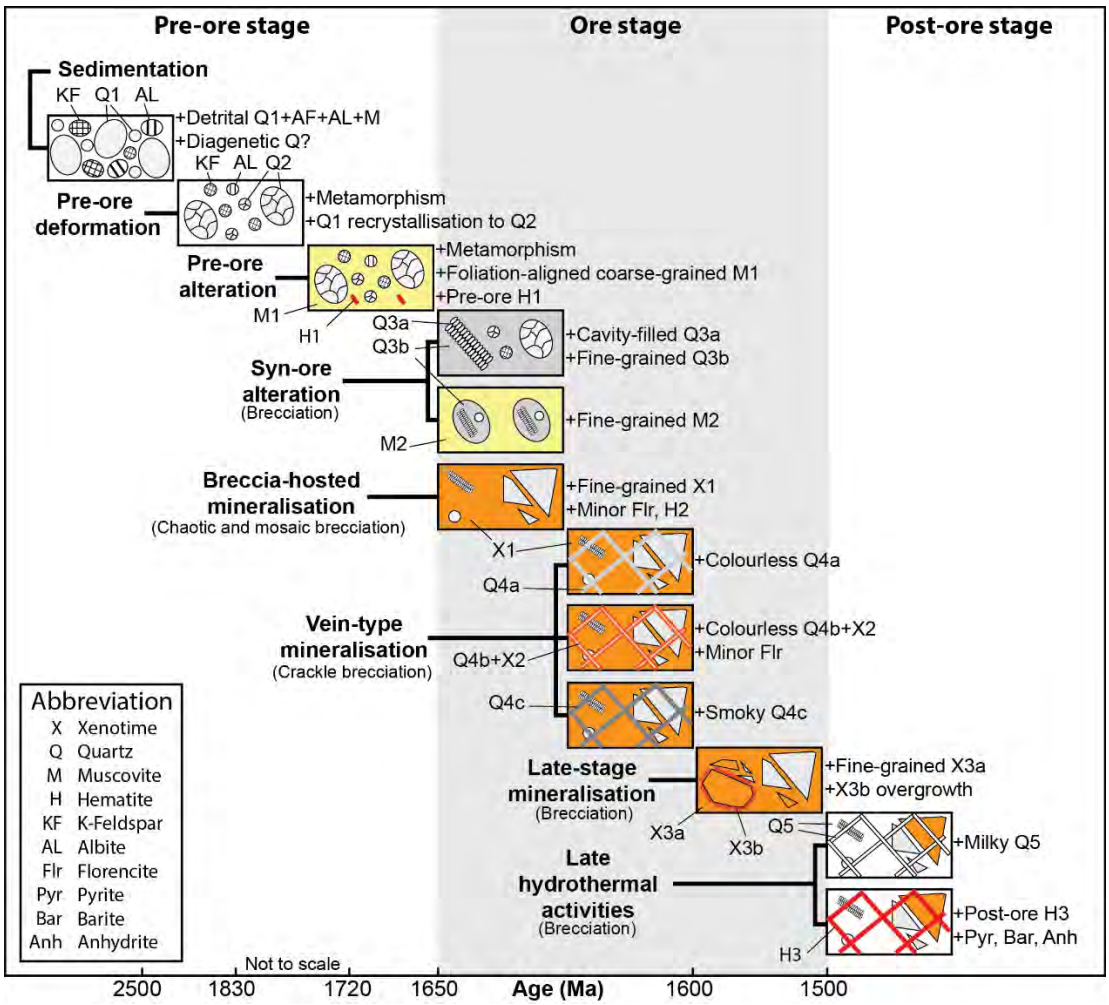

Fig. 3-7: Three-stage mineral paragenesis associated the HREE mineralisation and the host metasedimentary rocks. See text for details.

Stage 1: Pre-mineralisation alteration stage

The BRM consists of detrital phases including quartz and feldspar of variable morphology and size, and also detrital zircon. However, subsequent metamorphic and hydrothermal overprints

led to a nearly complete obliteration of the original grain textures and morphology (Nazari-Dehkordi et al., 2017). The first recognisable post-sedimentation mineral/structural paragenesis in the BRM is a locally well-developed schistose foliation associated with the recrystallisation of detrital quartz (Q1) into poly-crystalline quartz patches (Q2) that have undulose extinction and tangential, concavo-convex or sutured contacts between grains (Fig. 3-8A). These features are interpreted to be the result of deformation and greenschist-grade metamorphism related to the regional Tanami event at ca. 1.83 Ga (Crispe et al., 2007).

The pre-mineralisation alteration stage also includes a sericite + muscovite (M1) alteration assemblage that replaced detrital alkali feldspar of the BRM (Fig. 3-8B). The white mica alteration manifests as platy coarse muscovite grains of up to 0.5 mm in length, aligned in the metamorphic foliation (Fig. 3-8B). This foliation-parallel assemblage occurs most prominently with mineralisation, but is traceable for several metres away from the orebodies. Additionally, hematite (H1) may occur as interlayers with sericite and larger muscovite grains (Fig. 3-8C), but is absent where overprinted by later alteration stages.

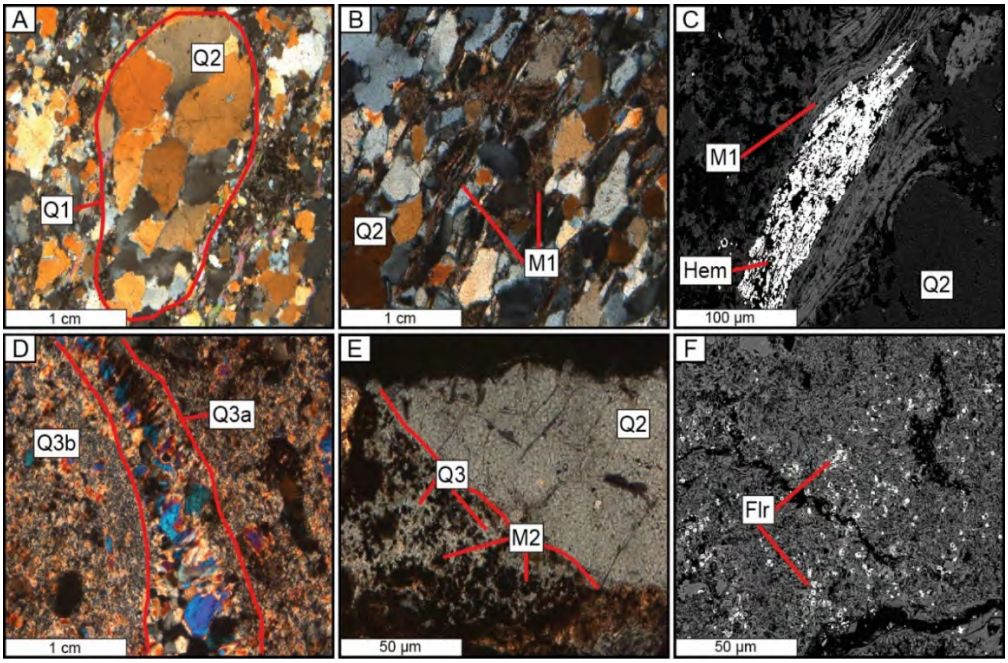

Fig. 3-8: Back-scattered electron and cross-polarised transmitted-light microscopic images of samples of the BRM. (A) A primarily large detrital quartz (Q1) recrystallised into a polycrystalline quartz (Q2); (B) Course-grained muscovite aligned in the pre-ore foliation; (C) Interlayer of hematite and pre-ore course-grained muscovite; (D) Syn-ore quartz alteration appearing as cavity-filled (Q3a) and fine-grained (Q3b) in breccia; (E) Regrowth of a detrital quartz during quartz-white mica alteration; (F) Tiny authigenic florencite enclosed in clay. Q = quartz; M = muscovite; H = hematite; Flr = florencite.

Stage 2: Syn-mineralisation alteration, veining and breccia

Syn-mineralisation alteration consists dominantly of fine-grained quartz and muscovite-sericite-illite (white mica, M2) that also contains minor hematite (H2) developed mainly in the fault zones. The quartz appears as cavity- and fracture-filled quartz (Q3a), which typically displays radial extinction, cemented by finer grained quartz (Q3b) (Fig. 3-8D), and also as quartz replacing pre-existing detrital quartz (Q2) (Fig. 3-8E). This fine-grained association is more intense adjacent to the HREE mineralisation and related faults, and is characterised in part by overprinting and replacement of the earlier-formed, foliation-parallel assemblages described above (Fig. 3-8B).

The syn-ore alteration event was succeeded by the earliest phase of the ore mineralisation, herein called “breccia-hosted” mineralisation. The breccia system is characterised by a set of chaotic and mosaic breccias occurring along steeply dipping major faults of usually a few meters width. The chaotic breccias tend to occupy a narrow (~1 m) core of the mineralised zone and are composed primarily of small rounded to sub-rounded clasts of the metasedimentary rocks of variable size (rarely >3 cm), with no traces of earlier mineralisation. The breccia matrix is largely composed of ore minerals and associated syn-ore quartz-white mica alterations. Chaotic breccias are enveloped by mosaic breccias, which consist mainly of medium to large (2 mm to >20 cm) clasts of metasedimentary rocks that display fitted-fabric texture. The mosaic breccias tend to occupy wider intervals (up to 4 m in width) of the mineralisation zones, and host ore of variable grade, depending on the relative volume of the breccia matrix.

The breccia-hosted mineralisation (Figs. 3-9A-C) is dominated by xenotime (X1) and minor florencite, which occur in the breccia matrix, as well as in fractures, cavities, and also within quartz-white mica alteration assemblages. Morphologically, X1 appears as clusters or as individual crystals (Fig. 3-10A) of dominantly anhedral grains that range in size from a few µm to over 200 µm. X1 also appears as pyramid-shaped overgrowths on detrital zircon (Fig. 3-10B). Xenotime (X1), particularly as coarser grains, is partially replaced by late florencite (Fig. 3-10C).

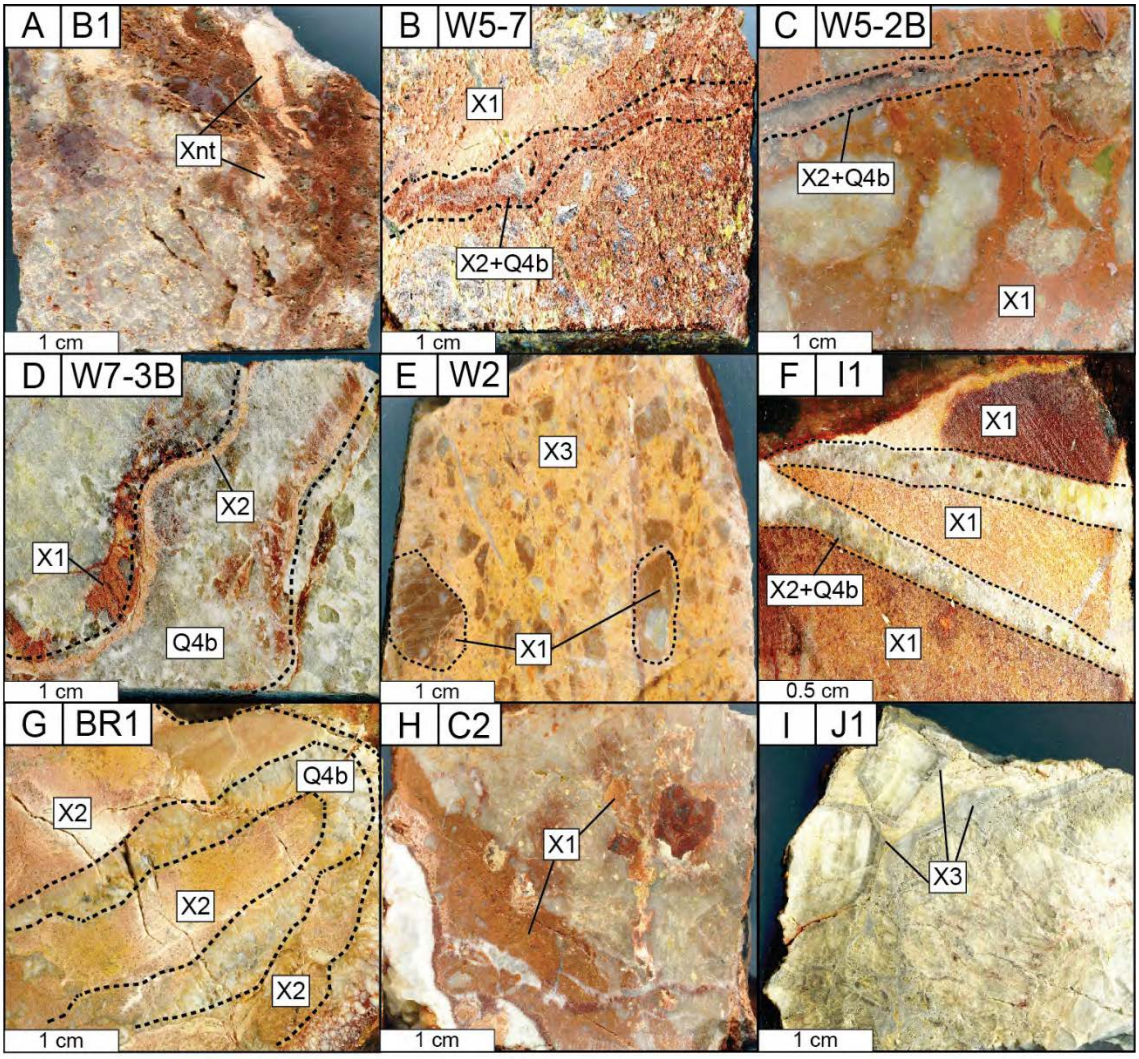

Fig. 3-9: Hand specimen photos of ore from various HREE deposits/prospects. (A) Sample B1 from Banshee; (B-E) Samples W5-7, W5-2B, W7-3B, W2; (F) Sample I1 from Iceman; (G) Sample BR1 from Boulder Ridge; (H) Sample C2 from Cyclops; (I) Sample J1 from John Galt. X = xenotime; Q = quartz.

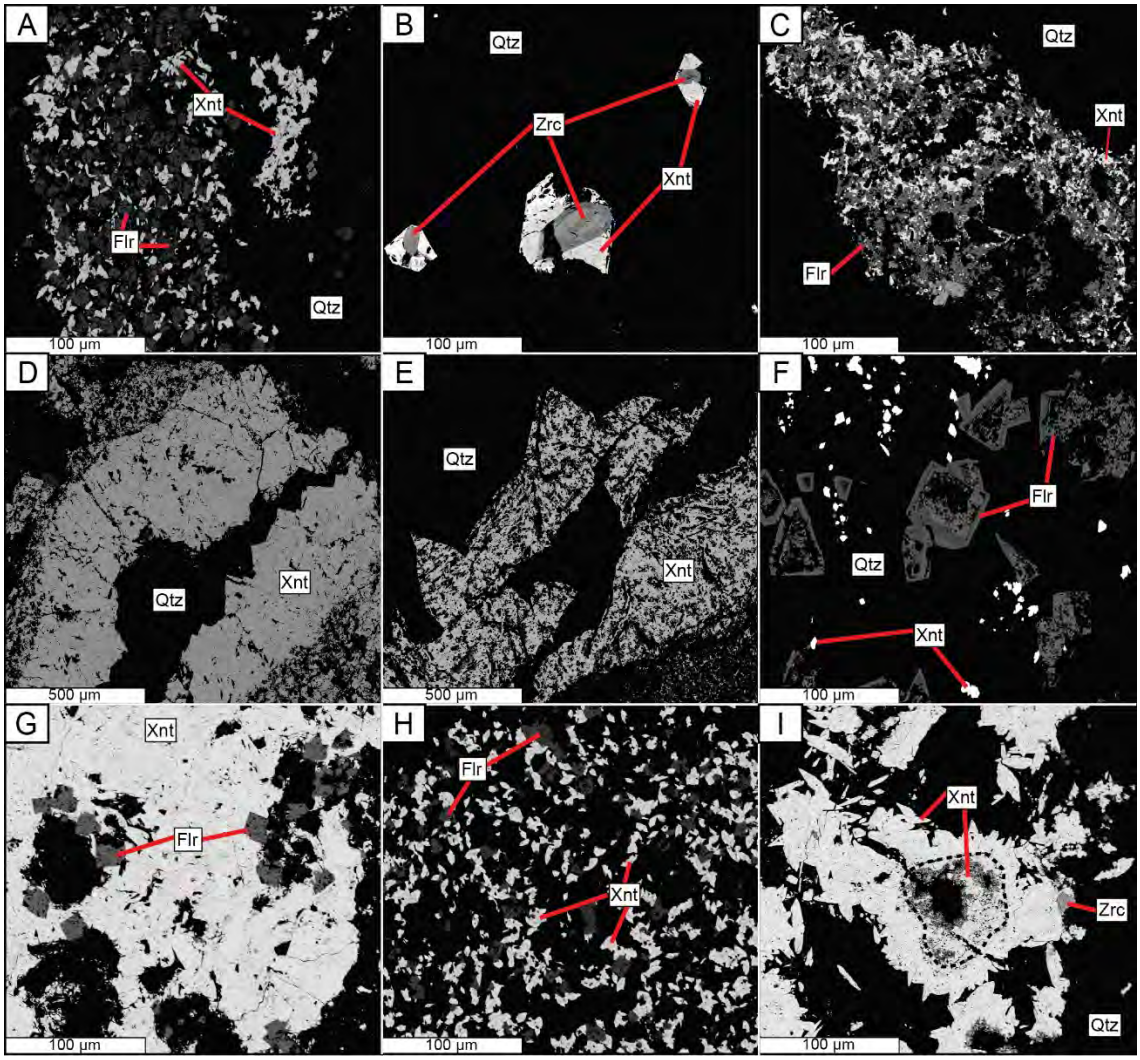

Fig. 3-10: Back-scattered electron microscopic images of ore minerals from Wolverine deposit. (A) Euhedral to anhedral fine-grained breccia-hosted xenotime and associated florencite; (B) Xenotime overgrowing detrital zircons; (C) Breccia-hosted xenotime almost entirely replaced by florencite; (D) Course-grained xenotime cross-cutting breccia-hosted xenotime; (E) Vein-type pyramid-shaped xenotime ore (F) Florencite and xenotime distributed within a mineralised hydrothermal quartz vein; (G) Co-genetic xenotime and florencite; (H) Late fine-grained xenotime in the matrix of a breccia containing mineralised clasts; (I) Late pyramid-shaped xenotime overgrowing earlier fine-grained xenotime.

Stage 3: Vein-type mineralisation

The breccia-hosted mineralisation and adjacent hosting rock are crosscut by hydrothermal veins (Figs. 3-9B-C), which in the most intense cases have formed crackle breccias in which the angular clasts of the metasedimentary rocks (themselves commonly already brecciated) are

arranged in a jigsaw puzzle pattern with no major displacement. The hydrothermal veins vary from a few mm up to 20 cm in width and are composed of quartz (Q4) and xenotime (X2). Q4 includes multiple quartz types. Q4a is colourless and transparent quartz that pre-dates xenotime (X2) (Fig. 3-11A), and likely marks the onset of the hydrothermal event associated with the "vein-type" mineralisation stage. X2 + Q4b veins overprint Q4a (Fig. 3-11A), and consist primarily of colourless quartz veins of usually ~1 cm in width, which are in turn cut by smoky Q4c veins that have a vuggy texture (Fig. 3-11B). In places the primary X2 veins were reopened (Fig. 3-11C) or broken and offset (Fig. 3-11D) due to repeated fracturing and minor fault displacement of the host rocks.

Xenotime (X2) occurs as blade- or pyramid-shaped grains ranging in size from 50 µm to 1000 µm (Fig. 3-10D). X2 is usually fractured and pitted, and displays subtle zoning in BSE images, (Fig. 3-10E). Euhedral equant florencite grains (~1 to ~30 µm) occur within Q4 (Fig. 10F) or X2 (Fig. 3-10G) and are interpreted to be co-genetic to Q4 + X2 veins. Typically, large florencite grains demonstrate a subtle oscillatory zoning in BSE, in which the rim appears to be brighter than the core zone (Fig. 3-10F).

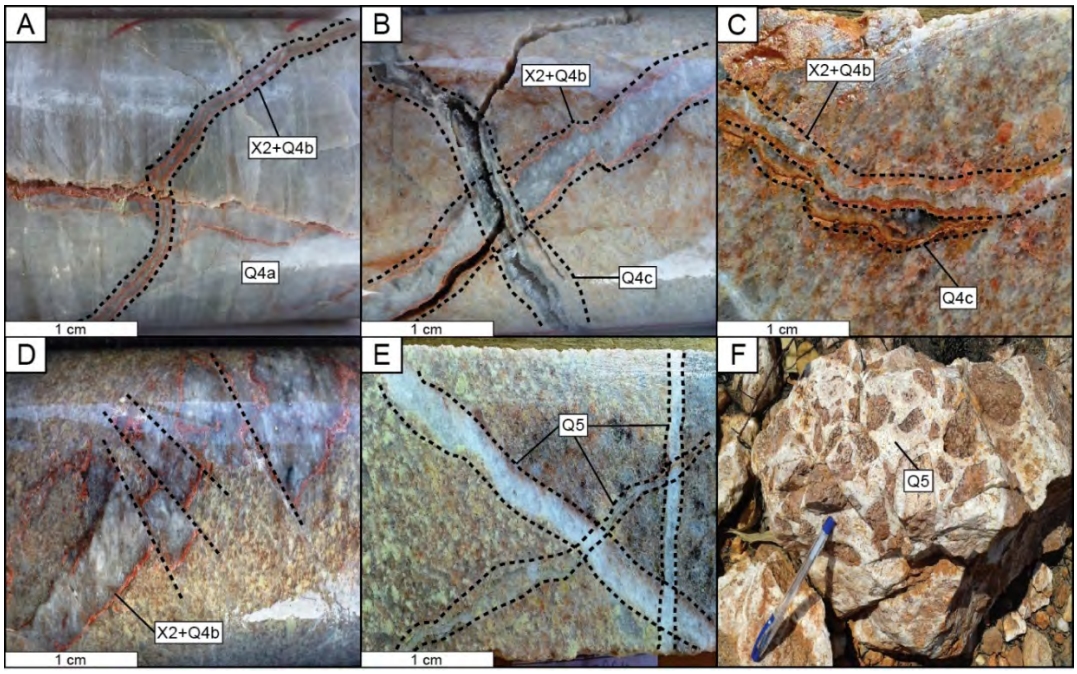

Fig. 3-11: Hydrothermal veins associated with the HREE mineralisation. (A) Quartz-xenotime vein cross-cutting a pre-existing quartz vein; (B) Quartz-xenotime vein being cut by a smoky quartz vein; (C) Smoky quartz vein cutting a quartz-xenotime vein; (D) Minor fault dislocations of a quartz-xenotime vein; (E) Multiple generations of late milky quartz veins; (F) Late breccia containing milky quartz in the matrix. Q = quartz; X = xenotime.

Stage 4: Late-stage mineralisation

The youngest xenotime mineralisation event is represented by fine-grained euhedral xenotime (X3a) that dominantly occurs in breccias (Fig. 3-9E) containing mineralised and non-mineralised clasts (Fig. 3-10H), and pyramid-shaped xenotime overgrowths (X3b) on the pre-existing xenotime (Fig. 3-10I). These are termed "late-stage" mineralisation. X3 grains rarely exceed 30 µm in size and show no evidence for co-genetic florencite or quartz, although they are occasionally replaced by secondary florencite.

Stage 5: Late hydrothermal phases

Post-dating the breccia-hosted and vein-type mineralisation and their associated alteration are veins containing quartz (Q5), barite, anhydrite, pyrite and hematite (H3). These veins (up to 10 cm in width) display vuggy and drusy textures, and are distinguished by a characteristic milky colour. They are composed primarily of several generations of large (1-5 cm in size) intergrown quartz (Fig. 3-11E). Occasionally, Q5 veins manifest as breccias (Fig. 3-11F) alongside previously mineralised major faults and fractures that may therefore contain mineralised clasts.

The final hydrothermal event of the paragenetic sequence is the partial replacement of pre- and syn-ore white mica by clays and clusters of tiny (<5 µm) authigenic florencite grains that tend to have cubic forms with a skeletal texture in which only a narrow rim of the original grain remains (Fig. 3-8F).

White mica composition

A complete list of major element analyses of the pre- (M1) and syn-ore (M2) white mica are presented in Appendix 3-4. Both mica types have relatively low FeO, MnO and TiO_2 contents and conform well to the muscovite [$KAl_2(Si_3Al)O_{10}(OH,F)_2$] to alumino-celadonite [$K(Mg,Fe^{2+})(Al)[Si_4O_{10}](OH)_2$] solid solution system (Rieder et al., 1999), and hence have phengitic compositions (Figs. 3-12A-B). The pre-ore mica has relatively low Si (Si a.p.f.u = 3.1 to 3.3) and K+Na a.p.f.u. close to 1, as is typical for natural muscovite. The syn-ore white mica extends to more phengitic compositions with higher Si contents (3.3 to 3.5 a.p.f.u.) and lower Al (2.2 to 2.5 a.p.f.u.) (Fig. 3-12A), and is K deficient, with K+Na a.p.f.u. between 0.75

and 0.88 (Fig. 3-12B). This interlayer deficiency is typical of illite series micas (Rieder et al., 1999) and may be due to pyrophyllite-type exchange of Si + vacancy = Al^{iv} + (K+Na) (Rosenberg, 2002). Most notably, the syn-ore mica is significantly richer in F (up to 0.5 wt.%) and Cl (up to 0.09 wt.%) than the pre-ore muscovite (F = <0.06 wt.%; Cl = <0.02 wt.%) (Fig. 3-12C).

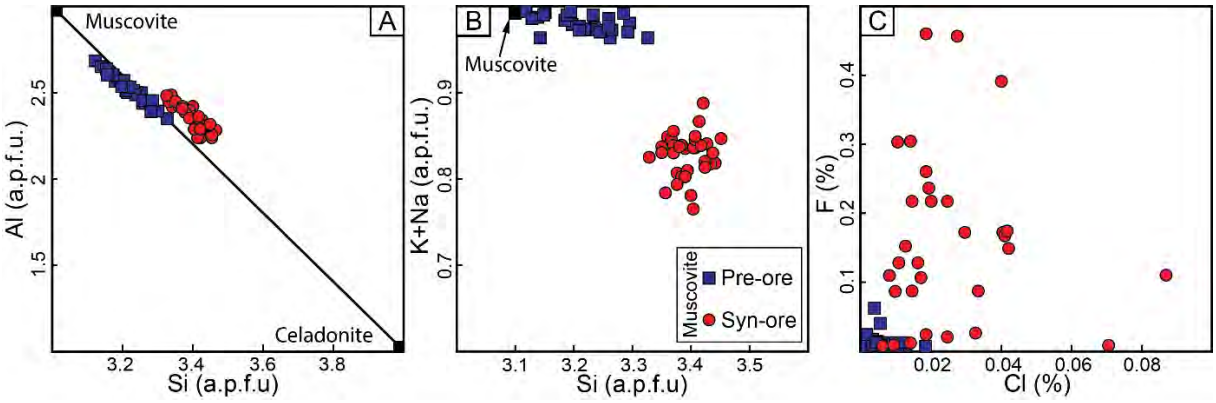

Fig. 3-12: Chemical composition of the pre- and syn-ore muscovite. (A) Aluminum (atoms-per-formula-unit; a.p.f.u.) versus Si (a.p.f.u.); (B) Si (a.p.f.u.) versus K+Na (a.p.f.u.); (C) F (wt.%) versus Cl (wt.%). Note, syn-ore muscovite is relatively enriched in F and Cl.

Geochronology

^{40}Ar-^{39}Ar geochronology of white mica

^{40}Ar/^{39}Ar dating results of four white mica-bearing samples from Wolverine and one sample from Area 5 are presented in Table 3-2. The quoted uncertainties in the ages incorporate uncertainties in the peak signals, system blanks, spectrometer mass discrimination, reactor corrections and J values. Superficial ^{40}Ar loss observed in the samples had no major impact on the validity of the ages and Ar release spectra are relatively flat in all samples. The sample from Area 5 yielded a ^{40}Ar/^{39}Ar total gas age of 1727 ± 9 Ma, which is in the range of the ages of three samples from Wolverine (1712 ± 8 Ma, 1714 ± 9 Ma, 1719 ± 9 Ma). The final Wolverine sample returned a slightly older age of 1746 ± 9 Ma.

Table 3-2: Ar-Ar data for pre-ore muscovite from the Wolverine and Area 5 deposits

	No.	Prospect/deposit	Drill core	Depth (m)	Easting	Northing	Total gas age
1	A2-22	Area 5	BRAD0002	159.1	492231.3	7909977	1727 ± 9
2	W5-4	Wolverine	BRWT0332W5	503.2	493508.1	7915069	1746 ± 9
3	W5-6	Wolverine	BRWT0332W5	505.2	493508.1	7915069	1714 ± 9
4	W5-8	Wolverine	BRWT0332W5	510.6	493508.1	7915069	1712 ± 8
5	W324-2	Wolverine	BRWT0324	372.9	493541.1	7914983	1719 ± 9

Uranium-Pb geochronology of xenotime

Sixteen samples from nine deposits/prospects were selected for U-Pb dating, with relevant hand specimen images shown in Fig. 3-9. Uranium-Pb concordia diagrams, calculated ages and isotope data for the samples are provided in Figure 3-13 and Appendix 3-5. Sample location information is provided in Appendix 3-2.

Xenotime from Banshee (sample B1) returned the oldest ages in this study, including several concordant analyses between ca. 1800 Ma and 1860 Ma that collectively gave a weighted mean age of 1821 ± 19 Ma (MSWD = 0.6) (Fig. 3-13A). Banshee also returned one slightly younger concordant age of ca. 1700 Ma from a xenotime overgrowth on a detrital clast. Uranium-Pb ages for various stages of xenotime from all other deposits and prospects examined are between ca. 1650 Ma and ca. 1510 Ma (Figs. 3-13, 3-14). Breccia-hosted xenotime (X1) dated from Wolverine, Cyclops, Dazzler, Iceman and Longshot yielded concordant ages between ca. 1650 Ma to ca. 1620 Ma. Assuming a single age event, these data produce a weighted mean age of 1645 ± 18 Ma (MSWD = 2.1). The vein-type xenotime (X2) present in most deposits/prospects returned mainly concordant, but slightly younger ages at ca. 1620 Ma, albeit with some overlap within uncertainty of the breccia-hosted xenotime age. Nevertheless, given the textural observation of vein xenotime forming after the breccia xenotime, we are confident that we can treat the vein xenotime analyses as a separate younger event. The weighted mean of the vein xenotime data is 1616 ± 4 Ma (MSWD = 1.1). Multiple younger ages were generated from xenotime (X3) overgrowths from Wolverine, Boulder Ridge and John Galt that extend from ca. 1600 Ma to ca. 1510 Ma (Fig. 3-13). Many of these analyses, particularly for John Galt, are discordant, likely due to Pb loss, so for John Galt the upper intercept is taken to be the crystallisation age. The lower intercept ages tend to be between ca. 300 to ca. 500 Ma, which is similar to lower intercept ages found for detrital zircons from the BRM (Nazari-Dehkordi et

al., 2017), and is attributed to disturbance during the Alice Springs Orogeny (450-300 Ma; Raimondo et al., 2011).

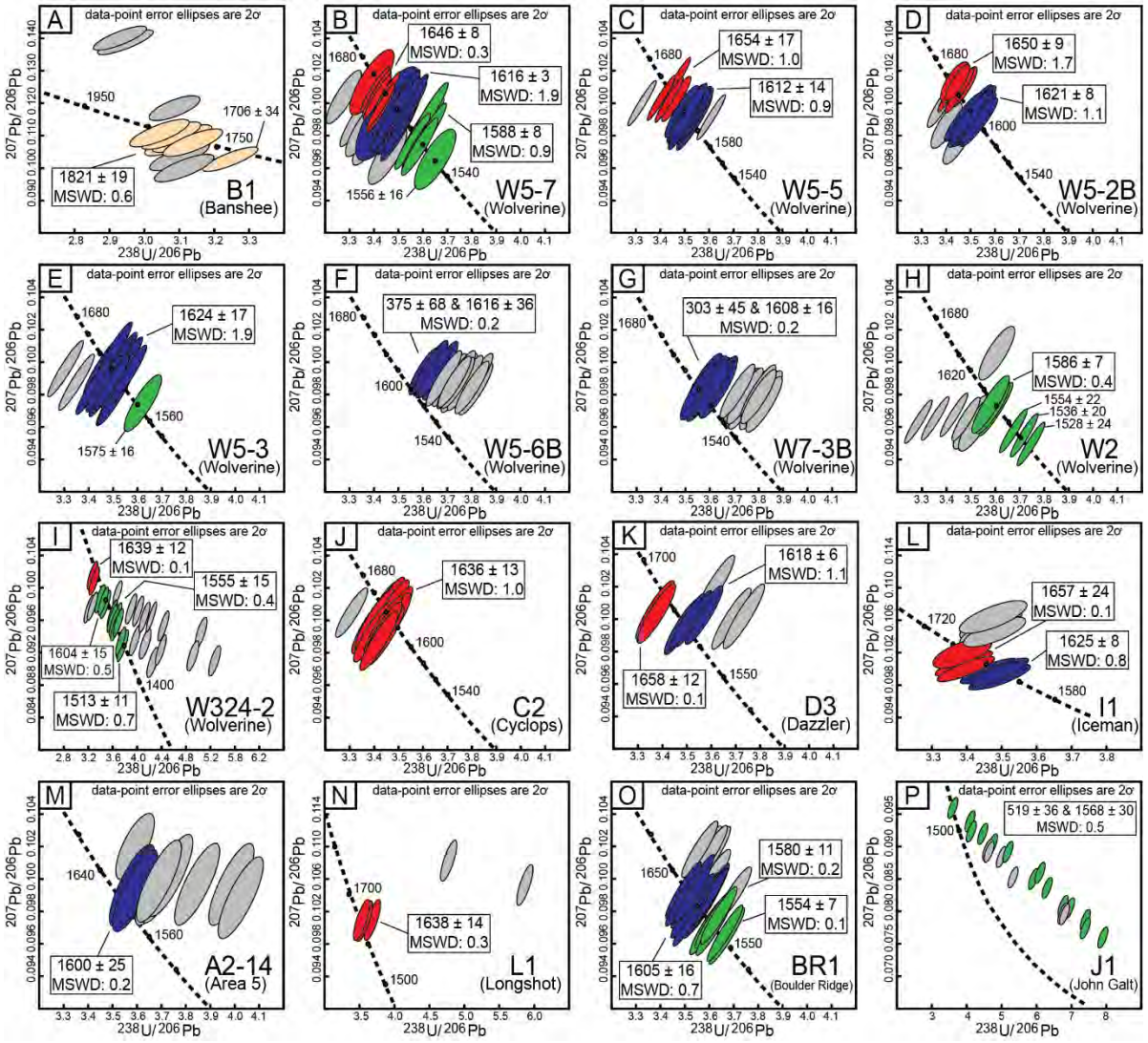

Fig. 3-13: Tera-Wasserburg concordia diagrams for U-Pb isotope analysis of ore xenotime. Grey coloured analyses are discordant and were excluded from age calculations. Note, colour coding refers to different generations of xenotime defined by the paragenetic relationships. Red = breccia-hosted; Blue = vein-type, Green = late overgrowths.

Discussion

Mineralisation style

Field observations and core log datasets indicate remarkable similarities between different HREE deposits/prospects across the NAHREY mineral field. All of the deposits/prospects have a similar ore mineralogy composed entirely of xenotime and florencite, and all are associated with an intense syn-ore quartz and white mica alteration. Mineralisation is clearly of hydrothermal origin and mainly occurs along steeply dipping faults and major structures of variable orientation and close to regional unconformities, in most cases between the BRM and overlying Birrindudu Group sandstones. Although some deposits appear to be distant from the unconformity, a reconstruction of the timing of the ore formation shows significantly close occurrence to the unconformity. For example, assuming a shallow dipping (5°) Birrindudu Group, the Wolverine orebody, now almost 2 km away from the unconformity, formed nearly 170 m underneath the unconformity. We propose that the ore-hosting structures acted as fluid pathways that witnessed large fluid fluxes, alongside which a breccia core of high grade ore is surrounded commonly by a halo of lower grade ore, as is typical of vein-type mineralisation. In such systems, orebodies sharing similar geological setting, ore-associated alteration and mineralogy, emplacement age and structural controls can be considered as discrete parts of a larger hydrothermal system with a common fluid source. In particular, structural correlation of most of the deposits/prospects of the Tanami Region with the BRD supports a large hydrothermal mineralising system. The variability in size of the HREE deposits/prospects is likely linked to fluid flux, which, at least in part, relates to the dilatency and permeability of each individual fault system. For example, the largest known deposit, Wolverine, is located at the conjunction of two major faults (Fig. 3-4), where sufficient space accommodation allowed large fluxes (and mixing, see below) of fluids.

The HREE mineralisation in the NAHREY mineral field is accommodated completely within metasedimentary rocks with no apparent link to magmatism or surficial process, and hence is unlike other REE ore styles (Nazari-Dehkordi et al., 2018). The simple ore mineralogy of NAHREY deposits also contrasts with the complex ore mineralogy of most other REE deposits (e.g., Weng et al., 2015). Although the HREE deposits/prospects studied here are restricted to northern Australia, the HREE mineralisation of the Maw Zone, Canada is directly comparable

to the NAHREY mineralisation. The Maw zone consists of hydrothermal xenotime hosted within brecciated sandstones close to the Archean-Proterozoic unconformity in the Athabasca Basin (Rabiei et al., 2017). Anomalous REE concentrations associated with hydrothermal alteration near regional unconformities have also been reported from the McArthur Basin of northern Australia, and the Athabasca and Thelon Basins of Canada (Fayek and Kyser, 1997; Davis et al., 2011; Orth et al., 2014). Xenotime- and florencite-rich quartz veins also occur within altered metasedimentary rocks of the sub-polar Urals (Repina, 2010). Accordingly, these reports indicate that there may be a global distribution for this particular ore style.

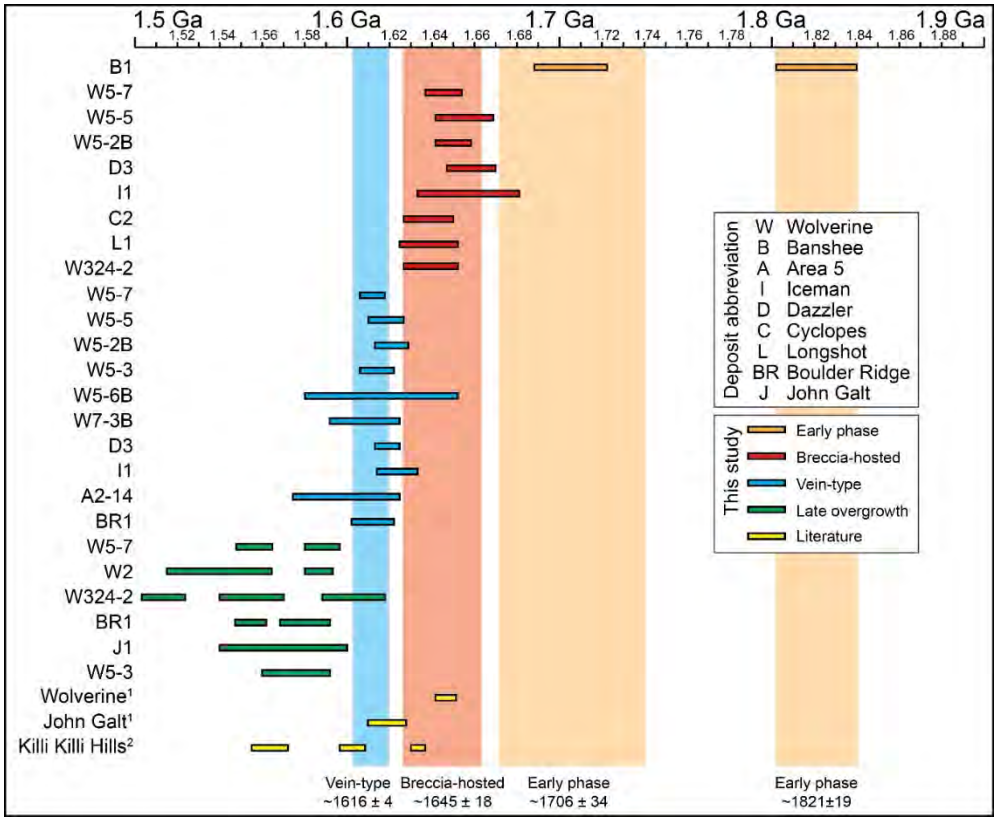

Fig. 3-14: Time plot of xenotime U-Pb ages for nine HREE deposits/prospects dated here, as well as from the literature (1 = Morin-Ka et al., 2016; 2 = Vallini et al., 2007). Note, the main stage of the HREE mineralisation across the NAHREY mineral field was between 1.65 Ga and 1.60 Ga.

Temporal evolution of mineralisation and relationship to regional-scale tectonics

Collectively, the ages of hydrothermal xenotime from nine HREE deposits/prospects in the Tanami Region and the Halls Creek Orogen span a range of ca. 300 m.y, from ca. 1800 Ma to ca. 1500 Ma (Fig. 3-14). This age range is interpreted to reflect multiple episodes of xenotime

growth, and probably dissolution and regrowth, during both regional metamorphism and hydrothermal alteration.

The Tanami Event (ca. 1820 Ma)

The earliest phase of xenotime mineralisation recorded only at Banshee is 1821 ± 19 Ma (Fig. 3-13A), which corresponds well to xenotime age data from Au deposits of the Pine Creek Orogen (Mount Todd: 1819 ± 9 Ma, Sener, 2004) and Tanami Region (Callie: 1803 ± 19 Ma, Cross et al., 2005). This age also coincides with the ca. 1820 to ca. 1835 Ma Tanami Orogeny (Bagas et al., 2007) that was responsible for regional metamorphism of greenschist facies to locally amphibolite facies conditions, and was broadly synchronous with widespread compressional deformation across a large part of central Australia (e.g., Bagas, 2004). This timeframe was also associated with extensive Au mineralisation in the Tanami Region (Bagas et al., 2007; Huston et al., 2007), the sedimentation of the Mount Charles Formation (Crispe et al., 2007), and with intrusion of the Birthday, Grimwade and Frederick granitic Suites (Huston et al., 2007). We speculate that fault (re)activation and fluid flow in the BRM during the Tanami Orogeny led to the formation of the Banshee deposit. In this case, mineralisation may have been localised by fluid reduction during interaction with the chloritic schist below the BRM, as discussed below.

1720-1700 Ma stage

The Banshee deposit also records a single xenotime age of 1706 ± 34 Ma (Fig. 3-13A), which is comparable to the xenotime ages reported from Pine Creek Orogen (Union Reefs Au deposit: 1701 ± 13 Ma, Sener, 2004) and Kimberley Basin (Pentecost Sandstone: 1704 ± 14 Ma, Warton Sandstone: 1704 ± 7 Ma, McNaughton et al., 1999). These ages are in agreement with our pre-ore muscovite $^{40}Ar/^{39}Ar$ age of ca. 1720 Ma reported for Wolverine and Area 5, and are also comparable to numerous $^{40}Ar/^{39}Ar$ ages for the Tanami Region (e.g., Dead Bullock Formation: ca. 1718 Ma, Li et al., 2014), and Halls Creek Orogen (e.g., Mabel Downs Tonalite: ca. 1705 Ma, Bodorkos and Reddy, 2004). Generally, ca. 1720 Ma is interpreted to correlate with the Strangways Orogeny (Fraser, 2002), which was a major tectonic event in the eastern part of the Arunta Orogeny associated with pervasive high-grade metamorphism, west-directed thrusting and hydrothermal fluid circulation (Maidment et al., 2005). At Banshee, we suggest

that this age records mobilisation and recrystallization of the ca. 1820 Ma stage of xenotime mineralisation during a regional scale metamorphism.

Main HREE mineralisation stage (1650-1600 Ma)

The major REE mineralisation event producing the breccia ore is constrained to 1645 ± 18 Ma for most of the studied deposits/prospects, including Wolverine (Fig. 3-14). This age is indistinguishable from a previously-reported age on Wolverine (1646 ± 5 Ma) by Morin-Ka et al. (2016), and is also within error of the age of the Killi Killi Hills xenotime hosted within the Birrindudu Group sandstones (1633 ± 4 Ma, but up to 1639 Ma, Vallini et al., 2007). A well-constrained xenotime age of 1616 ± 4 Ma (Fig. 3-14) is also inferred for the vein-type HREE mineralisation at Wolverine and several other deposits/prospects (Area 5, Iceman, Dazzler, Boulder Ridge). This age also compares well to the age previously reported from John Galt (1619 ± 9 Ma, Morin-Ka et al., 2016), suggesting that the hydrothermal activity responsible for vein formation was a regional scale event that extended from Halls Creek Orogen to the Tanami Region. The younger age for vein-type xenotime compared to breccia-hosted xenotime also conforms to petrographic observations that quartz-xenotime veins cross-cut the pre-existing breccia-hosted xenotime (Figs. 3-9B-D).

The period around 1650 Ma that records the bulk of the HREE mineralisation represents a time of complex geological activity in the North Australian Craton. Within this timeframe, the Mount Isa Inlier, lying on the eastern margin of the North Australian Craton, underwent major sedimentation (e.g., Soldiers Cap Group, Young Australia Group, Mount Albert Group, Foster and Austin, 2008; Mount Isa Group and McNamara Group; Page et al., 2000), magmatism (e.g., the 1670-1650 Ma Sybella Batholith and Ernest Henry Diorite, Page et al., 2000) and base metal mineralisation (Dugald River, Cannington, Mount Isa, Hilton-George Fisher, and McArthur River deposits all formed between 1665 to 1640; Page et al., 2000). These ages are broadly correlated to the ca. 1650 Ma assembly of the North Australian Craton and Laurentia (Pisarevsky et al., 2014), both of which subsequently underwent crustal extension at ca. 1640 Ma and re-assembly at ca. 1620 Ma during the Isan Orogeny (Gibson et al., 2017). Concurrently, collision of the Arunta Inlier with the Warumpi Province along the southern margin of the North Australian Craton during the Liebig Orogeny caused significant magmatism (1644 Ma Kakalyi Gneiss, Wyborn et al., 1998; and 1635 Ma Andrew Young Igneous Complex, Young et al., 1995) and metamorphism (e.g., ca. 1640-1635 Ma Yaya

Metamorphic Complex, Scrimgeour et al., 2005; ca. 1615 Ma Iwupataka Metamorphic Complex, Zhao and Bennett, 1995).

The broadly coeval collisions of the North Australian Craton with the Arunta Inlier to the south and Laurentia to the east caused abrupt changes in the apparent polar wander path of the North Australia Craton at ca. 1650 Ma and ca. 1640 Ma (Idnurm, 2000). Although distal from these tectonic and magmatic events, we suggest that associated far-field effects caused faulting and large-scale fluid flow in the northern Tanami and Halls Creek zones, which provided suitable conditions for formation of HREE mineralisation. A similar suggestion has been proposed for the base metal (e.g., Gibson et al., 2017), and uranium (e.g., ca. 1680 Ma Jabiluka and ca. 1640 Ma Nabarlek, Polito et al., 2005) deposits of the North Australia Craton.

Post ore stages (1600 -1500 Ma)

The latest phase of the HREE mineralisation, from ca. 1600 Ma to ca. 1500 Ma (Fig. 3-14), relates primarily to xenotime overgrowths on pre-existing xenotime. Two age populations of the xenotime from Killi Killi Hills within the Birrindudu Group sandstones (1602 ± 5 Ma and 1564 ± 8, Vallini et al., 2007), also fall into this ca. 100 m.y. timespan. The xenotime overgrowths likely formed by the relatively minor dissolution and subsequent overgrowth of earlier xenotime during a series of deformation/fluid events that postdate the main mineralisation stage. The 1600-1500 Ma timespan of the late xenotime overgrowths corresponds well to far field tectonic events including the crustal shortening associated with the Isan Orogeny in the North Australian Craton that continued until ca. 1500 Ma (Gibson et al., 2017), and the Chewings Orogeny in the Arunta Inlier (ca. 1600-1525 Ma, Collins et al., 1995; Vallini et al., 2007). These major tectonic events resulted in substantial magmatism and metamorphism in both the Arunta Inlier (Zhao and Bennett, 1995 and references therein) and the Mount Isa Inlier (Page and Sun, 1998 and references therein). We suggest that further reworking of the North Australian Craton during the Isan Orogeny and the Chewings Orogeny was likely responsible for the formation of this younger generation of xenotime.

Implications of a prolonged temporal evolution

The total geochronological dataset implies that evolution of mineralisation in the NAHREY mineral field was a prolonged and multi-stage process extending from ca. 1800 Ma, down to

ca. 1500 Ma (Fig. 3-14). Such long-lived episodic growth of REE-bearing minerals have been reported from REE deposits worldwide (ca. 1520 Ma to ca. 350 Ma for the Nolans Bore REE deposit, Huston et al., 2016; ca. 1370 Ma to ca. 900 Ma for the Gifford Creek Carbonatite Complex, Zi et al., 2017; ca. 1300 Ma to ca. 400 Ma for the Bayan Obo deposit, Song et al., 2018). Similarly, U deposits tend to undergo intermittent stages of mineralisation and remobilisation over timespans of several 100 m.y. to over 1 b.y. (ca. 1590 Ma to ca. 500 Ma Olympic Dam, Cherry et al., 2018; ca. 1680 Ma to ca. 800 Ma Jabiluka, Polito et al., 2005; ca. 1740 Ma to ca. 1470 Ma Mary Kathleen, Oliver et al., 1999; ca. 1590 Ma to ca. 850 Ma Athabasca Basin, Alexandre et al., 2009). Such common features between REE and U deposits suggest that radiogenic isotopic systems were sporadically disturbed, with the age of disturbance at least partly controlled by radiogenic heat production and mineral recrystallistion, resulting in development of complex orebodies involving several stages of mineralisation (see also Huston et al., 2016). In this case, REE and U ore minerals may be especially effective as recorders of post formation thermo-tectonic events due to their susceptibility to hydrothermal recrystallisation and an inherent high level of radiogenic heat production due to their high U and Th contents.

Towards an ore genesis model

Traditionally, alkaline and peralkaline igneous complexes have been linked with REE enrichment processes (e.g., Strange Lake, Salvi and Williams-Jones, 2006; Thor Lake, Sheard et al., 2012). Indeed, mid Paleoproterozoic (1870 to 1790 Ma) igneous rocks are a major component of the Tanami Region (Smith, 2001), and Browns Range Dome (Page et al., 1995; Cross and Crispe, 2007), prompting Cook et al. (2013) to suggest a magmatic source for the HREE mineralisation. However, the age dataset reported here demonstrates that the main stage (ca. 1650 to ca. 1600 Ma) of the HREE mineralisation in the NAHREY mineral field was not coincident with any local or regional magmatic activity. Magmatic rocks of coeval age are limited only to the Mount Isa Inlier well to the east, and the Arunta Inlier far to the south (Fig. 3-15). Furthermore, the unradiogenic Nd isotopic composition of the orebodies is inconsistent with that of any igneous rocks from across the North Australian Craton (Nazari-Dehkordi et al., 2018).

The geological relationships of the ore and petrographic textures of the ore minerals and associated quartz veins all suggest a hydrothermal origin for the HREE mineralisation. Indeed,

the mineralisation setting of the NAHREY mineral field is remarkably similar to that of unconformity-related U deposits of the Athabasca Basin and the Pine Creek Orogen; both ore styles are structurally controlled and are associated with regional unconformities between Paleoproterozoic sedimentary packages and underlying Archean basement dominated by metasedimentary rocks (e.g., Richard et al., 2016). Much of the U mineralisation in the Athabasca Basin and Pine Creek Orogen formed between 1620 and 1590 Ma (Polito et al., 2005; Alexandre et al., 2009), which is broadly comparable with the main stage (ca. 1650-1600 Ma) of the HREE mineralisation presented here (Fig. 3-14). There are also similarities in ore–related alteration styles, with intense muscovite-illite alteration zones intimately associated with many unconformity-related U deposits (e.g., Alexandre et al., 2005). In contrast, the ore mineral assemblage associated with unconformity-related U deposits usually contains abundant chlorite but is more depleted in quartz.

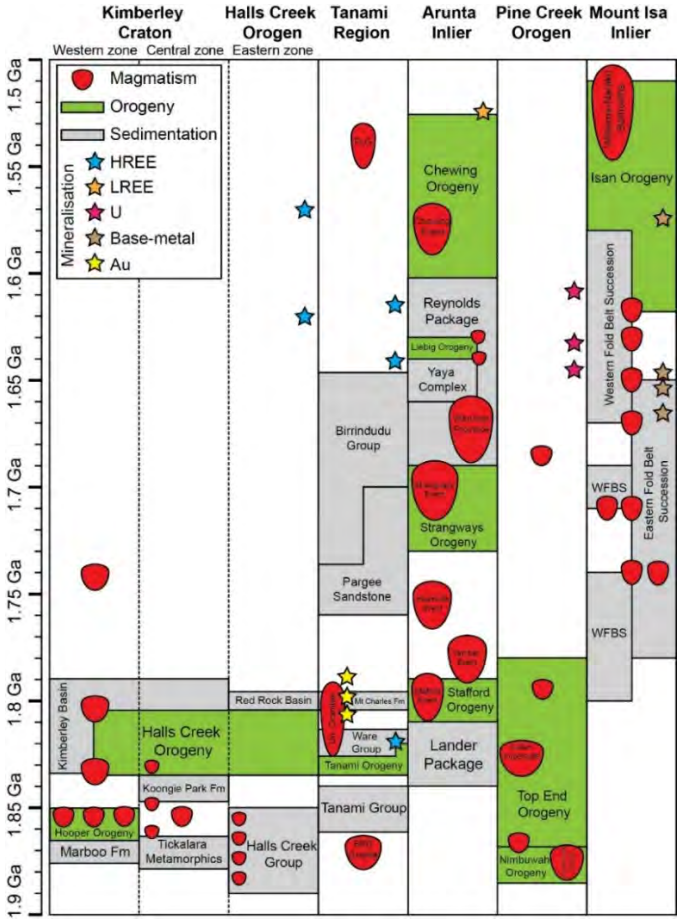

Fig. 3-15: Time-space plot of the 1.9-1.5 Ga events in the North Australian Craton. Data sources are Gibson et al. (2017) for the Mount Isa Inlier; Mercadier et al. (2013) for the Pine Creek Orogen; Scrimgeour et al. (2005) for the Arunta Inlier; Bagas et al. (2008) for the Tanami Region; Sheppard et al. (1999) for the Halls Creek Orogen, and Lan and Chen (2012) for the Kimberley Craton.

Given these similarities in geological setting, aspects of ore genesis models for unconformity-related U deposits are likely to be applicable for mineralisation in the NAHREY mineral field. The most accepted genetic models for the unconformity-related U deposits involve mixing of an oxidizing basinal fluid with a reducing fluid, with U being sourced either from the overlying sandstones (e.g., Kyser et al., 2000) or the underlying basement (e.g., Richard et al., 2010). Similarly, we suggest that mineralisation in the NAHREY mineral field was produced by mixing of hydrothermal fluids along sub-vertical faults near the regional unconformity between the underlying Archean basement rocks (mainly the BRM) and overlying Proterozoic sandstones. Fluid mixing not only conforms to the structural and geological setting, but is considered essential to explain the concentration of REE phosphate minerals in the ore zones. Xenotime has extremely low solubility in hydrothermal fluids (Gysi et al., 2015; Migdisov et al., 2016), so hydrothermal transport of REE+Y and P to the site of mineralisation requires separate fluids. Nazari-Dehkordi et al. (2018) presented compelling Nd isotope evidence that REE+Y were sourced from the Archean basement (BRM) in acidic, highly-saline fluids. Such fluid compositions may be effective at transporting REE+Y (e.g., Migdisov et al., 2016) and are entirely consistent with the formation of halogen-rich syn-ore white mica (Fig. 3-12C) alteration replacing K-Feldspar (Fig. 3-6) in the ore zones.

The phosphorus for ore mineral formation is proposed to have been leached from the overlying apatite-bearing Birrindudu Group sandstones. Detrital apatite in the Birrindudu Group sandstones originated from the ca. 1.83 to ca. 1.79 Ga granites in the Tanami Region (Crispe et al., 2007). Phosphate dissolution was likely driven via low-pH meteoric fluids circulating through the Birrindudu Group sandstones, as has been reported for other sandstone units (e.g., Morton, 1986). The bulk of the HREE mineralisation (at 1.65-1.60 Ga) formed in fault zones where upwelling BRM-derived REE+Y-bearing fluid mixed with P-bearing fluid derived from the Birrindudu Group sandstones. Mixing of fluids of varying salinity is also consistent with the compositions of fluid inclusions trapped within ore associated quartz (Nazari-Dehkordi et al., in prep.). Temperatures of ore formation are expected to be between 150 and 350 °C (Nazari-Dehkordi et al., 2018) based on alteration mineral assemblages and fluid inclusion data (Richter et al., 2018; Nazari-Dehkordi et al., in prep.). These temperature conditions are consistent with the preservation of primary Ar of the pre-ore muscovite (indicating T <420 ºC; Harrison et al., 2009), and the formation of K-deficient syn-ore mica (Fig. 3-12B), which is only expected to be stable below 400 ºC (Rosenberg, 2002). Under these conditions xenotime (and florencite) solubility in fluids is extremely low, so fluid mixing would result in very

efficient precipitation of ore minerals in fault zones. HREE (+Y) are considered to be the most insoluble of the REE (e.g., Williams-Jones et al., 2012), and hence would have been most easily lost from the reacting fluid. In this case, it is likely that some portion of LREE remained dissolved in the fluids to be transported out of the ore zone.

The Area 5 orebody formed during the main stage of the REE mineralisation, but is distinct from other deposits/prosects as it is dominated by florencite, with subordinate xenotime, and hence, is relatively LREE rich (Fig. 3-5A). We propose that this LREE favour of Area 5 may reflect more comprehensive precipitation of the dissolved load of REE from the fluids or, more likely, that Area 5 formed from hydrothermal fluids that had already seen partial and preferential HREE depletion via prior xenotime precipitation. A similar process was proposed by Williams-Jones et al. (2015) to explain HREE and LREE rich zones of the Lofdal HREE deposit in Namibia. In this case, Area 5 can be considered to be 'distal' to the other HREE-rich orebodies (e.g., Wolverine), in terms of evolution of the hydrothermal system.

The Banshee deposit is also distinct from other orebodies of the NAHREY mineral field, as it is relatively U rich and LREE poor (Fig. 3-5), and it formed at ca. 1.82 Ga, nearly 200 m.y., earlier than the main HREE mineralisation episode (Fig. 3-14). This time corresponds to a period of granitic magmatism in the Tanami Region (Fig. 3-15). Mineralisation is hosted in the BRM close to the contact with underlying package of quartz-chlorite schists. For Banshee, we speculate that ore formation may have been driven by magmatism, or magmatic-derived fluids, with the high U signature obtained via interaction of oxidized U^{6+}-bearing brines with the reductant agents such as Fe^{2+} bearing chlorite in the basement schists. This very process of reacting oxidised fluids with chlorite is widely considered to be a crucial mechanism for ore formation in unconformity-related U deposits (e.g., Fayek and Kyser, 1997; Alexandre et al., 2005).

Exploration implications

Identification of the ore-associated structures has significant implications for exploration, particularly for structurally-controlled regional-scale orebody occurrences, such as in the NAHREY mineral field. The ore-bearing structures distributed within and around the BRD are of variable strike, suggesting that the HREE mineralisation was associated with major faulting

and/or reactivating of older faults in the basement. Conjugate fracture sets, especially involving E-W striking structures tend to be favoured site for mineralisation (e.g. Wolverine). These structures are typical of the dome-related structures (Cooper et al., 2006), so we suggest that doming of the BRD may have provided suitable structural architecture for the HREE mineralisation. Hence, the dome-related structures, particularly E-W trending faults, can be considered as potential exploration targets for the discovery of further HREE orebodies.

The spatial and genetic association between regional unconformity structures and mineralisation in the NAHREY field raises the potential for further HREE mineralisation to be found associated with other regional unconformities within intercontinental sedimentary basins. Indeed, a number of the HREE deposits/prospects studied here (Cyclops and Dazzler; see Fig. 3-2B) are hosted directly along the unconformity structure. As mineralisation requires a source of P, overlying sedimentary units rich in phosphate could also be considered as potential exploration targets for mineralisation. Source rocks for ore metals need not be particularly REE-rich (see Nazari-Dehkordi et al., 2018), but should be depleted in P and Ca to avoid fluorite and/or apatite saturation that would serve to greatly restrict REE mobility.

The strong association of U with HREE (Fig. 3-5) has proved very useful for exploration using remotely sensed radiometric surveys. Here, we recognise ore-associated white mica alteration compositions (phengite-illite; Fig. 3-12) that are quite distinct from the pre-ore metamorphic muscovite of the region. This distinctive ore-associated mica is potentially well resolved by hyperspectral remote sensing techniques (Van der Meer et al., 2012), meaning hyperspectral mapping combined with regional radiometric surveys has great potential to be an effective regional-scale exploration tool.

Conclusion

Major findings of this study include:

(1) HREE mineralisation in the NAHREY mineral field is of hydrothermal origin. Ore formation was a multi-stage process that primarily occurred between 1.65-1.60 Ga, with several subsequent episodes of xenotime growth and regrowth.

(2) Ore formation is not related to any local or regional magmatism, but coincided with the initiation of the Isan and Liebig Orogenies to the west and south, respectively. Far field stresses from these events are the potential drivers of large-scale fluid flow leading to the ore formation.

(3) We propose an ore genesis model that involves mixing of discrete hydrothermal fluids that separately carried REE+Y and P from the BRM and the overlying Birrindudu Group sandstones, respectively. Ore formation is best developed at fault intersections and along the unconformity surface where fluid mixing was facilitated.

Acknowledgments

This work was supported by Northern Minerals Ltd and an ARC Future Fellowship (FT 120100198) to CS. We also thank the reviewers for their insightful comments.

References

Aleinikoff, J.D., Selby, D., Slack, J.F., Day, W.C., Pillers, R.M., Cosca, M.A., Seeger, C.M., Fanning, C.M., and Samson, I.M., 2016. U-Pb, Re-Os, and Ar/Ar Geochronology of Rare Earth Element (REE)-Rich Breccia Pipes and Associated Host Rocks from the Mesoproterozoic Pea Ridge Fe-REE-Au Deposit, St. Francois Mountains, Missouri. Economic Geology, v. 111, p 1883-1914.

Alexandre, P., Kyser, K., and Jiricka, D., 2009. Critical geochemical and mineralogical factors for the formation of unconformity-related uranium deposits: Comparison between barren and mineralized systems in the Athabasca Basin, Canada. Economic Geology, v. 104, p. 413–435.

Alexandre, P., Kyser, K., Polito, P., and Thomas, D., 2005. Alteration mineralogy and stable isotope geochemistry of Paleoproterozoic basement-hosted unconformity-type uranium deposits in the Athabasca Basin, Canada. Economic Geology, v. 100, p. 1547–1563.

Armstrong, J.T., 1991. Quantitative elemental analysis of individual microparticles with electron beam instruments, in Heinrich, K.F.J., and Newbery, D.E., eds., Electron Probe Quantitation: Plenum Press.

Bagas, L., 2004. Proterozoic evolution and tectonic setting of the northwest Paterson Orogen, Western Australia. Precambrian Research, v. 128, p. 475–496.

Bagas, L., Bierlein, F.P., English, L., Anderson, J., Maidment, D., and Huston, D.L., 2008. An example of a Palaeoproteozoic back-arc basin: petrology and geochemistry of the ca. 1864 Ma Stubbins Formation as an aid towards an improved understanding of the Granites-Tanami Orogen, Western Australia. Precambrian Research, v. 166, p. 168–184.

Bagas, L., Huston, D.L., Anderson, J., and Mernagh, T.P., 2007. Paleoproterozoic gold deposits in the Bald Hill and Coyote areas, Western Tanami, Western Australia. Mineralium Deposita, v. 42, p. 127–144.

Blake, D.H, Hodgson, I.M., and Smith, P.A., 1975. Geology of the Birrindudu and Tanami 1:2500000 Sheet Areas, Northern Territory. Canberra ACT: Bureau of Mineral Resources, Australia, Report 174.

Blake, D.H., Tyler, I.M., and Page, R.W., 2000. Regional geology of the Halls Creek Orogen. In: Hoatson, D.M., and Blake, D.H., (Eds.). Geology and economic potential of the

Palaeoproterozoic layered mafic/ultramafic intrusions in the East Kimberley, Western Australia. Australian Geological Survey Organisation Bulletin, v. 246, p. 35–62.

Bodorkos, S., and Reddy, S.M., 2004. Proterozoic cooling and exhumation of the northern central Halls Creek Orogen, Western Australia: Constraints from a reconnaissance $^{40}Ar/^{39}Ar$ study. Australian Journal of Earth Sciences, v. 51, p. 591–609.

Brown, S.M., Fletcher, I.R., Stein, H.J., Snee, L.W., and Groves, D.I., 2002. Geochronological constraints on pre-, syn-, and post-mineralization events at the world-class Cleo gold deposit, Eastern Goldfields Province, Western Australia. Economic Geology, v. 97, p. 541–559.

Busch, J.P., van der Pluijm, B.A., Hall, C.M., and Essene, E.J., 1996. Listric normal faulting during postorogenic extension revealed by $^{40}Ar/^{39}Ar$ thermochronology near the Robertson Lake shear zone, Grenville Orogen, Canada. Tectonics, v. 15, p. 387–402.

Chakhmouradian, A.R., and Zaitsev, A.N., 2012. Rare earth mineralization in igneous rocks: sources and processes. Elements, v. 8, p. 347–353.

Cherry, A.R., Kamenetsky, V.S., McPhie, J., Thompson, J.M., Ehrig, K., Meffre, S., Kamenetsky, M.B., and Krneta, S., 2018. Tectonothermal events in the Olympic IOCG Province constrained by apatite and REE-phosphate geochronology. Australian Journal of Earth Sciences, v. 65, p. 643–659.

Clark, A.B., and Blockley, J.G., 1960. A report on a geological reconnaissance, Billiluna Area (authority to prospect 769, Northern Territory). Open File, New Consolidated Gold Fields (Australasia) Pty Limited, pp 1–9.

Collins, W.J., Williams, I.S., Shaw, S.E., and McLaughlin, N.A., 1995. The age of the Ormiston Pound Granite: implications for Mesoproterozoic evolution of the Arunta Inlier, central Australia. Precambrian Research, v. 71, p. 91–105.

Cook, N.J., Ciobanu, C.L., O'Rielly, D., Wilson, R., Das, K., and Wade, B., 2013. Mineral chemistry of Rare Earth Element (REE) mineralization, Browns Ranges, Western Australia. Lithos, v. 172-173, p. 192–213.

Cooper, S.P., Goodwin, L.B., and Lorenz, J.C., 2006. Fracture and fault patters associated with basement-cored anticlines: The example of Teapot Dome, Wyoming. American Association of Petroleum Geologists (AAPG) Bulletin, v. 90, p. 1903–1920.

Crispe, A., and Vandenberg, L., 2005. Geology of the Tanami Region, Northern Territory. Northern Territory Geological Survey Bulletin.

Crispe, A.J., Vandenberg, L.C., and Scrimgeour, I., 2007. Geological framework of the Archaean and Palaeoproterozoic Tanami Region, Northern Territory. Mineralium Deposita, v. 42, p. 1–26.

Cross, A., and Crispe, A., 2007. SHRIMP U-Pb analyses of detrital zircon: a window to understanding the Paleoproterozoic development of the Tanami Region, northern Australia. Mineralium Deposita, v. 42, p. 27-50.

Cross, A.J., Claoue-Long, J.C., Scrimgeour, I.R., Ahmad, M., and Kruse, P.D., 2005. Summary of results. Joint NTGS-GA geochronology project: Rum Jungle, basement to southern Georgina Basin and eastern Arunta Region 2001–2003. Northern Territory Geological Survey, Record 2005–006.

Davis, W.J., Gall, Q., Jefferson, C.W., and Rainbird, R.H., 2011. Fluorapatite in the Paleoproterozoic Thelon Basin: structural-stratigraphic context, in-situ ion microprobe U-Pb ages, and fluid flow history. Geological Society of America Bulletin, v. 123, p. 1056–1073.

Dawson, G.C., Krapez, B., Fletcher, I.R., McNaughton, N.J., and Rasmussen, B., 2003. 1.2 Ga thermal metamorphism in the Albany–Fraser Orogen of Western Australia: consequence of collision or regional heating by dyke swarms? Journal of the Geological Society of London, v. 160, p. 29–37.

Fayek, M., and Kyser, T.K., 1997. Characterization of multiple fluid-flow events and rare-earth element mobility associated with formation of unconformity-type uranium deposits in the Athabasca Basin. Saskatchewan. Canadian Mineralogist, v. 35, p. 627–658.

Fletcher, I.R., McNaughton, N.J., Aleinikoff, J.A., Rasmussen, B., and Kamo, S.L., 2004. Improved calibration procedures and new standards for U-Pb and Th-Pb dating of Phanerozoic xenotime by ion microprobe. Chemical Geology, v. 209, p. 295–314.

Foster, D.R.W., and Austin, J.R., 2008. The 1800-1610 Ma stratigraphic and magmatic history of the Eastern Succession, Mount Isa Inlier, and correlations with adjacent Paleoproterozoic terranes. Precambrian Research, v. 163, p. 7–30.

Fraser, G., 2002. Geochronology of Tanami ores and host rocks. In: Munson, T.J., and Scrimgeour, I., (Eds.). Northern Territory Geological Survey Record, 2002/0003.

Gibson, G.M., Hutton, L.J., and Holzschuh, J., 2017. Basin inversion and supercontinent assembly as drivers of sediment-hosted Pb–Zn mineralization in the Mount Isa region, northern Australia. Journal of the Geological Society, v. 174, p. 773–786.

Goodenough, K.M, Wall, F., and Merriman, D., 2018. The Rare Earth Elements: Demand, Global Resources, and Challenges for Resourcing Future Generations. Natural Resources Research, v. 27, p. 201–216.

Gysi, A.P., Williams-Jones, A.E., and Harlov, D., 2015. The solubility of xenotime-(Y) and other HREE phosphates (DyPO4, ErPO4 and YbPO4) in aqueous solutions from 100 to 250°C and psat. Chemical Geology, v. 41, p. 83–95.

Hancock, S.L., and Rutland, R.W.R., 1984. Tectonics of an early Proterozoic geosuture: the Halls Creek orogenic sub province, northern Australia. Journal of Geodynamics, v. 1, p. 387–432.

Harrison, T.M., Celerier, J., Aikman, A.B., Hermann, J., and Heizler, M.T., 2009. Diffusion of ^{40}Ar in muscovite. Geochimica et Cosmochimica Acta, v. 73, p. 1039–1051.

Hendrickx, M.A., Slater, K., Crispe, A.J., Dean, A.A., Vandenberg, L.C., and Smith, J.B., 2000. Paleoproterozoic stratigraphy of the Tanami Region: regional correlations realisation preliminary results. Darwin NT. Northern Territory Geological Survey Record, 71 pp.

Huston, D.L., Vandenberg, L., Wygralak, A.S., Mernagh, T.P., Bagas, L., Crispe, A., Lambeck, A., Cross, A., Fraser, G., Williams, N., Worden, K., Meixner, T., Goleby, B., Jones, L., Lyons, P., and Maidment, D., 2007. Lode-gold mineralization in the Tanami region, northern Australia. Mineralium Deposita, v. 42, p. 175–204.

Huston, D.L., Maas, R., Cross, A., Hussey, K.J., Mernagh, T.P., Fraser, G., and Champion, D.C., 2016. The Nolans Bore rare-earth element-phosphorus-uranium mineral system: geology, origin and post-depositional modifications. Mineralium Deposita, v. 51, p. 797–822.

Idnurm, M., 2000. Towards a high resolution late Palaeoproterozoic-earliest Mesoproterozoic apparent polar wander path for northern Australia. Australian Journal of Earth Sciences, v. 47, p. 405–429.

Keane, S.D., Dewolf, C.P., Essene, E.J., Halliday, A.N., Hall, C.M., and Cosca, M.A., 2006. Isotopic constraints on the thermal history of the Wind River Range, Wyoming: implications for Archean metamorphism. Canadian Journal of Earth Sciences, v. 43, p. 1511–1532.

Korzhinskii, D.S., 1970. Theory of metasomatic zoning. Clarendon Press, Oxford, 162 p.

Kyser, K., Hiatt, E.E., Renac, C., Durocher, K., Holk, G., and Deckart, K., 2000. Diagenetic fluids in paleo- and meso-proterozoic sedimentary basins and their implications for

long protracted fluid histories. In: Kyser, T.K., (Ed.). Fluids and basin evolution. Mineralogical Association of Canada, v. 28, p. 225–262.

Lan, Z-W., and Chen, Z-Q., 2012. New xenotime ages obtained from the Paleoproterozoic Kimberley Group, NW Australia: implications for regional hydrothermal events. Australian Journal of Earth Sciences, v. 59, p. 119–133.

Li, B., Bagas, L., and Jourdan, F., 2014. Tectono-thermal evolution of the Palaeoproterozoic Granites–Tanami Orogen, North Australian Craton: Implications from hornblende and biotite $^{40}Ar/^{39}Ar$ geochronology. Lithos, v. 206, p. 262–276.

Maidment, D.W., Hand, M., and Williams, I.S., 2005. Tectonic cycles in the Strangways Metamorphic Complex, Arunta Inlier, central Australia: Geochronological evidence for exhumation and basin formation between two high-grade metamorphic events. Australian Journal of Earth Sciences, v. 52, p. 205–215.

McNaughton, N.J., Rasmussen, B., and Fletcher, I.R., 1999. SHRIMP uranium-lead dating of diagenetic xenotime in siliciclastic sedimentary rocks. Science, v. 285, p. 78–80.

Meert, J.G., Hargraves, R.B., van der Voo, R., Hall, C.M., and Halliday, A.N., 1994. Paleomagnetic and $^{40}Ar/^{39}Ar$ studies of Late Kibaran intrusives in Burundi, East Africa: implications for Late Proterozoic supercontinents. The Journal of Geology, v. 102, p. 621–637.

Meisel, T., Schoner, N., Paliulionyte, V., and Kahr, E., 2002. Determination of rare earth elements, Y, Th, Zr, Hf, Nb and Ta in geological reference materials G-2, G-3, SCo-1 and WGB-1 by sodium peroxide sintering and inductively coupled plasma-mass spectrometry. Geostandards Newsletter, v. 26, p. 53–61.

Mercadier, J., Annesley, I.R., McKechnie, C.L., Bogdan, T.S., and Creighton, S., 2013. Magmatic and metamorphic uraninite mineralization in the western margin of the Trans-Hudson Orogen (Saskatchewan, Canada): a uranium source for unconformity-related uranium deposits? Economic Geology, v. 108, p. 1037–1065.

Migdisov, A., Williams-Jones, A.E., Brugger, J., and Caporuscio, F., 2016. Hydrothermal transport, deposition, and fractionation of REE: experimental data and thermodynamic calculations. Chemical Geology, v. 439, p. 13–42.

Morin-Ka, S., Beardsmore, T.J., Hancock, E.A., Rasmussen, B., Dunkley, D., Muhling, J., Zi, J., Wilson, R., and Champion, J., 2016. Alteration and Age of the Browns Range Rare Earth Element Deposits. Western Australian Department of Mines and Petroleum.

Morton, A.C., 1986. Dissolution of apatite in North Sea Jurassic sandstones: Implications for the generation of secondary porosity. Clay Minerals, v. 21, p. 711–733.

Nazari-Dehkordi, T., Spandler, C., Oliver, N.H.S., and Wilson, R., 2018. Unconformity–Related Rare Earth Element deposits: A regional-scale hydrothermal mineralization type of northern Australia. Economic Geology, v. 113, 1297–1305.

Nazari-Dehkordi, T., Spandler, C., Oliver, N.H.S., Chapman, J., and Wilson, R., 2017. Provenance, tectonic setting and source of Archean metasedimentary rocks of the Browns Range Metamorphics, Tanami Region, Western Australia. Australian Journal of Earth Sciences, v. 64, p. 723–741.

Northern Minerals, 2015. Increased mineral resource delivers more good news: Australian Stock Exchange release, www.asx.com.au/asxpdf/20150223/pdf/42ws7ycqttdwn1.pdf.

Oliver, N.H.S., Bodorkos, S., Nemchin, A.A., Kinny, P.D., and Watt, G.R., 1999. Relationships between zircon U–Pb SHRIMP ages and leucosome type in migmatites of the Halls Creek Orogen, Western Australia. Journal of Petrology, v. 40, p. 1553–1575.

Orth, K., Meffre, S., and Davidson, G., 2014. Age and paragenesis of mineralisation at Coronation Hill uranium deposit, Northern Territory, Australia. Mineralium Deposita, v. 49, p. 595-623.

Page, R.W., Griffin, T.J., Tyler, I.M., and Sheppard, S., 2001. Geochronological constraints on tectonic models for Australian Palaeoproterozoic high-K granites. Journal of the Geological Society of London, v. 158, p. 535-545.

Page, R.W., Jackson, M.J., and Krassay, A.A., 2000. Constraining sequence stratigraphy in North Australian basins: SHRIMP U–Pb zircon geochronology between Mt Isa and McArthur River. Australian Journal of Earth Sciences, v. 47, p. 431–459.

Page, R.W., and Sun, S.S., 1998. Aspects of geochronology and crustal evolution in the Eastern Fold Belt, Mt Isa Inlier. Australian Journal of Earth Sciences, v. 45, p. 343–361.

Page, R.W., Sun, S.S., Blake, D., Edgecombe, D., and Pearcey, D., 1995. Geochronology of an exposed late Archean basement terrane in the Granites-Tanami region. Australian Geological Survey Organisation Research Newsletter, v. 22, p. 21-22.

Pettke, T., Oberli, F., Audetat, A., Guillong, M., Simon, A.C., Hanley, J.J., and Klemm, L.M., 2012. Recent developments in element concentration and isotope ratio analysis of individual fluid inclusions by laser ablation single and multiple collector ICP-MS. Ore Geology Reviews, v. 44, p. 10–38.

Pisarevsky, S.A., Elming, S.A., Pesonen, L.J., and Li, Z.X., 2014. Mesoproterozoic paleogeography: supercontinent and beyond. Precambrian Research, v. 244, p. 207–225.

Polito, P.A., Kyser, T.K., Thomas, D., Marlatt, J., and Drever, G., 2005. Re-evaluation of the petrogenesis of the Proterozoic Jabiluka unconformity-related uranium deposit, Northern Territory, Australia. Mineralium Deposita, v. 40, p. 238–257.

Rabiei, M., Chi, G., Normand, C., Davis, W.J., Fayek, M., and Blamey, N.J.F., 2017. Hydrothermal Rare Earth Element (Xenotime) Mineralization at Maw Zone, Athabasca Basin, Canada, and Its Relationship to Unconformity-Related Uranium Deposits. Economic Geology, v. 112, p. 1483–1507.

Raimondo, T., Clark, C., Hand, M., and Faure, K., 2011. Assessing the geochemical and tectonic impacts of fluid–rock interaction in mid-crustal shear zones: a case study from the intracontinental Alice Springs Orogen, central Australia. Journal of Metamorphic Geology, v. 29, p. 821–850.

Rieder, M., Cavazzini, G., Yakonov, Y.S., Frank-Kamenetskii, V.A., Gottard, G., Guggenheim, S., Koval, P.V., Muller, G., Neiva, M.A.R., Radoslovic, E.W., Robert, J.L., Sassi, S.P., Takeda, H., Weiss, Z., and Wones, D.R., 1999. Nomenclature of the micas. Mineralogical Magazine, v. 63, p. 267–279.

Repina, S.A., 2010. Zoning and sectoriality of the florencite and xenotime group minerals from quartz veins, the Subpolar Urals. Geology of Ore Deposits, v. 52, p. 821–836.

Richard, A., Cathelineau, M., Boiron, M.C., Mercadier, J., Banks, D.A., and Cuney, M., 2016. Metal-rich fluid inclusions provide new insights into unconformity-related U deposits (Athabasca Basin and Basement, Canada). Mineralium Deposita, v. 51, p. 249–270.

Richard, A., Pettke, T., Cathelineau, M., Boiron, M.C., Mercadier, J., Cuney, M., and Derome, D., 2010. Brine-rock interaction in the Athabasca basement (McArthur River U deposit, Canada): consequences for fluid chemistry and uranium uptake. Terra Nova, v. 22, p. 303–308.

Richter, L., Diamond, L.W., Atanasova, P., Banks, D.A., and Gutzmer, J., 2018. Hydrothermal formation of heavy rare earth element (HREE)-xenotime deposits at 100 °C in a sedimentary basin. Geology, DOI: https://doi.org/10.1130/G39871.1.

Rosenberg, P.E., 2002. The nature, formation, and stability of end-member illite: A hypothesis. American Mineralogist, v. 87, p. 103–107.

Salvi, S., and Williams-Jones, A.E., 2006. Alteration, HFSE mineralisation and hydrocarbon formation in peralkaline igneous systems: insights from the Strange Lake Pluton, Canada. Lithos, v. 91, p. 19–34.

Samson, S.D., and Alexander, E.C.J., 1987. Calibration of the interlaboratory $^{40}Ar/^{39}Ar$ dating standard, MMhb-1. Chemical Geology, v. 66, p. 27–34.

Scrimgeour, I.R., Kinny, P.D., Close, D.F., and Edgoose, C.J., 2005. High-T granulites and polymetamorphism in the southern Arunta region, central Australia: evidence for a 1.64 Ga accretional event. Precambrian Research, v. 142, p. 1–27.

Sener, A.K., 2004. Characteristics, distribution and timing of gold mineralisation in the Pine Creek Orogen, Northern Territory, Australia. PhD thesis, University of Western Australia, Perth.

Sheard, E.R., Williams-Jones, A.E., Heiligmann, M., Pederson, C., and Trueman, D.L., 2012. Controls on the concentration of zirconium, niobium, and the rare earth elements in the Thor lake rare metal deposit, Northwest Territories, Canada. Economic Geology, v. 107, p. 81–104.

Sheppard, S., Rasmussen, B., Muhling, J.R., Farrell, T.R., and Fletcher, I.R., 2007. Grenvillian-aged orogenesis in the Palaeoproterozoic Gascoyne Complex, Western Australia: 1030–950 Ma reworking of the Proterozoic Capricorn Orogen. Journal of Metamorphic Geology, v. 25, p. 477–494.

Sheppard, S., Tyler, I.M., Griffin, T.G., and Taylor, W.R., 1999. Paleoproterozoic subduction-related and passive margin basins in the Halls Creek Orogen, northwest Australia. Australian Journal of Earth Sciences, v. 46, p. 679–690.

Smith, J.B., 2001. Summary of results, joint NTGS-AGSO age determination program 1999-2001. Darwin NT. Northern Territory Geological Survey, Record 2001–007.

Song, W., Xu, C., Smith, M.P., Chakhmouradian, A.R., Brenna, M., Kynicky, J., Chen, W., Yang, Y., Deng, M., and Tang, H., 2018. Genesis of the world's largest rare earth element deposit, Bayan Obo, China: Protracted mineralization evolution over ~1 b.y. Geology, v. 46, p. 323–326.

Spandler, C., Hammerli, J., Sha, P., Hilbert-Wolf, H., Hu, Y., Roberts, E., and Schmitz, M., 2016. MKED1: a new titanite standard for in situ analysis of Sm-Nd isotopes and U-Pb geochronology. Chemical Geology, v. 425, p. 110–126.

Streepey, M.A., van der Pluijm, B.A., Essene, E.J., Hall, C.M., and Magloughlin, J.F., 2000. Late Proterozoic (ca. 930 Ma) extension in eastern Laurentia. Geological Society of America Bulletin, v. 112, p. 1522–1530.

Tyler, I.M, Griffin, T.J, Page, R.W., and Shaw, R.D., 1995. Are there terranes within the Lamboo Complex of the Halls Creek Orogen? Geological Survey of Western Australia, Annual Review 1993-94, p. 37-46.

Vallini, D., Rasmussen, B., Krapez, B., Fletcher, I.R., and McNaughton, N.J., 2002. Obtaining diagenetic ages from metamorphosed sedimentary rocks: U–Pb dating of unusually coarse xenotime cement in phosphatic sandstone. Geology, v. 30, p. 1083–1086.

Vallini, D.A., Groves, D.I., McNaughton, N.J., and Fletcher, I.R., 2007. Uraniferous diagenetic xenotime in northern Australia and its relationship to unconformity-associated uranium mineralisation. Mineralium Deposita, v. 42, p. 51–64.

Van Achterbergh, E., Ryan, C.G., Jackson, S.E., and Griffin, W.L., 2001. Data reduction software for LA-ICP-MS, in: Sylvester, P.J., (Ed.), Laser Ablation-ICP Mass Spectrometry in the Earth Sciences: Principles and Applications. Mineralogical Association of Canada, v. 29, p. 239–243.

Van der Meer, F.D., Van der Werff, H.M., Van Ruitenbeek, F.J., Hecker, C.A., Bakker, W. H., Noomen, M.F., and Woldai, T., 2012. Multi-and hyperspectral geologic remote sensing: A review. International Journal of Applied Earth Observation and Geoinformation, v. 14, p. 112–128.

Weng, Z, Jowitt S.M., Mudd, G.M., and Nawshad, H.A., 2015. A detailed assessment of global rare earth element resources: Opportunities and challenges. Economic Geology, v. 110, p. 1925–1952.

Williams-Jones, A.E., Migdisov, A.A., and Samson, I.M., 2012. Hydrothermal mobilization of the rare earth elements – a tale of “Ceria” and “Yttria”. Elements, v. 8, p. 355–360.

Williams-Jones, A.E., Wollenberg, R., and Bodeving, S., 2015, Hydrothermal fractionation of the rare earth elements and the genesis of the Lofdal REE deposit, Namibia. Symposium on critical and strategic materials. British Columbia Geological Survey Paper 2015–3.

Wyborn, L., Hazell, M., Page, R., Idnurm, M., and Sun S., 1998. A newly discovered major Proterozoic granite alteration system in the Mount Webb region, central Australia, and implications for Cu-Au mineralisation. AGSO Research Newsletter, v. 28, p. 1–6.

Young, D.N., Fanning, C.M., Shaw, R.D., Edgoose, C.J., Blake, D.H., Page, R.W., and Camacho, A., 1995. U-Pb zircon dating of tectonomagmatic events in the northern Arunta Inlier, central Australia. Precambrian Research, v. 71, p. 45–68.

Zhao, J.X., and Bennett, V.C., 1995. HRIMP U–Pb zircon geochronology of granites in the Arunta Inlier, central Australia: implications for Proterozoic crustal evolution. Precambrian Research, v. 71, p. 17–43.

Zi, J-W., Courtney, J.G., Rasmussen, B., Sheppard, S., and Muhling, J.R., 2017. Using monazite geochronology to test the plume model for carbonatites: The example of Gifford Creek Carbonatite Complex, Australia. Chemical Geology, v. 463, p. 50–60.

Chapter 4

Unconformity–Related Rare Earth Element deposits: A regional-scale hydrothermal mineralization type of northern Australia

Teimoor Nazari-Dehkordi[1*], Carl Spandler[1], Nicholas H.S. Oliver[1, 2], Robin Wilson[3]

[1]Department of Geosciences, James Cook University, Townsville, QLD 4811, Australia
[2]HCOVGlobal Consultants, PO Box 3533, Hermit Park, QLD 4812, Australia
[3]Northern Minerals, PO Box 669, West Perth, WA 6872, Australia

Published in *Economic Geology*
https://doi.org/10.5382/econgeo.2018.4592

Abstract

Rare earth element (REE) orebodies are typically associated with alkaline igneous rocks or develop as placer or laterite deposits. Here, we describe an economically-important heavy (H)REE mineralization type that is entirely hydrothermal in origin with no demonstrable links to magmatism. The mineralization occurs as numerous xenotime-rich vein and breccia orebodies across a large area of northern Australia, but particularly close to a regional unconformity between Archean metasedimentary rocks of the Browns Range Metamorphics (BRM) and overlying Proterozoic sandstones of the Birrindudu Group. The deposits formed at 1.65-1.61 Ga along steeply-dipping faults; there is no known local igneous activity at this time.

Depletion of HREE in the BRM, together with the similar non-radiogenic Nd isotope composition of the orebodies and the BRM, indicate that ore metals were leached directly from the BRM. We propose an ore genesis model that involves fluid leaching HREE from the BRM and subsequently mixing with P-bearing acidic fluid from the overlying sandstones in fault zones near the unconformity. The union of P and HREE via fluid mixing in a low Ca environment triggered extensive xenotime precipitation.

This mineralization is unlike that of any other class of REE ore deposit but has a similar setting to unconformity-related U deposits of Australia and Canada, so we assign it the label “unconformity-related REE”. Further discoveries of this REE mineralization type are expected near regional unconformities within Proterozoic intracontinental sedimentary basins across the globe.

Keywords: Rare earth element, unconformity, hydrothermal, xenotime, florencite, Browns Range, Western Australia

Introduction

The supply of rare earth elements (REE) is essential to delivering clean energy technologies and other modern technological applications, yet almost all of the world's REE production is currently sourced from just a few ore deposits (mainly Bayan Obo, China; Weng et al., 2015). As a result, many of the REEs, particularly the heavy (H)REE, are considered to be metals of critical supply risk (e.g., Hatch, 2012; Goodenough et al., 2017). Recent efforts to redress this supply risk have identified REE resources from across the globe; of which >95% of known REE resources are directly hosted within alkaline magmatic rocks and carbonatites, or have genetic links with magmatic rocks (e.g., laterite, skarns, IOCG deposits, Weng et al., 2015). Less than 3% of REE global resources are in placer-type deposits. Exploration efforts, therefore, tend to focus on magmatic systems, with carbonatites, peralkaline silicate intrusions and pegmatites considered to be the most prospective targets. However, these rock-types are relatively rare in the rock record, so discovery of alternative geological environments for REE mineralization would greatly benefit future resource security.

Hydrothermal processes can mobilize and redistribute REE at the deposit scale (Gysi et al., 2015; Migdisov et al., 2016) and there is potential for REE orebodies to form via purely hydrothermal processes (Migdisov et al., 2016). Across the globe, there are a number of vein and breccia style REE orebodies (e.g., Steenkampskraal, Hoidas Lake, Nolans Bore, Gallinas, Olserum-Djupedal) with inferred hydrothermal origins, but almost all of these deposits have demonstrable links with magmatism (Williams Jones et al., 2000; Harmer and Nex, 2016; Anenburg et al., 2018). Indeed, Anenburg et al. (2018) suggest that many REE vein deposits, such as Nolans Bore and Hoidas Lake, are direct products of wall-rock reaction with carbonatitic rocks, rather than of hydrothermal activity. Therefore, with the exception of placer and supergene deposits, there are very few reported examples of economically-significant REE mineralization without links to magmatism. One such deposit is the Maw Zone, which consists of hydrothermal xenotime mineralization hosted within brecciated sandstones of the Athabasca Basin, Canada (Quirt et al., 1991; Rabiei et al., 2017). The Maw zone, however, is a relatively small mineral resource and it is unclear whether it is unique, or an example of a regional (or globally) significant mineralization style for which other deposits are yet to be discovered.

In this paper, we describe HREE+Y mineralization that occurs as numerous structurally-controlled deposits and prospects across a large part of the North Australian Craton; an area henceforth labelled the North Australian HREE+Y (NAHREY) mineral field. Combining ore petrology, mineral chemistry, geochronology, and Sm-Nd isotope analysis of a number of these deposits, we show that this mineralization type has no genetic link to magmatism, but rather represents hydrothermal mineralization that formed via REE leaching from the metasedimentary host rocks under conditions somewhat akin to those proposed for mid Proterozoic unconformity-related U deposits of Australia and Canada, and that proposed for the Maw Zone (Rabiei et al., 2017). The recognition of this regionally significant HREE+Y mineralization type expands current definitions of REE ore formation settings, which in turn may lead to alternative exploration strategies for delineating new REE resources.

Geological Setting

The North Australian HREE+Y (NAHREY) mineral field extends over a distance of ca. 300 km from the John Galt REE Deposit in the east Kimberley of Western Australia, through to the Killi Killi Hills in the Tanami Region (Fig. 4-1A; Vallini et al., 2007). Most of the known mineralization, which consists of around 20 deposits and prospects (Fig. 4-1), is centered on the western side of the ~60 × ~30 km Browns Range Dome in the northwest of the Tanami Region (Cook et al., 2013). The Wolverine Deposit is the largest of these orebodies, and is the main focus of this study, although it shares fundamental characteristics with all the other deposits and prospects (e.g., Iceman, Cyclops, Boulder Ridge, John Galt; Fig. 4-1). Wolverine occurs as a near vertical ore lens at the intersection of two steeply dipping faults and has a strike length of over 400 m and extends from the surface to over 550 m depth. The total mineral resource of 4.97 Mt at 0.86% total rare earth oxide (Northern Minerals, 2015), represents a significant resource, particularly considering the high contents of HREE and Y (Fig. 4-2), rare metals that are among the most critical with respect to supply risk (Goodenough et al., 2017).

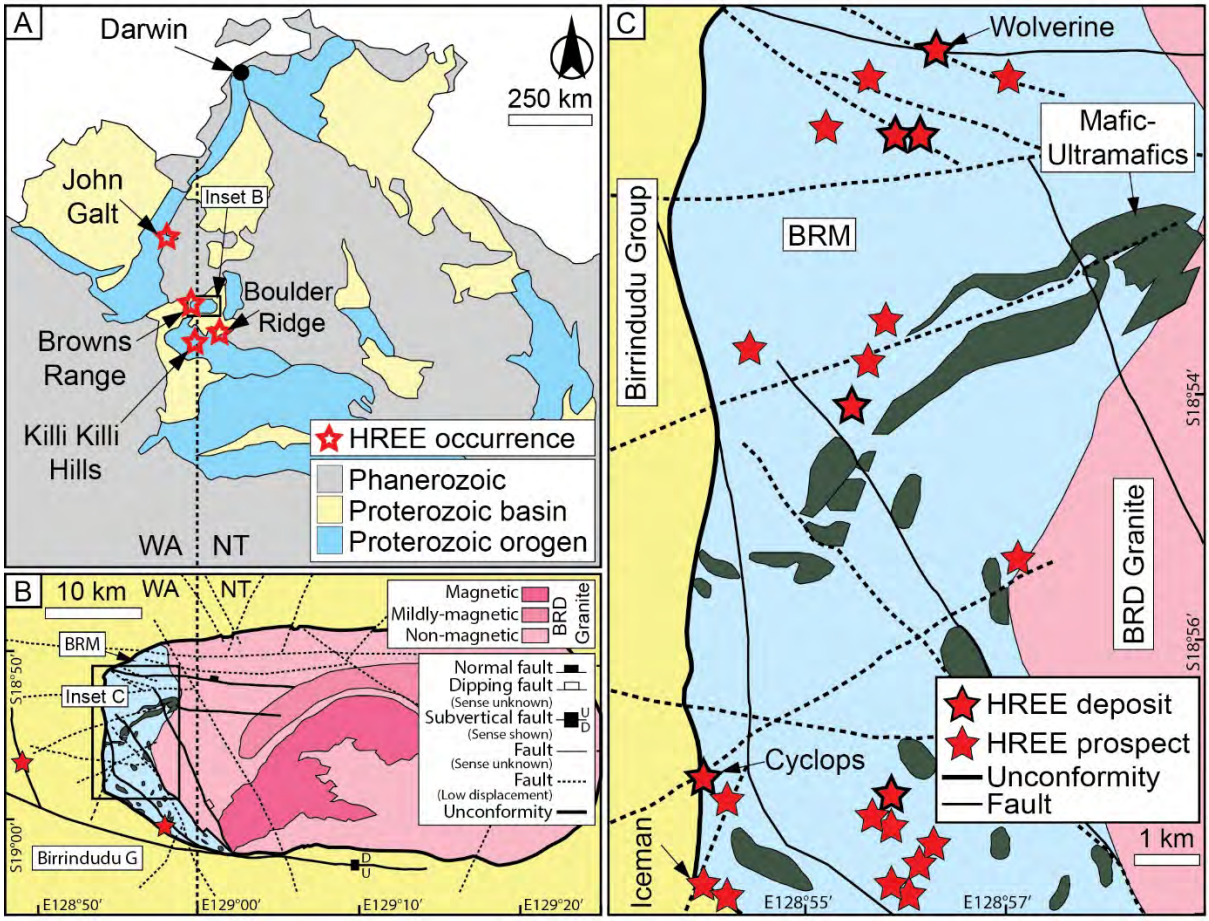

Fig. 4-1: Known distribution of the hydrothermal unconformity-related HREE+Y mineralization in northern Australia (A); (B) A simplified geological map of the Browns Range Dome (BRD); and (C) Geological map of the western section of the Browns Range Dome (BRD) with the locations of HREE deposits and prospects indicated. For more detail, see Crispe et al. (2007) and Nazari-Dehkordi et al. (2017). Note, the mafic/ultramafic bodies are largely inferred from regional magnetic imagery.

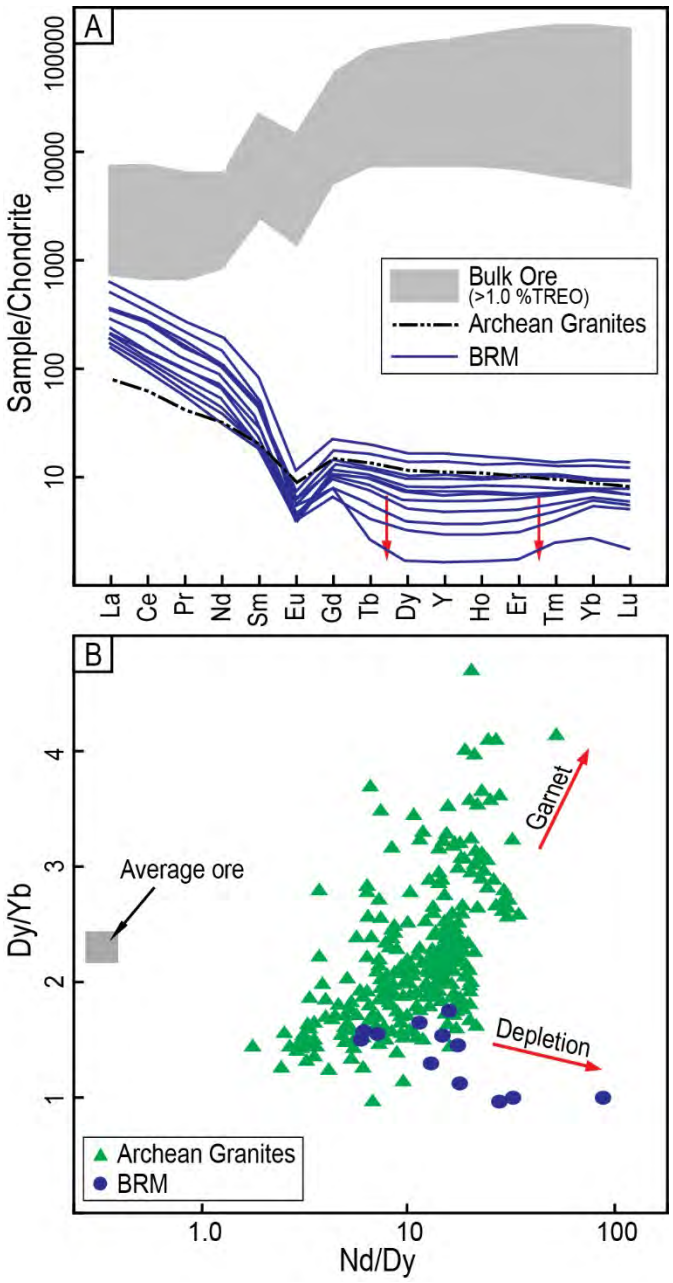

Fig. 4-2: REE charactersitics of the BRM. (A) Chondrite-normalized REE+Y profiles for the Browns Range Metamorphics (BRM), average Australian Archean Granite (from Champion and Smithies, 2007) and bulk ore from the Wolverine Deposit. The chondrite values are from Taylor and McLennan (1985). (B) La/Dy versus Dy/Yb of BRM, average bulk ore from the Wolverine Deposit and granitoids from Archean cratons across the globe (n = 256). Note, the REE depletion signature of the BRM is quite distinct from the REE signature of Archean granitoids (which is partly controlled by garnet in the source) but does mirror the REE signature of the Wolverine ore, and is consistent with the results of experimental leaching of REE from sedimentary rocks (Ohr et al., 1994). Archean granitoid data are from the GeoRoc Database (accessed May 2018).

Mineralization within and around the Browns Range Dome is spatially associated with the regional unconformity between the Brown Range Metamorphics (BRM) that hosts most of the mineralization (e.g., Wolverine, Iceman and Cyclops), and the overlying Paleoproterozoic Gardiner Sandstone of the 6 km-thick Birrindudu Group (Fig. 4-1). The BRM crop out over an area of ~100 km^2 and consist of a package of immature quartz-feldspar meta-arkosic sandstones, with minor interbedded conglomerates and semi-pelitic schists. The BRM represent clastic detritus deposited between 3.1 and 2.5 Ga from erosion of Mesoarchean granitic source (Nazari-Dehkordi et al., 2017). These rocks experienced greenschist metamorphism at ca. 1.83 Ga (Crispe et al., 2007), and are relatively depleted in Na, Ca and P (Appendix 4-1). The chondrite-normalized REE profiles are characterized by distinct HREE+Y depletion that is unlike that of other clastic sedimentary rocks (McLennan, 1989) or Archean granites (Fig. 4-2). Intruding the BRM is the ca. 1.88 Ga Browns Range Dome granite (Cross and Crispe, 2007), minor ca. 2.5 Ga granitic to pegmatitic intrusions (Nazari-Dehkordi et al., 2017), and a sequence of mafic-ultramafic rocks that were affected by regional metamorphism, and hence predate the ca. 1.83 Ga metamorphic activity. Some mineralization extends into the overlying unmetamorphosed ca. 1.66 to 1.64 Ga Gardiner Sandstone (e.g., at Killi Killi Hills; Vallini et al., 2007), implying that mineralization post-dated cooling and exhumation of the BRM. There is thus no evidence of magmatic activity in the local region after ca. 1.8 Ga.

Mineralization Style

The style of mineralization across the NAHREY field is remarkably uniform, consisting of planar orebodies of quartz-xenotime-(Y) veins and breccias hosted in steeply-dipping fault zones (Fig. 4-3; Cook et al., 2013). The highest-grade mineralization occurs as chaotic to mosaic breccias with altered and rounded clasts of BRM (<0.1 m) set within a xenotime-(Y)-rich matrix. These breccia zones are commonly cross-cut and mantled by crackle breccias with networks of crustiform to comb-textured quartz-xenotime veins (Fig. 4-3B). The ore mineralogy is relatively simple, consisting only of xenotime-(Y) with subordinate florencite-(Ce) [$LREEAl_3(PO_4)_2(OH)_6$]. This simple mineralogy is rather distinctive, as other REE deposits generally consist of highly complex REE mineral assemblages (Weng et al., 2015). The major mineral assemblages associated with the mineralization and host metasedimentary rocks include; (1) a pre-ore detrital and metamorphic assemblage, including quartz (several generations), alkali feldspar and coarse-grained muscovite aligned in a pre-mineralization

foliation (Fig. 4-4A); this assemblage reflects mainly a greenschist-facies overprint on the predominantly meta-arkosic host rocks; (2) a syn-ore hydrothermal mineral assemblage consisting of xenotime-(Y), florencite-(Ce), quartz and fine-grained hydrothermal muscovite (Fig. 4-4A). The ore minerals are subhedral to euhedral, and are morphologically distinct from the highly pitted and corroded REE phosphates that occur as fine accessory grains in the host BRM (Fig. 4-4B). Hematite is locally abundant in fault zone breccias and veins associated with mineralization, but largely predates or postdates xenotime-(Y) formation. Of note, carbonate minerals are completely absent, and the syn-ore fine-grained muscovite is distinctly enriched in F (up to 0.5 wt. %, Fig. 4-4C) compared to the pre-ore muscovite (Appendix 4-2).

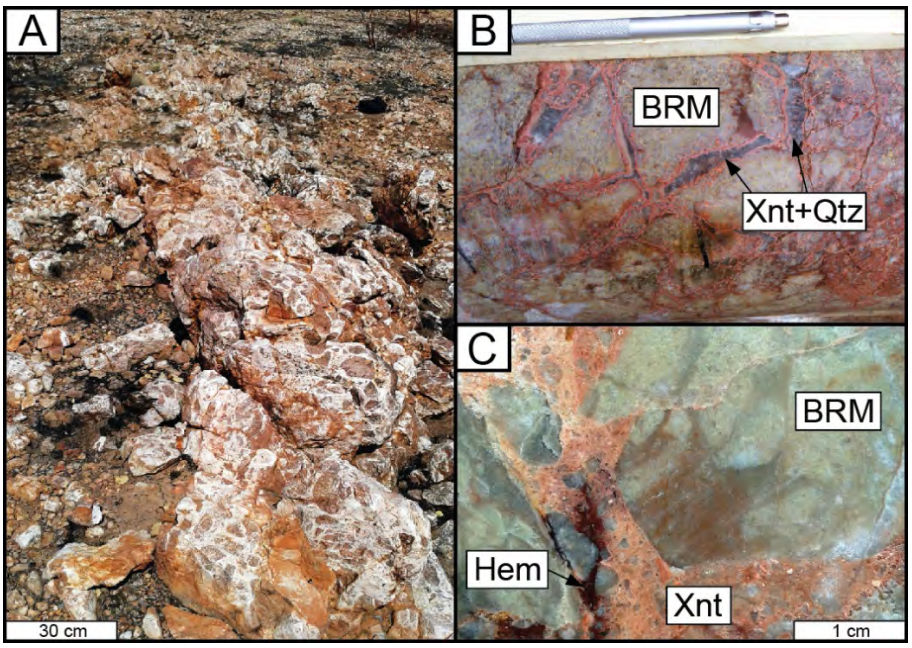

Fig. 4-3: Ore-associated hydrothermal breccias developed along a major fault structure near the Wolverine Deposit (A). Note the clasts of Browns Range Metamorphic (BRM) within a vein quartz matrix; (B) Core sample of pink xenotime-(Y) (Xnt) + quartz (Qtz) crackle veins in the BRM (Wolverine Deposit). The xenotime-(Y) occurs between the quartz and host rock in these veins; (C) Cut surface of a core sample of a mineralized breccia (Wolverine Deposit) consisting of silicified clasts of BRM within a xenotime matrix (salmon color). Note the post-ore hematite (Hem) vein to the bottom left of the image.

We have assessed mineralization processes using bulk-rock geochemical data from the Wolverine Deposit (Fig. 4-5). These data were collected as part of Northern Minerals Ltd mineral exploration and resource definition work (see Appendix 4-1). Examination of the three most abundant components (K_2O, Al_2O_3, SiO_2) reveals that most of the BRM (host rocks to the ore) have compositions that are consistent with a mineralogy dominated by quartz, alkali-feldspar (predominantly K-feldspar) and muscovite in variable proportions, which is in agreement with petrographic observations (Nazari-Dehkordi et al., 2017). However, almost all of the bulk ore samples (Fig. 4-5) fall fairly sharply around the tie line between muscovite and quartz, with quartz being a key vein constituent with xenotime-(Y). These data are consistent with wholesale conversion of K-feldspar to muscovite in alteration zones associated with ore, which, together with the simple REE mineralogy, is a classic indicator of large metasomatic fluid fluxes (Korzhinskii, 1970).

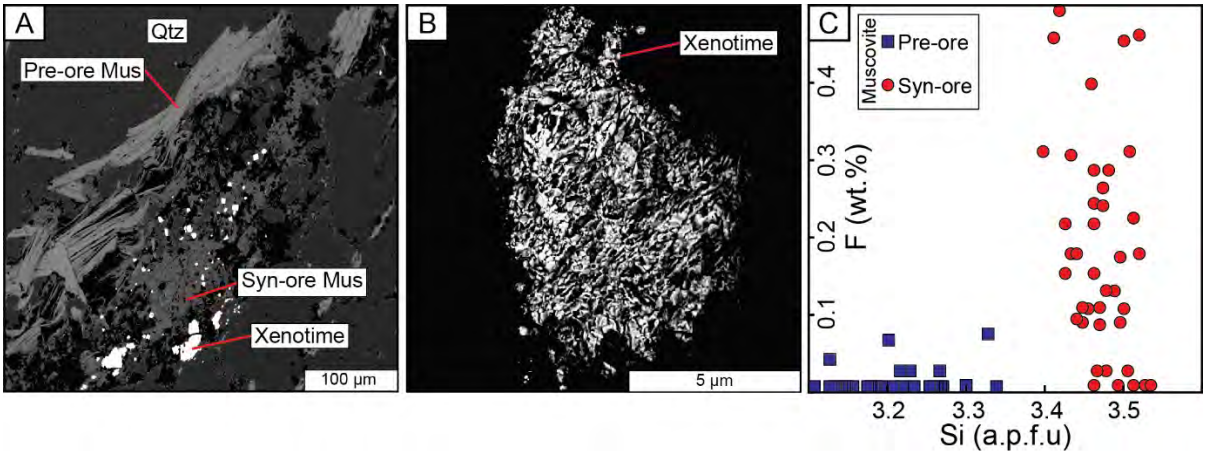

Fig. 4-4: Backscattered electron image of the xenotime-(Y) ore assemblage, with two generations of muscovite (Mus) (A). (B) Backscattered electron image of a highly pitted and corroded primary xenotime grain from the BRM. The nature of these grains is consistent with reaction and partial dissolution by hydrothermal fluids. (C) Fluorine (wt.%) versus Si (atoms-per-formula-unit; a.p.f.u.) diagram for pre- and syn-ore muscovite. Note, syn-ore muscovite is relatively enriched in F.

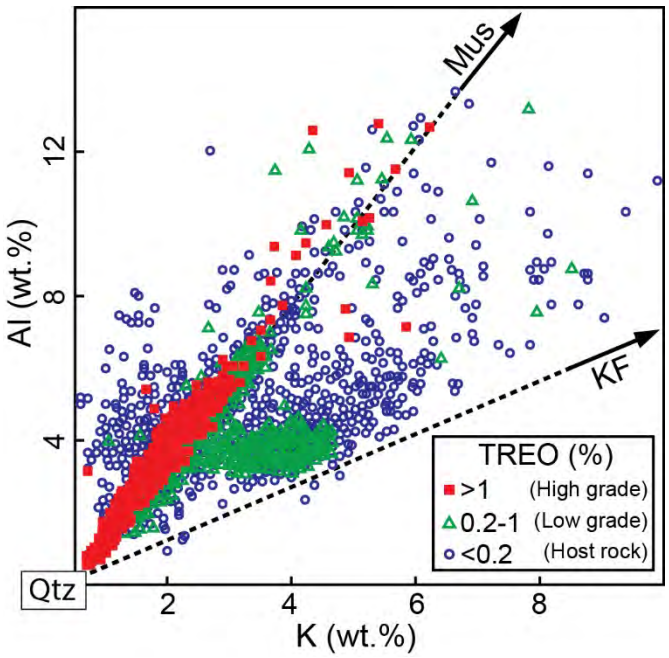

Fig. 4-5: Whole-rock Al (wt.%) versus K (wt.%) for the core samples (n = ca. 8300) from the Wolverine Deposit. The samples are color-coded according to ore grade, with blue samples representing unmineralized BRM host rock. Qtz = quartz, KF = K-feldspar, Mus = muscovite. Note, most of the ore samples plot along the Qtz+Mus tie-line.

Timing of Mineralization

Previous U-Pb age dating of primary xenotime-(Y) from a number of occurrences across the NAHREY mineral field has yielded mineralization ages of between 1.65 and 1.61 Ga (Vallini et al., 2007; Morin-Ka et al., 2016). To further constrain the timing of the HREE mineralization, we have conducted U-Pb dating of ore xenotime-(Y) from samples of the Wolverine (samples W5-5 and W5-3), Cyclops (sample C2), and Boulder Ridge (sample BR1) orebodies. The analyses were conducted using laser ablation ICP-MS, with calibration against well-characterized xenotime-(Y) standards, as outlined in Appendix 4-3. All samples returned concordant ages between 1.64 Ga to 1.60 Ga, with a clustering around ca. 1.62 Ga (Fig. 4-6). These results are consistent with the previous dating results of Vallini et al. (2007) and Morin-Ka et al. (2016) and indicate a relatively short time frame of xenotime-(Y) mineralization across the region. The mineralization age postdates known magmatism in the region but is close in age to the deposition of the Gardiner Sandstone of the Birrindudu Group (Vallini et al., 2007).

Sm-Nd Isotopes

Samarium-Nd isotope data can effectively trace the source of metals for REE deposits, with most large deposits having clear affinities with mantle sources (Smith et al., 2016). We have determined the Nd isotope composition of xenotime-(Y) ore from several deposits/prospects across the region via conventional bulk-rock isotope analysis and by in situ microanalysis of xenotime-(Y) (by TIMS and laser ablation multi-collector ICP-MS, respectively; see Appendix 4-4 for analytical methods). Values of εNd calculated to the approximate age of mineralization (1.62 Ga) are between -12 to -16 for the bulk ore, and between -12 and -27 for in situ xenotime-(Y) (Fig. 4-7; Appendix 4-4). The relatively large range of εNd values, even at the individual sample scale, is an artefact of micro-scale Sm/Nd zoning within the xenotime-(Y) crystals that returns highly variable analytical signals during laser ablation sampling (see Appendix 4-4 for more details). Nevertheless, the range of in-situ values broadly agrees with the bulk ore values. For comparison, the BRM that host the mineralization have $\varepsilon Nd_{(1.62\ Ga)}$ values of -15 and -23, and give a model age (T_{DM}) of 3.0 to 3.2 Ga (with the exception of sample G5-5 that is characterized by relatively high $^{147}Sm/^{144}Nd$ likely owing to late stage LREE mobilization), which is entirely consistent with the Mesoarchean age and Lu-Hf isotope signature of detrital zircons from these rocks (Nazari-Dehkordi et al., 2017), as well as the evolved Nd and Pb isotopic signature of the Browns Range Dome overall (Champion, 2013; D. Huston, pers. comm.). The commonality of Nd isotope signatures of the HREE+Y ore and the BRM is even more apparent when compared to other potential REE sources in the region (Fig. 4-7). The Birrindudu Group sandstones that unconformably overlie the BRM have $\varepsilon Nd_{(1.62\ Ga)}$ values between +1 and -5 (Champion, 2013), reflecting a more juvenile source for these sedimentary rocks. Mafic igneous rocks of the North Australia Craton provide constraints on the mantle $\varepsilon Nd_{(1.62\ Ga)}$ signature of between +5 and -5 (Champion, 2013).

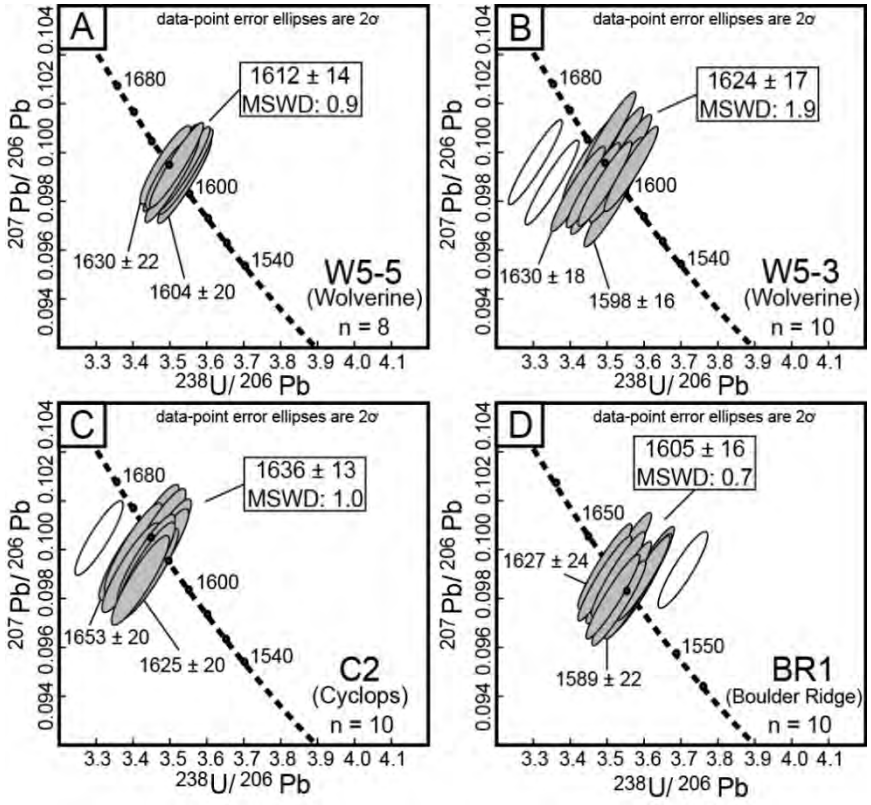

Fig. 4-6: Tera-Wasserburg plots of in situ U-Pb dating of xenotime-(Y) from ore samples from Wolverine (A-B), Cyclops (C), and Boulder Ridge (D). See Figure 4-1 for deposit/prospect locations. Unfilled ellipses were excluded from the age calculations. Note that the age of all samples is between ca. 1640 and ca. 1600 Ma.

Discussion

The mineralization of the NAHREY mineral field is unlike that of any known REE ore deposit, with the exception of the Maw Zone of Canada (see below; Rabiei et al., 2017). Whereas most other REE deposits are hosted in - or associated with - magmatic rocks, the NAHREY mineralization is of regional extent; it is structurally controlled and is hosted in metasedimentary rocks. The ore occurs as veins and breccias, and the ore mineralogy is relatively simple, being dominated by xenotime-(Y) and quartz, with an intense muscovite halo. The mineralization has clear hydrothermal affinity, despite the fact that REE+Y are regarded as relatively immobile under most hydrothermal conditions (e.g., Williams-Jones et al., 2012; Migdisov et al., 2016). Our ore genesis model for this enigmatic REE mineralization style attempts to reconcile these issues.

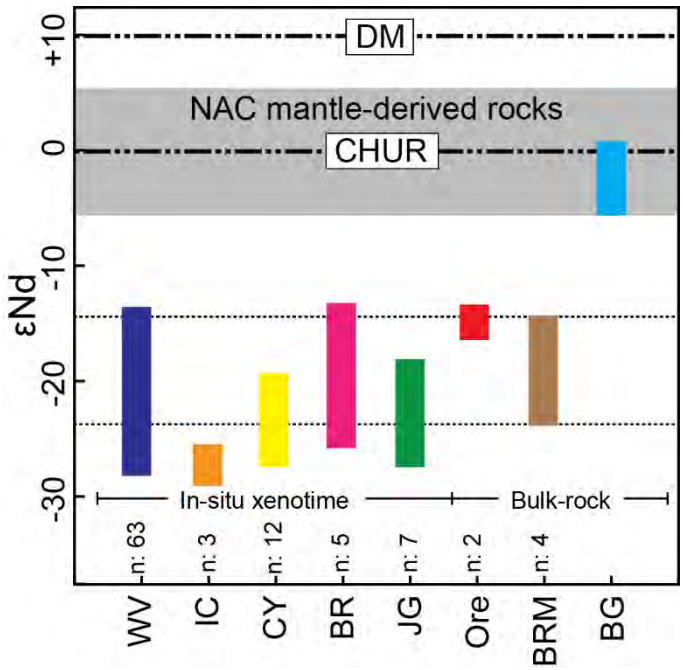

Fig. 4-7: εNd values (t = 1.62 Ga) of HREE+Y orebodies and the host rock units. BG = Birrindudu Group, NAC = North Australian Craton. Data for NAC mantle-derived rocks and BG are from Champion (2013). Deposit/prospect abbreviations; WV = Wolverine, IC = Iceman, CY = Cyclops, BR = Boulder Ridge, JG = John Galt. See Figure 4-1 for deposit/prospect locations.

Source of REE for ore formation

The timing of ore formation (1.61 to 1.65 Ga) in the NAHREY mineral field does not correlate with any known magmatic activity in the wider region, and the orebodies have highly non-radiogenic Nd isotope compositions that are inconsistent with the REE originating from the overlying sedimentary rocks, or from mantle or juvenile igneous sources. The Nd isotope signatures do, however, match those of the hosting BRM (Fig. 4-7), identifying these metasedimentary rocks as the only plausible source of the ore metals. This premise is supported by the distinctive signature of HREE+Y depletion of the BRM that is not shared by granitic or sedimentary protoliths but does mirror the REE enrichment signature of the ore (Fig. 4-2). We discount fluid leaching of REE from zircon, as our previous study of zircons from the BRM (Nazari-Dehkordi et al., 2017) found no evidence of zircon dissolution or modification at ca. 1.62 Ma (i.e., the timing of mineralization). Garnet is an important HREE sink, but garnet does not occur in the BRM, and the REE depletion signature is inconsistent with a garnet source (Fig. 4-2B). Instead, we propose that REE+Y were leached from accessory REE-bearing

phosphates (apatite, monazite-(Ce) or xenotime-(Y)) from the BRM by acidic fluids. A similar process has been proposed for hydrothermal mobility of REE in environments of unconformity U deposits (Gaboreau et al., 2007), and is consistent with the results of experimental leaching of sedimentary rocks by acidic fluids (Ohr et al., 1994).

As well as acidic conditions, hydrothermal transport of REE requires complexation with species such as Cl^-, F^-, CO_3^{2-} and SO_4^{2-} (e.g., Migdisov et al., 2016; Zhou et al., 2016). The ore mineral paragenesis at Browns Range is free of carbonate or sulphate but does include F-rich hydrothermal muscovite (Fig. 4-4) and Cl-bearing fluid inclusions hosted in quartz (Richter et al., 2018; Nazari-Dehkordi et al., in prep). Therefore, REE leaching of the BRM was likely caused by percolation of low pH saline (Cl, ±F) fluids. The source of these fluids (and halogens) may be the metamorphic basement rocks, or basinal brines, both of which can contain appreciable halogen contents (e.g., Chae et al., 2007; Kharaka and Hanor, 2014).

Under most conditions hydrothermal fluids preferentially mobilize LREE over HREE+Y (Migdisov et al., 2016). This, together with the LREE rich nature of the BRM, conflicts with the observed depletion trend of the BRM (Fig. 4-2) and HREE+Y rich nature of the ore. We suspect that the Al-rich, Ca-poor BRM favoured florencite (LREE-Al phosphate) stability, which is supported by the presence of secondary florencite in the BRM (Nazari-Dehkordi et al., 2017) and in other analogous metasedimentary units, such as those around unconformity U deposits (e.g., Gaboreau et al., 2007). Drawing on the proposed phase relationships of Ohr et al. (1994) and Doroshkevich et al. (2009), we suggest that REE phosphate dissolution is coupled to hydrothermal formation of florencite according to the generalized reaction [1]:

$$\underset{\text{xenotime}}{YPO_4} + \underset{\text{monazite}}{CePO_4} + \underset{\text{K-feldspar}}{3KAlSi_3O_8} + 6H(F,Cl)_{(aq)} = \underset{\text{florencite}}{CeAl_3(PO_4)_2} + \underset{\text{quartz}}{9SiO_2} + 3K(F,Cl)_{(aq)} + Y(F,Cl)_{3\,(aq)} \quad [1]$$

Where ‘Ce’ represents LREE, and ‘Y’ represents HREE+Y. The proposed reaction is speculative, as there is currently no experimental or thermodynamic data on florencite stability. Nonetheless, progress of this reaction would be consistent with the presence of highly corroded and pitted accessory REE phosphates found within the BRM (i.e., the remnants of the dissolution reaction; Fig. 4-4B), and can explain the preferential mobility of HREE+Y and, hence, the observed depletion trend in the BRM.

After dissolution of REE+Y from the basement metasedimentary rocks, the percolating hydrothermal fluids then migrated into fault structures where REE+Y phosphate minerals were precipitated in the vicinity of regional unconformities. In the following section we evaluate the processes responsible for ore mineral deposition.

A model for ore genesis

In many respects, the setting of the mineralization in the NAHREY mineral field is similar to that of the unconformity-related U deposits of northern Australia and the Athabasca Basin, Canada; both ore types are structurally controlled, are hosted in Precambrian metasedimentary sequences, and are found in close proximity to regional unconformities (Cuney, 2009). Formation of unconformity-related U deposits involves redox-driven U mineral precipitation due to mixing or reaction of fluid(s) at or near the unconformity (Cuney, 2009); however, the solubilities of HREE and Y in hydrothermal fluids are unlikely to be strongly affected by redox reactions (Migdisov et al., 2016), so another mechanism is required to precipitate ore grade levels of xenotime-(Y).

The ore minerals across the NAHREY mineral field are exclusively phosphates, indicating that P also plays an important role in ore formation. Phosphorous has low solubility in hydrothermal fluids and is considered to be effective in binding with soluble REE to drive mineral precipitation (Williams-Jones et al., 2012; Gysi et al., 2015; Migdisov et al., 2016). The BRM has a low phosphate content so the required P likely originated from a different source to that of HREE, and also was likely transported in an acidic environment under which P is highly soluble, possibly as H_3PO_4 (Gysi et al., 2015). We propose that P was supplied from Birrindudu Group sandstones that lie above unconformity, as this unit is reported to contain Fe-stained phosphate (Vallini et al., 2007) and detrital apatite, derived mainly from apatite-rich ~1.83 Ga granites in the Tanami Region (Crispe et al., 2007). Phosphate dissolution was likely driven via low-pH meteoric fluids circulating through the Birrindudu Group sandstones, as has been reported for other sandstone units (e.g., Morton, 1986).

H_3PO_4–bearing fluids derived from the Birrindudu Group migrated down into fault structures in the vicinity of the regional unconformity, and there mixed with up-flowing saline HREE+Y–bearing fluids from the BRM (Fig. 4-8). Mixing of the fluids converted detrital K-feldspar and other minerals into F–bearing muscovite, and produced highly insoluble REE phosphates, mainly xenotime-(Y). The reaction [2] can be generalized as follows:

$$Y(F,Cl)_{3\,(aq)} + HCl_{\,(aq)} + H_3PO_{4\,(aq)} + 3KAlSi_3O_8 = KAl_3Si_3O_{10}(F)_2 + YPO_4 + 6SiO_2 + 2H_2O_{(aq)} + 2KCl_{\,(aq)} \quad [2]$$

(BRM) (BRM) (BG) K-Feldspar muscovite xenotime quartz

(where ‘Y’ represents HREE+Y, BRM = Browns Range Metamorphics, and BG = Birrindudu Group). Based on the limited syn-ore thermal overprint and the fluid inclusion data of Richter et al. (2018), we estimate the temperature of ore formation to have been between 150 and 350 °C. These temperatures are consistent with expected geothermal gradients to the base of the Birrindudu Group (~6 kms) and with hydrothermal temperatures proposed for unconformity U deposits that form in similar geological settings (Derome et al., 2005). This model not only produces the observed simple ore assemblage of quartz, F-rich muscovite and xenotime-(Y), but also provides a connection between ore genesis, fault structures and the regional unconformity, and hence also an association with unconformity-related U mineralization models. Ore mineral precipitation was largely driven by the extremely low solubility of the REE in the presence of P, and neutralization of acidic fluids (e.g., see Gysi et al. 2015) through conversion of K-feldspar to muscovite. The source fluids were not likely highly enriched in REE, so we expect the fault systems that host mineralization were witness to very high fluid fluxes, which would be consistent with the generation of a very simple metasomatic assemblage in the altered ore hosts. The distinctive HREE-Y rich nature of the ore may be due to prior LREE depletion from the fluid by florencite precipitation, as outlined above. Alternatively, REE fractionation may have occurred at the site of ore formation due to the lower solubility of HREE+Y compared to LREE (see Migdisov et al., 2016). In this case, the LREE remained soluble during fluid mixing, and were subsequently transported (with Cl) out of the mineralization zones. A similar ore genesis process has been proposed for the xenotime-(Y) rich Lofdal deposit in Namibia (Williams-Jones et al., 2015).

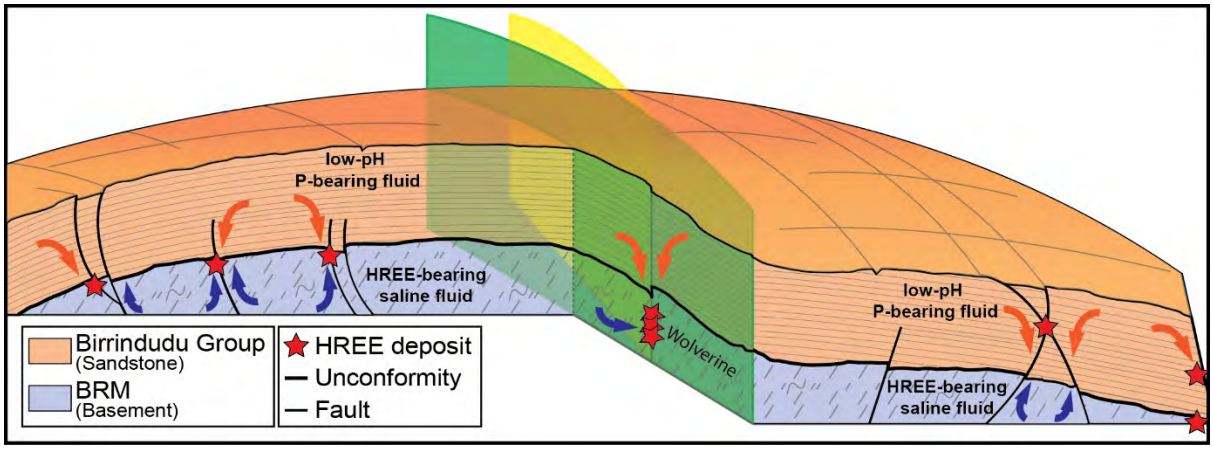

Fig. 4-8: An ore genesis model for the HREE ore formation. Three-dimensional cartoon of the Browns Range Dome illustrating the mixing of fluids leading to ore formation along fault zones in the vicinity of the regional unconformity between the BRM and the Birrindudu Group sandstones. Wolverine, the largest known deposit, developed at the intersection of two steeply dipping faults.

Tectonic drivers of mineralization

The formation of the NAHREY mineral field at 1.65-1.61 Ga was not associated with any local-scale magmatism or orogeny, but coincided with an abrupt change in the apparent polar wandering path of northern Australia (Idnurm, 2000), which has been ascribed to major continental collision events involving the North Australian Craton (Pisarevsky et al., 2014). This time period corresponds to the initiation of the Isan Orogeny (Gibson et al., 2017) and accretion of the Warumpi Province (i.e., Liebig Orogeny: Scrimgeour et al., 2005) along the eastern and southern margins of the North Australian Craton, respectively. In these areas, records of the collisional events include high-grade metamorphism and deformation, and mafic to felsic magmatism (e.g., Andrew Young and Papunya Igneous Complexes in the Arunta regions; Young et al., 1995). This time period also saw the formation of the Nabarlek U deposit in the Pine Creek Orogen (Polito et al., 2004), as well as large stratiform Pb-Zn-Ag orebodies in the McArthur River (HYC) and Mount Isa (Hilton-George Fisher, Mount Isa, Cannington) districts (Large et al., 2005).

There is little evidence to suggest that this tectonothermal activity extended throughout the interior of the North Australian Craton (including the Browns Range area) at this time (Fraser et al., 2012; Li et al., 2014). Therefore, we propose that far-field effects of these distal orogenic

events caused faulting and/or fault reactivation and doming in the Browns Range area, which initiated fluid circulation within the upper crust leading to REE mineralization. Similar tectonic and geological conditions have been proposed for unconformity-related U deposits that formed during the same broad time period (Cui et al., 2012).

Global correlatives and implications for exploration

The regional extent and large number of deposits/prospects within the NAHREY mineral field provides encouragement that hydrothermal REE mineralization of similar style may occur elsewhere in northern Australia, and the world. Indeed, the Maw Zone deposit of Canada shares many of the distinctive features of the NAHREY mineralization. The Maw Zone consists of hydrothermal xenotime-(Y) mineralization within brecciated sandstone close to the Archean-Proterozoic unconformity of the Athabasca Basin (Rabiei et al., 2017). The fluid mixing ore genesis model proposed by Rabiei et al. (2017) for the Maw Zone is similar to that proposed here, and hence may describe an essential process for formation of this type of REE deposit. Collectively, this mineralization style is unlike other established REE ore types, and accordingly is labelled Unconformity-Related.

Exploration for Unconformity-Related REE mineralization would require a very different approach than that taken for other types of REE ore deposits. Unlike other REE ore deposits, an association with magmatism is not required; rather, the key ingredients for ore formation appear to be fault structures close to regional unconformities within intercontinental sedimentary basins. Metasedimentary rocks that supply the REE need not be especially REE rich but do need to be Ca and P depleted to avoid fluorite and apatite saturation during hydrothermal fluid flow. Meeting these criteria are arkosic sediments derived from granitic sources (such as the BRM). Mineral deposition is achieved by mixing low pH saline fluids carrying REE, with acidic fluids carrying P, so overlying sedimentary units rich in phosphate could be considered as potential indicators for exploration of hydrothermal REE mineralization. Other prospective areas include the McArthur Basin of northern Australia, and the Athabasca and Thelon Basins of Canada, all of which host significant unconformity-related U deposits, and are noted to contain anomalous levels of REE phosphates in hydrothermally altered rocks (Quirt et al., 1991; Fayek and Kyser, 1997; Gaboreau et al., 2007; Davis et al., 2011; Orth et al., 2014; Rabiei et al., 2017).

Acknowledgments

This work was supported by Northern Minerals Ltd and an ARC Future Fellowship (FT 120100198) to CS. The authors acknowledge Northern Minerals Ltd for logistical support. We also thank Anthony Williams-Jones, Kathryn Goodenough and David Huston for their insightful comments.

References

Anenburg, M., and Mavrogenes, J., 2018. Carbonatitic versus hydrothermal origin for fluorapatite REE-Th deposits: Experimental study of REE transport and crustal “antiskarn” metasomatism. American Journal of Science, v. 318, p. 335–366.

Chae, G.T., Yun, S.T., Mayer, B., Kim, K.H., Kim, S.Y., Kwon, J.S., and Koh, Y.K., 2007. Fluorine geochemistry in bedrock groundwater of South Korea. Science of the Total Environment, v. 385, p. 272–283.

Champion, D.C., and Smithies, R.H., 2007. Three billion years of granite magmatism: Palaeo-Archaean to Permian granites of Australia: Sixth International Hutton Symposium, Origin of granites and related rocks. University of Stellenbosch, South Africa.

Champion, D.C., 2013. Neodymium depleted mantle model age map of Australia: explanatory notes and user guide: Record 2013/44. Geoscience Australia, Canberra.

Cook, N.J., Ciobanu, C.L., O'Rielly, D., Wilson, R., Das, K., and Wade, B., 2013. Mineral chemistry of Rare Earth Element (REE) mineralization, Browns Ranges, Western Australia. Lithos, v. 172-173, p. 192–213.

Crispe, A.J., Vandenberg, L.C., and Scrimgeour, I., 2007. Geological framework of the Archaean and Palaeoproterozoic Tanami Region, Northern Territory. Mineralium Deposita, v. 42, p. 1–26.

Cross, A., and Crispe, A., 2007. SHRIMP U-Pb analyses of detrital zircon: a window to understanding the Paleoproterozoic development of the Tanami Region, northern Australia. Mineralium Deposita, v. 42, p. 27–50.

Cui, T., Yang, J., and Samson, I.M., 2012. Tectonic deformation and fluid flow: Implications for the formation of unconformity-related uranium deposits. Economic Geology, v. 107, p. 147–163.

Cuney, M., 2009. The extreme diversity of uranium deposits. Mineralium Deposita, v. 44, p. 3–9.

Davis, W.J., Gall, Q., Jefferson, C.W., and Rainbird, R.H., 2011. Fluorapatite in the Paleoproterozoic Thelon Basin: structural-stratigraphic context, in-situ ion microprobe U-Pb ages, and fluid flow history. Geological Society of America Bulletin, v. 123, p. 1056–1073.

Derome, D., Cathelineau, M., Cuney, M., Fabre, C., Lhomme, T., and Banks, D.A., 2005. Mixing of sodic and calcic brines and uranium deposition at the McArthur River,

Saskatchewan, Canada. A Raman and Laser-Induced Breakdown Spectroscopic study of fluid inclusions. Economic Geology, v. 100, p. 1529–45.

Doroshkevich, A.G., Viladkar, S.G., Ripp, G.S., and Burtseva, M.V., 2009. Hydrothermal REE mineralization in the Amba Dongar carbonatite complex, Gujarat, India. The Canadian Mineralogist, v. 47, p. 1105–1116.

Fayek, M., and Kyser, T.K., 1997. Characterization of multiple fluid-flow events and rare-earth-element mobility associated with formation of unconformity-type uranium deposits in the Athabasca basin, Saskatchewan. Canadian Mineralogist, v. 35, p. 627–658.

Fraser, G.L., Bagas, L., and Huston, D.L., 2012. $^{40}Ar/^{39}Ar$ evidence for the timing of Paleoproterozoic gold mineralisation at the Sandpiper Deposit, Tanami region, northern Australia. Australian Journal of Earth Sciences, v. 59, p. 399–409.

Gaboreau, S., Cuney, M., Quirt, D., Beaufort, D., Patrier, D., and Mathieu, R., 2007. Significance of aluminum phosphate-sulphate minerals associated with U unconformity-type deposits. The Athabasca Basin, Canada. American Mineralogist, v. 92, p. 267–280.

Gibson, G.M., Hutton, L.J., and Holzschuh, J., 2017. Basin inversion and supercontinent assembly as drivers of sediment-hosted Pb-Zn mineralization in the Mount Isa region, northern Australia. Journal of the Geological Society, v. 174, p. 773–786.

Goodenough, K.M, Wall, F., and Merriman, D., 2017. The Rare Earth Elements: Demand, Global Resources, and Challenges for Resourcing Future Generations. Natural Resources Research, DOI:10.1007/s11053-017-9336-5.

Gysi, A.P., Williams-Jones, A.E., and Harlov, D., 2015. The solubility of xenotime-(Y) and other HREE phosphates ($DyPO_4$, $ErPO_4$ and $YbPO_4$) in aqueous solutions from 100 to 250°C and p_{sat}. Chemical Geology, v. 41, p. 83–95.

Harmer, R.E., and Nex, P.A.M., 2016. Rare earth deposits of Africa. Episodes, v. 39, p. 381–406.

Hatch, G.P., 2012. Dynamics in the global market for rare earths. Elements, v. 8, p. 341-346.

Idnurm, M., 2000. Towards a high resolution late Palaeoproterozoic-earliest Mesoproterozoic apparent polar wander path for northern Australia. Australian Journal of Earth Sciences, v. 47, p. 405–429.

Kharaka Y.K., and Hanor, J.S., 2014. Deep fluids in sedimentary basins. Treatise on Geochemistry, v. 7, p. 471–515.

Korzhinskii, D.S., 1970. Theory of metasomatic zoning. Clarendon Press, Oxford, 162 p.

Large, R.R., Bull, S.W., McGoldrick, P.J., and Walters, S.G., 2005. Stratiform and strata-bound Zn-Pb-Ag deposits in Proterozoic sedimentary basins, northern Australia. Economic Geology, v. 100, p. 931–963.

Li, B., Bagas, L., and Jourdan, F., 2014. Tectono-thermal evolution of the Palaeoproterozoic Granites–Tanami Orogen, North Australian Craton: Implications from hornblende and biotite $^{40}Ar/^{39}Ar$ geochronology. Lithos, v. 206, p. 262–276.

McLennan, M.S., 1989. Rare earth elements in sedimentary rocks; influence of provenance and sedimentary processes. Reviews in Mineralogy and Geochemistry, v. 21, p. 169–200.

Migdisov, A., Williams-Jones, A.E., Brugger, J., and Caporuscio, F., 2016. Hydrothermal transport, deposition, and fractionation of REE. Experimental data and thermodynamic calculations: Chemical Geology, v. 439, p. 13–42.

Morin-Ka, S., Beardsmore, T.J., Hancock, E.A., Rasmussen, B., Dunkley, D., Muhling, J., Zi, J., Wilson, R., and Champion, J., 2016. Alteration and Age of the Browns Range Rare Earth Element Deposits. Western Australian Department of Mines and Petroleum.

Morton, A.C., 1986. Dissolution of apatite in North Sea Jurassic sandstones: Implications for the generation of secondary porosity. Clay Minerals, v. 21, p. 711–733.

Nazari-Dehkordi, T., Spandler, C., Oliver, N.H.S., Chapman, J., and Wilson, R., 2017. Provenance, tectonic setting and source of Archean metasedimentary rocks of the Browns Range Metamorphics, Tanami Region, Western Australia. Australian Journal of Earth Sciences, v. 64, p. 723–741.

Northern Minerals, 2015. Increased mineral resource delivers more good news. Australian Stock Exchange release, www.asx.com.au/asxpdf/20150223/pdf/42ws7ycqttdwn1.pdf.

Ohr, M., Halliday, A.N., and Peacor, D.R., 1994. Mobility and fractionation of rare earth elements in argillaceous sediments: implications for dating diagenesis and low-grade metamorphism. Geochimica et Cosmochimica Acta, v. 58, p. 289–312.

Orth, K., Meffre, S., Davidson, G., 2014. Age and paragenesis of mineralisation at Coronation Hill uranium deposit, Northern Territory, Australia. Mineralium Deposita, v. 49, p. 595-623.

Pisarevsky, S.A., Elming, S.A., Pesonen, L.J., and Li, Z.X., 2014. Mesoproterozoic paleogeography: supercontinent and beyond. Precambrian Research, v. 244, p. 207–225.

Polito, P.A., Kyser, T.K., Marlatt, J., Alexandre, P., Bajwah, Z., and Drever, G., 2004. Significance of alteration assemblages for the origin and evolution of the Proterozoic Nabarlek unconformity-related uranium deposit, Northern Territory, Australia. Economic Geology, v. 99, p. 113–139.

Quirt, D., Kotzer, and Kyser, T.K., 1991. Tourmaline, phosphate minerals, zircon and pitchblende in the Athabasca Group; Maw Zone and McArthur River Areas, Saskatchewan, In: Saskatchewan: Summary of Investigations. Saskatchewan Geological Survey, Miscellaneous Report 91–4.

Rabiei, M., Chi, G., Normand, C., Davis, W.J., Fayek, M., and Blamey, N.J.F., 2017. Hydrothermal Rare Earth Element (Xenotime) Mineralization at Maw Zone, Athabasca Basin, Canada, and Its Relationship to Unconformity-Related Uranium Deposits. Economic Geology, v. 112, p. 1483–1507.

Richter, L., Diamond, L.W., Atanasova, P., Banks, D.A., and Gutzmer, J., 2018. Hydrothermal formation of heavy rare earth element (HREE)–xenotime deposits at 100 °C in a sedimentary basin. Geology, doi: https://doi.org/10.1130/G39871.1.

Scrimgeour, I., Kinny, P.D., Close, D.F., and Edgoose, C.J., 2005. High-T granulites and polymetamorphism in the southern Arunta region, central Australia: evidence for a 1.64 Ga accretional event. Precambrian Research, v. 142, p. 1–27.

Smith, M., Moore, K., Kavecsanszki, D., Finch, A., Kynicky, J., and Wall, F., 2016. From mantle to critical zone: a review of large and giant sized deposits of the rare earth elements. Geoscience Frontiers, v. 7, p. 315–334.

Taylor, S.R., and McLennan, S.M., 1985. The continental crust: Its composition and evolution. Oxford, UK: Blackwell.

Vallini, D.A., Groves, D.I., McNaughton, N.J., and Fletcher, I.R., 2007. Uraniferous diagenetic xenotime in northern Australia and its relationship to unconformity-associated uranium mineralisation. Mineralium Deposita, v. 42, p. 51–64.

Weng, Z, Jowitt S.M., Mudd, G.M., and Nawshad, H.A., 2015. A detailed assessment of global rare earth element resources: Opportunities and challenges. Economic Geology, v. 110, p. 1925–1952.

Williams-Jones, A.E., Migdisov, A.A., and Samson, I.M., 2012. Hydrothermal mobilization of the rare earth elements – a tale of “Ceria” and “Yttria”. Elements, v. 8, p. 355–360.

Williams-Jones, A.E., Samson I.M, and Olivo, G.R., 2000. The genesis of hydrothermal fluorite-REE deposits in the Gallinas Mountains, New Mexico. Economic Geology, v. 95, p. 327–342.

Williams-Jones, A.E., Wollenberg, R., and Bodeving, S., 2015. Hydrothermal fractionation of the rare earth elements and the genesis of the Lofdal REE deposit, Namibia, Symposium on critical and strategic materials. British Columbia Geological Survey Paper 2015–3.

Young, D.N., Fanning, C.M., Shaw, R.D., Edgoose, C.J., Blake, D.H., Page, R.W., and Camacho, A., 1995. U-Pb zircon dating of tectonothermal events in the northern Arunta Inlier, central Australia. Precambrian Research, v. 71, p. 45–68.

Zhou, L., Mavrogenes, J., Spandler, C., and Li, H., 2016. A synthetic fluid inclusion study of the solubility of monazite-(La) and xenotime-(Y) in H_2O-Na-K-Cl-F-CO_2 fluids at 800°C and 0.5 GPa. Chemical Geology, v. 442, p. 121–129.

Chapter 5

Paragenesis and chemistry of the xenotime and florencite from unconformity-related heavy rare earth element mineralisation of northern Western Australia

Teimoor Nazari-Dehkordi[1*], Carl Spandler[1], Nicholas H.S. Oliver[1, 2], Robin Wilson[3]

[1]Economic Geology Research Centre, Department of Geoscience, James Cook University, Townsville, QLD 4811, Australia

[2]HCOVGlobal Consultants, PO Box 3533, Hermit Park, QLD 4812, Australia

[3]Northern Minerals, PO Box 669, West Perth, WA 6872, Australia

Abstract

This study investigates the paragenesis and ore mineral chemistry of xenotime [(Y,HREE)PO_4] and florencite [LREE$Al_3(PO_4)_2(OH)_6$] from heavy rare earth element (HREE) deposits/prospects of the northwest Tanami and Hall Creek regions of Western Australia. Multiple stages of xenotime formation are recognised: (1) Early xenotime (up to 1 mm) in breccias (breccia-hosted) and in quartz-xenotime veins (vein-type); (2) Late xenotime (<100 µm) occurs largely as pyramid-shaped overgrowths on the pre-existing xenotime. Similarly, florencite formed in several stages including: (1) Early florencite (~20 µm), coexisting with early xenotime, is enclosed by early xenotime and occurs within mineralised quartz veins; and (2) Late florencite that largely replaces early xenotime and also appears as narrow rims on early florencite.

Analysis of a number of the HREE deposits/prospects characterised xenotime with elevated U content, and marked Eu anomaly inherited from the Browns Range Metamorphics (source rocks). Late xenotime is richer in HREE and depleted in P compared with the early xenotime, owing to the formation of the coexisting late florencite. Moreover, early florencite has a nearly pure florencite composition similar to that of the unconformity-related U deposits, whereas late florencite sits on the florencite-svanbergite compositional spectrum. We indicate that the high U content of xenotime and composition of early florencite potentially support a genetic association between the HREE mineralisation and the coeval U deposits of northern Australia that formed across the same basin.

Keywords: xenotime, florencite, APS minerals, mineral chemistry, hydrothermal, unconformity, Tanami Region, Halls Creek Orogen

Introduction

Rare earth element (REE) rich minerals are accessory components of most rocks of the continental crust. Due to their affinity to incorporate a range of trace elements and radiogenic isotopes (Nd, Sr, U, Th, Pb), REE-rich minerals can provide important information on the nature and timing of geological events, including igneous crystallisation, metamorphism, and hydrothermal alteration (e.g., Engi, 2017). In rare cases where REE-rich minerals are sufficiently concentrated to form REE orebodies, these minerals may provide crucial information on the age and processes of ore formation (e.g., Andreoli et al., 1994; Harlov et al., 2002; Schoneveld et al., 2015). Phosphates are arguably the most important of REE-minerals, with monazite and apatite being a focus of research in recent years (e.g., Williams, 2001; Ehlers and Farley, 2003; Krenn et al., 2008; Chu et al., 2009; Patino Douce et al., 2011; Harlov et al., 2011; Slezak et al., 2018). By comparison, xenotime [(Y,HREE)PO_4] and florencite [LREE$Al_3(PO_4)_2(OH)_6$] have received much less attention.

Xenotime is often the primary HREE+Y host in crustal rocks. It is stable over a broad range of P-T conditions, and can form in a range of geological environments (igneous, metamorphic, diagenetic and hydrothermal; Rasmussen, 1996; McNaughton and Rasmussen, 2017). Xenotime is also considered a reliable mineral for U-Pb geochronology (Spear and Pyle, 2002), but is often overlooked due to its low modal abundance and frequent fine grainsize (typically <10 μm), which hinders in situ analysis. For these reasons, there are relatively few comprehensive studies of xenotime geochemistry, and of these most have been published in the last few years (e.g., Aleinikoff et al., 2015; Zi et al., 2015; McNaughton and Rasmussen, 2017).

Florencite is the LREE+P end-member of the aluminium phosphate-sulfate (APS) mineral group [$AB_3(XO_4)_2(OH)_6$], where A = LREE, Sr, Ca, Th; B = Al, Fe^{3+}; X = P, S, Si (e.g., Bayliss et al., 2010). Florencite is found as an accessory phase in a range of near-surface geological environments (e.g., sedimentary, diagenetic), but may also be formed under hydrothermal and metamorphic conditions (Nagy et al., 2002; Hikov et al., 2010), and is likely to be more widespread than currently recognised (Rasmussen, 1996). Florencite crystal chemistry allows for solid solution with other APS end-member components (florencite-goyazite-svanbergite-woodhouseite; e.g., Nagy et al., 2002; Bayliss et al., 2010), which can be employed as sensitive

monitors of the physicochemical conditions of formation, such as fO_2 and pH (e.g., Dill, 2001; Gaboreau et al., 2005, 2007; Adlakha and Hattori, 2015). Nonetheless, conditions of florencite stability and occurrence are currently not well understood, with most available information coming from clay assemblages associated with sandstones of northern Australia and Canada (e.g., Rasmussen, 1996; Gaboreau et al., 2005).

The northern Tanami and Halls Creek regions of central Australia are host to HREE+Y mineralised veins and breccias that consist primarily of hydrothermal xenotime and florencite, plus quartz (Cook et al., 2013; Nazari-Dehkordi et al., 2018). This mineralisation district is known as the North Australian HREE+Y (NAHREY) mineral field (Nazari-Dehkordi et al., 2018). The HREE+Y mineralisation reaches grades of economic significance, with the largest deposit, the Wolverine deposit, containing a total mineral resource of 4.97 Mt at 0.86% total rare earth oxides. Mineralisation is hosted with Archean metasedimentary rocks in close proximity to regional-scale unconformities, and hence are known as unconformity-related REE ore deposits (Nazari-Dehkordi et al., 2018). In this paper, we combine detailed petrographic studies and geochemical data for various different generations of xenotime and florencite from several deposits/prospects from across the NAHREY mineral field. These data allow us to evaluate the composition and distribution of trace elements between xenotime and florencite formed under hydrothermal conditions, and hence contributes to understanding of the conditions of formation of these REE phosphate minerals.

Geological setting and mineralisation

The NAHREY mineral field encompasses a relatively vast area that extends ca. 300 km from the Halls Creek Orogen (Red Rock Basin) to the Tanami Region (Fig. 5-1A). Detailed geological descriptions of the Tanami Region and Halls Creek Orogen are presented elsewhere (e.g., Crispe et al., 2007; Bagas et al., 2008; Nazari-Dehkordi et al., 2017 for the Tanami Region, and Griffin et al., 2000; Page et al., 2001; Ahmad and Munson, 2013, for the Halls Creek Orogen). Here we present a brief overview of the geology of these regions, with particular reference to the HREE+Y mineralisation.

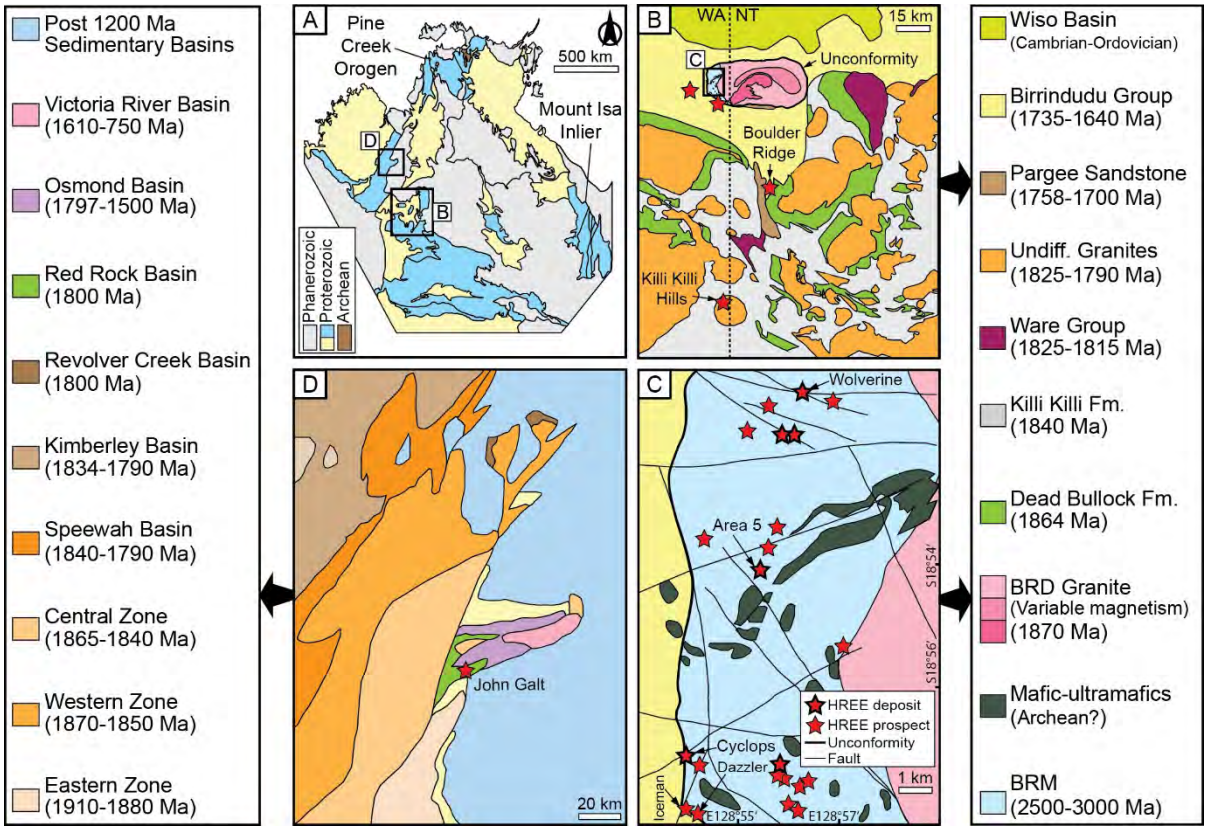

Fig. 5-1: Geological maps of the Tanami Region and Halls Creek Orogen. (A) Distribution of the hydrothermal HREE mineralisation in the NAHREY mineral field, northern Australia; (B) Simplified geological map of the Tanami Region; (C) Geological map of the western section of the Browns Range Dome (BRD) with the locations of HREE deposits/prospects indicated; (D) Simplified geological map of the Hall Creek Orogen.

Tanami Region

Situated in the northwest of the Tanami Region (Fig. 5-1B), the Browns Range Dome is an east-west trending ovoid-shaped structure measuring ca. 60 km by ca. 30 km, cored by the 1 to 3 km thick, ca. 1.87 Ga Browns Range Dome granite (Page et al., 1995; Hendrickx et al., 2000; Cross and Crispe, 2007). The western section of the Dome comprises Archean metasedimentary rocks (mainly immature quartz arkose) of the Browns Range Metamorphics (BRM) (Fig. 5-1C), that was crosscut by small ca. 2.5 Ga granitic, syenitic and pegmatitic intrusions (Nazari-Dehkordi et al., 2017). These rocks experienced regional metamorphism, mostly of greenschist facies, at ca. 1.8 Ga.

Unconformably overlying the BRM are sedimentary sequences including the ca. 1.78 to ca. 1.64 Ga Pargee Sandstone and Birrindudu Group (Crispe et al., 2007; Vallini et al., 2007), and the <1.8 Ga Tanami Group and Ware Group (Smith, 2001). Of most significance here is the Gardiner Sandstone of the Birrindudu Group, as this unit overlies the BRM along the western margin of the Browns Range Dome in close proximity to most of the HREE mineralisation (Fig. 5-1).

Most of the known mineralisation occurrences (including deposits having >0.1 Mt of ore grading at > 0.2% TREO, and prospects) of the NAHREY mineral field are hosted by the BRM (Fig. 5-1). Each of these deposits and prospects have been individually named after characters of the X-men comic series. In all cases, the mineralisation is characterised by a simple ore mineralogy of xenotime and florencite, and consists primarily of quartz-xenotime veins and breccias accommodated in sub-vertical faults, surrounded by a halo of low grade ore extended into the host rock. The largest deposit, Wolverine, is a steeply (~75° N) dipping planar orebody, up to 5 m wide, that extends over 400 m in strike length and from the surface to at least 550 metres in depth. The orebody lies within a WNW-striking fault in association with an intersecting N-E trending fault. Most other deposits/prospects (e.g., Iceman and Cyclops, and including Boulder Ridge, 40 km SE of the Browns Range Dome; Fig. 5-1) occur close to, or within, the unconformity with the overlying Birrindudu Group sandstones, and are developed along dominantly steeply-dipping W- to SW-striking structures with limited surface exposure. All of these deposits/prospects are rich in xenotime, with only subordinate florencite. The Area 5 orebody (Fig. 5-1) is compositionally distinct, as it is dominated by florencite with only minor amounts of xenotime. This orebody occurs at an intersection of sub-vertical fault zones with prominent WNW and NE strikes, alongside which the orebody appears as discontinuous pods.

Geochronological studies conducted on primary xenotime indicate that the HREE+Y mineralisation throughout the NAHREY mineral field formed between ca. 1.65 to ca. 1.60 Ga (Vallini et al., 2007; Morin-Ka et al., 2016; Nazari-Dehkordi et al., 2018). This time period postdates all known magmatic and metamorphic events in the region (Nazari-Dehkordi et al., 2018).

Halls Creek Orogen

Bounding the Tanami Region to the northwest is the north-northeast trending Halls Creek Orogen (Fig. 5-1D), which consists of three distinct metamorphic zones including Eastern, Central and Western Zones (Tyler et al., 1995). During the ca. 1.87-1.85 Ga Hooper Orogeny, metamorphic sequences of the Western Zone were deformed, due to the accretion of the Central Zone island arc terrane onto the eastern margin of the Kimberley Craton (Sheppard et al., 1999). Subsequent collision of the North Australian Craton (Halls Creek Group of the Eastern Zone) with the Kimberley Craton, and associated intrusive magmatism is marked by the ca. 1.84 to 1.81 Ga Halls Creek Orogeny (Sheppard et al., 1999). All Zones were later unconformably overlain by the Speewah Group and the Kimberley Basin, which are broadly equivalent to the ca. 1.80 Ga Red Rock Basin (Griffin et al., 2000; Page et al., 2001). The Red Rock Basin is host to the John Galt HREE+Y mineralisation but to date has received very little study. The Red Rock Basin is bounded by the prominent Angelo–Halls Creek–Osmond Fault System (Sheppard et al., 1999) and is composed of a sequence of fine- to coarse-grained quartz-rich sandstones with interlayers of pebbly sandstone, conglomerate and basaltic lavas (Blake et al., 2000).

To date, only one xenotime-rich HREE+Y orebody, known as John Galt, has been identified within the Halls Creek Orogen. John Galt consists of steeply-dipping quartz-xenotime veins that crop out along major N-S oriented faults and, most distinctively, along a ~100 metre high ENE-trending escarpment. Mineralisation extends to at least 100 m depth, based on limited exploration drilling. The mineralised structure cuts metasedimentary rocks of the Red Rock Basin, and appears to extend into the metamorphic rocks of the Central and, potentially, Western Zones that underlie the unconformity. The timing of mineralisation at John Galt is similar to other areas of the NAHREY mineral field, being ca. 1.62 Ga (Morin-Ka et al., 2016; Nazari-Dehkordi et al., 2018).

Analytical methods

Sampling and petrography

Drill core and outcrop samples of most of the deposits/prospects were collected, although sampling efforts focussed in and around the Wolverine deposit. Prior to analysis, the samples were lightly brushed and washed in an ultrasonic bath to remove any loose soil or contamination from drilling mud. Thin sections of representative samples were examined using conventional optical microscopy and electron microscopy (backscattered electron imaging; BSE) to identify the ore mineral assemblages and characterise textural relationships among the ore minerals and the host rock. A complete list of the sample locations and information is provided in Appendix 5-1.

Electron probe microanalysis

Wavelength dispersive spectrometry (WDS) analyses of florencite were performed using JEOL-JXA8200 superprobe at the Advanced Analytical Centre (AAC) at James Cook University (JCU), using a 20 nÅ electron beam defocused to 3 µm, and accelerating voltage of 15 kV. Florencite analyses were made on polished thin sections prepared from ore samples of Wolverine and Area 5 deposits. Back-scattered electron (BSE) images were obtained prior to the quantitative analysis to identify compositional variations or assess internal zonings of ore minerals. The elements measured in a single analysis were P, Fe, Gd, F, Ca, Y, Nd, Sm, Al, Th, Si, Ce, Pr, Cl, La, S and Sr. WDS analysis of xenotime were not completed owing to the complications of multiple WDS peak overlaps associated with HREE; instead xenotime analyses were conducted by LA-ICP-MS, as outlined below. Further information on the analytical conditions are presented in Appendix 5-2.

Laser ablation ICP-MS analysis

The composition of xenotime was obtained using laser ablation inductively-coupled plasma mass spectroscopy (LA-ICP-MS) at the AAC, JCU, using a GeoLas 193-nm ArF Excimer laser ablation system coupled with a Bruker (formally Varian) 820-MS ICP MS. Ablation was conducted in a custom-build large volume cell as described by Fricker et al. (2011) using high-

purity He as the carrier gas, which was subsequently mixed with Ar prior to introduction into the ICP-MS. The ICP-MS was tuned for maximum sensitivity under robust plasma conditions (Th/U sensitivity ratio ~1; e.g., Pettke, 2008) and maintaining oxide production rates (monitored by ThO/Th) to below 0.4%. For spot analyses, the laser fluence was set to 6 J/cm^2 at the sample site with laser repetition rate and beam diameter set to 10 Hz and 60 μm, respectively. These conditions provide excellent analyte sensitivity with controlled ablation, which results in smooth time-integrated analytical signals. Bracketing analyses of NIST-SRM-612 and NIST-SRM-610 glasses were used for external standardisation, employing the elemental reference values of Spandler et al. (2011). Internal standardisation was completed by summing all elements as oxides to 100%. This approach introduces an additional degree of uncertainty to the data, as P (a major element) is poorly determined by LA-ICP-MS. Nonetheless, our calculated Y and HREE contents are comparable to reported Y and HREE contents of xenotime from several HREE deposits/prospects by Cook et al. (2013). Data reduction was carried out using the GLITTER software (Van Achterbergh et al., 2001).

Result

Ore petrography and paragenesis

The mineralisation of the NAHREY mineral field is characterised by a simple ore mineralogy of xenotime and florencite only, with no trace of carbonates (e.g., bastnaesite) or any other REE-bearing minerals (e.g., monazite). A mineral paragenetic sequence was developed based mainly on the samples collected from Wolverine, as this is the largest and most comprehensively sampled deposit in the NAHREY mineral field. Nevertheless, available field data, sample petrography and geochemical and isotopic data illustrate remarkable similarities among different deposits/prospects. Collectively, three major mineral assemblages are associated with the mineralisation and the host metasedimentary rocks:

(1) A pre-ore detrital and metamorphic assemblage, including quartz (several generations), alkali feldspar, hematite and coarse-grained muscovite aligned in pre-mineralisation foliation. The pre-ore assemblage chiefly reflects a greenschist-facies overprint on the predominantly arkosic host rocks, resulting in locally well-developed schistose foliation, which is expected to have formed during the widespread ca. 1.83 Ga Tanami Event (Crispe et al., 2007).

(2) A syn-ore hydrothermal mineral assemblage consisting predominantly of xenotime, florencite, and an association of fine-grained, cavity-filled and/or cemented quartz and muscovite-sericite-illite assemblages, entirely enclosing the ore minerals. The intensity of the quartz-muscovite alteration is greatest in close proximity to the HREE+Y mineralisation, but does extend for several metres into the surrounding BRM in some cases.

Multiple stages of xenotime and florencite formation are recognised based on petrographic examinations of ore samples from across the NAHREY mineral field. The earliest stages of the HREE mineralisation are represented by xenotime formed in highly brecciated zones and quartz-xenotime veins, herein referred to as “breccia-hosted” (Figs. 5-2A-B), and “vein-type” (Fig. 5-2C) mineralisation, respectively. These early stages of xenotime (early xenotime) were subsequently overgrown by euhedral pyramid-shaped xenotime (late xenotime; Fig. 5-2D). Similarly, the occurrence of florencite can be classified into (early) syn-ore and (late) post-ore parageneses. The early florencite appears as equant euhedral crystals in the breccias (Fig. 5-2B) and as disseminations in the quartz-xenotime veins (Fig. 5-2E). These crystals show no signs of replacement and are interpreted to have co-crystallised with early xenotime. Occasionally, the early florencite, particularly the coarser grains in the mineralised veins, shows a zonation in BSE imaging of a darker core and a brighter rim (Fig. 5-2E). The rims are here considered as late florencite that postdate the early florencite core. Florencite replacing early stage xenotime, characterised by irregular resorbed boundaries between the two minerals, is also considered as late florencite (Fig. 5-2F).

(3) A post-ore mineral assemblage consisting mainly of quartz (multiple generations), hematite, barite and anhydrite within veins, varying in size from fine- to coarse-grained (up to 5 cm in size), that cross-cut the early stage of xenotime mineralisation (breccia-hosted and vein-type). In places post-ore quartz veins form a wide range of breccias mostly alongside previously mineralised major faults and fractures.

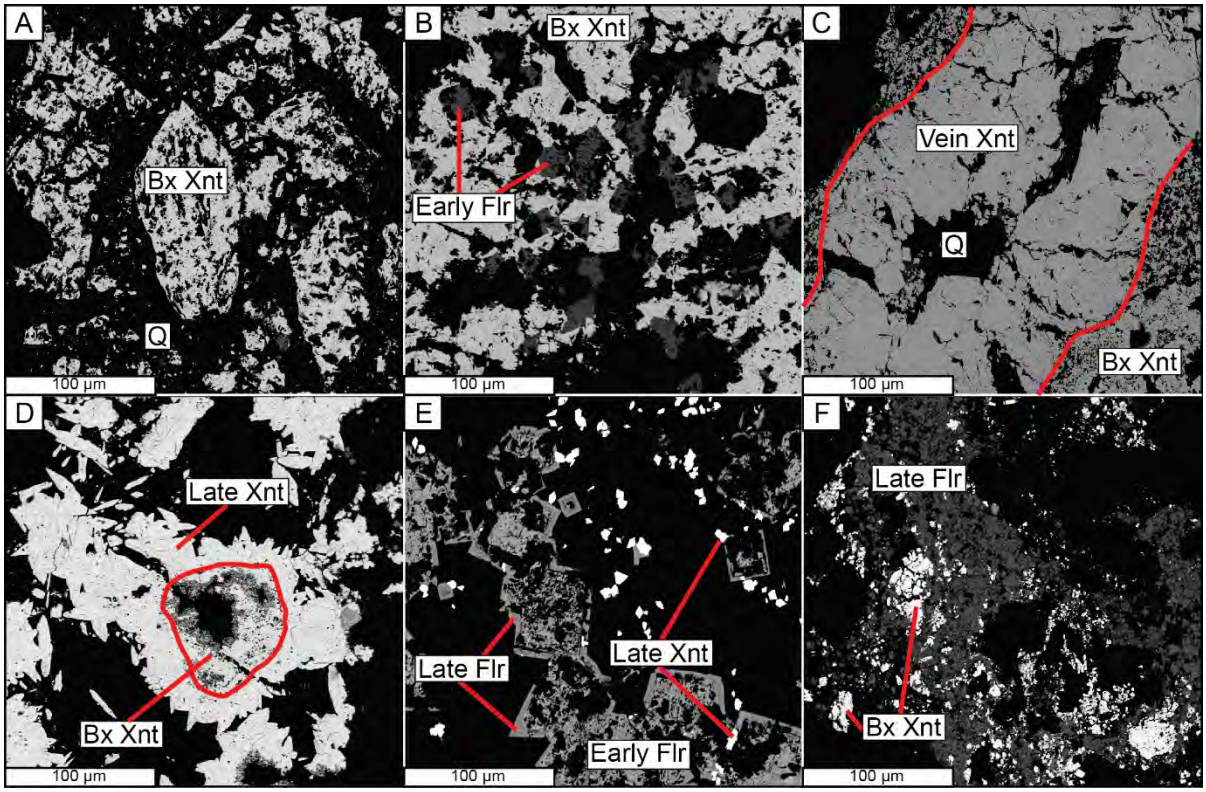

Fig. 5-2: Backscattered electron images of the ore mineral assemblage. (A) Breccia-hosted (Bx) xenotime; (B) Breccia-hosted xenotime and associated early florencite (Flr); (C) Hydrothermal quartz-xenotime vein cross-cutting breccia-hosted xenotime; (D) Late pyramid-shaped xenotime overgrowths; (E) Late rim-type florencite overgrowths on early florencite; (F) Late florencite replacing xenotime.

Composition of xenotime and florencite

The LA-ICP-MS data of xenotime are presented in Appendix 5-3 and Figure 5-3. Average composition of xenotime of various generation from different HREE deposits/prospects is also presented in Table 5-1. All xenotime samples are highly enriched in HREE from Gd to Lu, depleted in La, Ce, and Pr, and have distinct negative Eu anomalies (between 0.34 and 0.6) (Fig. 5-3A). The REE patterns illustrate a relatively wide concentration range for LREE, and comparatively limited variation for the HREE. Late overgrowth xenotime tends to be richer in HREE and more depleted in LREE and P compared with the early (breccia-hosted and vein-type) xenotime (Figs. 5-3B-C, and Fig. 5-4A-D). Analyses of xenotime from Iceman and Boulder Ridge have a relatively flat LREE pattern, from La to Pr (Fig. 5-3A) and variable apparent Al concentrations, owing primarily to the presence of tiny LREE-dominated florencite that could not be avoided during analysis.

Calcium and Fe contents of xenotime are generally within the range of 1000 to 2000 ppm, and 20 to 2500 ppm, respectively, although xenotime from Iceman and Wolverine has Fe contents covering a wide range from ca. 100 ppm up to ca. 28000 ppm (Fig. 5-4E). Similarly, Wolverine and Iceman xenotime have significant variation in Sc content (up to ca. 2000 ppm; Figs. 5-4C-D), whereas other deposits/prospects have comparatively low Sc (mean = 300 ppm). Silicon contents are mostly below detection limits (ca. 0.3 wt.%), with only a limited number of analyses from Boulder Ridge and Iceman containing higher values (up to 0.6 wt.%). All deposits/prospects have low contents of Th (mean = 50 ppm) and Zr (mean = 50 ppm), whereas U content is relatively high with values reaching 6000 ppm (mean = 3000 ppm). In general, xenotime from Iceman contains the highest amounts of trace elements, whereas those of John Galt and Cyclops have the least variation and contain the lowest contents of these elements.

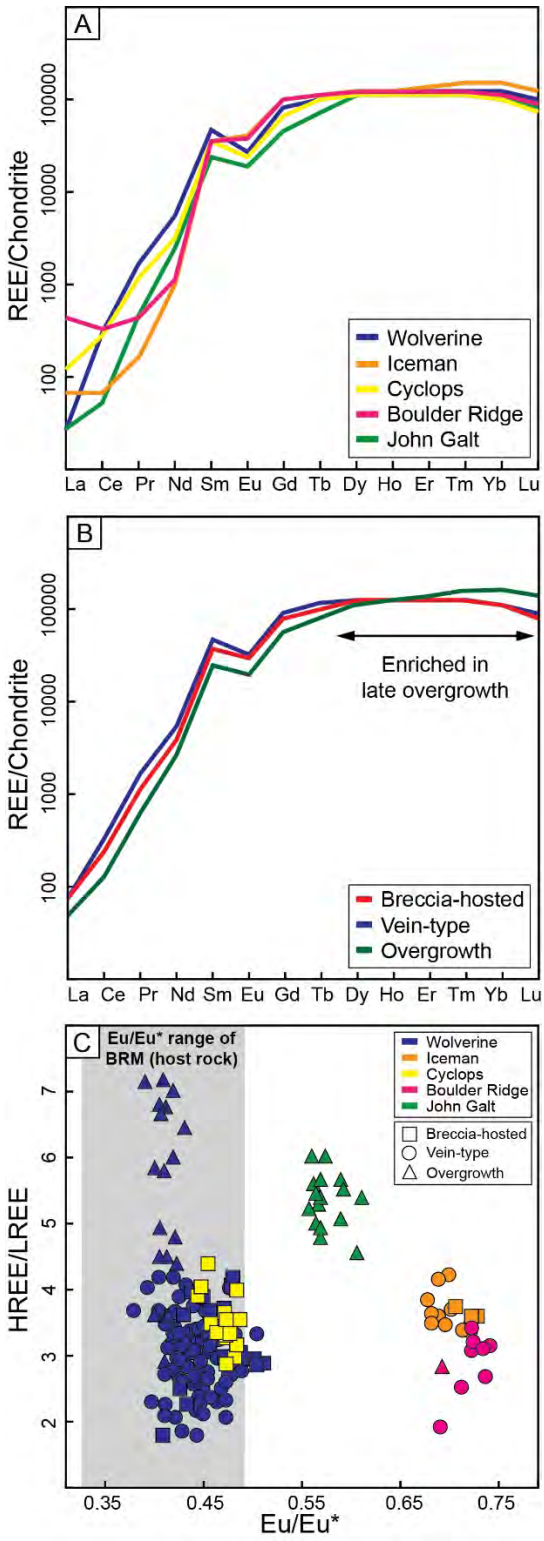

Fig. 5-3: REE characteristics of xenotime. (A) Chondrite-normalized REE patterns for xenotime from different deposits/prospects; (B) Chondrite-normalized REE patterns for different generations of xenotime. Note that breccia-hosted and vein-type xenotime have comparable patterns, whereas late xenotime is richer in HREE and more depleted in LREE; (C) HREE/LREE versus Eu/Eu* plot for xenotime. Note that most of the xenotime samples share a similar Eu anomaly with the source rocks (BRM). Chondrite normalization values are form McDonough and Sun (1995).

Table 5-1: Average composition of xenotime from different HREE deposits/prospects

Deposit	**Wolverine**			**Boulder Ridge**		**Cyclops**	**Iceman**		**John Galt**
Number	n = 19	n = 100	n = 19	n = 8	n = 1	n = 15	n = 3	n = 11	n = 16
Paragenesis	Breccia	Vein-type	Overgrowth	Vein-type	Overgrowth	Breccia	Breccia	Vein-type	Overgrowth
(ppm)									
Al	315	230	374	1244	1999	551	172	427	51
Si	3730	3376	3094	3678	2823	3566	4174	3355	3159
P	135269	130955	127051	132162	119226	127354	132084	128444	113220
Ca	1039	1008	1187	1386	1580	831	1710	1861	156
Sc	164	243	1432	619	534	180	1398	1411	344
Ti	101	20	11	21	2	15	39	62	2
Mn	15	13	8	10	14	4	9	8	4
Fe	10308	8464	4608	905	321	243	2273	8389	30
Sr	4	6	11	25	401	4	18	14	7
Zr	26	18	25	247	179	75	133	162	13
Nb	1	0	0	0	0	0	0	0	0
Sb	3	3	1	1	0	0	1	2	0
Ba	4	5	4	4	46	15	3	4	4
La	7	12	7	23	352	8	22	18	10
Ce	210	326	136	61	703	208	60	51	50
Pr	175	257	113	18	100	140	21	21	60
Nd	3269	4420	2410	601	956	2261	676	700	1755
Sm	10227	11030	7182	7208	7197	8377	7446	7461	5578
Eu	2461	2503	1586	3628	3462	2049	3476	3369	1646
Gd	26641	26728	19304	32873	32412	20933	29544	29185	13635
Tb	6473	6482	5271	6708	6579	5824	6631	6486	4337
Dy	47062	47205	44313	44972	45594	45004	47518	47871	40967
Ho	10337	10297	10951	10010	10232	9934	11172	11299	10445
Er	27783	28084	34657	27467	28315	26526	33173	33639	29465
Tm	4115	4239	6127	4114	4276	3881	5394	5538	4266
Yb	26041	27482	45191	26188	27541	24025	37229	38510	26604
Lu	3269	3433	5970	3310	3320	2937	4784	4885	3261
Hf	6	6	6	11	10	7	7	7	5
W	16	10	11	7	7	14	11	11	7
Pb	4	4	19	12	81	1	26	27	3
Th	24	39	141	53	28	70	34	30	20
U	1841	1426	1548	3291	3022	1969	5056	5257	2858
Eu/Eu*	0.46	0.45	0.41	0.72	0.69	0.47	0.72	0.70	0.58
Al	0.00	0.00	0.00	0.01	0.02	0.00	0.00	0.00	0.00
Si	0.03	0.03	0.02	0.03	0.02	0.03	0.03	0.03	0.03
P	0.93	0.92	0.91	0.93	0.89	0.93	0.92	0.90	0.89
Ca	0.01	0.01	0.01	0.01	0.01	0.00	0.01	0.01	0.00
Sc	0.00	0.00	0.01	0.00	0.00	0.00	0.01	0.01	0.00
Mn	0.00	0.00	0.00	0.00	0.00	0.00	0.00	0.00	0.00
Fe	0.04	0.03	0.02	0.00	0.00	0.00	0.01	0.03	0.00
Y	0.82	0.83	0.84	0.83	0.88	0.86	0.82	0.83	0.93
Zr	0.00	0.00	0.00	0.00	0.00	0.00	0.00	0.00	0.00
La	0.00	0.00	0.00	0.00	0.00	0.00	0.00	0.00	0.00
Ce	0.00	0.00	0.00	0.00	0.00	0.00	0.00	0.00	0.00
Pr	0.00	0.00	0.00	0.00	0.00	0.00	0.00	0.00	0.00
Nd	0.00	0.01	0.00	0.00	0.00	0.00	0.00	0.00	0.00
Sm	0.01	0.02	0.01	0.01	0.01	0.01	0.01	0.01	0.01
Eu	0.00	0.00	0.00	0.01	0.01	0.00	0.00	0.00	0.00
Gd	0.04	0.04	0.03	0.05	0.05	0.03	0.04	0.04	0.02
Tb	0.01	0.01	0.01	0.01	0.01	0.01	0.01	0.01	0.01
Dy	0.06	0.06	0.06	0.06	0.06	0.06	0.06	0.06	0.06
Ho	0.01	0.01	0.01	0.01	0.01	0.01	0.01	0.01	0.02
Er	0.04	0.04	0.05	0.04	0.04	0.04	0.04	0.04	0.04
Tm	0.01	0.01	0.01	0.01	0.01	0.01	0.01	0.01	0.01
Yb	0.03	0.03	0.06	0.03	0.04	0.03	0.05	0.05	0.04
Lu	0.00	0.00	0.01	0.00	0.00	0.00	0.01	0.01	0.00
Th	0.00	0.00	0.00	0.00	0.00	0.00	0.00	0.00	0.00
U	0.00	0.00	0.00	0.00	0.00	0.00	0.00	0.00	0.00
Total	2.04	2.05	2.06	2.04	2.07	2.04	2.05	2.06	2.06
REE site	0.95	0.94	0.93	0.96	0.91	0.96	0.95	0.93	0.92
P site	1.04	1.06	1.09	1.06	1.12	1.07	1.07	1.08	1.14

*Y = 33.9 wt.% (Cook et al., 2013)

**Formulae on basis of 4 a.p.f.u.

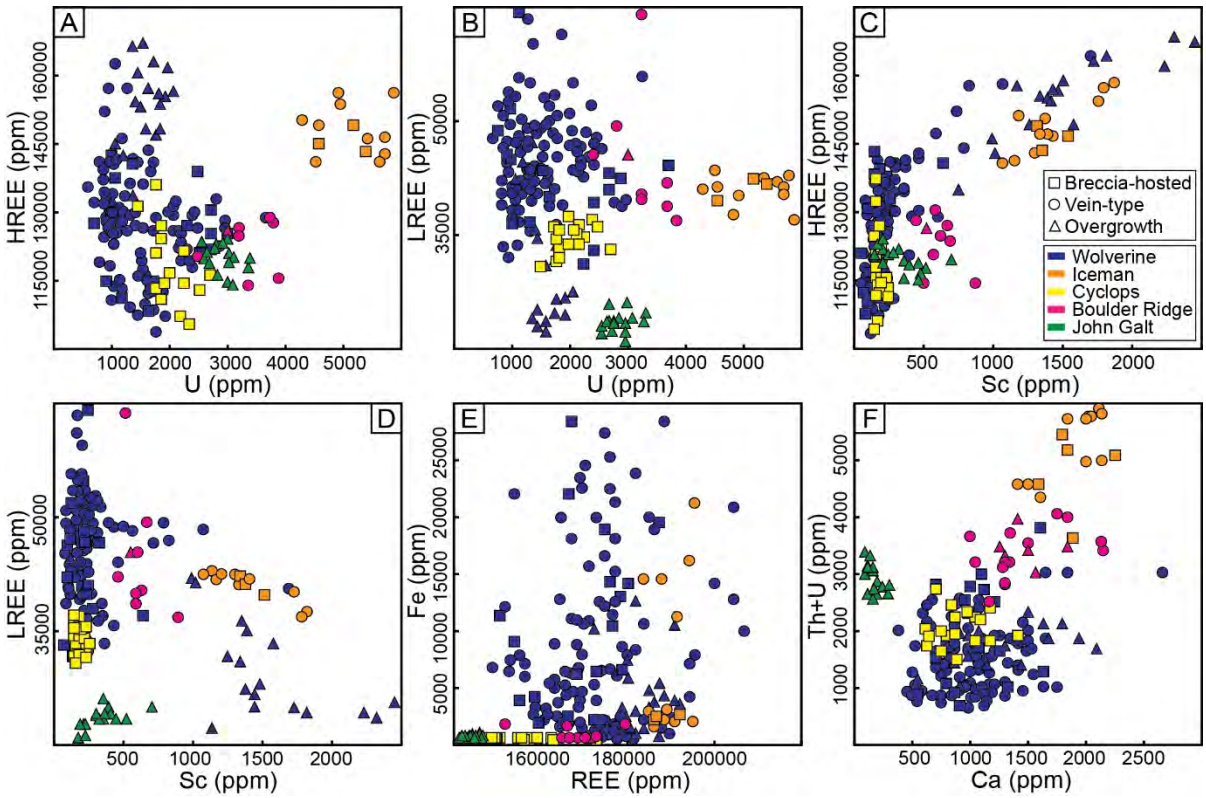

Fig. 5-4: Scatterplots of element compositions of xenotime from different deposits/prospects.

Representative electron probe data of florencite from Wolverine and Area 5 are shown in Tables 5-2 and 5-3, respectively, with the full dataset available in Appendix 5-4. The analytical results returned relatively low totals (between 80 to 90 wt.%) for the analyses, which is for the most part consistent with the expected ca. 10.5 wt.% structurally-bound H_2O (Roberts et al., 1990). Florencite from Wolverine generally returned lower totals (between 80 to 85 wt.%) that cannot be ascribed entirely due to H_2O, but may reflect deficiency of cations in the REE site (see Appendix 5-4) due either to the presence of carbon in the crystal structure (undetectable by microprobe) or to radiation damage induced by actinides (Mordberg, 2004; Gaboreau et al., 2007).

Florencite from the Wolverine and Area 5 deposits (Fig. 5-5A) contains wt.% levels of Ce (ca. 10 wt.% Ce_2O_3), Nd (ca. 6.5 wt.% Nd_2O_3) and La (ca. 5 wt.% La_2O_3), and hence can be classified as florencite-(Ce) (Fig. 5-5A). Early florencite is the relatively enriched in Pr, Nd, Sm, Gd, whereas the late florencite from the same deposit has markedly higher contents of La and Ce (Fig. 5-5B). The early florencite has a limited compositional range characterised by relatively high P_2O_5 (ca. 22-24 wt.%), and low SrO (ca. 0.9-2.9 wt.%) and SO_3 (ca. 0.4-1.9

wt.%), and so is close to the end member composition of florencite. In contrast, the late florencite has a wider compositional range with overall lower P_2O_5 (ca. 21-26 wt.%), and higher SrO (ca. 1.7-6.0 wt.%) and SO_3 (ca. 1.4-5.1 wt.%). The Th content is generally low (<0.4 wt.% ThO), whereas CaO content varies from ca. 0.8 wt.% in early florencite to ca. 1.2 wt.% in late florencite. There is no systematic relationship in SiO_2 content, although early florencite tends to have greater variability in SiO_2, reaching up to 2.7 wt.%, compared to ~1.8 wt.% for late florencite. Although bulk of the analyses have FeO <1.5 wt.% (0.15 a.p.f.u.) and Al_2O_3 >30 wt.% (3 a.p.f.u.), a number of analyses of early florencite from Area 5 and late florencite from Wolverine, have FeO values that reach 9 wt.% and are conversely depleted in Al_2O_3 (27 wt.%). Major element chemistry of both generations of florencite is consistent largely with a florencite composition with components of Sr- (svanbergite [$SrAl_3(SO_4)(PO_4)(OH)_6$] and goyazite [$SrAl_3(PO_4)_2(OH)_5H_2O$]) and Ca- (woodhouseite [$CaAl_3(SO_4)(PO_4)(OH)_6$]) end members of the APS mineral group (Fig. 5-5C).

Table 5-2: Representative electron probe micro-analytical data for florencite from Wolverine

	W1	W2	W3	W4	W5	W6	W7	W8	W9	W33	W39	W43	W46	W48	W57	W63	W64	W67	W77
	Wolverine (early)									Wolverine (late)									
CaO	0.86	0.90	0.91	0.89	0.99	1.12	1.24	0.99	0.99	0.99	0.95	0.99	1.05	0.94	1.11	1.35	1.49	1.25	1.03
Y_2O_3	0.00	0.00	0.00	0.00	0.00	0.00	0.00	0.00	0.00	0.00	0.00	0.00	0.00	0.00	0.00	0.00	0.00	0.00	0.00
La_2O_3	4.16	3.27	3.77	3.50	3.49	3.47	3.54	3.72	3.73	4.68	4.81	4.58	4.65	3.91	3.55	3.84	4.16	3.53	3.98
Ce_2O_3	8.49	8.01	8.57	8.47	8.42	8.23	7.95	9.64	9.52	12.51	11.19	11.31	10.68	9.69	8.83	7.66	8.15	8.70	8.66
Nd_2O_3	7.73	8.37	7.78	6.95	7.25	6.34	6.94	7.33	7.49	5.92	5.48	5.86	5.29	5.75	6.41	4.59	3.02	4.91	5.36
Pr_2O_3	1.61	1.52	1.57	1.49	1.63	1.60	1.63	1.91	1.64	1.71	1.39	1.82	1.50	1.41	1.17	1.36	1.14	1.57	1.30
Sm_2O_3	1.08	0.93	1.01	0.98	1.11	1.01	0.93	0.74	0.87	0.83	0.98	0.64	0.69	0.79	0.72	0.52	0.24	0.53	0.82
Gd_2O_3	0.18	0.14	0.15	0.17	0.31	0.09	0.16	0.13	0.00	0.01	0.32	0.18	0.26	0.21	0.11	0.24	0.07	0.24	0.00
ThO_2	0.00	0.06	0.00	0.08	0.00	0.00	0.12	0.00	0.04	0.01	0.03	0.00	0.00	0.11	0.39	0.31	0.21	0.03	0.21
SrO	1.32	1.38	1.31	1.34	1.37	1.40	1.50	0.89	1.01	1.87	2.11	2.24	1.92	2.55	4.15	5.40	6.02	4.12	4.69
FeO	0.09	0.32	0.38	0.12	0.13	0.47	0.33	0.75	0.19	0.62	0.11	0.10	1.17	0.95	1.80	0.69	1.89	1.05	1.00
SiO_2	0.40	0.08	0.92	2.07	0.95	2.07	0.52	0.09	0.56	0.07	0.25	0.00	0.24	0.61	0.13	0.67	0.99	1.79	0.00
Al_2O_3	30.82	30.44	30.17	30.44	30.61	29.27	31.76	30.56	28.72	31.15	30.93	30.97	30.49	30.50	30.52	30.63	30.75	30.32	30.76
P_2O_5	25.88	25.30	25.74	24.97	25.30	25.02	25.31	25.43	26.07	25.80	25.67	26.08	25.41	24.62	23.58	21.89	21.28	23.29	23.20
SO_3	0.90	0.89	0.77	0.88	0.71	0.91	0.80	0.74	0.74	1.70	2.09	1.75	1.81	2.07	2.85	4.05	5.14	3.02	3.47
F	0.18	0.00	0.18	0.49	0.00	0.35	0.00	0.44	0.02	0.62	0.60	0.35	0.82	0.72	0.56	0.64	0.83	0.43	0.40
Cl	0.04	0.02	0.00	0.01	0.03	0.01	0.03	0.00	0.01	0.01	0.03	0.03	0.03	0.01	0.07	0.09	0.05	0.04	0.03
Total	83.74	81.64	83.24	82.85	82.30	81.36	82.76	83.35	81.58	88.49	86.95	86.91	86.00	84.86	85.94	83.91	85.42	84.81	84.90
Ca	0.08	0.09	0.08	0.08	0.09	0.11	0.11	0.09	0.09	0.09	0.09	0.09	0.10	0.09	0.10	0.13	0.14	0.12	0.10
Y	0.00	0.00	0.00	0.00	0.00	0.00	0.00	0.00	0.00	0.00	0.00	0.00	0.00	0.00	0.00	0.00	0.00	0.00	0.00
La	0.13	0.11	0.12	0.11	0.11	0.11	0.11	0.12	0.12	0.15	0.15	0.14	0.15	0.13	0.11	0.13	0.13	0.11	0.13
Ce	0.27	0.26	0.27	0.27	0.27	0.26	0.25	0.30	0.31	0.39	0.35	0.35	0.34	0.31	0.28	0.25	0.26	0.28	0.28
Nd	0.24	0.26	0.24	0.21	0.22	0.20	0.21	0.23	0.24	0.18	0.17	0.18	0.16	0.18	0.20	0.15	0.09	0.15	0.17
Pr	0.05	0.05	0.05	0.05	0.05	0.05	0.05	0.06	0.05	0.05	0.04	0.06	0.05	0.04	0.04	0.04	0.04	0.05	0.04
Sm	0.03	0.03	0.03	0.03	0.03	0.03	0.03	0.02	0.03	0.02	0.03	0.02	0.02	0.02	0.02	0.02	0.01	0.02	0.02
Gd	0.01	0.00	0.00	0.00	0.01	0.00	0.00	0.00	0.00	0.00	0.01	0.01	0.01	0.01	0.00	0.01	0.00	0.01	0.00
Th	0.00	0.00	0.00	0.00	0.00	0.00	0.00	0.00	0.00	0.00	0.00	0.00	0.00	0.00	0.01	0.01	0.00	0.00	0.00
Sr	0.07	0.07	0.07	0.07	0.07	0.07	0.07	0.04	0.05	0.09	0.10	0.11	0.10	0.13	0.21	0.28	0.30	0.21	0.24
∑REE	0.88	0.87	0.86	0.82	0.85	0.83	0.83	0.86	0.89	0.97	0.94	0.96	0.93	0.91	0.97	1.02	0.97	0.95	0.98
Fe	0.01	0.02	0.03	0.01	0.01	0.03	0.02	0.05	0.01	0.04	0.01	0.01	0.08	0.07	0.13	0.05	0.14	0.08	0.07
Al	3.13	3.15	3.08	3.10	3.13	3.02	3.19	3.11	3.01	3.09	3.11	3.11	3.09	3.12	3.12	3.21	3.16	3.09	3.18
∑Al	3.14	3.17	3.11	3.11	3.14	3.05	3.21	3.16	3.02	3.13	3.12	3.12	3.17	3.19	3.25	3.26	3.3	3.17	3.25
Si	0.03	0.01	0.08	0.18	0.08	0.18	0.04	0.01	0.05	0.01	0.02	0.00	0.02	0.05	0.01	0.06	0.09	0.15	0.00
P	1.89	1.88	1.89	1.83	1.86	1.85	1.83	1.86	1.96	1.84	1.86	1.88	1.85	1.81	1.73	1.65	1.57	1.71	1.72
S	0.06	0.06	0.05	0.06	0.05	0.06	0.05	0.05	0.05	0.11	0.13	0.11	0.12	0.14	0.19	0.27	0.34	0.20	0.23
∑P	1.98	1.95	2.02	2.07	1.99	2.09	1.92	1.92	2.06	1.96	2.01	1.99	1.99	2.00	1.93	1.98	2.00	2.06	1.95
F	0.05	0.00	0.05	0.13	0.00	0.10	0.00	0.12	0.01	0.16	0.16	0.09	0.22	0.20	0.15	0.18	0.23	0.12	0.11
Cl	0.01	0.00	0.00	0.00	0.00	0.00	0.00	0.00	0.00	0.00	0.00	0.00	0.00	0.00	0.01	0.01	0.01	0.01	0.00
OH	5.94	6.00	5.95	5.86	6.00	5.90	6.00	5.88	5.99	5.83	5.83	5.90	5.77	5.80	5.84	5.81	5.76	5.88	5.89
∑OH	6.00	6.00	6.00	6.00	6.00	6.00	6.00	6.00	6.00	6.00	6.00	6.00	6.00	6.00	6.00	6.00	6.00	6.00	6.00
Flr	0.78	0.76	0.76	0.73	0.74	0.70	0.72	0.78	0.79	0.81	0.78	0.78	0.77	0.73	0.68	0.61	0.56	0.65	0.66
Wdh	0.13	0.14	0.13	0.14	0.14	0.16	0.18	0.14	0.13	0.11	0.12	0.11	0.14	0.13	0.13	0.14	0.17	0.15	0.12
Svb	0.00	0.00	0.00	0.00	0.00	0.00	0.00	0.00	0.00	0.05	0.04	0.03	0.03	0.06	0.14	0.22	0.26	0.12	0.18
Gyz	0.13	0.15	0.16	0.15	0.16	0.19	0.17	0.12	0.17	0.06	0.09	0.10	0.11	0.11	0.11	0.08	0.07	0.12	0.09
Hut	0.02	0.01	0.04	0.09	0.04	0.09	0.02	0.01	0.03	0.01	0.01	0.00	0.01	0.03	0.01	0.04	0.05	0.08	0.00

Early florencite (Wolverine) = $[REE_{(0.70)}, Th_{(0.0005)}, Ca_{(0.08)}, Sr_{(0.06)}][Al_{(3.11)}, Fe_{(0.02)}][(P_{(1.87)}, S_{(0.04)}, Si_{(0.05)})O_4][(OH)_6]$
Late florencite (Wolverine) = $[REE_{(0.66)}, Th_{(0.0015)}, Ca_{(0.15)}, Sr_{(0.09)}][Al_{(3.11)}, Fe_{(0.07)}][(P_{(1.80)}, S_{(0.15)}, Si_{(0.02)})O_4][(OH)_6]$

*Flr = Florencite, Wdh = Woodhouseite, Svb = Svanbergite, Gyz = Goyazite, Hut = Huttonite

**Formulae on basis of 14 atoms per formula unit (a.p.f.u.)

Table 5-3: Representative electron probe micro-analytical data for florencite from Area 5

	A1	A2	A3	A4	A7	A13	A14	A19	A20	A22	A23	A24	A26	A29	A34	A51	A54	A55	A86
	Area 5 (late)					Area 5 (early)													
CaO	1.86	1.31	0.91	1.75	1.37	0.57	0.64	0.73	0.76	0.70	0.77	0.92	0.61	0.65	0.67	0.55	0.47	0.39	0.61
Y_2O_3	0.00	0.00	0.00	0.00	0.00	0.00	0.00	0.00	0.00	0.00	0.00	0.00	0.00	0.00	0.00	0.00	0.00	0.00	0.00
La_2O_3	6.03	8.61	9.87	7.16	7.54	6.06	5.91	5.65	6.09	6.25	6.03	4.75	5.82	6.37	5.87	5.76	5.91	6.90	4.70
Ce_2O_3	10.02	11.59	12.19	10.92	10.91	10.50	10.39	10.87	10.53	10.15	9.91	10.56	11.03	10.77	9.88	10.50	10.76	10.98	9.34
Nd_2O_3	2.78	2.97	2.10	3.00	2.52	7.49	6.70	7.06	7.21	6.72	6.44	6.66	6.97	7.58	8.03	7.53	7.61	7.01	7.38
Pr_2O_3	1.03	1.03	0.93	1.08	0.89	1.48	1.39	1.48	1.33	1.56	1.40	1.47	1.50	1.54	1.44	1.43	1.53	1.36	1.50
Sm_2O_3	0.00	0.13	0.00	0.16	0.04	0.93	0.85	1.01	0.85	0.96	0.84	0.90	1.02	0.75	0.94	0.89	0.87	0.71	0.79
Gd_2O_3	0.11	0.00	0.00	0.08	0.00	0.06	0.00	0.21	0.02	0.00	0.16	0.14	0.13	0.06	0.21	0.27	0.04	0.08	0.05
ThO_2	0.01	0.06	0.05	0.00	0.01	0.00	0.00	0.05	0.01	0.00	0.00	0.10	0.02	0.16	0.00	0.00	0.00	0.00	0.14
SrO	4.80	2.59	3.18	3.58	4.45	1.95	2.12	2.24	2.20	2.40	2.72	2.10	1.38	1.72	1.96	1.80	1.51	1.52	1.69
FeO	1.18	1.00	1.00	0.91	0.86	1.30	2.57	1.10	0.79	1.81	0.96	3.96	3.05	0.41	0.64	0.52	1.13	0.37	6.97
SiO_2	0.00	0.15	0.03	0.00	0.08	0.00	0.00	0.00	0.00	0.00	0.04	0.03	0.00	0.18	0.00	0.00	0.00	0.00	0.06
Al_2O_3	31.69	30.48	31.42	32.08	31.88	31.72	30.83	32.03	31.39	30.96	31.41	31.18	30.39	32.50	32.14	31.87	31.24	31.49	29.86
P_2O_5	24.28	24.89	24.01	24.42	23.94	25.98	25.43	25.74	25.76	25.77	25.82	24.83	25.78	26.12	26.03	26.04	25.99	26.15	24.26
SO_3	4.70	3.11	3.00	3.55	4.29	1.33	1.44	1.54	1.47	1.38	1.72	1.85	1.00	1.05	1.22	1.12	0.95	0.83	1.34
F	0.34	0.41	0.11	0.45	0.37	0.00	0.91	0.39	0.28	0.22	0.16	0.23	0.49	0.44	0.22	0.17	0.05	0.40	0.31
Cl	0.02	0.03	0.00	0.01	0.03	0.05	0.03	0.04	0.03	0.06	0.02	0.02	0.02	0.04	0.04	0.01	0.02	0.00	0.04
Total	88.85	88.37	88.80	89.14	89.18	89.42	89.22	90.15	88.71	88.94	88.42	89.70	89.20	90.33	89.29	88.45	88.08	88.18	89.04
Ca	0.17	0.12	0.08	0.15	0.12	0.05	0.06	0.06	0.07	0.06	0.07	0.08	0.05	0.06	0.06	0.05	0.04	0.03	0.05
Y	0.00	0.00	0.00	0.00	0.00	0.00	0.00	0.00	0.00	0.00	0.00	0.00	0.00	0.00	0.00	0.00	0.00	0.00	0.00
La	0.18	0.27	0.30	0.21	0.23	0.18	0.18	0.17	0.19	0.19	0.18	0.14	0.18	0.19	0.18	0.18	0.18	0.21	0.14
Ce	0.30	0.36	0.36	0.33	0.33	0.31	0.32	0.33	0.32	0.31	0.30	0.32	0.33	0.32	0.30	0.32	0.33	0.34	0.28
Nd	0.08	0.09	0.06	0.09	0.07	0.22	0.20	0.21	0.21	0.20	0.19	0.19	0.21	0.22	0.24	0.22	0.23	0.21	0.22
Pr	0.03	0.03	0.03	0.03	0.03	0.04	0.04	0.04	0.04	0.05	0.04	0.04	0.05	0.05	0.04	0.04	0.05	0.04	0.04
Sm	0.00	0.00	0.00	0.00	0.00	0.03	0.02	0.03	0.02	0.03	0.02	0.03	0.03	0.02	0.03	0.03	0.02	0.02	0.02
Gd	0.00	0.00	0.00	0.00	0.00	0.00	0.00	0.01	0.00	0.00	0.00	0.00	0.00	0.00	0.01	0.01	0.00	0.00	0.00
Th	0.00	0.00	0.00	0.00	0.00	0.00	0.00	0.00	0.00	0.00	0.00	0.00	0.00	0.00	0.00	0.00	0.00	0.00	0.00
Sr	0.23	0.13	0.15	0.17	0.21	0.09	0.10	0.11	0.11	0.12	0.13	0.10	0.07	0.08	0.09	0.09	0.07	0.07	0.08
∑REE	0.99	1.00	0.98	0.98	0.99	0.92	0.92	0.96	0.96	0.96	0.93	0.9	0.92	0.94	0.95	0.94	0.92	0.92	0.83
Fe	0.08	0.07	0.07	0.06	0.06	0.09	0.18	0.08	0.05	0.13	0.07	0.27	0.21	0.03	0.04	0.04	0.08	0.03	0.48
Al	3.10	3.02	3.01	3.08	3.08	3.02	3.01	3.09	3.07	3.02	3.08	3.01	2.96	3.12	3.12	3.13	3.07	3.11	2.89
∑Al	3.18	3.09	3.08	3.14	3.14	3.11	3.19	3.17	3.12	3.15	3.15	3.28	3.17	3.15	3.16	3.17	3.15	3.14	3.37
Si	0.00	0.01	0.00	0.00	0.01	0.00	0.00	0.00	0.00	0.00	0.00	0.00	0.00	0.01	0.00	0.00	0.00	0.00	0.01
P	1.70	1.77	1.65	1.68	1.66	1.78	1.78	1.79	1.81	1.81	1.82	1.72	1.80	1.80	1.82	1.84	1.83	1.86	1.69
S	0.29	0.20	0.18	0.22	0.26	0.08	0.09	0.09	0.09	0.09	0.11	0.11	0.06	0.06	0.08	0.07	0.06	0.05	0.08
∑P	1.99	1.98	1.83	1.9	1.93	1.86	1.87	1.88	1.90	1.90	1.93	1.83	1.86	1.87	1.9	1.91	1.89	1.91	1.78
F	0.09	0.11	0.03	0.12	0.10	0.00	0.24	0.10	0.07	0.06	0.04	0.06	0.13	0.11	0.06	0.04	0.01	0.10	0.08
Cl	0.00	0.00	0.00	0.00	0.00	0.01	0.00	0.01	0.00	0.01	0.00	0.00	0.00	0.00	0.01	0.00	0.00	0.00	0.01
OH	5.91	5.88	5.97	5.88	5.90	5.99	5.76	5.89	5.92	5.93	5.95	5.94	5.87	5.88	5.94	5.95	5.98	5.90	5.91
∑OH	6.00	6.00	6.00	6.00	6.00	6.00	6.00	6.00	6.00	6.00	6.00	6.00	6.00	6.00	6.00	6.00	6.00	6.00	6.00
Flr	0.61	0.76	0.76	0.67	0.67	0.81	0.80	0.81	0.80	0.80	0.76	0.77	0.84	0.83	0.82	0.83	0.84	0.85	0.78
Wdh	0.19	0.13	0.09	0.16	0.13	0.08	0.10	0.08	0.09	0.08	0.10	0.13	0.09	0.09	0.08	0.08	0.07	0.06	0.13
Svb	0.14	0.10	0.17	0.12	0.19	0.07	0.07	0.09	0.06	0.07	0.06	0.08	0.04	0.06	0.07	0.06	0.05	0.05	0.06
Gyz	0.11	0.04	0.00	0.06	0.03	0.05	0.07	0.05	0.07	0.08	0.10	0.07	0.06	0.04	0.05	0.06	0.05	0.05	0.10
Hut	0.00	0.01	0.00	0.00	0.01	0.00	0.00	0.00	0.00	0.00	0.00	0.00	0.00	0.01	0.00	0.00	0.00	0.00	0.01

Early florencite (Area 5) = $[REE_{(0.77)}, Th_{(0.0005)}, Ca_{(0.06)}, Sr_{(0.09)}][Al_{(3.08)}, Fe_{(0.07)}][(P_{(1.82)}, S_{(0.07)}, Si_{(0.01)})O_4][(OH)_6]$
Late florencite (Area 5) = $[REE_{(0.69)}, Th_{(0.0004)}, Ca_{(0.11)}, Sr_{(0.16)}][Al_{(3.06)}, Fe_{(0.06)}][(P_{(1.68)}, S_{(0.21)}, Si_{(0.01)})O_4][(OH)_6]$

*Flr = Florencite, Wdh = Woodhouseite, Svb = Svanbergite, Gyz = Goyazite, Hut = Huttonite

**Formulae on basis of 14 atoms per formula unit (a.p.f.u.)

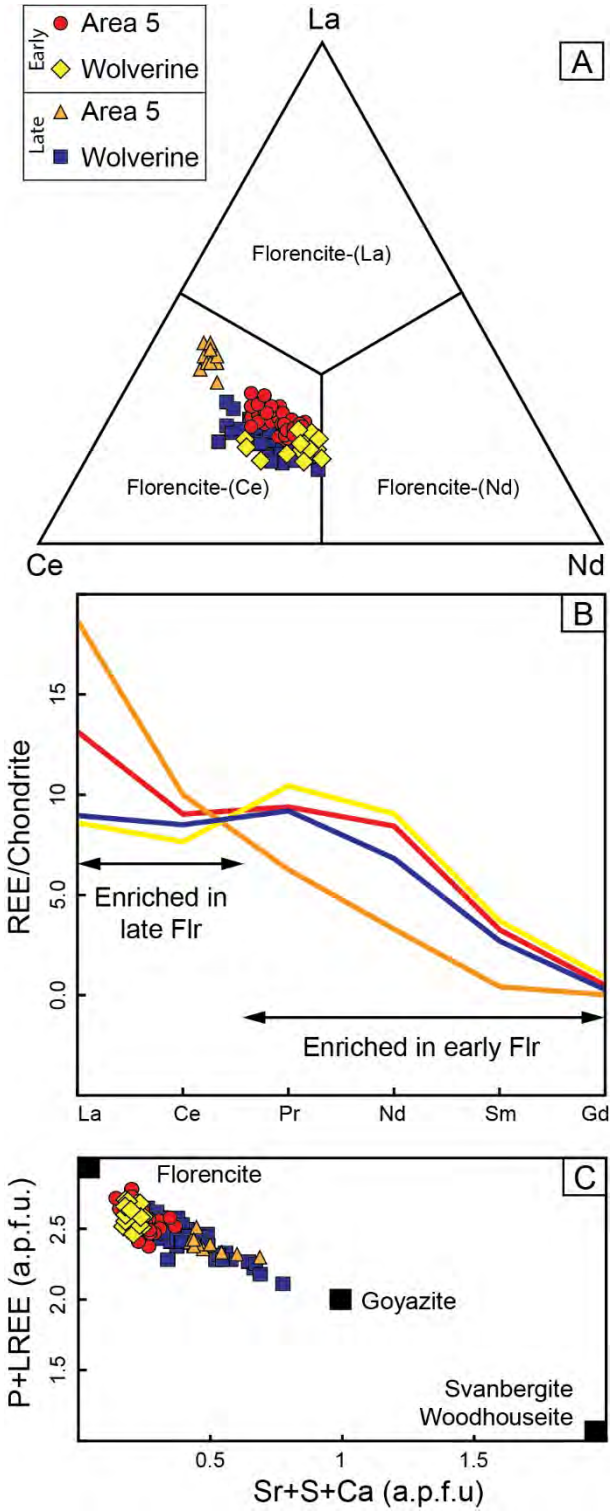

Fig. 5-5: Electron probe data for florencite from Area 5 and Wolverine. (A) Ce-La-Nd ternary plot; (B) Partial (La to Gd) chondrite-normalized REE patterns; (C) P+LREE versus Sr+S plot. Note that both early and late florencite analyses contain components of goyazite, svanbergite, woodhouseite compositions. Chondrite normalization values are form McDonough and Sun (1995).

Discussion

Compositional evolution of the HREE+Y mineralisation

The mineralisation in the NAHREY mineral field is of hydrothermal origin (Nazari-Dehkordi et al., 2018), and hence the ore minerals can reveal significant information about the ore-forming hydrothermal fluids and potentially the source rocks. Incorporation of the REE (and Y) into REE-bearing phases varies with REE ionic radii, and depends on temperature, redox conditions and fluid composition (Bau, 1991; Bau and Moller, 1992), as well as whether there are co-crystallising phases with the ability to preferentially fractionate the REE. Such features need to be taken into consideration here because the HREE+Y mineralisation contains two coexisting REE phases with distinct preferences for various REE groups (HREE-rich xenotime and LREE-rich florencite).

A recent geochemical and isotopic study by Nazari-Dehkordi et al. (2018) showed that the REE+Y for xenotime mineralisation derived from the host rocks (BRM), illustrating that the ore minerals likely inherited compositional features from the BRM. Indeed, the negative Eu anomalies of xenotime are similar to those of the BRM (Fig. 5-3C, Nazari-Dehkordi et al., 2017). Therefore, we do not ascribe the negative Eu anomalies to redox conditions of ore formation (e.g., Bau, 1991; Bau and Moller, 1992), rather the Eu anomalies were inherited directly from the REE source rock. Xenotime analyses from John Galt, Boulder Ridge and Iceman have higher Eu anomalies, but these prospects are either not hosted by the BRM (John Galt, Boulder Ridge) or only partly hosted by the BRM (Iceman).

The trace element data reveal a fairly similar composition for both breccia-hosted and vein-type xenotime, which represent the earliest stage of the HREE mineralisation. The late xenotime overgrowths are comparatively richer in the HREE (Fig. 5-3B, Fig. 5-4A) and more depleted in P and LREE, which we interpret to be an effect of co-precipitation of late florencite, which preferentially sequesters LREE and P. The relative enrichment in HREE in this xenotime reflects residual enrichment after repartitioning of LREE and P in florencite. Moreover, the dataset, particularly from Wolverine, indicates higher Th and Ca in the late xenotime overgrowth compared with early (breccia-hosted and vein-type) xenotime (Fig. 5-4F), while other major and trace elements remain in a relatively comparable range. As discussed in detail

later, preferential incorporation of these elements into the late xenotime overgrowth is consistent with relatively low Th and Ca concentrations in the coexisting late florencite.

Mechanisms of element substitution in xenotime

Our mineral compositional dataset indicates that non-REE trace elements (e.g., Fe, Sc, U, Th, Zr, and Ca) can be present in xenotime. Incorporation of these elements into the xenotime structure is possible through a number of charge-balanced substitution mechanisms involving exchange of both REE^{3+} and P^{5+}.

The resolution of the laser ablation ICP-MS data does not allow for precise evaluation of element substitution mechanisms, but does provide general trends between various trace elements that allow qualitative assessment of how elements are incorporated in the NAHREY xenotime. Zircon is isostructural with xenotime and follows $Zr^{4+} + Si^{4+} = REE^{3+} + P^{5+}$ exchange (Spear and Pyle, 2002). However, xenotime has low Zr content (ca. 50 ppm), ruling out a significant zircon type substitution. The distinct positive relationship between Th, U and Ca (Fig. 5-4F) is consistent with the cheralite type $(U, Th)^{4+} + Ca^{2+} = 2(REE, Y)^{3+}$ substitution mechanism (Spear and Pyle, 2002). This substitution has also been reported from several other xenotime occurrences (e.g., Forster, 1998; Ondrejka et al., 2007). However, the relatively low Th, U, and Ca values are consistent only with a very minor cheralite component in the NAHREY xenotime. Uranium and Sc both display a positive relationship with HREE, and an inverse correlation with LREE (Figs. 5-4A-D), further demonstrating preferential incorporation of elements with comparable atomic radius to that of HREE in xenotime (Van Emden et al., 1997; Franz et al., 1996). In contrast, Fe content shows no demonstrable relationship with REE (Fig. 5-4E), potentially ruling out simple Fe^{3+} for REE^{3+} exchange as a significant constituent in xenotime. The Fe data are discussed in more detail below.

From our dataset we identified variable amounts of Si in xenotime. Although not common, percentage levels of Si have also been documented in xenotime of variable origin (magmatic: Ondrejka et al., 2007; Hetherington et al., 2008, diagenetic: Kositcin et al., 2003, hydrothermal: Lan et al., 2013). Apart from a zircon type substitution, Si can be incorporated in xenotime via thorite ($ThSiO_4$) and coffinite ($USiO_4$) substitution mechanisms. In particular, the thorite-coffinite substitution is likely to be most important in the Ca depleted, hence cheralite-free,

xenotime of John Galt and Cyclops. Nevertheless, in general, the concentrations of U, Th are very low indicating that thorite and coffinite components are present at very low levels.

Despite the similar characteristics and timing of formation of these HREE deposits/prospects, the extent to which xenotime incorporated trace elements is variable. In particular, xenotime from John Galt has the lowest contents of most trace elements, and also has the lowest of REE and P concentrations. This distinct chemistry potentially suggests that the hydrothermal fluids responsible for the formation of the John Galt ore in Halls Creek Orogen had significantly different composition compared to those in the Tanami Region. Among the deposits/prospects hosted in the Tanami Region, Cyclops (hosted by BRM) and Boulder Ridge (hosted by the Birrindudu Group sandstones) show restricted elemental variation, and contain low trace element contents (e.g., Fe, Sc). In contrast, xenotime analyses from Wolverine and Iceman, both hosted by the BRM, show the largest variation in trace element content. A number of analyses from Wolverine and Iceman contain very high Fe (up to 2.5 wt.%) values, which are consistent with the high Fe values reported by Cook et al. (2013) for xenotime from the HREE deposits/prospects hosted by BRM. However, incorporation of more than 1 wt.% of Fe structurally bound in xenotime is very rare (e.g., Kositcin et al., 2003), and is ascribed largely to Fe-rich mineral inclusions (e.g., Forster, 2006). Hence such high Fe values documented in xenotime are unlikely to represent any exchange mechanism. Instead, all the high Fe values observed in xenotime analyses have time-resolved analytical signals consistent with micro inclusions. These inclusions are potentially hematite that, to some extent and largely within shear zones, appears to be associated with the ore formation. Nazari-Dehkordi et al. (2018) also, based on whole-rock geochemistry of the host rocks at Wolverine, demonstrated that ore formation was associated with some Fe enrichment in the form of hematite. These data illustrate that the ore-forming hydrothermal fluids contained oxidised Fe. Iron enrichment mainly in breccia-hosted and vein-type (early stage) xenotime from Wolverine, the largest deposit in the NAHREY mineral field, also suggests that ore forming hydrothermal fluids were relatively oxidising.

Mechanisms of element substitution in florencite

Early florencite generations generally have fairly uniform compositions, although early florencite from Wolverine has somewhat lower LREE, Sr and S contents compared with the

early florencite from Area 5 (Fig. 5-6). The higher degree of compositional variability of the late florencite may reflect differing conditions of ore mineral precipitation, with the late florencite forming from different fluids and possibly under different conditions than that of the early mineralisation. These aspects are discussed in more detail below.

Overall the range of chemical compositions recorded in both the early and late florencite conforms well to a coupled substitution of Sr (+Ca) + S for LREE + P (Figs. 5-6A-F; Scott, 1987; Jambor, 1999; Dill, 2001), which represents a compositional spectrum from the florencite [$LREEAl_3(PO_4)_2(OH)_6$] end-member to the svanbergite/woodhouseite [$(Sr,Ca)Al_3(SO_4)(PO_4)(OH)_6$] end-members. We note that the Sr content of the late florencite reaches up to 6 wt.% SrO, which is distinctly higher than other florencite occurrences (Eastern Alps = 0.67 wt.%; Nagy et al., 2002; Witwatersrand Basin = 1.82 wt.%; Rasmussen and Muhling, 2009), but is closer to those associated with the unconformity-related U deposits (McArthur Basin = 2.3 wt.%; Gaboreau et al., 2005; Athabasca Basin = 5 wt.%; Gaboreau et al., 2007). The Sr-poor florencite occurrences are associated with phases that have a strong preference for Sr (Eastern Alps = apatite; Witwatersrand Basin = epidote, calcite, titanite), whereas these other phases are minor or absent from unconformity-related U deposits. Consequently, we consider the relatively high Sr contents of our florencite to reflect the lack of any coexisting mineral with a strong affinity for Sr (e.g., Ca-bearing minerals).

The well-defined inverse relationship between Al and Fe (Fig. 5-6G) is consistent with Fe^{3+} substitution for Al. However, some analyses of early florencite from Area 5, and late florencite from Wolverine have high Fe contents that would require an additional substitution mechanism, possibly Fe^{3+} for LREE. The appreciable levels of Si and Th are not accounted for by the standard florencite-svanbergite substitutions, and there is little evidence for a cheralite-type ($Th^{4+}+Ca^{2+} = 2REE^{3+}$) substitution (Fig. 5-6H), as Ca is likely incorporated via a woodhouseite (Ca+S for LREE+P) substitution. Instead, we do observe a broad negative correlation between Th + Si and LREE + P (Fig. 5-6I), which supports a huttonite-type ($Th^{4+}+Si^{4+} = P^{5+}+REE^{3+}$) substitution mechanism. Incorporation of Th, and by analogy U, by this mechanism raises the potential to use florencite for U-Th-Pb geochronology.

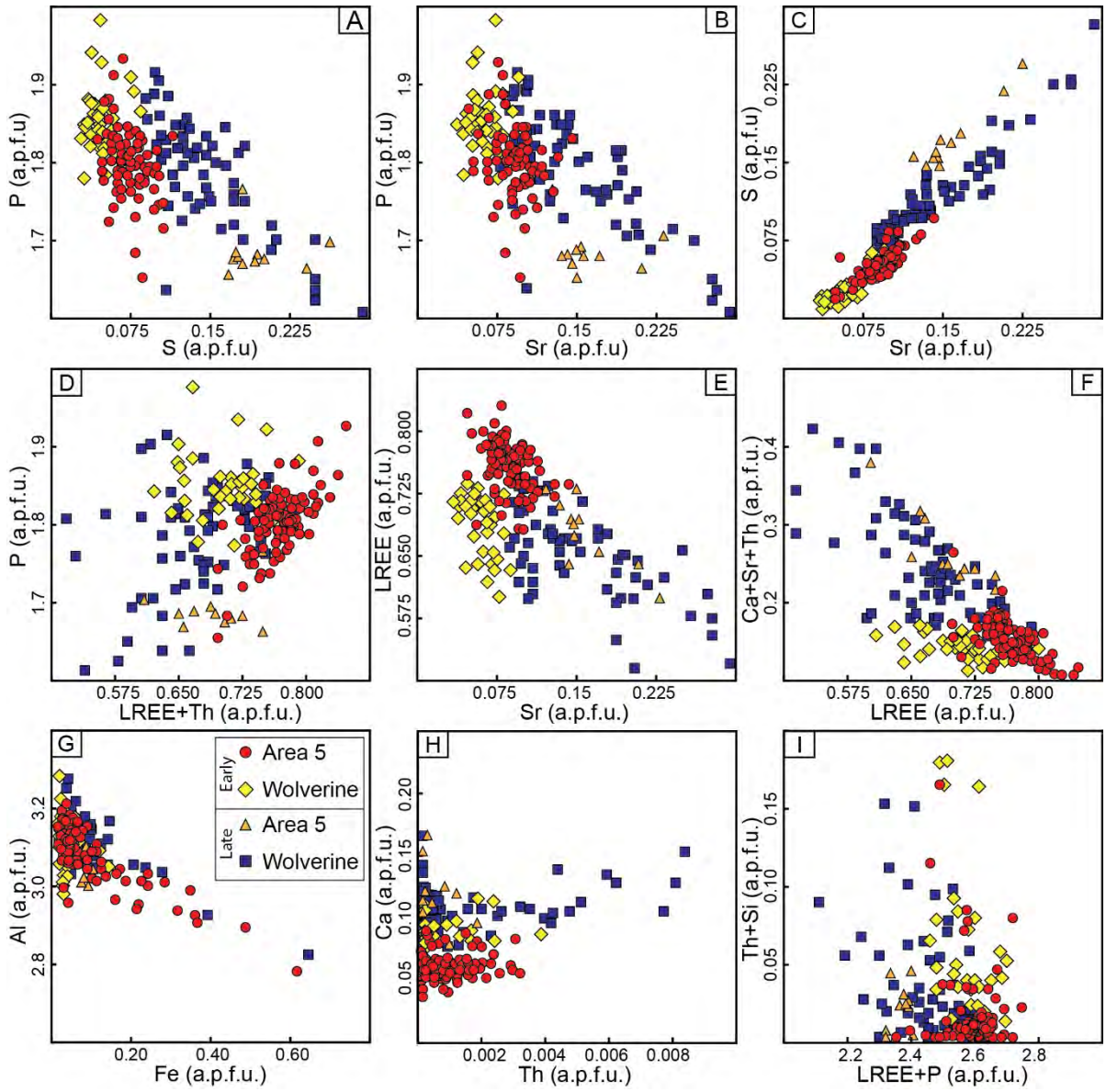

Fig. 5-6: Scatterplots of element compositions of florencite from Area 5 and Wolverine.

Comparison with unconformity-related APS minerals

Most available mineral chemistry data for florencite and other APS minerals come from unconformity-related U mineralisation settings (e.g., Athabasca Basin, Canada: Wilson, 1984; Quirt et al., 1991; Lorilleux et al., 2003; Gaboreau et al., 2007, and McArthur Basin, northern Australia: Beaufort et al., 2005; Gaboreau et al., 2005). The early and late florencite from the Wolverine and Area 5 deposits sit within the compositional field defined by the APS minerals associated with the U ore deposits of the Athabasca Basin, Canada, and McArthur Basin,

northern Australia (Fig. 5-7A). Such compositional trend potentially indicates a close association between the HREE mineralisation in the NAHREY mineral field and unconformity-related U deposits. The composition of the APS minerals can be also used as an indicator of fO_2-pH conditions during mineral formation (Kister et al., 2005, 2006). The Sr-S-rich APS minerals (e.g., svanbergite-rich) are stabilized by relatively low pH and high fO_2 conditions, where sulphate is the dominate form of S, whereas LREE-P-rich APS mineral compositions (e.g., florencite-rich) are favoured by relatively high pH and low fO_2 conditions (Komninou and Sverjensky, 1996; Gaboreau et al., 2005). Therefore, P/S versus LREE can be used as a guide to conditions of APS formation (Fig. 5-7B). The early florencite, with close to end-member florencite composition, formed with the early xenotime mineralisation at relatively high pH and possibly low fO_2. These conditions fit with the findings of Nazari-Dehkordi et al. (2018) that the ore formation occurred via neutralisation of ore-bearing fluids and formation of a widespread muscovite alteration. Moreover, near-svanbergite mineral composition of late florencite demonstrates a more oxidised (higher fO_2) and/or low pH environment, which is consistent with the occurrence of oxidised sulphate minerals (barite and anhydrite) which appear late in the overall paragenetic sequence. Influx of SO_3^{2-}-bearing fluids is suggested to be the source of S for the late florencite and sulphate minerals. Evaporate horizons of the Paleo-Mesoproterozoic sedimentary rocks overlying the Birrindudu Group sandstones (Ahmad and Munson, 2013) may be the potential source of S.

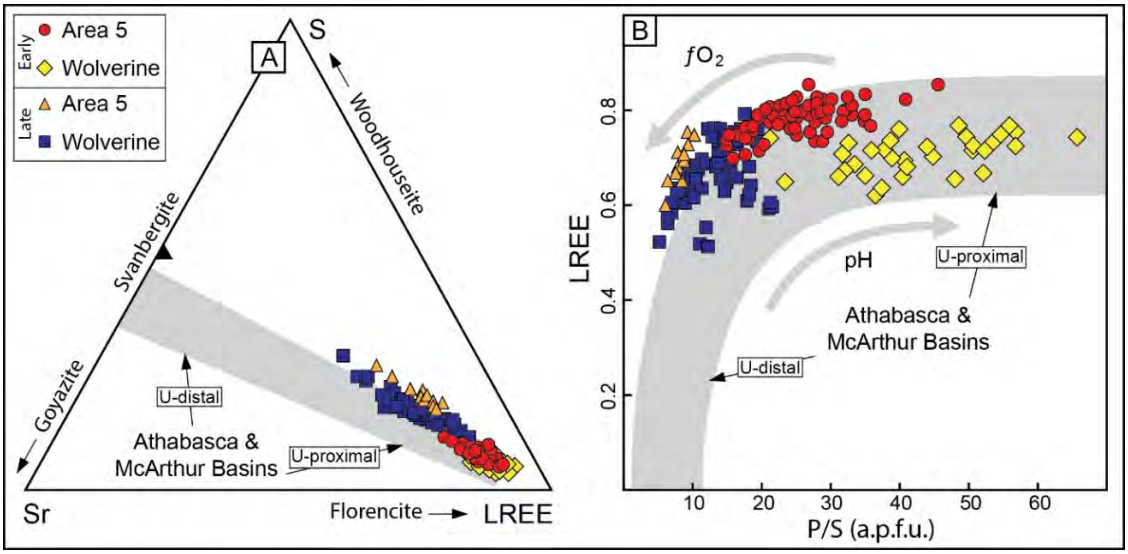

Fig. 5-7: (A) Plot of Sr, S, and LREE, and; (B) Plot of LREE versus P/S for florencite from Area 5 and Wolverine. Compositional fields of APS minerals associated with the unconformity-related U deposits of Australia and Canada are also shown for comparison (Data are from Gaboreau et al., 2005, 2007).

Xenotime formation environment

Several publications have attempted to provide insights into xenotime formation environment using Th and U contents of xenotime from a range of geological settings, including igneous, metamorphic hydrothermal and diagenetic (Aleinikoff et al., 2015; Zi et al., 2015; McNaughton and Rasmussen, 2017). Our xenotime trace element dataset allows for testing of the applicability of using xenotime geochemistry to define formation environments as suggested by McNaughton and Rasmussen (2017).

All of our xenotime are of hydrothermal origin (Cook et al., 2013; Nazari-Dehkordi et al., 2018), yet our dataset shows variable U and U/Th values that span most of the formation environment fields as defined by McNaughton and Rasmussen (2017) (Fig. 5-8). The majority of data points do not fall within the defined field for hydrothermal xenotime, but rather conform most closely to the U-low diagenetic field. These results indicate that geochemistry of xenotime alone is unlikely to provide definitive information on the geological setting of formation. As outlined above, the composition of xenotime is governed by many factors, not the least of which is the control of coexisting REE-bearing, or other, accessory phases (xenotime with florencite in this case). Many accessory minerals have a strong preference for Th over U (e.g., monazite; Stepanov et al., 2012), or vice versa, so crystallisation of even trace levels of these phases will strongly influence the U and Th uptake by any co-crystallising xenotime (e.g., , Bea, 1996; Aubert et al., 2001). We therefore urge caution in using the trace element compositions of xenotime to classify the geological environment of formation.

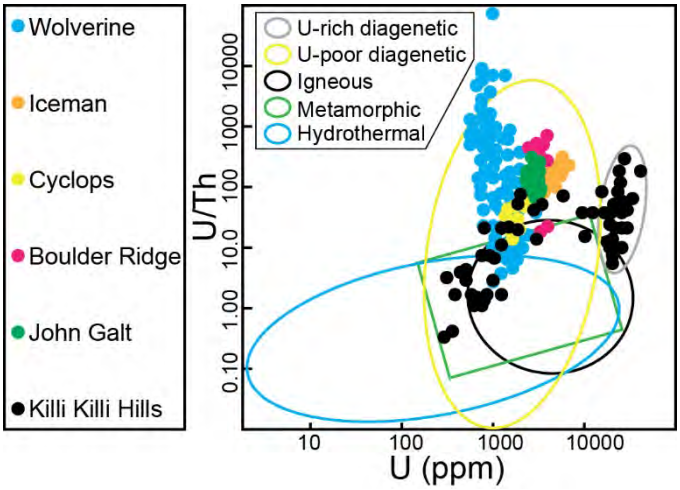

Fig. 5-8: Uranium (ppm) versus U/Th for xenotime from different HREE deposits/prospects. Compositional fields for xenotime of various origin are from McNaughton and Rasmussen (2017). The Killi Killi Hills xenotime data points are from Vallini et al. (2007). Note, all xenotime presented here is hydrothermal in origin, yet the compositional data span all of field of environment of formation.

Conclusion

The major findings of this study include:

(1) Ore petrography and paragenesis studies show a multistage ore mineral formation of xenotime and florencite throughout the NAHREY mineral field.

(2) Xenotime displays marked Eu anomalies that were directly inherited from the metasedimentary source rocks for the HREE. Compared with early xenotime, the late xenotime overgrowths are richer in the HREE and more depleted in P and LREE, owing to co-crystallisation of late florencite.

(3) Xenotime contains variable, but generally low, amounts of trace elements, particularly U, Th, Si and Ca. Incorporation of these elements into the xenotime structure occurred mainly via cheralite and, to a lesser extent, thorite/coffinite substitutions. Moreover, Sc^{3+}, and possibly Fe^{3+} were incorporated in xenotime in exchange for REE^{3+}.

(4) Late florencite that largely replaces early xenotime or overgrows early florencite, has variable compositions that accord with the florencite-svanbergite/woodhouseite-type [$(Sr^{2+},Ca^{2+}) + S^{6+} = P^{5+} + LREE^{3+}$] and huttonite-type ($Th^{4+} + Si^{4+} = P^{5+} + LREE^{3+}$) substitution mechanism.

(5) High concentration of U in xenotime along with comparable chemical composition of early florencite to that of APS minerals associated with the unconformity-related U deposits of northern Australia provide support for a genetic association between the two mineralisation styles.

(6) Hydrothermal xenotime can vary significantly in U and U/Th contents, so these parameters may not be effective for distinguishing the environment of xenotime formation.

Acknowledgments

This work was financially and logistically supported by Northern Minerals Ltd and by an ARC Future Fellowship (FT 120100198) to CS. We also thank the reviewers for their insightful comments.

References

Adlakha, E.E., and Hattori, K., 2015. Compositional variation and timing of aluminum phosphate-sulfate minerals in the basement rocks along the P2 fault and in association with the McArthur River uranium deposit, Athabasca Basin, Saskatchewan, Canada. American Mineralogist, v. 100, p. 1386–1399.

Ahmad, M., and Munson, T.J., 2013. Geology and mineral resources of the Northern Territory, Northern Territory Geological Survey. Special Publication 5.

Aleinikoff, J.N., Lund, K., and Fanning, C.M., 2015. SHRIMP U-Pb and REE data pertaining to the origins of xenotime in Belt Supergroup rocks: evidence for ages of deposition, hydrothermal alteration, and metamorphism. Canadian Journal of Earth Sciences, v. 52, p. 722–745.

Andreoli, M.A.G., Smith, C.B., Watkeys, M., Moore, J.M., Ashwal, L.D., and Hart, R.J., 1994. The geology of the Steenkampskraal monazite deposit, South Africa: implications for REE-Th-Cu mineralization in charnockite-granulite terrains. Economic Geology, v. 89, p. 994–1016.

Aubert, D., Stille, P., and Probst, A., 2001. REE fractionation during granite weathering and removal by waters and suspended loads: Sr and Nd isotopic evidence. Geochimica et Cosmochimica Acta, v. 65, p. 387–406.

Bagas, L., Bierlein, F.P., English, L., Anderson, J., Maidment, D., and Huston, D.L., 2008. An example of a Palaeoproteozoic back-arc basin: petrology and geochemistry of the ca. 1864 Ma Stubbins Formation as an aid towards an improved understanding of the Granites-Tanami Orogen, Western Australia. Precambrian Research, v. 166, p. 168–184.

Bau, M., 1991. Rare-earth element mobility during hydrothermal and metamorphic fluid-rock interaction and the significance of the oxidation state of europium. Chemical Geology, v. 93, p. 219–230.

Bau, M., and Moller, P., 1992. Rare earth element fractionation in metamorphogenic hydrothermal calcite, magnesite and siderite. Mineralogy and Petrology, v. 45, p. 231–246.

Bayliss, P., Kolitsch, U., Nickel, E.H., and Pring, A., 2010. Alunite supergroup: recommended nomenclature. Mineralogical Magazine, v. 74, p. 919–927.

Bea, F., 1996. Residence of REE, Y, Th and U in granites and crustal protoliths: Implications for the chemistry of crustal melts. Journal of Petrology, v. 37, p. 521–552.

Beaufort, D., Patrier, P., Laverret E., Bruneton, P., and Mondy, J., 2005. Clay alteration associated with Proterozoic unconformity-type deposits in the East Alligator River Uranium Field, Northern Territory, Australia. Economic Geology, v. 100, p. 515–536.

Blake, D.H, Hodgson, I.M., and Smith, P.A., 1975. Geology of the Birrindudu and Tanami 1:2500000 Sheet Areas, Northern Territory. Canberra ACT: Bureau of Mineral Resources, Australia, Report 174.

Blake, D.H., Tyler, I.M., and Page, R.W., 2000. Regional geology of the Halls Creek Orogen. In: Hoatson, D.M., and Blake, D.H., (Eds.). Geology and economic potential of the Palaeoproterozoic layered mafic/ultramafic intrusions in the East Kimberley, Western Australia. Australian Geological Survey Organisation Bulletin, v. 246, p. 35–62.

Chu, M., Wang, K., Griffin, W., Chung, S., OReilly, S., Pearson, N., and Iizuka, I., 2009. Apatite composition: tracing petrogenetic processes in Transhimalayan granitoids. Journal of Petrology, v. 50, p. 1829–1855.

Cook, N.J., Ciobanu, C.L., O'Rielly, D., Wilson, R., Das, K., and Wade, B., 2013. Mineral chemistry of Rare Earth Element (REE) mineralization, Browns Ranges, Western Australia: Lithos, v. 172-173, p. 192–213.

Crispe, A., and Vandenberg, L., 2005. Geology of the Tanami Region, Northern Territory. Northern Territory Geological Survey Bulletin.

Crispe, A.J., Vandenberg, L.C., and Scrimgeour, I., 2007. Geological framework of the Archaean and Palaeoproterozoic Tanami Region, Northern Territory: Mineralium Deposita, v. 42, p. 1–26.

Cross, A., and Crispe, A., 2007. SHRIMP U-Pb analyses of detrital zircon: a window to understanding the Paleoproterozoic development of the Tanami Region, northern Australia: Mineralium Deposita, v. 42, p. 27–50.

Dill, H.G., 2001. The geology of aluminium phosphates and sulfates of the alunite group minerals: a review. Earth Science Reviews, v. 53, p. 35–93.

Ehlers, T.A., and Farley, K.A., 2003. Apatite (U-Th)/He thermochronometry: methods and applications to problems in tectonic and surface processes. Earth and Planetary Science Letters, v. 206, p. 1–14.

Engi, M., 2017. Petrochronology based on REE-minerals: monazite, allanite, xenotime, apatite. Reviews in Mineralogy and Geochemistry, v. 83, p. 365–418.

Forster, H.J., 1998. The chemical composition of REE-Y-Th-U-rich accessory minerals in peraluminous granites of the Erzgebirge-Fichtelgebirge region, Germany. Part II: Xenotime. American Mineralogist, v. 83, p. 1302–1315.

Forster, H.-J., 2006. Composition and origin of intermediate solid solutions in the system thorite–xenotime–zircon–coffinite. Lithos, v. 88, p. 35–55.

Fricker, M.B., Kutscher, D., Aeschlimann, B., Frommer, J., Dietiker, R., Bettmer, J., and Günther, D., 2011. High spatial resolution trace element analysis by LA-ICP-MS using a novel ablation cell for multiple or large samples. International Journal of Mass Spectrometry, v. 307, p. 39–45.

Gaboreau, S., Beaufort, D., Vieillard, Ph., Patrier, P., and Bruneton, P., 2005. Aluminum phosphate-sulphate minerals associated with Proterozoic unconformity-type uranium deposits in the East Alligator River Uranium Field, Northern Territories, Australia. The Canadian Mineralogist, v. 43, p. 813–827.

Gaboreau, S., Cuney, M., Quirt, D., Beaufort, D., Patrier, P., and Mathieu, R., 2007. Significance of aluminium phosphate-sulfate minerals associated with U unconformity-type deposits: The Athabasca basin, Canada. American Mineralogist, v. 92, p. 267–280.

Griffin, T.J., Page, R.W., Sheppard, S., and Tyler, I.M., 2000. Tectonic implications of Palaeoproterozoic post-collisional, high-K felsic igneous rocks from the Kimberley Region of Northwestern Australia. Precambrian Research, v. 101, p. 1–23.

Harlov, D.E., Andersson, U.B., Forster, H.-J., Nystrom, J.O., Dulski, P., and Broman, C., 2002. Apatite-monazite relations in the kiirunavaara magnetite-apatite ore, northern Sweden. Chemical Geology, v. 191, p. 47–72.

Harlov, D.E., Wirth, R., and Hetherington, C.J., 2011. Fluid-mediated partial alteration in monazite: the role of coupled dissolution-reprecipitation in element redistribution and mass transfer. Contributions to Mineralogy and Petrology, v. 162, p. 329–348.

Hendrickx, M.A., Slater, K., Crispe, A.J., Dean, A.A., Vandenberg, L.C., and Smith, J.B., 2000. Paleoproterozoic stratigraphy of the Tanami Region: regional correlations realisation preliminary results. Darwin NT: Northern Territory Geological Survey Record, 71 pp.

Hetherington, C.J., Jercinovic, M.J., Williams, M.L., and Mahan, K., 2008. Understanding geologic processes with xenotime: composition, chronology, and a protocol for electron probe microanalysis. Chemical Geology, v. 254, p. 133–147.

Hikov, A., Lerouge, C., and Velinova, N., 2010. Geochemistry of alunite group minerals in hydrothermally altered rocks from the Asarel porphyry copper deposit, Central Srednogorie. Review of the Bulgarian Geological Society, v. 71, p. 133–148.

Jambor, J.L., 1999. Nomenclature of the alunite supergroup. The Canadian Mineralogist, v. 37, p. 1323–1341.

Kister, Ph., Laverret, E., Quirt, D., Cuney, M., Patrier, P., Beaufort, D., and Bruneton, P., 2006. Mineralogy and geochemistry of the host-rock alterations associated to the Shea Creek unconformity-type uranium deposits (Saskatchewan, Canada), Part 2. Spatial distribution of the Athabasca Group sandstone matrix minerals. Clays and Clay Minerals, v. 54, p. 295–313.

Kister, Ph., Vieillard, Ph., Cuney, M., Quirt, D., and Laverret, E., 2005. Thermodynamic constraints on the mineralogical and fluid composition evolution in a clastic sedimentary basin: the Athabasca basin (Saskatchewan, Canada). European Journal of Mineralogy, v. 17, p. 325–342.

Kolitsch, U., and Pring, A., 2001. Crystal chemistry of the crandallite, beudantite, and alunite groups: a review and evaluation of the suitability as storage materials for toxic metals. Journal of Mineralogy and Petrology Sciences, v. 96, p. 67–78.

Komninou, A., and Sverjensky, D.A., 1996. Geochemical modeling of the formation of an unconformity-type uranium deposit. Economic Geology, v. 91, p. 590–606.

Kositcin, N., McNaughton, N.J., Griffin, B.J., Fletcher, I.R., Groves, D.I., and Rasmussen, B., 2003. Textural and geochemical discrimination between xenotime of different origin in the Archaean Witwatersrand Basin, South Africa. Geochimica et Cosmochimica Acta, v. 67, p. 709–731.

Krenn, E., Ustaszewski. K., and Finger, F., 2008. Detrital and newly formed metamorphic monazite in amphibolite-facies metapelites from the Motajica Massif, Bosnia. Chemical Geology, v. 254, p. 164–174.

Lan, Z.W., Chen, Z.Q., Li, X.H., Li, B., and Adams, D., 2013. Hydrothermal origin of the Paleoproterozoic xenotime from the King Leopold Sandstone of the Kimberley Group, Kimberley, NW Australia: Implications for a ca 1.7 Ga far-field hydrothermal event. Australian Journal of Earth Sciences, v. 60, p. 497–508.

Lorilleux, G., Cuney, M., Jebrak, M., Rippert, J.C., and Portella, P., 2003. Chemical brecciation processes in the Sue unconformity-type uranium deposits, eastern Athabasca Basin (Canada). Journal of Geochemical Exploration, v. 80, p. 241–258.

McDonough, W.F., and Sun, S.S., 1995. Composition of the Earth. Chemical Geology, v. 120, p. 223–253.

McNaughton, N.J., and Rasmussen, B., 2017. Geochemical characterisation of xenotime formation environments using U-Th. Chemical Geology, v. 484, p. 109–119.

Mordberg, L.E., 2004. Thorium in crandallite-group minerals: an example from a Devonian bauxite deposit, Timan, Russia. Russian Research Geological institute (VSEGEI), St. Petersburg, Russia. Mineralogical Magazine, v. 68, p. 489–497.

Morin-Ka, S., Beardsmore, T.J., Hancock, E.A., Rasmussen, B., Dunkley, D., Muhling, J., Zi, J., Wilson, R., and Champion, J., 2016. Alteration and Age of the Browns Range Rare Earth Element Deposits: Western Australian Department of Mines and Petroleum.

Nagy, G., Draganits, E., Demeny, A., Panto, G., and Arkai, P., 2002. Genesis and transformations of monazite, florencite, and rhabdophane during medium grade metamorphism: examples from the Sopron Hills, Eastern Alps. Chemical Geology, v. 191, p. 25–46.

Nazari-Dehkordi, T., Spandler, C., Oliver, N.H.S., and Wilson, R., 2018. Unconformity–Related Rare Earth Element deposits: A regional-scale hydrothermal mineralization type of northern Australia. Economic Geology, v. 113, p. 1297–1305.

Nazari-Dehkordi, T., Spandler, C., Oliver, N.H.S., Chapman, J., and Wilson, R., 2017. Provenance, tectonic setting and source of Archean metasedimentary rocks of the Browns Range Metamorphics, Tanami Region, Western Australia. Australian Journal of Earth Sciences, v. 64, p. 723–741.

Ni, Y., Hughes, J.M., and Mariano, A.N., 1995. Crystal chemistry of the monazite and xenotime structures. American Mineralogist, v. 80, p. 21–26.

Ondrejka, M., Uher, P., Prsek, J., Ozdin, D., 2007. Arsenian monazite-(Ce) and xenotime-(Y), REE arsenates and carbonates from the Tisovec-Rejkovo rhyolite, Western Carpathians, Slovakia: composition and substitutions in the (REE,Y)XO_4 system (X = P, As, Si, Nb, S). Lithos, v. 95, p. 116–129.

Page, R., Sun, S.S., Blake, D., Edgecombe, D., and Pearcey, D., 1995. Geochronology of an exposed late Archean basement terrane in the Granites-Tanami region. Australian Geological Survey Organisation Research Newsletter, v. 22, p. 21–22.

Page, R.W., Griffin, T.J., Tyler, I.M., and Sheppard, S., 2001. Geochronological constraints on tectonic models for Australian Palaeoproterozoic high-K granites. Journal of the Geological Society of London, v. 158, p. 535–545.

Patino Douce, A.E., Roden, M.F., Chaumba, J., Fleisher, C., and Yogodzinski, G., 2011. Compositional variability of terrestrial mantle apatites, thermodynamic modeling of apatite volatile contents, and the halogen and water budgets of planetary mantles. Chemical Geology, v. 288, p. 14–31.

Pettke, T., 2008. Analytical protocols for element concentration and isotope ratio measurements in fluid inclusions by LA-(MC)-ICP-MS. Laser ablation ICP-MS in the earth sciences: current practices and outstanding issues. Mineralogical Association of Canada Short Course Series, v. 40, p. 189–218.

Polito, P.A., Kyser, T.K., Marlatt, J., Alexandre, P., Bajwah, Z., and Drever, G., 2004. Significance of alteration assemblages for the origin and evolution of the Proterozoic Nabarlek unconformity-related uranium deposit, Northern Territory, Australia. Economic Geology, v. 99, p. 113–139.

Quirt, D., Kotzer, T., and Kyser, T.K., 1991. Tourmaline, phosphate minerals, zircon and pitchblende in the Athabasca group: Maw Zone and McArthur Rivers areas, Saskatchewan. In summary of investigations, Saskatchewan Geological Survey, Saskatchewan Energy and Mines, v. 4, p. 181–191.

Rasmussen, B., 1996. Early-diagenetic REE-phosphate minerals (florencite, gorceixite, crandallite, and xenotime) in marine sandstones; a major sink for oceanic phosphorus. American Journal of Science, v. 296, p. 601–632.

Rasmussen, B., and Muhling, J.R., 2009. Reactions destroying detrital monazite in greenschist-facies sandstones from the Witwatersrand basin, South Africa. Chemical Geology, v. 264, p. 311–327.

Roberts, W.L., Campbell, T.J., and Rapp, G.R., 1990. Encyclopedia of Minerals. Van Nostrand Reinhold, 2nd edition, New York, pp. 979.

Scott, K.M., 1987. Solid solution in, and classification of, gossan-derived members of the alunite-jarosite family, northwest Queensland, Australia. American Mineralogist, v. 72, p. 178–187.

Sheppard, S., Tyler, I.M., Griffin, T.G., and Taylor, W.R., 1999. Paleoproterozoic subduction-related and passive margin basins in the Halls Creek Orogen, northwest Australia. Australian Journal of Earth Sciences, v. 46, p. 679–690.

Slezak, P.R., Spandler, C., and Blake, K., 2018. Ghosts of apatite past: Using hyperspectral CL and micro-geochemical data to reveal multi-generational apatite in the Gifford Creek Carbonatite Complex, Australia. The Canadian Mineralogist, v. 56, p. 1–25.

Smith, J.B., 2001. Summary of results, joint NTGS-AGSO age determination program 1999-2001. Darwin NT: Northern Territory Geological Survey, Record 2001–007.

Spandler, C., Pettke, T., and Rubatto, D., 2011. Internal and external fluid sources for eclogite-facies veins in the Monviso meta-ophiolite, Western Alps: Implications for fluid flow in subduction zones. Journal of Petrology, v. 52, p. 1207–1236.

Spear, F.S., and Pyle, J.M., 2002. Apatite, monazite and xenotime in metamorphic rocks. In: Kohn, M.J., Rakovan, J., Hughes, J.M. (Eds.), Phospates. Geochemical, geobiological and materials importance. Reviews in Mineralogy and Geochemistry, v. 48, p. 293–335.

Stepanov, A.S., Hermann, J., Rubatto, D., and Rapp, R.P., 2012. Experimental study of monazite/melt partitioning with implications for the REE, Th and U geochemistry of crustal rocks. Chemical Geology, v. 300, p. 200–220.

Tyler, I.M, Griffin, T.J, Page, R.W., and Shaw, R.D., 1995. Are there terranes within the Lamboo Complex of the Halls Creek Orogen? Geological Survey of Western Australia, Annual Review 1993-94, p. 37–46.

Vallini, D.A., Groves, D.I., McNaughton, N.J., and Fletcher, I.R., 2007. Uraniferous diagenetic xenotime in northern Australia and its relationship to unconformity-associated uranium mineralisation. Mineralium Deposita, v. 42, p. 51–64.

Van Achterbergh, E., Ryan, C.G., Jackson, S.E., and Griffin, W.L., 2001. Data reduction software for LA-ICP-MS, in: Sylvester, P.J., (Ed.), Laser Ablation-ICP Mass Spectrometry in the Earth Sciences: Principles and Applications. Mineralogical Association of Canada, v. 29, 239–243.

Van Emden, B., Thornber, M.R., Graham, J., and Lincoln, F.J., 1997. The incorporation of actinides in monazite and xenotime from placer deposits in western Australia. Canadian Mineralogist, v. 35, p. 95–104.

Williams, I.S., 2001. Response of detrital zircon and monazite, and their U-Pb isotopic systems, to regional metamorphism and host-rock partial melting, Cooma Complex, southeastern Australia. Australian Journal of Earth Sciences, p. 48, v. 557–580.

Wilson, J.A., 1984. Crandallite group minerals in the Helikian Athabasca group in Alberta, Canada. Canadian Journal of Earth Science, v. 22, p. 637–641.

Zi, J.-W., Rasmussen, B., Muhling, J.R., Fletcher, I.R., Thorne, A.M., Johnson, S.P., Cutten, H.N., Dunkley, D.J., and Korhonen, F.J., 2015. In situ U-Pb geochronology of xenotime and monazite from the Abra polymetallic deposit in the Capricorn Orogen,

Australia: dating hydrothermal mineralization and fluid flow in a long-lived crustal structure. Precambrian Research, v. 260, p. 91–112.

Chapter 6

Fluid inclusion and stable isotope constraints on the heavy rare earth element mineralisation in the Browns Range Dome, Tanami Region, Western Australia

Teimoor Nazari-Dehkordi[1*], Jan Marten Huizenga[1,2], Carl Spandler[1], Nicholas H.S. Oliver[1, 3]

[1]Economic Geology Research Centre, Department of Geoscience, James Cook University, Townsville, QLD 4811, Australia

[2]Department of Geology, University of Johannesburg, PO Box 524, Auckland Park 2006, South Africa

[3]HCOVGlobal Consultants, PO Box 3533, Hermit Park, QLD 4812, Australia

Abstract

This study reports on fluid inclusion and oxygen isotope compositions of mineralised and barren hydrothermal quartz veins and hosting metasedimentary rocks associated with the heavy rare earth element (HREE) mineralisation in the Browns Range Dome of the Tanami Region, Western Australia. The HREE mineralisation consists largely of quartz and xenotime-bearing hydrothermal veins and breccias that occurs along sub-vertical faults within Archean to Paleoproterozoic metasedimentary rocks. Analysis of nearly 550 primary fluid inclusions in quartz identified three types of hydrothermal fluids; type I low salinity H_2O-NaCl (largely <5 wt.% NaCl; consistent with meteoric water); type II medium salinity H_2O-NaCl (12-18 wt.% NaCl), and; type III high salinity H_2O-$CaCl_2$-NaCl (up to 25 wt.% NaCl). Quartz from a vein that is barren of mineralisation contains only type I low salinity H_2O-NaCl fluid inclusions, whereas the mineralised quartz samples contain all three types of fluid inclusions with homogenisation temperatures varying over a relatively wide range from 100 to 250 °C.

The Raman analyses of the fluid inclusions confirmed their hydrous composition with no hydrocarbon or CO_2 species identified. Limited LA-ICP-MS analysis found detectable Y, Ce, U and Cl only in the type III fluid inclusions, which indicates that transport of ore metals was (at least partly) by Cl complexes in the type III fluid. The $\delta^{18}O_{fluid}$ values calculated from quartz from mineralised samples are in the range defined by the Archean metasedimentary host rocks of the Browns Range Metamorphics ($\delta^{18}O_{fluid}$ = +1.8 to +5.2‰) and the Paleoproterozoic Birrindudu Group sandstones ($\delta^{18}O_{fluid}$ = +8‰) that unconformably overly the Browns Range Metamorphics. Collectively, our fluid inclusion and oxygen isotope data, together with other field, mineralogical and geochemical data, support an ore genesis model involving mixing of distinct hydrothermal fluids in fault zones and along unconformity surfaces in, and around, the Browns Range Dome; one fluid type (likely type I) potentially carried P from the Birrindudu Group sandstones, and one fluid type (type III) carried HREE+Y derived from metasedimentary rocks of the Browns Range Metamorphics. The trapping temperature and pressure during the fluid mixing was between 100 to 250 °C and between 0.4 and 1.6 Kbar.

Keywords: Fluid inclusion, stable isotope, hydrothermal, xenotime, unconformity

Introduction

The rare earth elements (REE) have been traditionally considered to be relatively immobile in hydrothermal fluids. However, recent studies have determined a hybrid magmatic-hydrothermal origin for a number of deposits that were originally regarded to be solely of magmatic origin (Salvi and Williams-Jones, 1996; Sheard et al., 2012). Experimental work has also demonstrated that solubilities of REE can be relatively high in certain hydrothermal environments, which raises the possibility of formation of REE deposits via purely hydrothermal processes (Migdisov et al., 2009; Williams-Jones et al., 2012; Loges et al., 2013; Migdisov and Williams-Jones, 2014; Timofeev et al., 2015, 2017). Nonetheless, we have an incomplete understanding of how REE - particularly the highly-sought after heavy (H)REE - are mobilised and precipitated by hydrothermal fluids. Available data on natural samples of REE-bearing hydrothermal fluids are restricted mostly to high temperature magmatic systems (e.g., Campbell et al., 1995; Williams-Jones et al., 2000). A detailed understanding of hydrothermally-formed REE deposits can, therefore, enhance our knowledge of hydrothermal REE mobility and deposition.

Recently-discovered HREE mineralisation in north-western Australia defines a rather poorly understood hydrothermal vein and breccia ore system with ore metals contained predominantly in xenotime [$(Y,HREE)PO_4$] and minor florencite [$LREEAl_3(PO_4)_2(OH)_6$] (Cook et al., 2013; Nazari-Dehkordi et al., 2018). The orebodies are hosted by Archean metasedimentary rocks of the Browns Range Metamorphics (BRM) and the Paleoproterozoic Birrindudu Group sandstones of the Tanami Region, and also Red Rock Basin of the Halls Creek Orogen, in an area known as the "North Australian HREE+Y" (NAHREY) mineral field (Nazari-Dehkordi et al., 2018) (Fig. 6-1). The bulk of the mineralisation appears in close proximity to a regional unconformity between the BRM and overlying Birrindudu Group (Richter et al., 2018; Nazari-Dehkordi et al., 2018), so this mineralisation style has been labelled unconformity-related REE deposits (Nazari-Dehkordi et al., 2018). Of these deposits, Wolverine is the largest with a total mineral resource of 4.97 Mt at 0.86% total rare earth oxides. These deposits/prospects are unusually enriched in HREE and show no apparent link to magmatic sources (Nazari-Dehkordi et al., 2018), and therefore provide a unique opportunity to study aqueous transport and deposition of HREE.

Studies of fluid inclusion and oxygen isotope compositions place valuable constraints on hydrothermal fluids and associated mineralisation (e.g., Criss and Farquhar, 2008). Here, we present a detailed fluid inclusion study incorporating fluid inclusion petrography, microthermometry, laser Raman spectroscopy analysis, and trace element microanalysis by laser ablation inductively coupled plasma mass spectrometry (LA-ICP-MS). We complement these data with oxygen isotope analysis of hydrothermally-formed xenotime and quartz from ore veins, as well as the metasedimentary host rocks, to allow inferences on the nature, composition and evolution of the ore-forming fluids.

Geological setting

All of the HREE deposits/prospects studied here occur near, or within, the Browns Range Dome of the Tanami Region (Fig. 6-1A), and in particular, near a regional unconformity that separates the underlying Archean metasedimentary rocks of the BRM from the overlying Birrindudu Group sandstones (Fig. 6-1B). Geological aspects of the Tanami Region are published in detail elsewhere (e.g., Crispe et al., 2007; Bagas et al., 2008; Nazari-Dehkordi et al., 2017), so only a brief review of the Browns Range Dome is presented here.

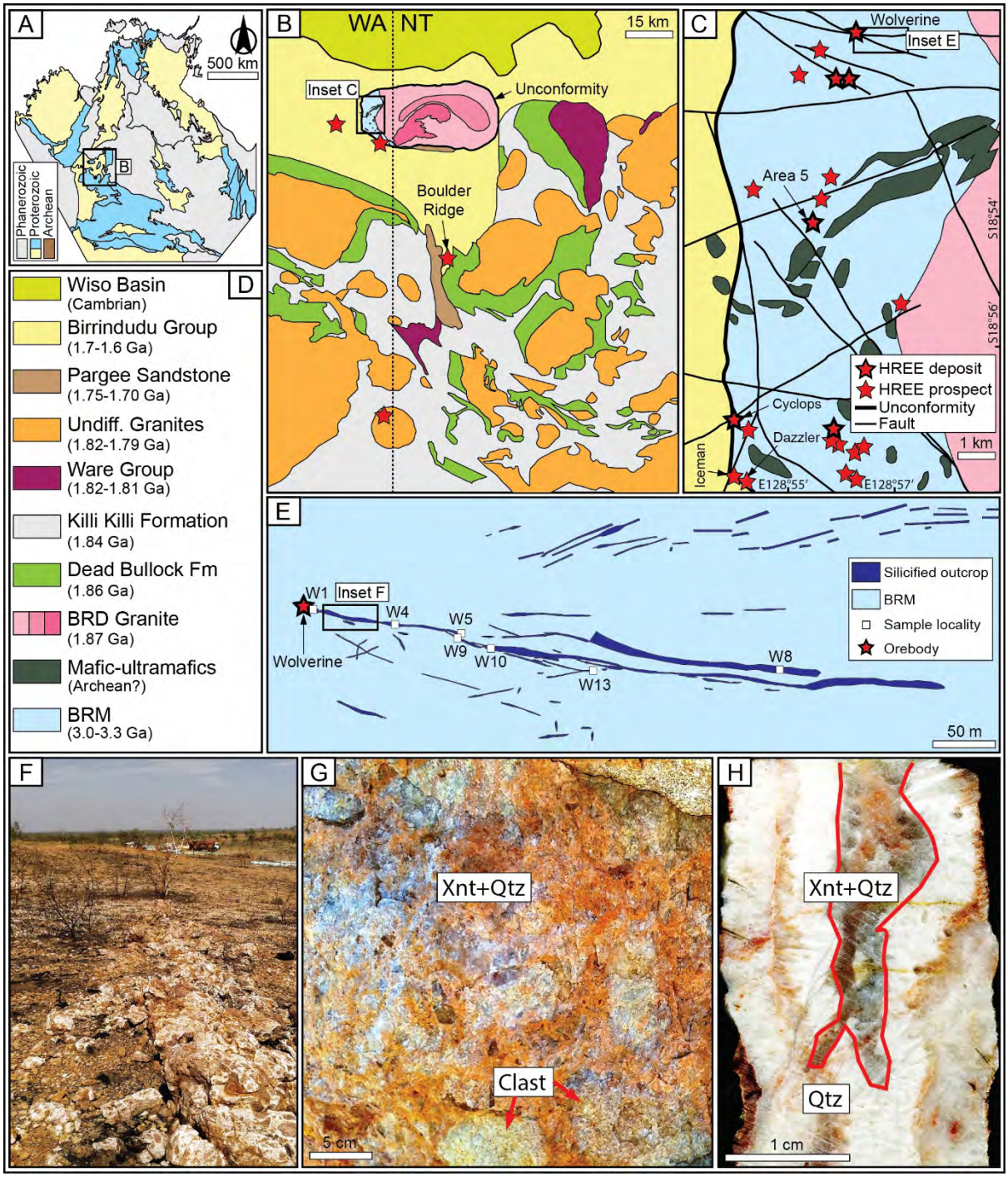

Fig. 6-1: Geological maps of the Tanami Region and Browns Range. (A) Distribution of the HREE mineralisation in the NAHREY mineral field; (B) simplified geological map of the Tanami Region; (C) Simplified geological map of the Browns Range area; (D) Stratigraphy of the Tanami Region; (E) Sample locality along the structure that hosts the Wolverine orebody for oxygen isotope analysis; (F) Breccia outcrop along the structure; (G) Orebody outcrop; (H) Multiple generations of quartz (milky-coloured and ore-bearing transparent). Qtz = quartz; Xnt = xenotime.

Browns Range Dome

Located in the northwest of the Tanami Region (Fig. 6-1C), the Browns Range Dome (BRD) is an east-west trending ovoid-shaped structure measuring ca. 60 km by ca. 30 km, cored by a 1-3 km thick ca. 1.87 Ga Browns Range Dome Granite (Page et al., 1995; Hendrickx et al., 2000; Cross and Crispe, 2007). Archean metasedimentary rocks of the BRM and minor mafic-ultramafic rocks occupy the western section of the Dome (Nazari-Dehkordi et al., 2017). The BRM comprises mainly arkosic metasandstones locally containing interbedded medium- to coarse-grained conglomerates and semi-pelitic schists that experienced regional metamorphism, mostly of greenschist facies, but locally up to amphibolite grade. The BRM were derived from a Mesoarchean granitic source, and were deposited between ca. 3.0 Ga (age of the detrital zircons in the BRM) and ca. 2.5 Ga (emplacement timing of the cross-cutting granitic, syenitic and pegmatitic intrusions measuring 10s to 100s of metres in dimension; Nazari-Dehkordi et al., 2017).

The BRM are unconformably overlain by a thick sequence of low grade Paleoproterozoic sedimentary rocks with rare volcanic units (Fig. 6-1D), the characteristics of which are presented in detail by Bagas et al. (2008) and Crispe et al. (2007). These include the ca. 1.78 to ca. 1.64 Ga Pargee Sandstone and Birrindudu Group (Crispe et al., 2007; Vallini et al., 2007), and the Tanami and Ware Groups, both of which were intruded by ca. 1.8 Ga granites (Smith, 2001). The ~3.5 to ~6 km thick Birrindudu Group consists of three conformable units including the basal Gardiner Sandstone, the fine-grained and calcareous Talbot Well Formation, and the Coomarie Sandstone (Blake et al., 1975). The Gardiner Sandstone is slightly metamorphosed and deformed, and unconformably overlies deeply weathered and metamorphosed rocks of the BRM, Tanami Group, Ware Group and Pargee Sandstone (Crispe and Vandenberg, 2005). The Gardiner Sandstone forms the outer margins of the BRD and dips gently (5 to 25º) to the west near the HREE mineralisation in the western part of the dome, and dips to the east in the eastern part of the dome (Fig. 6-1C). The western part of the dome shows some faulting.

HREE mineralisation

Mineralisation and ore geometry

Mineralisation throughout the NAHREY mineral field displays a spatial relationship with faults and some lithological boundaries. All the deposits/prospects have a strongly structurally-controlled mineralisation style characterised by a simple ore mineralogy of xenotime and subordinate florencite. Other REE minerals, such as REE carbonates (e.g., bastnaesite) or monazite are absent, which is unusual for a REE ore deposit (e.g., Weng et al., 2015). The HREE mineralisation consists primarily of quartz-xenotime veins and breccias accommodated in sub-vertical faults, surrounded by a halo of low-grade ore extended into the host rock. This study focuses on two of the larger deposits, namely Wolverine and Area 5, from which fluid inclusion samples and bulk of the oxygen isotope separates were collected.

The largest deposit, Wolverine, is a steeply (ca. 75° to the north) dipping planar orebody, up to 5 m wide, that extends over 400 m in strike length and from the surface to at least ca. 550 metres in depth. The orebody lies within a WNW-striking fault in association with an intersecting W-E trending fault (Fig. 6-1E). Similarly, the Area 5 orebody occurs at an intersection of sub-vertical fault zones with prominent WNW and W strikes, alongside which the orebody appears as discontinuous pods. Area 5 is compositionally distinct, as it is dominated by florencite with only minor amounts of xenotime.

Ore mineral paragenesis

There are three major mineral assemblages associated with the mineralisation and the metasedimentary host rocks across the NAHREY mineral field.

(1) A pre-ore detrital and metamorphic assemblage, including quartz (several generations), alkali feldspar, hematite and coarse-grained muscovite aligned in pre-mineralisation foliation. The pre-ore assemblage chiefly reflects a greenschist-facies overprint on the predominantly meta-arkosic host rocks, resulting in locally well-developed schistose foliation in the metasedimentary rocks, which potentially occurred during the widespread ca. 1830 Ma Tanami Event (Crispe et al., 2007).

(2) A syn-ore hydrothermal mineral assemblage consisting predominantly of the ore minerals (xenotime, florencite), quartz and fine-grained muscovite (Fig. 6-2A). The syn-ore quartz-muscovite alteration consists dominantly of coarse- to fine-grained, cavity-filled and/or cemented, quartz and muscovite-sericite-illite assemblages, entirely enclosing the ore minerals. The main stage of the HREE mineralisation is characterised by fine-grained xenotime occurring in quartz + F-rich muscovite alteration assemblage within highly brecciated zones and coarse-grained quartz-xenotime veins (Figs. 6-2B-C).

(3) A post-ore mineral assemblage consisting mainly of multiple generations of quartz, hematite, barite and anhydrite within veins of up to 5 cm in width, that cross-cut the early stages of the paragenetic sequence.

Previous U-Pb age dating of xenotime from a number of deposits/prospects from across the NAHREY mineral field has yielded mineralization ages of between ca. 1.65 and ca. 1.60 Ga (Vallini et al., 2007; Morin-Ka et al., 2016; Nazari-Dehkordi et al., 2018). Therefore, the mineralisation across the NAHREY mineral field occurred within a relatively narrow 50 m.y. timeframe.

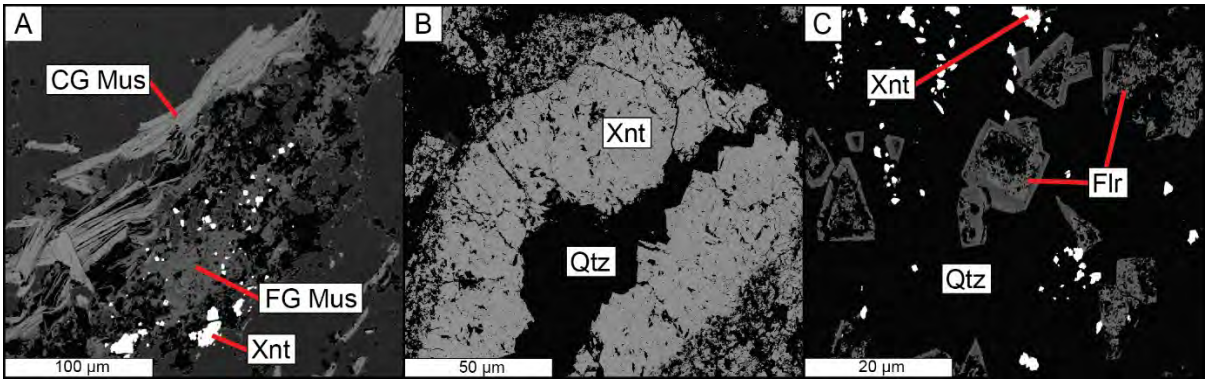

Fig. 6-2: Mineral assemblage associated with the HREE mineralisation and metasedimentary rocks. (A) Pre-ore coarse-grained muscovite and a syn-ore assembly of fine-grained muscovite and ore minerals; (B) Hydrothermal quartz-xenotime vein with very coarse-grained (1 mm) xenotime; (C) Dissemination of xenotime and florencite in hydrothermal quartz vein. Qtz = quartz; Xnt = xenotime; Flr = florencite; FG Mus = fine-grained muscovite; CG Mus = course-grained muscovite.

Sampling for fluid inclusion analysis

Localities of the samples for fluid inclusion analyses are listed in Table 6-1. The opaque nature and relatively fine grainsize of the REE-bearing ore minerals hindered direct study of the fluid inclusions trapped within these phases. Therefore, hydrothermal quartz that displays a paragenetic association with the mineralisation was targeted for analysis. The investigated samples include two mineralised hydrothermal vein quartz samples from drill cores of the Area 5 (sample A2-14) and Wolverine (sample W7-3) deposits (Figs. 6-3A-B), as well as mineralisation-barren hydrothermal vein quartz (sample W8; Fig. 6-3C) collected from an outcrop about 500 m east of the Wolverine orebody (see Fig. 6-1E). None of these samples was interrupted by post-depositional veining or fracturing. The barren quartz sample W8 shares a similar host structure and hydrothermal texture with the mineralised sample W7-3 from Wolverine. However, the precise timing of formation of the barren quartz vein is not known, leaving the possibility that this quartz could be syn-ore, or pre-/post-date the mineralisation. In either case, a comparison between the fluid inclusion assemblages present in the mineralised and barren samples can provide important constraints on the hydrothermal fluids involved in mineralisation.

Table 6-1: Location and available fluid inclusion types in the studied samples

Sample	Deposit	Easting	Northing	Depth	FIs Type	Ore
W8	Wolverine	494124	7914636	Surface	I	Barren
A2-14	Area 5	492231	7909976	135m	I, II, III	Mineralise
W7-3	Wolverine	493695	7914741	41m	I, II, III	Mineralise

*Coordinate system: UTM zone 52S.

Doubly-polished ~0.2 mm thick sections of the three samples were prepared. After initial microscopic evaluation of the sections, cathodoluminescence (CL) imaging of several quartz grains containing abundant and representative fluid inclusions was conducted. These CL images were used to identify internal textures, and potential multi-stage growth zones in quartz that are not evident from standard optical microscope petrography. Association of these CL zones with the ore minerals was used to infer ore-related quartz-hosted fluid inclusions. Initial fluid inclusion analysis involved thorough fluid inclusion petrography including documentation of the fluid inclusion shapes, spatial distribution, fluid composition types, and vapour/liquid ratios. Detailed grain-scale maps showing all fluid inclusions as a function of depth within the section were prepared for each quartz grain (see Appendix 6-1).

Sampling for oxygen isotope analysis

Thirty-four samples, including 4 xenotime, 24 quartz and 6 bulk-rock powders, were selected for oxygen isotope analysis. These samples are divided into three groups based on association with the mineralisation and sample type:

(1) Ore-related samples (12 quartz and 4 xenotime) derived from ore-bearing veins and/or breccias of several HREE deposits/prospects (Wolverine, Boulder Ridge, Cyclops, Dazzler, and Iceman; see Fig. 6-1). Coexisting quartz and xenotime were sampled from 4 mineralised veins from Wolverine.

(2) Seven quartz samples collected from outcrops as a ~500 m sampling traverse along the prominent WNW striking fault structure that hosts the Wolverine orebody (Figs. 6-1E-F). The sub-vertical structure cuts the BRM and consists largely of a zone of breccias and vein networks up to 5 metres wide with numerous splays and vein offshoots that extend into the BRM. The vein and breccia infill is predominantly coarse-grained hydrothermal quartz occasionally with hematite. Wolverine orebody lies at the western-most extent of the sampling traverse at, or adjacent to, the conjunction of the WNW and W-E faults. Here the brecciated ore samples are highly complex, containing high grade ore, rounded to sub-rounded clasts of the BRM, and interrelated hydrothermal quartz in the matrix (Fig. 6-1G). Further to the east away from the ore zone, the breccias consist principally of large (30 cm wide) angular clasts of the BRM enclosed within hydrothermal quartz. These large clasts occasionally contain traces of ore minerals, particularly florencite. Examination of the hand specimens revealed multiple generations of hydrothermal quartz veins of variable width, which can be generally classified as transparent and milky-coloured (Fig. 6-1H). Microprobe examination identified minor occurrences of ore minerals only in the transparent quartz vein. The structure terminates to the east with a poorly exposed silicified zone composed largely of hydrothermal quartz veins without any ore minerals. Based on the distribution of the ore minerals, the outcrops along the structure are variably mineralised, from the surface exposure of the Wolverine orebody through a barely mineralised zone to a silicified zone entirely barren of the mineralisation. All the outcrops are overprinted by the late quartz and hematite. We selected the least altered hydrothermal quartz samples along the structure (Fig. 6-1E) to investigate possible lateral variations in oxygen isotope composition along the structure, with one sample collected from

surface exposures of the Wolverine orebody and one sample with no traces of mineralisation collected from the silicified zone furthest from Wolverine. Five other samples represent slightly mineralised transparent quartz veins.

(3) Four detrital quartz and five bulk-rock samples from the BRM, and one bulk-rock sample from the Birrindudu Group sandstones lying above the unconformity with the BRM.

The samples were carefully washed in an ultrasonic bath to ensure complete removal of dust and associated contaminations, and then dried in an oven for 24 hours at 100 °C. Quartz and xenotime samples were subsequently lightly grounded in a small mortar, and then a minimum of 50 mg of the target mineral was manually handpicked under a binocular microscope. Whole-rock samples were dried, crushed, split and then finely-milled using a ring mill. A minimum 20 mg of the milled powder was used for analysis.

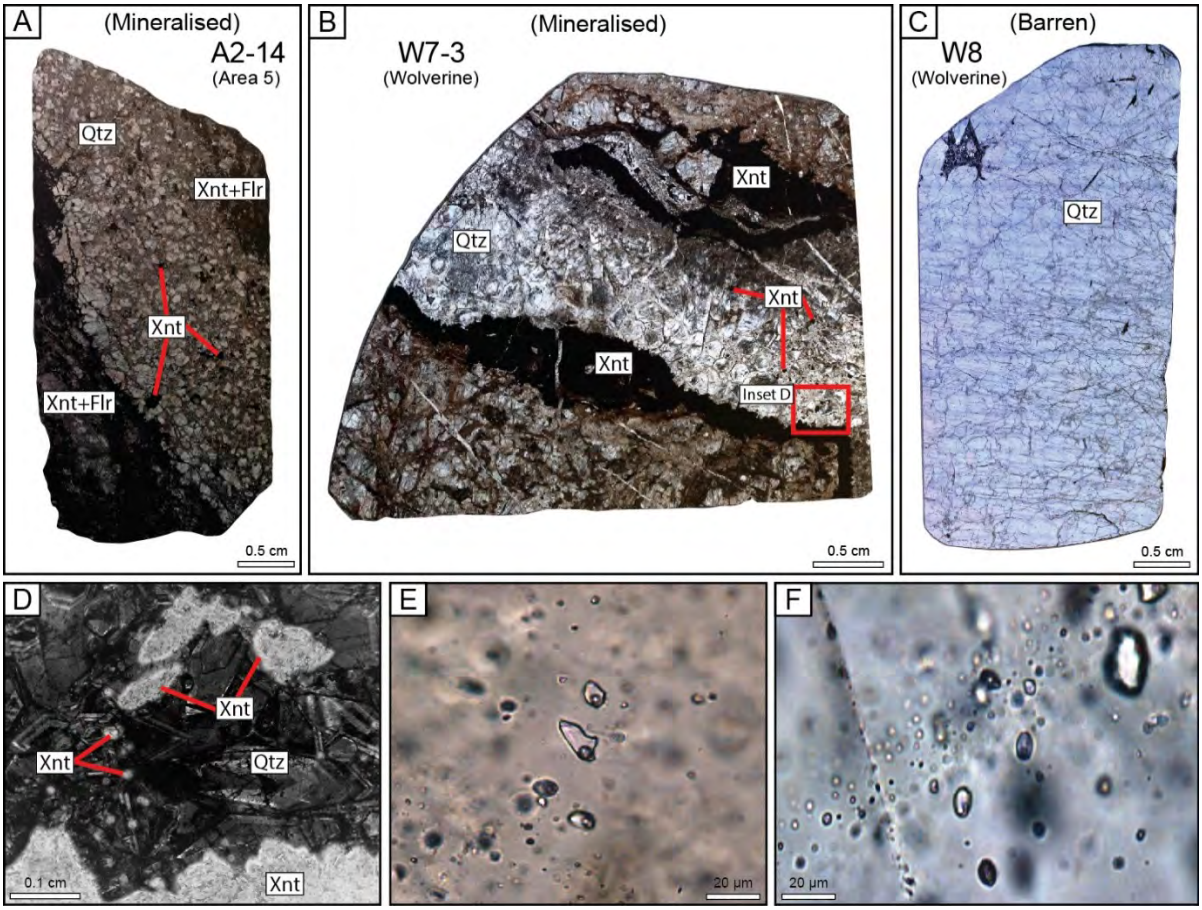

Fig. 6-3: Photographs of the hydrothermal quartz samples selected for fluid inclusion studies. (A) Mineralised sample A2-14 from Area 5 deposit; (B) Mineralised sample W7-3 from Wolverine deposit; (C) Barren sample W8 from Wolverine deposit; (D) A CL image of a mineralised quartz vein showing random distribution of ore minerals throughout both the dark and bright zonings; (E) Assembly of primary fluid inclusions; (F) Distribution of individual isolated fluid inclusions. Note that the fluid inclusions are at different depths. Qtz = quartz; Xnt = xenotime; Flr = florencite.

Analytical Methods

Cathodoluminescence (CL) imaging

Cathodoluminescence images of the representative quartz grains from the fluid inclusion samples were obtained by a JEOL-JSM5410LV scanning electron microprobe equipped with a Robinson CL detector and photomultiplier at the Advanced Analytical Centre (AAC), James Cook University (JCU), Australia. Instrument operating conditions were set to an accelerating

voltage of 20 kV, a beam current of ~10 nA and acquisition time of 200 s. Samples were uncoated and the chamber was flushed with Ar.

Fluid inclusion microthermometry

Fluid inclusion microthermometry was carried out using an Olympus-BX51 microscope, attached to a Linkam-MDS600 heating-freezing stage, located at the Department of Geoscience, JCU. The sample was located within an insulated stage on a 10 mm diameter quartz lens, housed in a stainless steel ring, all of which was placed on a thick silver block that serves as a thermal resister for sample heating. Caution was taken to avoid any contact between the sample and the steel ring to prevent uneven heating. The temperature within the stage was controlled through interaction between a heating element and liquid nitrogen within the silver block. The temperature range of the instrument is –190 °C to +600 °C, and the precision and accuracy of the microthermometry measurements, based on standard calibration procedures, were estimated to be ±2 °C for homogenization temperatures and ±0.1 °C for final ice melting temperatures. The stage was calibrated with a standard synthetic CO_2-H_2O fluid inclusion at the triple points of CO_2 (–56.6 °C) and H_2O (0.0 °C). The following phase transitions were measured systematically during heating:

(1a) Initial melting (H_2O-NaCl-$CaCl_2$): T_{mi} (antarcticite (aa) + hydrohalite (hh) + ice + vapour (vap) = liquid (liq) + hh + ice + vap).
(1b) Initial melting (H_2O-NaCl): T_{mi} (hydrohalite (hh) + ice + vapour (vap) = liquid (liq) + ice + vap).
(2) Final melting of ice: T_m (ice + liq + vap = liq + vap).
(3) Homogenisation by the disappearance of the vapour bubble into the liquid phase: T_h (liq + vap = liq).

Initial melting (T_{mi}) and final ice melting measurements (T_m) were carried out on numerous fluid inclusions. The temperature was decreased to –100 °C at a rate of ca. 20 °C/min to assure complete freezing. Freezing was usually marked by a sudden contraction of the vapour bubble that occasionally turned a brown-orange colour during cooling, which is typical for the H_2O-NaCl-$CaCl_2$ system (Zwart and Touret, 1994). The initial melting temperature measurements (T_{mi}) are imprecise, owing primarily to difficulty of observations at very low temperatures,

particularly for saline fluid inclusions with very low T_{mi}. This issue becomes more acute with the relatively small-sized fluid inclusions (<30 µm) studied here, as well as the possibility that the data may reflect metastable melting rather than eutectic melting (Bodnar, 2003). Nonetheless, the T_{mi} measurements, although imprecise, provide valuable insights into the composition of the ore-forming hydrothermal fluids. Hence, caution was taken to record the very first stage of melting. Final melting of ice was measured with a heating rate of 0.2 °C/min. For homogenization experiments (T_h), the temperature was initially increased at a rate of 20 °C/min until the vapour bubble nearly disappeared. Thereafter, the heating rate was reduced to 0.5 °C/min to ensure accurate recording of homogenization. Salinities and densities of the fluid inclusions were calculated using the Microsoft Excel-based program of Steele-MacInnis et al. (2012) developed for the H_2O-NaCl fluid system.

Raman spectroscopy analysis

Raman analyses of vapour, solid and liquid compositions of individual representative fluid inclusions were conducted at the AAC, JCU using a WITec Alpha Access 300 instrument connected to a modified Zeiss microscope with a 100 times objective. The Raman was equipped with a diode-generated 532 nm green laser. The focus diameter was approximately 2 µm and the measurement time was 30 s with three accumulations. To correct for any influence from the matrix, analyses of the host mineral were performed under identical conditions and orientation. Data processing was done with WITec Project Data Analysis Software 4.1. The Raman database for fluid inclusions of Frezzotti et al. (2012) was used for qualitative evaluation.

Fluid inclusion element analysis

Elemental microanalysis of individual fluid inclusions was conducted by LA-ICP-MS at AAC, JCU, using a GeoLas 193-nm ArF Excimer laser ablation system coupled with a Bruker (formally Varian) 820-MS ICP-MS. Ablation was conducted in a custom-build large volume cell as described by Fricker et al. (2011) using high-purity He as the carrier gas, which was subsequently mixed with Ar prior to introduction into the ICP-MS. Analysis was carried out with a beam diameter of between 20 µm and 35 µm (depending on the inclusion size) and beam energy density on the sample of 10 J/cm^2. The following analytes were collected: ^{23}Na, ^{29}Si,

^{31}P, ^{35}Cl, ^{39}K, ^{44}Ca, ^{57}Fe, ^{89}Y, ^{140}Ce and ^{238}U. NIST-SRM-610 glass was used as the bracketing external standard, using the reference values of Spandler et al. (2011), and MPI-DING glass T1-G and GSD-1G glass were used as secondary check standards for all elements. Analysis of the secondary standards compare well with the published values (see Appendix 6-2), demonstrating the accuracy of the analyses. Fluid inclusion element concentrations were quantified from raw signals using the software SILLS (Guillong et al., 2008), and involved deconvolution for fluid inclusion + host and host-only signals after calculation of background-corrected count rates for each isotope. Internal standardization was performed using Na concentrations assumed to be equal to the average salinity determined for the respective fluid inclusion type based on microthermometry measurements. Owing to the small size, large salinity range, and analytical challenges of measuring quartz-hosted fluid inclusions by LA-ICP-MS (e.g., Audetat and Pettke, 2003), trace element concentrations carry relative uncertainties of at least 30%. Despite the large uncertainty in absolute concentration, the relative concentrations of elements in each analysis are much better constrained, so that elemental ratios can be compared with greater confidence.

Oxygen isotope analysis

Oxygen isotope analysis was carried out at the Department of Geological Sciences, University of Cape Town, South Africa. Quartz and xenotime samples were analysed using laser fluorination methods described in detail in Harris and Vogeli (2010). The purified O_2, formed from each sample reaction with 10 kPa BrF_5, was collected onto a 5 Å molecular sieve contained in a stoppered glass storage bottle. Isotope ratios were measured using a Finnegan Mat Delta XP mass spectrometer in dual-inlet mode. All data are reported in the standard δ-notation relative to Standard Mean Ocean Water (SMOW), where δ (‰) = $((R_{sample}/R_{standard}) - 1) \times 1000$, with R being the measured ratio (e.g., $^{18}O/^{16}O$). Raw data were converted to the SMOW scale using the ratios obtained for duplicates of the internal standard MON GT ($\delta^{18}O$ = 5.38 per mil) run with each batch of 10 samples. The long-term average difference in $\delta^{18}O$ values of the 2 internal MONT-GT standards in each run is 0.11‰ (n = 216), corresponding to a 2σ value of 0.15‰.

Results

Fluid inclusion petrography

An important aspect of fluid inclusion studies on hydrothermal ore deposits is interpreting the relationship between the fluid inclusions and the mineralisation event (e.g., Roedder and Bodnar, 1997). This requires a careful sample selection and detailed petrographic study in order to identify fluid inclusion assemblages of primary origin representing the ore-forming hydrothermal fluid (e.g., Goldstein, 2003).

A large number of primary and secondary fluid inclusions were identified in the studied quartz grains. These quartz grains derive from hydrothermal veins that are devoid of any other minerals (except xenotime and florencite in the mineralised samples), and show no evidence for disruption by later alteration. The CL images of the representative quartz grains reveal oscillatory zonation with variable luminescence intensity (Fig. 6-3D), which is commonly reported from hydrothermal quartz grains from a range of geological settings (e.g., Muller et al., 2010). The well-preserved oscillatory zonation within euhedral quartz grains also demonstrates undeformed nature of the studied samples (e.g., Muller et al., 2010; Fig. 6-3D). In some cases, a CL dark quartz generation is seen occupying the interstices between these euhedral quartz grains. Associated ore minerals are of variable size and are distributed randomly throughout the host quartz grains with no preferential association with any of the CL zones (Fig. 6-3). Therefore, the isolated fluid inclusions and irregularly distributed clusters of fluid inclusions hosted in intra-granular quartz (Figs. 6-3E-F) are interpreted to be primary in origin and related directly to ore mineral formation. These primary inclusions are the focus of this study. Fluid inclusions in trans-granular trails were considered as secondary inclusions (e.g., Roedder, 1984), and were not further studied here.

A summary of the characteristics of the fluid inclusion types present in each grain is listed in Appendix 6-3. A complete list of the details of nearly 550 fluid inclusions analysed in this study is also available in Appendix 6-4.

Fluid inclusion types in the mineralised samples

Using petrography (e.g., available phases), microthermometry and Raman analysis, three types of primary aqueous fluid inclusions were identified in the two mineralised samples (samples W7-3 and A2-14): (1) type I low salinity H_2O-NaCl, (2) type II medium salinity H_2O-NaCl and (3) type III high salinity H_2O-NaCl-$CaCl_2$. Raman spectroscopy analyses indicated that all of the inclusions are H_2O rich (Figs. 6-4A-D), with no detectable CO_2, CH_4, or other C-bearing species (Fig. 6-4). A summary of the main characteristics of the different fluid inclusion types are provided in Table 6-2, with further information presented in Figs. 6-5, 6-6 and 6-7.

Table 6-2: Characteristics of the different fluid inclusion types

Type	**Composition**	**Host**	**Phase**	**T_{mi} (°C)**	**T_m (°C)**	**T_h (°C)**	**Salinity (wt.% NaCl)**	**Density (g/cm^3)**
Mineralised								
Type I	H_2O-NaCl	Quartz	L-V±S	-4.4 – -19	-0.1 – -6.5	99.1 – 272.3	0.2 – 9.9	0.76 – 1.0
Type II	H_2O-NaCl	Quartz	L-V	-13 – -21	-8.8 – -14.4	155.6 – 222.2	12.6 – 18.1	0.94 – 1.0
Type III	H_2O-$CaCl_2$-NaCl	Quartz	L-V±S	-22.9 – -51.3	-0.5 – -25.8	102.7 – 241.2	0.5 – 25.8	0.87 – 1.1
Barren								
Type I	H_2O-NaCl	Quartz	L-V	-4.4 – -19	-0.1 – -6.5	99.1 – 350	0.2 – 8.5	0.63 – 0.94

*Note that due to the lack of a next-to-last solid phase, accurate calculation of the salinity of the type III fluid inclusions was not possible. Instead, T_m was used to approximate the salinity.

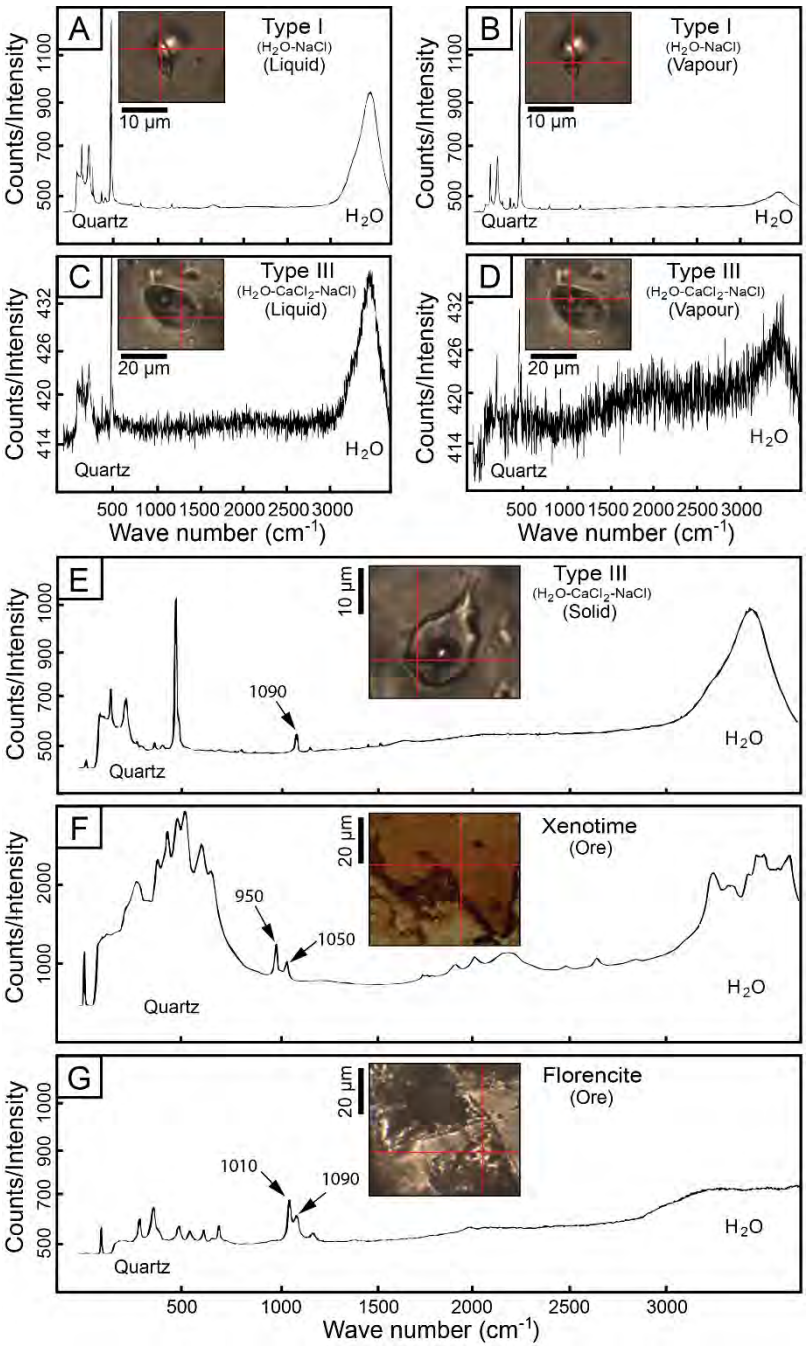

Fig. 6-4: Representative Laser Raman spectra of fluid inclusions. (A) Spectrum for liquid phase of type I fluid inclusion (low salinity H_2O-NaCl); (B) Spectrum for vapour phase of type I fluid inclusion; (C) Spectrum for liquid phase of type III fluid inclusion (high salinity H_2O-$CaCl_2$-NaCl); (D) Spectrum for vapour phase of type III fluid inclusion; (E) Spectrum for solid (florencite) phase of type III fluid inclusion; (F) Spectrum for xenotime associated with the ore; (G) Spectrum for ore-related florencite. Note that the solid phase in the type III fluid inclusion and florencite ore have comparable vibrational regions.

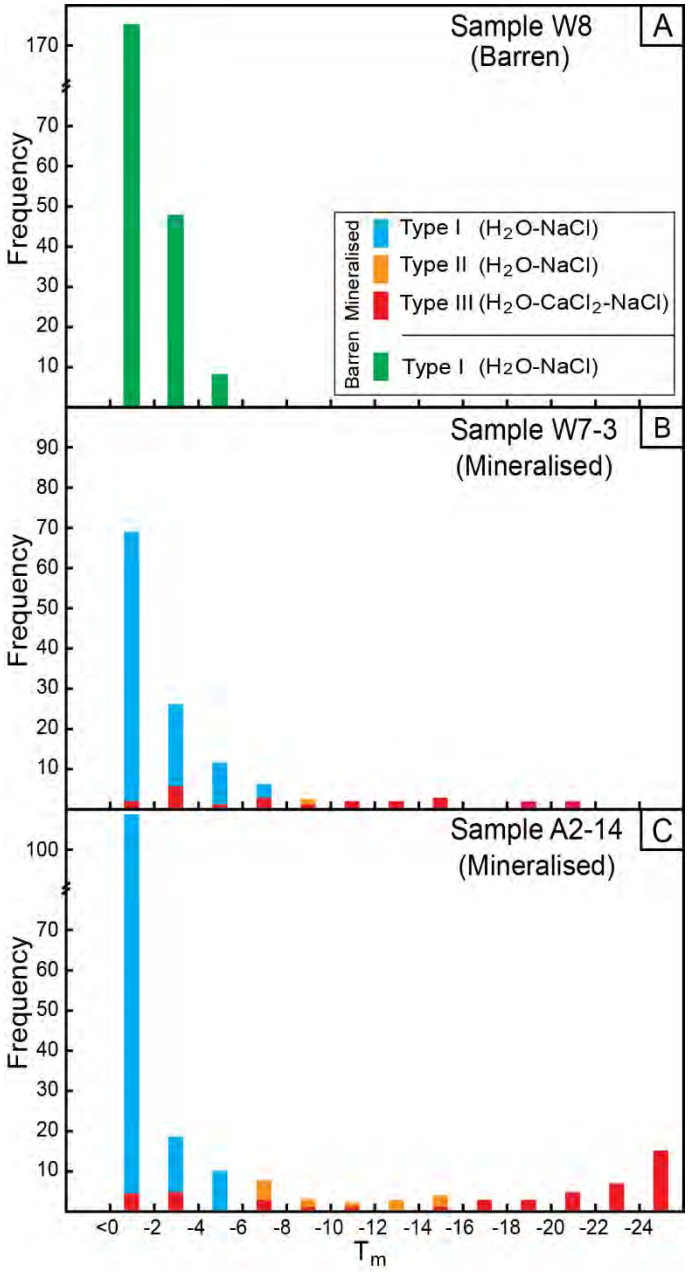

Fig. 6-5: Histogram of the T_m of the fluid inclusion types in the mineralised and barren samples.

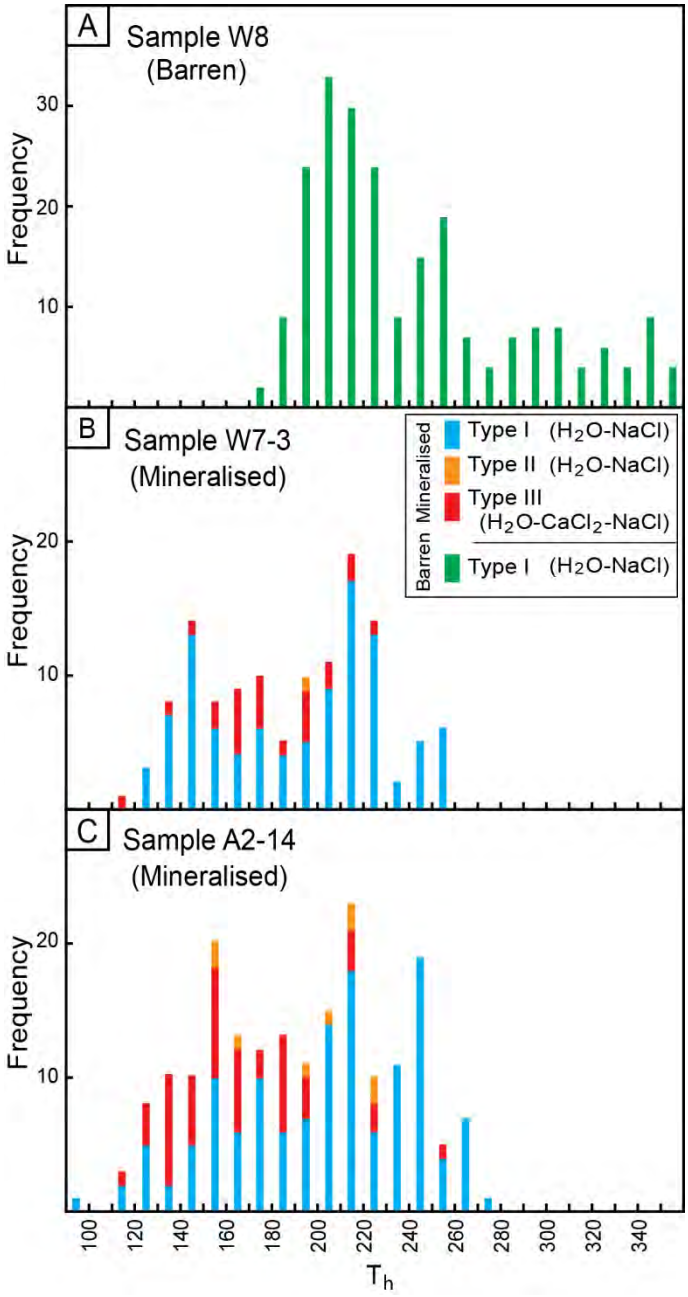

Fig. 6-6: Histogram of the T_h of the fluid inclusion types in the mineralised and barren samples.

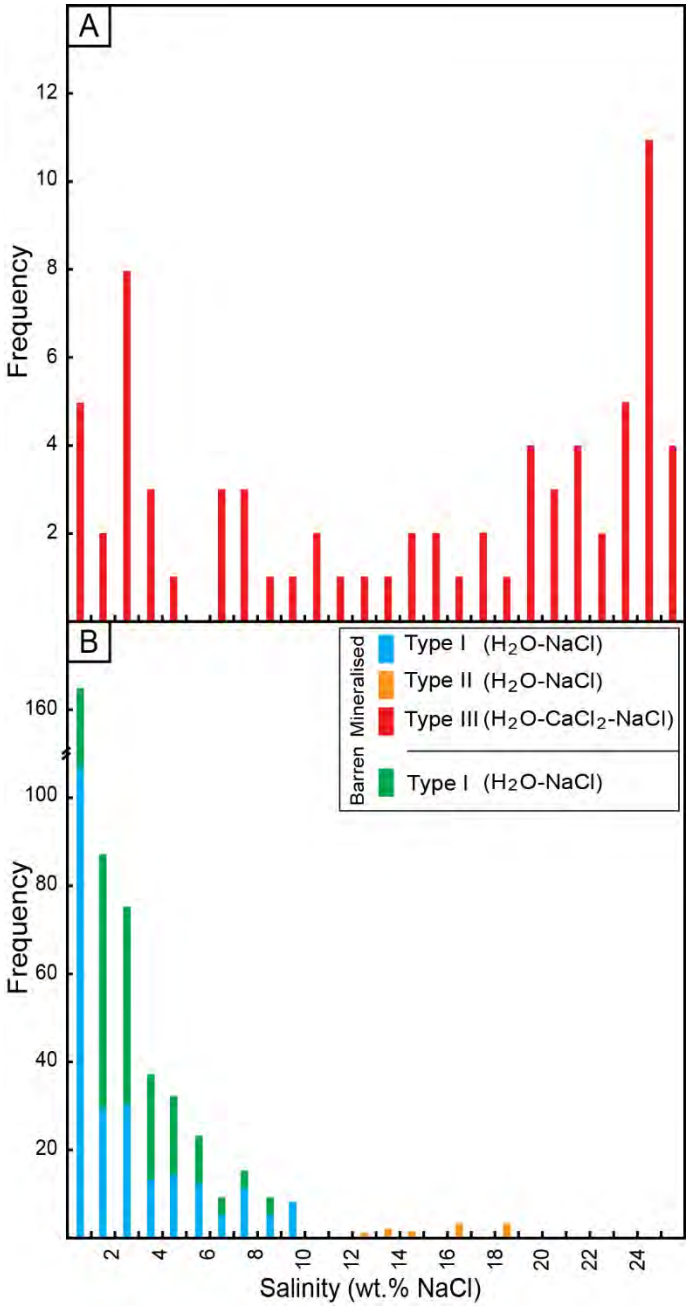

Fig. 6-7: Histogram of the salinity of the fluid inclusion types in the mineralised and barren samples. Note that due to the lack of a next-to-last solid phase, precise calculation of the salinity of the type III fluid inclusions was not possible. Instead, the T_m was used as a rough estimation of the salinity.

Type I low salinity H_2O-NaCl fluid inclusions

The type I fluid inclusions consist primarily of H_2O-bearing liquid + vapour phases, and account for nearly 70% of the total fluid inclusion population. These fluid inclusions vary in size from 5 to 20 μm, and show variable liquid/vapour ratios, which allows further subdivision into inclusions with small (~5 to ~10 vol.% of the inclusion) and large (~50 vol.% of the inclusion) vapour phases. These fluid inclusions usually occur in clusters, and locally as isolated inclusions and generally display negative-crystal, elliptical, and occasionally irregular morphologies (Figs. 6-3E-F). Only one of the type I fluid inclusions contained a tiny (~1 μm) solid phase. Solid phases are more common in the type III fluid inclusions (n = 5), as discussed below. Additionally, about 20 mono-phase liquid H_2O-rich fluid inclusions were identified. These mono-phase fluid inclusions vary from 5 to 20 μm in size and have dominantly elliptical and minor irregular shapes, and share similar petrographic features with the two-phase fluid inclusions. However, these fluid inclusions were not used for microthermometry as melting temperatures measured in absence of a vapour phase cannot be used (e.g., Goldstein and Reynolds, 1994).

Initial melting temperatures (T_{mi}) of around -20 °C were observed in relatively large type I fluid inclusions (Fig. 6-8A), whereas initial melting could only be observed at around -5°C for small fluid inclusions with low salinities. Final ice melting temperatures range between -0.1 °C to -7 °C, corresponding to a salinity of lower than 10 (largely <5) wt.% NaCl. Type I low salinity H_2O-NaCl fluid inclusions have a variable homogenisation temperatures (T_h) of between 100 °C and 250 °C, largely clustering around 200 °C (Fig. 6-8).

Type II medium salinity H_2O-NaCl fluid inclusions

The type II fluid inclusions (medium salinity H_2O-NaCl) are composed of two phases (liquid + vapour), both of which consist largely of H_2O. These fluid inclusions are relatively rare, with only 10 inclusions (i.e., less than 2% of the total fluid inclusion population) analysed in this study. The type II fluid inclusions vary in size from 5 to 20 μm and show an overall constant liquid/vapour ratio of 2/1. These fluid inclusions occur individually as isolated inclusions in quartz, and demonstrate negative-crystal and elliptical shapes, and are petrographically indistinguishable from the type I low salinity H_2O-NaCl fluid inclusions (Figs. 6-3E-F).

Nonetheless, the types I and II fluid inclusions can be discriminated based on microthermometry measurements.

Initial melting and final ice melting for type II fluid inclusions, characteristically lower than those of the type I fluid inclusions, vary within a relatively narrow range from ca. -20 °C to ca. -15 °C, and from -8 °C to ca. -15 °C, respectively (Fig. 6-8A). These final ice melting temperatures correspond to a range of salinities from ca. 12 to ca. 18 wt.% NaCl, which are significantly greater than those of the type I fluid inclusions. The type II fluid inclusions are defined by a rather variable T_h range between 150 °C and 220 °C, which is comparable to the type I fluid inclusions.

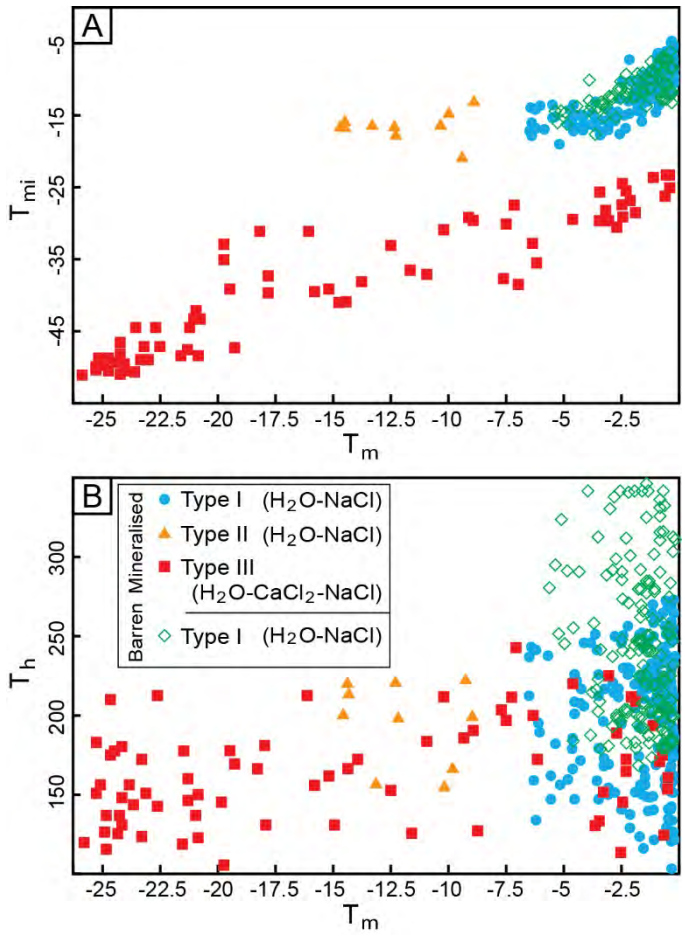

Fig. 6-8: (A) T_m-T_{mi} and (B) T_m-T_h relationships of the fluid inclusions in the mineralised and barren samples.

Type III high salinity H_2O-NaCl-$CaCl_2$ fluid inclusions

These liquid-vapour±solid (florencite) fluid inclusions account for about 15% of the total fluid inclusion population and are exclusively present within the mineralised samples (samples A2-14 and W7-3). The type III fluid inclusions vary in size from 10 to 30 μm and generally have negative-crystal or rounded shapes. Similar to the type I fluid inclusions (low salinity H_2O-NaCl), the vapour phase in these fluid inclusions is volumetrically variable, varying between ~10 to ~40 vol.%. The fluid inclusions generally appear as two-phase (liquid + vapour) fluid inclusions. However, a tiny solid phase with a significant Raman peak at a wavenumber of ~1090 cm^{-1} (Fig. 6-4E) was also identified (occupying about 5-10 vol.%) in 5 fluid inclusions with between 10 and 20 vol.% vapour. The two-phase fluid inclusions randomly occur throughout the host quartz either in clusters or as isolated individual inclusions. The three-phase fluid inclusions only occur as isolated individual inclusions.

The type III fluid inclusions characteristically display a brown-orange colour at freezing temperatures, which is typical for the H_2O-NaCl-$CaCl_2$ system (Goldstein and Reynolds, 1994; Zwart and Touret, 1994). The fluid inclusions show a T_{mi} ranging from ca. -25 °C to ca. -52 °C. Accurate calculation of the fluid composition and salinity was not possible owing to the difficulties associated with the observation of the melting temperature of the next-to-last solid phase (e.g., hydrohalite). In the absence of CO_2 (as confirmed by Raman spectroscopy), T_m can provide reliable estimates of salinity with the depression of the freezing point of water correlated with the content and type of salt (Shepherd et al., 1985). However, in the presence of Ca (and K), the salinity estimations based on T_m values likely have on the order of 5% uncertainty (Shepherd et al., 1985). The type III fluid inclusions have T_m of between -0.5 °C to -25 °C, corresponding to salinities from ~1 wt.% up to at least 25 wt.% NaCl. Further division based on salinity can divide type III fluid inclusions into “low” (<5 wt.% NaCl equivalent), “medium” (6-19 wt.% NaCl equivalent) and “high” (>19 wt.% NaCl equivalent) salinity fluid inclusions (Fig. 6-7). The observations that type III fluid inclusions lack halite and hydrohalite solid phases suggest that the H_2O-$CaCl_2$-NaCl fluid sits compositionally within the ice field (Fig. 6-9). Moreover, the type III fluid inclusions yielded T_h values varying within a relatively narrow range between 100 °C and 250 °C, somewhat similar to those documented for the types I and II fluid inclusions (low and medium salinity H_2O-NaCl), all derived from the same mineralised samples.

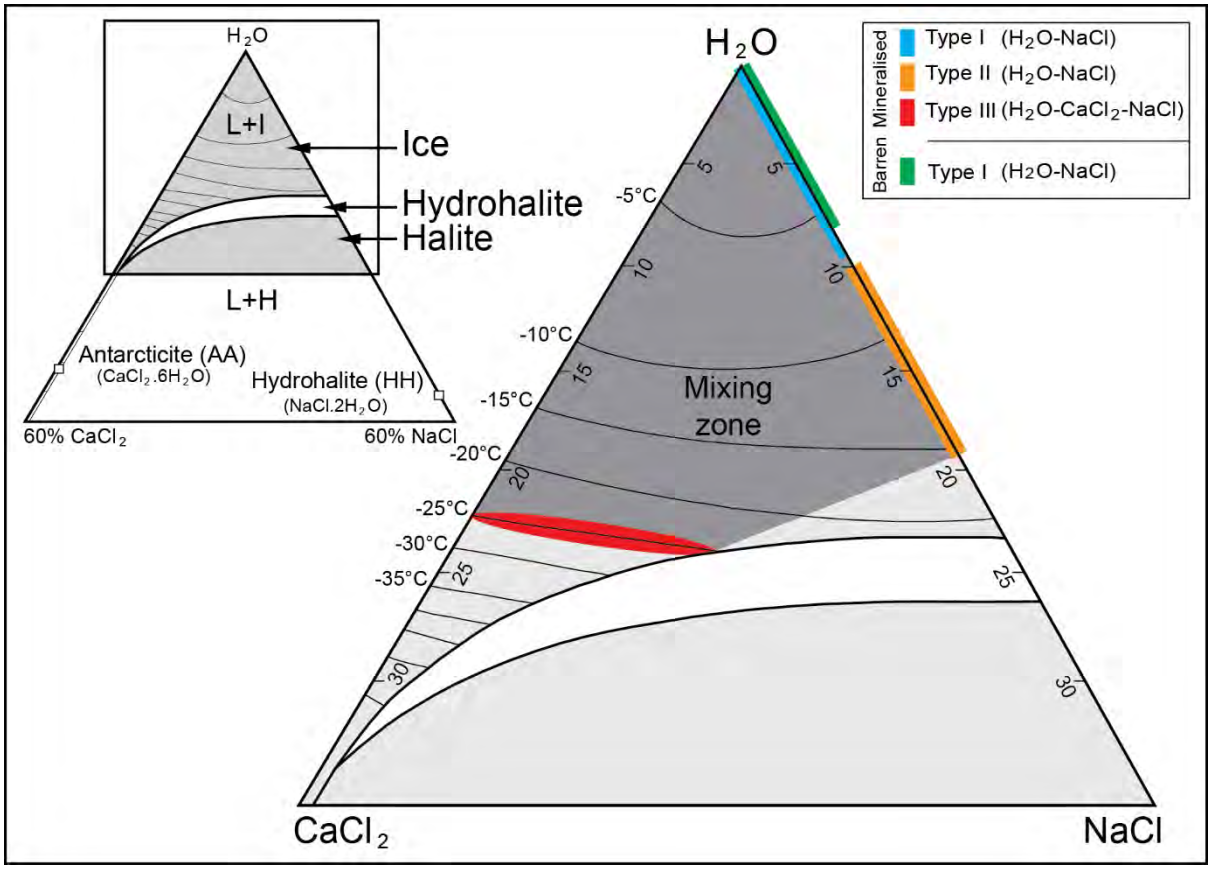

Fig. 6-9: Compositional fields of the hydrothermal fluid types on the H_2O-NaCl-$CaCl_2$ diagram.

Fluid inclusion type in the mineralisation–barren sample

Petrographic examinations combined with the microthermometry and Raman analyses, identified a different assemblage of primary fluid inclusions in the sample barren of mineralisation (sample W8). Fluid inclusions in this sample are composed of only two phases (liquid + vapour) with no trace of any solid phase. Raman spectroscopy analyses indicated no traces of any other component other than H_2O and NaCl in these fluid inclusions. These inclusions are usually small, rarely exceeding 10 µm in size, but display an overall constant liquid to vapour ratio of 3:1. They typically have negative-crystal, elliptical, and rarely irregular shapes, and occur as both clusters and isolated inclusions in quartz (Figs. 6-3E-F). All of the primary fluid inclusions in this sample yielded microthermometry measurements rather comparable to those of the type I low salinity H_2O-NaCl documented in the mineralised samples (Table 6-2; Figs. 6-5, 6-7 and 6-8). Initial and final melting temperatures of these inclusions vary from around -20 °C to -10 °C, and -0.1 to ca. -7 °C, respectively (Fig. 6-8A),

which corresponds to a narrow range of relatively low salinity from 0.2 to 5 wt.% NaCl. Nevertheless, the fluid inclusions in the mineralisation-barren sample are distinguished by their highly variable T_h temperatures between ca. 100 °C and ca. 350 °C.

Fluid inclusion elemental composition

The elemental composition of 15 fluid inclusions covering all inclusion types from the mineralised and barren samples are presented in Table 6-3. Detection limits by the LA-ICP-MS technique tend to be high due to the small size of most of the inclusions; therefore many elements were not measured above these detection limits. Nonetheless, the data demonstrate that the major cations in the fluid inclusions are Na and K, with Na/K ratio varying within a relatively narrow range from 4.1 to 6.7. Potassium and Na contents respectively range from ~0.15 wt.% and ~0.8 wt.% in the type I low salinity fluid inclusions to nearly 1.7 wt.% and 8.6 wt.% in the type III high salinity fluid inclusions (Fig. 6-10). No other elements were above the detection limits in the types I and II fluid inclusions. Some of the type III fluid inclusions were found to contain appreciable levels of Cl (2.4 to 6.3 wt.%), Ca (0.6 to 1.4 wt.%), Fe (0.04 to 0.6 wt.%), U (0.2 to 161 ppm) and REE (Y+Ce = 0.8 to 2.3 ppm), with the highest REE (and U) content recorded from the most saline fluid inclusions.

Table 6-3: Composition of the primary fluid inclusions

Samples	Type	FI No	T_m	T_h	Salinity	Na	P	Cl	K	Ca	Fe	Y	Ce	U	Na/K
A2-14 (ore-related)	I	E_K13	-1.2	250	2.1	0.79	<0.7	<6.5	0.1	<3.0	<0.20	<1.6	<1.8	<1.1	5.6
W8 (Barren)	I	C_N10	-1.5	187.7	2.6	0.79	<0.8	<8.0	0.1	<3.5	<0.20	<1.6	<1.8	<1.1	5.4
A2-14 (ore-related)	I	B_Y13	-2.8	250	4.6	1.97	<0.2	<1.6	0.3	<0.7	<0.04	<0.4	<0.4	<0.3	5.4
A2-14 (ore-related)	II	A_O29	-10.1	155.6	14	3.93	<6.3	<6.4	0.9	<2.8	<1.51	<21.7	<17.6	<11.0	4.4
A2-14 (ore-related)	III	B_AF19	-2.7	187.8	5.1	1.97	<3.4	<3.5	0.4	<1.5	<0.90	<11.6	<9.4	<5.9	4.9
W7-3 (ore-related)	III	A_Z24	-6.1	171.9	10	3.93	<0.2	5.1	0.6	<0.9	<0.05	<0.7	<0.5	<0.3	6.6
W7-3 (ore-related)	III	A_V54	-6.3	198.8	10.2	3.93	<0.4	6.4	1	<1.8	0.1	<1.2	<1.0	<0.6	4.1
A2-14 (ore-related)	III	G_L12-2	-6.9	241.2	11	4.33	<0.1	3.5	0.7	1.2	<0.03	<0.4	<0.3	<0.2	6
A2-14 (ore-related)	III	G_L12-2	-6.9	241.2	11	4.33	<0.2	3.5	0.8	0.9	0.2	<0.5	0.9	<0.3	5.1
A2-14 (ore-related)	III	G_N25	-7.2	210	11.2	4.33	<0.0	4.8	0.8	0.8	<0.03	<0.2	<0.1	0.2	5.7
W7-3 (ore-related)	III	A_P25	-7.5	198	11.5	4.33	<0.2	3.2	0.8	<0.9	0.1	1	<0.5	<0.3	5.1
A2-14 (ore-related)	III	C_N17	-7.6	201	11.8	4.72	<0.1	4.4	0.7	0.6	0.05	<0.3	<0.2	<0.1	6.8
A2-14 (ore-related)	III	G_K22	-9.2	185	13.3	5.11	<0.1	2.4	0.9	1.4	0.05	<0.2	0.8	<0.1	6
W7-3 (ore-related)	III	H_L15	-19.1	168.8	20.2	7.87	<2.1	2.5	1.7	<9.5	0.7	<5.5	<4.5	<2.8	4.6
A2-14 (ore-related)	III	G_L20-1	-24.5	174	22.8	8.65	<0.6	3	1.5	<2.6	<0.14	<1.9	2.3	161	5.7

*Type I: Low salinity H_2O-NaCl; Type II: Medium salinity H_2O-NaCl; Type III: High salinity H_2O-$CaCl_2$-NaCl.

**All major elements are in wt.%, whereas the trace elements (Y, Ce and U) are in ppm.

***bdl: below detection limit.

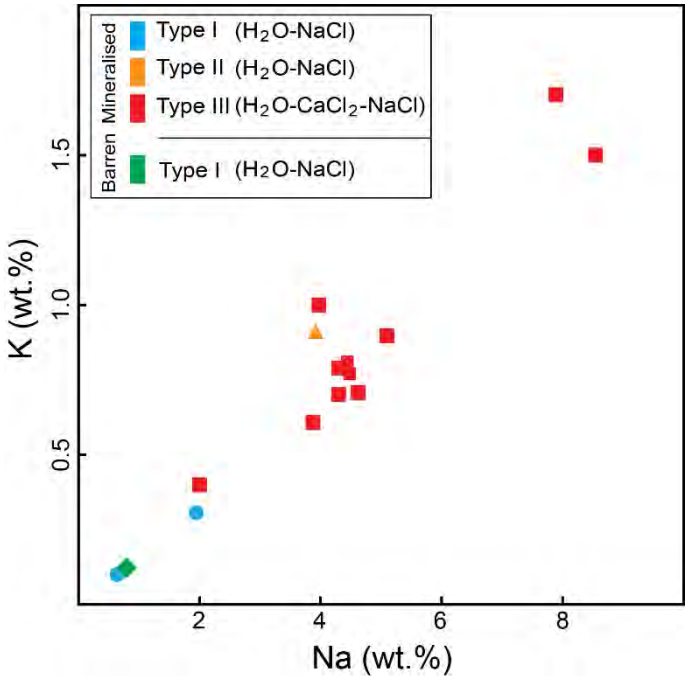

Fig. 6-10: Na versus K (in wt.%) plot for the three types of fluid inclusions.

Oxygen isotope results

Oxygen isotope data are presented in Table 6-4 and Figure 6-11. The $\delta^{18}O$ values of ore-related quartz from Wolverine and several other HREE deposits/prospects range from +11.3 to +20.2‰. Quartz samples collected from the outcrops of the structure that hosts the Wolverine orebody have variable $\delta^{18}O_{quartz}$ values ranging from +20.2‰ near to the orebody, to +10.3‰ for the mineralisation-barren quartz sample furthest from Wolverine (Fig. 6-1E).

The $\delta^{18}O$ values obtained for detrital quartz samples and bulk rock samples from the BRM (host rocks) display a limited variation in the range from +10.7 to +13.3‰, and +12.4 to +14.1‰, respectively. One sample of the Birrindudu Group sandstones returned a distinctively higher $\delta^{18}O$ value of +16.9‰ (Fig. 6-11).

The $\delta^{18}O$ values of four quartz-xenotime pairs from Wolverine show a relatively limited variation from +14.6 to +17.2‰ for quartz, and from +6.3 to +7.3‰ for xenotime, which corresponds to a difference in $\delta^{18}O$ between quartz and xenotime of +7.7 to +9.8.

Table 6-4: Oxygen isotope compositions.

Location	Deposit/prospect	Sample No.	Longitude	Latitude	Drill core	Depth	Type	$\delta^{18}O_{qtz}$	$\delta^{18}O_{xnt}$	$\delta^{18}O_{fluid}$	$2\sigma\ \delta^{18}O_{fluid}$
Ore-related quartz and xenotime											
Boulder Ridge	Prospect	BR1	545197	7827868	-	Outcrop	Ore-related	15.0		6.1	0.9
Dazzler	Prospect	D3	490384	7902004	-	Outcrop	Ore-related	14.8		5.9	0.9
Iceman	Prospect	I1	490746	7901660	-	Outcrop	Ore-related	14.8		5.9	0.9
Cyclops	Deposit	C2	489782	7904619	-	Outcrop	Ore-related	12.6		3.7	0.6
Wolverine	Deposit	W5-2	493508	7915069	BRWT0332W5	487.6	Ore-related	15.8		6.9	1.0
Wolverine	Deposit	W5-4	493508	7915069	BRWT0332W5	503.1	Ore-related	11.3		2.4	0.4
Wolverine	Deposit	W5-7	493508	7915069	BRWT0332W5	505.5	Ore-related	17.2	7.3	8.3	1.2
Wolverine	Deposit	W7-2	493696	7914741	BRWD0007	36.5	Ore-related	14.6	6.8	5.7	0.9
Wolverine	Deposit	W7-3	493696	7914741	BRWD0007	41.6	Ore-related	14.7	6.3	5.8	0.9
Wolverine	Deposit	W14	n.a.	n.a.	n.a.	n.a.	Ore-related	15.3	7.3	6.4	1.0
Wolverine	Deposit	W16-3	493599	7914773	BRWD0016	88.7	Ore-related	19.2		11.4	1.7
Wolverine	Deposit	W324-3	493541	7914984	BRWT0324	384.8	Ore-related	20.3		6.1	0.9
Wolverine ore hosting structure											
Wolverine	Deposit	W1	493723	7914708	-	Outcrop	Ore-related	20.2		11.3	1.7
Wolverine	Deposit	W4	493796	7914690	-	Outcrop	Ore-related	16.2		7.3	1.1
Wolverine	Deposit	W5	493850	7914682	-	Outcrop	Ore-related	15.2		6.3	0.9
Wolverine	Deposit	W9	493852	7914677	-	Outcrop	Ore-related	16.1		7.2	1.1
Wolverine	Deposit	W10	493872	7914660	-	Outcrop	Ore-related	13.9		5	0.8
Wolverine	Deposit	W13	493967	7914637	-	Outcrop	Ore-related	17.8		8.9	1.3
Wolverine	Deposit	W8	494125	7914636	-	Outcrop	Barren	10.3		1.4	0.2
BRM											
Wolverine	Deposit	W16-1	493599	7914773	BRWD0016	47.8	Detrital Quartz	10.7		1.8	0.3
Gambit	Deposit	G4-8	493210	7913635	BRGD0004	70.8	Detrital Quartz	12.7		3.8	0.6
Gambit	Deposit	G5-1	493098	7913652	BRGD0005	11.2	Detrital Quartz	13.3		4.4	0.7
Wolverine	Deposit	W7-1	493696	7914741	BRWD0007	22.1	Detrital Quartz	12.4		3.5	0.5
Wolverine	Deposit	W5-1	493508	7915069	BRWT0332W5	441.2	Whole-rock	12.5		3.6	0.5
Wolverine	Deposit	W5-10	493508	7915069	BRWT0332W5	529	Whole-rock	13.0		4.1	0.6
Wolverine	Deposit	W5-12	493508	7915069	BRWT0332W5	545	Whole-rock	14.1		5.2	0.8
Wolverine	Deposit	W5-13	493508	7915069	BRWT0332W5	550.7	Whole-rock	12.9		4	0.6
Wolverine	Deposit	W16-4	493599	7914773	BRWD0016	103.5	Whole-rock	12.4		3.5	0.5
Birrindudu Group sandstones											
Cyclops	Prospect	C1	489642	7904606	-	Outcrop	Whole-rock	16.9		8	1.2

*The $\delta^{18}O_{fluid}$ values were calculated based on $\delta^{18}O_{qtz}$ and T_h = 250 °C using equation of Clayton et al. (1972).

**Qtz = quartz, Xnt = xenotime, BRM = Browns Range Metamorphics.

***Uncertainty (2σ) is 0.15‰ of the $\delta^{18}O_{fluid}$ value calculated based on the long-term average difference in $\delta^{18}O$ values of the internal standards (see Analytical Methods).

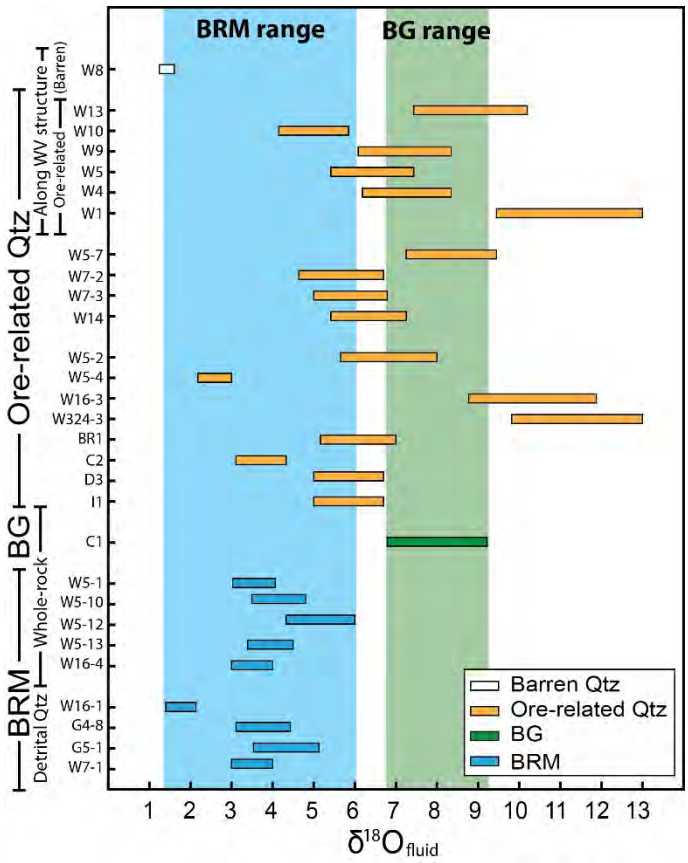

Fig. 6-11: Oxygen isotope compositions of the ore-related and barren quartz separates and the metasedimentary/sedimentary rocks of the BRM and the Birrindudu Group sandstones. Note that the ore-related quartz separates are characterised by $\delta^{18}O_{fluid}$ largely in the range defined by the BRM and the Birrindudu Group sandstones. The $\delta^{18}O_{fluid}$ bars include 2σ.

Discussion

Characteristics of the ore-forming hydrothermal fluids

The microthermometry dataset (Fig. 6-8) yielded comparable results for the mineralised samples derived from Wolverine (sample W7-3) and Area 5 (sample A2-14) deposits, despite the fact that Wolverine is distinctly xenotime rich whereas the Area 5 deposit is dominated by florencite. Therefore, the microthermometry dataset presented here can be used to effectively identify hydrothermal fluids involved in the HREE ore formation in the Browns Range Dome.

The mineralised samples have fluid inclusions characterised with variable T_{mi}, T_m and T_h, consistent with the occurrence of multiple distinct hydrothermal fluids of varying salinity,

composition and temperature. In particular, T_{mi} values define two arrays of fluid inclusions, one of which is characterised by T_{mi} values greater than ca. -20 °C, and one of which has T_{mi} in the range of -25 °C to -52 °C (Fig. 6-8A). The first array with relatively high T_{mi} values is consistent with having H_2O-NaCl compositions (eutectic melting at -21.1 °C) with a wide range of T_m (Fig. 6-8), and hence salinity. A large portion of these inclusions yielded very low salinities (largely <5 wt.% NaCl) referred to here as type I low salinity H_2O-NaCl fluid. These low salinity fluid inclusions are abundant in the mineralised samples and are the only fluid inclusion type identified in the sample barren of mineralisation. These fluid inclusions potentially record the circulation of meteoric water in the hydrothermal system, which is known to be of low salinity in nature and the most common type of fluid in most sedimentary basins (e.g., Seward and Barnes, 1997; Kharaka and Hanor, 2007). However, meteoric water alone is very unlikely to explain the high salinity H_2O-NaCl fluid inclusions (up to ca. 18 wt.%) of the same array ($T_{mi} \geq$ -20 °C, Fig. 6-8A) in the mineralised samples. These are interpreted to represent traces of a distinct hydrothermal fluid, which is here labelled as type II medium salinity H_2O-NaCl fluid. The relatively wide range of T_m, and hence salinity, observed in the type II fluid inclusions is due potentially to a variable mixing with meteoric water causing dilution and subsequently reduction in the salinity (e.g., Seward and Barnes, 1997).

The second array of fluid inclusions has T_{mi} values that are distinctively lower than -21.1 °C (Fig. 6-8A) and, hence, are inconsistent with the H_2O-NaCl system. These low T_{mi} values are commonly reported from H_2O-$CaCl_2$-NaCl (-52 °C), H_2O-FeCl-NaCl (-37 °C), H_2O-MgCl-NaCl (-35 °C), and H_2O-KCl-NaCl (-23 °C) systems (e.g., Crawford, 1981; Bodnar, 2003). Based on our elemental compositional dataset (Table 6-3), the large proportion of inclusions with <-40 °C $T_{mi,}$ and the brown-orange colour visible during freezing (Zwart and Touret, 1994), we favour the H_2O-$CaCl_2$-NaCl compositional system for all of the fluid inclusions that have T_{mi} lower than -25 °C, here classified as the type III high salinity fluid inclusions. The type III fluid inclusion population has significantly variable T_m values (Fig. 6-8) corresponding to a wide range of salinities from very saline (up to 25 wt.% NaCl, see Fig. 6-7) to very low (<5 wt.%) partially overlapping those of the meteoric water. The spatial distribution of the microthermometry data points conforms well to varying degrees of mixing between the end-member high salinity H_2O-NaCl-$CaCl_2$ fluid and meteoric water (type I), resulting in formation of the type III fluid inclusions that have a broad range of salinity.

Collectively, the microthermometry dataset identified three distinct types of hydrothermal fluids including type I low salinity H_2O-NaCl fluid (meteoric water) which underwent various degrees of mixing with the type II medium salinity H_2O-NaCl fluid and type III high salinity H_2O-NaCl-$CaCl_2$ fluid. The estimated composition of all of the hydrothermal fluid types recognised in both the mineralised and barren samples can be expressed on the H_2O-$CaCl_2$-NaCl ternary diagram (Fig. 6-9). Accordingly, the type I low salinity H_2O-NaCl fluid inclusions documented in both mineralised and barren samples are located near the H_2O apex, whereas the type II medium salinity H_2O-NaCl fluid inclusions, present only in the mineralised samples, sit on the H_2O-NaCl line near the hydrohalite field. The type II fluid inclusions are comparatively rare comprising only 10 out of 550 fluid inclusions analysed here, so the type II fluid may not have had a significant role in HREE ore formation. The type III high salinity H_2O-NaCl-$CaCl_2$ fluid inclusions, found only in the mineralised samples, fall into the ice field with the most saline inclusions plotting toward the $CaCl_2$ apex. Compositionally-defined hydrothermal fluid types are also supported by our limited elemental analysis of a number of representative fluid inclusions (Table 6-3). Principally, the H_2O-NaCl rich fluid inclusions (type I low salinity and type II medium salinity) have fairly simple compositions composed largely of Na and K. In contrast, the H_2O-$CaCl_2$-NaCl rich fluid inclusions (type III high salinity fluid) contain, in addition to elevated Na and K, appreciable quantities of Cl and also occasionally detectable Ca and to a lesser extent Fe. Additionally, the water rich nature of all the fluid types is confirmed by Raman spectroscopy showing H_2O in liquid and vapour phases of various fluid inclusions. According to the elemental composition of the fluid inclusions (Fig. 6-10), all three fluid inclusion types (types I and II with a H_2O-NaCl composition, and type III with a H_2O-$CaCl_2$-NaCl composition) also contain appreciable amounts of K.

Detailed petrographic investigations identified tiny solid phases only in the types I and III fluids within the mineralised samples, whose Raman spectra displays peaks at wavenumbers of ~1090 cm^{-1} (Fig. 6-4E). These peaks are similar to those returned by a range of carbonates (see Frezzotti et al., 2012), but the fluid inclusions do not contain CO_2, as shown by the Raman analyses, and carbonate minerals are entirely absent from the ore assemblage. Therefore, a carbonate composition for the solid phases is deemed unlikely. Instead, we attribute these phases to be florencite, as the major Raman peak for florencite also occurs between 1000 and 1100 cm^{-1} (Fig. 6-4G; Frost et al., 2013), and florencite is a major ore mineral (note, xenotime has a distinctly lower Raman peak at ~950 cm^{-1}; Fig. 6-4F). We interpret these florencite daughter phases to be syn-ore florencite that was accidentally trapped during fluid inclusion

formation. This premise is consistent with their most common occurrence in the type III fluid inclusions.

Trapping conditions of the hydrothermal fluids

Microthermometry data can be used to constrain physical conditions during fluid entrapment (e.g., Dubessy et al., 2003; Boiron et al., 2010; Bons et al., 2014), although direct determination of the pressure-temperature conditions of the fluid entrapments from fluid inclusion data requires an independent estimate of either pressure or temperature. Widely-used are geothermometers that employ temperature sensitive oxygen isotope exchange between coexisting minerals, such as quartz-monazite, quartz-magnetite, and quartz-apatite. Xenotime and quartz are interpreted to have crystallized together in the studied mineralised samples, so their oxygen isotope compositions have the potential to provide an estimate for the trapping temperature, provided isotope fractionation factors are known. However, as discussed below, oxygen isotope fractionation factors for this mineral pair are unconstrained, so this approach could not be applied here. In the case of boiling, the homogenisation temperature would indicate the true trapping temperature (e.g., Bodnar et al., 1985; Wilkinson, 2001; Moncada et al., 2012). However, the fluid inclusion assemblages consist mainly of a mono-modal group of dominantly liquid-rich inclusions with relatively consistent liquid to vapour ratios, with no coexisting liquid-rich and vapour-rich inclusions. These features are inconsistent with boiling.

As an alternative, we investigated mineral assemblages associated with the HREE mineralisation and the metasedimentary rocks of the BRM that host the orebodies. A significant feature of the pre-ore mineral paragenesis is the occurrence of a coarse-grained muscovite aligned in the pre-mineralisation foliation (Fig. 6-2A) that has been dated (Ar-Ar) to ca. 1720 Ma (Nazari-Dehkordi et al., in review); this significantly predates the timing of the HREE ore formation (ca. 1.65 to ca. 1.60 Ga, Vallini et al., 2007; Morin-Ka et al. 2016; Nazari-Dehkordi et al., 2018). Consequently, the pre-ore muscovite has remained a closed system for Ar through the hydrothermal activity associated with the HREE mineralisation. Harrison et al. (2009) experimentally calculated an Ar closure temperature of 420 °C for muscovite, so this temperature represents the maximum possible fluid trapping temperature. Furthermore, based on the 3.5 to 6 km thick Birrindudu Group sandstones that unconformably overly the metasedimentary rocks of the BRM (host rocks), we calculated a lithostatic pressure of 0.9 to

1.6 Kbar, and a corresponding hydrostatic pressure of 0.4 to 0.6 Kbar, constraining the pressure to between 0.4 to 1.6 Kbar (Fig. 6-12).

The mineralised samples contain all three types of fluid inclusions, which collectively have a range of T_h values of between ~100 and ~250 °C (Fig. 6-6C). Such a wide variation in T_h values is not expected of an isothermal fluid mixing process (e.g., Lecuyer et al., 1999; Derome et al., 2003; Dubessy et al., 2003). Instead, the mineralised samples appear to record circulation of fluids of varying temperature, including probably two hot (~250 °C) medium and high salinity fluids (types II and III) and one cold low salinity fluid (~100 °C; type I), which subsequently mixed to form fluid inclusions with a wide range of T_h values. A geothermal gradient of ~35 °C/km, suggested by Gerner and Holgate (2010) for northern Tanami Region, corresponds to a temperature range of between 120 °C (3.5 km-thick Birrindudu Group) and 210 °C (6 km-thick Birrindudu Group), which is entirely consistent with P-T constraints provided here (Fig. 6-12).

The trapping temperature of the type I low salinity H_2O-NaCl fluid inclusions in the barren sample (with higher T_h values), are between 350 °C (highest T_h value) and 100 °C (lowest T_h value). In regard to the trapping pressure, a hydrostatic pressure between 0.4 to 0.6 Kbar is plausible for reasonable geothermal gradients, whereas the higher lithostatic pressures are inconsistent with the 420 °C temperature limit defined by the pre-ore muscovite (Fig. 6-12). We speculate that the barren sample may indeed post-date the ore formation, and so formed under lower pressure conditions likely following the partial removal (by erosion or tectonics) of the overlying Birrindudu Group sandstones. Indeed, the wide range of T_h values (100-350 °C) combined with very limited variation in T_m and hence salinity, are inconsistent with occurrence of multiple fluids with distinct temperatures in the barren sample, but may record circulation and gradual cooling of a hot fluid (350 °C) in relatively shallow and cold environments which also resulted in formation of fluid inclusions with very low T_h.

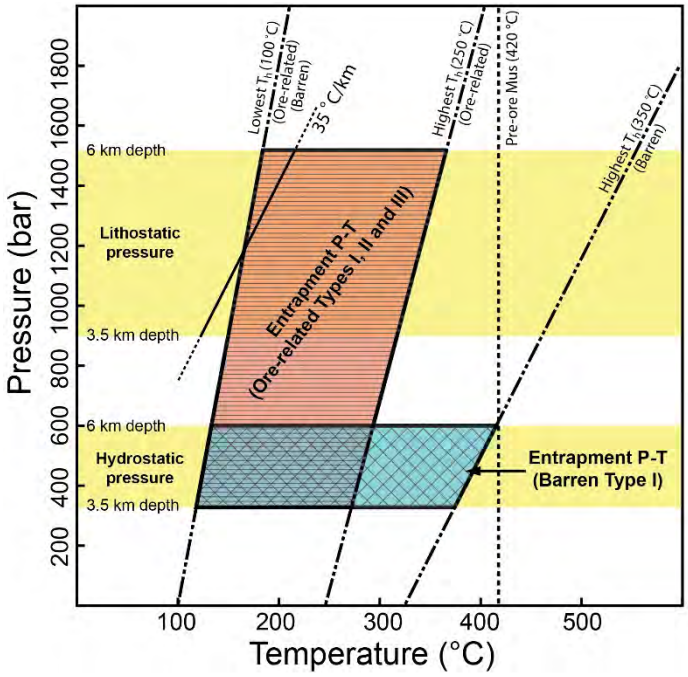

Fig. 6-12: The estimated trapping pressure-temperature diagram of the three types of fluid inclusions. Note that the type I fluid inclusions in the barren quartz may have formed at lower pressure following the erosion of the Birrindudu Group sandstones.

Origin of the hydrothermal fluids

The formation of the HREE deposits/prospects of the NAHREY mineral field was associated with mixing of ore-forming hydrothermal fluids that carried the required components for ore phosphate mineral (xenotime and florencite) formation (Nazari-Dehkordi et al., 2018). Considering the extremely low solubility of REE-P-complexes in hydrothermal systems (Williams-Jones et al., 2012; Migdisov et al., 2016), REE+Y and P were most likely transported by different hydrothermal fluids with contrasting sources.

The association of Ce, Y and U exclusively with the type III fluid inclusions illustrates that transport of the ore metals and U was by saline hydrothermal fluid of H_2O-$CaCl_2$-NaCl composition. This premise is consistent with current understanding that hydrothermal transport of REE is greatly enhanced in Cl-bearing saline fluids (e.g., Williams-Jones et al., 2012). The hydrothermal source of P for ore formation is not so clear. None of the measured fluid inclusions contained detectable P content. However, P has a very high detection limit (around 1 wt.%) in these analyses, and it is expected that the contents of P in the fluid would have been

relatively low at these conditions (<1000 ppm based on extrapolation of the results of Antignano and Manning (2008)).

As discussed above, the fluid inclusions in the mineralised samples record the mixing between cold (~100 °C) and hot (~250 °C) hydrothermal fluids derived from different sources. Elemental compositions of the fluid inclusions combined with the isotopic and geochemical datasets of Nazari-Dehkordi et al. (2018) demonstrate transportation of ore metals by saline fluids derived from the BRM unconformably buried under a thick sedimentary sequence (Birrindudu Group sandstones). Accordingly, the saline fluids (type III H_2O-$CaCl_2$-NaCl fluid and potentially type II medium salinity H_2O-NaCl fluid) represent the hot fluids, whereas the type I H_2O-NaCl fluid represents cold meteoric water originated from the shallow depths of the sedimentary rocks of the Birrindudu Group, indicating a different source for P to that of ore metals as required for simultaneous transport of P and REE+Y. The identification of a tiny florencite solid phase in a type I fluid inclusion can provide further support for transportation of P by the type I low salinity fluid (meteoric water). Therefore, although precise determination of the P-bearing fluid is not possible, we assume that P was most likely transported by the type I low salinity H_2O-NaCl fluid.

To place further constraints on the possible origin of these ore-forming hydrothermal fluids, we also compared oxygen isotope composition of the ore-related quartz samples with that of the BRM (host rocks) and overlying Birrindudu Group sandstones. Using quartz-fluid isotope fractionation factors of Clayton et al. (1972) and our oxygen isotope compositions of the detrital quartz and whole-rock analyses (Table 6-4), and assuming a hydrothermal fluid T of 250 °C (Fig. 6-12; see also Nazari-Dehkordi et al., 2018) we calculate that the hydrothermal fluids that leached the BRM (host rock) had $\delta^{18}O_{fluid}$ values ranging from +1.8 to +5.2‰ (Fig. 6-11). These values are distinctly lower than the calculated $\delta^{18}O_{fluid}$ of putative hydrothermal fluid derived from the Birrindudu Group sandstones ($\delta^{18}O_{fluid}$ = +8‰). The $\delta^{18}O_{fluid}$ values derived from the ore-related quartz separates vary from +2.4‰ to +11.3‰, with the great majority overlapping with the $\delta^{18}O_{fluid}$ range defined by both the BRM and the Birrindudu Group sandstones (Fig. 6-11), further supporting the premise that mineralisation involved significant contributions from fluids derived from both the BRM and the Birrindudu Group.

The role of fluid mixing in ore formation

The microthermometry measurements demonstrated that the mineralisation-barren quartz only contained a single fluid inclusion type (type I fluid inclusions) highlighting the significant role of fluid mixing in ore formation. Further support for fluid mixing is provided by the occurrence of florencite solid phases, identified in a limited number of types I and III fluid inclusions, only in the mineralised samples.

Fluid mixing along with boiling are indeed considered to be the most important physical processes affecting ore deposition in general (e.g., Wilkinson, 2001), the latter of which was not observed in the studied samples. Thus, our results are in contrary to the findings of Richter et al. (2018) who suggested that fluid boiling promoted ore formation at Wolverine. A boiling mechanism is associated with a drop in pressure (e.g., pressure release at high depth as a result of fracturing of the BRM, or complete removal of the overlying Birrindudu Group sandstone prior to ore formation or ore mineralisation before deposition of the overlying Birrindudu Group sandstones, and hence exposure of the ore-bearing fluids to near surface environments). However, field interpretations and age dataset from the mineralisation and the host rocks do not appear to support a low pressure environment for the ore formation. In fact, the BRM is underlain by a thick sedimentary sequence of the Birrindudu Group sandstones, and also the mineralisation appears on the unconformity itself, and also extends into the overlying Birrindudu Group sandstones (Fig. 6-1). These observations combined with the timing of the ore deposition across the NAHREY mineral field (ca. 1.65-1.60 Ga; Vallini et al., 2007; Morin-Ka et al., 2016; Nazari-Dehkordi et al., 2018) that partially coincided with the formation of the Birrindudu Group sandstones (ca. 1.78-1.64 Ga, Crispe et al., 2007; Vallini et al., 2007), indicate that ore formation occurred under a thick sedimentary sequence. Therefore, these data rule out a near surface environment (e.g., ore formation after partial or complete removal of the overlying Birrindudu Group), and also suggest that even fracturing of the BRM, potentially during the doming of the BRD, would not lead to pressure release and so boiling, considering significant pressure imposed by the 3.5 to 6 km-thick Birrindudu Group overlying the BRM during the ore formation. Collectively, our fluid inclusion dataset combined with the age dataset reported from the NAHREY mineral field and also field observations support fluid mixing (rather than boiling) as the main physical trigger for ore formation.

Fluid mixing usually causes a change in temperature, acidity and redox properties (e.g., Wilkinson, 2001). As the experimental works have shown that REE form trivalent cations in both solid and aqueous states (Migdisov et al., 2016), so variation in redox conditions was unlikely to trigger ore deposition. Mixing of hydrothermal fluids of contrasting temperature as well as the association of the ore minerals with a widespread fine-grained muscovite crystallisation suggesting of an increase in pH, as described by Nazari-Dehkordi et al. (2018) (Fig. 6-2A), potentially contributed to the ore formation. Nonetheless, due largely to the extremely low solubility of the P and REE complexes in aqueous fluids, as discussed above, we suggest that introduction of P to the REE-bearing fluids resulted in immediate ore mineral formation.

Applicability of available fractionation factors to quartz-xenotime pair

The oxygen isotope composition of coexisting minerals with well-known fractionation factors (e.g., quartz-monazite, Breecker and Sharp, 2007; quartz-tourmaline, Slack and Trumbull, 2011, quartz-garnet, Quinn et al., 2017) is particularly useful for geothermometry of metamorphic and hydrothermal systems. Although commonly reported from a variety of geological environment (e.g., sedimentary, diagenetic, magmatic, metamorphic), little effort has been made to calculate and employ the oxygen isotope composition of xenotime. Currently, the available data of quartz-xenotime oxygen isotope fractionations are limited only to the theoretical dataset reported by Zheng (1996).

Employing the data derived from this study, we examine oxygen isotope fractionation between coexisting xenotime and quartz as a potential geothermometer. Assuming an ore formation temperature of 250 °C, as discussed above, the quartz–xenotime fractionation calculations of Zheng (1996) would return an oxygen isotope fractionation factor ($\Delta_{(1000 \ln \alpha)}$) of around –0.9 ‰. The oxygen isotope fractionation factor, based on the quartz–xenotime fractionation calculations of Zheng (1996), shows limited change with temperature ($\Delta_{(1000 \ln \alpha)}$ = –1.7, T = 100 °C). In contrast, the $\Delta_{(1000 \ln \alpha)}$ values calculated based on the $\delta^{18}O$ values of xenotime (+6.3 to +7.3‰) and coexisting quartz (+14.6 to +17.2‰) separates, using the fractionation factor formula of $\alpha_{qtz\text{-}xnt} = 1000 \ln [(1000 + \delta^{18}O_{qtz}) / (1000 + \delta^{18}O_{xnt})]$, yields $\Delta_{(1000 \ln \alpha)}$, in the range between +7.7 to +9.8 ‰; values that are very different from those calculated using the isotope fractionation parameterisation of Zheng (1996). These data indicate that the oxygen isotope

fractionations factors of Zheng (1996) cannot be used to calculate reliable temperatures from natural quartz-xenotime pairs. Nevertheless, the relatively large values of $\alpha_{qtz\text{-}xnt}$ found here provides encouragement that oxygen isotope analysis of quartz-xenotime pairs may serve as an effective geothermometer, provided future experimental and empirical studies are conducted to establish the systematics of oxygen isotope exchange between xenotime and quartz over a range of temperatures.

Conclusions

The major findings of this study include:

(1) Studies of fluid inclusions in quartz from HREE mineralised veins detected three types of hydrothermal fluids including type I low salinity H_2O-NaCl (meteoric fluid), type II medium salinity H_2O-NaCl, and type III high salinity H_2O-$CaCl_2$-NaCl.
(2) The mineralised samples contain all three types of fluid inclusions, whereas the sample barren of mineralisation only contains type I fluid inclusions.
(3) Microthermometry measurements show a relatively wide range of salinity for the types II and III fluids, potentially as a result of various degrees of mixing with the meteoric water (type I).
(4) Ore metals were transported, at least partially, as Cl complexes by the type III fluid.
(5) The $\delta^{18}O_{fluid}$ values of the ore-related quartz separates suggest contribution from the Archean metasedimentary rocks of the BRM (host rocks) and the unconformably-overlying Birrindudu Group sandstones.

Acknowledgments

This work was financially and logistically supported by Northern Minerals Ltd and by an ARC Future Fellowship (FT 120100198) to CS. Special thanks to Robin Wilson from Northern Minerals Ltd for helping with the field work and sampling, and also to Chris Harris from University of Cape Town for conducting the oxygen isotope analyses. We also thank the reviewers for their constructive comments.

References

Antignano, A., and Manning, C.E., 2008. Rutile solubility in H_2O, H_2O–SiO_2, and H_2O–$NaAlSi_3O_8$ fluids at 0.7–2.0 GPa and 700–1000 °C: implications for mobility of nominally insoluble elements. Chemical Geology, v. 255, p. 283–293.

Audetat, A., and Pettke, T., 2003. The magmatic-hydrothermal evolution of two barren granites: A melt and fluid inclusion study of the Rito del Medio and Canada Pinabete plutons in northern New Mexico (USA). Geochimica et Cosmochimica Acta, v. 67, p. 97–121.

Bagas, L., Bierlein, F.P., English, L., Anderson, J., Maidment, D., and Huston, D.L., 2008. An example of a Palaeoproteozoic back-arc basin: petrology and geochemistry of the ca. 1864 Ma Stubbins Formation as an aid towards an improved understanding of the Granites-Tanami Orogen, Western Australia. Precambrian Research, v. 166, p. 168–184.

Blake, D.H, Hodgson, I.M., and Smith, P.A., 1975. Geology of the Birrindudu and Tanami 1:2500000 Sheet Areas, Northern Territory. Canberra ACT. Bureau of Mineral Resources, Australia, Report 174.

Bodnar, R.J., 2003. Formation of fluid inclusions. In Fluid Inclusions: Analysis and Interpretation. In: Samson, I., Anderson, A., and Marshall, D. (Eds.). Mineralogical Association of Canada, Short Course 32, p. 1–8.

Bodnar, R.J., Reynolds, T.J., and Kuehn, C.A., 1985. Fluid inclusion systematics in epithermal systems: Geology and Geochemistry of Epithermal Systems. In: Berger, B.R., and Bethke, P.M. (Eds.). Reviews in Economic Geology, v. 2, p. 73–98.

Boiron, M.C., Cathelineau, M., Richard, A., 2010. Fluid flows and metal deposition near basement/cover unconformity: lessons and analogies from Pb-Zn-F-Ba systems for the understanding of Proterozoic U deposits. Geofluids, v. 10, p. 270–292.

Bons, P.D., Fusswinkel, T., Gomez-Rivas, E., Markl, G., Wagner, T., Walter, B., 2014. Fluid mixing from below in unconformity-related ore deposits. Geology, v. 42, p. 1035–1038.

Breecker, D.O., and Sharp, Z.D., 2007. A monazite oxygen isotope thermometer. American Mineralogist, v. 92, p. 1561–1572.

Campbell, A.R., Banks, D.A., Phillips, R.S., Yardley, B.W.D., 1995. Geochemistry of Th-U-REE mineralizing magmatic fluids, Captain Mountains, New Mexico. Economic Geology, v. 90, p. 1271–1287.

Clayton, R.N., O'Neil, J.R., and Mayeda, T.K., 1972. Oxygen isotope exchange between quartz and water. Journal of Geophysical Research, v. B77, p. 3057–3067.

Cook, N.J., Ciobanu, C.L., O'Rielly, D., Wilson, R., Das, K., and Wade, B., 2013. Mineral chemistry of Rare Earth Element (REE) mineralization, Browns Ranges, Western Australia: Lithos, v. 172-173, p. 192–213.

Crawford, M.L., 1981. Phase equilibria in aqueous fluid inclusions. In: Hollister, L.S., and Crawford, M.L. (Eds.). Short course in fluid inclusions. Applications to Petrology. Mineralogical Association of Canada, v. 6, p. 75–100.

Crispe, A., and Vandenberg, L., 2005. Geology of the Tanami Region, Northern Territory. Northern Territory Geological Survey Bulletin.

Crispe, A.J., Vandenberg, L.C., and Scrimgeour, I., 2007. Geological framework of the Archaean and Palaeoproterozoic Tanami Region, Northern Territory. Mineralium Deposita, v. 42, p. 1–26.

Criss, R.E., and Farquhar, J., 2008. Abundance, notation, and fractionation of light stable isotopes. Reviews in Mineralogy and Geochemistry, v. 68, p. 15–30.

Cross, A., and Crispe, A., 2007. SHRIMP U-Pb analyses of detrital zircon: a window to understanding the Paleoproterozoic development of the Tanami Region, northern Australia. Mineralium Deposita, v. 42, p. 27–50.

Derome, D., Cuney, M., Cathelineau, C., Fabre, M., Dubessy, J., Bruneton, P., and Hubert, A., 2003. A detailed fluid inclusion study in silicified breccias from the Kombolgie sandstones (Northern Territory, Australia): inferences for the genesis of middle-Proterozoic unconformity-type uranium deposits. Journal of Geochemical Exploration, v. 80, p. 259–275.

Dubessy, J., Derome, D., and Sausse, J., 2003. Numerical modelling of fluid mixings in the H_2O-NaCl system. Applications to the North Caramal uranium prospect (Australia). Chemical Geology, v. 194, p. 25–39.

Frezzotti, M.L., Tecce, F., and Casagli, A., 2012. Raman spectroscopy for fluid inclusion analysis. Journal of Geochemical Exploration, v. 112, p. 1–20.

Fricker, M.B., Kutscher, D., Aeschlimann, B., Frommer, J., Dietiker, R., Bettmer, J., and Günther, D., 2011. High spatial resolution trace element analysis by LA-ICP-MS

using a novel ablation cell for multiple or large samples. International Journal of Mass Spectrometry, v. 307, p. 39–45.

Frost, R.L., Xi, Y., Scholz, R., and Tazava, E., 2013. Spectroscopic characterization of the phosphate mineral florencite-La –$LaAl_3(PO_4)_2(OH, H_2O)_6$, a potential tool in the REE mineral prospection. Journal of Molecular Structure, v. 1037, p. 148–153.

Gerner, E., and Holgate, F., 2010. Oztemp interpreted temperature at 5 km depth. Canberra: Digital data, Geoscience Australia. GEOCAT reference 71143.

Goldstein, R.H., 2003. Petrographic analysis of fluid inclusions studies. Chapter 2 in Introduction to Fluid Inclusions: Analysis and Interpretation. Mineralogical Association of Canada, Short Course, v. 32, p. 9–53.

Goldstein, R.H., and Reynolds, T.J., 1994. Systematics of fluid inclusions in diagenetic minerals. Society for Sedimentary Geology, Short Course, v. 31, p. 1–199.

Guillong, M., Meier, D.L., Allan, M.M., Heinrich, C.A., Yardley, B.W.D., 2008. SILLS: A MATLAB-based program for the reduction of laser ablation ICP-MS data of homogeneous materials and inclusions. In: Sylvester, P. (Ed.). Laser Ablation ICP-MS in the Earth Sciences: Current Practices and Outstanding Issues. Mineralogical Association of Canada, Short Course, v. 40, p. 328–333.

Harris, C., and Vogeli, J., 2010. Oxygen isotope composition of garnet in the Peninsula Granite, Cape Granite Suite, South Africa: constraints on melting and emplacement mechanisms. South African Journal of Geology, v. 113, p. 401–412.

Harrison, T.M., Celerier, J., Aikman, A.B., Hermann, J., and Heizler, M.T., 2009. Diffusion of ^{40}Ar in muscovite. Geochimica et Cosmochimica Acta, v. 73, p. 1039–1051.

Hendrickx, M.A., Slater, K., Crispe, A.J., Dean, A.A., Vandenberg, L.C., and Smith, J.B., 2000. Paleoproterozoic stratigraphy of the Tanami Region: regional correlations realisation preliminary results. Darwin NT: Northern Territory Geological Survey Record, 71 pp.

Kharaka, Y.K., and Hanor, J.S., 2007. Deep fluids in the continents: I. Sedimentary basins. In: Drever, J.I., (Ed.). Surface and Ground Water, Weathering and Soils. Treatise on Geochemistry, v. 5, Elsevier, 48 pp.

Lecuyer, C., Dubois, M., Marignac, C., Gruau, G., Fouquet, Y., and Ramboz, C., 1999. Phase separation and fluid mixing in subseafloor back arc hydrothermal systems: A microthermometric and oxygen isotope study of fluid inclusions in barite-sulfide chimneys of the Lau basin. Journal of Geophysical Research, v. 104, p. B17911–B17927.

Loges, A., Migdisov, A.A., Wagner, T., Williams-Jones, A.E., and Markl, G., 2013. An experimental study of the aqueous solubility and speciation of Y(III) fluoride at temperatures up to 250 °C. Geochimica et Cosmochimica Acta, v. 123, p. 403–415.

Migdisov A.A., Williams-Jones A.E., and Wagner T., 2009. An experimental study of the solubility and speciation of the Rare Earth Elements (III) in fluoride- and chloride-bearing aqueous solutions at temperatures up to 300 C. Geochimica et Cosmochimica Acta, v. 73, p. 7087–7109.

Migdisov, A., Williams-Jones, A.E., Brugger, J., and Caporuscio, F., 2016. Hydrothermal transport, deposition, and fractionation of REE: experimental data and thermodynamic calculations. Chemical Geology, v. 439, p. 13–42.

Migdisov, A.A., and Williams-Jones, A.E., 2014. Hydrothermal transport and deposition of the rare earth elements by fluorine-bearing aqueous liquids. Mineral Deposita, v. 49, p. 987–997.

Moncada, D., Mutchler, S., Nieto, A., Reynolds, T.J., Rimstidt, J.D., and Bodnar, R.J., 2012. Mineral textures and fluid inclusion petrography of the epithermal Ag-Au deposits at Guanajuato, Mexico: Application to exploration. Journal of Geochemical Exploration, v. 114, p. 20–35.

Morin-Ka, S., Beardsmore, T.J., Hancock, E.A., Rasmussen, B., Dunkley, D., Muhling, J., Zi, J., Wilson, R., and Champion, J., 2016. Alteration and Age of the Browns Range Rare Earth Element Deposits: Western Australian Department of Mines and Petroleum.

Muller, A., Herrington, R., Armstrong, R., Seltmann, R., Kirwin, D.J., Stenina, N.J., and Kronz, A., 2010. Trace elements and cathodoluminescence of quartz in stockwork veins of Mongolian porphyry-style deposits. Mineralium Deposita, v. 45, p. 707–727.

Nazari-Dehkordi, T., Spandler, C., Oliver, N.H.S., and Wilson, R., 2018. Unconformity-Related Rare Earth Element deposits: A regional-scale hydrothermal mineralization type of northern Australia. Economic Geology, v. 113, p. 1297–1305.

Nazari-Dehkordi, T., Spandler, C., Oliver, N.H.S., Chapman, J., and Wilson, R., 2017. Provenance, tectonic setting and source of Archean metasedimentary rocks of the Browns Range Metamorphics, Tanami Region, Western Australia. Australian Journal of Earth Sciences, v. 64, p. 723–741.

Page, R., Sun, S.S., Blake, D., Edgecombe, D., and Pearcey, D., 1995. Geochronology of an exposed late Archean basement terrane in the Granites-Tanami region. Australian Geological Survey Organisation Research Newsletter, v. 22, p. 21–22.

Quinn, R.J., Kitajima, K., Nakashima, D., Spicuzza, M.J., Valley, J.W., 2017. Oxygen isotope thermometry using quartz inclusions in garnet. Journal of Metamorphic Geology, v. 35, p. 231–252.

Richter, L., Diamond, L.W., Atanasova, P., Banks, D.A., and Gutzmer, J., 2018. Hydrothermal formation of heavy rare earth element (HREE)-xenotime deposits at 100 °C in a sedimentary basin. Geology, doi: https://doi.org/10.1130/G39871.1.

Roedder, E., 1984. Fluid inclusions. Reviews in Mineralogy, v. 12, 644 pp.

Roedder, E., and Bodnar, R.J., 1997. Fluid inclusion studies of hydrothermal ore deposits. In: Barnes, H.L. (Ed.). Geochemistry of hydrothermal ore deposits. John Wiley & Sons, Inc. New York, p. 657–698.

Salvi, S., and Williams-Jones, A.E., 1996. The role of hydrothermal processes in concentrating high-field strength elements in the Strange Lake peralkaline complex, northeastern Canada. Geochimica et Cosmochimica Acta, v. 60, p. 1917–1932.

Seward, T.M., and Barnes, H.L., 1997. Metal transport by hydrothermal ore fluids. In: Barnes, H.L., (Ed.). Geochemistry of hydrothermal ore deposits. John Wiley and Sons, New York, p. 435–486.

Sheard, E.R., Williams-Jones, A.E., Heiligmann, M., Pederson, C., and Trueman, D.L., 2012. Controls on the concentration of zirconium, niobium, and the rare earth elements in the Thor Lake Rare Metal Deposit, Northwest Territories, Canada. Economic Geology, v. 107, p. 81–104.

Shepherd, T.J., Rankin, A.H., and Alderton, D.H.M., 1985. A Practical Guide to Fluid Inclusion Studies. Blackie, London, 239 pp.

Slack, J.F., and Trumbull, R.B., 2011. Tourmaline as a recorder of ore-forming processes. Elements, v. 7, p. 321–326.

Smith, J.B., 2001. Summary of results, joint NTGS-AGSO age determination program 1999-2001. Darwin NT: Northern Territory Geological Survey, Record 2001–007.

Spandler, C., Pettke, T., and Rubatto, D., 2011. Internal and external fluid sources for eclogite-facies veins in the Monviso meta-ophiolite, Western Alps: Implications for fluid flow in subduction zones. Journal of Petrology, v. 52, p. 1207–1236.

Steele-MacInnis M., Lecumberri-Sanchez P., and Bodnar R.J., 2012. HOKIEFLINCS_H_2ONACL: A Microsoft Excel spreadsheet for interpreting microthermometric data from fluid inclusions based on the PVTX properties of H_2O-NaCl. Computers and Geoscience, v. 49, p. 334–337.

Timofeev, A., Migdisov, A.A., and Williams-Jones, A.E., 2015. An experimental study of the solubility and speciation of niobium in fluoride-bearing aqueous solutions at elevated temperature. Geochimica et Cosmochimica Acta, v. 158, p. 103–111.

Timofeev, A., Migdisov, A.A., and Williams-Jones, A.E., 2017. An experimental study of the solubility and speciation of tantalum in fluoride-bearing aqueous solutions at elevated temperature. Geochimica et Cosmochimica Acta, v. 197, p. 294–304.

Vallini, D.A., Groves, D.I., McNaughton, N.J., and Fletcher, I.R., 2007. Uraniferous diagenetic xenotime in northern Australia and its relationship to unconformity-associated uranium mineralisation. Mineralium Deposita, v. 42, p. 51–64.

Weng, Z, Jowitt S.M., Mudd, G.M., and Nawshad, H.A., 2015. A detailed assessment of global rare earth element resources: Opportunities and challenges. Economic Geology, v. 110, p. 1925–1952.

Wilkinson, J.J., 2001. Fluid inclusions in hydrothermal ore deposits. Lithos, v. 55, p. 229–272.

Williams-Jones, A.E., Migdisov, A.A., and Samson, I.M., 2012. Hydrothermal mobilisation of the rare earth elements: A tale of “Ceria” and “Yttria”. Elements, v. 8, p. 355–360.

Williams-Jones, A.E., Samson, I.M., and Olivo, G.R., 2000. The genesis of hydrothermal fluorite-REE deposits in the Gallinas Mountains, New Mexico. Economic Geology, v. 95, p. 327–342.

Zheng, Y.F., 1996. Oxygen isotope fractionations involving apatites: Application to paleotemperature determination. Chemical Geology, v. 127, p. 177–178.

Zwart, E.W., and Touret, L.R., 1994. Melting behaviour and composition of aqueous fluid inclusions in fluorite and calcite: applications within the system H_2O-$CaCl_2$-NaCl. European Journal of Mineralogy, v. 6, p. 773–786.

Chapter 7

Conclusion

Overview

Extended from the east Kimberly Craton through to the Tanami Region, the North Australia HREE+Y (NAHREY) mineral field contains numerous structurally controlled HREE deposits and prospects of variable size and grade. As discussed in detail in this thesis, these deposits/prospects share remarkably similar geological setting, host rocks, ore mineralogy and ore-related alterations, incomparable to those documented from other well-studied REE orebodies. Combined with a proposed ore genesis model unique among REE ore models, these features inform on a new ore style, herein labelled "Unconformity-Related REE deposit". This ore style composed only of ore phosphate minerals, is completely hydrothermal in origin and shows no demonstrable link to magmatic rocks. Ore-forming hydrothermal fluids, driven by far field stresses during large scale tectonic events (e.g., orogenies), leached the REE and phosphorous from metasedimentary or sedimentary rocks. Hydrothermal transportation of the REE was enhanced particularly by Cl- and F-bearing complexes. Ore deposition occurred along near-unconformity structures and major faults, following mixing of ore-forming hydrothermal fluids, one carrying REE and another one carrying P from contrasting sources. Associated with a pervasive syn-ore quartz-muscovite alteration assemblage, precipitation of the REE-bearing ore minerals required introduction of P and also neutralisation of acidic ore-forming hydrothermal fluids.

In addition to the NAHREY mineral field, reports of a similar style of REE ore from Pine Creek Orogen, northern Australia, and Thelon and Athabasca Basins, Canada, demonstrate a global extent for the Unconformity-Related REE deposits. Exploration of such ore system involves approaches different from those traditionally employed for discovery of REE orebodies. The most important regional scale exploration vectors include:

(1) Identification of ore-related structures: Most notable feature of this style of REE ore is a strong association with major structures spatially related to regional unconformities in the intracontinental sedimentary basins. Hence, the unconformity itself and associated structures, particularly at the conjunction of multiple faults, can be potential targets.

(2) Recognition of P-rich sedimentary rock units: This style of REE ore is composed exclusively of phosphate ore minerals. Therefore, sedimentary rocks containing abundant apatite or other P-bearing phases are ideal sources of phosphorous.

(3) Determination of P-Ca-depleted sedimentary/metasedimentary rock units: The ore-forming hydrothermal fluids leach the ore metals (REE) from a relatively large volume of metasedimentary rocks. Hence, the source rocks are not required to be remarkably rich in REE. However, these rocks must be depleted in P and Ca to avoid fluorite and/or apatite saturation that would greatly restrict REE mobility. Consequently, sedimentary/metasedimentary rock units unusually depleted in Ca and P can also be targeted.

(4) Detection of U anomaly: REE are usually associated with anomalous concentrations of U, and occasionally Th, implying that remotely sensed radiometric surveys can also be employed for REE exploration.

Future research

Additional research is recommended on the following topics:

(1) The research reported in this thesis further highlights the significant role of halogens (Cl, F) in leaching and transportation of REE to an economic grade. However, the ultimate source of these elements remains a question. Further research is required to provide insights into the source of halogens in the NAHREY mineral field.

(2) The ore genesis model reported in this thesis defines the source of the ore metals and P for the HREE deposits/prospects of the Tanami Region, particularly for those hosted by the BRM and also for Longshot, hosted by the Birrindudu Group sandstones along structures spatially correlated to the BRD. More research is needed to determine the sources of REE and P for the John Galt prospect in the Halls Creek Orogen.

(3) Fluid inclusion studies documented in this thesis, provide estimates on the P-T conditions of the ore mineralisation in the basement (BRM). However, the

mineralisation occurs on the unconformity itself, and also extends into the overlying sandstones (Birrindudu Group sandstones). Therefore, further fluid inclusion studies can inform on the physical conditions of the ore-forming hydrothermal fluids at shallower levels.

Appendices

Appendix 2

Chapter 2

Appendix 2.1: Zircon U-Pb isotopic data

Appendix 2-1: Zircon U-Pb isotopic data

	U (ppm)	Th (ppm)	Th/U	$^{207}Pb/^{206}Pb$	±1s	$^{207}Pb/^{235}U$	±1s	$^{206}Pb/^{238}U$	±1s	$^{207}Pb/^{206}Pb$ age (Ma)	±1s	$^{207}Pb/^{235}U$ age (Ma)	±1s	$^{206}Pb/^{238}U$ age (Ma)	±1s	Discordance (%)
NM1 (BRM)																
NM1_1*	39	16	0.4	0.2414	0.0027	21.50	0.2389	0.6463	0.0066	3129	18	3161	11	3213	25	0
NM1_2	47	27	0.6	0.2261	0.0026	15.26	0.1707	0.4895	0.005	3025	18	2831	11	2568	21	-9
NM1_3*	100	55	0.6	0.2405	0.0026	18.32	0.1989	0.5528	0.0055	3123	17	3007	10	2836	23	-6
NM1_4	307	336	1.1	0.2213	0.0025	3.775	0.0415	0.1237	0.0012	2990	18	1587	9	752	7	-53
NM1_5*	27	13	0.5	0.2402	0.0028	21.41	0.2422	0.6465	0.0066	3121	18	3157	11	3214	26	0
NM1_7	170	196	1.2	0.2182	0.0024	7.159	0.0784	0.238	0.0024	2967	18	2131	10	1376	12	-35
NM1_9	341	983	2.9	0.2063	0.0023	3.600	0.0396	0.1266	0.0013	2877	18	1549	9	768	7	-50
NM1_10	292	577	2.0	0.1897	0.0025	2.739	0.0354	0.1048	0.0011	2739	22	1339	10	642	6	-52
NM1_11	161	587	3.6	0.2496	0.0028	7.310	0.0815	0.2125	0.0021	3182	18	2150	10	1242	11	-42
NM1_12*	109	116	1.1	0.2381	0.0026	15.94	0.1743	0.4856	0.0049	3107	17	2873	10	2551	21	-11
NM1_13	419	767	1.8	0.1944	0.0025	1.707	0.021	0.0637	0.0007	2779	21	1011	8	398	4	-61
NM1_14	59	38	0.6	0.2244	0.0025	16.16	0.1789	0.5225	0.0053	3012	18	2886	11	2710	22	-6
NM1_15	314	419	1.3	0.2302	0.0026	4.538	0.0496	0.143	0.0014	3054	18	1738	9	861	8	-50
NM1_16	223	243	1.1	0.2299	0.0027	5.125	0.0583	0.1617	0.0016	3052	18	1840	10	966	9	-48
NM1_17	484	704	1.5	0.1915	0.0044	0.954	0.0206	0.0361	0.0005	2755	38	680	11	228	3	-66
NM1_18*	94	61	0.6	0.2388	0.0027	12.51	0.1375	0.3801	0.0038	3112	18	2644	10	2076	18	-21
NM1_19	24	40	1.7	0.1909	0.0042	5.744	0.1186	0.2182	0.0028	2750	35	1938	18	1272	15	-34
NM1_21	300	748	2.5	0.2047	0.0023	4.919	0.0537	0.1743	0.0017	2864	18	1805	9	1036	9	-43
NM1_22	282	440	1.6	0.2446	0.0029	0.465	0.0054	0.0138	0.0001	3150	19	387	4	88	1	-77
NM1_23	142	537	3.8	0.1704	0.002	0.604	0.007	0.0257	0.0003	2562	20	480	4	163	2	-66
NM1_24	516	1762	3.4	0.2272	0.0037	1.229	0.0191	0.0392	0.0004	3032	26	813	9	248	3	-69
NM1_25	520	492	0.9	0.2091	0.0023	2.390	0.0263	0.0829	0.0008	2898	18	1239	8	513	5	-59
NM1_26	239	377	1.6	0.252	0.0028	18.39	0.2003	0.5293	0.0053	3197	17	3010	10	2738	22	-9
NM1_27*	133	282	2.1	0.2088	0.0024	5.416	0.0601	0.1882	0.0019	2896	18	1887	9	1111	10	-41
NM1_28	48	25	0.5	0.2402	0.0027	20.18	0.2231	0.6095	0.0062	3121	18	3100	11	3068	25	-1
NM1_29	551	840	1.5	0.1576	0.0118	0.310	0.0219	0.0143	0.0004	2430	21	274	17	91	2	-67
NM1_30	396	330	0.8	0.2379	0.009	1.826	0.0631	0.0557	0.001	3106	58	1054	23	349	6	-67
NM1_32	93	66	0.7	0.2241	0.0025	14.16	0.1568	0.4584	0.0046	3010	18	2760	10	2432	20	-12
NM1_33	167	139	0.8	0.2315	0.0026	9.738	0.106	0.3051	0.0031	3063	17	2410	10	1716	15	-29
NM1_34	241	355	1.5	0.2327	0.0026	6.480	0.0707	0.202	0.002	3071	17	2043	10	1186	11	-42
NM1_35	172	294	1.7	0.1869	0.0023	1.920	0.0275	0.0745	0.001	2715	20	1088	10	463	6	-57
NM1_36*	164	237	1.4	0.2368	0.0025	12.26	0.164	0.3758	0.0049	3098	17	2624	13	2056	23	-22
NM1_37	1244	1016	0.8	0.1711	0.0019	0.558	0.0077	0.0237	0.0003	2567	19	450	5	151	2	-66
NM1_38	157	354	2.3	0.2333	0.0026	0.426	0.0058	0.0132	0.0002	3075	18	360	4	85	1	-76
NM1_39	647	938	1.4	0.184	0.002	1.530	0.0208	0.0603	0.0008	2689	18	942	8	378	5	-60
NM1_40	650	805	1.2	0.1716	0.0019	2.975	0.04	0.1258	0.0016	2573	18	1401	10	762	9	-46
NM1_41	139	98	0.7	0.2578	0.0028	17.20	0.23	0.4843	0.0063	3233	17	2946	13	2546	27	-14
NM1_42	229	518	2.3	0.1374	0.0015	0.819	0.011	0.0432	0.0006	2195	19	607	6	273	3	-55
NM1_43*	261	818	3.1	0.162	0.0018	0.612	0.0083	0.0274	0.0004	2477	19	484	5	174	2	-64
NM1_44	282	224	0.8	0.242	0.0026	15.43	0.2057	0.4626	0.006	3133	17	2842	13	2451	26	-14
NM1_45	438	662	1.5	0.2166	0.0035	3.680	0.0637	0.1233	0.0017	2955	26	1567	14	749	10	-52
NM1_46	187	245	1.3	0.1654	0.0018	0.784	0.0106	0.0344	0.0004	2512	18	587	6	218	3	-63
NM1_47	453	935	2.1	0.1565	0.0017	0.569	0.0077	0.0264	0.0003	2418	18	457	5	168	2	-63
NM1_48	404	774	1.9	0.1491	0.0016	0.671	0.0091	0.0327	0.0004	2334	19	521	6	207	3	-60
NM1_49	138	230	1.7	0.2407	0.0026	0.977	0.0132	0.0294	0.0004	3125	17	692	7	187	2	-73
NM1_50	289	313	1.1	0.2403	0.0028	0.415	0.0058	0.0125	0.0002	3122	18	352	4	80	1	-77
NM1_51	471	865	1.8	0.1957	0.0022	0.565	0.0077	0.021	0.0003	2791	18	455	5	134	2	-71
NM1_52	149	418	2.8	0.1574	0.0017	0.541	0.0074	0.0249	0.0003	2428	19	439	5	159	2	-64
NM1_53	193	484	2.5	0.182	0.002	0.931	0.0127	0.0371	0.0005	2671	18	668	7	235	3	-65
NM1_54	266	307	1.2	0.1551	0.0017	1.069	0.0144	0.05	0.0006	2403	18	738	7	314	4	-57
NM1_55	319	736	2.3	0.2063	0.0023	0.409	0.0056	0.0144	0.0002	2876	18	348	4	92	1	-74
W5-1 (BRM)																
W5-1_1*	49	26	0.5	0.2412	0.0027	19.78	0.2231	0.6105	0.0062	3121	18	3100	11	3069	25	-1
W5-1_2*	169	190	1.1	0.2732	0.003	9.640	0.1255	0.3117	0.0031	3324	17	2584	10	1749	15	-32
W5-1_3*	319	301	0.9	0.1999	0.0021	5.775	0.0563	0.1987	0.002	2825	17	1896	9	1168	10	-38
W5-1_4*	439	316	0.7	0.2983	0.0031	6.205	0.0878	0.2118	0.0021	3461	16	2307	9	1237	11	-46
W5-1_5*	489	705	1.4	0.186	0.002	2.339	0.0264	0.099	0.001	2707	17	1283	8	608	6	-53
W5-1_7*	861	775	0.9	0.2023	0.0022	1.572	0.0225	0.0778	0.0008	2845	17	1172	7	483	5	-59
W5-1_8*	452	539	1.2	0.2039	0.0021	4.596	0.047	0.1635	0.0016	2857	17	1748	8	976	9	-44
W5-1_9*	66	50	0.8	0.2256	0.0024	15.42	0.1564	0.4829	0.0048	3021	17	2817	10	2540	21	-10
W5-1_10*	120	140	1.2	0.1386	0.0015	1.507	0.0145	0.0736	0.0007	2209	18	892	6	458	4	-49
W5-1_14*	183	187	1.0	0.2275	0.0024	12.17	0.1238	0.3882	0.0038	3034	17	2618	10	2114	18	-19
W5-1_15*	112	140	1.3	0.1455	0.0016	0.8048	0.0115	0.0546	0.0005	2294	18	751	5	342	3	-54
W5-1_16*	474	487	1.0	0.1929	0.002	3.553	0.0364	0.1335	0.0013	2767	17	1539	8	808	8	-47
W16-4 (BRM)																
W16-4_1*	231	572	2.5	0.166	0.0021	1.917	0.0219	0.075	0.0008	2518	21	1015	8	466	5	-54
W16-4_2*	171	197	1.2	0.2192	0.0024	7.159	0.0784	0.239	0.0024	2968	18	2130	10	1377	12	-35
W16-4_5*	747	962	1.3	0.2115	0.0023	3.312	0.0408	0.1205	0.0013	2917	18	1530	9	733	7	-52
W16-4_7*	651	641	1.0	0.2039	0.0022	3.946	0.0455	0.1404	0.0015	2857	18	1623	9	847	8	-48
W16-4_8*	168	140	0.8	0.2305	0.0026	9.338	0.106	0.3061	0.0031	3065	17	2412	10	1718	15	-29
W16-4_9*	246	600	2.4	0.2094	0.0023	4.046	0.047	0.1401	0.0015	2901	19	1643	10	845	8	-49
W16-4_10*	896	996	1.1	0.1205	0.0014	0.5514	0.0066	0.0332	0.0004	1963	20	446	4	210	2	-53
W16-4_11*	95	62	0.7	0.2378	0.0027	11.71	0.1375	0.3811	0.0038	3110	18	2642	11	2075	18	-21
W16-4_12*	94	67	0.7	0.2251	0.0025	14.16	0.1568	0.4594	0.0046	3009	18	2761	10	2431	20	-12
W16-4_13*	344	495	1.4	0.1789	0.0019	3.137	0.032	0.1149	0.0012	2643	17	1365	8	701	7	-49
W16-4_14*	646	665	1.0	0.1361	0.0015	2.668	0.0213	0.0995	0.0011	2178	19	1070	8	611	6	-43
W16-4_15*	48	28	0.6	0.2291	0.0026	15.26	0.1707	0.4925	0.005	3024	18	2830	11	2567	21	-9
W16-4_18*	110	117	1.1	0.2361	0.0026	15.14	0.1743	0.4866	0.0049	3105	17	2871	10	2550	21	-11
W16-4_19*	60	39	0.7	0.2254	0.0025	16.56	0.1789	0.5325	0.0053	3011	18	2888	11	2709	22	-6

(Continued)

	U (ppm)	Th (ppm)	Th/U	$^{207}Pb/^{206}Pb$	±1s	$^{207}Pb/^{235}U$	±1s	$^{206}Pb/^{238}U$	±1s	$^{207}Pb/^{206}Pb$ age (Ma)	±1s	$^{207}Pb/^{235}U$ age (Ma)	±1s	$^{206}Pb/^{238}U$ age (Ma)	±1s	Discordance (%)
W324-7 (BRM)																
W324-7_1*	634	972	1.5	0.114	0.0012	2.093	0.0204	0.1142	0.0013	1865	19	1043	7	697	7	-33
W324-7_2*	149	126	0.8	0.2392	0.0027	20.49	0.2231	0.6105	0.0062	3119	18	3101	11	3070	25	-1
W324-7_3*	223	438	2.0	0.2343	0.0024	7.376	0.0922	0.2533	0.0028	3082	17	2250	10	1455	14	-35
W324-7_4*	94	67	0.7	0.2251	0.0025	14.76	0.1568	0.4594	0.0046	3007	18	2762	10	2429	20	-12
W324-7_6*	791	977	1.2	0.1124	0.0012	1.839	0.0187	0.1058	0.0012	1838	19	985	7	648	7	-34
W324-7_7*	166	138	0.8	0.2315	0.0026	9.238	0.106	0.3051	0.0031	3066	17	2408	10	1720	15	-29
W324-7_8*	501	754	1.5	0.1834	0.0019	4.152	0.0479	0.1684	0.0019	2683	17	1684	9	1003	10	-40
W324-7_9*	101	56	0.6	0.2415	0.0026	18.32	0.1989	0.5538	0.0055	3121	17	3001	10	2832	23	-6
W324-7_10*	334	742	2.2	0.1417	0.0015	5.963	0.0485	0.2184	0.0024	2248	18	1686	9	1273	13	-24
W324-7_12*	93	60	0.6	0.1607	0.0018	12.01	0.014	0.0526	0.0006	2463	19	784	6	330	3	-58
W324-7_14*	373	690	1.8	0.1443	0.0016	2.981	0.0333	0.1398	0.0015	2279	19	1350	9	843	9	-38
W324-7_15*	473	629	1.3	0.1563	0.0018	2.850	0.0341	0.1323	0.0014	2416	19	1369	9	801	8	-41
W324-7_16*	148	553	3.7	0.1181	0.0014	1.673	0.0205	0.1027	0.0011	1928	21	998	8	630	6	-37
W324-7_17*	498	702	1.4	0.1168	0.0013	2.407	0.0243	0.1247	0.0014	1907	20	1118	8	757	8	-32
W324-7_20*	565	453	0.8	0.1511	0.0017	2.654	0.0315	0.1274	0.0014	2358	19	1315	9	773	8	-41
G5-5 (BRM)																
G5-5_2*	539	928	1.7	0.215	0.0031	1.660	0.0228	0.0459	0.0006	2943	23	872	10	289	4	-67
G5-5_3*	92	65	0.7	0.2415	0.0026	10.15	0.106	0.3151	0.0031	3060	17	2408	10	1710	15	-29
G5-5_4*	780	923	1.2	0.2702	0.0039	2.456	0.0453	0.0726	0.001	3307	22	1330	12	452	6	-66
G5-5_5*	92	59	0.6	0.2488	0.0027	12.25	0.1375	0.3811	0.0038	3116	18	2640	10	2080	18	-21
G5-5_7*	409	872	2.1	0.2663	0.0038	1.899	0.0333	0.0544	0.0007	3284	22	1115	11	342	5	-69
G5-5_8*	177	453	2.6	0.2506	0.0066	7.086	0.1963	0.2195	0.0038	3188	41	2183	23	1279	20	-41
G5-5_9*	769	868	1.1	0.1591	0.0018	3.480	0.025	0.1062	0.001	2550	18	1250	7	645	6	-48
G5-5_10*	650	1357	2.1	0.2049	0.0029	2.753	0.0394	0.0833	0.0011	2865	23	1228	12	515	7	-58
G5-5_13*	271	391	1.4	0.2356	0.0024	15.59	0.1564	0.4859	0.0048	3017	17	2813	10	2542	21	-10
G5-5_14*	555	981	1.8	0.2253	0.0034	1.852	0.0282	0.0531	0.0007	3019	24	990	11	334	4	-66
G5-5_16*	135	429	3.2	0.2199	0.0026	1.679	0.0583	0.1656	0.0016	3049	18	1845	10	969	9	-47
G5-5_17*	575	925	1.6	0.2684	0.0039	2.229	0.0402	0.0656	0.0009	3296	22	1251	12	409	5	-67
G5-5_20*	97	111	1.1	0.294	0.0043	5.325	0.0178	0.0265	0.0004	3439	22	741	8	168	2	-77
G5-5_21*	507	978	1.9	0.2861	0.0034	1.282	0.019	0.0351	0.0004	3396	19	881	8	222	3	-75
G5-5_22*	186	649	3.5	0.2861	0.0035	1.120	0.0162	0.0297	0.0004	3396	19	787	7	189	2	-76
G5-5_30*	495	751	1.5	0.2013	0.0026	2.284	0.0271	0.068	0.0009	2837	21	1075	9	424	5	-61
2ENM1 (Intrusive)																
2ENM1_3	1228	1566	1.3	0.1245	0.0014	1.865	0.0259	0.1078	0.0014	2022	20	1069	9	660	8	-38
2ENM1_4	150	88	0.6	0.2413	0.0025	18.62	0.2516	0.5436	0.0072	3129	17	3001	13	2798	30	-7
2ENM1_5	681	577	0.8	0.2172	0.0024	6.688	0.0919	0.2216	0.0029	2960	17	2071	12	1290	15	-38
2ENM1_6	543	760	1.4	0.1937	0.0022	4.338	0.0608	0.1612	0.0021	2774	18	1700	11	963	12	-43
2ENM1_7*	601	247	0.4	0.1468	0.0016	5.513	0.076	0.2703	0.0036	2309	19	1902	12	1542	18	-19
2ENM1_8	261	171	0.7	0.2788	0.0031	13.49	0.2091	0.3921	0.0052	3356	17	2827	13	2132	24	-25
2ENM1_9*	56	29	0.5	0.2584	0.0028	17.96	0.2474	0.5003	0.0066	3237	17	2987	13	2615	28	-12
2ENM1_10*	308	129	0.4	0.2802	0.0031	19.27	0.3061	0.5721	0.0075	3364	17	3195	13	2916	31	-9
2ENM1_11	496	472	1.0	0.2316	0.0025	11.70	0.1665	0.3661	0.0052	3063	17	2580	13	2011	25	-22
2ENM1_12	945	1508	1.6	0.1549	0.0015	3.067	0.0439	0.1435	0.0021	2400	18	1424	11	864	11	-39
2ENM1_13	352	222	0.6	0.2165	0.0023	9.430	0.1343	0.3158	0.0045	2954	17	2380	13	1769	22	-26
2ENM1_14*	138	107	0.8	0.2528	0.0027	19.18	0.2901	0.579	0.0083	3202	17	3100	14	2944	34	-5
2ENM1_15*	553	225	0.4	0.2468	0.0026	20.00	0.287	0.5933	0.0085	3164	17	3101	14	3003	34	-3
2ENM1_16	866	363	0.4	0.2118	0.0022	7.615	0.1082	0.2606	0.0037	2919	17	2186	13	1493	19	-32
2ENM1_17	390	213	0.5	0.2603	0.0028	11.34	0.1759	0.3436	0.0049	3249	17	2630	13	1904	23	-28
2ENM1_18*	128	45	0.4	0.2362	0.0025	21.12	0.302	0.6481	0.0093	3094	17	3144	14	3221	36	0
2ENM1_19	870	368	0.4	0.2023	0.0021	7.398	0.1053	0.265	0.0038	2845	17	2161	13	1515	19	-30
2ENM1_20	372	329	0.9	0.2518	0.0027	13.20	0.188	0.3801	0.0054	3196	17	2694	13	2076	25	-23
2ENM1_21*	77	32	0.4	0.2387	0.0028	19.81	0.2887	0.6018	0.0083	3111	19	3082	14	3037	33	-1
2ENM1_22*	305	120	0.4	0.1708	0.002	11.45	0.168	0.4989	0.0068	2565	19	2584	13	2609	29	0
2ENM1_23	662	669	1.0	0.2154	0.0025	14.53	0.1925	0.4555	0.0062	2947	18	2717	13	2419	27	-11
2ENM1_24	508	315	0.6	0.2346	0.0027	12.62	0.181	0.3904	0.0053	3083	18	2652	13	2124	25	-20
2ENM1_25*	456	371	0.8	0.2274	0.0026	18.76	0.2502	0.5633	0.0077	3034	18	2971	14	2880	31	-3
2ENM1_26	145	54	0.4	0.2403	0.0028	13.68	0.195	0.413	0.0056	3122	18	2728	13	2229	26	-18
2ENM1_27*	211	124	0.6	0.2373	0.0028	20.77	0.298	0.6347	0.0087	3102	18	3127	14	3168	34	0
2ENM1_28	365	433	1.2	0.2659	0.0031	8.781	0.1396	0.2668	0.0036	3282	18	2414	13	1524	18	-37
2ENM1_29*	557	265	0.5	0.199	0.0023	8.958	0.1578	0.3994	0.0055	2818	19	2519	13	2166	25	-14
2ENM1_30	556	761	1.4	0.2285	0.0088	6.372	0.2336	0.2023	0.0045	3041	60	2028	32	1187	24	-41
2ENM1_31*	277	141	0.5	0.2635	0.0029	18.58	0.2662	0.5253	0.0071	3267	17	3046	13	2721	30	-11
2ENM1_32*	739	318	0.4	0.1474	0.0016	6.141	0.0825	0.2924	0.0039	2316	19	1967	12	1653	19	-16
2ENM1_33*	538	461	0.9	0.1397	0.0016	5.586	0.0743	0.2745	0.0037	2223	19	1866	12	1563	19	-16
2ENM1_34	778	429	0.6	0.1549	0.0017	4.124	0.0652	0.2189	0.0029	2400	18	1762	12	1276	15	-28
2ENM1_35	671	547	0.8	0.2552	0.0028	7.721	0.1073	0.2195	0.0029	3217	17	2199	12	1279	15	-42
2ENM1_36*	166	51	0.3	0.2548	0.0028	18.81	0.266	0.5412	0.0073	3215	17	3042	13	2788	30	-8
2ENM1_37*	185	97	0.5	0.1699	0.0019	5.459	0.0878	0.2671	0.0036	2557	18	2012	12	1526	18	-24
2ENM1_38*	301	245	0.8	0.156	0.0018	3.652	0.0615	0.2023	0.0027	2413	19	1703	12	1188	15	-30
2ENM1_39	287	280	1.0	0.2335	0.0026	15.88	0.2171	0.4843	0.0065	3076	17	2851	13	2546	28	-11
2ENM1_40	207	99	0.5	0.2175	0.0024	9.651	0.1344	0.3218	0.0043	2962	17	2402	13	1798	21	-25
M1 (Intrusive)																
M1_1*	215	66	0.3	0.2269	0.0024	13.53	0.1664	0.4132	0.0052	3030	17	2675	12	2230	24	-17
M1_2*	1220	1463	1.2	0.3157	0.0034	7.933	0.1183	0.212	0.0027	3549	16	2361	12	1239	14	-48
M1_3*	153	117	0.8	0.2505	0.0027	10.15	0.1312	0.2939	0.0037	3187	17	2448	12	1661	18	-32
M1_4*	560	523	0.9	0.2743	0.0029	8.872	0.1178	0.2424	0.0031	3331	17	2355	12	1399	16	-41
M1_5*	779	742	1.0	0.2654	0.0028	6.936	0.0838	0.1786	0.0022	3279	17	2051	11	1059	12	-48
M1_6*	709	214	0.3	0.2398	0.0026	13.35	0.171	0.4036	0.0051	3118	17	2704	12	2185	23	-19
M1_7*	234	99	0.4	0.2308	0.0025	18.29	0.2351	0.5745	0.0073	3058	17	3005	12	2926	30	-3

(Continued)

	U (ppm)	Th (ppm)	Th/U	$^{207}Pb/^{206}Pb$	±1s	$^{207}Pb/^{235}U$	±1s	$^{206}Pb/^{238}U$	±1s	$^{207}Pb/^{206}Pb$ age (Ma)	±1s	$^{207}Pb/^{235}U$ age (Ma)	±1s	$^{206}Pb/^{238}U$ age (Ma)	±1s	Discordance (%)
M1 (Intrusive)																
M1_9*	179	83	0.5	0.2591	0.0028	13.29	0.1851	0.4028	0.0051	3141	17	2776	12	2182	23	-21
M1_11*	751	1287	1.7	0.3215	0.0035	9.040	0.1461	0.2489	0.0032	3577	17	2526	12	1433	16	-43
M1_12*	320	118	0.4	0.27	0.0029	12.01	0.1737	0.352	0.0046	3106	17	2687	12	1944	22	-28
M1_13*	290	175	0.6	0.1694	0.0019	8.536	0.1074	0.344	0.0045	2551	18	2235	12	1906	21	-15
M1_14*	228	166	0.7	0.1923	0.0021	6.729	0.0826	0.2337	0.003	2762	18	2004	12	1353	16	-32
M1_15*	297	358	1.2	0.2229	0.0024	14.47	0.1832	0.4477	0.0058	3002	17	2733	13	2385	26	-13
M1_17*	287	162	0.6	0.2958	0.0032	11.51	0.183	0.3386	0.0044	3448	17	2737	13	1880	21	-31
M1_18*	449	549	1.2	0.2675	0.0029	10.94	0.1557	0.3183	0.0041	3291	17	2584	12	1781	20	-31
M1_19*	713	559	0.8	0.3024	0.0033	7.492	0.1085	0.1964	0.0025	3482	17	2252	12	1156	14	-49
M1_20*	172	58	0.3	0.2659	0.0029	12.53	0.182	0.3744	0.0049	3082	17	2731	12	2050	23	-25
M1_21*	383	143	0.4	0.2337	0.0025	15.88	0.2104	0.4929	0.0064	3077	17	2869	13	2583	28	-10
M1_23*	302	181	0.6	0.2126	0.0023	11.49	0.133	0.3399	0.0044	2925	18	2431	12	1886	21	-22
M1_24*	333	158	0.5	0.1656	0.0018	10.33	0.1357	0.4478	0.0058	2514	18	2455	12	2385	26	-3
M1_26*	286	152	0.5	0.2719	0.0029	9.639	0.1354	0.2731	0.0035	3317	17	2456	12	1556	18	-37
M1_28*	613	855	1.4	0.2675	0.0037	4.611	0.0614	0.1087	0.0015	3291	22	1636	12	665	8	-59
M1_30*	720	205	0.3	0.2169	0.0024	11.14	0.1321	0.3323	0.0043	2958	17	2429	12	1849	21	-24
N1 (Intrusive)																
N1_1	269	99	0.4	0.2331	0.0026	12.79	0.1716	0.3979	0.005	3073	18	2664	13	2159	23	-19
N1_2	462	202	0.4	0.2602	0.0029	11.28	0.1513	0.3144	0.004	3248	18	2546	13	1762	19	-31
N1_3	241	196	0.8	0.2953	0.0033	9.936	0.1328	0.244	0.0031	3446	17	2429	12	1407	16	-42
N1_4	470	400	0.9	0.311	0.0036	8.015	0.1088	0.1869	0.0024	3526	18	2232	12	1105	13	-50
N1_6*	180	150	0.8	0.1551	0.0018	8.016	0.0949	0.3282	0.0042	2402	20	2113	12	1829	21	-13
N1_7*	255	109	0.4	0.2355	0.0026	17.63	0.2357	0.543	0.0069	3089	18	2969	13	2796	29	-6
N1_8	351	324	0.9	0.2263	0.0026	5.225	0.0706	0.1675	0.0021	3026	19	1856	12	998	12	-46
N1_9*	231	113	0.5	0.2346	0.0026	18.17	0.2435	0.5617	0.0071	3084	18	2999	13	2874	30	-4
N1_11	291	262	0.9	0.2475	0.0029	10.62	0.1496	0.3126	0.0041	3168	19	2490	13	1753	20	-30
N1_12*	111	39	0.4	0.2606	0.0031	14.31	0.2163	0.428	0.0056	3250	19	2834	13	2296	25	-19
N1_13*	261	219	0.8	0.196	0.0023	6.376	0.0914	0.2408	0.0032	2793	20	2042	12	1390	16	-32
N1_14	627	1221	1.9	0.1653	0.0019	3.159	0.0448	0.1393	0.0018	2510	20	1447	11	840	10	-42
N1_16*	79	32	0.4	0.1657	0.002	11.20	0.1602	0.4924	0.0065	2515	20	2540	13	2581	28	0
N1_17*	176	105	0.6	0.2344	0.0027	17.57	0.2472	0.5462	0.0072	3082	19	2966	13	2809	30	-5
N1_18	937	1332	1.4	0.1836	0.0022	2.877	0.0405	0.1142	0.0015	2686	20	1376	11	697	8	-49
N1_19*	67	30	0.4	0.2477	0.003	17.53	0.2619	0.5393	0.0071	3170	19	3007	14	2780	30	-8
N1_22*	187	82	0.4	0.2343	0.0026	20.76	0.2723	0.6428	0.0081	3082	18	3127	13	3200	31	0
N1_23*	39	15	0.4	0.2318	0.0027	18.82	0.2554	0.5893	0.0075	3064	19	3032	13	2986	30	-2
N1_24*	191	205	1.1	0.1729	0.0019	8.804	0.1163	0.3696	0.0046	2586	19	2318	12	2027	22	-13
N1_25	459	388	0.8	0.2856	0.0032	12.40	0.1626	0.3151	0.0039	3394	17	2635	12	1766	20	-33
N1_26	625	594	1.0	0.2885	0.0032	8.693	0.114	0.2187	0.0027	3409	17	2306	12	1275	14	-45
N1_27*	96	71	0.7	0.1642	0.0018	11.84	0.1568	0.5235	0.0066	2499	19	2592	12	2714	28	0
N1_29*	39	17	0.4	0.2377	0.0027	21.48	0.2887	0.6559	0.0083	3104	18	3160	13	3251	32	0
N1_30*	240	89	0.4	0.2347	0.0026	21.20	0.2787	0.6557	0.0082	3084	18	3148	13	3250	32	0
C1 (Gardiner Sandstone)																
C1_1*	101	42	0.4	0.1074	0.0012	4.452	0.0508	0.3008	0.0032	1756	20	1722	9	1695	16	-2
C1_2*	103	45	0.4	0.1061	0.0012	4.215	0.0485	0.2882	0.0031	1733	20	1677	9	1632	15	-3
C1_3*	87	45	0.5	0.1035	0.0011	4.633	0.0535	0.3247	0.0035	1688	20	1755	10	1812	17	0
C1_4*	277	170	0.6	0.1121	0.0012	2.464	0.028	0.1594	0.0017	1834	20	1261	8	953	9	-24
C1_5*	488	311	0.6	0.1068	0.0011	1.829	0.0206	0.1242	0.0013	1746	20	1056	7	755	8	-29
C1_6*	108	88	0.8	0.1189	0.0013	4.207	0.0495	0.2566	0.0028	1940	20	1675	10	1472	15	-12
C1_7*	614	171	0.3	0.1204	0.0013	1.689	0.0196	0.1018	0.0011	1961	20	1004	7	625	6	-38
C1_8*	69	37	0.5	0.1076	0.0012	5.093	0.0596	0.3434	0.0037	1759	20	1835	10	1903	18	0
C1_10*	554	243	0.4	0.103	0.0011	1.784	0.0201	0.1257	0.0013	1679	20	1039	7	763	8	-27
C1_11*	52	26	0.5	0.1113	0.0013	5.093	0.0611	0.3318	0.0035	1821	21	1835	11	1847	17	0
C1_12*	87	60	0.7	0.1104	0.0013	4.814	0.0595	0.3163	0.0034	1806	22	1787	11	1771	17	-1
C1_13*	97	65	0.7	0.11	0.0013	4.549	0.054	0.2998	0.0032	1800	21	1740	10	1690	16	-3
C1_14*	121	86	0.7	0.1186	0.0014	5.149	0.061	0.3148	0.0034	1935	21	1844	10	1764	16	-4
C1_15*	28	32	1.1	0.1123	0.0016	3.934	0.0555	0.2541	0.0028	1836	25	1620	11	1459	14	-10
C1_16*	980	1055	1.1	0.137	0.0015	1.134	0.013	0.06	0.0006	2189	19	769	6	376	4	-51
C1_17*	90	60	0.7	0.1129	0.0013	4.275	0.0509	0.2746	0.0029	1846	21	1688	10	1564	15	-7
C1_18*	624	660	1.1	0.1282	0.0014	1.923	0.0222	0.1088	0.0012	2074	20	1089	8	665	7	-39
C1_19*	33	23	0.7	0.1092	0.0014	4.685	0.0603	0.3111	0.0034	1786	23	1764	11	1746	16	-1
C1_20*	77	75	1.0	0.1248	0.0015	3.891	0.0474	0.226	0.0024	2026	21	1612	10	1313	13	-19
C1_21*	87	32	0.4	0.107	0.0012	5.009	0.0572	0.3395	0.0036	1734	21	1808	10	1873	18	0
C1_22*	170	129	0.8	0.1263	0.0014	0.787	0.0315	0.0452	0.0017	2011	20	1331	9	950	10	-29
C1_23*	39	32	0.8	0.1112	0.0017	3.714	0.1117	0.2423	0.0049	2378	19	2392	11	2408	22	0
C1_24*	166	66	0.4	0.1143	0.0012	4.248	0.0396	0.2696	0.0025	1725	20	1520	9	1377	13	-9
C1_25*	171	81	0.5	0.1091	0.0014	4.506	0.0364	0.2997	0.0019	2039	20	1436	9	1065	11	-26
C1_26*	158	176	1.1	0.1184	0.0016	1.328	0.0693	0.0813	0.0032	2362	19	2000	10	1669	16	-17
C1_27*	175	162	0.9	0.132	0.0016	4.149	0.0503	0.228	0.0023	2338	19	1711	9	1247	12	-27
C1_28*	96	36	0.4	0.1166	0.0013	5.340	0.0699	0.3321	0.0039	1974	19	1989	10	2004	19	0
C1_29*	113	102	0.9	0.1586	0.0018	10.64	0.1031	0.4865	0.0044	2480	18	2350	10	2202	20	-6
C1_30*	461	457	1.0	0.1731	0.0014	9.051	0.0236	0.3793	0.0013	2039	19	1142	8	730	7	-36
C1_31*	82	37	0.5	0.1075	0.0012	4.922	0.0576	0.3322	0.0035	1758	21	1806	9	1849	17	0
C1_32*	1047	1349	1.3	0.1265	0.0014	0.749	0.0086	0.043	0.0004	2049	20	567	5	271	3	-52
C1_33*	195	208	1.1	0.1113	0.0013	3.471	0.04	0.2264	0.0024	1820	21	1520	9	1315	12	-13
C1_34*	130	67	0.5	0.1153	0.0013	4.219	0.049	0.2655	0.0028	1885	21	1677	9	1518	14	-9
C1_35*	113	38	0.3	0.1093	0.0012	4.520	0.0523	0.3	0.0031	1788	21	1734	10	1691	16	-2
C1_36*	325	449	1.4	0.1199	0.0014	1.331	0.0156	0.0806	0.0008	1955	21	859	7	499	5	-42
C1_37*	268	80	0.3	0.1335	0.0015	4.238	0.0475	0.2304	0.0024	2144	19	1681	9	1336	12	-21
C1_38*	16	14	0.9	0.1165	0.0018	5.341	0.0832	0.3327	0.0037	1903	28	1875	13	1851	18	-1

(Continued)

	U (ppm)	Th (ppm)	Th/U	$^{207}Pb/^{206}Pb$	±1s	$^{207}Pb/^{235}U$	±1s	$^{206}Pb/^{238}U$	±1s	$^{207}Pb/^{206}Pb$ age (Ma)	±1s	$^{207}Pb/^{235}U$ age (Ma)	±1s	$^{206}Pb/^{238}U$ age (Ma)	±1s	Discordance (%)
C1 (Gardiner Sandstone)																
C1_39*	29	16	0.6	0.1594	0.0019	10.58	0.1273	0.4816	0.0051	2449	20	2487	11	2534	22	0
C1_40*	116	57	0.5	0.1745	0.0019	9.916	0.1108	0.4123	0.0043	2601	18	2427	10	2225	20	-8
C1_41*	136	34	0.3	0.1097	0.0012	3.530	0.0391	0.2337	0.0023	1795	20	1534	8	1353	12	-12
C1_42*	376	389	1.0	0.1164	0.0013	1.866	0.0205	0.1165	0.0011	1901	20	1069	7	710	6	-34
C1_43*	41	26	0.6	0.1118	0.0013	5.135	0.0592	0.3335	0.0033	1829	21	1842	8	1855	16	0
C1_44*	319	184	0.6	0.1228	0.0014	2.018	0.0222	0.1194	0.0012	1997	20	1121	7	727	7	-35
C1_45*	100	79	0.8	0.1103	0.0013	3.446	0.0387	0.227	0.0023	1803	21	1515	9	1319	12	-13
C1_46*	102	46	0.5	0.1611	0.0018	6.366	0.0689	0.287	0.0028	2467	19	2027	9	1626	14	-20
C1_47*	79	34	0.4	0.1437	0.0016	8.698	0.0946	0.4397	0.0044	2272	19	2307	10	2349	20	0
C1_48*	145	126	0.9	0.1267	0.0015	1.532	0.0177	0.0878	0.0009	2053	21	943	7	542	5	-43
C1_49*	68	29	0.4	0.1236	0.0014	6.185	0.0693	0.3636	0.0036	2008	20	2002	10	1999	17	0
C1_50*	126	174	1.4	0.1989	0.0023	4.618	0.0523	0.1686	0.0017	2817	19	1752	9	1004	9	-43
C1_51*	128	140	1.1	0.1709	0.0019	6.734	0.0725	0.2857	0.0028	2567	19	2077	9	1620	14	-22
C1_52*	208	267	1.3	0.1277	0.0014	3.361	0.0364	0.1908	0.0018	2067	20	1495	8	1126	10	-25
C1_53*	127	110	0.9	0.1152	0.0013	3.220	0.0356	0.2028	0.002	1882	20	1462	8	1190	11	-19
C1_54*	96	91	0.9	0.1632	0.0018	7.566	0.0823	0.3363	0.0033	2488	19	2181	10	1869	16	-14
C1_55*	182	140	0.8	0.1149	0.0013	3.440	0.0378	0.2172	0.0021	1878	21	1513	10	1267	11	-16
C1_56*	49	22	0.4	0.151	0.0017	8.650	0.096	0.4155	0.0041	2357	20	2302	10	2240	18	-3
C1_57*	95	43	0.5	0.1142	0.0013	4.465	0.0505	0.2835	0.0028	1867	21	1724	9	1609	14	-7
C1_58*	425	428	1.0	0.1165	0.0013	2.127	0.0234	0.1323	0.0013	1904	20	1157	8	801	7	-31
C1_59*	76	25	0.3	0.177	0.002	11.69	0.1254	0.4791	0.0047	2624	18	2580	10	2523	20	-2
C1_60*	66	45	0.7	0.1092	0.0013	3.940	0.0457	0.2618	0.0026	1785	22	1622	9	1499	13	-8

*Analyses used for age calculations. Note that the ages reported from the metasedimentary samples W5-1, W324-7, W16-4 and G5-5 were calculated based on all the analyses. Similar approach was used to calculate the ~2.5 Ga and ~3.1 Ga ages of the intrusive sample M1, and the ~2.5 Ga ages of the intrusive samples N1 and 2ENM1. However, for the ~3.1 Ga age of the intrusive samples N1 and 2ENM1 along with the metasedimentary sample NM1 only concordant and near concordant ages were counted. Discordance = $(1-(1-^{206}Pb/^{23}8U/^{207}Pb/^{235}U))*100$.

Appendix 3

Chapter 3

Appendix 3-1: Analytical conditions for EPMA measurement of white mica

Appendix 3-2: Sample locations

Appendix 3-3: $^{40}Ar/^{39}Ar$ analytical results

Appendix 3-4: EPMA analyses of pre- and syn-ore muscovite

Appendix 3-5: Xenotime U-Pb data

Appendix 3-1: Analytical conditions for EPMA measurement of white mica

				Count time (sec.)	
Element	**Standard**	**Line**	**Channel**	**Peak**	**Background**
Na	Na_2O	Kα	TAP	20	10
Fe	FeO	Kα	LIF	20	10
Ca	CaO	Kα	PETH	20	10
Si	SiO_2	Kα	TAP	20	10
K	K_2O	Kα	PETJ	20	10
Al	Al_2O_3	Kα	TAP	20	10
Mn	MnO	Kα	LIF	20	10
Cl	Cl	Kα	PETH	20	10
Mg	MgO	Kα	TAP	20	10
Ti	TiO_2	Kα	LIF	20	10
F	F	Kα	TAP	20	10

Appendix 3-2: Sample locations

	No.	Prospect/deposit	Rock type	Drill core	Depth (m)	Easting	Northing
	$^{40}Ar/^{39}Ar$						
1	A2-4	Area 5	BRM	BRAD0002	84.5	492231.3	7909977
2	A2-22	Area 5	BRM	BRAD0002	159.1	492231.3	7909977
3	W16-1	Wolverine	BRM	BRWD0016	47.8	493599.4	7914772
4	W324-7	Wolverine	BRM	BRWT0324	441.6	493541.1	7914983
5	W5-4	Wolverine	BRM	BRWT0332W5	503.2	493508.1	7915069
6	W5-6	Wolverine	BRM	BRWT0332W5	505.2	493508.1	7915069
7	W5-8	Wolverine	BRM	BRWT0332W5	510.6	493508.1	7915069
	Uranium-Pb						
1	B1	Banshee	Ore	-	Surface	492363	7903981
2	W5-7	Wolverine	Ore	BRWT0332W5	505.8	493508.1	7915069
3	W5-5	Wolverine	Ore	BRWT0332W5	504.6	493508.1	7915069
4	W5-2B	Wolverine	Ore	BRWT0332W5	487.6	493508.1	7915069
5	W5-3	Wolverine	Ore	BRWT0332W5	490.3	493508.1	7915069
6	W5-6B	Wolverine	Ore	BRWT0332W5	505.1	493508.1	7915069
7	W7-3B	Wolverine	Ore	BRWD0007	41.6	493695.9	7914741
8	W2	Wolverine	Ore	-	Surface	493723	7914707
9	W324-2	Wolverine	Ore	BRWT0324	372.9	493541.1	7914983
10	C2	Cyclops	Ore	-	Surface	489782	7904619
11	D3	Dazzler	Ore	-	Surface	490384	7902004
12	I1	Iceman	Ore	-	Surface	490746	7901660
13	A2-14	Area 5	Ore	BRAD0002	135.1	492231.3	7909976
14	L1	Longshot	Ore	-	Surface	480968	7905671
15	BR1	Boulder Ridge	Ore	-	Surface	526100	7808681
16	J1	John Galt	Ore	-	Surface	417650	8087517

Appendix 3-3: $^{40}Ar/^{39}Ar$ analytical results

F39	Laser Power (Mw)	Peak36	Err36	Peak37	Err37	Peak38	Err38	Peak39	Err39	Peak40	Err40	Age (Ma)	Age Err
Sample W5-4													
0.055482	100	2.13E-02	1.83E-03	4.87E-02	9.12E-03	3.27E-02	3.05E-03	5.17E+00	1.48E-02	3.13E+03	5.13E+00	1657.405	3.586
0.217884	200	1.89E-02	1.56E-03	8.40E-02	6.99E-03	4.84E-02	3.76E-03	1.51E+01	3.57E-02	9.73E+03	1.58E+01	1725.333	3.181
0.492258	300	2.14E-02	2.22E-03	1.34E-01	5.38E-03	8.21E-02	3.90E-03	2.56E+01	5.43E-02	1.69E+04	3.13E+01	1760.162	3.163
0.844304	400	2.24E-02	2.76E-03	1.86E-01	6.83E-03	1.26E-01	3.95E-03	3.28E+01	1.02E-01	2.18E+04	4.41E+01	1760.776	4.162
0.993086	600	1.48E-02	1.28E-03	1.42E-01	6.11E-03	1.59E-01	4.16E-03	1.39E+01	3.80E-02	9.07E+03	2.19E+01	1745.471	4.088
0.996343	800	-4.29E-04	1.47E-03	6.90E-02	9.09E-03	1.82E-02	1.92E-03	3.04E-01	3.28E-03	1.79E+02	1.42E-01	1631.073	11.91
0.99692	1000	2.95E-04	1.30E-03	-5.40E-03	6.92E-03	1.31E-03	1.86E-03	5.38E-02	3.21E-03	3.48E+01	5.80E-02	1731.345	67.614
0.997623	1200	-1.49E-04	1.36E-03	-1.13E-02	6.50E-03	1.79E-03	1.69E-03	6.55E-02	3.11E-03	4.28E+01	6.10E-02	1746.17	54.181
0.99835	1400	-1.50E-03	9.98E-04	-6.98E-03	1.05E-02	1.10E-03	1.65E-03	6.78E-02	3.74E-03	4.57E+01	6.47E-02	1790.585	62.991
0.999186	1600	-1.44E-04	1.29E-03	-1.52E-02	7.91E-03	4.61E-04	2.45E-03	7.79E-02	3.34E-03	5.04E+01	7.35E-02	1735.409	48.499
0.999502	1800	1.18E-03	1.46E-03	-1.12E-02	6.66E-03	1.67E-03	1.77E-03	2.94E-02	3.34E-03	1.68E+01	2.40E-02	1577.511	122.548
0.999775	2000	3.48E-03	2.16E-03	-5.53E-05	1.09E-02	6.14E-03	1.76E-03	2.55E-02	3.20E-03	1.19E+01	2.58E-02	1305.74	128.97
0.999948	2400	4.07E-04	1.48E-03	-3.54E-03	6.32E-03	1.81E-03	1.87E-03	1.61E-02	3.60E-03	9.78E+00	2.33E-02	1647.946	246.046
1.000094	2800	3.67E-03	1.47E-03	-6.24E-03	6.76E-03	3.48E-03	1.95E-03	1.36E-02	2.96E-03	7.98E+00	1.99E-02	1477.245	228.991
1.000051	3200	1.25E-03	1.21E-03	-9.73E-04	4.91E-03	-5.28E-04	1.96E-03	-3.95E-03	2.54E-03	1.21E+00	9.52E-03	-1358.04	1570.144
1	4000	-2.42E-03	1.34E-03	2.47E-03	5.23E-03	-2.22E-03	2.03E-03	-4.78E-03	2.82E-03	1.45E-01	9.41E-03	-1072.27	1099.231
Mass=1	J=0.00249582 +/- 0.0000211079; Total gas age= 1746.49 +/- 9.651												

(Continued)

F39	Laser Power (Mw)	Peak36	Err36	Peak37	Err37	Peak38	Err38	Peak39	Err39	Peak40	Err40	Age (Ma)	Age Err
Sample W5-8													
0.135298	100	1.72E-02	1.54E-03	4.26E-02	8.63E-03	2.55E-02	3.93E-03	8.56E+00	2.50E-02	5.14E+03	9.62E+00	1646.967	3.748
0.490699	200	2.00E-02	9.78E-04	1.03E-01	1.01E-02	6.60E-02	4.08E-03	2.25E+01	6.29E-02	1.44E+04	2.86E+01	1721.05	3.804
0.812096	300	1.02E-02	1.58E-03	7.61E-02	9.77E-03	9.70E-02	3.25E-03	2.03E+01	4.87E-02	1.31E+04	2.50E+01	1726.842	3.405
0.967258	400	9.23E-03	1.48E-03	3.67E-02	7.11E-03	6.87E-02	2.90E-03	9.81E+00	2.36E-02	6.27E+03	1.22E+01	1713.931	3.431
0.991951	600	3.44E-03	2.20E-03	1.17E-02	5.24E-03	2.91E-02	1.33E-03	1.56E+00	4.84E-03	1.01E+03	1.84E+00	1723.444	4.06
0.996155	800	1.81E-04	1.34E-03	7.53E-03	8.24E-03	4.00E-04	2.36E-03	2.66E-01	5.51E-03	1.76E+02	1.66E-01	1752.037	23.407
0.997866	1000	-1.98E-03	1.44E-03	2.14E-03	1.12E-02	-1.85E-03	2.54E-03	1.08E-01	4.54E-03	7.09E+01	6.88E-02	1752.763	47.554
0.9987	1200	4.16E-05	2.03E-03	3.26E-03	9.64E-03	-5.26E-04	2.43E-03	5.28E-02	3.92E-03	3.65E+01	4.48E-02	1804.705	86.754
0.999476	1400	5.05E-04	1.48E-03	4.80E-03	9.37E-03	-1.14E-03	2.39E-03	4.91E-02	3.74E-03	3.55E+01	5.08E-02	1851.286	89.514
0.999666	1600	2.01E-03	1.61E-03	-2.83E-03	8.99E-03	-3.24E-03	2.39E-03	1.20E-02	4.78E-03	7.87E+00	3.63E-02	1656.062	437.048
0.999716	1800	1.07E-03	2.52E-03	5.55E-03	7.81E-03	1.51E-04	1.80E-03	3.18E-03	3.57E-03	3.26E+00	1.40E-02	2156.499	1448.437
1	4000	2.21E-02	2.48E-03	1.51E-03	8.61E-03	1.19E-02	2.22E-03	1.80E-02	4.12E-03	1.69E+01	7.22E-01	1608.615	265.833
Mass=1	J=J=0.00248391 +/- 0.0000211219; Total gas age= 1712.374 +/- 9.594												

(Continued)

F39	Laser Power (Mw)	Peak36	Err36	Peak37	Err37	Peak38	Err38	Peak39	Err39	Peak40	Err40	Age (Ma)	Age Err
Sample W5-6													
0.126235	100	7.00E-03	2.64E-03	5.02E-03	9.29E-03	3.25E-02	1.62E-03	2.31E+00	5.94E-03	1.37E+03	2.09E+00	1631.947	3.269
0.445461	200	3.28E-03	2.02E-03	5.85E-03	1.05E-02	2.72E-02	1.91E-03	5.85E+00	1.28E-02	3.75E+03	5.65E+00	1721.43	2.944
0.930832	300	1.46E-03	2.36E-03	2.96E-02	7.62E-03	3.05E-02	2.68E-03	8.90E+00	1.79E-02	5.77E+03	8.55E+00	1733.643	2.79
0.991637	400	-1.34E-03	1.99E-03	-1.59E-02	8.41E-03	9.26E-03	2.24E-03	1.12E+00	6.93E-03	6.95E+02	4.82E-01	1692.452	6.925
0.992493	600	-3.16E-03	1.94E-03	-2.47E-02	7.68E-03	-1.26E-03	1.62E-03	1.57E-02	2.78E-03	1.14E+01	2.50E-02	1954.515	218.924
0.993326	800	1.86E-03	1.94E-03	6.31E-03	7.45E-03	7.63E-03	2.13E-03	1.53E-02	2.59E-03	6.23E+00	1.64E-02	1182.813	171.027
0.994217	1000	2.16E-03	1.58E-03	7.35E-03	9.69E-03	5.79E-03	1.63E-03	1.63E-02	2.67E-03	6.28E+00	2.07E-02	1120.011	152.839
0.995325	1200	1.92E-03	1.28E-03	2.57E-02	1.04E-02	6.24E-03	1.78E-03	2.03E-02	3.08E-03	7.76E+00	1.43E-02	1141.61	135.945
0.996179	1400	5.95E-04	1.52E-03	1.86E-02	8.17E-03	7.14E-03	1.72E-03	1.57E-02	2.43E-03	5.40E+00	1.22E-02	1091.084	145.129
0.996873	1600	-1.85E-04	1.85E-03	1.22E-02	9.37E-03	8.11E-03	2.22E-03	1.27E-02	2.45E-03	5.47E+00	1.86E-02	1321.033	202.713
0.998469	1800	9.80E-03	1.82E-03	1.07E-02	9.33E-03	2.27E-02	1.44E-03	2.93E-02	2.00E-03	2.30E+01	2.71E-02	1801.407	83.413
0.999074	2000	3.60E-03	2.46E-03	1.15E-02	8.33E-03	1.87E-02	1.83E-03	1.11E-02	2.36E-03	1.48E+01	1.91E-02	2541.969	298.262
0.999462	2400	6.15E-03	1.89E-03	1.24E-02	5.76E-03	1.43E-02	1.45E-03	7.10E-03	2.60E-03	8.50E+00	1.91E-02	2179.501	474.405
0.999686	2800	7.18E-03	1.84E-03	2.17E-02	6.48E-03	9.41E-03	1.75E-03	4.12E-03	2.27E-03	6.81E+00	1.60E-02	2425.28	752.353
0.999881	3200	1.05E-03	1.54E-03	2.34E-03	4.84E-03	5.55E-03	1.76E-03	3.57E-03	2.27E-03	4.79E+00	1.22E-02	2558.088	882.413
1	4000	1.96E-03	1.78E-03	1.34E-02	5.62E-03	1.61E-03	1.71E-03	2.19E-03	2.64E-03	9.42E-01	5.61E-03	624.019	995.077
Mass=1	J=0.00249208 +/- 0.0000211316; Total gas age= 1713.974 +/- 9.56												

(Continued)

F39	Laser Power (Mw)	Peak36	Err36	Peak37	Err37	Peak38	Err38	Peak39	Err39	Peak40	Err40	Age (Ma)	Age Err
Sample W324-7													
0.066802	100	7.66E-03	2.37E-03	-1.46E-02	9.40E-03	1.40E-02	2.72E-03	2.20E+00	6.83E-03	1.40E+03	1.88E+00	1701.856	3.768
0.216198	200	2.54E-03	2.37E-03	5.56E-03	9.85E-03	1.36E-02	2.08E-03	4.92E+00	1.73E-02	3.18E+03	4.89E+00	1719.124	4.255
0.587602	300	3.81E-03	1.99E-03	2.62E-02	8.60E-03	3.89E-02	1.96E-03	1.22E+01	3.26E-02	8.01E+03	1.20E+01	1732.837	3.405
0.979497	400	1.88E-03	2.06E-03	3.11E-02	9.19E-03	1.66E-01	3.42E-03	1.29E+01	3.94E-02	8.29E+03	1.20E+01	1710.811	3.735
0.99862	600	-4.32E-04	2.66E-03	-2.15E-02	8.45E-03	4.20E-02	1.58E-03	6.29E-01	4.46E-03	4.08E+02	2.42E-01	1722.555	8.166
0.999126	800	-1.33E-03	1.60E-03	-3.59E-03	6.84E-03	7.38E-03	2.01E-03	1.67E-02	4.05E-03	9.05E+00	2.21E-02	1575.668	260.551
0.999251	1000	-5.36E-04	1.85E-03	7.74E-03	1.17E-02	2.80E-03	2.26E-03	4.10E-03	2.89E-03	4.44E+00	1.22E-02	2388.679	947.825
0.999424	1200	-1.11E-03	1.64E-03	-1.10E-02	5.65E-03	1.22E-03	1.86E-03	5.69E-03	2.86E-03	1.97E+00	1.75E-02	1245.256	489.823
0.999643	1400	-5.21E-04	1.72E-03	-2.60E-03	5.09E-03	1.94E-03	2.15E-03	7.21E-03	3.31E-03	3.31E+00	1.84E-02	1407.928	471.421
0.999568	1600	-1.39E-03	2.03E-03	-3.77E-03	5.67E-03	-1.28E-03	2.27E-03	-2.46E-03	3.27E-03	1.37E+00	1.42E-02	-30534.3	5615.343
0.999601	1800	2.61E-03	1.74E-03	1.09E-02	1.04E-02	-3.99E-03	2.34E-03	1.10E-03	2.72E-03	1.26E+00	1.27E-02	1330.987	2544.97
0.999594	2000	-2.52E-03	1.40E-03	1.22E-02	1.15E-02	-2.01E-03	2.20E-03	-2.41E-04	2.69E-03	8.13E-01	8.82E-03	-5.3E+09	21487.99
0.999694	2400	6.90E-04	1.41E-03	1.30E-02	1.14E-02	-1.14E-03	1.55E-03	3.30E-03	2.43E-03	2.33E+00	1.37E-02	1714.461	844.929
0.999872	2800	1.97E-03	1.34E-03	1.57E-02	1.10E-02	-3.58E-04	2.22E-03	5.85E-03	2.51E-03	1.23E+00	9.64E-03	431.346	288.825
0.999927	3200	1.12E-04	1.23E-03	-4.45E-03	4.79E-03	1.15E-06	1.28E-03	1.81E-03	2.15E-03	1.09E+00	1.29E-02	1603.459	1312.223
1	4000	3.49E-04	8.79E-04	-3.41E-03	4.27E-03	-1.90E-03	1.37E-03	2.40E-03	2.55E-03	1.28E-01	1.07E-02	45.459	472.096
Mass=1	J=0.00246217 +/- 0.0000209339; Total gas age= 1719.804 +/- 9.654												

(Continued)

F39	Laser Power (Mw)	Peak36	Err36	Peak37	Err37	Peak38	Err38	Peak39	Err39	Peak40	Err40	Age (Ma)	Age Err
Sample A2-22													
0.081408	100	5.74E-02	1.41E-03	3.91E-02	5.88E-03	6.53E-02	3.48E-03	9.97E+00	2.20E-02	6.18E+03	9.87E+00	1667.763	2.965
0.315194	200	7.33E-02	2.33E-03	1.31E-01	8.26E-03	8.95E-02	4.82E-03	2.86E+01	6.40E-02	1.82E+04	2.97E+01	1699.292	3.045
0.656863	300	3.21E-02	6.50E-04	1.96E-01	5.09E-03	9.51E-02	4.55E-03	4.18E+01	8.28E-02	2.79E+04	4.71E+01	1751.966	2.914
0.946427	400	2.00E-02	1.32E-03	1.85E-01	9.35E-03	1.13E-01	7.21E-03	3.55E+01	6.02E-02	2.37E+04	4.14E+01	1751.534	2.733
0.978794	600	3.62E-04	2.56E-03	1.93E-02	1.02E-02	3.07E-02	3.27E-03	3.96E+00	6.82E-03	2.63E+03	4.08E+00	1744.669	2.611
0.983247	800	-1.28E-04	2.21E-03	2.11E-02	1.01E-02	4.18E-03	1.30E-03	5.45E-01	6.31E-03	3.02E+02	2.31E-01	1550.065	12.272
0.985526	1000	3.02E-04	1.32E-03	9.00E-03	9.97E-03	5.03E-03	1.39E-03	2.79E-01	1.86E-03	1.33E+02	7.97E-02	1396.67	7.102
0.989387	1200	-1.44E-03	1.71E-03	1.04E-02	8.46E-03	2.98E-03	1.98E-03	4.73E-01	4.27E-03	2.46E+02	1.51E-01	1489.195	9.399
0.993456	1400	-1.34E-04	1.41E-03	1.21E-02	6.96E-03	7.06E-03	1.73E-03	4.98E-01	1.33E-03	2.60E+02	1.50E-01	1488.504	3.206
0.995742	1600	-9.43E-04	1.43E-03	3.05E-03	6.99E-03	4.54E-03	1.87E-03	2.80E-01	2.87E-03	1.35E+02	1.65E-01	1413.343	10.585
0.99826	1800	-6.80E-04	1.64E-03	2.21E-03	7.02E-03	1.09E-03	1.99E-03	3.08E-01	2.86E-03	1.53E+02	1.21E-01	1441.074	9.742
0.998851	2000	6.77E-04	1.72E-03	4.99E-05	9.05E-03	9.16E-04	1.33E-03	7.23E-02	2.94E-03	4.06E+01	5.02E-02	1561.467	44.568
0.999526	2400	1.81E-03	1.34E-03	-5.83E-03	7.43E-03	1.25E-04	1.77E-03	8.27E-02	2.47E-03	4.19E+01	5.68E-02	1446.689	31.282
0.999972	2800	2.42E-04	1.09E-03	-1.24E-02	8.92E-03	2.42E-03	1.72E-03	5.47E-02	2.59E-03	3.02E+01	2.10E-02	1546.675	50.494
1	3200	-1.47E-03	1.33E-03	3.81E-04	5.30E-03	-1.65E-03	1.61E-03	3.41E-03	2.31E-03	1.98E+00	1.72E-02	1820.193	799.258
1	4000	-2.48E-03	1.40E-03	9.19E-03	7.67E-03	-1.24E-03	1.26E-03	2.03E-05	2.84E-03	3.14E-01	1.54E-02	8748.793	250738.6
Mass=1	J=0.00245947 +/- 0.0000209101; Total gas age= 1727.284 +/- 9.566												

Appendix 3-4: EPMA analyses of pre- and syn-ore muscovite

Paragenesis	Pre-ore	Pre-ore	Pre-ore	Pre-ore	Pre-ore	Pre-ore	Pre-ore	Pre-ore	Pre-ore	Pre-ore	Pre-ore	Pre-ore	Pre-ore	Pre-ore
Sample No	NM1_2	NM1_3	NM1_4	NM1_5	NM1_6	NM1_7	NM1_8	NM1_9	NM1_10	NM1_11	NM1_12	NM1_14	NM1_17	NM1_18
SiO_2	49.94	48.88	49.39	49.87	50.21	48.75	49.24	49.81	48.27	51.25	50.02	49.65	49.95	49.70
TiO_2	0.05	0.06	0.07	0.03	0.03	0.02	0.01	0.07	0.00	0.02	0.07	0.04	0.08	0.01
Al_2O_3	31.74	33.96	32.64	30.90	30.98	32.48	32.72	31.46	32.57	30.82	31.95	32.63	32.85	31.88
FeO	0.56	0.56	0.70	0.72	0.41	0.93	0.67	0.53	0.65	0.39	0.54	0.59	0.38	0.65
MnO	0.04	0.02	0.02	0.03	0.00	0.00	0.00	0.00	0.00	0.00	0.00	0.01	0.05	0.03
MgO	3.00	2.03	2.63	3.23	3.15	3.01	3.02	3.13	2.89	3.26	2.94	2.71	2.44	2.82
CaO	0.00	0.00	0.00	0.00	0.00	0.00	0.00	0.00	0.00	0.00	0.00	0.00	0.00	0.00
Na_2O	0.16	0.20	0.22	0.18	0.12	0.24	0.21	0.18	0.19	0.13	0.20	0.20	0.16	0.20
K_2O	11.39	11.51	11.32	11.53	11.45	11.33	11.35	11.30	11.29	11.43	11.54	11.54	11.46	11.20
F (%)	0.00	0.00	0.02	0.00	0.00	0.00	0.00	0.02	0.00	0.00	0.00	0.00	0.00	0.00
Cl (%)	0.00	0.00	0.00	0.00	0.00	0.01	0.00	0.00	0.00	0.00	0.00	0.01	0.00	0.01
Total	96.9	97.2	97.0	96.5	96.4	96.8	97.2	96.5	95.9	97.3	97.3	97.4	97.4	96.5
Si	6.52	6.37	6.45	6.55	6.59	6.40	6.42	6.53	6.38	6.65	6.51	6.46	6.48	6.51
Ti	0.01	0.01	0.01	0.00	0.00	0.00	0.00	0.01	0.00	0.00	0.01	0.00	0.01	0.00
Al	4.88	5.21	5.02	4.79	4.79	5.02	5.02	4.86	5.08	4.71	4.90	5.00	5.02	4.92
Al iv	1.48	1.63	1.55	1.45	1.41	1.60	1.58	1.47	1.62	1.35	1.49	1.54	1.52	1.49
Al vi	3.41	3.58	3.47	3.34	3.38	3.42	3.44	3.39	3.46	3.36	3.41	3.46	3.50	3.44
Fe	0.06	0.06	0.08	0.08	0.05	0.10	0.07	0.06	0.07	0.04	0.06	0.06	0.04	0.07
Mn	0.00	0.00	0.00	0.00	0.00	0.00	0.00	0.00	0.00	0.00	0.00	0.00	0.01	0.00
Mg	0.58	0.39	0.51	0.63	0.62	0.59	0.59	0.61	0.57	0.63	0.57	0.53	0.47	0.55
Ca	0.00	0.00	0.00	0.00	0.00	0.00	0.00	0.00	0.00	0.00	0.00	0.00	0.00	0.00
Na	0.04	0.05	0.06	0.05	0.03	0.06	0.05	0.05	0.05	0.03	0.05	0.05	0.04	0.05
K	1.90	1.91	1.89	1.93	1.92	1.90	1.89	1.89	1.90	1.89	1.92	1.92	1.90	1.87
Total (cation)	14.00	14.00	14.01	14.04	13.99	14.07	14.04	14.00	14.05	13.96	14.02	14.02	13.97	13.99

(Continued)

Paragenesis	Pre-ore	Pre-ore	Pre-ore	Pre-ore	Pre-ore	Pre-ore	Pre-ore	Pre-ore	Pre-ore	Pre-ore	Pre-ore	Pre-ore	Pre-ore
Sample No	NM1_19	W5-1_2	W5-1_4	W5-1_6	W5-1_7	W5-1_9	W5-1_11	W5-1_12	W5-1_13	W5-1_14	W5-1_15	W5-1_16	W5-1_20
SiO_2	49.32	47.11	46.98	46.49	46.92	47.67	46.83	50.12	46.77	46.96	46.99	47.74	48.63
TiO_2	0.03	0.14	0.04	0.15	0.06	0.18	0.10	0.04	0.16	0.11	0.16	0.09	0.08
Al_2O_3	32.83	33.56	33.59	34.05	33.94	32.66	33.27	31.88	33.37	33.00	33.26	32.48	32.79
FeO	0.73	1.91	1.92	1.91	1.96	1.95	1.95	1.24	1.90	1.86	2.00	1.83	1.63
MnO	0.00	0.00	0.00	0.00	0.01	0.00	0.00	0.00	0.03	0.00	0.05	0.03	0.00
MgO	2.92	1.37	1.36	1.27	1.28	1.49	1.49	1.86	1.44	1.40	1.42	1.66	1.67
CaO	0.00	0.00	0.00	0.00	0.00	0.00	0.00	0.00	0.02	0.00	0.00	0.00	0.01
Na_2O	0.23	0.41	0.38	0.39	0.37	0.28	0.34	0.24	0.39	0.40	0.35	0.30	0.29
K_2O	11.43	11.16	11.00	11.02	10.99	11.19	11.25	11.20	10.61	11.01	11.05	11.22	11.07
F (%)	0.07	0.00	0.00	0.00	0.04	0.00	0.00	0.00	0.00	0.00	0.00	0.00	0.00
Cl (%)	0.00	0.01	0.00	0.00	0.01	0.00	0.01	0.01	0.00	0.02	0.01	0.00	0.01
Total	97.5	95.7	95.3	95.3	95.5	95.4	95.2	96.6	94.7	94.7	95.3	95.4	96.2
Si	6.41	6.28	6.29	6.23	6.26	6.37	6.28	6.57	6.29	6.32	6.29	6.38	6.42
Ti	0.00	0.01	0.00	0.02	0.01	0.02	0.01	0.00	0.02	0.01	0.02	0.01	0.01
Al	5.03	5.28	5.30	5.37	5.34	5.14	5.26	4.92	5.29	5.23	5.25	5.12	5.10
Al iv	1.59	1.72	1.71	1.77	1.74	1.63	1.72	1.43	1.71	1.68	1.71	1.62	1.58
Al vi	3.44	3.56	3.58	3.60	3.60	3.51	3.54	3.49	3.57	3.55	3.55	3.50	3.53
Fe	0.08	0.21	0.21	0.21	0.22	0.22	0.22	0.14	0.21	0.21	0.22	0.20	0.18
Mn	0.00	0.00	0.00	0.00	0.00	0.00	0.00	0.00	0.00	0.00	0.01	0.00	0.00
Mg	0.57	0.27	0.27	0.25	0.25	0.30	0.30	0.36	0.29	0.28	0.28	0.33	0.33
Ca	0.00	0.00	0.00	0.00	0.00	0.00	0.00	0.00	0.00	0.00	0.00	0.00	0.00
Na	0.06	0.11	0.10	0.10	0.10	0.07	0.09	0.06	0.10	0.10	0.09	0.08	0.07
K	1.90	1.90	1.88	1.88	1.87	1.91	1.93	1.87	1.82	1.89	1.89	1.91	1.87
Total (cation)	14.05	14.07	14.05	14.06	14.05	14.03	14.08	13.93	14.02	14.05	14.05	14.04	13.99

(Continued)

Paragenesis	Syn-ore	Syn-ore	Syn-ore	Syn-ore	Syn-ore	Syn-ore	Syn-ore	Syn-ore	Syn-ore	Syn-ore	Syn-ore	Syn-ore	Syn-ore
Sample No	W5-6B_4	W5-6B_5	W5-6B_8	W5-6B_9	W5-6B_10	W5-8_2	W5-8_3	W5-8_5	W5-8_7	W5-8_8	W5-8_10	W5-12_3	W5-12_6
SiO_2	52.68	53.99	52.24	52.94	52.94	52.00	51.28	51.89	50.99	51.92	52.62	52.31	50.18
TiO_2	0.03	0.00	0.05	0.01	0.04	0.01	0.07	0.00	0.00	0.00	0.06	0.00	0.17
Al_2O_3	30.09	30.37	29.30	29.25	30.02	31.57	31.67	30.54	30.80	32.10	30.94	29.40	27.99
FeO	0.88	0.78	0.92	0.84	0.90	0.77	0.76	0.85	0.70	0.58	0.88	1.13	1.04
MnO	0.02	0.00	0.00	0.06	0.00	0.03	0.00	0.01	0.00	0.00	0.02	0.00	0.02
MgO	2.41	2.66	2.64	2.65	2.72	2.01	1.80	2.20	1.99	1.98	2.30	2.84	2.58
CaO	0.01	0.01	0.02	0.01	0.01	0.09	0.02	0.01	0.05	0.03	0.03	0.02	0.01
Na_2O	0.03	0.05	0.07	0.06	0.07	0.08	0.05	0.03	0.08	0.04	0.02	0.04	0.08
K_2O	10.06	9.98	9.78	10.07	9.75	10.10	9.29	9.07	9.29	10.02	9.42	10.33	10.02
F (%)	0.46	0.00	0.00	0.46	0.02	0.31	0.11	0.31	0.09	0.15	0.09	0.24	0.02
Cl (%)	0.02	0.01	0.07	0.03	0.02	0.01	0.02	0.01	0.01	0.01	0.01	0.02	0.03
Total	96.2	97.8	95.0	95.9	96.4	96.7	94.9	94.6	93.9	96.7	96.3	96.1	92.1
Si	6.84	6.88	6.87	6.90	6.85	6.73	6.72	6.81	6.76	6.70	6.80	6.83	6.84
Ti	0.00	0.00	0.00	0.00	0.00	0.00	0.01	0.00	0.00	0.00	0.01	0.00	0.02
Al	4.61	4.56	4.54	4.49	4.58	4.81	4.89	4.72	4.81	4.88	4.71	4.53	4.50
Al iv	1.16	1.12	1.13	1.10	1.15	1.27	1.28	1.19	1.24	1.30	1.20	1.17	1.16
Al vi	3.45	3.44	3.40	3.39	3.42	3.54	3.60	3.54	3.57	3.58	3.51	3.36	3.34
Fe	0.10	0.08	0.10	0.09	0.10	0.08	0.08	0.09	0.08	0.06	0.10	0.12	0.12
Mn	0.00	0.00	0.00	0.01	0.00	0.00	0.00	0.00	0.00	0.00	0.00	0.00	0.00
Mg	0.47	0.51	0.52	0.51	0.52	0.39	0.35	0.43	0.39	0.38	0.44	0.55	0.52
Ca	0.00	0.00	0.00	0.00	0.00	0.01	0.00	0.00	0.01	0.00	0.00	0.00	0.00
Na	0.01	0.01	0.02	0.01	0.02	0.02	0.01	0.01	0.02	0.01	0.00	0.01	0.02
K	1.67	1.62	1.64	1.67	1.61	1.67	1.55	1.52	1.57	1.65	1.55	1.72	1.74
Total (cation)	13.69	13.66	13.69	13.70	13.67	13.71	13.62	13.59	13.64	13.69	13.62	13.77	13.77

(Continued)

Paragenesis	Syn-ore	Syn-ore	Syn-ore	Syn-ore	Syn-ore	Syn-ore	Syn-ore	Syn-ore	Syn-ore	Syn-ore	Syn-ore	Syn-ore	Syn-ore
Sample No	W5-12_9	W5-12_11	W5-4_1	W5-4_3	W5-4_5	W5-4_7	W5-4_13	W5-4_15	W5-6_2	W5-6_3	W5-6_7	W5-6_8	W5-6_9
SiO_2	50.57	50.52	52.11	51.70	51.73	52.27	52.91	52.68	53.38	50.61	52.50	52.09	52.32
TiO_2	0.04	0.03	0.06	0.00	0.00	0.08	0.00	0.00	0.00	0.00	0.00	0.03	0.00
Al_2O_3	31.94	28.83	31.46	31.60	31.16	29.98	31.66	31.27	30.79	30.10	31.33	30.66	32.09
FeO	0.63	1.01	0.58	0.54	0.69	0.61	0.55	0.72	0.59	0.51	0.55	0.59	0.51
MnO	0.00	0.00	0.00	0.00	0.00	0.00	0.00	0.00	0.01	0.00	0.00	0.02	0.00
MgO	1.66	2.68	2.11	1.92	2.09	2.15	2.18	2.26	2.67	2.15	2.46	2.43	2.22
CaO	0.04	0.03	0.04	0.05	0.06	0.10	0.03	0.04	0.03	0.03	0.05	0.06	0.04
Na_2O	0.09	0.07	0.10	0.10	0.08	0.09	0.09	0.06	0.09	0.23	0.06	0.12	0.10
K_2O	9.67	9.77	10.10	10.03	10.14	9.66	10.12	10.08	10.09	9.41	9.72	9.88	10.06
F (%)	0.46	0.02	0.09	0.18	0.18	0.22	0.22	0.15	0.13	0.11	0.39	0.24	0.22
Cl (%)	0.02	0.02	0.03	0.04	0.03	0.02	0.01	0.04	0.01	0.09	0.04	0.02	0.02
Total	94.6	92.9	96.6	95.9	95.9	94.9	97.5	97.1	97.6	93.0	96.7	95.9	97.3
Si	6.66	6.81	6.74	6.73	6.74	6.86	6.76	6.77	6.82	6.78	6.76	6.78	6.71
Ti	0.00	0.00	0.01	0.00	0.00	0.01	0.00	0.00	0.00	0.00	0.00	0.00	0.00
Al	4.96	4.58	4.79	4.84	4.78	4.63	4.77	4.74	4.64	4.75	4.76	4.70	4.85
Al iv	1.34	1.19	1.26	1.27	1.26	1.14	1.24	1.23	1.18	1.22	1.24	1.22	1.29
Al vi	3.62	3.39	3.53	3.57	3.53	3.49	3.54	3.51	3.45	3.52	3.52	3.48	3.55
Fe	0.07	0.11	0.06	0.06	0.07	0.07	0.06	0.08	0.06	0.06	0.06	0.06	0.05
Mn	0.00	0.00	0.00	0.00	0.00	0.00	0.00	0.00	0.00	0.00	0.00	0.00	0.00
Mg	0.33	0.54	0.41	0.37	0.41	0.42	0.42	0.43	0.51	0.43	0.47	0.47	0.42
Ca	0.01	0.00	0.01	0.01	0.01	0.01	0.00	0.01	0.00	0.00	0.01	0.01	0.01
Na	0.02	0.02	0.02	0.03	0.02	0.02	0.02	0.02	0.02	0.06	0.02	0.03	0.03
K	1.63	1.68	1.67	1.66	1.69	1.62	1.65	1.65	1.64	1.61	1.60	1.64	1.64
Total (cation)	13.68	13.75	13.70	13.70	13.72	13.64	13.69	13.69	13.70	13.68	13.67	13.70	13.71

(Continued)

Paragenesis	Syn-ore	Syn-ore	Syn-ore	Syn-ore
Sample No	W5-6_10	W5-6_13	W5-6_19	W5-6_20
SiO_2	52.44	52.77	51.61	51.77
TiO_2	0.00	0.00	0.01	0.00
Al_2O_3	31.44	31.02	29.80	31.12
FeO	0.54	0.47	0.50	0.57
MnO	0.04	0.00	0.01	0.00
MgO	2.10	2.61	2.34	2.28
CaO	0.04	0.05	0.04	0.09
Na_2O	0.10	0.11	0.08	0.10
K_2O	9.59	9.70	9.78	9.85
F (%)	0.13	0.26	0.18	0.11
Cl (%)	0.02	0.02	0.04	0.01
Total	96.3	96.7	94.2	95.8
Si	6.77	6.79	6.83	6.74
Ti	0.00	0.00	0.00	0.00
Al	4.79	4.70	4.65	4.78
Al iv	1.23	1.21	1.17	1.26
Al vi	3.56	3.49	3.48	3.52
Fe	0.06	0.05	0.06	0.06
Mn	0.00	0.00	0.00	0.00
Mg	0.40	0.50	0.46	0.44
Ca	0.01	0.01	0.01	0.01
Na	0.03	0.03	0.02	0.02
K	1.58	1.59	1.65	1.64
Total (cation)	13.64	13.67	13.68	13.70

*Mineral formulae (a.p.f.u.) are normalised to 22 oxygen, assuming all Fe as Fe^{2+}.

Appendix 3-5: Xenotime U-Pb data

Spot No.	U (ppm)	Th (ppm)	Th/U	$^{207}Pb/^{206}Pb$	±1s	$^{207}Pb/^{235}U$	±1s	$^{206}Pb/^{238}U$	±1s	$^{207}Pb/^{206}Pb$ Age (Ma)	±1s	$^{207}Pb/^{235}U$ Age (Ma)	±1s	$^{206}Pb/^{238}U$ Age (Ma)	±1s
Sample W5-7 (Wolverine)															
W5-7_1*	1407	0	0.00	0.1000	0.0019	3.9552	0.0754	0.2870	0.0034	1624	36	1625	15	1626	17
W5-7_2*	2753	65	0.02	0.1000	0.0011	3.9462	0.0466	0.2863	0.0031	1624	21	1623	10	1623	15
W5-7_3*	2119	0	0.00	0.0991	0.0011	3.9022	0.0437	0.2855	0.0030	1608	20	1614	9	1619	15
W5-7_4*	2140	0	0.00	0.0979	0.0011	3.7610	0.0460	0.2788	0.0031	1584	21	1585	10	1585	16
W5-7_5*	2078	7	0.00	0.1020	0.0014	4.0925	0.0568	0.2931	0.0031	1661	25	1659	11	1657	16
W5-7_6*	1959	400	0.20	0.0995	0.0011	3.9127	0.0448	0.2852	0.0031	1615	20	1616	9	1617	15
W5-7_7*	2839	16	0.01	0.0997	0.0011	3.9478	0.0452	0.2872	0.0030	1619	21	1624	9	1627	15
W5-7_8*	2795	3	0.00	0.0985	0.0012	3.8739	0.0490	0.2852	0.0033	1596	22	1608	10	1617	16
W5-7_9*	2802	0	0.00	0.0966	0.0014	3.6298	0.0521	0.2726	0.0030	1559	27	1556	11	1554	15
W5-7_10*	2636	265	0.10	0.1001	0.0013	3.9546	0.0519	0.2865	0.0031	1626	24	1625	11	1624	15
W5-7_11	2838	29	0.01	0.0983	0.0010	3.9570	0.0411	0.2921	0.0031	1592	19	1625	8	1652	15
W5-7_12	1854	1	0.00	0.0987	0.0010	3.9696	0.0419	0.2919	0.0031	1599	19	1628	9	1651	15
W5-7_14*	4129	347	0.08	0.0984	0.0010	4.0064	0.0415	0.2953	0.0031	1634	18	1636	8	1640	15
W5-7_15*	3753	83	0.02	0.0996	0.0010	3.9076	0.0405	0.2846	0.0030	1617	18	1615	8	1614	15
W5-7_17*	3603	91	0.03	0.0989	0.0010	3.9232	0.0408	0.2877	0.0030	1604	19	1619	8	1630	15
W5-7_18*	2940	0	0.00	0.0989	0.0010	3.9476	0.0413	0.2895	0.0030	1604	19	1624	8	1639	15
W5-7_19*	2918	0	0.00	0.1001	0.0010	4.0930	0.0428	0.2966	0.0031	1651	19	1653	9	1659	15
W5-7_20*	3107	3	0.00	0.0995	0.0010	3.9128	0.0409	0.2852	0.0030	1615	19	1616	8	1618	15
W5-7_21*	2196	4	0.00	0.0992	0.0010	3.7376	0.0403	0.2734	0.0029	1582	19	1580	9	1576	15
W5-7_22*	4128	50	0.01	0.0986	0.0010	3.8778	0.0409	0.2854	0.0030	1597	19	1609	9	1619	15
W5-7_23*	3161	260	0.08	0.0984	0.0010	3.8248	0.0409	0.2822	0.0030	1593	19	1598	9	1602	15
W5-7_24*	4687	57	0.01	0.0986	0.0010	3.8612	0.0406	0.2842	0.0030	1597	19	1606	8	1613	15
W5-7_25*	3665	91	0.02	0.0986	0.0010	3.7991	0.0402	0.2797	0.0030	1597	19	1593	8	1590	15
W5-7_26*	2972	160	0.05	0.1004	0.0010	3.8044	0.0410	0.2748	0.0029	1597	19	1594	9	1588	15
W5-7_27*	2375	3	0.00	0.0985	0.0010	3.9473	0.0423	0.2908	0.0031	1619	19	1623	9	1625	15
W5-7_28	4874	17	0.00	0.0995	0.0010	4.0531	0.0427	0.2956	0.0031	1640	19	1645	9	1650	16
W5-7_29*	2028	1	0.00	0.0966	0.0010	3.8524	0.0417	0.2892	0.0031	1560	19	1604	9	1638	15
W5-7_30*	2059	5	0.00	0.0978	0.0010	3.9071	0.0422	0.2897	0.0031	1583	19	1615	9	1640	15
W5-7_31*	2512	3	0.00	0.0996	0.0010	4.0691	0.0449	0.2962	0.0032	1642	19	1648	9	1653	16
W5-7_32*	2306	660	0.29	0.0974	0.0010	3.8047	0.0421	0.2832	0.0030	1586	20	1594	9	1601	15
W5-7_33*	3096	390	0.13	0.1005	0.0011	3.9083	0.0435	0.2822	0.0030	1623	20	1615	9	1612	15
W5-7_34*	1994	354	0.18	0.0986	0.0010	3.8639	0.0426	0.2842	0.0031	1598	19	1606	9	1612	15
W5-7_35*	4342	11	0.00	0.0977	0.0010	3.7282	0.0405	0.2769	0.0030	1580	19	1577	9	1576	15
W5-7_36*	3943	75	0.02	0.0985	0.0010	4.0070	0.0433	0.2950	0.0032	1630	19	1636	9	1647	16
W5-7_37*	2818	10	0.00	0.0996	0.0011	4.1060	0.0456	0.2930	0.0032	1653	20	1656	9	1658	16
W5-7_38	1360	1	0.00	0.0974	0.0010	4.0172	0.0442	0.2992	0.0032	1575	19	1638	9	1687	16
W5-7_39	2412	0	0.00	0.0997	0.0011	4.2291	0.0473	0.3077	0.0033	1618	20	1680	9	1730	16
W5-7_40*	4250	68	0.02	0.0993	0.0010	3.9250	0.0423	0.2866	0.0031	1612	19	1619	9	1624	15
Sample W324-2 (Wolverine)															
W324-2_1	3862	162	0.04	0.0967	0.0010	3.1647	0.0353	0.2375	0.0026	1560	19	1449	9	1374	14
W324-2_2*	3064	54	0.02	0.0940	0.0010	3.3917	0.0383	0.2619	0.0029	1507	20	1503	9	1503	15
W324-2_3	5116	110	0.02	0.0965	0.0010	3.0606	0.0339	0.2301	0.0025	1557	19	1423	8	1335	13
W324-2_4*	3113	492	0.16	0.0940	0.0010	3.3711	0.0378	0.2601	0.0028	1509	20	1507	9	1507	15
W324-2_5	2644	625	0.24	0.1000	0.0011	3.7305	0.0426	0.2707	0.0030	1623	20	1578	9	1545	15
W324-2_6*	4867	295	0.06	0.0972	0.0011	3.6598	0.0421	0.2733	0.0030	1570	20	1563	9	1557	15
W324-2_7	2843	1117	0.39	0.0992	0.0010	4.0310	0.0452	0.2948	0.0032	1639	19	1641	9	1642	16
W324-2_8	3507	814	0.23	0.0959	0.0010	3.3637	0.0371	0.2544	0.0028	1546	19	1496	9	1461	14
W324-2_9	5149	834	0.16	0.0977	0.0010	3.2847	0.0362	0.2440	0.0027	1580	19	1477	9	1407	14
W324-2_10*	5037	217	0.04	0.0971	0.0010	3.6200	0.0406	0.2704	0.0030	1552	20	1554	9	1552	15
W324-2_11	4205	471	0.11	0.0954	0.0010	2.9084	0.0289	0.2212	0.0022	1536	19	1384	7	1288	11
W324-2_12*	2510	607	0.24	0.0990	0.0010	3.8901	0.0388	0.2850	0.0028	1611	19	1612	8	1617	14
W324-2_13*	2426	675	0.28	0.0971	0.0010	3.5884	0.0360	0.2682	0.0026	1549	19	1547	8	1546	13
W324-2_14	4695	101	0.02	0.0927	0.0009	2.8383	0.0281	0.2221	0.0022	1482	19	1366	7	1293	11
W324-2_15	4786	187	0.04	0.0912	0.0010	2.3189	0.0236	0.1845	0.0018	1451	20	1218	7	1091	10
W324-2_16	4729	478	0.10	0.0949	0.0010	2.5349	0.0259	0.1938	0.0019	1526	20	1282	7	1142	10
W324-2_17	2336	333	0.14	0.0943	0.0010	3.1939	0.0325	0.2459	0.0024	1513	20	1456	8	1417	12
W324-2_18*	3440	368	0.11	0.0979	0.0010	3.6761	0.0363	0.2724	0.0027	1565	19	1566	8	1563	13
W324-2_19*	4086	265	0.06	0.0947	0.0010	3.3069	0.0328	0.2533	0.0025	1523	19	1520	8	1515	13
W324-2_20	3933	201	0.05	0.0921	0.0010	2.5114	0.0254	0.1978	0.0019	1470	20	1275	7	1163	10
W324-2_21	4687	213	0.05	0.0981	0.0010	4.0262	0.0394	0.2978	0.0029	1638	19	1640	8	1641	14
W324-2_22	3972	147	0.04	0.0941	0.0010	3.0391	0.0305	0.2343	0.0023	1510	20	1418	8	1357	12
W324-2_23*	2021	194	0.10	0.0963	0.0010	3.5705	0.0370	0.2691	0.0026	1543	20	1543	8	1546	13
W324-2_24*	3211	299	0.09	0.0980	0.0011	3.8804	0.0399	0.2871	0.0028	1607	20	1610	8	1617	14
W324-2_25*	4730	248	0.05	0.0979	0.0010	3.9286	0.0385	0.2911	0.0028	1619	19	1620	8	1622	14
W324-2_27	4113	401	0.10	0.0976	0.0010	3.3907	0.0338	0.2520	0.0024	1579	19	1502	8	1449	13
W324-2_28	5114	430	0.08	0.0966	0.0010	3.5148	0.0347	0.2639	0.0025	1560	19	1531	8	1510	13
W324-2_30	4373	415	0.09	0.0912	0.0010	2.8861	0.0315	0.2296	0.0022	1450	22	1378	8	1332	12
Sample W5-3 (Wolverine)															
W5-3_1*	4080	35	0.01	0.0990	0.0010	3.8501	0.0385	0.2820	0.0028	1606	19	1603	8	1602	14
W5-3_3*	3216	16	0.00	0.1008	0.0010	3.9546	0.0397	0.2845	0.0028	1630	19	1625	8	1614	14
W5-3_4*	2001	5	0.00	0.0986	0.0010	3.8260	0.0392	0.2815	0.0028	1598	19	1598	8	1599	14
W5-3_10*	2610	3	0.00	0.1000	0.0010	3.9828	0.0406	0.2888	0.0029	1625	19	1631	8	1636	14
W5-3_11*	2475	11	0.00	0.0993	0.0011	3.9040	0.0404	0.2852	0.0028	1611	20	1615	8	1618	14
W5-3_12*	2060	13	0.01	0.0997	0.0011	3.9546	0.0414	0.2877	0.0028	1619	20	1625	8	1630	14
W5-3_13*	2399	1	0.00	0.0997	0.0011	3.9685	0.0411	0.2889	0.0028	1618	20	1628	8	1626	14
W5-3_15	2494	5	0.00	0.0993	0.0011	4.2177	0.0433	0.3080	0.0030	1612	20	1678	8	1731	15
W5-3_16*	2298	12	0.01	0.0991	0.0011	3.8596	0.0399	0.2824	0.0028	1608	20	1605	8	1603	14
W5-3_17*	2020	23	0.01	0.0981	0.0011	3.7180	0.0392	0.2749	0.0027	1589	20	1575	8	1565	14
W5-3_18*	2253	6	0.00	0.0983	0.0011	3.8620	0.0400	0.2851	0.0028	1603	20	1606	8	1617	14
W5-3_19*	4171	183	0.04	0.0988	0.0010	3.9051	0.0393	0.2867	0.0028	1613	19	1615	8	1625	14
W5-3_20	2466	7	0.00	0.0985	0.0011	4.0717	0.0421	0.3000	0.0029	1595	20	1649	8	1691	15

(Continued)

Spot No.	U (ppm)	Th (ppm)	Th/U	$^{207}Pb/^{206}Pb$	±1s	$^{207}Pb/^{235}U$	±1s	$^{206}Pb/^{238}U$	±1s	$^{207}Pb/^{206}Pb$ Age (Ma)	±1s	$^{207}Pb/^{235}U$ Age (Ma)	±1s	$^{206}Pb/^{238}U$ Age (Ma)	±1s
Sample W5-5 (Wolverine)															
W5-5-1	4993	58	0.01	0.0999	0.0010	4.2086	0.0549	0.3057	0.0041	1622	18	1676	11	1719	20
W5-5-2*	1456	3	0.00	0.0987	0.0010	3.8565	0.0513	0.2834	0.0038	1600	19	1605	11	1608	19
W5-5-4*	6240	95	0.02	0.0995	0.0010	4.0946	0.0533	0.2987	0.0040	1654	18	1653	11	1659	20
W5-5-5*	4630	77	0.02	0.0994	0.0010	4.1559	0.0542	0.3032	0.0041	1653	18	1665	11	1657	20
W5-5-6*	5575	68	0.01	0.0993	0.0010	4.0509	0.0528	0.2959	0.0040	1642	18	1645	11	1641	20
W5-5-7*	1359	2	0.00	0.1000	0.0010	3.9206	0.0520	0.2845	0.0038	1623	19	1618	11	1614	19
W5-5-8*	1694	7	0.00	0.0985	0.0010	3.9072	0.0517	0.2879	0.0039	1611	19	1615	11	1620	19
W5-5-9*	1914	10	0.01	0.1022	0.0010	4.1095	0.0540	0.2917	0.0039	1664	18	1656	11	1650	19
W5-5-10*	1945	13	0.01	0.0996	0.0010	3.9454	0.0521	0.2874	0.0039	1622	19	1623	11	1628	19
W5-5-11*	2336	2	0.00	0.0998	0.0010	3.8780	0.0511	0.2819	0.0038	1611	19	1609	11	1601	19
W5-5-12*	1763	0	0.00	0.0997	0.0010	3.9306	0.0520	0.2861	0.0038	1618	19	1620	11	1622	19
W5-5-13*	1855	2	0.00	0.0994	0.0010	3.9564	0.0521	0.2887	0.0039	1613	19	1625	11	1635	19
W5-5-14	2353	2	0.00	0.0996	0.0010	3.8076	0.0501	0.2773	0.0037	1617	18	1594	11	1578	19
W5-5-15*	2830	3	0.00	0.1003	0.0010	3.9808	0.0522	0.2881	0.0039	1629	18	1630	11	1632	19
Sample W5-2B (Wolverine)															
W5-2B-1	3887	19	0.00	0.0988	0.0010	4.0008	0.0524	0.2938	0.0039	1601	18	1634	11	1660	20
W5-2B-2*	5528	9	0.00	0.1002	0.0010	3.9891	0.0521	0.2887	0.0039	1629	18	1632	11	1635	19
W5-2B-3*	4391	4	0.00	0.0994	0.0010	3.9332	0.0515	0.2869	0.0039	1619	18	1621	11	1626	19
W5-2B-4*	3380	4	0.00	0.0996	0.0010	3.9819	0.0523	0.2900	0.0039	1626	18	1631	11	1632	19
W5-2B-5*	5077	16	0.00	0.1004	0.0010	3.9985	0.0522	0.2890	0.0039	1631	18	1634	11	1637	19
W5-2B-6*	4693	15	0.00	0.0998	0.0010	4.0529	0.0530	0.2947	0.0040	1640	18	1645	11	1655	20
W5-2B-7*	3390	36	0.01	0.0983	0.0010	3.8667	0.0507	0.2854	0.0038	1601	18	1607	11	1619	19
W5-2B-8	4334	48	0.01	0.0984	0.0010	4.1346	0.0541	0.3049	0.0041	1594	18	1661	11	1715	20
W5-2B-10*	2899	10	0.00	0.0983	0.0010	3.8613	0.0507	0.2848	0.0038	1603	18	1606	11	1615	19
W5-2B-11*	3198	12	0.00	0.0985	0.0010	3.9070	0.0510	0.2877	0.0039	1616	18	1615	11	1630	19
W5-2B-12*	4075	19	0.00	0.0999	0.0010	4.0719	0.0530	0.2958	0.0040	1631	18	1649	11	1658	20
W5-2B-13	3124	12	0.00	0.0982	0.0010	3.9179	0.0511	0.2894	0.0039	1590	18	1617	11	1639	19
W5-2B-14*	2934	14	0.00	0.0997	0.0010	4.0001	0.0522	0.2910	0.0039	1629	18	1634	11	1636	19
W5-2B-15*	3490	29	0.01	0.1016	0.0010	4.0987	0.0534	0.2927	0.0039	1653	18	1654	11	1655	20
W5-2B-16*	3023	28	0.01	0.0991	0.0010	4.0092	0.0523	0.2934	0.0039	1628	18	1636	11	1638	20
W5-2B-17*	4470	46	0.01	0.0992	0.0010	4.0508	0.0527	0.2962	0.0040	1639	18	1645	11	1653	20
W5-2B-18*	3401	29	0.01	0.0993	0.0010	3.8481	0.0501	0.2810	0.0038	1611	18	1603	11	1596	19
W5-2B-19*	3360	48	0.01	0.0985	0.0010	3.9311	0.0512	0.2894	0.0039	1606	18	1620	11	1629	19
W5-2B-20*	3336	49	0.01	0.0998	0.0010	3.9598	0.0516	0.2877	0.0039	1621	18	1626	11	1630	19
Sample W5-6B (Wolverine)															
W5-6B-2	1535	6	0.00	0.0981	0.0010	3.6327	0.0480	0.2686	0.0036	1588	19	1557	18	1534	18
W5-6B-3	1605	2	0.00	0.0984	0.0010	3.7133	0.0490	0.2737	0.0037	1594	19	1574	19	1559	19
W5-6B-4*	2081	35	0.02	0.0992	0.0010	3.7803	0.0496	0.2763	0.0037	1610	18	1589	19	1573	19
W5-6B-5*	1818	11	0.01	0.0993	0.0010	3.7535	0.0495	0.2741	0.0037	1611	19	1583	19	1562	19
W5-6B-6*	3264	67	0.02	0.0992	0.0010	3.6334	0.0460	0.2658	0.0035	1608	18	1557	18	1519	18
W5-6B-7	2366	14	0.01	0.0985	0.0010	3.5804	0.0456	0.2637	0.0034	1596	19	1545	17	1509	17
W5-6B-8*	3381	49	0.01	0.0995	0.0010	3.7346	0.0473	0.2723	0.0035	1614	18	1579	18	1553	18
W5-6B-9	2566	70	0.03	0.0984	0.0010	3.6214	0.0460	0.2670	0.0035	1594	18	1554	18	1525	18
W5-6B-10*	2877	118	0.04	0.0997	0.0010	3.7286	0.0473	0.2711	0.0035	1619	18	1578	18	1547	18
W5-6B-11	1619	4	0.00	0.0984	0.0010	3.5257	0.0452	0.2599	0.0034	1594	19	1533	17	1489	17
W5-6B-12*	1317	6	0.00	0.0987	0.0010	3.5833	0.0462	0.2632	0.0034	1600	19	1546	17	1506	17
W5-6B-13	1843	3	0.00	0.0984	0.0010	3.6610	0.0469	0.2698	0.0035	1595	19	1563	18	1540	18
W5-6B-14*	2208	1	0.00	0.0991	0.0010	3.6203	0.0462	0.2650	0.0034	1607	19	1554	18	1516	18
W5-6B-15	1730	12	0.01	0.0985	0.0010	3.6618	0.0468	0.2697	0.0035	1596	19	1563	18	1539	18
W5-6B-16	1605	2	0.00	0.0983	0.0010	3.5357	0.0454	0.2609	0.0034	1592	19	1535	17	1494	17
W5-6B-17*	1594	6	0.00	0.0992	0.0010	3.8348	0.0492	0.2805	0.0036	1608	19	1600	18	1594	18
W5-6B-18	2424	2	0.00	0.0984	0.0010	3.6693	0.0468	0.2706	0.0035	1593	19	1565	18	1544	18
W5-6B-19	1680	7	0.00	0.0989	0.0010	3.6117	0.0464	0.2650	0.0034	1603	19	1552	18	1515	18
W5-6B-20	2570	21	0.01	0.0990	0.0010	3.5447	0.0451	0.2597	0.0034	1606	18	1537	17	1488	17
Sample W7-3B (Wolverine)															
W7-3B-1	4151	121	0.03	0.0992	0.0010	3.6952	0.0466	0.2702	0.0035	1609	18	1570	10	1542	18
W7-3B-2	3643	668	0.18	0.0990	0.0010	3.6448	0.0460	0.2670	0.0035	1606	18	1559	10	1526	18
W7-3B-3*	5383	203	0.04	0.0996	0.0010	3.9566	0.0497	0.2880	0.0037	1617	18	1625	10	1632	19
W7-3B-4*	4528	279	0.06	0.0988	0.0010	3.9411	0.0496	0.2895	0.0038	1613	18	1622	10	1629	19
W7-3B-5*	4292	442	0.10	0.0996	0.0010	3.9035	0.0491	0.2844	0.0037	1616	18	1614	10	1613	18
W7-3B-6	3396	321	0.09	0.0985	0.0010	3.8043	0.0480	0.2802	0.0036	1596	18	1594	10	1592	18
W7-3B-7*	3871	399	0.10	0.0989	0.0010	3.8576	0.0486	0.2830	0.0037	1603	18	1605	10	1606	18
W7-3B-8	2212	210	0.09	0.0982	0.0010	3.5780	0.0454	0.2643	0.0034	1590	18	1545	10	1512	17
W7-3B-9	2822	137	0.05	0.0989	0.0010	3.6181	0.0458	0.2653	0.0034	1604	18	1554	10	1517	18
W7-3B-10	3523	44	0.01	0.0991	0.0010	3.8214	0.0483	0.2798	0.0036	1607	18	1597	10	1590	18
W7-3B-11	3197	71	0.02	0.0988	0.0010	3.7049	0.0468	0.2721	0.0035	1601	18	1572	10	1551	18
W7-3B-12*	3700	146	0.04	0.0992	0.0010	3.8599	0.0487	0.2822	0.0037	1609	18	1605	10	1603	18
W7-3B-13	3604	90	0.03	0.0991	0.0010	3.7947	0.0478	0.2777	0.0036	1607	18	1592	10	1580	18
W7-3B-14	2309	29	0.01	0.0981	0.0010	3.5903	0.0457	0.2655	0.0034	1588	19	1547	10	1518	18
W7-3B-15	1980	98	0.05	0.0982	0.0010	3.5444	0.0452	0.2617	0.0034	1591	19	1537	10	1499	17
Sample W2 (Wolverine)															
W2-1	4162	134	0.03	0.0965	0.0009	3.9227	0.0485	0.2953	0.0038	1558	18	1618	10	1668	19
W2-2	3385	62	0.02	0.0962	0.0009	3.7834	0.0469	0.2857	0.0037	1552	18	1589	10	1620	19
W2-4*	2228	141	0.06	0.0962	0.0010	3.5065	0.0441	0.2649	0.0035	1551	19	1529	10	1515	18
W2-6	3838	66	0.02	0.0964	0.0009	3.8542	0.0477	0.2904	0.0038	1556	18	1604	10	1644	19
W2-7*	2196	70	0.03	0.0964	0.0010	3.6218	0.0453	0.2729	0.0036	1556	18	1554	10	1556	18
W2-8	2297	57	0.02	0.1008	0.0010	3.8755	0.0485	0.2795	0.0036	1638	18	1609	10	1589	18
W2-9*	2069	269	0.13	0.0972	0.0010	3.7552	0.0469	0.2808	0.0037	1581	18	1583	10	1585	18
W2-10*	2178	337	0.15	0.0977	0.0010	3.7787	0.0475	0.2812	0.0037	1590	19	1588	10	1587	18
W2-11*	3015	173	0.06	0.0966	0.0010	3.5392	0.0444	0.2662	0.0035	1560	18	1536	10	1521	18
W2-12*	2482	22	0.01	0.0974	0.0010	3.7788	0.0470	0.2819	0.0037	1585	18	1588	10	1591	18

(Continued)

Spot No.	U (ppm)	Th (ppm)	Th/U	$^{207}Pb/^{206}Pb$	±1s	$^{207}Pb/^{235}U$	±1s	$^{206}Pb/^{238}U$	±1s	$^{207}Pb/^{206}Pb$ Age (Ma)	±1s	$^{207}Pb/^{235}U$ Age (Ma)	±1s	$^{206}Pb/^{238}U$ Age (Ma)	±1s
Sample W2 (Wolverine)															
W2-13	4366	69	0.02	0.0967	0.0009	4.0567	0.0499	0.3050	0.0040	1561	18	1646	10	1716	20
W2-14	4077	314	0.08	0.0963	0.0009	4.0269	0.0497	0.3038	0.0039	1554	18	1640	10	1710	19
W2-15	3457	75	0.02	0.0960	0.0009	3.7954	0.0471	0.2874	0.0037	1547	18	1592	10	1629	19
Sample C2 (Cyclops)															
C2-1*	4850	107	0.02	0.0991	0.0010	3.9332	0.0495	0.2879	0.0037	1617	18	1621	10	1631	18
C2-2*	5110	120	0.02	0.0999	0.0010	3.9846	0.0501	0.2892	0.0037	1633	18	1631	10	1637	19
C2-3*	5780	154	0.03	0.1004	0.0010	3.9761	0.0501	0.2872	0.0037	1632	18	1629	10	1628	18
C2-4*	3349	257	0.08	0.0987	0.0010	3.9182	0.0495	0.2880	0.0037	1619	18	1617	10	1621	18
C2-5*	4219	93	0.02	0.0997	0.0010	3.9562	0.0499	0.2878	0.0037	1629	18	1625	10	1630	18
C2-6*	3926	137	0.03	0.0982	0.0010	3.9320	0.0496	0.2903	0.0037	1611	18	1620	10	1623	19
C2-7*	4655	114	0.02	0.0996	0.0010	3.9949	0.0504	0.2910	0.0037	1626	18	1633	10	1637	19
C2-8*	4150	124	0.03	0.0996	0.0010	4.0502	0.0510	0.2949	0.0038	1627	18	1644	10	1646	19
C2-9*	4989	118	0.02	0.1001	0.0010	4.0856	0.0514	0.2960	0.0038	1646	18	1651	10	1651	19
C2-10*	3761	183	0.05	0.0998	0.0010	4.0912	0.0516	0.2972	0.0038	1651	18	1653	10	1657	19
C2-11*	3995	154	0.04	0.1004	0.0010	4.0149	0.0506	0.2900	0.0037	1632	18	1637	10	1641	19
C2-12*	4559	117	0.03	0.0994	0.0010	4.0335	0.0507	0.2943	0.0038	1640	18	1641	10	1643	19
C2-13*	5306	111	0.02	0.1005	0.0010	4.1066	0.0516	0.2963	0.0038	1654	18	1656	10	1653	19
C2-14*	4920	134	0.03	0.1001	0.0010	4.0724	0.0512	0.2952	0.0038	1645	18	1649	10	1647	19
C2-15	4951	119	0.02	0.0999	0.0010	4.1886	0.0527	0.3040	0.0039	1623	18	1672	10	1711	19
Sample J1 (John Galt)															
J1-1	5931	34	0.01	0.0803	0.0008	1.6229	0.0208	0.1467	0.0020	1203	19	979	8	882	11
J1-2*	5440	42	0.01	0.0905	0.0009	2.6813	0.0341	0.2150	0.0029	1435	18	1323	9	1255	15
J1-3	6478	73	0.01	0.0778	0.0008	1.4265	0.0182	0.1330	0.0018	1142	19	900	8	805	10
J1-4	5782	90	0.02	0.0866	0.0008	1.9393	0.0247	0.1624	0.0022	1352	19	1095	9	970	12
J1-5	4908	29	0.01	0.0858	0.0008	1.9831	0.0253	0.1677	0.0022	1333	19	1110	9	1000	12
J1-6*	5806	44	0.01	0.0893	0.0009	2.4296	0.0309	0.1973	0.0026	1411	18	1251	9	1161	14
J1-7*	4832	46	0.01	0.0904	0.0009	2.6782	0.0340	0.2149	0.0029	1433	18	1322	9	1255	15
J1-8*	4563	18	0.00	0.0856	0.0008	2.2162	0.0282	0.1879	0.0025	1328	19	1186	9	1110	14
J1-9*	4983	25	0.00	0.0931	0.0009	2.8330	0.0359	0.2208	0.0029	1489	18	1364	10	1286	15
J1-10*	4547	17	0.00	0.0933	0.0009	3.0766	0.0390	0.2391	0.0032	1494	18	1427	10	1382	16
J1-11	5627	18	0.00	0.0811	0.0008	1.6466	0.0209	0.1472	0.0020	1225	19	988	8	885	11
J1-12	5643	24	0.00	0.0803	0.0008	1.6253	0.0207	0.1467	0.0019	1205	19	980	8	883	11
J1-13*	5293	19	0.00	0.0952	0.0009	3.1996	0.0404	0.2438	0.0032	1532	18	1457	10	1407	17
J1-14*	4733	20	0.00	0.0901	0.0009	2.3721	0.0301	0.1911	0.0025	1427	18	1234	9	1127	14
J1-15*	3933	13	0.00	0.0912	0.0009	2.6441	0.0335	0.2104	0.0028	1450	18	1313	9	1231	15
J1-16	4475	18	0.00	0.0787	0.0010	1.4490	0.0217	0.1336	0.0017	1164	26	910	9	808	10
J1-17	5058	33	0.01	0.0770	0.0010	1.3108	0.0196	0.1234	0.0016	1122	26	851	9	750	9
J1-18*	3756	13	0.00	0.0981	0.0013	3.7103	0.0553	0.2745	0.0036	1575	24	1574	12	1571	18
J1-19	6346	49	0.01	0.0805	0.0011	1.5844	0.0237	0.1428	0.0019	1208	25	964	9	861	10
J1-20	3493	27	0.01	0.0850	0.0011	1.8081	0.0271	0.1543	0.0020	1315	25	1048	10	925	11
Sample I1 (Iceman)															
I1-2*	9371	51	0.01	0.1024	0.0010	4.1024	0.0524	0.2950	0.0039	1667	18	1667	10	1666	19
I1-3	7980	48	0.01	0.1058	0.0010	4.2382	0.0533	0.2905	0.0038	1729	18	1682	10	1644	19
I1-4*	8982	68	0.01	0.0993	0.0010	3.9652	0.0499	0.2896	0.0038	1621	18	1627	10	1630	19
I1-5	9617	52	0.01	0.1073	0.0010	4.3281	0.0543	0.2925	0.0038	1754	18	1699	10	1654	19
I1-6	9316	50	0.01	0.1049	0.0010	4.2056	0.0528	0.2909	0.0038	1712	18	1675	10	1646	19
I1-9*	8911	72	0.01	0.0994	0.0010	4.0645	0.0510	0.2966	0.0039	1643	18	1647	10	1644	19
I1-10	7826	52	0.01	0.1058	0.0010	4.2145	0.0529	0.2891	0.0038	1727	18	1677	10	1637	19
I1-11*	10056	45	0.00	0.1004	0.0010	3.9953	0.0500	0.2886	0.0037	1632	18	1633	10	1635	19
I1-12*	7484	131	0.02	0.1004	0.0010	4.0237	0.0505	0.2908	0.0038	1643	18	1639	10	1646	19
I1-13*	9268	47	0.01	0.1003	0.0010	4.1079	0.0514	0.2970	0.0039	1660	18	1656	10	1657	19
I1-14*	8399	48	0.01	0.1001	0.0010	3.9832	0.0499	0.2886	0.0037	1626	18	1631	10	1635	19
I1-15*	8504	50	0.01	0.1002	0.0010	4.0136	0.0502	0.2904	0.0038	1628	18	1637	10	1634	19
Sample BR1 (Boulder Ridge)															
BR1-2	5511	12	0.00	0.1011	0.0010	3.8487	0.0467	0.2762	0.0034	1644	18	1603	10	1572	17
BR1-4*	5434	8	0.00	0.0988	0.0010	3.9429	0.0478	0.2894	0.0036	1619	19	1623	10	1629	18
BR1-6	5829	14	0.00	0.1023	0.0010	3.9639	0.0479	0.2810	0.0035	1667	18	1627	10	1596	17
BR1-7	6010	13	0.00	0.1020	0.0010	3.9381	0.0476	0.2801	0.0034	1660	18	1622	10	1592	17
BR1-8*	5619	11	0.00	0.0991	0.0010	3.8311	0.0463	0.2805	0.0034	1607	19	1599	10	1594	17
BR1-9	5050	11	0.00	0.1022	0.0010	3.9411	0.0477	0.2797	0.0034	1665	18	1622	10	1590	17
BR1-10*	5843	11	0.00	0.0986	0.0010	3.8292	0.0462	0.2818	0.0035	1597	19	1599	10	1600	17
BR1-12	6029	14	0.00	0.1000	0.0010	3.7083	0.0447	0.2689	0.0033	1625	19	1573	10	1535	17
BR1-13	5937	19	0.00	0.1035	0.0011	3.9057	0.0474	0.2738	0.0034	1688	19	1615	10	1560	17
BR1-17*	6547	7	0.00	0.0997	0.0011	3.9649	0.0559	0.2884	0.0041	1625	20	1627	11	1633	20
BR1-18*	6620	7	0.00	0.0991	0.0011	3.9387	0.0555	0.2882	0.0040	1618	20	1622	11	1623	20
BR1-19*	8164	10	0.00	0.0985	0.0011	3.7508	0.0531	0.2784	0.0039	1590	20	1589	11	1583	20
BR1-20*	8174	11	0.00	0.0997	0.0011	3.8973	0.0547	0.2836	0.0040	1618	20	1613	11	1610	20
BR1-21*	6224	32	0.01	0.0978	0.0011	3.6989	0.0528	0.2744	0.0038	1574	20	1571	11	1569	19
BR1-22*	6019	30	0.00	0.0966	0.0011	3.6532	0.0513	0.2721	0.0038	1560	20	1555	11	1551	19
BR1-23*	6879	8	0.00	0.0989	0.0011	3.9044	0.0547	0.2865	0.0040	1613	20	1615	11	1616	20
BR1-25*	5720	11	0.00	0.0975	0.0011	3.6185	0.0509	0.2691	0.0038	1558	20	1554	11	1549	19
BR1-27*	6228	9	0.00	0.0985	0.0011	3.8743	0.0544	0.2853	0.0040	1596	20	1608	11	1618	20
BR1-28*	5723	10	0.00	0.0978	0.0011	3.7540	0.0527	0.2783	0.0039	1583	20	1583	11	1583	20
BR1-30*	6253	19	0.00	0.0983	0.0011	3.7960	0.0531	0.2803	0.0039	1591	20	1592	11	1593	20
Sample D3 (Dazzler)															
D3-3	4350	123	0.03	0.1006	0.0013	3.6961	0.0567	0.2665	0.0036	1635	24	1571	12	1523	18
D3-4	4740	131	0.03	0.1004	0.0013	3.7645	0.0577	0.2719	0.0036	1632	24	1585	12	1551	18
D3-5*	5211	159	0.03	0.1018	0.0014	3.8751	0.0594	0.2760	0.0037	1611	24	1609	12	1611	19
D3-6*	6099	121	0.02	0.0994	0.0013	3.9450	0.0604	0.2879	0.0038	1622	24	1623	12	1631	19
D3-7*	5869	136	0.02	0.0986	0.0013	3.9497	0.0604	0.2905	0.0039	1621	25	1624	12	1624	19
D3-8*	7323	163	0.02	0.0997	0.0013	4.1206	0.0630	0.2999	0.0040	1656	24	1658	12	1661	20
D3-11*	5685	197	0.03	0.1002	0.0013	3.9095	0.0600	0.2831	0.0038	1617	25	1616	12	1607	19
D3-12*	7816	789	0.10	0.0989	0.0013	4.1254	0.0631	0.3026	0.0040	1653	25	1659	13	1654	20
D3-15*	4198	142	0.03	0.1065	0.0014	3.9383	0.0606	0.2683	0.0035	1630	25	1622	12	1632	18

(Continued)

Spot No.	U (ppm)	Th (ppm)	Th/U	$^{207}Pb/^{206}Pb$	±1s	$^{207}Pb/^{235}U$	±1s	$^{206}Pb/^{238}U$	±1s	$^{207}Pb/^{206}Pb$ Age (Ma)	±1s	$^{207}Pb/^{235}U$ Age (Ma)	±1s	$^{206}Pb/^{238}U$ Age (Ma)	±1s
Sample L1 (Longshot)															
L1-1*	10670	552	0.05	0.1004	0.0013	3.8634	0.0576	0.2791	0.0036	1632	24	1636	12	1633	18
L1-2*	15818	560	0.04	0.1010	0.0013	3.7203	0.0555	0.2671	0.0035	1643	24	1646	12	1626	18
L1-3*	10477	712	0.07	0.1007	0.0013	4.0246	0.0600	0.2898	0.0038	1638	24	1639	12	1640	19
L1-4	10453	907	0.09	0.1047	0.0014	2.4742	0.0371	0.1714	0.0022	1709	24	1265	11	1020	12
L1-5	10593	781	0.07	0.1090	0.0014	2.9925	0.0470	0.2084	0.0027	1783	24	1441	12	1220	14
Sample A2-14 (Area 5))															
A2-14-1	11030	3269	0.30	0.1009	0.0016	3.6794	0.0632	0.2646	0.0036	1640	28	1567	14	1513	18
A2-14-2	10960	2130	0.19	0.1008	0.0016	3.7075	0.0639	0.2669	0.0036	1638	29	1573	14	1525	18
A2-14-3	10599	3139	0.30	0.1032	0.0016	3.9037	0.0675	0.2745	0.0037	1682	29	1614	14	1563	19
A2-14-4	11812	3118	0.26	0.1003	0.0016	3.6866	0.0638	0.2667	0.0036	1629	29	1569	14	1524	18
A2-14-5	10471	5513	0.53	0.1002	0.0016	3.4337	0.0597	0.2486	0.0034	1628	29	1512	14	1431	17
A2-14-6*	12097	3181	0.26	0.1005	0.0016	3.6906	0.0642	0.2663	0.0036	1633	29	1569	14	1522	18
A2-14-7*	12590	6545	0.52	0.1009	0.0016	3.5579	0.0622	0.2558	0.0035	1640	29	1540	14	1468	18
A2-14-8*	7133	1290	0.18	0.0993	0.0016	3.7870	0.0663	0.2766	0.0038	1600	29	1595	14	1594	19
A2-14-9*	7552	1940	0.26	0.0982	0.0016	3.7442	0.0657	0.2765	0.0038	1599	29	1597	14	1594	19
A2-14-10	8300	7534	0.91	0.0985	0.0016	3.3672	0.0591	0.2480	0.0034	1596	29	1497	14	1428	17
Sample B1 (Banshee)															
B1-1*	3435	2363	0.69	0.1106	0.0021	5.0129	0.1016	0.3294	0.0047	1819	34	1822	17	1825	23
B1-2*	3486	2200	0.63	0.1092	0.0021	4.9052	0.0997	0.3265	0.0047	1811	34	1818	17	1822	23
B1-3*	3615	2129	0.59	0.1073	0.0020	4.7310	0.0964	0.3206	0.0046	1790	34	1791	17	1793	22
B1-4*	3730	2203	0.59	0.1088	0.0021	4.8486	0.0991	0.3241	0.0046	1819	34	1793	17	1810	23
B1-5*	3712	2254	0.61	0.1142	0.0022	5.2636	0.1080	0.3353	0.0048	1867	34	1863	18	1864	23
B1-6	4965	3704	0.75	0.1396	0.0027	6.5381	0.1345	0.3408	0.0049	2222	33	2051	18	1891	24
B1-7	4886	3674	0.75	0.1402	0.0027	6.5868	0.1361	0.3420	0.0049	2229	33	2058	18	1896	24
B1-8	4186	2017	0.48	0.1032	0.0020	4.5852	0.0947	0.3233	0.0047	1683	35	1747	17	1806	23
B1-9*	4286	1899	0.44	0.1019	0.0020	4.3691	0.0905	0.3121	0.0045	1702	35	1707	17	1711	22
B1-10	4257	2057	0.48	0.0997	0.0019	4.4149	0.0918	0.3226	0.0047	1618	35	1715	17	1802	23
B1-11*	4252	2270	0.53	0.1070	0.0021	4.8014	0.1002	0.3269	0.0047	1821	35	1825	18	1824	23
B1-12	4194	2074	0.49	0.1197	0.0023	5.3981	0.1129	0.3286	0.0048	1952	34	1885	18	1832	23

*Analysis included in the age calculations.

Appendix 4

Chapter 4

Appendix 4-1: Whole-rock geochemistry

Appendix 4-2: EPMA analyses

Appendix 4-3: U-Pb isotopic analysis

Appendix 4-4: Sm-Nd isotopic analysis

Appendix 4-1: Whole-rock geochemistry

Sampling and sample preparation

Twelve samples of the Browns Range Metamorphics (BRM) that are least affected by weathering and hydrothermal alteration were analysed for whole-rock geochemistry. Sampling was focussed in the northern portion of the field area, although from field observations it appears that the general sedimentary characteristics of the metasedimentary rocks do not vary significantly throughout the district. To best avoid surface weathering, the majority of the samples were taken from core samples drilled in the vicinity of REE orebodies. All of the collected samples were lightly brushed and washed in an ultrasonic bath to remove any contamination from drilling mud. Thin sections of representative samples were prepared for textural characterisation and mineralogical identification using petrographic and scanning electron microscopy (SEM) techniques. The modal composition of the samples was determined using the classic Gazzi-Dickinson point-counting method on a petrographic microscope (Dickinson, 1970).

In addition to our analysis of the BRM, we also utilised bulk rock geochemical data of diamond core and drill chip samples from the HREE+Y orebodies of the Brown Range Dome. These data were collected as an integral part of Northern Minerals Ltd mineral exploration and resource definition work. The assay data can be accessed through Northern Minerals Ltd (www.northernminerals.com.au).

Analytical Techniques

The whole-rock geochemical analyses of BRM samples were carried out by Bureau Veritas Laboratories in Vancouver, Canada. Approximately 100 mg of finely milled powder of each sample was fused to glass using lithium metaborate/tetraborate flux. The fused discs were then digested in nitric acid and analysed for major elements by ICP-OES. A full suite of trace elements were analysed using the 1:1:1 Aqua Regia Ultratrace ICP-MS procedure, which utilises 1:1:1 $HCl:HNO_3:H_2O$ combination to achieve ultra-low detection limits. Sample preparation and analytical procedures are as outlined in Jarvis and Jarvis (1995) and Pearce et al. (1999). Briefly, the procedure starts with the addition of 4 ml HF and 1 ml HNO_3 (SPA, ROMIL Cambridge) to 100 mg of powdered sample within a Teflon vial which is then sealed

and left on a hot plate at 150 °C for 48 h. Followed by a two-step addition of 1 ml HNO_3 into the moist residue, the insoluble fluoride species convert into soluble nitrate species. Moreover, an internal standard combined with 2.5 ml HNO_3 are supplemented, following which the mixture is diluted to 50 ml, generating a final concentration of 20 ppb Re and Rh. The internal standard is, then, used to compensate for any analytical drift and matrix suppression effects. The relative analytical uncertainty on these data is <1% for elements that are substantially above their detection limits, including 0.005 wt.% for most major elements, ~4 ppm for transition metals and <1 ppm for most lithophile trace elements.

The diamond core and drill chip samples collected by Northern Minerals Ltd were analyses for REE and selected major and minor element composition by Genalysis. The samples were dried, crushed, split and pulverised, and then fused with sodium peroxide within a nickel crucible and dissolved with hydrochloric acid. Fusion digestion ensured complete dissolution of the refractory minerals such as xenotime. Subsequently, the suitably diluted digestion solution was analysed by Inductively Coupled Plasma Mass Spectrometry (ICP-MS).

Table 1: Major (wt. %) and trace element (ppm) concentrations of the BRM

Sample No	**A2-2**	**A2-3**	**A2-16**	**A2-25**	**W5-1**	**W5-2**	**W5-13**	**W324-5**	**W324-7**	**NM1**	**W16-4**	**G5-5**
Easting	492231.3	492231.3	492231.3	492231.3	493508.1	493508.1	493508.1	493541.2	493541.2	494489	493599.5	493098.1
Northing	7909977	7909977	7909977	7909977	7915069	7915069	7915069	7914984	7914984	7912111	7914773	7913652
Depth	46.9	51.3	138.2	187.5	441.2	487.6	550.7	409.5	441.6	Surface	103.5	98.1
SiO_2	88	83	86	88	88	91	87	94	90	72	77	78
Al_2O_3	8.5	11.5	7.4	6	8.2	5.5	7.1	4.1	6.7	19.6	16.6	13.6
TiO_2	0.06	0.16	0.15	0.04	0.10	0.07	0.06	0.06	0.06	0.22	0.11	0.15
Fe_2O_3	0.7	0.8	0.4	1.4	0.9	0.8	0.5	0.5	0.5	1.4	0.8	0.3
MnO	0.02	0.02	0.02	0.02	0.02	0.02	0.02	0.02	0.02	0.02	0.02	0.02
MgO	0.40	0.77	0.05	0.08	0.37	0.40	0.19	0.25	0.26	0.34	0.31	0.26
CaO	0.02	0.02	0.01	0.03	0.02	0.03	0.02	0.02	0.02	0.07	0.04	0.05
Na_2O	0.02	0.02	0.15	0.10	0.04	0.02	0.09	0.01	0.01	0.04	0.11	0.21
K_2O	2.2	3.8	5.9	4.3	2.6	1.7	4.4	1.3	2.1	5.7	4.9	7.5
P_2O_5	0.02	0.04	0.04	0.02	0.02	0.05	0.03	0.04	0.02	0.12	0.08	0.10
LOI	2.2	2.1	0.7	1	1.7	1.4	1	0.9	1.3	3.0	2.6	1.5
K_2O/Na_2O	112	189	39	43	66	86	49	127	207	143	44	36
Al_2O_3/TiO_2	142	72	49	150	82	79	118	68	112	89	151	91
Ba	21	61	465	655	84	645	459	37	25	158	78	855
Sc	1.0	2.0	2.0	0.5	2.0	5.0	0.5	2.0	1.0	5.0	1.5	3.0
Cs	1.5	1.9	0.8	1.2	1.3	0.5	0.9	0.4	0.3	2.5	2.2	1.8
Ga	9.7	17.1	3.7	3.3	9.7	7.1	6.1	5.4	7.1	22.6	20	19
Hf	2.7	3.6	2.4	2.2	2.6	1.9	2.5	1.4	2.6	5.2	6.2	5.5
Nb	1.9	5.4	2.6	1.8	3.3	2.3	1.7	1.7	2.0	6.1	5.2	4.9
Rb	56	102	143	109	69	27	95	24	27	170	176	160
Sr	17	87	61	70	28	145	53	54	55	175	147	197
Ta	0.3	0.5	0.3	0.3	0.4	0.3	0.2	0.2	0.2	1.0	0.5	0.6
Th	25	41	24	19	25	22	25	12	27	103	87	47
U	2.1	2.1	2.2	2.5	1.3	2.0	0.7	1.6	1.0	1.0	1.8	4.5
V	14	19	6.0	6.0	9.0	16	6.0	13	6.0	20	17	14
Mo	0.08	0.03	0.06	0.07	0.06	0.07	0.08	0.09	0.05	1.6	5.7	5.4
Cu	1.6	1.2	1.1	5.5	0.6	139	0.8	18.5	0.5	15.6	5.0	20.5
Pb	0.8	1.2	1.5	3.2	1.3	1.3	1.3	0.9	1.0	42	6.5	40
Zn	2.4	2.0	0.9	3.0	1.0	0.8	0.4	0.5	0.4	13.4	7.6	13
Ni	2.7	1.7	0.7	0.9	0.8	2.9	1.9	2.6	0.6	3.2	2.9	4.5
Co	2.0	0.6	0.3	0.8	0.3	1.5	1.2	3.1	0.2	5.7	5.8	3.1
Mn	25	13	38	60	26	21	28	28	23	34	25	31
As	0.1	1.0	3.2	1.1	0.4	6.4	2.3	2.5	1.3	9.5	10	9.6
Cr	2.4	2.6	2.5	5.7	2.6	2.0	2.0	2.8	2.5	5.6	3.7	2.8
Li	0.4	0.2	0.3	0.2	0.6	0.3	0.1	0.3	0.2	0.2	0.3	0.4
F	343	202	46	50	129	174	87	122	126	101	95	125
Zr	93	123	85	73	92	81	82	40	84	151	180	170
Y	15	23.3	10.3	8.4	12	6.8	17.3	20.1	5.4	3.11	14.1	16.03
La	27.3	85.0	32.2	36.2	25.3	42.8	29.8	51.9	32.8	70.1	51.4	51.4
Ce	47.9	152.1	55.0	61.0	42.9	81.8	50.3	103	58.8	130.1	107.7	103.7
Pr	4.33	15.9	5.51	6.61	4.03	8.41	4.77	10.7	6.41	12.8	9.87	9.88
Nd	14.1	57.7	18.9	21.9	12.4	30.6	15.9	35.1	24.6	45.5	33.1	34.6
Sm	2.50	8.96	2.78	2.88	2.39	4.44	2.61	5.37	3.44	5.59	4.81	5.58
Eu	0.34	0.62	0.30	0.25	0.24	0.30	0.42	0.43	0.25	0.28	0.38	0.37
Gd	2.42	4.00	1.91	1.90	2.02	1.60	2.86	3.12	1.32	1.55	2.26	2.62
Tb	0.38	0.63	0.30	0.26	0.34	0.21	0.49	0.53	0.16	0.11	0.36	0.43
Dy	2.29	3.65	1.50	1.20	1.80	1.00	2.61	3.15	0.88	0.50	1.90	2.41
Ho	0.50	0.77	0.35	0.29	0.40	0.24	0.59	0.67	0.19	0.11	0.48	0.54
Er	1.52	2.15	1.07	0.87	1.10	0.75	1.75	2.01	0.59	0.33	1.41	1.61
Tm	0.24	0.30	0.17	0.15	0.17	0.13	0.27	0.29	0.11	0.07	0.20	0.25
Yb	1.45	2.08	1.16	1.06	1.17	1.00	1.69	1.90	0.90	0.50	1.30	1.56
Lu	0.22	0.31	0.17	0.15	0.17	0.14	0.25	0.28	0.13	0.06	0.19	0.23
$(Gd/Yb)_N$	1.3	1.6	1.3	1.4	1.4	1.3	1.4	1.3	1.2	2.5	1.4	1.4
$(La/Sm)_N$	6.9	6	7.3	7.9	6.6	6	7.2	6.1	6	7.9	6.7	5.8

Major elements are normalised to 100% on a LOI-free basis.

References

Dickinson, W.R., 1970. Interpreting detrital modes of graywacke and arkose. Journal of Sedimentary Petrology, v. 40, p. 695–707.

Jarvis, I., and Jarvis, K.E., 1995. Plasma spectrometry in earth sciences: techniques, applications and future trends. Chemical Geology, v. 95, p. 1–33.

Pearce, T.J., Besly, B.M., Wray, D.S., and Wright, D.K., 1999. Chemostratigraphy: a method to improve interwell correlation in barren sequences, a case study using onshore

Duckmantian/Stephanian sequences (West Midlands, U.K.). Sedimentary Geology, v. 124, p. 197–220.

Appendix 4-2: EPMA analyses

Analytical technique

Backscattered electron (BSE) imaging and mineral identification and characterisation for many samples was undertaken using a JEOL-JXA8200 super probe with the Armstrong-CITZAF (phi-rho-Z) matrix correction program (Armstrong, 1988, 1991), housed at Advanced Analytical Centre (AAC), James Cook University (JCU). Quantitative Wavelength Dispersive Spectrometry (WDS) analyses were conducted on carbon-coated polished thin sections using a 20 nA beam defocused to 5 µm, and accelerating voltage of 15 kV. The elements measured were Na, Fe, Ca, Si, K, Al, Mn, Cl, Mg, Ti and F. Mineral formulae of white mica is normalised to 11 oxygen, assuming all Fe as Fe^{2+}. Natural and synthetic standards were used for calibration. Further information on the electron probe microanalysis (EPMA) analytical conditions are presented in Table 1. Compositional mineral analysis of pre- and syn-ore white mica is presented in Table 2.

Table 1: Analytical conditions for EPMA measurement of white mica

				Count time (sec.)	
Element	**Standard**	**Line**	**Channel**	**Peak**	**Background**
Na	Na_2O	Kα	TAP	20	10
Fe	FeO	Kα	LIF	20	10
Ca	CaO	Kα	PETH	20	10
Si	SiO_2	Kα	TAP	20	10
K	K_2O	Kα	PETJ	20	10
Al	Al_2O_3	Kα	TAP	20	10
Mn	MnO	Kα	LIF	20	10
Cl	Cl	Kα	PETH	20	10
Mg	MgO	Kα	TAP	20	10
Ti	TiO_2	Kα	LIF	20	10
F	F	Kα	TAP	20	10

Table 2: EPMA analyses of pre- and syn-ore muscovite

Paragenesis	Pre-ore	Pre-ore	Pre-ore	Pre-ore	Pre-ore	Pre-ore	Pre-ore	Pre-ore	Pre-ore	Pre-ore	Pre-ore	Pre-ore	Pre-ore	Pre-ore	Pre-ore
Sample No	NM1_2	NM1_3	NM1_4	NM1_5	NM1_6	NM1_7	NM1_8	NM1_9	NM1_10	NM1_11	NM1_12	NM1_14	NM1_16	NM1_17	NM1_18
CaO	0.00	0.00	0.00	0.00	0.00	0.00	0.00	0.00	0.00	0.00	0.00	0.00	0.00	0.00	0.00
Na_2O	0.16	0.20	0.22	0.18	0.12	0.24	0.21	0.18	0.19	0.13	0.20	0.20	0.18	0.16	0.20
K_2O	11.39	11.51	11.32	11.53	11.45	11.33	11.35	11.3	11.29	11.43	11.54	11.54	11.31	11.46	11.2
FeO	0.56	0.56	0.70	0.72	0.41	0.93	0.67	0.53	0.65	0.39	0.54	0.59	0.32	0.38	0.65
TiO_2	0.05	0.06	0.07	0.03	0.03	0.02	0.01	0.07	0.00	0.02	0.07	0.04	0.02	0.08	0.01
MgO	3.00	2.03	2.63	3.23	3.15	3.01	3.02	3.13	2.89	3.26	2.94	2.71	1.88	2.44	2.82
SiO_2	49.94	48.88	49.39	49.87	50.21	48.75	49.24	49.81	48.27	51.25	50.02	49.65	49.10	49.95	49.70
MnO	0.04	0.02	0.02	0.03	0.00	0.00	0.00	0.00	0.00	0.00	0.00	0.01	0.00	0.05	0.03
Al_2O_3	31.74	33.96	32.64	30.90	30.98	32.48	32.72	31.46	32.57	30.82	31.95	32.63	34.79	32.85	31.88
F	0.00	0.00	0.02	0.00	0.00	0.00	0.00	0.02	0.00	0.00	0.00	0.00	0.00	0.00	0.00
Cl	0.00	0.00	0.00	0.00	0.00	0.01	0.00	0.00	0.00	0.00	0.00	0.01	0.01	0.00	0.01
Total	96.88	97.22	97.02	96.50	96.36	96.77	97.22	96.51	95.86	97.30	97.27	97.37	97.61	97.37	96.49
Ca	0.00	0.00	0.00	0.00	0.00	0.00	0.00	0.00	0.00	0.00	0.00	0.00	0.00	0.00	0.00
Na	0.02	0.03	0.03	0.02	0.02	0.03	0.03	0.02	0.02	0.02	0.03	0.02	0.02	0.02	0.03
K	0.95	0.96	0.94	0.96	0.96	0.94	0.94	0.94	0.95	0.95	0.96	0.96	0.94	0.95	0.94
Fe	0.03	0.03	0.04	0.04	0.02	0.05	0.04	0.03	0.04	0.02	0.03	0.03	0.02	0.02	0.04
Ti	0.00	0.00	0.00	0.00	0.00	0.00	0.00	0.00	0.00	0.00	0.00	0.00	0.00	0.00	0.00
Mg	0.29	0.20	0.26	0.32	0.31	0.29	0.29	0.31	0.28	0.32	0.28	0.26	0.18	0.24	0.28
Mn	0.00	0.00	0.00	0.00	0.00	0.00	0.00	0.00	0.00	0.00	0.00	0.00	0.00	0.00	0.00
Al	2.44	2.61	2.51	2.39	2.40	2.50	2.51	2.43	2.53	2.36	2.45	2.50	2.66	2.52	2.46
Total	3.74	3.82	3.78	3.73	3.70	3.82	3.80	3.74	3.82	3.67	3.75	3.78	3.82	3.75	3.74
Si	3.26	3.18	3.22	3.27	3.30	3.18	3.20	3.26	3.18	3.33	3.25	3.22	3.18	3.25	3.26
Total	7	7	7	7	7	7	7	7	7	7	7	7	7	7	7
F	0.00	0.00	0.00	0.00	0.00	0.00	0.00	0.00	0.00	0.00	0.00	0.00	0.00	0.00	0.00
Cl	0.00	0.00	0.00	0.00	0.00	0.00	0.00	0.00	0.00	0.00	0.00	0.00	0.00	0.00	0.00
OH	2.00	2.00	2.00	2.00	2.00	2.00	2.00	2.00	2.00	2.00	2.00	2.00	2.00	2.00	2.00
Total	2	2	2	2	2	2	2	2	2	2	2	2	2	2	2

(Continued)

Paragenesis	Pre-ore	Pre-ore	Pre-ore	Pre-ore	Pre-ore	Pre-ore	Pre-ore	Pre-ore	Pre-ore	Pre-ore	Pre-ore	Pre-ore	Pre-ore	Pre-ore	Pre-ore
Sample No	NM1_19	NM1_20	W5-1_2	W5-1_4	W5-1_6	W5-1_7	W5-1_8	W5-1_9	W5-1_11	W5-1_12	W5-1_13	W5-1_14	W5-1_15	W5-1_16	W5-1_20
CaO	0.00	0.00	0.00	0.00	0.00	0.00	0.00	0.00	0.00	0.00	0.02	0.00	0.00	0.00	0.01
Na_2O	0.23	0.21	0.41	0.38	0.39	0.37	0.40	0.28	0.34	0.24	0.39	0.40	0.35	0.30	0.29
K_2O	11.43	11.32	11.16	11	11.02	10.99	10.78	11.19	11.25	11.2	10.61	11.01	11.05	11.22	11.07
FeO	0.73	0.73	1.91	1.92	1.91	1.96	1.87	1.95	1.95	1.24	1.90	1.86	2.00	1.83	1.63
TiO_2	0.03	0.07	0.14	0.04	0.15	0.06	0.12	0.18	0.10	0.04	0.16	0.11	0.16	0.09	0.08
MgO	2.92	2.97	1.37	1.36	1.27	1.28	1.27	1.49	1.49	1.86	1.44	1.40	1.42	1.66	1.67
SiO_2	49.32	49.69	47.11	46.98	46.49	46.92	45.64	47.67	46.83	50.12	46.77	46.96	46.99	47.74	48.63
MnO	0.00	0.00	0.00	0.00	0.00	0.01	0.00	0.00	0.00	0.00	0.03	0.00	0.05	0.03	0.00
Al_2O_3	32.83	32.62	33.56	33.59	34.05	33.94	32.36	32.66	33.27	31.88	33.37	33.00	33.26	32.48	32.79
F	0.07	0.02	0.00	0.00	0.00	0.04	0.00	0.00	0.00	0.00	0.00	0.00	0.00	0.00	0
Cl	0.00	0.00	0.01	0.00	0.00	0.01	0.14	0.00	0.01	0.01	0.00	0.02	0.01	0.00	0.01
Total	97.56	97.63	95.67	95.26	95.28	95.57	92.57	95.43	95.24	96.59	94.70	94.76	95.28	95.36	96.18
Ca	0.00	0.00	0.00	0.00	0.00	0.00	0.00	0.00	0.00	0.00	0.00	0.00	0.00	0.00	0.00
Na	0.03	0.03	0.05	0.05	0.05	0.05	0.05	0.04	0.04	0.03	0.05	0.05	0.05	0.04	0.04
K	0.94	0.94	0.95	0.94	0.94	0.93	0.95	0.95	0.96	0.94	0.91	0.94	0.94	0.95	0.93
Fe	0.04	0.04	0.11	0.11	0.11	0.11	0.11	0.11	0.11	0.07	0.11	0.10	0.11	0.10	0.09
Ti	0.00	0.00	0.01	0.00	0.01	0.00	0.01	0.01	0.01	0.00	0.01	0.01	0.01	0.00	0.00
Mg	0.28	0.29	0.14	0.13	0.13	0.13	0.13	0.15	0.15	0.18	0.14	0.14	0.14	0.16	0.16
Mn	0.00	0.00	0.00	0.00	0.00	0.00	0.00	0.00	0.00	0.00	0.00	0.00	0.00	0.00	0.00
Al	2.51	2.49	2.63	2.64	2.67	2.66	2.62	2.57	2.61	2.47	2.64	2.61	2.62	2.55	2.55
Total	3.80	3.78	3.87	3.87	3.90	3.88	3.86	3.82	3.88	3.70	3.86	3.85	3.86	3.82	3.78
Si	3.20	3.22	3.13	3.13	3.10	3.12	3.14	3.18	3.12	3.30	3.14	3.15	3.14	3.18	3.22
Total	7	7	7	7	7	7	7	7	7	7	7	7	7	7	7
F	0.01	0.00	0.00	0.00	0.00	0.01	0.00	0.00	0.00	0.00	0.00	0.00	0.00	0.00	0.00
Cl	0.00	0.00	0.00	0.00	0.00	0.00	0.02	0.00	0.00	0.00	0.00	0.00	0.00	0.00	0.00
OH	1.99	2.00	2.00	2.00	2.00	1.99	1.98	2.00	2.00	2.00	2.00	2.00	2.00	2.00	2.00
Total	2	2	2	2	2	2	2	2	2	2	2	2	2	2	2

(Continued)

Paragenesis	Syn-ore	Syn-ore	Syn-ore	Syn-ore	Syn-ore	Syn-ore	Syn-ore	Syn-ore	Syn-ore	Syn-ore	Syn-ore	Syn-ore	Syn-ore	Syn-ore	Syn-ore
Sample No	W5-6B_1	W5-6B_2	W5-6B_4	W5-6B_5	W5-6B_8	W5-6B_9	W5-6B_10	W5-8_2	W5-8_3	W5-8_5	W5-8_7	W5-8_8	W5-8_10	W5-12_3	W5-12_4
CaO	0.00	0.00	0.01	0.01	0.02	0.01	0.01	0.09	0.02	0.01	0.05	0.03	0.03	0.02	0.01
Na_2O	0.07	0.07	0.03	0.05	0.07	0.06	0.07	0.08	0.05	0.03	0.08	0.04	0.02	0.04	0.04
K_2O	10.02	10.02	10.06	9.98	9.78	10.07	9.75	10.10	9.29	9.07	9.29	10.02	9.42	10.33	10.16
FeO	0.88	0.86	0.88	0.78	0.92	0.84	0.90	0.77	0.76	0.85	0.70	0.58	0.88	1.13	1.00
TiO_2	0.00	0.02	0.03	0.00	0.05	0.01	0.04	0.01	0.07	0.00	0.00	0.00	0.06	0.00	0.00
MgO	2.72	2.79	2.41	2.66	2.64	2.65	2.72	2.01	1.80	2.20	1.99	1.98	2.30	2.84	2.74
SiO_2	53.39	54.08	52.68	53.99	52.24	52.94	52.94	52.00	51.28	51.89	50.99	51.92	52.62	52.31	49.09
MnO	0.00	0.00	0.02	0.00	0.00	0.06	0.00	0.03	0.00	0.01	0.00	0.00	0.02	0.00	0.00
Al_2O_3	30.40	30.19	30.09	30.37	29.30	29.25	30.02	31.57	31.67	30.54	30.80	32.10	30.94	29.40	27.33
F	0.00	0.00	0.46	0.00	0.00	0.46	0.02	0.31	0.11	0.31	0.09	0.15	0.09	0.24	0.00
Cl	0.01	0.01	0.02	0.01	0.07	0.03	0.02	0.01	0.02	0.01	0.01	0.01	0.01	0.02	0.04
Total	97.49	98.05	96.69	97.85	95.10	96.37	96.49	96.98	95.07	94.92	94.00	96.83	96.39	96.34	90.42
Ca	0.00	0.00	0.00	0.00	0.00	0.00	0.00	0.01	0.00	0.00	0.00	0.00	0.00	0.00	0.00
Na	0.01	0.01	0.00	0.01	0.01	0.01	0.01	0.01	0.01	0.00	0.01	0.00	0.00	0.00	0.01
K	0.84	0.83	0.85	0.83	0.84	0.86	0.82	0.85	0.80	0.78	0.81	0.84	0.80	0.88	0.91
Fe	0.05	0.05	0.05	0.04	0.05	0.05	0.05	0.04	0.04	0.05	0.04	0.03	0.05	0.06	0.06
Ti	0.00	0.00	0.00	0.00	0.00	0.00	0.00	0.00	0.00	0.00	0.00	0.00	0.00	0.00	0.00
Mg	0.27	0.27	0.24	0.26	0.26	0.26	0.27	0.20	0.18	0.22	0.20	0.19	0.23	0.28	0.29
Mn	0.00	0.00	0.00	0.00	0.00	0.00	0.00	0.00	0.00	0.00	0.00	0.00	0.00	0.00	0.00
Al	2.35	2.32	2.35	2.34	2.32	2.30	2.34	2.46	2.51	2.43	2.47	2.50	2.42	2.30	2.27
Total	3.51	3.48	3.50	3.48	3.49	3.47	3.50	3.57	3.55	3.49	3.53	3.57	3.51	3.53	3.54
Si	3.49	3.52	3.50	3.52	3.51	3.53	3.50	3.43	3.45	3.51	3.47	3.43	3.49	3.47	3.46
Total	7	7	7	7	7	7	7	7	7	7	7	7	7	7	7
F	0.00	0.00	0.10	0.00	0.00	0.10	0.00	0.06	0.02	0.07	0.02	0.03	0.02	0.05	0.00
Cl	0.00	0.00	0.00	0.00	0.01	0.00	0.00	0.00	0.00	0.00	0.00	0.00	0.00	0.00	0.01
OH	2.00	2.00	1.90	2.00	1.99	1.90	1.99	1.93	1.97	1.93	1.98	1.97	1.98	1.95	1.99
Total	2	2	2	2	2	2	2	2	2	2	2	2	2	2	2

(Continued)

Paragenesis	Syn-ore	Syn-ore	Syn-ore	Syn-ore	Syn-ore	Syn-ore	Syn-ore	Syn-ore	Syn-ore	Syn-ore	Syn-ore	Syn-ore	Syn-ore	Syn-ore	Syn-ore
Sample No	W5-12_6	W5-12_9	W5-12_11	W5-12_12	W5-4_1	W5-4_2	W5-4_3	W5-4_5	W5-4_7	W5-4_8	W5-4_13	W5-4_15	W5-4_16	W5-6_2	W5-6_3
CaO	0.01	0.04	0.03	0.02	0.04	0.05	0.05	0.06	0.10	0.06	0.03	0.04	0.01	0.03	0.03
Na_2O	0.08	0.09	0.07	0.07	0.10	0.10	0.10	0.08	0.09	0.04	0.09	0.06	0.04	0.09	0.23
K_2O	10.02	9.67	9.77	10.40	10.10	9.47	10.03	10.14	9.66	9.78	10.12	10.08	9.70	10.09	9.41
FeO	1.04	0.63	1.01	1.07	0.58	0.60	0.54	0.69	0.61	0.63	0.55	0.72	0.58	0.59	0.51
TiO_2	0.17	0.04	0.03	0.02	0.06	0.00	0.00	0.00	0.08	0.00	0.00	0.00	0.00	0.00	0.00
MgO	2.58	1.66	2.68	2.67	2.11	2.09	1.92	2.09	2.15	2.25	2.18	2.26	1.96	2.67	2.15
SiO_2	50.18	50.57	50.52	50.29	52.11	49.55	51.70	51.73	52.27	50.88	52.91	52.68	48.53	53.38	50.61
MnO	0.02	0.00	0.00	0.01	0.00	0.00	0.00	0.00	0.00	0.01	0.00	0.00	0.00	0.01	0.00
Al_2O_3	27.99	31.94	28.83	28.01	31.46	29.86	31.60	31.16	29.98	28.73	31.66	31.27	30.21	30.79	30.10
F	0.02	0.46	0.02	0.29	0.09	0.09	0.18	0.18	0.22	0.18	0.22	0.15	0.31	0.13	0.11
Cl	0.03	0.02	0.02	0.02	0.03	0.03	0.04	0.03	0.02	0.04	0.01	0.04	0.02	0.01	0.09
Total	92.15	95.12	92.99	92.88	96.68	91.84	96.16	96.15	95.18	92.60	97.77	97.31	91.37	97.79	93.24
Ca	0.00	0.00	0.00	0.00	0.00	0.00	0.00	0.00	0.01	0.00	0.00	0.00	0.00	0.00	0.00
Na	0.01	0.01	0.01	0.01	0.01	0.01	0.01	0.01	0.01	0.01	0.01	0.01	0.01	0.01	0.03
K	0.89	0.83	0.86	0.91	0.85	0.84	0.85	0.86	0.83	0.86	0.84	0.84	0.87	0.84	0.82
Fe	0.06	0.04	0.06	0.06	0.03	0.04	0.03	0.04	0.03	0.04	0.03	0.04	0.03	0.03	0.03
Ti	0.01	0.00	0.00	0.00	0.00	0.00	0.00	0.00	0.00	0.00	0.00	0.00	0.00	0.00	0.00
Mg	0.27	0.17	0.27	0.27	0.21	0.22	0.19	0.21	0.22	0.23	0.21	0.22	0.20	0.26	0.22
Mn	0.00	0.00	0.00	0.00	0.00	0.00	0.00	0.00	0.00	0.00	0.00	0.00	0.00	0.00	0.00
Al	2.29	2.54	2.33	2.27	2.45	2.45	2.48	2.44	2.38	2.34	2.44	2.42	2.49	2.37	2.43
Total	3.52	3.59	3.53	3.54	3.56	3.56	3.56	3.56	3.48	3.48	3.54	3.54	3.60	3.52	3.53
Si	3.48	3.41	3.47	3.46	3.44	3.44	3.44	3.44	3.52	3.52	3.46	3.46	3.40	3.48	3.47
Total	7	7	7	7	7	7	7	7	7	7	7	7	7	7	7
F	0.00	0.10	0.00	0.06	0.02	0.02	0.04	0.04	0.05	0.04	0.05	0.03	0.07	0.03	0.02
Cl	0.00	0.00	0.00	0.00	0.00	0.00	0.00	0.00	0.00	0.00	0.00	0.00	0.00	0.00	0.01
OH	1.99	1.90	1.99	1.94	1.98	1.98	1.96	1.96	1.95	1.96	1.95	1.96	1.93	1.97	1.97
Total	2	2	2	2	2	2	2	2	2	2	2	2	2	2	2

(Continued)

Paragenesis	Syn-ore	Syn-ore	Syn-ore	Syn-ore	Syn-ore	Syn-ore	Syn-ore	Syn-ore	Syn-ore	Syn-ore
Sample No	W5-6_6	W5-6_7	W5-6_8	W5-6_9	W5-6_10	W5-6_12	W5-6_13	W5-6_15	W5-6_19	W5-6_20
CaO	0.04	0.05	0.06	0.04	0.04	0.07	0.05	0.04	0.04	0.09
Na_2O	0.09	0.06	0.12	0.10	0.10	0.05	0.11	0.09	0.08	0.10
K_2O	9.83	9.72	9.88	10.06	9.59	7.78	9.70	9.93	9.78	9.85
FeO	0.57	0.55	0.59	0.51	0.54	0.28	0.47	0.49	0.50	0.57
TiO_2	0.00	0.00	0.03	0.00	0.00	0.07	0.00	0.00	0.01	0.00
MgO	2.53	2.46	2.43	2.22	2.10	1.58	2.61	2.36	2.34	2.28
SiO_2	54.11	52.50	52.09	52.32	52.44	49.88	52.77	53.30	51.61	51.77
MnO	0.00	0.00	0.02	0.00	0.04	0.00	0.00	0.00	0.01	0.00
Al_2O_3	31.48	31.33	30.66	32.09	31.44	33.56	31.02	31.55	29.80	31.12
F	0.11	0.39	0.24	0.22	0.13	0.50	0.26	0.29	0.18	0.11
Cl	0.01	0.04	0.02	0.02	0.02	0.03	0.02	0.03	0.04	0.01
Total	98.76	97.11	96.13	97.58	96.44	93.79	97.01	98.08	94.40	95.90
Ca	0.00	0.00	0.00	0.00	0.00	0.00	0.00	0.00	0.00	0.01
Na	0.01	0.01	0.02	0.01	0.01	0.01	0.01	0.01	0.01	0.01
K	0.81	0.82	0.84	0.84	0.81	0.68	0.82	0.83	0.85	0.84
Fe	0.03	0.03	0.03	0.03	0.03	0.02	0.03	0.03	0.03	0.03
Ti	0.00	0.00	0.00	0.00	0.00	0.00	0.00	0.00	0.00	0.00
Mg	0.24	0.24	0.24	0.22	0.21	0.16	0.26	0.23	0.24	0.23
Mn	0.00	0.00	0.00	0.00	0.00	0.00	0.00	0.00	0.00	0.00
Al	2.40	2.44	2.40	2.48	2.46	2.71	2.41	2.43	2.38	2.44
Total	3.50	3.54	3.54	3.58	3.52	3.58	3.52	3.52	3.50	3.55
Si	3.50	3.46	3.46	3.42	3.48	3.42	3.48	3.48	3.50	3.45
Total	7	7	7	7	7	7	7	7	7	7
F	0.02	0.08	0.05	0.05	0.03	0.11	0.05	0.06	0.04	0.02
Cl	0.00	0.00	0.00	0.00	0.00	0.00	0.00	0.00	0.00	0.00
OH	1.98	1.91	1.95	1.95	1.97	1.89	1.94	1.94	1.96	1.98
Total	2	2	2	2	2	2	2	2	2	2

Formula (a.p.f.u.) calculated based on 11 oxygen

References

Armstrong, J.T., 1988. Quantitative analysis of silicate and oxide minerals: Comparison of Monte-Carlo, ZAF, and phi-rho-Z procedures. In Newbery, D.E., (Ed.), Microbeam Analysis: San Francisco, p. 239-246.

Armstrong, J.T., 1991. Quantitative elemental analysis of individual microparticles with electron beam instruments. In Heinrich, K.F.J., and Newbery, D.E., (Eds.), Electron Probe Quantitation: Plenum Press.

Appendix 4-3: U-Pb isotopic analysis

Sampling and Petrography

The representative ore samples were selected from a much larger set of outcrop and core samples collected by the authors between 2014 and 2016. The samples were lightly brushed and washed in an ultrasonic bath to remove any contamination from drilling mud. A slice of the sample was used for thin section and petrographic studies using conventional optical microscopy under a transmitted and reflected light microscope. Microscopic studies were further complimented by backscattered electron imaging (BSE).

Analytical Technique

In-situ laser ablation inductively-coupled plasma mass spectroscopy (LA-ICP-MS) U-Pb dating of xenotime was conducted at Advanced Analytical Centre (AAC), James Cook University (JCU), using a GeoLas Pro 193 nm excimer laser, and a Bruker (formally Varian) 820-MS ICP-MS. The ICP-MS was tuned to ensure approximately equal sensitivity of U, Th and Pb to minimize isotope fractionation due to matrix effect. Further details of the instrumental and analytical set-up are available in Spandler et al. (2016). Analytes collected were ^{31}P, ^{89}Y, ^{204}Pb, ^{206}Pb, ^{207}Pb, ^{208}Pb, ^{232}Th, ^{235}U and ^{238}U. The standards used in the analyses included z6413 (primary), MG-1 and BS-1 (secondary) xenotime (Fletcher et al., 2004). For quantification of U and Th concentration in xenotime, analysis of the NIST-SRM-612 reference glass conducted at the beginning, middle and end of every analytical session with ^{89}Y used as the internal standard assuming perfect xenotime stoichiometry. Xenotime analysis was undertaken using a beam diameter of 24 µm, and laser energy of 6 J/cm^2. All data reduction was carried out by GLITTER software (Van Achterbergh et al., 2001). All time-resolved single isotope signals from standards and samples were filtered for signal spikes or perturbations related to inclusions and fractures. Subsequently, the most stable and representative ratios were selected taking into account possible mixing of different age domains and zoning. Analysis of secondary standards MG-1 (492 ± 3 Ma) and BS-1 (506 ± 5 Ma) compare well with the published values of 490.1 Ma for MG-1 and 508.8 Ma for BS-1 (Fletcher et al., 2004), demonstrating the accuracy of our technique.

Table 1: U-Pb isotopic data

	U (ppm)	Th (ppm)	Th/U	$^{207}Pb/^{206}Pb$	±1s	$^{207}Pb/^{235}U$	±1s	$^{206}Pb/^{238}U$	±1s	$^{207}Pb/^{206}Pb$ age (Ma)	±1s	$^{207}Pb/^{235}U$ age (Ma)	±1s	$^{206}Pb/^{238}U$ age (Ma)	±1s	Discordance (%)
W5-3_1*	4080	35	0.01	0.0990	0.0010	3.8501	0.0385	0.2820	0.0028	1606	19	1603	8	1602	14	0.3
W5-3_3*	3216	16	0.00	0.1008	0.0010	3.9546	0.0397	0.2845	0.0028	1630	19	1625	8	1614	14	0.9
W5-3_4*	2001	5	0.00	0.0986	0.0010	3.8260	0.0392	0.2815	0.0028	1598	19	1598	8	1599	14	-0.1
W5-3_10*	2610	3	0.00	0.1000	0.0010	3.9828	0.0406	0.2888	0.0029	1625	19	1631	8	1636	14	-0.7
W5-3_11*	2475	11	0.00	0.0993	0.0011	3.9040	0.0404	0.2852	0.0028	1611	20	1615	8	1618	14	-0.4
W5-3_12*	2060	13	0.01	0.0997	0.0011	3.9546	0.0414	0.2877	0.0028	1619	20	1625	8	1630	14	-0.7
W5-3_13*	2399	1	0.00	0.0997	0.0011	3.9685	0.0411	0.2889	0.0028	1618	20	1628	8	1626	14	-0.5
W5-3_15	2494	5	0.00	0.0993	0.0011	4.2177	0.0433	0.3080	0.0030	1612	20	1678	8	1731	15	-7.4
W5-3_16*	2298	12	0.01	0.0991	0.0011	3.8596	0.0399	0.2824	0.0028	1608	20	1605	8	1603	14	0.3
W5-3_18*	2253	6	0.00	0.0983	0.0011	3.8620	0.0400	0.2851	0.0028	1603	20	1606	8	1617	14	-0.8
W5-3_19*	4171	183	0.04	0.0988	0.0010	3.9051	0.0393	0.2867	0.0028	1613	19	1615	8	1625	14	-0.8
W5-3_20	2466	7	0.00	0.0985	0.0011	4.0717	0.0421	0.3000	0.0029	1595	20	1649	8	1691	15	-6.0
W5-5-2*	1456	3	0.00	0.0987	0.0010	3.8565	0.0513	0.2834	0.0038	1600	19	1605	11	1608	19	-0.5
W5-5-7*	1359	2	0.00	0.1000	0.0010	3.9206	0.0520	0.2845	0.0038	1623	19	1618	11	1614	19	0.6
W5-5-8*	1694	7	0.00	0.0985	0.0010	3.9072	0.0517	0.2879	0.0039	1611	19	1615	11	1620	19	-0.5
W5-5-10*	1945	13	0.01	0.0996	0.0010	3.9454	0.0521	0.2874	0.0039	1622	19	1623	11	1628	19	-0.4
W5-5-11*	2336	2	0.00	0.0998	0.0010	3.8780	0.0511	0.2819	0.0038	1611	19	1609	11	1601	19	0.6
W5-5-12*	1763	0	0.00	0.0997	0.0010	3.9306	0.0520	0.2861	0.0038	1618	19	1620	11	1622	19	-0.2
W5-5-13*	1855	2	0.00	0.0994	0.0010	3.9564	0.0521	0.2887	0.0039	1613	19	1625	11	1635	19	-1.4
W5-5-15*	2830	3	0.00	0.1003	0.0010	3.9808	0.0522	0.2881	0.0039	1629	18	1630	11	1632	19	-0.2
C2-2*	5110	120	0.02	0.0999	0.0010	3.9846	0.0501	0.2892	0.0037	1633	18	1631	10	1637	19	-0.3
C2-3*	5780	154	0.03	0.1004	0.0010	3.9761	0.0501	0.2872	0.0037	1632	18	1629	10	1628	18	0.3
C2-5*	4219	93	0.02	0.0997	0.0010	3.9562	0.0499	0.2878	0.0037	1629	18	1625	10	1630	18	-0.1
C2-7*	4655	114	0.02	0.0996	0.0010	3.9949	0.0504	0.2910	0.0037	1626	18	1633	10	1637	19	-0.6
C2-8*	4150	124	0.03	0.0996	0.0010	4.0502	0.0510	0.2949	0.0038	1627	18	1644	10	1646	19	-1.2
C2-9*	4989	118	0.02	0.1001	0.0010	4.0856	0.0514	0.2960	0.0038	1646	18	1651	10	1651	19	-0.3
C2-10*	3761	183	0.05	0.0998	0.0010	4.0912	0.0516	0.2972	0.0038	1651	18	1653	10	1657	19	-0.4
C2-11*	3995	154	0.04	0.1004	0.0010	4.0149	0.0506	0.2900	0.0037	1632	18	1637	10	1641	19	-0.6
C2-12*	4559	117	0.03	0.0994	0.0010	4.0335	0.0507	0.2943	0.0038	1640	18	1641	10	1643	19	-0.2
C2-14*	4920	134	0.03	0.1001	0.0010	4.0724	0.0512	0.2952	0.0038	1645	18	1649	10	1647	19	-0.1
C2-15	4951	119	0.02	0.0999	0.0010	4.1886	0.0527	0.3040	0.0039	1623	18	1672	10	1711	19	-5.4
BR1-4*	5434	8	0.00	0.0988	0.0010	3.9429	0.0478	0.2894	0.0036	1619	19	1623	10	1629	18	-0.6
BR1-8*	5619	11	0.00	0.0991	0.0010	3.8311	0.0463	0.2805	0.0034	1607	19	1599	10	1594	17	0.8
BR1-10*	5843	11	0.00	0.0986	0.0010	3.8292	0.0462	0.2818	0.0035	1597	19	1599	10	1600	17	-0.2
BR1-12	6029	14	0.00	0.1000	0.0010	3.7083	0.0447	0.2689	0.0033	1625	19	1573	10	1535	17	5.5
BR1-17*	6547	7	0.00	0.0997	0.0011	3.9649	0.0559	0.2884	0.0041	1625	20	1627	11	1633	20	-0.5
BR1-18*	6620	7	0.00	0.0991	0.0011	3.9387	0.0555	0.2882	0.0040	1618	20	1622	11	1623	20	-0.3
BR1-19*	8164	10	0.00	0.0985	0.0011	3.7508	0.0531	0.2784	0.0039	1590	20	1589	11	1583	20	0.4
BR1-20*	8174	11	0.00	0.0997	0.0011	3.8973	0.0547	0.2836	0.0040	1618	20	1613	11	1610	20	0.5
BR1-23*	6879	8	0.00	0.0989	0.0011	3.9044	0.0547	0.2865	0.0040	1613	20	1615	11	1616	20	-0.2
BR1-27*	6228	9	0.00	0.0985	0.0011	3.8743	0.0544	0.2853	0.0040	1596	20	1608	11	1618	20	-1.4
BR1-30*	6253	19	0.00	0.0983	0.0011	3.7960	0.0531	0.2803	0.0039	1591	20	1592	11	1593	20	-0.1

Discordance = $100*(^{207}Pb/^{206}Pb-^{238}U/^{206}Pb)/(^{207}Pb/^{206}Pb)$.

References

Fletcher, I.R., McNaughton, N.J., Aleinikoff, J.A., Rasmussen, B., and Kamo, S.L., 2004. Improved calibration procedures and new standards for U-Pb and Th-Pb dating of Phanerozoic xenotime by ion microprobe. Chemical Geology, v. 209, p. 295–314.

Spandler, C., Hammerli, J., Sha, P., Hilbert-Wolf, H., Hu, Y., Roberts, E., and Schmitz, M., 2016. MKED1: a new titanite standard for in situ analysis of Sm-Nd isotopes and U-Pb geochronology. Chemical Geology, v. 425, p. 110–126.

Van Achterbergh, E., Ryan, C.G., Jackson, S.E., and Griffin, W.L., 2001. Data reduction software for LA-ICP-MS. In: Sylvester, P.J., (Ed.), Laser Ablation-ICP Mass Spectrometry in the Earth Sciences: Principles and Applications. Mineralogical Association of Canada, v. 29, p. 239–243.

Appendix 4-4: Sm-Nd isotopic analysis

Introduction

In this contribution we have determined the Sm-Nd isotope composition of the xenotime orebodies using two approaches: (1) Bulk analysis of two orebody samples by TIMS, and (2) In situ microanalysis of xenotime from a number of deposits/prospects by laser ablation multi-collector ICP-MS. We have also analysed the isotopic composition of four samples of the Browns Range Metamorphic (BRM) that host the ore.

Whole-Rock Sm-Nd Isotopic Analysis

Whole-rock Sm-Nd isotopic analysis was conducted on two samples of ore from the Wolverine Deposit (samples W5-2 and W5-6) and four representative samples of the BRM (samples W5-1, W5-13, W16-4, and G5-5). Samarium-Nd isotope analysis of selected rock powders was performed at the University of Adelaide with a Finnigan-MAT262 thermal ionization mass spectrometer (TIMS), in static and quadruple cup dynamic measurement modes following the routine described in Wade et al. (2006). Between 50 to 200 mg of the samples were digested in PARR acid (HNO_3-HF acid mix) digestion bombs at 190 ºC for 96 hours, then evaporated to dryness and bombed with 6M HCl overnight. The samples were then spiked with a ^{150}Nd-^{147}Sm spike. The measurements were corrected for mass fractionation by normalization to $^{146}Nd/^{144}Nd = 0.7219$. Neodymium and Sm concentrations were calculated by isotope dilution and were corrected for 200 pg and 150 pg blanks, respectively. Reference material JNdi-1 was 0.512083 ± 13 (2σ) (n=9). $^{143}Nd/^{144}Nd$ ratios were normalized to the TIMS value of the JNdi-1 glass (0.512098 ± 13; Fisher et al. 2011).

In-Situ Sm-Nd Isotopic Analysis

Laser ablation Nd isotope analyses of xenotime were undertaken at the Advanced Analytical Centre (AAC), James Cook University (JCU), using a GeoLas 193nm ArF Excimer laser ablation system connected to a Thermo-Scientific Neptune multi-collector ICP-MS, following the set-up outlined in Hammerli et al. (2014). In-situ laser ablation analyses were conducted on polished thin sections over 60s with spot sizes of 16-90 μm, pulse rates of 4 Hz and a laser energy density at the sample site of 5 to 6 J/cm^2, as determined by an energy meter. Ablation

was carried out in He (typical flow rate ~0.9 l/min), which was combined with Ar (~0.8 l/min, optimized daily) and N_2 (~0.005 l/min) prior to transport into the torch. Interference and mass bias corrections were made according to the method of Fisher et al. (2011). The $^{147}Sm/^{144}Nd$ ratios were calibrated against a synthetic LREE-rich silicate glass ($^{147}Sm/^{144}Nd$ = 0.2451; Fisher et al., 2011), which was routinely analysed throughout each session. Sample mineral $^{143}Nd/^{144}Nd$ ratios were further normalised to bracketing analyses of Nd-doped glass (JNdi-1, TIMS $^{143}Nd/^{144}Nd$, Fisher et al., 2011). Overall, three apatite grains were used as quality control material including Ap1, Ap2 and Durango Apatite. The $^{143}Nd/^{144}Nd$ results for Ap1 and Ap2 are 0.511341 ± 23 (2SD) and 0.510999 ± 56 (2SD), respectively, which agree well with the published data (Ap1: 0.511342 ± 31 (2SD) and Ap2: 0.510977 ± 39 (2SD)) of Yang et al. (2008). The analyses of Durango apatite produced $^{143}Nd/^{144}Nd$ value of 0.512467 ± 48 (2SD), which is in good agreement with the ratios acquired by LA-MC-ICP-MS reported by Foster and Vance (2006) (0.512469 ± 25) (2SD) and Fisher et al. (2011) (0.512463 ± 48), and the TIMS value of 0.512489 ± 12 (Fisher et al. 2011). The $^{143}Nd/^{144}Nd$ result for the LREE glass is 0.512096 ± 16 (2SD) which is indistinguishable from the value determined by TIMS (0.512098 ± 13, Fisher et al., 2011).

Complications with In-Situ Sm-Nd Isotopic Analysis

The in-situ Sm-Nd isotopic analyses revealed that the ore xenotime from all samples is invariably zoned in Sm/Nd (and hence $^{143}Nd/^{144}Nd$) at the micrometer scale. This resulted in time resolved analytical signal for $^{143}Nd/^{144}Nd$ and $^{147}Sm/^{144}Nd$ that varied to a much larger degree that expected for the analytical precision (see Fig. 1). Although a limited number of analytical signals contained segments with relatively constant $^{143}Nd/^{144}Nd$ and $^{147}Sm/^{144}Nd$ ratios (Figs. 1A-B), most of the analyses produced relatively smooth patterns (e.g., relatively precise analyses) that varied significantly over the analysis period of ca. 60s (Figs. 1C-D). Additionally, some analyses illustrate two relatively flat plateaus with distinct isotopic compositions (Figs. 1E-F). We interpret these signals to represent sampling of micrometer-scale zoning of the xenotime grains, rather than contamination by inclusions or other analytical artefacts. During data processing, care was taken to select only relatively flat and stable intervals of the signals. In many cases this could not be completed, and these analyses were not further used (e.g., Figs. 1G-H). Nevertheless, despite careful signal processing, the results returned large analytical errors on the calculated isotope ratios.

Results

All analytical results are presented in Table 1 and Table 2. Although our in situ analysis of xenotime revealed highly variable $^{147}Sm/^{144}Nd$ (0.03636 to 6.41526) and $^{143}Nd/^{144}Nd$ (0.51030 to 0.57800) ratios, εNd values, calculated to 1.62 Ga (the age of ore formation) for all five HREE deposits/prospects, studied here (Wolverine, Area 5, Cyclops, Boulder Ridge and John Galt) fall within a similar (albeit broad) range from -12 to -28. These values are similar to εNd values calculated from the bulk ore samples of -13 and -17, and bulk rock values for the BRM of -15 to -24 (see manuscript text for more details).

Table 1: In-situ Sm-Nd analysis of xenotime

Deposit	Sample	$^{147}Sm/^{144}Nd$	$^{143}Nd/^{144}Nd$	CHUR	$^{143}Nd/^{144}Nd$ (i)	εNd (T=1.62 Ga)	2σ
Wolverine	W5-7-1 A	0.93786	0.52067	0.51055	0.50984	-13.9	4.9
Wolverine	W5-7-6 A	0.94875	0.52007	0.51055	0.50913	-27.9	1.9
Wolverine	W5-7-14 A	0.04512	0.51064	0.51055	0.50937	-23.1	1.3
Wolverine	W5-7-15 A	0.04879	0.51065	0.51055	0.50934	-23.7	1.1
Wolverine	W5-7-16 A	0.04002	0.51050	0.51055	0.50929	-24.7	1.1
Wolverine	W5-7-16 B	0.03637	0.51030	0.51055	0.50913	-27.7	1.5
Wolverine	W5-7-17 A	0.05706	0.51073	0.51055	0.50934	-23.8	1.2
Wolverine	W5-7-17 B	0.06808	0.51109	0.51055	0.50958	-19.1	1.0
Wolverine	W5-3-1 A	1.41552	0.52462	0.51055	0.50961	-18.5	1.2
Wolverine	W5-3-1 B	1.60014	0.52636	0.51055	0.50938	-22.9	3.0
Wolverine	W5-3-2 A	1.30835	0.52349	0.51055	0.50961	-18.3	1.3
Wolverine	W5-3-3 A	1.37710	0.52419	0.51055	0.50958	-18.9	0.6
Wolverine	W5-3-3 B	1.45671	0.52485	0.51055	0.50940	-22.5	4.1
Wolverine	W5-3-4 A	1.18957	0.52221	0.51055	0.50959	-18.8	1.3
Wolverine	W5-3-5 A	1.80171	0.52870	0.51055	0.50958	-18.9	1.5
Wolverine	W5-3-7 A	1.25728	0.52292	0.51055	0.50958	-19.0	0.8
Wolverine	W5-3-7 B	1.29121	0.52321	0.51055	0.50952	-20.2	0.9
Wolverine	W5-3-8 A	0.92916	0.51962	0.51055	0.50977	-15.3	0.8
Wolverine	W5-3-9 A	1.04971	0.52080	0.51055	0.50967	-17.2	0.9
Wolverine	W5-3-10 A	1.11226	0.52155	0.51055	0.50975	-15.7	2.3
Wolverine	W5-3-11 A	1.43639	0.52483	0.51055	0.50959	-18.8	0.8
Wolverine	W5-3-11 B	1.57730	0.52615	0.51055	0.50942	-22.1	1.8
Wolverine	W5-3-12 A	1.27975	0.52318	0.51055	0.50960	-18.5	3.1
Wolverine	W5-4-1 A	1.21598	0.52261	0.51055	0.50971	-16.4	3.1
Wolverine	W5-4-1 B	1.30667	0.52340	0.51055	0.50954	-19.8	1.4
Wolverine	W5-4-2 A	1.14844	0.52189	0.51055	0.50971	-16.5	1.7
Wolverine	W5-4-2 B	1.29180	0.52331	0.51055	0.50961	-18.5	1.6
Wolverine	W5-4-3 A	2.97382	0.54102	0.51055	0.50947	-21.1	6.7
Wolverine	W5-4-4 A	1.21312	0.52258	0.51055	0.50971	-16.5	1.4
Wolverine	W5-4-5 A	2.07509	0.53128	0.51055	0.50927	-25.2	2.7
Wolverine	W5-4-14 A	1.23862	0.52278	0.51055	0.50964	-17.8	1.2
Wolverine	W5-4-14 B	1.69903	0.52779	0.51055	0.50977	-15.4	2.8
Wolverine	W5-4-15 A	1.08770	0.52120	0.51055	0.50967	-17.3	1.1
Wolverine	W5-4-15 B	1.13404	0.52179	0.51055	0.50976	-15.4	2.0
Wolverine	W5-4-16 A	1.12250	0.52162	0.51055	0.50972	-16.3	1.3
Wolverine	W5-4-1 A	1.62957	0.52681	0.51055	0.50952	-20.2	1.3
Wolverine	W5-4-1 B	2.00709	0.53072	0.51055	0.50943	-22.0	1.2
Wolverine	W5-4-2 A	1.40267	0.52447	0.51055	0.50959	-18.9	2.8
Wolverine	W5-4-3 A	2.00261	0.53073	0.51055	0.50949	-20.8	4.2
Wolverine	W5-4-3 B	2.18952	0.53264	0.51055	0.50941	-22.3	2.7
Wolverine	W7-3-1 A	1.24208	0.52293	0.51055	0.50976	-15.6	1.9
Wolverine	W7-3-2 A	1.55334	0.52606	0.51055	0.50958	-18.9	2.4
Wolverine	W7-3-2 B	1.89545	0.52957	0.51055	0.50946	-21.4	5.2
Wolverine	W7-3-3 A	1.17112	0.52226	0.51055	0.50984	-13.9	1.1
Wolverine	W7-3-4 A	2.28286	0.53361	0.51055	0.50940	-22.6	1.9
Wolverine	W7-3-4 B	3.04467	0.54155	0.51055	0.50925	-25.4	9.1
Wolverine	W7-3-5 A	0.44392	0.51443	0.51055	0.50972	-16.2	8.6
Wolverine	W7-3-5 B	1.40225	0.52419	0.51055	0.50932	-24.2	6.7
Wolverine	W7-3-7 A	0.28712	0.51289	0.51055	0.50985	-13.7	2.4
Wolverine	W7-3-8 A	1.10308	0.52147	0.51055	0.50977	-15.3	1.7
Wolverine	W7-3-9 A	1.34967	0.52398	0.51055	0.50966	-17.4	2.8
Wolverine	W7-3-9 B	2.58106	0.53680	0.51055	0.50941	-22.3	6.8
Wolverine	W7-3-10 A	1.40753	0.52455	0.51055	0.50962	-18.3	2.5
Wolverine	W7-3-12 A	2.43714	0.53511	0.51055	0.50925	-25.4	5.6
Wolverine	W5-2B-1	2.36269	0.53410	0.51055	0.50923	-25.9	5.5
Wolverine	W5-2B-2	3.33014	0.54443	0.51055	0.50937	-23.2	6.2
Wolverine	W5-2B-3	2.02327	0.53096	0.51055	0.50966	-17.5	3.3
Wolverine	W5-2B-4	3.22924	0.54360	0.51055	0.50960	-18.6	3.9
Wolverine	W5-2B-6	1.49082	0.52529	0.51055	0.50959	-18.8	2.1
Wolverine	W5-2B-7	1.91812	0.52975	0.51055	0.50955	-19.6	5.1
Wolverine	W5-2B-8	1.33662	0.52363	0.51055	0.50955	-19.5	3.9
Wolverine	W5-2B-9	2.37399	0.53463	0.51055	0.50963	-18.0	2.8
Wolverine	W5-2B-10	2.40285	0.53467	0.51055	0.50937	-23.2	6.9
Cyclops	C2-1	2.72913	0.53804	0.51055	0.50931	-24.4	7.2
Cyclops	C2-2	4.63989	0.55804	0.51055	0.50918	-26.8	7.2
Cyclops	C2-3	1.38805	0.52416	0.51055	0.50954	-19.8	3.4
Cyclops	C2-4	3.77585	0.54894	0.51055	0.50918	-26.8	5.6
Cyclops	C2-5	1.84146	0.52883	0.51055	0.50944	-21.7	4.8
Cyclops	C2-6 A	2.08121	0.53123	0.51055	0.50931	-24.2	4.5
Cyclops	C2-6 B	1.34541	0.52374	0.51055	0.50957	-19.2	1.3
Cyclops	C2-7	1.71176	0.52748	0.51055	0.50945	-21.5	4.9
Cyclops	C2-8	2.15197	0.53186	0.51055	0.50920	-26.5	4.3
Cyclops	C2-9 A	2.00259	0.53059	0.51055	0.50950	-20.6	5.3
Cyclops	C2-9 B	2.41124	0.53480	0.51055	0.50941	-22.3	5.1
Cyclops	C2-10	1.51791	0.52559	0.51055	0.50961	-18.5	5.7
Boulder Ridge	BR1-5	4.76393	0.56012	0.51055	0.50932	-24.0	9.3
Boulder Ridge	BR1-6 A	4.67901	0.55917	0.51055	0.50928	-24.9	6.3
Boulder Ridge	BR1-6 B	6.41526	0.57801	0.51055	0.50960	-18.6	6.8
Boulder Ridge	BR1-7	2.86480	0.53994	0.51055	0.50939	-22.6	7.6
Boulder Ridge	BR1-8	2.96408	0.54153	0.51055	0.50993	-12.1	6.5
Iceman	I1-4	2.25064	0.53312	0.51055	0.50913	-27.9	3.5
Iceman	I1-8	4.57305	0.55800	0.51055	0.50924	-25.7	8.3
Iceman	I1-13	4.59227	0.55823	0.51055	0.50926	-25.2	9.0
John Galt	J1-3	1.83126	0.52881	0.51055	0.50929	-24.8	5.3
John Galt	J1-5	2.11314	0.53177	0.51055	0.50924	-25.7	1.2
John Galt	J1-8	1.81313	0.52861	0.51055	0.50928	-24.8	1.6
John Galt	J1-9 A	2.03384	0.53113	0.51055	0.50945	-21.5	2.9
John Galt	J1-9 B	1.60950	0.52683	0.51055	0.50967	-17.2	2.6
John Galt	J1-10	1.62441	0.52682	0.51055	0.50951	-20.4	1.6
John Galt	J1-11	1.79334	0.52830	0.51055	0.50918	-26.8	5.8

Table 2: Whole-rock Sm-Nd analysis of ore and BRM

Deposit	Sample	Easting	Northing	Depth	Type	Sm (ppm)	Nd (ppm)	$^{147}Sm/^{144}Nd$	$^{143}Nd/^{144}Nd$	$^{143}Nd/^{144}Nd$ (i)	εNd (t=1.62 Ga)	2σ	T_{DM} (Ma)	T_{CHUR} (Ma)
Wolverine	W5-1	493508.1	7915069	441.2	BRM	2.39	12.4	0.10109	0.51067	0.50961	-18.7	0.08	3296	3105
Wolverine	W5-13	493508.1	7915069	550.7	BRM	2.61	16	0.10188	0.51085	0.50977	-15.5	0.02	3087	2855
Wolverine	W16-4	493599.5	7914773	103.5	BRM	4.81	33.1	0.08752	0.51059	0.50966	-17.4	0.06	3050	2842
Gambit	G5-5	493098.1	7913652	98.1	BRM	5.58	34.6	0.19176	0.51138	0.50934	-23.7	0.06	11472	35382
Wolverine	W5-2	493508.1	7915069	487.6	Ore	863	1200	0.43505	0.51451	0.50990	-13.0	0.06	943	1199
Wolverine	W5-6	493508.1	7915069	505.2	Ore	7907	2694	1.77450	0.52854	0.50969	-17.0	0.05	1501	1533

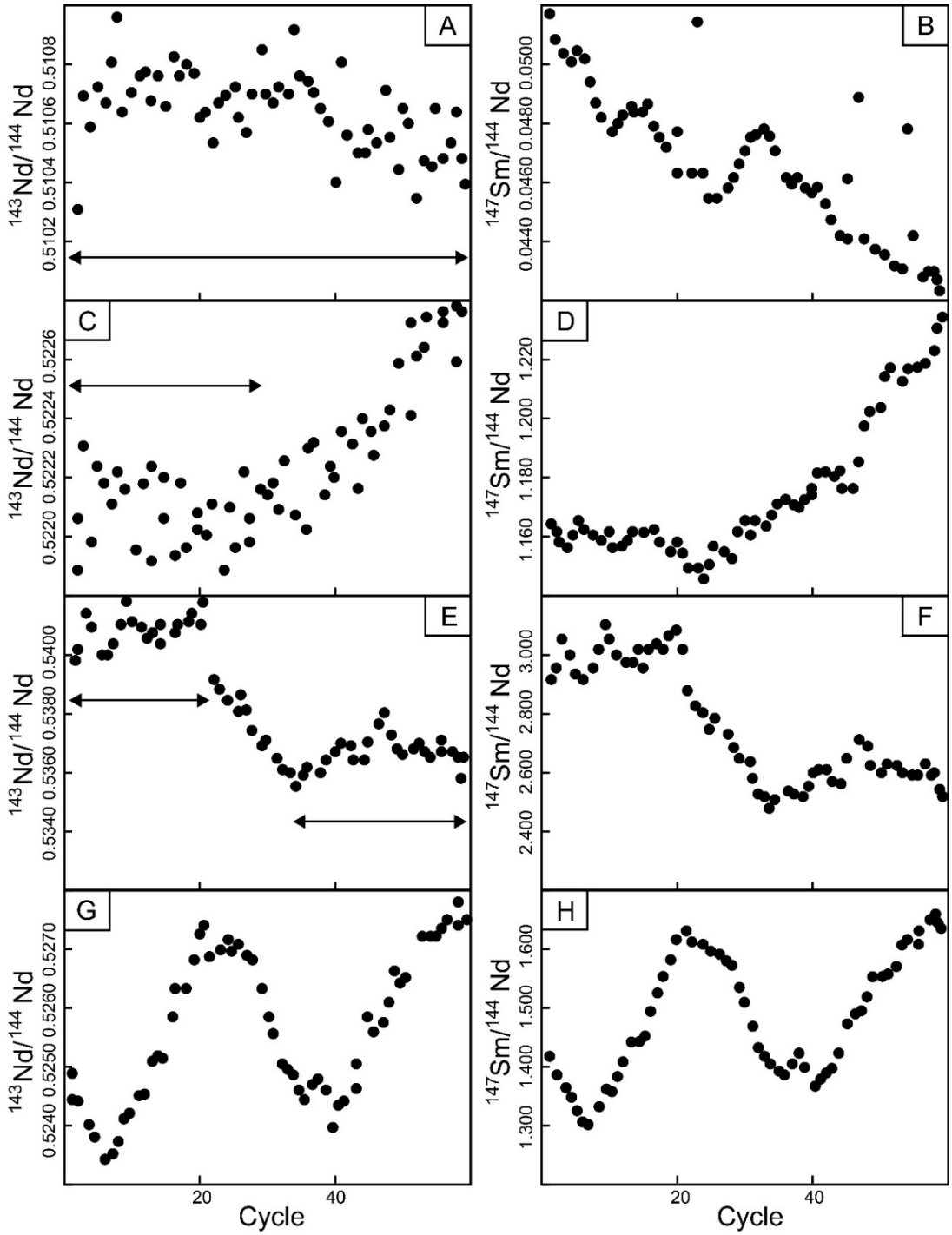

Figure 1. $^{143}Nd/^{144}Nd$ and $^{147}Sm/^{144}Nd$ ratios versus Cycle, showing xenotime with (A-B) limited isotopic variation, (C-D) limited variation interrupted by anomaly, (E-F) two stable plateaus, referred to with suffix "A" and "B" in Table 1, and (G-H) considerable isotopic variations.

References

Fisher, C.M., McFarlane, C.R.M., Hanchar, J.M., Schmitz, M.D., Sylvester, P.J., Lam, R., and Longerich, H.P., 2011. Sm-Nd isotope systematics by laser ablation-multi-collector-inductively coupled plasma mass spectrometry: methods and potential natural and synthetic reference materials. Chemical Geology, v. 284, p. 1–20.

Foster, G.L., and Vance, D., 2006. In situ Nd isotopic analysis of geological materials by laser ablation MC-ICP-MS. Journal of Analytical Atomic Spectrometry, v. 21, p. 288–296.

Hammerli, J., Kemp, A.I.S., and Spandler, C., 2014. Neodymium isotope equilibration during crustal metamorphism revealed by in situ microanalysis of REE-rich accessory minerals. Earth and Planetary Science Letters, v. 392, p. 133–142.

Wade, B.P., Barovich, K.M., Hand, M., Scrimgeour, I.R., and Close, D.F., 2006. Evidence for early Mesoproterozoic arc magmatism in the Musgrave Block, central Australia: implications for Proterozoic crustal growth and tectonic reconstructions of Australia. The Journal of Geology, v. 114, p. 43–63.

Yang, Y.H., Sun, J.F., Xie, L.W., Fan, H.R., and Wu, F.Y., 2008. In situ Nd measurement of natural geological materials by LA-MC-ICPMS. Chinese Science Bulletin, v. 53, p. 1062–1070.

Appendix 5

Chapter 5

Appendix 5-1: Sample locations

Appendix 5-2: Analytical conditions for EPMA measurement of florencite

Appendix 5-3: LA-ICP-MS spot analysis of xenotime

Appendix 5-4: Electron probe micro-analytical data of florencite from Wolverine and Area 5

Appendix 5-1: Sample locations

	No.	Prospect/deposit	Drill core	Depth (m)	Easting	Northing
	WDS					
1	A2-11	Area 5	BRAD0002	132.4	492231.3	7909977
2	A2-14	Area 5	BRAD0002	135	492231.3	7909976
3	W5-6	Wolverine	BRWT0332W5	505.2	493508.1	7915069
4	W5-4	Wolverine	BRWT0332W5	503.2	493508.1	7915069
5	W324-2	Wolverine	BRWT0324	372.9	493541.1	7914983
6	W5-7	Wolverine	BRWT0332W5	505.8	493508.1	7915069
7	W5-8	Wolverine	BRWT0332W5	510.6	493508.1	7915069
	LA-ICP-MS					
1	W5-7	Wolverine	BRWT0332W5	505.8	493508.1	7915069
2	W324-2	Wolverine	BRWT0324	372.9	493541.1	7914983
3	W5-3	Wolverine	BRWT0332W5	490.3	493508.1	7915069
4	W5-2B	Wolverine	BRWT0332W5	487.6	493508.1	7915069
5	W5-6B	Wolverine	BRWT0332W5	505.1	493508.1	7915069
6	W7-3B	Wolverine	BRWD0007	41.6	493695.9	7914741
7	W5-5	Wolverine	BRWT0332W5	504.6	493508.1	7915069
8	C2	Cyclops	-	Surface	489782	7904619
9	D3	Dazzler	-	Surface	490384	7902004
10	A2-14	Area 5	BRAD0002	135.1	492231.3	7909976
11	I1	Iceman	-	Surface	490746	7901660
12	BR1	Boulder Ridge	-	Surface	526100	7808681
13	J1	John Galt	-	Surface	417650	8087517

Appendix 5-2: Analytical conditions for EPMA measurement of florencite

			Count time (sec.)	
Element	Standard	Line	Peak	Background
P	P_2O_5	Kα	20	10
Fe	FeO	Kα	20	10
Gd	Gd_2O_3	Lβ	20	10
F	F	Kα	20	10
Ca	CaO	Kα	20	10
Y	Y_2O_3	La	20	10
Nd	Nd_2O_3	Lβ	20	10
Sm	Sm_2O_3	Lβ	20	10
Al	Al_2O_3	Kα	20	10
Th	ThO_2	Mα	20	10
Si	SiO_2	Kα	20	10
Ce	Ce_2O_3	Lα	20	10
Pr	Pr_2O_3	Lβ	20	10
Cl	Cl	Kα	20	10
La	La_2O_3	Lα	20	10
S	SO_3	Kα	20	10
Sr	SrO	Lα	20	10

Appendix 5-3: LA-ICP-MS spot analysis of xenotime

Deposit	Wolverine										
No	W5-7_3	W5-7_4	W5-7_10	W5-7_11	W5-7_23	W5-7_24	W5-7_25	W5-7_2	W5-7_5	W5-7_6	W5-7_8
Paragenesis	Breccia-hosted							Vein-type			
(ppm)											
Al	585	525	388	79	1336	817	157	263	20	358	106
Si	<2867	<3569	<2961	<3075	<3904	3503	<3184	<3581	<3088	<3522	<3625
P	121735	132612	130195	132141	137722	129428	130413	126091	130883	132570	136405
Ca	1003	499	1055	775	850	1316	910	977	776	895	1116
Sc	120	156	144	216	107	159	126	95	248	444	154
Ti	4	62	4	9	7	9	1	5	4	3	1
Mn	24	28	22	19	26	20	18	20	4	19	15
Fe	19443	28281	22064	10335	19001	13950	14175	23626	2093	18651	8061
Sr	5	4	4	2	5	5	4	5	3	5	5
Zr	2	3	1	1	2	3	3	1	5	2	1
Nb	0	0	0	0	0	0	0	0	0	0	0
Sb	4	8	12	3	5	3	3	9	0	6	2
Ba	10	7	5	3	18	3	5	4	1	5	2
La	21	8	22	2	13	12	14	31	1	22	11
Ce	531	238	602	78	382	355	320	776	61	553	291
Pr	379	207	443	97	325	295	248	550	73	406	220
Nd	5488	4053	6723	3070	5364	4824	4535	7646	2162	6117	3745
Sm	9624	12160	11616	15589	11002	9762	11866	11391	10728	10396	10964
Eu	2153	2811	2422	3400	2317	2152	2522	2298	2639	2159	2537
Gd	25101	32363	26259	42408	25379	24167	28941	26498	31844	24312	29636
Tb	6391	6993	6142	8262	6212	6138	6765	6452	7082	6213	6951
Dy	48875	47191	45127	49579	45789	46865	47238	48731	48430	48553	49203
Ho	11196	9765	10076	9454	10212	10659	10135	10775	10125	11112	10460
Er	31751	24507	26850	22077	29125	30628	27495	29410	27107	31822	28008
Tm	5206	3382	3840	2901	4548	4960	4187	4467	4007	5066	4477
Yb	34929	20268	22696	16703	29497	33720	28216	28448	25790	34541	29293
Lu	4368	2532	2840	2035	3782	4321	3548	3642	3200	4340	3718
Hf	5	4	5	5	2	5	5	5	5	5	5
W	11	18	13	8	11	11	8	11	6	20	9
Pb	3	1	1	3	2	2	0	1	6	9	0
Th	1	3	0	1	0	2	1	0	33	57	0
U	960	892	1460	1093	885	990	707	960	1719	981	684
Eu/Eu*	0.42	0.43	0.42	0.40	0.42	0.43	0.42	0.40	0.44	0.42	0.43
Al	0.00	0.00	0.00	0.00	0.01	0.01	0.00	0.00	0.00	0.00	0.00
Si	0.02	0.03	0.02	0.02	0.03	0.03	0.02	0.03	0.02	0.03	0.03
P	0.87	0.90	0.90	0.92	0.92	0.90	0.91	0.88	0.93	0.90	0.93
Ca	0.01	0.00	0.01	0.00	0.00	0.01	0.00	0.01	0.00	0.00	0.01
Sc	0.00	0.00	0.00	0.00	0.00	0.00	0.00	0.00	0.00	0.00	0.00
Mn	0.00	0.00	0.00	0.00	0.00	0.00	0.00	0.00	0.00	0.00	0.00
Fe	0.08	0.11	0.08	0.04	0.07	0.05	0.05	0.09	0.01	0.07	0.03
Y	0.84	0.80	0.82	0.82	0.79	0.82	0.82	0.82	0.84	0.80	0.81
Zr	0.00	0.00	0.00	0.00	0.00	0.00	0.00	0.00	0.00	0.00	0.00
La	0.00	0.00	0.00	0.00	0.00	0.00	0.00	0.00	0.00	0.00	0.00
Ce	0.00	0.00	0.00	0.00	0.00	0.00	0.00	0.00	0.00	0.00	0.00
Pr	0.00	0.00	0.00	0.00	0.00	0.00	0.00	0.00	0.00	0.00	0.00
Nd	0.01	0.01	0.01	0.00	0.01	0.01	0.01	0.01	0.00	0.01	0.01
Sm	0.01	0.02	0.02	0.02	0.02	0.01	0.02	0.02	0.02	0.01	0.02
Eu	0.00	0.00	0.00	0.00	0.00	0.00	0.00	0.00	0.00	0.00	0.00
Gd	0.04	0.04	0.04	0.06	0.03	0.03	0.04	0.04	0.04	0.03	0.04
Tb	0.01	0.01	0.01	0.01	0.01	0.01	0.01	0.01	0.01	0.01	0.01
Dy	0.07	0.06	0.06	0.07	0.06	0.06	0.06	0.06	0.07	0.06	0.06
Ho	0.02	0.01	0.01	0.01	0.01	0.01	0.01	0.01	0.01	0.01	0.01
Er	0.04	0.03	0.03	0.03	0.04	0.04	0.04	0.04	0.04	0.04	0.04
Tm	0.01	0.00	0.00	0.00	0.01	0.01	0.01	0.01	0.01	0.01	0.01
Yb	0.05	0.02	0.03	0.02	0.04	0.04	0.04	0.04	0.03	0.04	0.04
Lu	0.01	0.00	0.00	0.00	0.00	0.01	0.00	0.00	0.00	0.01	0.00
Th	0.00	0.00	0.00	0.00	0.00	0.00	0.00	0.00	0.00	0.00	0.00
U	0.00	0.00	0.00	0.00	0.00	0.00	0.00	0.00	0.00	0.00	0.00
Total	2.08	2.06	2.06	2.05	2.05	2.06	2.05	2.07	2.04	2.06	2.04
P site	0.89	0.93	0.93	0.94	0.95	0.93	0.93	0.91	0.95	0.93	0.96
REE site	1.10	1.02	1.04	1.06	1.01	1.06	1.06	1.07	1.07	1.05	1.04

*Y = 33.9 wt.% (Cook et al., 2013)

**Formulae on basis of 4 a.p.f.u.

(Continued)

Deposit	Wolverine								
No	W5-7_9	W5-7_12	W5-7_13	W5-7_14	W5-7_15	W5-7_17	W5-7_18	W5-7_21	W5-7_1
Paragenesis	Vein-type								Overgrowth
(ppm)									
Al	53	420	82	249	191	143	187	160	192
Si	<3036	<3310	<2870	<3088	<3512	<3163	<3133	<3316	<4221
P	127427	137729	134479	133203	137305	135794	138717	133260	132581
Ca	498	766	704	1024	1003	1111	707	1304	536
Sc	187	162	142	128	182	175	206	203	98
Ti	4	7	4	5	4	12	38	28	6
Mn	6	36	16	42	32	11	12	10	6
Fe	4628	28386	8149	25229	19868	8674	8807	4653	10037
Sr	4	5	4	5	3	2	4	2	4
Zr	29	1	1	1	1	10	10	42	5
Nb	0	0	0	0	0	0	0	0	0
Sb	1	6	2	6	8	1	3	1	3
Ba	1	7	7	36	2	2	3	1	2
La	1	9	9	10	12	9	7	8	8
Ce	43	274	252	320	280	356	235	274	254
Pr	52	233	235	278	212	308	196	239	263
Nd	1717	4414	4673	4971	4057	5646	3474	4736	5765
Sm	10378	11317	12251	11402	12456	14423	10591	14629	11536
Eu	2456	2421	2800	2492	2735	3226	2825	3220	2225
Gd	30045	27728	31887	27598	31500	36932	32014	36651	24044
Tb	6680	6536	7174	6192	7120	7531	6862	7486	5798
Dy	45748	48574	49871	45712	49580	46320	45508	46898	45673
Ho	9894	10807	10535	10351	10555	9164	9638	9175	10565
Er	27048	31096	27793	28910	28115	22049	24523	21739	29529
Tm	3959	5099	4121	4477	4430	2876	3416	2800	4501
Yb	25989	34303	26558	28852	30067	16980	20844	16647	28098
Lu	3320	4465	3236	3662	3684	2124	2672	2113	3613
Hf	6	5	5	5	5	5	5	6	5
W	7	19	7	12	12	8	11	8	14
Pb	4	2	0	1	2	2	3	3	0
Th	46	0	0	0	0	18	25	25	1
U	1025	787	855	1054	831	1857	1634	1384	1123
Eu/Eu*	0.43	0.42	0.43	0.43	0.42	0.43	0.47	0.42	0.41
Al	0.00	0.00	0.00	0.00	0.00	0.00	0.00	0.00	0.00
Si	0.02	0.02	0.02	0.02	0.03	0.02	0.02	0.03	0.03
P	0.92	0.91	0.93	0.90	0.92	0.93	0.95	0.93	0.92
Ca	0.00	0.00	0.00	0.01	0.01	0.01	0.00	0.01	0.00
Sc	0.00	0.00	0.00	0.00	0.00	0.00	0.00	0.00	0.00
Mn	0.00	0.00	0.00	0.00	0.00	0.00	0.00	0.00	0.00
Fe	0.02	0.10	0.03	0.09	0.07	0.03	0.03	0.02	0.04
Y	0.85	0.78	0.82	0.80	0.79	0.81	0.81	0.83	0.82
Zr	0.00	0.00	0.00	0.00	0.00	0.00	0.00	0.00	0.00
La	0.00	0.00	0.00	0.00	0.00	0.00	0.00	0.00	0.00
Ce	0.00	0.00	0.00	0.00	0.00	0.00	0.00	0.00	0.00
Pr	0.00	0.00	0.00	0.00	0.00	0.00	0.00	0.00	0.00
Nd	0.00	0.01	0.01	0.01	0.01	0.01	0.01	0.01	0.01
Sm	0.02	0.02	0.02	0.02	0.02	0.02	0.01	0.02	0.02
Eu	0.00	0.00	0.00	0.00	0.00	0.00	0.00	0.00	0.00
Gd	0.04	0.04	0.04	0.04	0.04	0.05	0.04	0.05	0.03
Tb	0.01	0.01	0.01	0.01	0.01	0.01	0.01	0.01	0.01
Dy	0.06	0.06	0.07	0.06	0.06	0.06	0.06	0.06	0.06
Ho	0.01	0.01	0.01	0.01	0.01	0.01	0.01	0.01	0.01
Er	0.04	0.04	0.04	0.04	0.03	0.03	0.03	0.03	0.04
Tm	0.01	0.01	0.01	0.01	0.01	0.00	0.00	0.00	0.01
Yb	0.03	0.04	0.03	0.04	0.04	0.02	0.03	0.02	0.04
Lu	0.00	0.01	0.00	0.00	0.00	0.00	0.00	0.00	0.00
Th	0.00	0.00	0.00	0.00	0.00	0.00	0.00	0.00	0.00
U	0.00	0.00	0.00	0.00	0.00	0.00	0.00	0.00	0.00
Total	2.05	2.06	2.04	2.06	2.05	2.04	2.03	2.04	2.04
P site	0.94	0.93	0.95	0.93	0.94	0.96	0.97	0.96	0.95
REE site	1.08	1.01	1.05	1.03	1.02	1.04	1.02	1.05	1.05

*Y = 33.9 wt.% (Cook et al., 2013)

**Formulae on basis of 4 a.p.f.u.

(Continued)

Deposit	Wolverine								
No	W324-2_1	W324-2_2	W324-2_5	W324-2_7	W324-2_10	W324-2_11	W324-2_12	W324-2_13	W324-2_14
Paragenesis	Overgrowth								
(ppm)									
Al	659	340	247	135	223	1081	1169	681	43
Si	<2785	<3998	<3205	<3501	<3758	<2687	<2999	<3719	<2947
P	130959	124528	115345	134576	132824	127783	126609	133294	127344
Ca	2097	1227	1128	982	1497	807	1769	1057	836
Sc	1152	1444	996	2480	1473	1789	1425	2324	2231
Ti	7	18	4	13	5	8	6	13	10
Mn	9	7	3	5	10	9	15	9	6
Fe	3244	1480	675	3474	3091	3618	2848	3615	4710
Sr	7	7	6	8	8	76	8	9	7
Zr	30	31	6	13	32	32	74	33	7
Nb	0	0	0	0	0	0	0	0	0
Sb	1	0	0	1	1	1	1	1	2
Ba	4	7	3	3	5	8	6	5	2
La	5	4	2	3	5	60	5	4	3
Ce	165	149	72	107	165	224	168	134	123
Pr	123	123	84	103	114	104	118	109	125
Nd	2208	2205	2378	2203	2111	1818	2096	2109	2598
Sm	5049	5252	10253	5855	6214	5122	5964	5077	5414
Eu	1087	1257	2283	1264	1354	1190	1359	1080	1182
Gd	13044	15183	26913	15339	17275	14707	16493	14578	14341
Tb	4532	4671	6436	4717	4911	4679	4963	4438	4616
Dy	43924	42814	47545	43798	44138	43534	43557	42300	43399
Ho	11288	11104	10947	11453	11189	11411	11104	11408	11326
Er	36871	35812	31748	37889	36274	37406	35761	38498	37549
Tm	6461	6493	5371	7050	6369	6859	6343	7064	6835
Yb	47463	48234	37950	53788	47834	51759	47135	55299	50425
Lu	6066	6247	4866	7174	6418	6857	6354	7517	6811
Hf	6	5	5	5	6	5	7	6	5
W	9	11	7	9	9	8	8	9	9
Pb	5	16	51	21	34	15	21	7	5
Th	41	105	350	140	251	123	177	54	33
U	1598	1788	1023	1413	2041	1656	1890	1414	1386
Eu/Eu*	0.41	0.43	0.42	0.41	0.40	0.42	0.42	0.38	0.41
Al	0.01	0.00	0.00	0.00	0.00	0.01	0.01	0.01	0.00
Si	0.02	0.03	0.03	0.03	0.03	0.02	0.02	0.03	0.02
P	0.92	0.90	0.87	0.93	0.92	0.91	0.91	0.92	0.91
Ca	0.01	0.01	0.01	0.01	0.01	0.00	0.01	0.01	0.00
Sc	0.01	0.01	0.01	0.01	0.01	0.01	0.01	0.01	0.01
Mn	0.00	0.00	0.00	0.00	0.00	0.00	0.00	0.00	0.00
Fe	0.01	0.01	0.00	0.01	0.01	0.01	0.01	0.01	0.02
Y	0.83	0.85	0.89	0.81	0.82	0.84	0.84	0.82	0.84
Zr	0.00	0.00	0.00	0.00	0.00	0.00	0.00	0.00	0.00
La	0.00	0.00	0.00	0.00	0.00	0.00	0.00	0.00	0.00
Ce	0.00	0.00	0.00	0.00	0.00	0.00	0.00	0.00	0.00
Pr	0.00	0.00	0.00	0.00	0.00	0.00	0.00	0.00	0.00
Nd	0.00	0.00	0.00	0.00	0.00	0.00	0.00	0.00	0.00
Sm	0.01	0.01	0.02	0.01	0.01	0.01	0.01	0.01	0.01
Eu	0.00	0.00	0.00	0.00	0.00	0.00	0.00	0.00	0.00
Gd	0.02	0.02	0.04	0.02	0.02	0.02	0.02	0.02	0.02
Tb	0.01	0.01	0.01	0.01	0.01	0.01	0.01	0.01	0.01
Dy	0.06	0.06	0.07	0.06	0.06	0.06	0.06	0.06	0.06
Ho	0.01	0.02	0.02	0.01	0.01	0.02	0.01	0.01	0.02
Er	0.05	0.05	0.04	0.05	0.05	0.05	0.05	0.05	0.05
Tm	0.01	0.01	0.01	0.01	0.01	0.01	0.01	0.01	0.01
Yb	0.06	0.06	0.05	0.07	0.06	0.07	0.06	0.07	0.07
Lu	0.01	0.01	0.01	0.01	0.01	0.01	0.01	0.01	0.01
Th	0.00	0.00	0.00	0.00	0.00	0.00	0.00	0.00	0.00
U	0.00	0.00	0.00	0.00	0.00	0.00	0.00	0.00	0.00
Total	2.05	2.06	2.08	2.04	2.04	2.05	2.06	2.05	2.06
P site	0.94	0.93	0.90	0.95	0.95	0.93	0.93	0.95	0.93
REE site	1.07	1.10	1.16	1.06	1.06	1.09	1.09	1.06	1.09

*Y = 33.9 wt.% (Cook et al., 2013)

**Formulae on basis of 4 a.p.f.u.

(Continued)

Deposit	Wolverine								
No	W324-2_15	W324-2_17	W324-2_18	W324-2_19	W324-2_20	W324-2_22	W324-2_23	W324-2_24	W324-2_25
Paragenesis	Overgrowth								
(ppm)									
Al	247	208	119	178	195	128	48	632	576
Si	<3144	<2618	<2645	<2484	<2757	<2871	<2838	<2739	<2863
P	129794	129483	127006	124700	125021	125027	119041	125179	122881
Ca	979	1493	780	912	1273	1049	1417	1053	1657
Sc	1580	1345	1390	1736	1343	1256	1012	766	1372
Ti	11	10	7	43	14	4	5	3	12
Mn	12	12	6	9	7	9	5	6	13
Fe	12583	7448	4151	5213	10571	2475	1665	970	5690
Sr	7	7	7	8	7	7	6	5	7
Zr	26	21	27	25	14	35	14	27	33
Nb	0	0	0	0	0	0	0	0	0
Sb	3	2	2	2	2	1	0	0	2
Ba	5	3	3	5	4	2	2	2	4
La	3	4	2	3	3	3	3	2	4
Ce	150	124	82	109	108	112	89	87	162
Pr	130	93	83	93	93	91	88	87	124
Nd	2841	2017	2136	1907	2230	2011	2355	2457	2352
Sm	8375	6675	8131	5467	8523	7107	9340	11027	6084
Eu	1695	1539	1820	1216	1926	1646	2115	2557	1342
Gd	20065	20067	22209	15380	22719	20158	27006	30818	16428
Tb	5425	5418	5586	4619	5818	5403	6441	6887	4793
Dy	43649	44121	44522	43187	45901	44028	46385	46895	42582
Ho	10448	10628	10802	11311	10963	10631	10478	10127	10888
Er	33075	33577	34463	37299	34433	33170	31193	28401	35534
Tm	5920	5889	6192	6882	6094	5875	5254	4629	6333
Yb	44201	43569	45729	51596	45291	42994	37726	32498	47051
Lu	5763	5734	6156	6807	5969	5633	4938	4190	6320
Hf	6	6	5	6	6	6	5	6	6
W	9	9	62	9	9	8	7	7	1
Pb	15	7	6	4	45	31	43	33	4
Th	99	72	50	34	330	244	295	243	42
U	1794	1575	1428	1930	1373	1723	1105	1326	1835
Eu/Eu*	0.40	0.41	0.41	0.41	0.42	0.42	0.41	0.42	0.41
Al	0.00	0.00	0.00	0.00	0.00	0.00	0.00	0.01	0.00
Si	0.02	0.02	0.02	0.02	0.02	0.02	0.02	0.02	0.02
P	0.90	0.91	0.91	0.90	0.89	0.91	0.89	0.91	0.89
Ca	0.01	0.01	0.00	0.01	0.01	0.01	0.01	0.01	0.01
Sc	0.01	0.01	0.01	0.01	0.01	0.01	0.01	0.00	0.01
Mn	0.00	0.00	0.00	0.00	0.00	0.00	0.00	0.00	0.00
Fe	0.05	0.03	0.02	0.02	0.04	0.01	0.01	0.00	0.02
Y	0.82	0.83	0.84	0.85	0.84	0.86	0.88	0.86	0.86
Zr	0.00	0.00	0.00	0.00	0.00	0.00	0.00	0.00	0.00
La	0.00	0.00	0.00	0.00	0.00	0.00	0.00	0.00	0.00
Ce	0.00	0.00	0.00	0.00	0.00	0.00	0.00	0.00	0.00
Pr	0.00	0.00	0.00	0.00	0.00	0.00	0.00	0.00	0.00
Nd	0.00	0.00	0.00	0.00	0.00	0.00	0.00	0.00	0.00
Sm	0.01	0.01	0.01	0.01	0.01	0.01	0.01	0.02	0.01
Eu	0.00	0.00	0.00	0.00	0.00	0.00	0.00	0.00	0.00
Gd	0.03	0.03	0.03	0.02	0.03	0.03	0.04	0.04	0.02
Tb	0.01	0.01	0.01	0.01	0.01	0.01	0.01	0.01	0.01
Dy	0.06	0.06	0.06	0.06	0.06	0.06	0.07	0.06	0.06
Ho	0.01	0.01	0.01	0.02	0.01	0.01	0.01	0.01	0.01
Er	0.04	0.04	0.05	0.05	0.05	0.04	0.04	0.04	0.05
Tm	0.01	0.01	0.01	0.01	0.01	0.01	0.01	0.01	0.01
Yb	0.06	0.06	0.06	0.07	0.06	0.06	0.05	0.04	0.06
Lu	0.01	0.01	0.01	0.01	0.01	0.01	0.01	0.01	0.01
Th	0.00	0.00	0.00	0.00	0.00	0.00	0.00	0.00	0.00
U	0.00	0.00	0.00	0.00	0.00	0.00	0.00	0.00	0.00
Total	2.06	2.05	2.06	2.06	2.07	2.06	2.07	2.06	2.07
P site	0.93	0.93	0.93	0.92	0.91	0.93	0.91	0.93	0.92
REE site	1.06	1.07	1.10	1.10	1.10	1.10	1.14	1.11	1.10

*Y = 33.9 wt.% (Cook et al., 2013)

**Formulae on basis of 4 a.p.f.u.

(Continued)

Deposit										
No	W5-3_1	W5-3_2	W5-3_3	W5-3_4	W5-3_5	W5-3_6	W5-3_7	W5-3_8	W5-3_9	W5-3_10
Paragenesis	Vein-type									
(ppm)										
Al	85	223	286	253	289	176	95	64	305	50
Si	<3353	<2855	<2411	<3364	<3201	<2716	<2530	<2829	<2825	<2907
P	126448	124002	117933	124415	119883	126168	118406	115130	118912	115313
Ca	450	1046	995	982	1076	1006	614	550	1193	752
Sc	149	141	290	254	274	238	134	154	347	206
Ti	30	6	7	9	10	2	9	5	9	12
Mn	9	9	17	27	26	12	8	5	9	5
Fe	24777	12521	10762	18059	22668	11260	6404	2554	5189	4317
Sr	5	6	5	5	5	5	4	5	6	5
Zr	11	3	2	1	2	1	9	7	1	16
Nb	0	0	0	0	0	0	0	0	0	0
Sb	2	5	5	8	15	7	2	1	2	1
Ba	1	5	2	4	3	2	3	22	11	1
La	16	25	14	12	8	22	11	9	12	3
Ce	454	633	426	408	266	486	345	233	362	119
Pr	330	471	335	296	229	332	297	182	274	100
Nd	5296	7006	5101	4200	4462	4958	5058	3130	4270	2067
Sm	10858	11118	9544	7889	10023	10940	10383	9298	9592	8960
Eu	2410	2320	2136	1760	2151	2404	2362	2248	2040	2547
Gd	24083	23003	22243	18842	23335	24553	24651	23974	20197	24333
Tb	6262	6158	5876	5301	5880	6175	6192	6136	5574	6111
Dy	46107	46501	45879	43669	45517	47447	46879	45703	44901	46090
Ho	10264	10259	10301	10608	10358	10446	10105	10060	10475	10175
Er	28007	29000	29262	30851	28879	29606	27463	27807	30629	28624
Tm	4282	4452	4574	4930	4604	4558	4065	4241	4913	4364
Yb	27614	28999	30242	33813	30143	30029	25885	27249	33871	27865
Lu	3534	3634	3739	4501	3804	3818	3172	3385	4307	3580
Hf	6	5	3	5	5	5	6	6	6	6
W	10	11	10	10	37	18	8	7	9	10
Pb	8	1	11	3	13	1	1	1	2	9
Th	16	1	71	1	86	0	5	11	8	87
U	931	845	1037	1002	1345	993	958	794	980	1133
Eu/Eu*	0.46	0.44	0.45	0.44	0.43	0.45	0.45	0.46	0.45	0.53
Al	0.00	0.00	0.00	0.00	0.00	0.00	0.00	0.00	0.00	0.00
Si	0.03	0.02	0.02	0.03	0.03	0.02	0.02	0.02	0.02	0.02
P	0.89	0.89	0.88	0.89	0.87	0.90	0.89	0.88	0.89	0.88
Ca	0.00	0.01	0.01	0.01	0.01	0.01	0.00	0.00	0.01	0.00
Sc	0.00	0.00	0.00	0.00	0.00	0.00	0.00	0.00	0.00	0.00
Mn	0.00	0.00	0.00	0.00	0.00	0.00	0.00	0.00	0.00	0.00
Fe	0.10	0.05	0.04	0.07	0.09	0.04	0.03	0.01	0.02	0.02
Y	0.83	0.85	0.88	0.84	0.85	0.84	0.89	0.91	0.88	0.90
Zr	0.00	0.00	0.00	0.00	0.00	0.00	0.00	0.00	0.00	0.00
La	0.00	0.00	0.00	0.00	0.00	0.00	0.00	0.00	0.00	0.00
Ce	0.00	0.00	0.00	0.00	0.00	0.00	0.00	0.00	0.00	0.00
Pr	0.00	0.00	0.00	0.00	0.00	0.00	0.00	0.00	0.00	0.00
Nd	0.01	0.01	0.01	0.01	0.01	0.01	0.01	0.01	0.01	0.00
Sm	0.02	0.02	0.01	0.01	0.01	0.02	0.02	0.01	0.01	0.01
Eu	0.00	0.00	0.00	0.00	0.00	0.00	0.00	0.00	0.00	0.00
Gd	0.03	0.03	0.03	0.03	0.03	0.03	0.04	0.04	0.03	0.04
Tb	0.01	0.01	0.01	0.01	0.01	0.01	0.01	0.01	0.01	0.01
Dy	0.06	0.06	0.07	0.06	0.06	0.06	0.07	0.07	0.06	0.07
Ho	0.01	0.01	0.01	0.01	0.01	0.01	0.01	0.01	0.01	0.01
Er	0.04	0.04	0.04	0.04	0.04	0.04	0.04	0.04	0.04	0.04
Tm	0.01	0.01	0.01	0.01	0.01	0.01	0.01	0.01	0.01	0.01
Yb	0.04	0.04	0.04	0.04	0.04	0.04	0.04	0.04	0.05	0.04
Lu	0.00	0.00	0.00	0.01	0.00	0.00	0.00	0.00	0.01	0.00
Th	0.00	0.00	0.00	0.00	0.00	0.00	0.00	0.00	0.00	0.00
U	0.00	0.00	0.00	0.00	0.00	0.00	0.00	0.00	0.00	0.00
Total	2.07	2.07	2.08	2.07	2.08	2.06	2.07	2.07	2.07	2.07
P site	0.91	0.92	0.90	0.92	0.89	0.92	0.91	0.91	0.91	0.91
REE site	1.05	1.09	1.12	1.07	1.09	1.08	1.13	1.15	1.12	1.14

*Y = 33.9 wt.% (Cook et al., 2013)

**Formulae on basis of 4 a.p.f.u.

(Continued)

Deposit	Wolverine									
No	W5-3_11	W5-3_12	W5-3_13	W5-3_14	W5-3_15	W5-3_16	W5-3_17	W5-3_18	W5-3_19	W5-3_20
Paragenesis	Vein-type									
(ppm)										
Al	376	15	285	316	62	121	191	93	78	127
Si	<3295	<2892	<2629	<2680	<2866	<3162	<2971	<2695	<3228	<2007
P	123739	116278	117155	119941	119209	119817	117005	119484	125018	113183
Ca	1641	1152	533	928	755	767	956	542	551	1177
Sc	242	128	139	228	111	113	128	167	102	128
Ti	9	1	2	12	7	9	3	9	5	2
Mn	24	9	9	14	9	9	20	15	15	95
Fe	12814	3265	4585	15489	6279	11234	19893	6341	10759	6145
Sr	5	4	5	6	3	3	3	5	4	4
Zr	4	3	9	1	5	1	1	4	1	1
Nb	0	0	0	0	0	0	0	0	0	0
Sb	5	2	2	6	2	7	10	3	5	4
Ba	4	0	5	2	1	3	12	2	3	17
La	13	2	12	16	15	25	21	17	21	11
Ce	421	81	306	481	417	657	538	371	587	295
Pr	295	85	228	354	349	525	436	284	482	256
Nd	4505	2137	3744	5332	6127	8147	7305	4847	7685	5231
Sm	7830	8603	9618	9336	12499	13035	13443	10871	13546	12894
Eu	1594	2312	2258	1878	2787	2818	2913	2445	2783	2809
Gd	17170	27323	24103	19269	27809	28165	28957	25393	27024	29119
Tb	5204	6573	6192	5318	6494	6776	6832	6383	6687	6880
Dy	44225	48541	45748	44446	46491	47145	46855	47760	47933	49900
Ho	10535	10527	10233	10431	9866	9779	9656	10450	10086	10530
Er	30622	28020	28560	30839	25558	24775	23758	28868	25911	27434
Tm	4914	4153	4386	4946	3502	3296	3091	4424	3609	3924
Yb	32593	25615	29155	33008	20810	19206	17580	29338	21430	25031
Lu	4226	3153	3737	4369	2652	2425	2163	3696	2674	2943
Hf	5	6	5	5	5	5	5	6	9	6
W	14	7	8	17	7	13	8	9	7	10
Pb	2	4	1	1	1	1	1	2	1	6
Th	1	23	4	1	3	3	1	1	0	1
U	985	1448	823	1154	1129	1002	927	861	723	819
Eu/Eu*	0.42	0.46	0.45	0.43	0.46	0.45	0.45	0.45	0.44	0.44
Al	0.00	0.00	0.00	0.00	0.00	0.00	0.00	0.00	0.00	0.00
Si	0.03	0.02	0.02	0.02	0.02	0.03	0.02	0.02	0.03	0.02
P	0.89	0.88	0.89	0.88	0.89	0.88	0.86	0.89	0.90	0.87
Ca	0.01	0.01	0.00	0.01	0.00	0.00	0.01	0.00	0.00	0.01
Sc	0.00	0.00	0.00	0.00	0.00	0.00	0.00	0.00	0.00	0.00
Mn	0.00	0.00	0.00	0.00	0.00	0.00	0.00	0.00	0.00	0.00
Fe	0.05	0.01	0.02	0.06	0.03	0.05	0.08	0.03	0.04	0.03
Y	0.85	0.90	0.89	0.87	0.88	0.87	0.87	0.88	0.85	0.90
Zr	0.00	0.00	0.00	0.00	0.00	0.00	0.00	0.00	0.00	0.00
La	0.00	0.00	0.00	0.00	0.00	0.00	0.00	0.00	0.00	0.00
Ce	0.00	0.00	0.00	0.00	0.00	0.00	0.00	0.00	0.00	0.00
Pr	0.00	0.00	0.00	0.00	0.00	0.00	0.00	0.00	0.00	0.00
Nd	0.01	0.00	0.01	0.01	0.01	0.01	0.01	0.01	0.01	0.01
Sm	0.01	0.01	0.01	0.01	0.02	0.02	0.02	0.02	0.02	0.02
Eu	0.00	0.00	0.00	0.00	0.00	0.00	0.00	0.00	0.00	0.00
Gd	0.02	0.04	0.04	0.03	0.04	0.04	0.04	0.04	0.04	0.04
Tb	0.01	0.01	0.01	0.01	0.01	0.01	0.01	0.01	0.01	0.01
Dy	0.06	0.07	0.07	0.06	0.07	0.07	0.07	0.07	0.07	0.07
Ho	0.01	0.02	0.01	0.01	0.01	0.01	0.01	0.01	0.01	0.02
Er	0.04	0.04	0.04	0.04	0.04	0.03	0.03	0.04	0.03	0.04
Tm	0.01	0.01	0.01	0.01	0.00	0.00	0.00	0.01	0.00	0.01
Yb	0.04	0.04	0.04	0.04	0.03	0.03	0.02	0.04	0.03	0.03
Lu	0.01	0.00	0.01	0.01	0.00	0.00	0.00	0.00	0.00	0.00
Th	0.00	0.00	0.00	0.00	0.00	0.00	0.00	0.00	0.00	0.00
U	0.00	0.00	0.00	0.00	0.00	0.00	0.00	0.00	0.00	0.00
Total	2.06	2.07	2.07	2.08	2.07	2.07	2.08	2.07	2.06	2.09
P site	0.92	0.91	0.91	0.90	0.91	0.91	0.89	0.91	0.93	0.88
REE site	1.08	1.14	1.14	1.10	1.12	1.11	1.11	1.13	1.09	1.16

*Y = 33.9 wt.% (Cook et al., 2013)

**Formulae on basis of 4 a.p.f.u.

(Continued)

Deposit	Wolverine								
No	W5-2B_3	W5-2B_5	W5-2B_16	W5-2B_18	W5-2B_20	W5-2B_1	W5-2B_2	W5-2B_4	W5-2B_6
Paragenesis	Breccia-hosted					Vein-type			
Al	55	85	103	33	259	151	385	383	46
Si	<2393	<2706	<3096	<3899	<2568	<2606	<3131	<2611	<2799
P	115198	118480	118120	117462	110189	123581	122542	117642	120317
Ca	997	715	1208	1081	1245	961	1490	1442	1023
Sc	128	92	64	91	73	99	117	91	83
Ti	46	23	32	438	9	133	14	57	59
Mn	9	8	9	8	15	10	29	13	8
Fe	1996	4142	8811	3940	11403	6004	22066	7584	3478
Sr	5	4	4	4	3	4	3	4	3
Zr	43	30	25	94	1	30	2	26	11
Nb	0	0	1	3	0	1	0	0	0
Sb	1	2	4	2	4	3	14	4	1
Ba	2	2	2	3	2	2	7	4	1
La	1	7	1	6	14	10	10	12	9
Ce	35	195	41	183	356	292	273	316	301
Pr	38	165	62	162	267	239	222	244	254
Nd	1147	3307	1998	3109	4462	4182	4637	4131	4708
Sm	7186	10703	8605	9790	10829	10699	13511	10273	12141
Eu	1929	2431	1952	2698	2371	2365	2630	2315	2576
Gd	20556	25899	19808	24170	23963	24905	29039	23775	26571
Tb	5685	6271	5616	5912	5850	6008	6221	5856	6333
Dy	46011	45128	45536	44531	42971	43895	42994	43924	45483
Ho	10481	9933	10344	9679	9655	9665	9006	9822	9649
Er	29231	25669	27848	25638	24767	25494	22786	25906	24660
Tm	4408	3643	4082	3605	3354	3573	2932	3605	3379
Yb	28110	21866	24379	22363	19315	21210	16940	21331	19712
Lu	3597	2637	3088	2754	2414	2736	2165	2702	2433
Hf	4	6	6	6	5	5	4	5	5
W	10	8	13	38	6	11	20	13	11
Pb	5	3	3	5	1	3	1	2	1
Th	45	22	20	38	1	25	3	22	9
U	2268	1539	2439	1686	1615	1607	1722	1721	1566
Eu/Eu*	0.49	0.45	0.46	0.54	0.45	0.44	0.41	0.45	0.44
Al	0.00	0.00	0.00	0.00	0.00	0.00	0.00	0.00	0.00
Si	0.02	0.02	0.03	0.03	0.02	0.02	0.02	0.02	0.02
P	0.89	0.90	0.89	0.89	0.86	0.91	0.88	0.89	0.90
Ca	0.01	0.00	0.01	0.01	0.01	0.01	0.01	0.01	0.01
Sc	0.00	0.00	0.00	0.00	0.00	0.00	0.00	0.00	0.00
Mn	0.00	0.00	0.00	0.00	0.00	0.00	0.00	0.00	0.00
Fe	0.01	0.02	0.04	0.02	0.05	0.02	0.09	0.03	0.01
Y	0.91	0.89	0.89	0.89	0.92	0.87	0.85	0.89	0.88
Zr	0.00	0.00	0.00	0.00	0.00	0.00	0.00	0.00	0.00
La	0.00	0.00	0.00	0.00	0.00	0.00	0.00	0.00	0.00
Ce	0.00	0.00	0.00	0.00	0.00	0.00	0.00	0.00	0.00
Pr	0.00	0.00	0.00	0.00	0.00	0.00	0.00	0.00	0.00
Nd	0.00	0.01	0.00	0.01	0.01	0.01	0.01	0.01	0.01
Sm	0.01	0.02	0.01	0.02	0.02	0.02	0.02	0.02	0.02
Eu	0.00	0.00	0.00	0.00	0.00	0.00	0.00	0.00	0.00
Gd	0.03	0.04	0.03	0.04	0.04	0.04	0.04	0.04	0.04
Tb	0.01	0.01	0.01	0.01	0.01	0.01	0.01	0.01	0.01
Dy	0.07	0.07	0.07	0.06	0.06	0.06	0.06	0.06	0.06
Ho	0.02	0.01	0.01	0.01	0.01	0.01	0.01	0.01	0.01
Er	0.04	0.04	0.04	0.04	0.04	0.03	0.03	0.04	0.03
Tm	0.01	0.01	0.01	0.01	0.00	0.00	0.00	0.00	0.00
Yb	0.04	0.03	0.03	0.03	0.03	0.03	0.02	0.03	0.03
Lu	0.00	0.00	0.00	0.00	0.00	0.00	0.00	0.00	0.00
Th	0.00	0.00	0.00	0.00	0.00	0.00	0.00	0.00	0.00
U	0.00	0.00	0.00	0.00	0.00	0.00	0.00	0.00	0.00
Total	2.07	2.06	2.07	2.06	2.09	2.05	2.07	2.07	2.06
P site	0.91	0.92	0.91	0.92	0.88	0.93	0.91	0.91	0.92
REE site	1.14	1.12	1.11	1.12	1.15	1.09	1.06	1.11	1.11

*Y = 33.9 wt.% (Cook et al., 2013)

**Formulae on basis of 4 a.p.f.u.

(Continued)

Deposit	Wolverine									
No	W5-2B_7	W5-2B_8	W5-2B_9	W5-2B_10	W5-2B_12	W5-2B_13	W5-2B_14	W5-2B_15	W5-2B_17	W5-2B_19
Paragenesis	Vein-type									
(ppm)										
Al	76	88	35	206	190	70	59	46	267	253
Si	<2277	<2024	<2766	<2743	<2785	<2633	<2125	<2720	<3078	<2682
P	115810	114485	116218	116823	117847	119945	116504	118693	114681	110240
Ca	1179	759	734	1366	1480	1071	1462	1401	966	1212
Sc	74	122	83	89	97	116	124	140	73	77
Ti	9	37	12	34	12	33	6	4	23	11
Mn	6	15	10	19	16	12	5	11	13	14
Fe	2820	2356	2484	11783	7379	4915	1935	3628	7391	6474
Sr	4	5	4	4	4	4	4	5	3	4
Zr	23	41	106	13	15	16	15	11	2	5
Nb	0	0	0	0	0	0	0	0	0	0
Sb	1	1	1	5	3	2	1	1	2	3
Ba	1	5	1	2	2	2	1	2	2	2
La	17	3	3	9	11	3	1	4	4	8
Ce	462	108	112	253	312	102	59	127	130	247
Pr	369	98	119	213	262	120	91	131	132	223
Nd	5953	2248	2847	3920	4937	3341	3197	3065	3100	4238
Sm	10585	9651	10216	9977	11957	11377	11369	9628	10835	11073
Eu	2407	2447	2529	2138	2443	2463	2557	2101	2332	2335
Gd	24914	26312	25977	22302	25243	25366	27390	20639	23862	23582
Tb	6134	6363	6328	5684	6070	6209	6737	5778	6080	5768
Dy	45019	46420	45388	43659	44372	45979	47921	46198	44912	43435
Ho	9833	10078	9947	9725	9589	10078	10366	10700	9698	9576
Er	25998	26786	25874	25627	24636	26793	27089	29439	25230	25323
Tm	3625	3780	3647	3620	3381	3851	3998	4403	3472	3436
Yb	22462	23401	22240	21379	20282	24273	25213	28176	20348	20022
Lu	2618	2778	2676	2631	2336	2797	2846	3325	2474	2449
Hf	5	6	6	5	5	5	5	5	5	5
W	7	8	6	10	8	9	7	7	9	7
Pb	2	4	2	2	1	2	3	13	2	1
Th	17	34	21	12	5	9	20	75	10	8
U	1552	1454	1401	1827	1836	2163	2159	1737	1721	1567
Eu/Eu*	0.45	0.47	0.47	0.44	0.43	0.44	0.44	0.46	0.44	0.44
Al	0.00	0.00	0.00	0.00	0.00	0.00	0.00	0.00	0.00	0.00
Si	0.02	0.02	0.02	0.02	0.02	0.02	0.02	0.02	0.03	0.02
P	0.89	0.89	0.89	0.88	0.89	0.90	0.89	0.89	0.88	0.87
Ca	0.01	0.00	0.00	0.01	0.01	0.01	0.01	0.01	0.01	0.01
Sc	0.00	0.00	0.00	0.00	0.00	0.00	0.00	0.00	0.00	0.00
Mn	0.00	0.00	0.00	0.00	0.00	0.00	0.00	0.00	0.00	0.00
Fe	0.01	0.01	0.01	0.05	0.03	0.02	0.01	0.02	0.03	0.03
Y	0.91	0.91	0.90	0.89	0.89	0.88	0.90	0.89	0.90	0.93
Zr	0.00	0.00	0.00	0.00	0.00	0.00	0.00	0.00	0.00	0.00
La	0.00	0.00	0.00	0.00	0.00	0.00	0.00	0.00	0.00	0.00
Ce	0.00	0.00	0.00	0.00	0.00	0.00	0.00	0.00	0.00	0.00
Pr	0.00	0.00	0.00	0.00	0.00	0.00	0.00	0.00	0.00	0.00
Nd	0.01	0.00	0.00	0.01	0.01	0.01	0.01	0.00	0.01	0.01
Sm	0.02	0.02	0.02	0.02	0.02	0.02	0.02	0.01	0.02	0.02
Eu	0.00	0.00	0.00	0.00	0.00	0.00	0.00	0.00	0.00	0.00
Gd	0.04	0.04	0.04	0.03	0.04	0.04	0.04	0.03	0.04	0.04
Tb	0.01	0.01	0.01	0.01	0.01	0.01	0.01	0.01	0.01	0.01
Dy	0.07	0.07	0.07	0.06	0.06	0.07	0.07	0.07	0.07	0.07
Ho	0.01	0.01	0.01	0.01	0.01	0.01	0.01	0.02	0.01	0.01
Er	0.04	0.04	0.04	0.04	0.03	0.04	0.04	0.04	0.04	0.04
Tm	0.01	0.01	0.01	0.01	0.00	0.01	0.01	0.01	0.00	0.00
Yb	0.03	0.03	0.03	0.03	0.03	0.03	0.03	0.04	0.03	0.03
Lu	0.00	0.00	0.00	0.00	0.00	0.00	0.00	0.00	0.00	0.00
Th	0.00	0.00	0.00	0.00	0.00	0.00	0.00	0.00	0.00	0.00
U	0.00	0.00	0.00	0.00	0.00	0.00	0.00	0.00	0.00	0.00
Total	2.07	2.07	2.07	2.07	2.07	2.06	2.07	2.07	2.07	2.08
P site	0.91	0.90	0.91	0.90	0.91	0.92	0.91	0.92	0.90	0.89
REE site	1.14	1.15	1.14	1.11	1.11	1.11	1.15	1.12	1.13	1.16

*Y = 33.9 wt.% (Cook et al., 2013)

**Formulae on basis of 4 a.p.f.u.

(Continued)

Deposit	Wolverine								
No	W5-6B_1	W5-6B_2	W5-6B_3	W5-6B_4	W5-6B_5	W5-6B_6	W5-6B_7	W5-6B_8	W5-6B_9
Paragenesis	Vein-type								
(ppm)									
Al	153	485	444	353	620	240	196	357	429
Si	<3151	<3327	<3013	<3385	<3936	<3763	3201	<3538	<3513
P	132153	130947	128560	130658	137727	133394	127999	130290	133076
Ca	1019	1028	1304	853	986	1129	760	1313	1115
Sc	180	242	364	245	263	338	209	137	136
Ti	7	6	4	7	26	6	9	8	11
Mn	17	31	23	17	24	21	11	23	13
Fe	10940	21546	19784	17957	27305	16672	6533	23229	12165
Sr	6	7	7	6	6	6	5	6	5
Zr	2	7	8	8	20	5	9	6	11
Nb	0	0	0	0	0	0	0	0	0
Sb	4	4	5	6	8	5	2	8	3
Ba	2	7	10	5	4	3	2	5	3
La	15	16	15	13	13	11	5	14	16
Ce	396	473	415	398	431	307	176	445	424
Pr	279	371	326	323	350	256	161	363	324
Nd	4060	6034	5136	5197	5596	4486	3231	5768	5071
Sm	10274	10184	8134	9521	9248	9373	10415	9607	11166
Eu	2268	2080	1591	2047	1852	1931	2301	1970	2541
Gd	24931	22112	17714	22937	20785	21821	25633	21326	28101
Tb	5991	5746	5192	5892	5459	5509	6269	5650	6437
Dy	43956	44838	44148	46016	44011	43890	46336	43816	46292
Ho	9965	10535	10540	10536	10466	10421	10318	10334	10145
Er	28288	30792	31747	30489	30974	30848	28929	29905	27977
Tm	4475	5009	5283	5001	5137	5118	4637	4753	4389
Yb	29817	34339	37470	34591	34773	34895	31460	31096	28155
Lu	3706	4302	4719	4312	4558	4504	3853	3985	3523
Hf	5	6	5	6	6	6	6	6	6
W	9	16	15	12	17	12	9	14	13
Pb	1	0	1	1	1	1	6	1	1
Th	5	0	0	1	3	3	40	3	3
U	1316	837	847	818	962	925	808	1159	1048
Eu/Eu*	0.43	0.42	0.41	0.42	0.41	0.41	0.43	0.42	0.44
Al	0.00	0.00	0.00	0.00	0.00	0.00	0.00	0.00	0.00
Si	0.02	0.03	0.02	0.03	0.03	0.03	0.03	0.03	0.03
P	0.92	0.90	0.90	0.90	0.91	0.91	0.91	0.90	0.92
Ca	0.01	0.01	0.01	0.00	0.01	0.01	0.00	0.01	0.01
Sc	0.00	0.00	0.00	0.00	0.00	0.00	0.00	0.00	0.00
Mn	0.00	0.00	0.00	0.00	0.00	0.00	0.00	0.00	0.00
Fe	0.04	0.08	0.08	0.07	0.10	0.06	0.03	0.09	0.05
Y	0.82	0.81	0.82	0.82	0.78	0.81	0.84	0.81	0.81
Zr	0.00	0.00	0.00	0.00	0.00	0.00	0.00	0.00	0.00
La	0.00	0.00	0.00	0.00	0.00	0.00	0.00	0.00	0.00
Ce	0.00	0.00	0.00	0.00	0.00	0.00	0.00	0.00	0.00
Pr	0.00	0.00	0.00	0.00	0.00	0.00	0.00	0.00	0.00
Nd	0.01	0.01	0.01	0.01	0.01	0.01	0.00	0.01	0.01
Sm	0.01	0.01	0.01	0.01	0.01	0.01	0.02	0.01	0.02
Eu	0.00	0.00	0.00	0.00	0.00	0.00	0.00	0.00	0.00
Gd	0.03	0.03	0.02	0.03	0.03	0.03	0.04	0.03	0.04
Tb	0.01	0.01	0.01	0.01	0.01	0.01	0.01	0.01	0.01
Dy	0.06	0.06	0.06	0.06	0.06	0.06	0.06	0.06	0.06
Ho	0.01	0.01	0.01	0.01	0.01	0.01	0.01	0.01	0.01
Er	0.04	0.04	0.04	0.04	0.04	0.04	0.04	0.04	0.04
Tm	0.01	0.01	0.01	0.01	0.01	0.01	0.01	0.01	0.01
Yb	0.04	0.04	0.05	0.04	0.04	0.04	0.04	0.04	0.04
Lu	0.00	0.01	0.01	0.01	0.01	0.01	0.00	0.00	0.00
Th	0.00	0.00	0.00	0.00	0.00	0.00	0.00	0.00	0.00
U	0.00	0.00	0.00	0.00	0.00	0.00	0.00	0.00	0.00
Total	2.05	2.06	2.06	2.06	2.05	2.05	2.05	2.06	2.05
P site	0.95	0.92	0.92	0.93	0.94	0.94	0.94	0.93	0.95
REE site	1.05	1.04	1.05	1.05	1.00	1.03	1.08	1.04	1.04

*Y = 33.9 wt.% (Cook et al., 2013)

**Formulae on basis of 4 a.p.f.u.

(Continued)

Deposit	Wolverine								
No	W5-6B_11	W5-6B_12	W5-6B_13	W5-6B_14	W5-6B_15	W5-6B_16	W5-6B_17	W5-6B_18	W5-6B_20
Paragenesis	Vein-type								
(ppm)									
Al	459	325	1084	40	2083	95	49	394	78
Si	<3437	3416	3381	<3185	<3322	<4268	<3294	<3120	<3597
P	136157	128241	128615	130080	125930	134833	128076	127333	133100
Ca	988	1303	892	831	1148	553	474	1144	822
Sc	271	314	165	156	275	149	138	611	403
Ti	12	11	3	2	6	5	3	14	3
Mn	11	19	14	5	12	15	9	13	11
Fe	10375	22546	12477	3207	6301	5218	5689	6101	7920
Sr	6	6	5	3	5	3	3	5	4
Zr	22	13	13	21	37	9	8	10	9
Nb	0	0	0	0	0	0	0	0	0
Sb	2	6	5	1	2	1	1	1	1
Ba	2	8	2	2	3	2	3	2	2
La	23	13	10	4	8	4	5	4	2
Ce	510	438	304	120	267	123	175	142	93
Pr	351	341	246	101	222	116	161	133	99
Nd	5285	5166	4204	2277	3936	2785	3600	2710	2499
Sm	11676	8605	10522	11976	10271	13433	13742	9327	11472
Eu	2534	1854	2396	2907	2231	2927	2939	2190	2740
Gd	27414	19733	26616	34225	25844	33714	34180	25319	31694
Tb	6554	5504	6282	7323	6196	7098	7250	6289	7015
Dy	47665	45197	45682	46540	46493	45364	46837	45995	47387
Ho	10421	10716	10286	9279	10185	9155	9281	10300	9857
Er	29106	31623	29470	22685	27852	23148	22641	28413	25881
Tm	4722	5299	4642	3021	4250	3069	2990	4439	3761
Yb	32323	37219	31626	17884	27431	18087	17054	29422	23905
Lu	3981	4687	3880	2144	3336	2310	2076	3619	2944
Hf	6	6	6	5	7	7	5	6	6
W	10	16	12	8	9	1	2	11	8
Pb	0	2	0	4	11	2	1	32	16
Th	1	7	1	28	88	18	8	230	109
U	596	972	877	1644	1211	1729	1279	1264	1441
Eu/Eu*	0.43	0.43	0.44	0.44	0.42	0.42	0.41	0.44	0.44
Al	0.00	0.00	0.01	0.00	0.02	0.00	0.00	0.00	0.00
Si	0.03	0.03	0.03	0.03	0.03	0.03	0.03	0.02	0.03
P	0.93	0.89	0.90	0.93	0.90	0.94	0.92	0.91	0.93
Ca	0.01	0.01	0.00	0.00	0.01	0.00	0.00	0.01	0.00
Sc	0.00	0.00	0.00	0.00	0.00	0.00	0.00	0.00	0.00
Mn	0.00	0.00	0.00	0.00	0.00	0.00	0.00	0.00	0.00
Fe	0.04	0.09	0.05	0.01	0.03	0.02	0.02	0.02	0.03
Y	0.80	0.82	0.83	0.84	0.85	0.82	0.85	0.85	0.82
Zr	0.00	0.00	0.00	0.00	0.00	0.00	0.00	0.00	0.00
La	0.00	0.00	0.00	0.00	0.00	0.00	0.00	0.00	0.00
Ce	0.00	0.00	0.00	0.00	0.00	0.00	0.00	0.00	0.00
Pr	0.00	0.00	0.00	0.00	0.00	0.00	0.00	0.00	0.00
Nd	0.01	0.01	0.01	0.00	0.01	0.00	0.01	0.00	0.00
Sm	0.02	0.01	0.02	0.02	0.02	0.02	0.02	0.01	0.02
Eu	0.00	0.00	0.00	0.00	0.00	0.00	0.00	0.00	0.00
Gd	0.04	0.03	0.04	0.05	0.04	0.05	0.05	0.04	0.04
Tb	0.01	0.01	0.01	0.01	0.01	0.01	0.01	0.01	0.01
Dy	0.06	0.06	0.06	0.06	0.06	0.06	0.06	0.06	0.06
Ho	0.01	0.01	0.01	0.01	0.01	0.01	0.01	0.01	0.01
Er	0.04	0.04	0.04	0.03	0.04	0.03	0.03	0.04	0.03
Tm	0.01	0.01	0.01	0.00	0.01	0.00	0.00	0.01	0.00
Yb	0.04	0.05	0.04	0.02	0.04	0.02	0.02	0.04	0.03
Lu	0.00	0.01	0.00	0.00	0.00	0.00	0.00	0.00	0.00
Th	0.00	0.00	0.00	0.00	0.00	0.00	0.00	0.00	0.00
U	0.00	0.00	0.00	0.00	0.00	0.00	0.00	0.00	0.00
Total	2.04	2.07	2.06	2.04	2.06	2.03	2.05	2.05	2.04
P site	0.95	0.92	0.93	0.96	0.93	0.97	0.95	0.94	0.95
REE site	1.04	1.05	1.06	1.06	1.08	1.04	1.07	1.08	1.05

*Y = 33.9 wt.% (Cook et al., 2013)

**Formulae on basis of 4 a.p.f.u.

(Continued)

Deposit	Wolverine									
No	W7-3B_2	W7-3B_3	W7-3B_4	W7-3B_5	W7-3B_6	W7-3B_7	W7-3B_8	W7-3B_9	W7-3B_10	W7-3B_11
Paragenesis	Vein-type									
(ppm)										
Al	50	102	352	143	246	142	125	347	9	186
Si	<2587	<2822	<4373	<3402	<3687	<4645	<2901	<3516	<3203	<4142
P	127676	128941	136931	129469	133942	142475	127611	130252	125808	136070
Ca	621	1086	888	868	834	1109	837	1087	643	614
Sc	240	199	197	293	223	282	193	249	181	193
Ti	5	34	40	18	78	50	26	25	14	102
Mn	2	4	6	6	5	7	5	4	3	3
Fe	329	568	1648	691	187	931	492	2155	275	701
Sr	7	7	5	6	27	19	4	19	4	23
Zr	8	37	107	48	55	120	20	18	100	73
Nb	1	1	0	0	1	1	0	0	0	1
Sb	0	1	2	1	1	1	1	2	1	2
Ba	6	2	2	2	18	17	1	15	1	18
La	3	12	12	14	19	35	3	23	8	20
Ce	80	313	334	417	333	797	111	463	205	246
Pr	70	267	279	314	291	549	102	326	168	164
Nd	1882	4828	5066	5050	5505	7990	2543	5128	3145	3134
Sm	10703	11120	11376	10626	14559	14806	11460	12688	10299	12871
Eu	2912	2773	2423	1805	3023	2709	2848	2593	2629	2800
Gd	31494	28860	24778	20421	30617	25873	29710	26053	28672	28050
Tb	7500	6856	6273	5949	7198	6684	7077	6750	6905	6899
Dy	51376	48098	45830	47636	49103	49752	48857	50156	49395	48778
Ho	10535	10038	9885	10916	10279	10809	10317	10810	10456	10497
Er	27059	26365	26887	31521	27434	30096	27148	29742	28059	28414
Tm	4003	3846	3899	5149	3956	4546	3948	4572	4103	4141
Yb	26114	23941	23965	34846	24989	30508	25298	30341	25928	26409
Lu	3222	2876	3030	4388	3081	3809	3077	3786	3215	3382
Hf	6	6	7	6	6	7	7	6	7	7
W	7	13	11	11	12	13	9	9	9	13
Pb	2	1	9	2	4	6	2	2	3	5
Th	30	95	161	151	176	228	106	59	191	146
U	2385	2282	2339	1623	2080	1504	2141	1263	2312	2078
Eu/Eu*	0.48	0.47	0.44	0.37	0.44	0.42	0.47	0.44	0.47	0.45
Al	0.00	0.00	0.00	0.00	0.00	0.00	0.00	0.00	0.00	0.00
Si	0.02	0.02	0.03	0.03	0.03	0.03	0.02	0.03	0.03	0.03
P	0.92	0.93	0.94	0.92	0.93	0.95	0.92	0.92	0.92	0.94
Ca	0.00	0.01	0.00	0.00	0.00	0.01	0.00	0.01	0.00	0.00
Sc	0.00	0.00	0.00	0.00	0.00	0.00	0.00	0.00	0.00	0.00
Mn	0.00	0.00	0.00	0.00	0.00	0.00	0.00	0.00	0.00	0.00
Fe	0.00	0.00	0.01	0.00	0.00	0.00	0.00	0.01	0.00	0.00
Y	0.85	0.85	0.81	0.84	0.82	0.79	0.85	0.83	0.86	0.82
Zr	0.00	0.00	0.00	0.00	0.00	0.00	0.00	0.00	0.00	0.00
La	0.00	0.00	0.00	0.00	0.00	0.00	0.00	0.00	0.00	0.00
Ce	0.00	0.00	0.00	0.00	0.00	0.00	0.00	0.00	0.00	0.00
Pr	0.00	0.00	0.00	0.00	0.00	0.00	0.00	0.00	0.00	0.00
Nd	0.00	0.01	0.01	0.01	0.01	0.01	0.00	0.01	0.00	0.00
Sm	0.02	0.02	0.02	0.02	0.02	0.02	0.02	0.02	0.02	0.02
Eu	0.00	0.00	0.00	0.00	0.00	0.00	0.00	0.00	0.00	0.00
Gd	0.04	0.04	0.03	0.03	0.04	0.03	0.04	0.04	0.04	0.04
Tb	0.01	0.01	0.01	0.01	0.01	0.01	0.01	0.01	0.01	0.01
Dy	0.07	0.07	0.06	0.06	0.07	0.06	0.07	0.07	0.07	0.06
Ho	0.01	0.01	0.01	0.01	0.01	0.01	0.01	0.01	0.01	0.01
Er	0.04	0.04	0.03	0.04	0.04	0.04	0.04	0.04	0.04	0.04
Tm	0.01	0.01	0.00	0.01	0.01	0.01	0.01	0.01	0.01	0.01
Yb	0.03	0.03	0.03	0.04	0.03	0.04	0.03	0.04	0.03	0.03
Lu	0.00	0.00	0.00	0.01	0.00	0.00	0.00	0.00	0.00	0.00
Th	0.00	0.00	0.00	0.00	0.00	0.00	0.00	0.00	0.00	0.00
U	0.00	0.00	0.00	0.00	0.00	0.00	0.00	0.00	0.00	0.00
Total	2.05	2.04	2.03	2.04	2.04	2.02	2.05	2.05	2.05	2.03
P site	0.94	0.95	0.98	0.95	0.96	0.98	0.94	0.95	0.94	0.97
REE site	1.10	1.08	1.03	1.08	1.06	1.03	1.09	1.08	1.10	1.05

*Y = 33.9 wt.% (Cook et al., 2013)

**Formulae on basis of 4 a.p.f.u.

(Continued)

Deposit	Wolverine								
No	W7-3B_12	W7-3B_13	W7-3B_14	W7-3B_15	W7-3B_16	W7-3B_17	W7-3B_18	W7-3B_19	W7-3B_20
Paragenesis	Vein-type								
(ppm)									
Al	226	301	131	143	475	364	744	180	240
Si	<3505	4084	<3070	<2865	<3946	<3285	5872	<3069	<2451
P	131751	131070	130608	126504	130580	132503	132661	129407	125302
Ca	602	682	873	891	381	1092	653	976	1507
Sc	169	209	222	224	155	362	165	249	310
Ti	66	29	44	89	98	33	75	29	53
Mn	3	6	5	4	5	5	3	6	4
Fe	863	1480	1580	703	1868	2581	553	1438	1346
Sr	24	17	12	11	36	11	28	5	14
Zr	16	5	23	73	14	26	12	52	13
Nb	1	0	0	1	1	0	1	0	0
Sb	1	2	3	2	2	2	1	1	1
Ba	13	10	6	7	43	11	16	1	18
La	16	9	8	14	21	21	17	12	20
Ce	269	148	141	324	218	491	234	368	475
Pr	218	108	107	251	164	353	166	312	367
Nd	4147	2512	2442	4259	3566	5761	2911	5371	5919
Sm	12017	12837	11613	11180	14234	13217	10273	10772	11202
Eu	2701	2756	2742	2722	3012	2733	2896	2365	2635
Gd	27303	27977	29761	27895	29710	26614	29808	23885	27568
Tb	6893	6900	7217	6920	7133	6846	7227	6365	6934
Dy	48638	49601	50424	49837	48829	50836	49672	47478	50543
Ho	10379	10556	10609	10660	10406	11029	10352	10536	11024
Er	28030	28763	28456	28430	27503	30610	27092	29418	30370
Tm	4068	4286	4242	4218	4011	4829	3914	4391	4791
Yb	25258	27236	27288	26320	25013	32184	24559	28373	31710
Lu	3129	3354	3427	3261	3141	3911	3051	3579	3877
Hf	6	6	6	7	6	6	6	5	6
W	10	7	11	14	10	5	12	10	10
Pb	2	2	2	3	4	2	4	3	2
Th	93	38	81	190	47	64	57	134	64
U	2185	2004	2046	2371	1985	1341	2457	1958	1642
Eu/Eu*	0.46	0.44	0.45	0.47	0.45	0.45	0.51	0.45	0.46
Al	0.00	0.00	0.00	0.00	0.00	0.00	0.01	0.00	0.00
Si	0.03	0.03	0.02	0.02	0.03	0.03	0.05	0.02	0.02
P	0.93	0.92	0.93	0.92	0.92	0.92	0.92	0.92	0.91
Ca	0.00	0.00	0.00	0.00	0.00	0.01	0.00	0.01	0.01
Sc	0.00	0.00	0.00	0.00	0.00	0.00	0.00	0.00	0.00
Mn	0.00	0.00	0.00	0.00	0.00	0.00	0.00	0.00	0.00
Fe	0.00	0.01	0.01	0.00	0.01	0.01	0.00	0.01	0.01
Y	0.83	0.83	0.84	0.85	0.83	0.82	0.82	0.84	0.85
Zr	0.00	0.00	0.00	0.00	0.00	0.00	0.00	0.00	0.00
La	0.00	0.00	0.00	0.00	0.00	0.00	0.00	0.00	0.00
Ce	0.00	0.00	0.00	0.00	0.00	0.00	0.00	0.00	0.00
Pr	0.00	0.00	0.00	0.00	0.00	0.00	0.00	0.00	0.00
Nd	0.01	0.00	0.00	0.01	0.01	0.01	0.00	0.01	0.01
Sm	0.02	0.02	0.02	0.02	0.02	0.02	0.01	0.02	0.02
Eu	0.00	0.00	0.00	0.00	0.00	0.00	0.00	0.00	0.00
Gd	0.04	0.04	0.04	0.04	0.04	0.04	0.04	0.03	0.04
Tb	0.01	0.01	0.01	0.01	0.01	0.01	0.01	0.01	0.01
Dy	0.07	0.07	0.07	0.07	0.07	0.07	0.07	0.06	0.07
Ho	0.01	0.01	0.01	0.01	0.01	0.01	0.01	0.01	0.01
Er	0.04	0.04	0.04	0.04	0.04	0.04	0.03	0.04	0.04
Tm	0.01	0.01	0.01	0.01	0.01	0.01	0.00	0.01	0.01
Yb	0.03	0.03	0.03	0.03	0.03	0.04	0.03	0.04	0.04
Lu	0.00	0.00	0.00	0.00	0.00	0.00	0.00	0.00	0.00
Th	0.00	0.00	0.00	0.00	0.00	0.00	0.00	0.00	0.00
U	0.00	0.00	0.00	0.00	0.00	0.00	0.00	0.00	0.00
Total	2.04	2.04	2.04	2.05	2.04	2.04	2.04	2.04	2.06
P site	0.96	0.96	0.95	0.94	0.95	0.95	0.97	0.95	0.93
REE site	1.07	1.07	1.08	1.10	1.07	1.07	1.05	1.08	1.11

*Y = 33.9 wt.% (Cook et al., 2013)

**Formulae on basis of 4 a.p.f.u.

(Continued)

Deposit	Wolverine									
No	W5-5_4	W5-5_5	W5-5_6	W5-5_7	W5-5_8	W5-5_12	W5-5_13	W5-5_1	W5-5_2	W5-5_3
Paragenesis	Breccia-hosted							Vein-type		
(ppm)										
Al	15	422	24	154	29	22	892	282	218	284
Si	<5046	<4515	<3846	<5224	<4662	<6061	<3787	<5266	<6350	<5008
P	156831	150070	149343	148026	152830	168286	151025	157221	158603	156785
Ca	702	950	1011	1090	1588	1123	1630	662	724	1196
Sc	180	185	128	189	198	124	626	810	719	571
Ti	5	6	10	1229	7	5	12	6	39	12
Mn	10	15	7	10	9	3	21	16	15	11
Fe	2288	6277	2324	2015	6544	6209	12657	20727	14315	7889
Sr	4	5	4	8	4	3	6	7	7	6
Zr	91	36	46	77	20	13	9	3	2	5
Nb	0	0	0	9	0	0	0	0	0	0
Sb	0	2	1	1	1	4	2	4	3	2
Ba	2	1	1	3	3	2	11	4	4	10
La	1	1	2	4	1	2	10	22	17	14
Ce	45	43	71	105	33	78	307	462	367	360
Pr	43	51	77	85	45	85	250	284	239	261
Nd	1264	1480	1904	1797	1422	2008	4148	4038	3696	4364
Sm	8972	9014	9138	9917	9561	10089	8899	11219	11534	10743
Eu	2608	2365	2395	2882	2828	2555	1973	2716	2763	2655
Gd	27801	25989	27031	28176	29832	27373	20962	28166	27832	29478
Tb	6796	6841	6835	6829	7086	6800	5567	6675	6599	6834
Dy	48321	49316	48988	47820	50233	48960	45696	50839	49863	49833
Ho	10351	11131	10895	10190	10716	10668	10872	11655	11159	11143
Er	27762	30809	29058	26649	28814	27319	31884	34394	33053	32388
Tm	3883	4757	4361	3741	4071	4000	5259	5832	5617	5339
Yb	24401	31814	27342	23175	24901	24687	36392	42434	40979	36584
Lu	2988	3859	3381	2907	3190	3181	4690	5334	5076	4550
Hf	9	7	7	8	8	7	6	6	7	6
W	8	9	9	89	8	11	11	16	12	11
Pb	8	6	6	12	6	8	2	1	1	1
Th	58	46	43	72	44	57	8	1	2	1
U	2703	2461	2706	2638	3713	2940	1282	862	815	1101
Eu/Eu*	0.50	0.47	0.47	0.53	0.51	0.47	0.44	0.47	0.47	0.46
Al	0.00	0.00	0.00	0.00	0.00	0.00	0.01	0.00	0.00	0.00
Si	0.04	0.03	0.03	0.04	0.03	0.04	0.03	0.04	0.04	0.03
P	0.99	0.97	0.98	0.97	0.98	1.01	0.96	0.95	0.96	0.97
Ca	0.00	0.00	0.01	0.01	0.01	0.01	0.01	0.00	0.00	0.01
Sc	0.00	0.00	0.00	0.00	0.00	0.00	0.00	0.00	0.00	0.00
Mn	0.00	0.00	0.00	0.00	0.00	0.00	0.00	0.00	0.00	0.00
Fe	0.01	0.02	0.01	0.01	0.02	0.02	0.04	0.07	0.05	0.03
Y	0.75	0.76	0.77	0.78	0.75	0.71	0.75	0.72	0.72	0.73
Zr	0.00	0.00	0.00	0.00	0.00	0.00	0.00	0.00	0.00	0.00
La	0.00	0.00	0.00	0.00	0.00	0.00	0.00	0.00	0.00	0.00
Ce	0.00	0.00	0.00	0.00	0.00	0.00	0.00	0.00	0.00	0.00
Pr	0.00	0.00	0.00	0.00	0.00	0.00	0.00	0.00	0.00	0.00
Nd	0.00	0.00	0.00	0.00	0.00	0.00	0.01	0.01	0.00	0.01
Sm	0.01	0.01	0.01	0.01	0.01	0.01	0.01	0.01	0.01	0.01
Eu	0.00	0.00	0.00	0.00	0.00	0.00	0.00	0.00	0.00	0.00
Gd	0.03	0.03	0.03	0.04	0.04	0.03	0.03	0.03	0.03	0.04
Tb	0.01	0.01	0.01	0.01	0.01	0.01	0.01	0.01	0.01	0.01
Dy	0.06	0.06	0.06	0.06	0.06	0.06	0.06	0.06	0.06	0.06
Ho	0.01	0.01	0.01	0.01	0.01	0.01	0.01	0.01	0.01	0.01
Er	0.03	0.04	0.04	0.03	0.03	0.03	0.04	0.04	0.04	0.04
Tm	0.00	0.01	0.01	0.00	0.00	0.00	0.01	0.01	0.01	0.01
Yb	0.03	0.04	0.03	0.03	0.03	0.03	0.04	0.05	0.05	0.04
Lu	0.00	0.00	0.00	0.00	0.00	0.00	0.01	0.01	0.01	0.00
Th	0.00	0.00	0.00	0.00	0.00	0.00	0.00	0.00	0.00	0.00
U	0.00	0.00	0.00	0.00	0.00	0.00	0.00	0.00	0.00	0.00
Total	1.99	2.01	2.01	2.01	2.01	1.98	2.02	2.02	2.01	2.01
P site	1.03	1.00	1.00	1.01	1.01	1.05	0.99	0.99	1.01	1.01
REE site	0.95	0.98	0.99	0.98	0.96	0.90	0.97	0.95	0.95	0.96

*Y = 33.9 wt.% (Cook et al., 2013)

**Formulae on basis of 4 a.p.f.u.

(Continued)

Deposit	Wolverine								
No	W5-5_9	W5-5_10	W5-5_11	W5-5_14	W5-5_15	W5-5_16	W5-5_17	W5-5_18	W5-5_19
Paragenesis	Vein-type								
(ppm)									
Al	15	118	870	61	14	32	81	29	105
Si	<5514	<4232	<4299	<3032	<3653	<3629	<4850	<4158	<3495
P	159261	157785	153921	144511	148701	149530	156622	150538	146687
Ca	1087	1509	1407	820	1145	1465	1646	840	932
Sc	233	460	431	162	112	91	97	133	254
Ti	1	10	18	6	29	7	14	37	15
Mn	7	17	17	9	11	8	7	10	8
Fe	1529	8628	14876	3786	3908	3598	5129	1970	7264
Sr	3	5	6	3	3	4	4	4	5
Zr	25	21	5	13	9	2	24	50	1
Nb	0	0	0	0	0	0	0	0	0
Sb	0	2	2	1	1	1	1	0	5
Ba	1	3	5	1	3	1	1	3	2
La	1	13	14	14	20	33	1	1	36
Ce	51	361	433	402	567	826	50	27	864
Pr	66	277	333	333	463	589	75	35	635
Nd	2125	4374	5175	5728	7419	8264	2031	1258	9055
Sm	11933	10762	8551	13351	12597	11857	8967	9462	12254
Eu	3082	2828	1854	3357	3100	2567	2397	2721	2777
Gd	34655	30157	19152	40473	31538	26513	25573	29833	26601
Tb	7571	6820	5610	7961	7255	6638	6668	6910	6739
Dy	48693	47903	46874	48460	48405	47975	48211	48611	49947
Ho	9619	10495	10964	9476	9820	10110	10497	10187	11186
Er	24729	28467	32202	22098	24085	26233	28749	26778	31027
Tm	3409	4357	5228	2884	3148	3645	4046	3799	4989
Yb	20683	28386	35640	15635	17857	20681	24934	23552	33234
Lu	2606	3590	4733	1878	2175	2552	3129	2950	3914
Hf	7	7	6	7	6	6	7	7	7
W	7	10	12	7	9	8	10	9	9
Pb	31	7	1	2	1	1	14	5	0
Th	169	46	2	16	10	5	86	35	0
U	2362	1959	1306	1278	1079	904	2949	2135	924
Eu/Eu*	0.46	0.48	0.44	0.44	0.48	0.44	0.48	0.49	0.47
Al	0.00	0.00	0.01	0.00	0.00	0.00	0.00	0.00	0.00
Si	0.04	0.03	0.03	0.02	0.03	0.03	0.03	0.03	0.03
P	1.00	0.98	0.97	0.96	0.97	0.98	0.99	0.98	0.96
Ca	0.01	0.01	0.01	0.00	0.01	0.01	0.01	0.00	0.00
Sc	0.00	0.00	0.00	0.00	0.00	0.00	0.00	0.00	0.00
Mn	0.00	0.00	0.00	0.00	0.00	0.00	0.00	0.00	0.00
Fe	0.01	0.03	0.05	0.01	0.01	0.01	0.02	0.01	0.03
Y	0.74	0.74	0.74	0.79	0.77	0.77	0.75	0.77	0.77
Zr	0.00	0.00	0.00	0.00	0.00	0.00	0.00	0.00	0.00
La	0.00	0.00	0.00	0.00	0.00	0.00	0.00	0.00	0.00
Ce	0.00	0.00	0.00	0.00	0.00	0.00	0.00	0.00	0.00
Pr	0.00	0.00	0.00	0.00	0.00	0.00	0.00	0.00	0.00
Nd	0.00	0.01	0.01	0.01	0.01	0.01	0.00	0.00	0.01
Sm	0.02	0.01	0.01	0.02	0.02	0.02	0.01	0.01	0.02
Eu	0.00	0.00	0.00	0.00	0.00	0.00	0.00	0.00	0.00
Gd	0.04	0.04	0.02	0.05	0.04	0.03	0.03	0.04	0.03
Tb	0.01	0.01	0.01	0.01	0.01	0.01	0.01	0.01	0.01
Dy	0.06	0.06	0.06	0.06	0.06	0.06	0.06	0.06	0.06
Ho	0.01	0.01	0.01	0.01	0.01	0.01	0.01	0.01	0.01
Er	0.03	0.03	0.04	0.03	0.03	0.03	0.03	0.03	0.04
Tm	0.00	0.00	0.01	0.00	0.00	0.00	0.00	0.00	0.01
Yb	0.02	0.03	0.04	0.02	0.02	0.02	0.03	0.03	0.04
Lu	0.00	0.00	0.01	0.00	0.00	0.00	0.00	0.00	0.00
Th	0.00	0.00	0.00	0.00	0.00	0.00	0.00	0.00	0.00
U	0.00	0.00	0.00	0.00	0.00	0.00	0.00	0.00	0.00
Total	1.99	2.00	2.01	2.02	2.01	2.01	2.00	2.00	2.02
P site	1.03	1.01	1.00	0.99	1.00	1.00	1.02	1.01	0.98
REE site	0.94	0.95	0.95	1.01	0.99	0.98	0.94	0.98	1.01

*Y = 33.9 wt.% (Cook et al., 2013)

**Formulae on basis of 4 a.p.f.u.

(Continued)

Deposit	Wolverine					Cyclops			
No	W5-5_21	W5-5_22	W5-5_23	W5-5_24	W5-5_25	C2_2	C2_3	C2_7	C2_8
Paragenesis	Vein-type					Breccia-hosted			
(ppm)									
Al	86	207	179	24	35	208	171	284	550
Si	<4294	<3218	<5007	<4001	<4659	<3107	<3437	<4370	<3139
P	158681	152123	155534	147355	148333	124675	127434	137794	129177
Ca	1548	1754	1045	1304	2682	1056	956	614	909
Sc	1072	1683	777	161	274	196	152	139	135
Ti	14	12	8	2	3	35	3	4	3
Mn	18	23	13	8	9	4	4	4	4
Fe	9785	12754	4363	1037	2096	291	217	180	324
Sr	7	7	5	4	4	7	3	5	5
Zr	1	4	2	35	24	83	71	44	1
Nb	0	0	0	0	0	0	0	0	0
Sb	3	2	1	0	0	0	0	0	0
Ba	2	5	6	2	4	208	5	1	2
La	25	15	17	2	2	5	5	15	9
Ce	519	481	407	61	71	129	138	455	249
Pr	353	353	266	73	92	95	104	329	181
Nd	5183	4697	3703	2042	2217	1810	2035	4506	2823
Sm	11068	9704	9908	9166	8668	8620	8979	8715	7560
Eu	2752	2328	2953	2312	2329	2328	2251	1887	1705
Gd	28763	22792	31670	25171	25218	23204	23302	19532	17816
Tb	6839	5849	7191	6512	6531	5981	5947	6069	5594
Dy	51597	48921	50673	49189	48698	43171	43331	48489	46661
Ho	11430	11497	10807	10699	10671	9162	9210	10996	10602
Er	33857	35713	30738	29528	28443	23555	23215	30607	29749
Tm	5881	6322	4957	4405	4032	3213	3057	4805	4726
Yb	42446	48536	35133	28729	26102	18873	17491	32126	30956
Lu	5548	6344	4413	3566	3300	2315	2155	3832	3658
Hf	6	6	7	7	7	6	6	7	6
W	10	14	9	8	9	6	6	86	39
Pb	1	2	0	6	6	0	1	0	0
Th	2	2	2	41	34	81	68	57	53
U	1227	977	1546	2767	2939	2142	2310	1686	1431
Eu/Eu*	0.47	0.48	0.51	0.47	0.48	0.50	0.48	0.44	0.45
Al	0.00	0.00	0.00	0.00	0.00	0.00	0.00	0.00	0.00
Si	0.03	0.02	0.03	0.03	0.03	0.03	0.03	0.03	0.02
P	0.97	0.96	0.98	0.97	0.97	0.93	0.93	0.95	0.93
Ca	0.01	0.01	0.01	0.01	0.01	0.01	0.01	0.00	0.01
Sc	0.00	0.01	0.00	0.00	0.00	0.00	0.00	0.00	0.00
Mn	0.00	0.00	0.00	0.00	0.00	0.00	0.00	0.00	0.00
Fe	0.03	0.04	0.02	0.00	0.01	0.00	0.00	0.00	0.00
Y	0.72	0.74	0.74	0.78	0.77	0.88	0.87	0.81	0.85
Zr	0.00	0.00	0.00	0.00	0.00	0.00	0.00	0.00	0.00
La	0.00	0.00	0.00	0.00	0.00	0.00	0.00	0.00	0.00
Ce	0.00	0.00	0.00	0.00	0.00	0.00	0.00	0.00	0.00
Pr	0.00	0.00	0.00	0.00	0.00	0.00	0.00	0.00	0.00
Nd	0.01	0.01	0.00	0.00	0.00	0.00	0.00	0.01	0.00
Sm	0.01	0.01	0.01	0.01	0.01	0.01	0.01	0.01	0.01
Eu	0.00	0.00	0.00	0.00	0.00	0.00	0.00	0.00	0.00
Gd	0.03	0.03	0.04	0.03	0.03	0.03	0.03	0.03	0.03
Tb	0.01	0.01	0.01	0.01	0.01	0.01	0.01	0.01	0.01
Dy	0.06	0.06	0.06	0.06	0.06	0.06	0.06	0.06	0.06
Ho	0.01	0.01	0.01	0.01	0.01	0.01	0.01	0.01	0.01
Er	0.04	0.04	0.04	0.04	0.03	0.03	0.03	0.04	0.04
Tm	0.01	0.01	0.01	0.01	0.00	0.00	0.00	0.01	0.01
Yb	0.05	0.06	0.04	0.03	0.03	0.03	0.02	0.04	0.04
Lu	0.01	0.01	0.00	0.00	0.00	0.00	0.00	0.00	0.00
Th	0.00	0.00	0.00	0.00	0.00	0.00	0.00	0.00	0.00
U	0.00	0.00	0.00	0.00	0.00	0.00	0.00	0.00	0.00
Total	2.01	2.02	2.01	2.01	2.01	2.04	2.04	2.02	2.04
P site	1.00	0.98	1.01	1.00	1.01	0.95	0.96	0.98	0.96
REE site	0.96	0.98	0.97	0.99	0.98	1.08	1.06	1.04	1.07

*Y = 33.9 wt.% (Cook et al., 2013)

**Formulae on basis of 4 a.p.f.u.

(Continued)

Deposit	Cyclops										
No	C2_9	C2_10	C2_11	C2_12	C2_13	C2_14	C2_15	C2_16	C2_17	C2_18	C2_20
Paragenesis	Breccia-hosted										
(ppm)											
Al	109	391	1624	235	347	629	1412	455	654	636	562
Si	<3881	<4088	<3231	<3351	5624	3261	<3163	<3427	<2861	<3159	<3386
P	128470	130862	123581	126109	132329	123410	123231	126125	122499	123590	131024
Ca	1145	639	798	816	840	1012	751	843	715	740	625
Sc	168	150	211	172	172	191	279	160	218	197	159
Ti	2	2	8	4	9	6	63	21	52	15	1
Mn	6	2	5	4	5	5	8	4	1	4	6
Fe	276	147	330	338	230	246	291	161	57	254	297
Sr	5	5	4	4	3	4	4	4	4	4	5
Zr	81	60	168	88	60	79	195	41	36	63	52
Nb	0	0	0	0	0	0	0	0	0	0	0
Sb	0	0	0	0	0	0	0	0	0	0	0
Ba	1	1	1	1	1	1	1	1	1	2	2
La	11	2	8	6	9	7	3	14	1	16	14
Ce	266	39	177	180	220	207	52	302	28	363	322
Pr	171	27	108	129	136	146	36	186	23	233	200
Nd	2663	844	1854	2126	2126	2384	1008	2759	923	3221	2837
Sm	7779	7598	8209	8340	8893	8279	8180	8125	8475	8700	9201
Eu	1770	1996	2063	2044	2189	1947	2083	2058	2038	2117	2261
Gd	18913	20523	21138	20614	22315	20501	21462	20633	20802	20956	22281
Tb	5688	5683	5744	5731	5883	5690	5767	5821	5798	5991	5966
Dy	46002	44579	44008	44213	45090	43668	42907	45906	44925	46192	45919
Ho	10359	10225	9723	9835	9733	9812	9488	10066	9799	10201	9805
Er	28275	27835	25677	26001	25613	25936	25014	27394	25903	27019	26104
Tm	4432	4283	3704	3693	3498	3701	3632	4026	3691	4017	3734
Yb	28388	27725	22146	22361	20836	22509	21841	24566	22856	25123	22580
Lu	3435	3619	2712	2791	2671	2758	2670	3013	2717	2954	2756
Hf	7	6	8	7	6	6	8	6	6	7	6
W	7	7	6	6	6	6	7	7	7	7	6
Pb	0	0	1	1	1	0	1	0	1	1	1
Th	77	70	104	77	48	86	122	48	46	56	60
U	1739	1742	1741	1891	2413	2163	1812	2166	2668	1665	1969
Eu/Eu*	0.45	0.49	0.48	0.48	0.47	0.46	0.48	0.49	0.47	0.48	0.48
Al	0.00	0.00	0.01	0.00	0.00	0.01	0.01	0.00	0.01	0.01	0.00
Si	0.03	0.03	0.03	0.03	0.04	0.03	0.03	0.03	0.02	0.03	0.03
P	0.93	0.94	0.92	0.93	0.94	0.92	0.92	0.92	0.92	0.91	0.94
Ca	0.01	0.00	0.00	0.00	0.00	0.01	0.00	0.00	0.00	0.00	0.00
Sc	0.00	0.00	0.00	0.00	0.00	0.00	0.00	0.00	0.00	0.00	0.00
Mn	0.00	0.00	0.00	0.00	0.00	0.00	0.00	0.00	0.00	0.00	0.00
Fe	0.00	0.00	0.00	0.00	0.00	0.00	0.00	0.00	0.00	0.00	0.00
Y	0.85	0.84	0.88	0.87	0.84	0.88	0.88	0.86	0.88	0.87	0.85
Zr	0.00	0.00	0.00	0.00	0.00	0.00	0.00	0.00	0.00	0.00	0.00
La	0.00	0.00	0.00	0.00	0.00	0.00	0.00	0.00	0.00	0.00	0.00
Ce	0.00	0.00	0.00	0.00	0.00	0.00	0.00	0.00	0.00	0.00	0.00
Pr	0.00	0.00	0.00	0.00	0.00	0.00	0.00	0.00	0.00	0.00	0.00
Nd	0.00	0.00	0.00	0.00	0.00	0.00	0.00	0.00	0.00	0.01	0.00
Sm	0.01	0.01	0.01	0.01	0.01	0.01	0.01	0.01	0.01	0.01	0.01
Eu	0.00	0.00	0.00	0.00	0.00	0.00	0.00	0.00	0.00	0.00	0.00
Gd	0.03	0.03	0.03	0.03	0.03	0.03	0.03	0.03	0.03	0.03	0.03
Tb	0.01	0.01	0.01	0.01	0.01	0.01	0.01	0.01	0.01	0.01	0.01
Dy	0.06	0.06	0.06	0.06	0.06	0.06	0.06	0.06	0.06	0.07	0.06
Ho	0.01	0.01	0.01	0.01	0.01	0.01	0.01	0.01	0.01	0.01	0.01
Er	0.04	0.04	0.04	0.04	0.03	0.04	0.03	0.04	0.04	0.04	0.03
Tm	0.01	0.01	0.01	0.00	0.00	0.01	0.00	0.01	0.01	0.01	0.00
Yb	0.04	0.04	0.03	0.03	0.03	0.03	0.03	0.03	0.03	0.03	0.03
Lu	0.00	0.00	0.00	0.00	0.00	0.00	0.00	0.00	0.00	0.00	0.00
Th	0.00	0.00	0.00	0.00	0.00	0.00	0.00	0.00	0.00	0.00	0.00
U	0.00	0.00	0.00	0.00	0.00	0.00	0.00	0.00	0.00	0.00	0.00
Total	2.04	2.03	2.05	2.04	2.03	2.05	2.05	2.04	2.05	2.05	2.03
P site	0.96	0.97	0.94	0.95	0.98	0.94	0.94	0.95	0.94	0.94	0.97
REE site	1.07	1.05	1.08	1.08	1.04	1.09	1.08	1.08	1.09	1.10	1.06

*Y = 33.9 wt.% (Cook et al., 2013)

**Formulae on basis of 4 a.p.f.u.

(Continued)

Deposit	Iceman							
No	I1_5	I1_8	I1_9	I1_1	I1_2	I1_3	I1_6	I1_7
Paragenesis	Breccia-hosted			Vein-type				
(ppm)								
Al	92	242	181	284	318	232	220	134
Si	<4479	<4407	<3635	<3043	<2751	<2957	<3608	<4172
P	135113	131869	129271	130673	128422	127057	130051	133149
Ca	1766	1568	1796	2118	1776	1804	1389	1500
Sc	1340	1520	1333	1746	1398	1357	1162	1344
Ti	29	42	46	45	51	45	84	26
Mn	8	12	7	8	7	8	6	9
Fe	1945	2255	2620	2069	2221	3377	2930	2304
Sr	6	39	8	44	14	16	8	12
Zr	144	181	73	152	168	128	169	187
Nb	0	0	0	0	0	0	0	0
Sb	1	2	1	1	1	2	3	1
Ba	2	4	3	7	9	5	3	5
La	8	41	17	51	37	32	10	11
Ce	29	117	36	107	69	67	34	35
Pr	15	32	16	27	21	21	15	13
Nd	626	821	582	742	701	708	637	586
Sm	7621	7344	7374	7517	7608	7550	7861	7726
Eu	3546	3324	3558	3243	3409	3412	3629	3493
Gd	29939	28043	30650	28481	30209	29833	30864	29490
Tb	6751	6464	6679	6230	6663	6709	6741	6518
Dy	47297	47223	48034	47048	47994	48519	48294	48063
Ho	11062	11143	11312	11430	11129	11274	10964	11232
Er	32849	33199	33471	35182	32890	33030	31515	33775
Tm	5329	5335	5518	5907	5449	5397	5040	5573
Yb	35448	37425	38812	42633	37484	36997	33707	38884
Lu	4565	4808	4980	5445	4743	4638	4367	4935
Hf	7	8	6	7	7	7	8	8
W	9	11	13	10	9	14	12	9
Pb	18	25	34	49	67	64	27	24
Th	37	38	27	26	33	32	41	25
U	5439	4538	5190	4927	5430	5701	4540	4553
Eu/Eu*	0.72	0.71	0.72	0.68	0.69	0.69	0.71	0.71
Al	0.00	0.00	0.00	0.00	0.00	0.00	0.00	0.00
Si	0.03	0.03	0.03	0.02	0.02	0.02	0.03	0.03
P	0.93	0.92	0.91	0.91	0.91	0.90	0.91	0.92
Ca	0.01	0.01	0.01	0.01	0.01	0.01	0.01	0.01
Sc	0.01	0.01	0.01	0.01	0.01	0.01	0.01	0.01
Mn	0.00	0.00	0.00	0.00	0.00	0.00	0.00	0.00
Fe	0.01	0.01	0.01	0.01	0.01	0.01	0.01	0.01
Y	0.81	0.82	0.83	0.83	0.84	0.84	0.83	0.82
Zr	0.00	0.00	0.00	0.00	0.00	0.00	0.00	0.00
La	0.00	0.00	0.00	0.00	0.00	0.00	0.00	0.00
Ce	0.00	0.00	0.00	0.00	0.00	0.00	0.00	0.00
Pr	0.00	0.00	0.00	0.00	0.00	0.00	0.00	0.00
Nd	0.00	0.00	0.00	0.00	0.00	0.00	0.00	0.00
Sm	0.01	0.01	0.01	0.01	0.01	0.01	0.01	0.01
Eu	0.00	0.00	0.01	0.00	0.00	0.00	0.01	0.00
Gd	0.04	0.04	0.04	0.04	0.04	0.04	0.04	0.04
Tb	0.01	0.01	0.01	0.01	0.01	0.01	0.01	0.01
Dy	0.06	0.06	0.06	0.06	0.06	0.07	0.06	0.06
Ho	0.01	0.01	0.01	0.01	0.01	0.02	0.01	0.01
Er	0.04	0.04	0.04	0.05	0.04	0.04	0.04	0.04
Tm	0.01	0.01	0.01	0.01	0.01	0.01	0.01	0.01
Yb	0.04	0.05	0.05	0.05	0.05	0.05	0.04	0.05
Lu	0.01	0.01	0.01	0.01	0.01	0.01	0.01	0.01
Th	0.00	0.00	0.00	0.00	0.00	0.00	0.00	0.00
U	0.00	0.00	0.00	0.00	0.01	0.01	0.00	0.00
Total	2.04	2.05	2.05	2.05	2.05	2.06	2.05	2.04
P site	0.96	0.95	0.94	0.94	0.93	0.93	0.94	0.95
REE site	1.05	1.06	1.08	1.08	1.09	1.09	1.08	1.06

*Y = 33.9 wt.% (Cook et al., 2013)

**Formulae on basis of 4 a.p.f.u.

(Continued)

Deposit	Iceman						Boulder Ridge		
No	I1_10	I1_11	I1_12	I1_13	I1_14	I1_15	BR1_1	BR1_2	BR1_3
Paragenesis	Vein-type						Vein-type		
(ppm)									
Al	113	550	736	683	846	576	2784	371	234
Si	4767	<3511	<3127	<3544	<2948	<2474	<3553	<4083	<4913
P	129067	129497	130006	124748	127789	122426	142440	141275	143156
Ca	2159	2001	2167	1977	1975	1600	1288	1178	1796
Sc	1308	1333	1792	1068	1829	1186	666	579	875
Ti	55	66	78	108	82	37	98	17	10
Mn	6	8	8	5	15	8	10	7	19
Fe	1385	14452	16200	14829	21431	11081	673	1673	1856
Sr	11	13	7	6	8	12	98	8	4
Zr	133	137	113	158	204	231	82	77	470
Nb	0	0	0	1	1	0	0	0	0
Sb	1	2	3	5	3	2	4	1	3
Ba	3	3	1	2	2	3	12	2	1
La	15	12	4	4	6	12	101	6	2
Ce	45	45	34	32	54	41	208	25	24
Pr	22	23	22	19	28	15	37	11	15
Nd	744	743	748	676	859	558	667	495	598
Sm	7646	7376	6925	7448	7058	7351	7545	7277	5970
Eu	3489	3374	3099	3504	3105	3302	3891	3753	2991
Gd	30508	28985	26252	30026	26601	29783	36947	33710	26825
Tb	6678	6493	6006	6689	6073	6546	6895	6904	6082
Dy	48000	47286	46879	47710	48041	48749	44134	44907	42110
Ho	11150	11299	11692	10956	11639	11520	9871	9668	9684
Er	32162	33377	35962	32123	36167	33845	27305	26342	26021
Tm	5093	5460	6250	4981	6153	5620	4228	3969	3763
Yb	35011	37926	44220	34002	43539	39212	27480	25241	23779
Lu	4478	4789	5721	4239	5516	4865	3346	3135	2920
Hf	7	7	7	7	8	8	7	7	17
W	9	12	12	12	14	10	5	7	6
Pb	27	11	5	7	5	8	12	2	28
Th	29	22	28	24	44	28	7	5	188
U	5836	5711	6236	5646	4938	4312	2805	2481	3899
Eu/Eu*	0.70	0.71	0.70	0.72	0.69	0.68	0.71	0.73	0.72
Al	0.00	0.00	0.01	0.01	0.01	0.00	0.02	0.00	0.00
Si	0.04	0.03	0.02	0.03	0.02	0.02	0.03	0.03	0.04
P	0.91	0.89	0.89	0.88	0.88	0.88	0.95	0.96	0.96
Ca	0.01	0.01	0.01	0.01	0.01	0.01	0.01	0.01	0.01
Sc	0.01	0.01	0.01	0.01	0.01	0.01	0.00	0.00	0.00
Mn	0.00	0.00	0.00	0.00	0.00	0.00	0.00	0.00	0.00
Fe	0.01	0.06	0.06	0.06	0.08	0.04	0.00	0.01	0.01
Y	0.83	0.82	0.81	0.83	0.81	0.85	0.79	0.80	0.79
Zr	0.00	0.00	0.00	0.00	0.00	0.00	0.00	0.00	0.00
La	0.00	0.00	0.00	0.00	0.00	0.00	0.00	0.00	0.00
Ce	0.00	0.00	0.00	0.00	0.00	0.00	0.00	0.00	0.00
Pr	0.00	0.00	0.00	0.00	0.00	0.00	0.00	0.00	0.00
Nd	0.00	0.00	0.00	0.00	0.00	0.00	0.00	0.00	0.00
Sm	0.01	0.01	0.01	0.01	0.01	0.01	0.01	0.01	0.01
Eu	0.01	0.00	0.00	0.01	0.00	0.00	0.01	0.01	0.00
Gd	0.04	0.04	0.04	0.04	0.04	0.04	0.05	0.04	0.04
Tb	0.01	0.01	0.01	0.01	0.01	0.01	0.01	0.01	0.01
Dy	0.06	0.06	0.06	0.06	0.06	0.07	0.06	0.06	0.05
Ho	0.01	0.01	0.02	0.01	0.02	0.02	0.01	0.01	0.01
Er	0.04	0.04	0.05	0.04	0.05	0.05	0.03	0.03	0.03
Tm	0.01	0.01	0.01	0.01	0.01	0.01	0.01	0.00	0.00
Yb	0.04	0.05	0.05	0.04	0.05	0.05	0.03	0.03	0.03
Lu	0.01	0.01	0.01	0.01	0.01	0.01	0.00	0.00	0.00
Th	0.00	0.00	0.00	0.00	0.00	0.00	0.00	0.00	0.00
U	0.01	0.01	0.01	0.01	0.00	0.00	0.00	0.00	0.00
Total	2.05	2.06	2.07	2.07	2.08	2.08	2.02	2.02	2.01
P site	0.94	0.92	0.91	0.91	0.90	0.90	0.98	0.99	1.00
REE site	1.08	1.06	1.06	1.08	1.06	1.11	1.01	1.01	0.99

*Y = 33.9 wt.% (Cook et al., 2013)

**Formulae on basis of 4 a.p.f.u.

(Continued)

Deposit	Boulder Ridge						John Galt	
No	BR1_13	BR1_14	BR1_21	BR1_22	BR1_25	BR1_19	J1_1	J1_2
Paragenesis	Vein-type					Overgrowth	Overgrowth	
(ppm)								
Al	717	1112	1730	1731	1269	1999	287	95
Si	<2968	<3268	<3131	<2946	<4562	2823	3528	<2483
P	123969	126924	123540	119795	136197	119226	115005	113129
Ca	1355	980	1301	1065	2123	1580	116	164
Sc	574	463	649	621	521	534	455	351
Ti	17	1	12	1	14	2	1	1
Mn	6	5	13	10	7	14	6	5
Fe	136	135	422	363	1982	321	22	25
Sr	27	14	33	5	8	401	4	6
Zr	38	41	148	82	1036	179	20	12
Nb	0	0	0	0	0	0	0	0
Sb	0	0	0	0	3	0	0	0
Ba	3	2	5	1	5	46	1	3
La	22	8	27	3	15	352	3	7
Ce	61	31	73	20	45	703	51	54
Pr	20	17	18	12	15	100	70	73
Nd	650	678	552	537	629	956	1921	2134
Sm	6538	7160	6620	6583	9972	7197	5911	6770
Eu	3176	3558	3300	3370	4989	3462	1671	1976
Gd	27775	30538	29330	29311	48550	32412	13675	14727
Tb	6082	6309	6505	6405	8484	6579	4426	4664
Dy	44145	44755	45530	45952	48244	45594	40601	40842
Ho	10421	10365	10352	10223	9499	10232	10227	10178
Er	30018	29330	28752	28099	23868	28315	28424	28039
Tm	4647	4509	4311	4322	3160	4276	3979	3938
Yb	30709	29074	27889	26482	18848	27541	24271	24318
Lu	3889	3696	3477	3551	2465	3320	2961	2922
Hf	6	6	9	7	31	10	6	6
W	7	7	7	8	5	7	7	7
Pb	4	3	8	2	33	81	1	3
Th	4	4	10	7	200	28	24	21
U	3715	3722	3177	3183	3344	3022	3056	2987
Eu/Eu*	0.72	0.74	0.72	0.74	0.69	0.69	0.57	0.60
Al	0.01	0.01	0.01	0.01	0.01	0.02	0.00	0.00
Si	0.02	0.03	0.03	0.02	0.03	0.02	0.03	0.02
P	0.91	0.92	0.90	0.89	0.93	0.89	0.90	0.89
Ca	0.01	0.01	0.01	0.01	0.01	0.01	0.00	0.00
Sc	0.00	0.00	0.00	0.00	0.00	0.00	0.00	0.00
Mn	0.00	0.00	0.00	0.00	0.00	0.00	0.00	0.00
Fe	0.00	0.00	0.00	0.00	0.01	0.00	0.00	0.00
Y	0.87	0.85	0.86	0.88	0.81	0.88	0.92	0.93
Zr	0.00	0.00	0.00	0.00	0.00	0.00	0.00	0.00
La	0.00	0.00	0.00	0.00	0.00	0.00	0.00	0.00
Ce	0.00	0.00	0.00	0.00	0.00	0.00	0.00	0.00
Pr	0.00	0.00	0.00	0.00	0.00	0.00	0.00	0.00
Nd	0.00	0.00	0.00	0.00	0.00	0.00	0.00	0.00
Sm	0.01	0.01	0.01	0.01	0.01	0.01	0.01	0.01
Eu	0.00	0.01	0.00	0.01	0.01	0.01	0.00	0.00
Gd	0.04	0.04	0.04	0.04	0.07	0.05	0.02	0.02
Tb	0.01	0.01	0.01	0.01	0.01	0.01	0.01	0.01
Dy	0.06	0.06	0.06	0.07	0.06	0.06	0.06	0.06
Ho	0.01	0.01	0.01	0.01	0.01	0.01	0.01	0.02
Er	0.04	0.04	0.04	0.04	0.03	0.04	0.04	0.04
Tm	0.01	0.01	0.01	0.01	0.00	0.01	0.01	0.01
Yb	0.04	0.04	0.04	0.04	0.02	0.04	0.03	0.03
Lu	0.01	0.00	0.00	0.00	0.00	0.00	0.00	0.00
Th	0.00	0.00	0.00	0.00	0.00	0.00	0.00	0.00
U	0.00	0.00	0.00	0.00	0.00	0.00	0.00	0.00
Total	2.05	2.05	2.06	2.06	2.04	2.07	2.06	2.06
P site	0.93	0.94	0.93	0.92	0.96	0.91	0.93	0.91
REE site	1.10	1.08	1.10	1.12	1.04	1.12	1.12	1.14

*Y = 33.9 wt.% (Cook et al., 2013)

**Formulae on basis of 4 a.p.f.u.

(Continued)

Deposit	John Galt									
No	J1_3	J1_4	J1_5	J1_6	J1_8	J1_9	J1_10	J1_11	J1_12	J1_13
Paragenesis	Overgrowth									
(ppm)										
Al	31	81	55	10	23	10	25	10	24	30
Si	<3085	3932	<2734	<3203	<3555	<3520	<3231	<3412	<2717	<3603
P	112447	113329	110653	113293	114575	115547	113022	114174	113510	115671
Ca	111	182	173	108	120	146	191	131	285	110
Sc	394	354	449	166	487	248	467	212	722	290
Ti	13	1	1	1	1	1	1	1	1	2
Mn	3	2	7	3	3	2	3	4	5	3
Fe	25	26	27	27	27	30	28	30	27	28
Sr	5	13	4	4	6	5	6	5	6	10
Zr	17	13	18	15	15	16	9	17	11	14
Nb	0	0	0	0	0	0	0	0	0	0
Sb	0	0	0	0	0	0	0	0	0	0
Ba	2	9	1	1	3	2	3	2	3	7
La	5	25	3	2	8	3	6	4	9	14
Ce	56	73	43	21	57	34	40	29	84	56
Pr	79	66	57	27	74	48	57	39	98	65
Nd	2163	1915	1723	1042	2015	1400	1767	1305	2567	1742
Sm	6093	5678	5442	4693	5590	5130	5728	5082	6371	5400
Eu	1737	1627	1710	1416	1582	1544	1730	1618	1780	1632
Gd	14123	13616	13409	12873	13493	13624	13986	13721	14229	14036
Tb	4454	4298	4257	4160	4221	4311	4366	4289	4383	4367
Dy	41082	40975	40996	40238	40389	40904	40193	40813	40902	41972
Ho	10371	10492	10395	10505	10290	10526	10198	10403	10550	10549
Er	29097	29163	29323	29931	28989	30031	28787	29362	29351	29886
Tm	4217	4221	4252	4386	4212	4392	4186	4224	4195	4244
Yb	26140	26697	26450	27511	25805	27343	25463	26583	26098	26789
Lu	3174	3196	3292	3389	3233	3350	3134	3273	3203	3311
Hf	6	5	5	6	5	5	5	5	5	5
W	7	7	7	7	7	7	7	7	7	7
Pb	2	3	2	3	2	2	1	1	2	6
Th	35	22	25	27	24	33	11	13	16	16
U	3287	3007	2559	3008	3279	2981	2822	2543	2638	2622
Eu/Eu*	0.57	0.57	0.61	0.56	0.56	0.56	0.59	0.59	0.57	0.57
Al	0.00	0.00	0.00	0.00	0.00	0.00	0.00	0.00	0.00	0.00
Si	0.03	0.03	0.02	0.03	0.03	0.03	0.03	0.03	0.02	0.03
P	0.89	0.89	0.88	0.89	0.89	0.90	0.89	0.89	0.89	0.90
Ca	0.00	0.00	0.00	0.00	0.00	0.00	0.00	0.00	0.00	0.00
Sc	0.00	0.00	0.00	0.00	0.00	0.00	0.00	0.00	0.00	0.00
Mn	0.00	0.00	0.00	0.00	0.00	0.00	0.00	0.00	0.00	0.00
Fe	0.00	0.00	0.00	0.00	0.00	0.00	0.00	0.00	0.00	0.00
Y	0.93	0.92	0.94	0.93	0.92	0.92	0.93	0.92	0.93	0.92
Zr	0.00	0.00	0.00	0.00	0.00	0.00	0.00	0.00	0.00	0.00
La	0.00	0.00	0.00	0.00	0.00	0.00	0.00	0.00	0.00	0.00
Ce	0.00	0.00	0.00	0.00	0.00	0.00	0.00	0.00	0.00	0.00
Pr	0.00	0.00	0.00	0.00	0.00	0.00	0.00	0.00	0.00	0.00
Nd	0.00	0.00	0.00	0.00	0.00	0.00	0.00	0.00	0.00	0.00
Sm	0.01	0.01	0.01	0.01	0.01	0.01	0.01	0.01	0.01	0.01
Eu	0.00	0.00	0.00	0.00	0.00	0.00	0.00	0.00	0.00	0.00
Gd	0.02	0.02	0.02	0.02	0.02	0.02	0.02	0.02	0.02	0.02
Tb	0.01	0.01	0.01	0.01	0.01	0.01	0.01	0.01	0.01	0.01
Dy	0.06	0.06	0.06	0.06	0.06	0.06	0.06	0.06	0.06	0.06
Ho	0.02	0.02	0.02	0.02	0.02	0.02	0.02	0.02	0.02	0.02
Er	0.04	0.04	0.04	0.04	0.04	0.04	0.04	0.04	0.04	0.04
Tm	0.01	0.01	0.01	0.01	0.01	0.01	0.01	0.01	0.01	0.01
Yb	0.04	0.04	0.04	0.04	0.04	0.04	0.04	0.04	0.04	0.04
Lu	0.00	0.00	0.00	0.00	0.00	0.00	0.00	0.00	0.00	0.00
Th	0.00	0.00	0.00	0.00	0.00	0.00	0.00	0.00	0.00	0.00
U	0.00	0.00	0.00	0.00	0.00	0.00	0.00	0.00	0.00	0.00
Total	2.07	2.06	2.07	2.06	2.06	2.06	2.06	2.06	2.06	2.06
P site	0.91	0.92	0.91	0.92	0.92	0.93	0.92	0.92	0.91	0.93
REE site	1.14	1.13	1.16	1.14	1.13	1.13	1.14	1.13	1.14	1.13

*Y = 33.9 wt.% (Cook et al., 2013)

**Formulae on basis of 4 a.p.f.u.

(Continued)

Deposit	John Galt			
No	J1_14	J1_15	J1_17	J1_19
Paragenesis	Overgrowth			
(ppm)				
Al	9	70	45	14
Si	<2879	<3017	<3067	<2566
P	112006	111396	114582	109188
Ca	175	104	288	90
Sc	202	179	320	217
Ti	1	1	1	3
Mn	1	3	6	1
Fe	27	25	25	73
Sr	4	17	10	10
Zr	9	8	8	10
Nb	0	0	0	0
Sb	0	0	0	1
Ba	1	12	8	7
La	3	35	20	13
Ce	17	71	80	41
Pr	25	57	83	45
Nd	1159	1673	2111	1451
Sm	5344	5369	5632	5022
Eu	1635	1563	1608	1505
Gd	13579	13143	13277	12642
Tb	4352	4368	4316	4165
Dy	41253	41478	41490	41345
Ho	10561	10677	10560	10640
Er	30036	30194	30182	30649
Tm	4333	4443	4484	4553
Yb	27384	28310	27914	28587
Lu	3352	3451	3369	3559
Hf	5	5	5	5
W	7	7	8	7
Pb	1	5	5	1
Th	10	19	9	17
U	2703	2553	2748	2935
Eu/Eu*	0.59	0.57	0.57	0.58
Al	0.00	0.00	0.00	0.00
Si	0.03	0.03	0.03	0.02
P	0.89	0.88	0.89	0.88
Ca	0.00	0.00	0.00	0.00
Sc	0.00	0.00	0.00	0.00
Mn	0.00	0.00	0.00	0.00
Fe	0.00	0.00	0.00	0.00
Y	0.94	0.94	0.92	0.95
Zr	0.00	0.00	0.00	0.00
La	0.00	0.00	0.00	0.00
Ce	0.00	0.00	0.00	0.00
Pr	0.00	0.00	0.00	0.00
Nd	0.00	0.00	0.00	0.00
Sm	0.01	0.01	0.01	0.01
Eu	0.00	0.00	0.00	0.00
Gd	0.02	0.02	0.02	0.02
Tb	0.01	0.01	0.01	0.01
Dy	0.06	0.06	0.06	0.06
Ho	0.02	0.02	0.02	0.02
Er	0.04	0.04	0.04	0.05
Tm	0.01	0.01	0.01	0.01
Yb	0.04	0.04	0.04	0.04
Lu	0.00	0.00	0.00	0.01
Th	0.00	0.00	0.00	0.00
U	0.00	0.00	0.00	0.00
Total	2.07	2.07	2.06	2.07
P site	0.91	0.91	0.92	0.90
REE site	1.15	1.15	1.13	1.17

*Y = 33.9 wt.% (Cook et al., 2013)

**Formulae on basis of 4 a.p.f.u.

Appendix 5-4: Electron probe micro-analytical data of florencite from Wolverine and Area 5

	A1	A2	A3	A4	A5	A6	A7	A8	A9	A10	A11	A12	A13	A14	A15	A16	A17	A18	A19
	Area 5 (late)											Area 5 (early)							
CaO	1.86	1.31	0.91	1.75	1.23	1.06	1.37	1.25	1.39	1.27	1.10	0.72	0.57	0.64	0.65	0.72	0.67	0.75	0.73
Y_2O_3	0.00	0.00	0.00	0.00	0.00	0.00	0.00	0.00	0.00	0.00	0.00	0.00	0.00	0.00	0.00	0.00	0.00	0.00	0.00
La_2O_3	6.03	8.61	9.87	7.16	7.76	8.81	7.54	7.83	7.11	8.25	7.94	5.29	6.06	5.91	5.70	5.84	5.68	5.59	5.65
Ce_2O_3	10.02	11.59	12.19	10.92	11.09	11.26	10.91	11.18	10.88	11.82	11.56	9.93	10.50	10.39	9.89	9.73	10.10	9.78	10.87
Nd_2O_3	2.78	2.97	2.10	3.00	2.71	2.10	2.52	2.76	2.48	2.71	2.62	7.24	7.49	6.70	6.71	6.65	6.64	6.77	7.06
Pr_2O_3	1.03	1.03	0.93	1.08	0.88	0.83	0.89	1.03	1.00	1.14	1.06	1.45	1.48	1.39	1.41	1.41	1.47	1.18	1.48
Sm_2O_3	0.00	0.13	0.00	0.16	0.00	0.07	0.04	0.00	0.00	0.09	0.17	0.78	0.93	0.85	0.63	0.83	0.78	0.79	1.01
Gd_2O_3	0.11	0.00	0.00	0.08	0.09	0.00	0.00	0.00	0.00	0.01	0.00	0.09	0.06	0.00	0.26	0.00	0.16	0.08	0.21
ThO_2	0.01	0.06	0.05	0.00	0.00	0.10	0.01	0.00	0.04	0.02	0.00	0.06	0.00	0.00	0.09	0.05	0.00	0.05	0.05
SrO	4.80	2.59	3.18	3.58	3.08	3.23	4.45	3.14	3.00	2.88	3.07	2.73	1.95	2.12	1.82	2.35	2.15	2.35	2.24
FeO	1.18	1.00	1.00	0.91	0.64	0.59	0.86	1.38	1.23	0.91	0.72	2.18	1.30	2.57	5.02	1.31	3.10	1.21	1.10
SiO_2	0.00	0.15	0.03	0.00	0.36	0.24	0.08	0.28	0.49	0.53	0.29	0.00	0.00	0.00	0.00	0.00	0.00	0.00	0.00
Al_2O_3	31.69	30.48	31.42	32.08	31.47	31.04	31.88	31.31	30.62	31.55	31.90	30.61	31.72	30.83	29.20	31.16	30.87	30.47	32.03
P_2O_5	24.28	24.89	24.01	24.42	23.82	23.63	23.94	24.26	23.91	24.09	23.91	25.52	25.98	25.43	24.30	25.49	25.41	25.50	25.74
SO_3	4.70	3.11	3.00	3.55	3.37	3.30	4.29	3.07	3.07	3.00	3.16	1.70	1.33	1.44	1.28	1.61	1.49	1.64	1.54
F	0.34	0.41	0.11	0.45	0.53	0.17	0.37	0.54	0.13	0.13	0.13	0.00	0.00	0.91	0.39	0.30	0.25	0.03	0.39
Cl	0.02	0.03	0.00	0.01	0.01	0.02	0.03	0.03	0.03	0.02	0.03	0.05	0.05	0.03	0.01	0.05	0.03	0.04	0.04
Total	88.85	88.37	88.80	89.14	87.03	86.45	89.18	88.05	85.38	88.42	87.67	88.35	89.42	89.22	87.36	87.49	88.79	86.23	90.15
Ca	0.17	0.12	0.08	0.15	0.11	0.10	0.12	0.11	0.12	0.11	0.10	0.06	0.05	0.06	0.06	0.06	0.06	0.07	0.06
Y	0.00	0.00	0.00	0.00	0.00	0.00	0.00	0.00	0.00	0.00	0.00	0.00	0.00	0.00	0.00	0.00	0.00	0.00	0.00
La	0.18	0.27	0.30	0.21	0.24	0.27	0.23	0.24	0.22	0.25	0.24	0.16	0.18	0.18	0.18	0.18	0.17	0.18	0.17
Ce	0.30	0.36	0.36	0.33	0.34	0.35	0.33	0.34	0.33	0.36	0.35	0.30	0.31	0.32	0.31	0.30	0.31	0.30	0.33
Nd	0.08	0.09	0.06	0.09	0.08	0.06	0.07	0.08	0.07	0.08	0.08	0.21	0.22	0.20	0.20	0.20	0.20	0.21	0.21
Pr	0.03	0.03	0.03	0.03	0.03	0.03	0.03	0.03	0.03	0.03	0.03	0.04	0.04	0.04	0.04	0.04	0.04	0.04	0.04
Sm	0.00	0.00	0.00	0.00	0.00	0.00	0.00	0.00	0.00	0.00	0.00	0.02	0.03	0.02	0.02	0.02	0.02	0.02	0.03
Gd	0.00	0.00	0.00	0.00	0.00	0.00	0.00	0.00	0.00	0.00	0.00	0.00	0.00	0.00	0.01	0.00	0.00	0.00	0.01
Th	0.00	0.00	0.00	0.00	0.00	0.00	0.00	0.00	0.00	0.00	0.00	0.00	0.00	0.00	0.00	0.00	0.00	0.00	0.00
Sr	0.23	0.13	0.15	0.17	0.15	0.16	0.21	0.15	0.14	0.14	0.15	0.13	0.09	0.10	0.09	0.11	0.10	0.12	0.11
∑REE	0.99	1.00	0.98	0.98	0.95	0.97	0.99	0.95	0.91	0.97	0.95	0.92	0.92	0.92	0.91	0.91	0.9	0.94	0.96
Fe	0.08	0.07	0.07	0.06	0.04	0.04	0.06	0.10	0.09	0.06	0.05	0.15	0.09	0.18	0.36	0.09	0.21	0.09	0.08
Al	3.10	3.02	3.01	3.08	3.10	3.07	3.08	3.04	3.00	3.06	3.11	2.96	3.02	3.01	2.91	3.08	3.01	3.05	3.09
∑Al	3.18	3.09	3.08	3.14	3.14	3.11	3.14	3.14	3.09	3.12	3.16	3.11	3.11	3.19	3.27	3.17	3.22	3.14	3.17
Si	0.00	0.01	0.00	0.00	0.03	0.02	0.01	0.02	0.04	0.04	0.02	0.00	0.00	0.00	0.00	0.00	0.00	0.00	0.00
P	1.70	1.77	1.65	1.68	1.69	1.68	1.66	1.69	1.68	1.68	1.67	1.77	1.78	1.78	1.74	1.81	1.78	1.83	1.79
S	0.29	0.20	0.18	0.22	0.21	0.21	0.26	0.19	0.19	0.19	0.20	0.10	0.08	0.09	0.08	0.10	0.09	0.10	0.09
∑P	1.99	1.98	1.83	1.9	1.93	1.91	1.93	1.9	1.91	1.91	1.89	1.87	1.86	1.87	1.82	1.91	1.87	1.93	1.88
F	0.09	0.11	0.03	0.12	0.14	0.05	0.10	0.14	0.04	0.03	0.03	0.00	0.00	0.24	0.10	0.08	0.06	0.01	0.10
Cl	0.00	0.00	0.00	0.00	0.00	0.00	0.00	0.00	0.00	0.00	0.00	0.01	0.01	0.00	0.00	0.01	0.00	0.01	0.01
OH	5.91	5.88	5.97	5.88	5.86	5.95	5.90	5.86	5.96	5.96	5.96	5.99	5.99	5.76	5.90	5.91	5.93	5.99	5.89
∑OH	6.00	6.00	6.00	6.00	6.00	6.00	6.00	6.00	6.00	6.00	6.00	6.00	6.00	6.00	6.00	6.00	6.00	6.00	6.00
Flr	0.61	0.76	0.76	0.67	0.71	0.72	0.67	0.71	0.68	0.73	0.72	0.76	0.81	0.80	0.81	0.78	0.79	0.78	0.81
Wdh	0.19	0.13	0.09	0.16	0.13	0.11	0.13	0.13	0.15	0.12	0.12	0.09	0.08	0.10	0.11	0.10	0.11	0.10	0.08
Svb	0.14	0.10	0.17	0.12	0.14	0.16	0.19	0.12	0.10	0.14	0.16	0.07	0.07	0.07	0.06	0.06	0.06	0.05	0.09
Gyz	0.11	0.04	0.00	0.06	0.03	0.01	0.03	0.05	0.07	0.02	0.01	0.09	0.05	0.07	0.08	0.09	0.09	0.10	0.05
Hut	0.00	0.01	0.00	0.00	0.02	0.01	0.01	0.01	0.02	0.02	0.01	0.00	0.00	0.00	0.00	0.00	0.00	0.00	0.00

*Flr = Florencite, Wdh = Woodhouseite, Svb = Svanbergite, Gyz = Goyazite, Hut = Huttonite

**Formulae on basis of 14 atoms per formula unit (a.p.f.u.)

(Continued)

	A20	A21	A22	A23	A24	A25	A26	A27	A28	A29	A30	A31	A32	A33	A34	A35	A36	A37	A38
	Area 5 (early)																		
CaO	0.76	0.73	0.70	0.77	0.92	0.56	0.61	0.69	0.67	0.65	0.65	0.61	0.67	0.58	0.67	0.56	0.91	0.68	0.68
Y_2O_3	0.00	0.00	0.00	0.00	0.00	0.00	0.00	0.00	0.00	0.00	0.00	0.00	0.00	0.00	0.00	0.00	0.00	0.00	0.00
La_2O_3	6.09	6.02	6.25	6.03	4.75	5.59	5.82	5.66	5.63	6.37	6.07	5.27	6.29	5.58	5.87	6.03	4.36	5.58	5.39
Ce_2O_3	10.53	9.57	10.15	9.91	10.56	9.87	11.03	10.14	10.13	10.77	10.63	9.96	10.39	9.84	9.88	9.77	8.95	9.77	10.16
Nd_2O_3	7.21	4.74	6.72	6.44	6.66	6.91	6.97	7.15	6.86	7.58	6.19	7.15	6.84	6.94	8.03	6.55	6.72	6.80	6.97
Pr_2O_3	1.33	1.28	1.56	1.40	1.47	1.50	1.50	1.52	1.44	1.54	1.37	1.43	1.42	1.45	1.44	1.34	1.32	1.34	1.61
Sm_2O_3	0.85	0.55	0.96	0.84	0.90	0.78	1.02	0.89	1.05	0.75	0.79	0.95	0.72	0.94	0.94	0.92	1.11	1.01	0.77
Gd_2O_3	0.02	0.15	0.00	0.16	0.14	0.00	0.13	0.00	0.04	0.06	0.06	0.00	0.03	0.15	0.21	0.11	0.16	0.17	0.06
ThO_2	0.01	0.00	0.00	0.00	0.10	0.07	0.02	0.09	0.11	0.16	0.15	0.01	0.02	0.00	0.00	0.00	0.02	0.00	0.03
SrO	2.20	1.96	2.40	2.72	2.10	1.53	1.38	2.31	2.04	1.72	2.14	2.00	1.55	2.13	1.96	1.62	2.01	2.27	1.98
FeO	0.79	8.42	1.81	0.96	3.96	4.98	3.05	0.33	0.30	0.41	0.23	2.92	0.47	0.61	0.64	4.28	1.62	0.89	0.25
SiO_2	0.00	0.03	0.00	0.04	0.03	0.00	0.00	0.00	0.05	0.18	0.00	0.17	0.00	0.00	0.00	0.00	1.36	0.00	0.00
Al_2O_3	31.39	27.40	30.96	31.41	31.18	29.74	30.39	31.70	31.05	32.50	31.07	29.08	30.86	31.75	32.14	29.04	30.67	31.57	31.80
P_2O_5	25.76	22.64	25.77	25.82	24.83	24.82	25.78	25.21	25.76	26.12	24.99	25.08	25.29	26.12	26.03	24.75	24.42	25.48	25.67
SO_3	1.47	1.45	1.38	1.72	1.85	1.03	1.00	1.48	1.26	1.05	1.39	1.27	1.08	1.34	1.22	1.12	1.69	1.55	1.22
F	0.28	0.25	0.22	0.16	0.23	0.41	0.49	0.36	0.68	0.44	0.58	0.14	0.32	0.63	0.22	0.58	0.16	0.00	0.52
Cl	0.03	0.01	0.06	0.02	0.02	0.03	0.02	0.03	0.00	0.04	0.02	0.01	0.02	0.05	0.04	0.03	0.05	0.05	0.02
Total	88.71	85.20	88.94	88.42	89.70	87.81	89.20	87.56	87.07	90.33	86.34	86.06	85.95	88.11	89.29	86.71	85.53	87.16	87.13
Ca	0.07	0.07	0.06	0.07	0.08	0.05	0.05	0.06	0.06	0.06	0.06	0.06	0.06	0.05	0.06	0.05	0.08	0.06	0.06
Y	0.00	0.00	0.00	0.00	0.00	0.00	0.00	0.00	0.00	0.00	0.00	0.00	0.00	0.00	0.00	0.00	0.00	0.00	0.00
La	0.19	0.19	0.19	0.18	0.14	0.17	0.18	0.18	0.18	0.19	0.19	0.17	0.20	0.17	0.18	0.19	0.14	0.17	0.17
Ce	0.32	0.30	0.31	0.30	0.32	0.30	0.33	0.31	0.32	0.32	0.34	0.31	0.33	0.30	0.30	0.31	0.28	0.30	0.31
Nd	0.21	0.15	0.20	0.19	0.19	0.21	0.21	0.22	0.21	0.22	0.19	0.22	0.21	0.21	0.24	0.20	0.20	0.20	0.21
Pr	0.04	0.04	0.05	0.04	0.04	0.05	0.05	0.05	0.04	0.05	0.04	0.04	0.04	0.04	0.04	0.04	0.04	0.04	0.05
Sm	0.02	0.02	0.03	0.02	0.03	0.02	0.03	0.03	0.03	0.02	0.02	0.03	0.02	0.03	0.03	0.03	0.03	0.03	0.02
Gd	0.00	0.00	0.00	0.00	0.00	0.00	0.00	0.00	0.00	0.00	0.00	0.00	0.00	0.00	0.01	0.00	0.00	0.00	0.00
Th	0.00	0.00	0.00	0.00	0.00	0.00	0.00	0.00	0.00	0.00	0.00	0.00	0.00	0.00	0.00	0.00	0.00	0.00	0.00
Sr	0.11	0.10	0.12	0.13	0.10	0.07	0.07	0.11	0.10	0.08	0.11	0.10	0.08	0.10	0.09	0.08	0.10	0.11	0.10
∑REE	0.96	0.87	0.96	0.93	0.9	0.87	0.92	0.96	0.94	0.94	0.95	0.93	0.94	0.9	0.95	0.9	0.87	0.91	0.92
Fe	0.05	0.61	0.13	0.07	0.27	0.35	0.21	0.02	0.02	0.03	0.02	0.21	0.03	0.04	0.04	0.31	0.11	0.06	0.02
Al	3.07	2.78	3.02	3.08	3.01	2.92	2.96	3.15	3.11	3.12	3.18	2.94	3.12	3.12	3.12	2.93	3.07	3.12	3.15
∑Al	3.12	3.39	3.15	3.15	3.28	3.27	3.17	3.17	3.13	3.15	3.2	3.15	3.15	3.16	3.16	3.24	3.18	3.18	3.17
Si	0.00	0.00	0.00	0.00	0.00	0.00	0.00	0.00	0.00	0.01	0.00	0.01	0.00	0.00	0.00	0.00	0.12	0.00	0.00
P	1.81	1.65	1.81	1.82	1.72	1.75	1.80	1.80	1.86	1.80	1.84	1.82	1.84	1.84	1.82	1.79	1.75	1.81	1.83
S	0.09	0.09	0.09	0.11	0.11	0.06	0.06	0.09	0.08	0.06	0.09	0.08	0.07	0.08	0.08	0.07	0.11	0.10	0.08
∑P	1.90	1.74	1.90	1.93	1.83	1.81	1.86	1.89	1.94	1.87	1.93	1.91	1.91	1.92	1.9	1.86	1.98	1.91	1.91
F	0.07	0.07	0.06	0.04	0.06	0.11	0.13	0.10	0.18	0.11	0.16	0.04	0.09	0.17	0.06	0.16	0.04	0.00	0.14
Cl	0.00	0.00	0.01	0.00	0.00	0.00	0.00	0.00	0.00	0.00	0.00	0.00	0.00	0.01	0.01	0.00	0.01	0.01	0.00
OH	5.92	5.93	5.93	5.95	5.94	5.89	5.87	5.90	5.82	5.88	5.84	5.96	5.91	5.83	5.94	5.84	5.95	5.99	5.86
∑OH	6.00	6.00	6.00	6.00	6.00	6.00	6.00	6.00	6.00	6.00	6.00	6.00	6.00	6.00	6.00	6.00	6.00	6.00	6.00
Flr	0.80	0.77	0.80	0.76	0.77	0.81	0.84	0.81	0.81	0.83	0.81	0.80	0.83	0.79	0.82	0.82	0.74	0.78	0.79
Wdh	0.09	0.14	0.08	0.10	0.13	0.11	0.09	0.08	0.09	0.09	0.09	0.09	0.09	0.09	0.08	0.10	0.13	0.10	0.09
Svb	0.06	0.07	0.07	0.06	0.08	0.04	0.04	0.09	0.04	0.06	0.07	0.03	0.05	0.05	0.07	0.04	0.06	0.07	0.06
Gyz	0.07	0.10	0.08	0.10	0.07	0.09	0.06	0.04	0.08	0.04	0.06	0.10	0.06	0.09	0.05	0.09	0.09	0.08	0.08
Hut	0.00	0.00	0.00	0.00	0.00	0.00	0.00	0.00	0.00	0.01	0.00	0.01	0.00	0.00	0.00	0.00	0.06	0.00	0.00

*Flr = Florencite, Wdh = Woodhouseite, Svb = Svanbergite, Gyz = Goyazite, Hut = Huttonite

**Formulae on basis of 14 atoms per formula unit (a.p.f.u.)

(Continued)

	A39	A40	A41	A42	A43	A44	A45	A46	A47	A48	A49	A50	A51	A52	A53	A54	A55	A56	A57
	Area 5 (early)																		
CaO	0.63	0.61	0.55	0.73	0.59	0.57	0.67	0.60	0.96	0.72	0.54	0.69	0.55	0.61	0.62	0.47	0.39	0.60	0.57
Y_2O_3	0.00	0.00	0.00	0.00	0.00	0.00	0.00	0.00	0.00	0.00	0.00	0.00	0.00	0.00	0.00	0.00	0.00	0.00	0.00
La_2O_3	5.41	5.62	5.86	5.53	5.53	5.76	6.17	5.62	5.33	5.35	5.54	5.49	5.76	5.53	5.46	5.91	6.90	5.52	5.57
Ce_2O_3	9.81	9.88	9.61	10.41	9.76	9.64	10.22	9.76	10.32	10.33	10.65	10.18	10.50	9.59	10.57	10.76	10.98	9.99	10.35
Nd_2O_3	7.09	6.48	7.36	7.44	7.12	6.45	6.88	7.30	5.83	6.76	7.74	7.10	7.53	7.19	7.40	7.61	7.01	7.19	7.14
Pr_2O_3	1.40	1.56	1.44	1.58	1.62	1.61	1.43	1.47	1.29	1.67	1.45	1.48	1.43	1.50	1.61	1.53	1.36	1.52	1.50
Sm_2O_3	0.83	0.86	1.03	1.07	0.76	0.98	0.76	0.76	0.70	0.85	0.88	0.97	0.89	0.75	0.95	0.87	0.71	0.89	1.09
Gd_2O_3	0.06	0.07	0.07	0.01	0.05	0.14	0.16	0.17	0.00	0.15	0.14	0.09	0.27	0.20	0.00	0.04	0.08	0.09	0.17
ThO_2	0.02	0.00	0.00	0.00	0.06	0.09	0.01	0.05	0.01	0.01	0.03	0.07	0.00	0.00	0.01	0.00	0.00	0.00	0.00
SrO	1.94	2.10	1.71	1.87	2.11	2.12	2.06	1.61	2.18	1.85	1.59	1.97	1.80	1.94	1.64	1.51	1.52	1.99	1.75
FeO	0.42	0.16	0.85	0.37	0.10	0.58	0.17	0.44	0.15	0.34	0.58	0.43	0.52	0.25	0.18	1.13	0.37	0.79	0.44
SiO_2	0.00	0.00	0.03	0.00	0.00	0.00	0.00	0.00	0.00	0.00	0.12	0.40	0.00	0.00	0.06	0.00	0.00	0.00	0.39
Al_2O_3	31.88	31.53	31.14	31.50	31.59	30.94	31.64	30.01	31.79	32.09	30.81	31.57	31.87	31.27	30.83	31.24	31.49	30.71	31.60
P_2O_5	25.80	25.77	25.38	25.60	25.80	25.79	26.50	26.05	25.43	25.94	25.72	25.63	26.04	26.11	26.28	25.99	26.15	25.45	25.49
SO_3	1.24	1.26	1.02	1.27	1.06	1.47	1.08	0.91	1.54	1.21	1.16	1.32	1.12	1.19	1.05	0.95	0.83	1.29	1.23
F	0.06	0.35	0.51	0.10	0.00	0.00	0.12	0.26	0.41	0.38	0.31	0.15	0.17	0.27	0.32	0.05	0.40	0.53	0.00
Cl	0.01	0.01	0.02	0.02	0.04	0.02	0.03	0.00	0.01	0.03	0.03	0.02	0.01	0.00	0.03	0.02	0.00	0.05	0.03
Total	86.60	86.26	86.57	87.51	86.19	86.15	87.90	85.01	85.95	87.67	87.28	87.55	88.45	86.41	87.00	88.08	88.18	86.61	87.32
Ca	0.06	0.06	0.05	0.07	0.05	0.05	0.06	0.06	0.09	0.06	0.05	0.06	0.05	0.05	0.06	0.04	0.03	0.05	0.05
Y	0.00	0.00	0.00	0.00	0.00	0.00	0.00	0.00	0.00	0.00	0.00	0.00	0.00	0.00	0.00	0.00	0.00	0.00	0.00
La	0.17	0.18	0.18	0.17	0.17	0.18	0.19	0.18	0.17	0.16	0.17	0.17	0.18	0.17	0.17	0.18	0.21	0.17	0.17
Ce	0.30	0.31	0.30	0.32	0.30	0.30	0.31	0.31	0.32	0.32	0.33	0.31	0.32	0.29	0.33	0.33	0.34	0.31	0.32
Nd	0.21	0.20	0.22	0.22	0.21	0.20	0.20	0.23	0.18	0.20	0.23	0.21	0.22	0.22	0.22	0.23	0.21	0.22	0.21
Pr	0.04	0.05	0.04	0.05	0.05	0.05	0.04	0.05	0.04	0.05	0.04	0.05	0.04	0.05	0.05	0.05	0.04	0.05	0.05
Sm	0.02	0.03	0.03	0.03	0.02	0.03	0.02	0.02	0.02	0.02	0.03	0.03	0.03	0.02	0.03	0.02	0.02	0.03	0.03
Gd	0.00	0.00	0.00	0.00	0.00	0.00	0.00	0.00	0.00	0.00	0.00	0.00	0.01	0.01	0.00	0.00	0.00	0.00	0.00
Th	0.00	0.00	0.00	0.00	0.00	0.00	0.00	0.00	0.00	0.00	0.00	0.00	0.00	0.00	0.00	0.00	0.00	0.00	0.00
Sr	0.09	0.10	0.08	0.09	0.10	0.10	0.10	0.08	0.11	0.09	0.08	0.10	0.09	0.09	0.08	0.07	0.07	0.10	0.09
∑REE	0.89	0.93	0.90	0.95	0.90	0.91	0.92	0.93	0.93	0.90	0.93	0.93	0.94	0.90	0.94	0.92	0.92	0.93	0.92
Fe	0.03	0.01	0.06	0.03	0.01	0.04	0.01	0.03	0.01	0.02	0.04	0.03	0.04	0.02	0.01	0.08	0.03	0.06	0.03
Al	3.16	3.15	3.10	3.11	3.15	3.10	3.11	3.06	3.18	3.15	3.09	3.11	3.13	3.10	3.09	3.07	3.11	3.09	3.12
∑Al	3.19	3.16	3.16	3.14	3.16	3.14	3.12	3.09	3.19	3.17	3.13	3.14	3.17	3.12	3.1	3.15	3.14	3.15	3.15
Si	0.00	0.00	0.00	0.00	0.00	0.00	0.00	0.00	0.00	0.00	0.01	0.03	0.00	0.00	0.01	0.00	0.00	0.00	0.03
P	1.84	1.85	1.82	1.82	1.85	1.86	1.87	1.91	1.83	1.83	1.85	1.81	1.84	1.86	1.89	1.83	1.86	1.84	1.81
S	0.08	0.08	0.06	0.08	0.07	0.09	0.07	0.06	0.10	0.08	0.07	0.08	0.07	0.08	0.07	0.06	0.05	0.08	0.08
∑P	1.92	1.93	1.88	1.9	1.92	1.95	1.94	1.97	1.93	1.91	1.93	1.92	1.91	1.94	1.97	1.89	1.91	1.92	1.92
F	0.02	0.09	0.14	0.03	0.00	0.00	0.03	0.07	0.11	0.10	0.08	0.04	0.04	0.07	0.09	0.01	0.10	0.14	0.00
Cl	0.00	0.00	0.00	0.00	0.01	0.00	0.00	0.00	0.00	0.00	0.00	0.00	0.00	0.00	0.00	0.00	0.00	0.01	0.00
OH	5.98	5.90	5.86	5.97	5.99	6.00	5.96	5.93	5.89	5.90	5.91	5.96	5.95	5.93	5.91	5.98	5.90	5.85	6.00
∑OH	6.00	6.00	6.00	6.00	6.00	6.00	6.00	6.00	6.00	6.00	6.00	6.00	6.00	6.00	6.00	6.00	6.00	6.00	6.00
Flr	0.79	0.80	0.81	0.81	0.79	0.80	0.79	0.82	0.76	0.79	0.83	0.80	0.83	0.80	0.83	0.84	0.85	0.81	0.81
Wdh	0.11	0.09	0.09	0.09	0.09	0.09	0.09	0.09	0.12	0.10	0.08	0.09	0.08	0.09	0.09	0.07	0.06	0.08	0.08
Svb	0.04	0.05	0.05	0.06	0.05	0.05	0.03	0.00	0.05	0.05	0.05	0.06	0.06	0.04	0.02	0.05	0.05	0.06	0.07
Gyz	0.09	0.08	0.07	0.06	0.10	0.09	0.11	0.11	0.10	0.08	0.06	0.07	0.06	0.09	0.08	0.05	0.05	0.07	0.05
Hut	0.00	0.00	0.00	0.00	0.00	0.00	0.00	0.00	0.00	0.00	0.01	0.02	0.00	0.00	0.01	0.00	0.00	0.00	0.02

*Flr = Florencite, Wdh = Woodhouseite, Svb = Svanbergite, Gyz = Goyazite, Hut = Huttonite

**Formulae on basis of 14 atoms per formula unit (a.p.f.u.)

(Continued)

	A58	A59	A60	A61	A62	A63	A64	A65	A66	A67	A68	A69	A70	A71	A72	A73	A74	A75	A76
	Area 5 (early)																		
CaO	0.49	0.56	0.64	0.61	0.56	0.83	0.69	0.61	0.54	0.67	0.64	0.60	0.73	0.53	0.58	0.47	0.49	0.76	0.75
Y_2O_3	0.00	0.00	0.00	0.00	0.00	0.00	0.00	0.00	0.00	0.00	0.00	0.00	0.00	0.00	0.00	0.00	0.00	0.00	0.00
La_2O_3	5.74	5.58	5.57	5.37	5.83	5.50	5.23	5.64	6.09	5.81	5.84	5.55	5.22	5.63	4.83	5.65	5.59	4.86	5.46
Ce_2O_3	10.96	9.86	9.97	10.54	10.39	10.15	9.81	10.19	10.30	10.15	10.03	9.60	10.14	9.90	10.85	10.66	10.77	9.41	10.74
Nd_2O_3	7.47	6.65	7.49	6.78	6.20	6.33	6.87	7.17	6.71	7.14	6.73	6.77	6.49	7.21	8.10	7.02	6.81	7.86	7.45
Pr_2O_3	1.54	1.55	1.57	1.47	1.54	1.37	1.48	1.68	1.57	1.41	1.49	1.48	1.41	1.63	1.91	1.57	1.36	1.53	1.34
Sm_2O_3	0.91	0.85	0.89	0.76	0.91	0.76	0.93	0.97	0.98	0.86	0.82	1.05	0.86	0.91	1.05	0.92	1.01	1.14	0.80
Gd_2O_3	0.24	0.02	0.07	0.25	0.03	0.06	0.14	0.11	0.11	0.03	0.09	0.15	0.04	0.09	0.00	0.00	0.16	0.09	0.08
ThO_2	0.00	0.11	0.04	0.08	0.00	0.00	0.00	0.05	0.00	0.01	0.00	0.00	0.00	0.00	0.00	0.04	0.00	0.00	0.07
SrO	1.59	1.45	1.68	1.99	1.80	2.36	2.08	2.02	1.55	2.12	2.07	1.96	2.07	1.67	1.36	1.93	1.62	2.20	1.99
FeO	0.50	4.80	1.06	1.42	1.44	0.79	0.47	0.58	0.62	0.28	1.44	0.44	0.70	2.21	0.22	0.65	0.28	0.65	0.20
SiO_2	0.00	0.00	0.00	0.02	0.08	0.00	0.09	0.00	0.08	0.00	0.25	0.15	0.92	0.07	0.27	0.39	0.26	0.00	0.00
Al_2O_3	28.84	30.35	31.98	31.22	30.83	31.68	31.52	30.72	31.12	30.84	31.21	30.68	30.57	30.53	30.83	30.53	29.13	31.31	30.33
P_2O_5	26.61	24.55	25.40	25.42	25.83	25.09	25.53	25.80	25.90	25.44	25.28	25.80	25.33	25.45	26.33	25.75	26.24	25.71	25.59
SO_3	1.13	0.93	1.26	1.10	1.20	1.61	1.29	1.30	1.02	1.42	1.21	1.24	1.47	1.17	0.91	1.41	1.04	1.51	1.19
F	0.31	0.00	0.09	0.27	0.24	0.14	0.49	0.16	0.28	0.39	0.06	0.15	0.53	0.38	0.47	0.42	0.24	0.24	0.54
Cl	0.03	0.03	0.01	0.04	0.04	0.02	0.03	0.01	0.02	0.01	0.01	0.00	0.03	0.01	0.05	0.03	0.04	0.00	0.00
Total	86.35	87.29	87.71	87.34	86.92	86.70	86.65	87.00	86.88	86.58	87.18	85.63	86.52	87.39	87.75	87.45	85.04	87.27	86.54
Ca	0.05	0.05	0.06	0.06	0.05	0.08	0.06	0.06	0.05	0.06	0.06	0.06	0.07	0.05	0.05	0.04	0.05	0.07	0.07
Y	0.00	0.00	0.00	0.00	0.00	0.00	0.00	0.00	0.00	0.00	0.00	0.00	0.00	0.00	0.00	0.00	0.00	0.00	0.00
La	0.18	0.17	0.17	0.17	0.18	0.17	0.16	0.18	0.19	0.18	0.18	0.18	0.16	0.18	0.15	0.18	0.18	0.15	0.17
Ce	0.35	0.30	0.30	0.33	0.32	0.31	0.30	0.32	0.32	0.32	0.31	0.30	0.32	0.31	0.33	0.33	0.34	0.29	0.34
Nd	0.23	0.20	0.22	0.20	0.18	0.19	0.21	0.22	0.20	0.22	0.20	0.21	0.20	0.22	0.24	0.21	0.21	0.24	0.23
Pr	0.05	0.05	0.05	0.05	0.05	0.04	0.05	0.05	0.05	0.04	0.05	0.05	0.04	0.05	0.06	0.05	0.04	0.05	0.04
Sm	0.03	0.02	0.03	0.02	0.03	0.02	0.03	0.03	0.03	0.03	0.02	0.03	0.03	0.03	0.03	0.03	0.03	0.03	0.02
Gd	0.01	0.00	0.00	0.01	0.00	0.00	0.00	0.00	0.00	0.00	0.00	0.00	0.00	0.00	0.00	0.00	0.00	0.00	0.00
Th	0.00	0.00	0.00	0.00	0.00	0.00	0.00	0.00	0.00	0.00	0.00	0.00	0.00	0.00	0.00	0.00	0.00	0.00	0.00
Sr	0.08	0.07	0.08	0.10	0.09	0.12	0.10	0.10	0.08	0.11	0.10	0.10	0.10	0.08	0.07	0.09	0.08	0.11	0.10
∑REE	0.98	0.86	0.91	0.94	0.9	0.93	0.91	0.96	0.92	0.96	0.92	0.93	0.92	0.92	0.93	0.93	0.93	0.94	0.97
Fe	0.04	0.34	0.07	0.10	0.10	0.06	0.03	0.04	0.04	0.02	0.10	0.03	0.05	0.16	0.02	0.05	0.02	0.05	0.01
Al	2.96	2.99	3.15	3.10	3.02	3.16	3.14	3.07	3.10	3.12	3.08	3.10	3.07	3.04	3.05	3.05	2.99	3.11	3.06
∑Al	3.00	3.33	3.22	3.20	3.12	3.22	3.17	3.11	3.14	3.14	3.18	3.13	3.12	3.20	3.07	3.10	3.01	3.16	3.07
Si	0.00	0.00	0.00	0.00	0.01	0.00	0.01	0.00	0.01	0.00	0.02	0.01	0.08	0.01	0.02	0.03	0.02	0.00	0.00
P	1.96	1.74	1.80	1.81	1.82	1.80	1.83	1.85	1.86	1.85	1.79	1.87	1.83	1.82	1.87	1.85	1.94	1.84	1.86
S	0.07	0.06	0.08	0.07	0.07	0.10	0.08	0.08	0.06	0.09	0.08	0.08	0.09	0.07	0.06	0.09	0.07	0.10	0.08
∑P	2.03	1.80	1.88	1.88	1.90	1.90	1.92	1.93	1.93	1.94	1.89	1.96	2.00	1.90	1.95	1.97	2.03	1.94	1.94
F	0.08	0.00	0.02	0.07	0.06	0.04	0.13	0.04	0.07	0.11	0.02	0.04	0.14	0.10	0.12	0.11	0.07	0.06	0.15
Cl	0.00	0.00	0.00	0.01	0.01	0.00	0.00	0.00	0.00	0.00	0.00	0.00	0.00	0.00	0.01	0.00	0.01	0.00	0.00
OH	5.91	6.00	5.98	5.92	5.93	5.96	5.86	5.96	5.92	5.89	5.98	5.96	5.85	5.90	5.87	5.88	5.93	5.93	5.85
∑OH	6.00	6.00	6.00	6.00	6.00	6.00	6.00	6.00	6.00	6.00	6.00	6.00	6.00	6.00	6.00	6.00	6.00	6.00	6.00
Flr	0.86	0.81	0.81	0.81	0.80	0.77	0.79	0.82	0.82	0.81	0.80	0.80	0.78	0.83	0.83	0.83	0.82	0.79	0.81
Wdh	0.06	0.12	0.10	0.09	0.09	0.12	0.10	0.08	0.08	0.08	0.10	0.09	0.10	0.09	0.07	0.07	0.07	0.10	0.08
Svb	0.00	0.06	0.07	0.06	0.04	0.07	0.05	0.05	0.03	0.06	0.07	0.04	0.04	0.05	0.02	0.06	0.00	0.06	0.04
Gyz	0.09	0.08	0.05	0.07	0.09	0.09	0.09	0.07	0.08	0.07	0.07	0.10	0.09	0.07	0.07	0.06	0.11	0.08	0.08
Hut	0.00	0.00	0.00	0.00	0.01	0.00	0.01	0.00	0.01	0.00	0.01	0.01	0.04	0.01	0.01	0.02	0.01	0.00	0.00

*Flr = Florencite, Wdh = Woodhouseite, Svb = Svanbergite, Gyz = Goyazite, Hut = Huttonite

**Formulae on basis of 14 atoms per formula unit (a.p.f.u.)

(Continued)

	A77	A78	A79	A80	A81	A82	A83	A84	A85	A86	A87	A88	A89	A90	A91	A92	A93	A94	A95
	Area 5 (early)																		
CaO	0.46	0.62	0.65	0.76	0.55	0.70	0.53	0.64	0.63	0.61	0.67	0.61	0.88	0.69	0.94	0.94	0.74	0.85	0.84
Y_2O_3	0.00	0.00	0.00	0.00	0.00	0.00	0.00	0.00	0.00	0.00	0.00	0.00	0.00	0.00	0.00	0.00	0.00	0.00	0.00
La_2O_3	5.52	4.75	6.20	6.34	5.69	5.22	5.40	6.01	5.11	4.70	4.70	5.04	5.93	5.66	4.95	5.38	5.36	5.63	4.51
Ce_2O_3	10.43	10.24	10.65	9.95	10.46	9.89	10.44	10.17	9.91	9.34	9.68	9.70	10.02	10.59	10.39	10.02	10.28	10.15	10.12
Nd_2O_3	7.31	6.82	6.88	6.08	7.48	6.87	7.34	6.60	7.70	7.38	8.03	7.29	5.91	7.32	6.86	6.01	7.12	6.72	7.74
Pr_2O_3	1.54	1.48	1.44	1.47	1.52	1.58	1.54	1.35	1.50	1.50	1.55	1.42	1.48	1.59	1.30	1.49	1.47	1.36	1.54
Sm_2O_3	0.90	0.88	0.76	0.73	0.84	0.84	0.87	0.69	1.06	0.79	1.04	0.94	0.70	0.70	0.91	0.81	0.91	0.75	1.05
Gd_2O_3	0.15	0.24	0.05	0.14	0.02	0.15	0.10	0.08	0.08	0.05	0.24	0.00	0.05	0.15	0.08	0.03	0.00	0.06	0.06
ThO_2	0.04	0.02	0.01	0.00	0.00	0.00	0.00	0.03	0.06	0.14	0.00	0.16	0.00	0.00	0.00	0.00	0.04	0.09	0.00
SrO	1.49	1.79	2.13	1.92	1.58	2.06	1.88	1.74	1.89	1.69	1.81	2.02	2.06	1.62	2.15	2.19	1.89	1.89	1.41
FeO	1.56	2.25	0.26	0.79	0.78	0.27	0.75	1.00	0.42	6.97	3.40	0.40	0.16	0.05	0.18	0.44	0.43	0.20	0.97
SiO_2	0.00	0.01	0.21	0.84	0.00	0.00	0.00	0.00	0.00	0.06	0.02	0.00	0.04	0.00	0.00	0.00	0.00	0.00	0.00
Al_2O_3	30.34	30.51	30.85	30.57	31.31	30.93	31.55	30.43	31.84	29.86	30.23	30.75	30.94	30.68	31.51	31.01	31.67	31.90	31.66
P_2O_5	25.60	25.40	26.07	25.21	25.97	25.36	25.65	25.41	26.00	24.26	24.74	25.69	25.75	25.28	24.29	24.75	24.74	24.89	25.48
SO_3	0.88	1.12	1.26	1.20	1.08	1.22	1.14	1.05	1.20	1.34	1.18	1.33	1.20	1.03	1.40	1.53	1.31	1.01	0.92
F	0.55	0.22	0.24	0.50	0.33	0.44	0.23	0.34	0.18	0.31	0.00	0.38	0.16	0.51	0.09	0.40	0.49	0.26	0.18
Cl	0.01	0.02	0.05	0.05	0.01	0.03	0.01	0.01	0.00	0.04	0.00	0.02	0.01	0.00	0.02	0.03	0.05	0.01	0.03
Total	86.80	86.36	87.70	86.55	87.62	85.55	87.43	85.56	87.58	89.04	87.28	85.75	85.30	85.88	85.07	85.03	86.50	85.76	86.52
Ca	0.04	0.06	0.06	0.07	0.05	0.06	0.05	0.06	0.06	0.05	0.06	0.06	0.08	0.06	0.09	0.09	0.07	0.08	0.08
Y	0.00	0.00	0.00	0.00	0.00	0.00	0.00	0.00	0.00	0.00	0.00	0.00	0.00	0.00	0.00	0.00	0.00	0.00	0.00
La	0.17	0.15	0.19	0.20	0.18	0.16	0.17	0.19	0.16	0.14	0.15	0.16	0.19	0.18	0.16	0.17	0.17	0.18	0.14
Ce	0.33	0.32	0.33	0.31	0.32	0.31	0.32	0.32	0.30	0.28	0.30	0.30	0.31	0.33	0.33	0.32	0.32	0.32	0.31
Nd	0.22	0.21	0.21	0.18	0.23	0.21	0.22	0.20	0.23	0.22	0.24	0.22	0.18	0.23	0.21	0.18	0.22	0.20	0.23
Pr	0.05	0.05	0.04	0.05	0.05	0.05	0.05	0.04	0.05	0.04	0.05	0.04	0.05	0.05	0.04	0.05	0.05	0.04	0.05
Sm	0.03	0.03	0.02	0.02	0.02	0.02	0.03	0.02	0.03	0.02	0.03	0.03	0.02	0.02	0.03	0.02	0.03	0.02	0.03
Gd	0.00	0.01	0.00	0.00	0.00	0.00	0.00	0.00	0.00	0.00	0.01	0.00	0.00	0.00	0.00	0.00	0.00	0.00	0.00
Th	0.00	0.00	0.00	0.00	0.00	0.00	0.00	0.00	0.00	0.00	0.00	0.00	0.00	0.00	0.00	0.00	0.00	0.00	0.00
Sr	0.07	0.09	0.10	0.09	0.08	0.10	0.09	0.09	0.09	0.08	0.09	0.10	0.10	0.08	0.11	0.11	0.09	0.09	0.07
∑REE	0.91	0.92	0.95	0.92	0.93	0.91	0.93	0.92	0.92	0.83	0.93	0.91	0.93	0.95	0.97	0.94	0.95	0.93	0.91
Fe	0.11	0.16	0.02	0.06	0.05	0.02	0.05	0.07	0.03	0.48	0.24	0.03	0.01	0.00	0.01	0.03	0.03	0.01	0.07
Al	3.05	3.05	3.06	3.06	3.11	3.12	3.13	3.07	3.14	2.89	3.00	3.10	3.13	3.12	3.19	3.15	3.18	3.19	3.14
∑Al	3.16	3.21	3.08	3.12	3.16	3.14	3.18	3.14	3.17	3.37	3.24	3.13	3.14	3.12	3.20	3.18	3.21	3.20	3.21
Si	0.00	0.00	0.02	0.07	0.00	0.00	0.00	0.00	0.00	0.01	0.00	0.00	0.00	0.00	0.00	0.00	0.00	0.00	0.00
P	1.85	1.82	1.86	1.81	1.85	1.84	1.83	1.84	1.84	1.69	1.76	1.86	1.87	1.85	1.76	1.80	1.78	1.79	1.81
S	0.06	0.07	0.08	0.08	0.07	0.08	0.07	0.07	0.08	0.08	0.07	0.09	0.08	0.07	0.09	0.10	0.08	0.06	0.06
∑P	1.91	1.89	1.96	1.96	1.92	1.92	1.90	1.91	1.92	1.78	1.83	1.95	1.95	1.92	1.85	1.90	1.86	1.85	1.87
F	0.15	0.06	0.06	0.13	0.09	0.12	0.06	0.09	0.05	0.08	0.00	0.10	0.04	0.14	0.02	0.11	0.13	0.07	0.05
Cl	0.00	0.00	0.01	0.01	0.00	0.00	0.00	0.00	0.00	0.01	0.00	0.00	0.00	0.00	0.00	0.00	0.01	0.00	0.00
OH	5.85	5.94	5.93	5.86	5.91	5.88	5.94	5.91	5.95	5.91	6.00	5.89	5.95	5.86	5.97	5.89	5.86	5.93	5.95
∑OH	6.00	6.00	6.00	6.00	6.00	6.00	6.00	6.00	6.00	6.00	6.00	6.00	6.00	6.00	6.00	6.00	6.00	6.00	6.00
Flr	0.84	0.81	0.81	0.79	0.83	0.79	0.82	0.80	0.81	0.78	0.82	0.79	0.78	0.83	0.79	0.77	0.82	0.79	0.80
Wdh	0.08	0.10	0.08	0.10	0.08	0.10	0.08	0.09	0.10	0.13	0.10	0.10	0.11	0.08	0.11	0.12	0.10	0.11	0.12
Svb	0.04	0.04	0.04	0.04	0.05	0.04	0.06	0.03	0.05	0.06	0.07	0.04	0.02	0.05	0.09	0.06	0.09	0.05	0.03
Gyz	0.07	0.09	0.08	0.08	0.06	0.09	0.06	0.09	0.07	0.10	0.06	0.10	0.11	0.05	0.04	0.08	0.03	0.07	0.08
Hut	0.00	0.00	0.01	0.04	0.00	0.00	0.00	0.00	0.00	0.01	0.00	0.00	0.00	0.00	0.00	0.00	0.00	0.00	0.00

*Flr = Florencite, Wdh = Woodhouseite, Svb = Svanbergite, Gyz = Goyazite, Hut = Huttonite

**Formulae on basis of 14 atoms per formula unit (a.p.f.u.)

(Continued)

	A96	A97	A98	A99	A100	A101	A102	A103	A104	A105	A106	A107	A108	A109	A110	A111	A112	A113
	Area 5 (early)																	
CaO	0.76	0.69	0.64	0.44	0.87	0.78	0.77	0.85	0.83	0.97	2.57	0.60	0.93	0.88	0.93	0.84	0.87	0.86
Y_2O_3	0.00	0.00	0.00	0.00	0.00	0.00	0.00	0.00	0.00	0.00	0.00	0.00	0.00	0.00	0.00	0.00	0.00	0.00
La_2O_3	5.21	5.58	5.39	6.70	6.08	5.24	4.96	5.95	5.80	6.11	4.86	6.26	4.48	5.35	4.83	4.34	4.63	5.53
Ce_2O_3	10.85	10.49	10.40	11.28	10.45	10.57	9.25	9.94	9.91	11.11	10.96	10.71	9.57	10.29	10.35	8.72	9.60	9.74
Nd_2O_3	7.07	7.36	7.27	6.45	6.10	7.44	7.02	6.32	6.67	5.56	5.58	7.02	7.40	6.91	7.00	7.79	7.12	6.81
Pr_2O_3	1.56	1.47	1.47	1.63	1.39	1.43	1.36	1.31	1.40	1.40	1.65	1.62	1.50	1.46	1.56	1.66	1.58	1.36
Sm_2O_3	0.99	0.65	1.13	0.77	0.76	0.83	0.91	0.40	0.78	0.64	0.22	0.68	1.09	0.92	1.34	1.36	1.01	0.87
Gd_2O_3	0.27	0.05	0.02	0.22	0.10	0.31	0.10	0.02	0.00	0.03	0.00	0.18	0.23	0.25	0.17	0.21	0.16	0.09
ThO_2	0.00	0.03	0.08	0.04	0.03	0.12	0.00	0.10	0.00	0.07	0.05	0.00	0.04	0.00	0.16	0.00	0.02	0.00
SrO	1.51	1.39	1.48	1.00	1.53	1.58	1.81	2.02	1.55	1.51	1.09	1.12	2.00	1.37	1.05	1.63	2.26	2.97
FeO	0.30	0.28	0.60	0.10	0.24	0.44	0.42	0.57	0.20	0.12	0.24	0.40	0.56	0.26	0.63	0.37	3.29	0.44
SiO_2	0.00	1.02	0.02	0.01	0.05	0.39	1.95	0.09	0.07	0.41	0.16	0.34	0.44	0.56	0.10	0.43	0.00	0.00
Al_2O_3	31.81	31.70	31.09	30.84	31.83	31.87	30.77	31.31	30.90	31.62	32.05	31.02	32.51	30.65	32.39	32.63	30.47	30.93
P_2O_5	25.54	25.37	25.93	26.15	25.38	25.49	24.64	25.43	25.35	25.43	25.94	25.81	25.35	26.64	25.63	25.35	24.56	25.75
SO_3	0.95	0.82	0.92	0.65	0.98	0.88	1.01	1.17	0.99	1.17	1.45	0.71	1.14	0.86	0.80	0.99	1.82	1.99
F	0.41	0.40	0.06	0.39	0.27	0.41	0.14	0.15	0.59	0.14	0.10	0.45	0.22	0.00	0.49	0.29	0.48	0.32
Cl	0.02	0.01	0.02	0.01	0.03	0.03	0.00	0.03	0.03	0.01	0.03	0.04	0.00	0.01	0.03	0.00	0.01	0.04
Total	87.24	87.31	86.52	86.69	86.10	87.82	85.10	85.67	85.08	86.31	86.96	86.96	87.47	86.41	87.46	86.61	87.87	87.70
Ca	0.07	0.06	0.06	0.04	0.08	0.07	0.07	0.08	0.08	0.09	0.23	0.05	0.08	0.08	0.08	0.07	0.08	0.08
Y	0.00	0.00	0.00	0.00	0.00	0.00	0.00	0.00	0.00	0.00	0.00	0.00	0.00	0.00	0.00	0.00	0.00	0.00
La	0.16	0.17	0.17	0.21	0.19	0.16	0.16	0.19	0.18	0.19	0.15	0.20	0.14	0.17	0.15	0.13	0.14	0.17
Ce	0.33	0.32	0.32	0.35	0.32	0.32	0.29	0.31	0.31	0.34	0.33	0.33	0.29	0.32	0.31	0.27	0.30	0.30
Nd	0.21	0.22	0.22	0.20	0.18	0.22	0.21	0.19	0.20	0.17	0.16	0.21	0.22	0.21	0.21	0.23	0.21	0.21
Pr	0.05	0.04	0.05	0.05	0.04	0.04	0.04	0.04	0.04	0.04	0.05	0.05	0.05	0.04	0.05	0.05	0.05	0.04
Sm	0.03	0.02	0.03	0.02	0.02	0.02	0.03	0.01	0.02	0.02	0.01	0.02	0.03	0.03	0.04	0.04	0.03	0.03
Gd	0.01	0.00	0.00	0.01	0.00	0.01	0.00	0.00	0.00	0.00	0.00	0.01	0.01	0.01	0.00	0.01	0.00	0.00
Th	0.00	0.00	0.00	0.00	0.00	0.00	0.00	0.00	0.00	0.00	0.00	0.00	0.00	0.00	0.00	0.00	0.00	0.00
Sr	0.07	0.07	0.07	0.05	0.07	0.08	0.09	0.10	0.08	0.07	0.05	0.06	0.10	0.07	0.05	0.08	0.11	0.15
∑REE	0.93	0.90	0.92	0.93	0.9	0.92	0.89	0.92	0.91	0.92	0.98	0.93	0.92	0.93	0.89	0.88	0.92	0.98
Fe	0.02	0.02	0.04	0.01	0.02	0.03	0.03	0.04	0.01	0.01	0.02	0.03	0.04	0.02	0.04	0.03	0.23	0.03
Al	3.16	3.12	3.10	3.10	3.16	3.13	3.08	3.12	3.12	3.14	3.11	3.10	3.18	3.05	3.17	3.21	3.03	3.10
∑Al	3.18	3.14	3.14	3.11	3.18	3.16	3.11	3.16	3.13	3.15	3.13	3.13	3.22	3.07	3.21	3.24	3.26	3.13
Si	0.00	0.08	0.00	0.00	0.00	0.03	0.17	0.01	0.01	0.03	0.01	0.03	0.04	0.05	0.01	0.04	0.00	0.00
P	1.82	1.79	1.86	1.89	1.81	1.80	1.77	1.82	1.84	1.81	1.81	1.85	1.78	1.90	1.80	1.79	1.75	1.85
S	0.06	0.05	0.06	0.04	0.06	0.06	0.06	0.07	0.06	0.07	0.09	0.05	0.07	0.05	0.05	0.06	0.12	0.13
∑P	1.88	1.92	1.92	1.93	1.87	1.89	2.00	1.90	1.91	1.91	1.91	1.93	1.89	2.00	1.86	1.89	1.87	1.98
F	0.11	0.11	0.02	0.10	0.07	0.11	0.04	0.04	0.16	0.04	0.03	0.12	0.06	0.00	0.13	0.08	0.13	0.09
Cl	0.00	0.00	0.00	0.00	0.00	0.00	0.00	0.00	0.00	0.00	0.00	0.01	0.00	0.00	0.00	0.00	0.00	0.01
OH	5.89	5.89	5.98	5.89	5.92	5.89	5.96	5.96	5.83	5.96	5.97	5.88	5.94	6.00	5.87	5.92	5.87	5.91
∑OH	6.00	6.00	6.00	6.00	6.00	6.00	6.00	6.00	6.00	6.00	6.00	6.00	6.00	6.00	6.00	6.00	6.00	6.00
Flr	0.82	0.81	0.82	0.87	0.79	0.80	0.77	0.77	0.78	0.79	0.71	0.85	0.78	0.81	0.81	0.78	0.77	0.77
Wdh	0.10	0.10	0.09	0.07	0.12	0.10	0.11	0.11	0.11	0.12	0.24	0.08	0.12	0.11	0.13	0.12	0.12	0.10
Svb	0.05	0.05	0.02	0.02	0.03	0.05	0.04	0.03	0.01	0.03	0.00	0.04	0.06	0.00	0.03	0.05	0.08	0.07
Gyz	0.06	0.06	0.08	0.05	0.08	0.07	0.09	0.10	0.10	0.07	0.15	0.05	0.08	0.12	0.07	0.08	0.07	0.10
Hut	0.00	0.04	0.00	0.00	0.00	0.02	0.09	0.01	0.01	0.02	0.01	0.02	0.02	0.03	0.01	0.02	0.00	0.00

*Flr = Florencite, Wdh = Woodhouseite, Svb = Svanbergite, Gyz = Goyazite, Hut = Huttonite

**Formulae on basis of 14 atoms per formula unit (a.p.f.u.)

(Continued)

	W1	W2	W3	W4	W5	W6	W7	W8	W9	W10	W11	W12	W13	W14	W15	W16	W17	W18	W19
	Wolverine (early)																		
CaO	0.86	0.90	0.91	0.89	0.99	1.12	1.24	0.99	0.99	0.99	1.01	0.97	0.88	1.03	0.86	0.99	0.85	0.87	1.17
Y_2O_3	0.00	0.00	0.00	0.00	0.00	0.00	0.00	0.00	0.00	0.00	0.00	0.00	0.00	0.00	0.00	0.00	0.00	0.00	0.00
La_2O_3	4.16	3.27	3.77	3.50	3.49	3.47	3.54	3.72	3.73	3.91	3.88	3.17	4.18	3.95	3.76	3.67	3.68	3.63	3.59
Ce_2O_3	8.49	8.01	8.57	8.47	8.42	8.23	7.95	9.64	9.52	8.69	8.37	8.57	8.94	9.31	9.10	8.23	8.49	8.40	8.79
Nd_2O_3	7.73	8.37	7.78	6.95	7.25	6.34	6.94	7.33	7.49	7.45	7.94	7.87	8.26	7.42	7.99	7.71	8.21	8.79	7.23
Pr_2O_3	1.61	1.52	1.57	1.49	1.63	1.60	1.63	1.91	1.64	1.50	1.76	1.61	1.89	1.71	1.72	1.39	1.63	1.61	1.67
Sm_2O_3	1.08	0.93	1.01	0.98	1.11	1.01	0.93	0.74	0.87	1.17	1.09	0.88	1.04	1.07	0.90	0.92	1.23	1.12	1.11
Gd_2O_3	0.18	0.14	0.15	0.17	0.31	0.09	0.16	0.13	0.00	0.27	0.10	0.28	0.29	0.26	0.03	0.21	0.14	0.00	0.10
ThO_2	0.00	0.06	0.00	0.08	0.00	0.00	0.12	0.00	0.04	0.08	0.06	0.20	0.01	0.00	0.12	0.00	0.00	0.00	0.00
SrO	1.32	1.38	1.31	1.34	1.37	1.40	1.50	0.89	1.01	1.49	1.07	1.12	1.07	0.89	1.01	1.40	0.89	1.17	1.08
FeO	0.09	0.32	0.38	0.12	0.13	0.47	0.33	0.75	0.19	0.25	0.16	0.62	0.59	0.18	0.55	0.31	0.31	0.23	0.39
SiO_2	0.40	0.08	0.92	2.07	0.95	2.07	0.52	0.09	0.56	1.91	0.17	1.07	0.25	0.84	0.43	0.37	1.96	0.25	0.47
Al_2O_3	30.82	30.44	30.17	30.44	30.61	29.27	31.76	30.56	28.72	29.69	30.27	30.98	30.88	30.74	30.24	30.62	30.67	30.76	29.05
P_2O_5	25.88	25.30	25.74	24.97	25.30	25.02	25.31	25.43	26.07	26.53	25.56	25.40	25.47	25.90	25.93	25.00	25.06	25.37	26.45
SO_3	0.90	0.89	0.77	0.88	0.71	0.91	0.80	0.74	0.74	0.83	0.53	0.63	0.59	0.44	0.52	0.72	0.55	0.57	0.53
F	0.18	0.00	0.18	0.49	0.00	0.35	0.00	0.44	0.02	0.05	0.66	0.19	0.49	0.17	0.33	0.40	0.33	0.25	0.62
Cl	0.04	0.02	0.00	0.01	0.03	0.01	0.03	0.00	0.01	0.03	0.02	0.02	0.04	0.01	0.03	0.03	0.02	0.01	0.00
Total	83.74	81.64	83.24	82.85	82.30	81.36	82.76	83.35	81.58	84.84	82.65	83.58	84.87	83.93	83.52	81.97	84.02	83.03	82.25
Ca	0.08	0.09	0.08	0.08	0.09	0.11	0.11	0.09	0.09	0.09	0.10	0.09	0.08	0.09	0.08	0.09	0.08	0.08	0.11
Y	0.00	0.00	0.00	0.00	0.00	0.00	0.00	0.00	0.00	0.00	0.00	0.00	0.00	0.00	0.00	0.00	0.00	0.00	0.00
La	0.13	0.11	0.12	0.11	0.11	0.11	0.11	0.12	0.12	0.12	0.13	0.10	0.13	0.12	0.12	0.12	0.11	0.12	0.12
Ce	0.27	0.26	0.27	0.27	0.27	0.26	0.25	0.30	0.31	0.27	0.27	0.27	0.28	0.29	0.29	0.26	0.26	0.27	0.28
Nd	0.24	0.26	0.24	0.21	0.22	0.20	0.21	0.23	0.24	0.23	0.25	0.24	0.25	0.22	0.25	0.24	0.25	0.27	0.23
Pr	0.05	0.05	0.05	0.05	0.05	0.05	0.05	0.06	0.05	0.05	0.06	0.05	0.06	0.05	0.05	0.04	0.05	0.05	0.05
Sm	0.03	0.03	0.03	0.03	0.03	0.03	0.03	0.02	0.03	0.03	0.03	0.03	0.03	0.03	0.03	0.03	0.04	0.03	0.03
Gd	0.01	0.00	0.00	0.00	0.01	0.00	0.00	0.00	0.00	0.01	0.00	0.01	0.01	0.01	0.00	0.01	0.00	0.00	0.00
Th	0.00	0.00	0.00	0.00	0.00	0.00	0.00	0.00	0.00	0.00	0.00	0.00	0.00	0.00	0.00	0.00	0.00	0.00	0.00
Sr	0.07	0.07	0.07	0.07	0.07	0.07	0.07	0.04	0.05	0.07	0.05	0.06	0.05	0.04	0.05	0.07	0.04	0.06	0.06
∑REE	0.88	0.87	0.86	0.82	0.85	0.83	0.83	0.86	0.89	0.87	0.89	0.85	0.89	0.85	0.87	0.86	0.83	0.88	0.88
Fe	0.01	0.02	0.03	0.01	0.01	0.03	0.02	0.05	0.01	0.02	0.01	0.04	0.04	0.01	0.04	0.02	0.02	0.02	0.03
Al	3.13	3.15	3.08	3.10	3.13	3.02	3.19	3.11	3.01	2.98	3.13	3.13	3.09	3.06	3.10	3.16	3.05	3.15	3.02
∑Al	3.14	3.17	3.11	3.11	3.14	3.05	3.21	3.16	3.02	3.00	3.14	3.17	3.13	3.07	3.14	3.18	3.07	3.17	3.05
Si	0.03	0.01	0.08	0.18	0.08	0.18	0.04	0.01	0.05	0.16	0.02	0.09	0.02	0.07	0.04	0.03	0.17	0.02	0.04
P	1.89	1.88	1.89	1.83	1.86	1.85	1.83	1.86	1.96	1.91	1.90	1.84	1.83	1.85	1.91	1.85	1.79	1.87	1.97
S	0.06	0.06	0.05	0.06	0.05	0.06	0.05	0.05	0.05	0.05	0.03	0.04	0.04	0.03	0.03	0.05	0.03	0.04	0.03
∑P	1.98	1.95	2.02	2.07	1.99	2.09	1.92	1.92	2.06	2.12	1.95	1.97	1.89	1.95	1.98	1.93	1.99	1.93	2.04
F	0.05	0.00	0.05	0.13	0.00	0.10	0.00	0.12	0.01	0.01	0.18	0.05	0.13	0.05	0.09	0.11	0.09	0.07	0.17
Cl	0.01	0.00	0.00	0.00	0.00	0.00	0.00	0.00	0.00	0.00	0.00	0.00	0.01	0.00	0.00	0.00	0.00	0.00	0.00
OH	5.94	6.00	5.95	5.86	6.00	5.90	6.00	5.88	5.99	5.98	5.81	5.94	5.86	5.95	5.90	5.89	5.91	5.93	5.83
∑OH	6.00	6.00	6.00	6.00	6.00	6.00	6.00	6.00	6.00	6.00	6.00	6.00	6.00	6.00	6.00	6.00	6.00	6.00	6.00
Flr	0.78	0.76	0.76	0.73	0.74	0.70	0.72	0.78	0.79	0.75	0.78	0.76	0.80	0.77	0.79	0.75	0.76	0.79	0.75
Wdh	0.13	0.14	0.13	0.14	0.14	0.16	0.18	0.14	0.13	0.13	0.14	0.15	0.12	0.14	0.13	0.14	0.13	0.13	0.15
Svb	0.00	0.00	0.00	0.00	0.00	0.00	0.00	0.00	0.00	0.00	0.00	0.00	0.00	0.00	0.00	0.00	0.00	0.00	0.00
Gyz	0.13	0.15	0.16	0.15	0.16	0.19	0.17	0.12	0.17	0.18	0.15	0.14	0.10	0.14	0.15	0.14	0.11	0.12	0.22
Hut	0.02	0.01	0.04	0.09	0.04	0.09	0.02	0.01	0.03	0.08	0.01	0.05	0.01	0.04	0.02	0.02	0.09	0.01	0.02

*Flr = Florencite, Wdh = Woodhouseite, Svb = Svanbergite, Gyz = Goyazite, Hut = Huttonite

**Formulae on basis of 14 atoms per formula unit (a.p.f.u.)

(Continued)

	W20	W21	W22	W23	W24	W25	W26	W27	W28	W29	W30	W31	W45	W49	W91	W32	W33	W34	W35
	Wolverine (early)															Wolverine (late)			
CaO	0.83	1.09	1.28	0.99	0.89	1.12	0.92	0.88	0.98	0.91	0.92	0.93	0.67	0.86	0.64	1.13	0.99	1.16	1.16
Y_2O_3	0.00	0.00	0.00	0.00	0.00	0.00	0.00	0.00	0.00	0.00	0.00	0.00	0.00	0.00	0.00	0.00	0.00	0.00	0.00
La_2O_3	4.17	3.64	3.63	3.64	4.05	3.82	3.79	3.63	3.47	2.85	3.54	3.85	3.74	3.53	3.74	3.92	4.68	4.81	3.70
Ce_2O_3	7.75	8.52	8.49	9.09	8.65	8.95	9.16	7.88	6.62	7.07	7.29	6.88	10.36	10.78	9.35	10.45	12.51	11.13	10.69
Nd_2O_3	6.97	6.66	6.39	7.55	7.64	7.17	7.88	7.94	6.75	7.45	6.70	5.64	8.26	6.09	4.30	5.42	5.92	5.74	6.42
Pr_2O_3	1.46	1.69	1.43	1.80	1.83	1.65	1.75	1.69	1.48	1.67	1.80	1.61	1.83	1.81	1.99	1.47	1.71	1.58	1.56
Sm_2O_3	1.02	0.87	0.79	1.25	0.95	1.01	0.98	0.85	0.97	1.29	0.97	0.69	1.13	0.95	0.55	0.73	0.83	0.57	0.64
Gd_2O_3	0.04	0.15	0.26	0.24	0.00	0.10	0.06	0.21	0.09	0.13	0.13	0.17	0.04	0.25	0.27	0.19	0.01	0.00	0.14
ThO_2	0.00	0.00	0.10	0.00	0.00	0.00	0.00	0.00	0.00	0.01	0.01	0.00	0.00	0.00	0.00	0.00	0.01	0.17	0.02
SrO	1.58	1.51	1.37	0.70	1.02	1.03	0.95	1.28	1.32	1.13	0.90	1.42	1.65	1.67	1.82	3.61	1.87	2.45	2.57
FeO	0.34	0.40	0.29	0.13	0.26	0.35	0.53	0.28	0.24	1.51	0.32	0.11	0.05	1.87	0.49	0.61	0.62	0.50	1.29
SiO_2	0.49	0.89	0.75	0.39	0.47	0.07	0.03	0.25	0.60	0.53	0.17	0.36	0.13	0.08	0.45	0.61	0.07	0.10	0.10
Al_2O_3	30.40	31.38	32.74	31.03	30.96	30.38	30.99	29.72	26.96	29.59	31.02	31.06	30.35	29.79	30.25	31.21	31.15	30.94	30.04
P_2O_5	24.66	24.66	25.83	25.73	25.74	25.40	25.35	25.01	25.14	25.15	25.36	24.61	26.06	25.73	25.83	24.58	25.80	24.71	25.10
SO_3	0.68	0.86	0.78	0.58	0.55	0.55	0.51	0.63	0.71	0.55	0.60	0.75	1.32	1.37	1.22	2.55	1.70	2.38	2.09
F	0.31	0.25	0.28	0.15	0.14	0.12	0.09	0.49	0.37	0.41	0.31	0.22	0.25	0.60	0.78	0.57	0.62	0.74	0.47
Cl	0.02	0.00	0.03	0.02	0.03	0.03	0.01	0.02	0.03	0.03	0.00	0.01	0.03	0.03	0.05	0.03	0.01	0.03	0.03
Total	80.72	82.56	84.42	83.29	83.19	81.76	83.00	80.76	75.73	80.27	80.04	78.32	85.87	85.40	81.73	87.08	88.49	87.00	86.04
Ca	0.08	0.10	0.11	0.09	0.08	0.10	0.09	0.08	0.10	0.09	0.09	0.09	0.06	0.08	0.06	0.10	0.09	0.11	0.11
Y	0.00	0.00	0.00	0.00	0.00	0.00	0.00	0.00	0.00	0.00	0.00	0.00	0.00	0.00	0.00	0.00	0.00	0.00	0.00
La	0.14	0.12	0.11	0.11	0.13	0.12	0.12	0.12	0.12	0.09	0.11	0.13	0.12	0.11	0.12	0.12	0.15	0.15	0.12
Ce	0.25	0.27	0.26	0.28	0.27	0.29	0.29	0.26	0.23	0.23	0.23	0.23	0.33	0.34	0.30	0.32	0.39	0.35	0.34
Nd	0.22	0.21	0.19	0.23	0.24	0.22	0.24	0.25	0.23	0.24	0.21	0.18	0.26	0.19	0.14	0.16	0.18	0.18	0.20
Pr	0.05	0.05	0.04	0.06	0.06	0.05	0.06	0.05	0.05	0.05	0.06	0.05	0.06	0.06	0.06	0.05	0.05	0.05	0.05
Sm	0.03	0.03	0.02	0.04	0.03	0.03	0.03	0.03	0.03	0.04	0.03	0.02	0.03	0.03	0.02	0.02	0.02	0.02	0.02
Gd	0.00	0.00	0.01	0.01	0.00	0.00	0.00	0.01	0.00	0.00	0.00	0.01	0.00	0.01	0.01	0.01	0.00	0.00	0.00
Th	0.00	0.00	0.00	0.00	0.00	0.00	0.00	0.00	0.00	0.00	0.00	0.00	0.00	0.00	0.00	0.00	0.00	0.00	0.00
Sr	0.08	0.08	0.07	0.03	0.05	0.05	0.05	0.07	0.07	0.06	0.05	0.07	0.08	0.08	0.09	0.18	0.09	0.12	0.13
∑REE	0.85	0.86	0.81	0.85	0.86	0.86	0.88	0.87	0.83	0.80	0.78	0.78	0.94	0.90	0.80	0.96	0.97	0.98	0.97
Fe	0.02	0.03	0.02	0.01	0.02	0.03	0.04	0.02	0.02	0.11	0.02	0.01	0.00	0.14	0.04	0.04	0.04	0.04	0.09
Al	3.18	3.19	3.22	3.13	3.14	3.14	3.18	3.12	3.01	3.09	3.20	3.28	3.09	3.04	3.15	3.12	3.09	3.13	3.05
∑Al	3.20	3.22	3.24	3.14	3.16	3.17	3.22	3.14	3.03	3.20	3.22	3.29	3.09	3.18	3.19	3.16	3.13	3.17	3.14
Si	0.04	0.08	0.06	0.03	0.04	0.01	0.00	0.02	0.06	0.05	0.02	0.03	0.01	0.01	0.04	0.05	0.01	0.01	0.01
P	1.85	1.80	1.83	1.86	1.88	1.89	1.87	1.89	2.02	1.89	1.88	1.87	1.91	1.89	1.93	1.77	1.84	1.79	1.83
S	0.05	0.06	0.05	0.04	0.04	0.04	0.03	0.04	0.05	0.04	0.04	0.05	0.09	0.09	0.08	0.16	0.11	0.15	0.14
∑P	1.94	1.94	1.94	1.93	1.96	1.94	1.90	1.95	2.13	1.98	1.94	1.95	2.01	1.99	2.05	1.98	1.96	1.95	1.98
F	0.09	0.07	0.07	0.04	0.04	0.03	0.03	0.14	0.11	0.11	0.09	0.06	0.07	0.16	0.22	0.15	0.16	0.20	0.13
Cl	0.00	0.00	0.00	0.00	0.00	0.01	0.00	0.00	0.00	0.01	0.00	0.00	0.00	0.00	0.01	0.00	0.00	0.00	0.00
OH	5.91	5.93	5.92	5.96	5.96	5.96	5.97	5.86	5.88	5.88	5.91	5.94	5.93	5.83	5.78	5.84	5.83	5.80	5.87
∑OH	6.00	6.00	6.00	6.00	6.00	6.00	6.00	6.00	6.00	6.00	6.00	6.00	6.00	6.00	6.00	6.00	6.00	6.00	6.00
Flr	0.75	0.74	0.70	0.78	0.78	0.76	0.79	0.77	0.72	0.73	0.72	0.71	0.83	0.79	0.73	0.70	0.81	0.77	0.75
Wdh	0.14	0.16	0.18	0.14	0.13	0.15	0.14	0.13	0.16	0.17	0.17	0.18	0.09	0.13	0.14	0.12	0.11	0.13	0.13
Svb	0.00	0.01	0.00	0.00	0.00	0.00	0.00	0.00	0.00	0.00	0.00	0.00	0.02	0.00	0.00	0.10	0.05	0.08	0.04
Gyz	0.15	0.13	0.18	0.12	0.13	0.16	0.13	0.15	0.27	0.21	0.19	0.19	0.08	0.13	0.20	0.10	0.06	0.05	0.11
Hut	0.02	0.04	0.03	0.02	0.02	0.01	0.00	0.01	0.03	0.03	0.01	0.02	0.01	0.01	0.02	0.03	0.01	0.01	0.01

*Flr = Florencite, Wdh = Woodhouseite, Svb = Svanbergite, Gyz = Goyazite, Hut = Huttonite

**Formulae on basis of 14 atoms per formula unit (a.p.f.u.)

(Continued)

	W36	W37	W38	W39	W40	W41	W42	W43	W44	W46	W47	W48	W50	W51	W49	W50	W51	W52
	Wolverine (late)																	
CaO	0.88	1.01	0.89	0.95	1.25	1.15	1.12	0.99	1.18	1.05	1.16	0.94	0.85	1.03	0.86	0.85	1.03	1.37
Y_2O_3	0.00	0.00	0.00	0.00	0.00	0.00	0.00	0.00	0.00	0.00	0.00	0.00	0.00	0.00	0.00	0.00	0.00	0.00
La_2O_3	3.66	4.08	4.46	4.81	3.87	3.88	4.95	4.58	3.99	4.65	4.11	3.91	4.86	3.89	3.53	4.86	3.89	4.29
Ce_2O_3	10.61	11.18	10.68	11.19	10.52	10.54	9.86	11.31	10.40	10.68	11.51	9.69	11.48	11.11	10.78	11.48	11.11	10.31
Nd_2O_3	6.92	6.38	6.89	5.48	5.00	5.30	5.08	5.86	5.92	5.29	4.42	5.75	5.65	5.83	6.09	5.65	5.83	4.85
Pr_2O_3	1.78	1.76	1.46	1.39	1.38	1.43	1.19	1.82	1.60	1.50	1.66	1.41	1.51	1.83	1.81	1.51	1.83	1.53
Sm_2O_3	0.94	0.81	0.60	0.98	0.58	0.58	0.84	0.64	0.62	0.69	0.80	0.79	0.91	0.69	0.95	0.91	0.69	0.76
Gd_2O_3	0.02	0.20	0.06	0.32	0.27	0.00	0.06	0.18	0.00	0.26	0.12	0.21	0.00	0.04	0.25	0.00	0.04	0.05
ThO_2	0.01	0.02	0.06	0.03	0.01	0.00	0.24	0.00	0.02	0.00	0.08	0.11	0.04	0.00	0.00	0.04	0.00	0.00
SrO	2.00	2.34	2.50	2.11	2.11	2.73	3.38	2.24	2.55	1.92	2.29	2.55	1.90	1.85	1.67	1.90	1.85	2.54
FeO	0.44	1.81	0.94	0.11	8.85	1.18	1.21	0.10	2.81	1.17	1.18	0.95	0.31	0.18	1.87	0.31	0.18	0.45
SiO_2	0.67	0.41	0.91	0.25	0.00	1.80	0.14	0.00	0.01	0.24	0.00	0.61	0.01	0.01	0.08	0.01	0.01	0.00
Al_2O_3	30.60	30.79	30.70	30.93	28.42	30.69	30.41	30.97	30.84	30.49	30.57	30.50	30.98	30.78	29.79	30.98	30.78	30.77
P_2O_5	25.24	25.09	24.48	25.67	22.89	24.09	23.95	26.08	24.66	25.41	25.75	24.62	26.11	26.27	25.73	26.11	26.27	25.58
SO_3	1.82	2.01	2.21	2.09	1.87	2.01	2.30	1.75	2.30	1.81	1.95	2.07	1.48	1.56	1.37	1.48	1.56	2.06
F	0.19	0.51	0.36	0.60	0.20	0.64	1.12	0.35	0.48	0.82	0.43	0.72	0.00	0.38	0.60	0.00	0.38	0.81
Cl	0.04	0.05	0.02	0.03	0.02	0.01	0.05	0.03	0.02	0.03	0.01	0.01	0.01	0.02	0.03	0.01	0.02	0.01
Total	85.84	88.45	87.22	86.95	87.24	86.03	85.90	86.91	87.41	86.00	86.03	84.86	86.10	85.48	85.40	86.10	85.48	85.37
Ca	0.08	0.09	0.08	0.09	0.11	0.10	0.10	0.09	0.11	0.10	0.11	0.09	0.08	0.09	0.08	0.08	0.09	0.13
Y	0.00	0.00	0.00	0.00	0.00	0.00	0.00	0.00	0.00	0.00	0.00	0.00	0.00	0.00	0.00	0.00	0.00	0.00
La	0.12	0.13	0.14	0.15	0.12	0.12	0.16	0.14	0.12	0.15	0.13	0.13	0.15	0.12	0.11	0.15	0.12	0.14
Ce	0.33	0.34	0.33	0.35	0.32	0.33	0.31	0.35	0.32	0.34	0.36	0.31	0.36	0.35	0.34	0.36	0.35	0.33
Nd	0.21	0.19	0.21	0.17	0.15	0.16	0.16	0.18	0.18	0.16	0.13	0.18	0.17	0.18	0.19	0.17	0.18	0.15
Pr	0.06	0.05	0.05	0.04	0.04	0.04	0.04	0.06	0.05	0.05	0.05	0.04	0.05	0.06	0.06	0.05	0.06	0.05
Sm	0.03	0.02	0.02	0.03	0.02	0.02	0.03	0.02	0.02	0.02	0.02	0.02	0.03	0.02	0.03	0.03	0.02	0.02
Gd	0.00	0.01	0.00	0.01	0.01	0.00	0.00	0.01	0.00	0.01	0.00	0.01	0.00	0.00	0.01	0.00	0.00	0.00
Th	0.00	0.00	0.00	0.00	0.00	0.00	0.00	0.00	0.00	0.00	0.00	0.00	0.00	0.00	0.00	0.00	0.00	0.00
Sr	0.10	0.11	0.12	0.10	0.10	0.13	0.17	0.11	0.12	0.10	0.11	0.13	0.09	0.09	0.08	0.09	0.09	0.13
∑REE	0.93	0.94	0.95	0.94	0.87	0.90	0.97	0.96	0.92	0.93	0.91	0.91	0.93	0.91	0.90	0.93	0.91	0.95
Fe	0.03	0.13	0.07	0.01	0.62	0.08	0.09	0.01	0.20	0.08	0.08	0.07	0.02	0.01	0.14	0.02	0.01	0.03
Al	3.09	3.05	3.09	3.11	2.82	3.07	3.11	3.11	3.06	3.09	3.08	3.12	3.12	3.11	3.04	3.12	3.11	3.13
∑Al	3.12	3.18	3.16	3.12	3.44	3.15	3.20	3.12	3.26	3.17	3.16	3.19	3.14	3.12	3.18	3.14	3.12	3.16
Si	0.06	0.03	0.08	0.02	0.00	0.15	0.01	0.00	0.00	0.02	0.00	0.05	0.00	0.00	0.01	0.00	0.00	0.00
P	1.83	1.78	1.77	1.86	1.63	1.73	1.76	1.88	1.76	1.85	1.86	1.81	1.89	1.91	1.89	1.89	1.91	1.87
S	0.12	0.13	0.14	0.13	0.12	0.13	0.15	0.11	0.15	0.12	0.13	0.14	0.09	0.10	0.09	0.09	0.10	0.13
∑P	2.01	1.94	1.99	2.01	1.75	2.01	1.92	1.99	1.91	1.99	1.99	2.00	1.98	2.01	1.99	1.98	2.01	2.00
F	0.05	0.13	0.10	0.16	0.05	0.17	0.31	0.09	0.13	0.22	0.12	0.20	0.00	0.10	0.16	0.00	0.10	0.22
Cl	0.01	0.01	0.00	0.00	0.00	0.00	0.01	0.00	0.00	0.00	0.00	0.00	0.00	0.00	0.00	0.00	0.00	0.00
OH	5.94	5.86	5.90	5.83	5.94	5.83	5.69	5.90	5.87	5.77	5.88	5.80	6.00	5.89	5.83	6.00	5.89	5.78
∑OH	6.00	6.00	6.00	6.00	6.00	6.00	6.00	6.00	6.00	6.00	6.00	6.00	6.00	6.00	6.00	6.00	6.00	6.00
Flr	0.78	0.77	0.78	0.78	0.73	0.71	0.72	0.78	0.73	0.77	0.73	0.73	0.79	0.77	0.79	0.79	0.77	0.72
Wdh	0.11	0.12	0.11	0.12	0.18	0.14	0.12	0.11	0.15	0.14	0.15	0.13	0.11	0.13	0.13	0.11	0.13	0.16
Svb	0.05	0.07	0.10	0.04	0.06	0.07	0.10	0.03	0.07	0.03	0.01	0.06	0.02	0.00	0.00	0.02	0.00	0.01
Gyz	0.08	0.07	0.05	0.09	0.11	0.10	0.09	0.10	0.10	0.11	0.14	0.11	0.11	0.14	0.13	0.11	0.14	0.15
Hut	0.03	0.02	0.04	0.01	0.00	0.08	0.01	0.00	0.00	0.01	0.00	0.03	0.00	0.00	0.01	0.00	0.00	0.00

*Flr = Florencite, Wdh = Woodhouseite, Svb = Svanbergite, Gyz = Goyazite, Hut = Huttonite

**Formulae on basis of 14 atoms per formula unit (a.p.f.u.)

(Continued)

	W53	W54	W55	W56	W57	W58	W59	W60	W61	W62	W63	W64	W65	W66	W67	W68	W69	W70	W71
	Wolverine (late)																		
CaO	1.03	1.02	1.10	1.25	1.11	1.07	1.08	1.18	1.79	1.34	1.35	1.49	1.10	1.08	1.25	1.40	1.10	1.10	1.21
Y_2O_3	0.00	0.00	0.00	0.00	0.00	0.00	0.00	0.00	0.00	0.00	0.00	0.00	0.00	0.00	0.00	0.00	0.00	0.00	0.00
La_2O_3	4.17	4.65	3.90	3.71	3.55	3.18	4.03	3.77	3.11	3.56	3.84	4.16	3.16	4.19	3.53	3.47	3.77	3.69	3.49
Ce_2O_3	10.62	10.77	10.74	8.29	8.83	9.35	9.75	9.98	8.81	9.92	7.66	8.15	8.76	9.25	8.70	7.22	8.99	8.92	9.21
Nd_2O_3	5.63	4.37	5.12	4.80	6.41	7.66	5.61	5.96	6.24	6.35	4.59	3.02	5.65	5.68	4.91	5.23	6.31	6.26	5.24
Pr_2O_3	1.70	1.44	1.56	1.40	1.17	1.64	1.62	1.48	1.53	1.62	1.36	1.14	1.42	1.58	1.57	1.26	1.46	1.61	1.39
Sm_2O_3	0.74	0.56	0.51	0.52	0.72	0.74	0.87	0.83	0.81	0.58	0.52	0.24	0.69	0.64	0.53	0.48	0.65	0.62	0.58
Gd_2O_3	0.14	0.16	0.00	0.18	0.11	0.26	0.19	0.18	0.01	0.05	0.24	0.07	0.12	0.15	0.24	0.00	0.07	0.02	0.28
ThO_2	0.00	0.05	0.00	0.08	0.39	0.21	0.13	0.00	0.00	0.01	0.31	0.21	0.17	0.05	0.03	0.30	0.09	0.13	0.00
SrO	2.01	3.71	1.82	5.24	4.15	3.11	2.88	2.75	2.78	2.84	5.40	6.02	3.66	3.18	4.12	5.44	2.93	3.95	4.32
FeO	1.35	0.49	5.48	0.71	1.80	0.90	0.63	0.23	0.66	0.19	0.69	1.89	0.32	0.65	1.05	0.42	1.03	0.17	1.84
SiO_2	0.01	0.27	0.17	0.26	0.13	0.22	0.19	0.08	0.83	0.11	0.67	0.99	0.03	0.76	1.79	0.54	0.09	0.37	0.22
Al_2O_3	30.39	31.41	29.14	31.77	30.52	29.44	30.99	31.28	29.89	30.72	30.63	30.75	29.77	31.30	30.32	31.32	29.70	30.87	30.95
P_2O_5	25.45	23.50	24.35	23.41	23.58	24.43	25.51	25.56	25.54	25.94	21.89	21.28	24.19	24.39	23.29	21.43	24.04	23.83	23.00
SO_3	1.73	2.65	1.85	4.26	2.85	2.21	2.08	2.45	2.73	2.16	4.05	5.14	2.88	2.51	3.02	4.04	2.49	3.02	3.43
F	0.20	0.42	0.24	0.45	0.56	0.28	0.19	0.82	0.00	0.30	0.64	0.83	0.37	0.01	0.43	0.65	0.59	0.68	0.53
Cl	0.03	0.06	0.04	0.03	0.07	0.08	0.01	0.02	0.02	0.05	0.09	0.05	0.05	0.01	0.04	0.06	0.03	0.04	0.00
Total	85.21	85.52	86.03	86.36	85.94	84.78	85.77	86.57	84.75	85.74	83.91	85.42	82.34	85.44	84.81	83.27	83.35	85.27	85.69
Ca	0.10	0.09	0.10	0.12	0.10	0.10	0.10	0.11	0.17	0.12	0.13	0.14	0.11	0.10	0.12	0.13	0.10	0.10	0.11
Y	0.00	0.00	0.00	0.00	0.00	0.00	0.00	0.00	0.00	0.00	0.00	0.00	0.00	0.00	0.00	0.00	0.00	0.00	0.00
La	0.13	0.15	0.12	0.12	0.11	0.10	0.13	0.12	0.10	0.11	0.13	0.13	0.10	0.13	0.11	0.11	0.12	0.12	0.11
Ce	0.34	0.34	0.33	0.26	0.28	0.30	0.31	0.31	0.28	0.31	0.25	0.26	0.29	0.29	0.28	0.23	0.29	0.29	0.29
Nd	0.17	0.14	0.16	0.15	0.20	0.24	0.17	0.18	0.19	0.19	0.15	0.09	0.18	0.17	0.15	0.17	0.20	0.20	0.16
Pr	0.05	0.05	0.05	0.04	0.04	0.05	0.05	0.05	0.05	0.05	0.04	0.04	0.05	0.05	0.05	0.04	0.05	0.05	0.04
Sm	0.02	0.02	0.01	0.02	0.02	0.02	0.03	0.02	0.02	0.02	0.02	0.01	0.02	0.02	0.02	0.01	0.02	0.02	0.02
Gd	0.00	0.00	0.00	0.01	0.00	0.01	0.01	0.00	0.00	0.00	0.01	0.00	0.00	0.00	0.01	0.00	0.00	0.00	0.01
Th	0.00	0.00	0.00	0.00	0.01	0.00	0.00	0.00	0.00	0.00	0.01	0.00	0.00	0.00	0.00	0.01	0.00	0.00	0.00
Sr	0.10	0.19	0.09	0.26	0.21	0.16	0.14	0.14	0.14	0.14	0.28	0.30	0.19	0.16	0.21	0.28	0.15	0.20	0.22
∑REE	0.91	0.98	0.86	0.98	0.97	0.98	0.94	0.93	0.95	0.94	1.02	0.97	0.94	0.92	0.95	0.98	0.93	0.98	0.96
Fe	0.10	0.04	0.39	0.05	0.13	0.07	0.05	0.02	0.05	0.01	0.05	0.14	0.02	0.05	0.08	0.03	0.08	0.01	0.13
Al	3.09	3.21	2.92	3.22	3.12	3.05	3.12	3.15	3.04	3.10	3.21	3.16	3.14	3.16	3.09	3.28	3.12	3.18	3.16
∑Al	3.19	3.25	3.31	3.27	3.25	3.12	3.17	3.17	3.09	3.11	3.26	3.3	3.16	3.21	3.17	3.31	3.20	3.19	3.29
Si	0.00	0.02	0.01	0.02	0.01	0.02	0.02	0.01	0.07	0.01	0.06	0.09	0.00	0.06	0.15	0.05	0.01	0.03	0.02
P	1.86	1.72	1.75	1.71	1.73	1.82	1.85	1.85	1.86	1.88	1.65	1.57	1.83	1.77	1.71	1.61	1.81	1.76	1.69
S	0.11	0.17	0.12	0.28	0.19	0.15	0.13	0.16	0.18	0.14	0.27	0.34	0.19	0.16	0.20	0.27	0.17	0.20	0.22
∑P	1.97	1.91	1.88	2.01	1.93	1.99	2.00	2.02	2.11	2.03	1.98	2.00	2.02	1.99	2.06	1.93	1.99	1.99	1.93
F	0.06	0.12	0.06	0.12	0.15	0.08	0.05	0.22	0.00	0.08	0.18	0.23	0.10	0.00	0.12	0.18	0.17	0.19	0.15
Cl	0.00	0.01	0.01	0.00	0.01	0.01	0.00	0.00	0.00	0.01	0.01	0.01	0.01	0.00	0.01	0.01	0.00	0.01	0.00
OH	5.94	5.88	5.93	5.87	5.84	5.91	5.95	5.77	6.00	5.91	5.81	5.76	5.89	6.00	5.88	5.81	5.83	5.81	5.85
∑OH	6.00	6.00	6.00	6.00	6.00	6.00	6.00	6.00	6.00	6.00	6.00	6.00	6.00	6.00	6.00	6.00	6.00	6.00	6.00
Flr	0.75	0.72	0.74	0.63	0.68	0.74	0.73	0.72	0.67	0.71	0.61	0.56	0.67	0.70	0.65	0.59	0.72	0.70	0.66
Wdh	0.14	0.11	0.17	0.15	0.13	0.12	0.13	0.15	0.20	0.15	0.14	0.17	0.14	0.14	0.15	0.16	0.14	0.12	0.14
Svb	0.01	0.16	0.02	0.20	0.14	0.07	0.04	0.05	0.00	0.01	0.22	0.26	0.07	0.09	0.12	0.23	0.08	0.14	0.17
Gyz	0.13	0.05	0.13	0.09	0.11	0.11	0.13	0.13	0.18	0.16	0.08	0.07	0.15	0.11	0.12	0.08	0.11	0.08	0.09
Hut	0.00	0.01	0.01	0.01	0.01	0.01	0.01	0.01	0.04	0.01	0.04	0.05	0.00	0.03	0.08	0.03	0.01	0.02	0.01

*Flr = Florencite, Wdh = Woodhouseite, Svb = Svanbergite, Gyz = Goyazite, Hut = Huttonite

**Formulae on basis of 14 atoms per formula unit (a.p.f.u.)

(Continued)

	W72	W73	W74	W75	W76	W77	W78	W79	W80	W81	W82	W83	W84	W85	W86	W87	W88	W89
	Wolverine (late)																	
CaO	1.57	1.20	1.17	1.35	1.11	1.03	1.25	0.98	1.10	1.07	0.79	0.95	1.15	1.09	1.17	1.07	0.94	1.47
Y_2O_3	0.00	0.00	0.00	0.00	0.00	0.00	0.00	0.00	0.00	0.00	0.00	0.00	0.00	0.00	0.00	0.00	0.00	0.00
La_2O_3	4.60	3.61	3.95	3.47	3.58	3.98	3.82	3.48	3.29	3.44	2.46	3.21	3.07	3.37	3.43	4.23	2.99	2.69
Ce_2O_3	9.67	8.54	9.05	8.80	9.36	8.66	9.59	9.26	8.94	7.94	7.52	8.25	8.70	9.46	8.39	7.56	7.95	6.82
Nd_2O_3	3.86	6.32	6.10	5.23	5.49	5.36	5.56	6.25	5.43	5.97	7.73	6.37	5.42	5.61	4.84	5.06	6.01	4.22
Pr_2O_3	1.38	1.37	1.61	1.06	1.53	1.30	1.66	1.69	1.53	1.37	1.63	1.65	1.64	1.81	1.43	1.48	1.68	1.59
Sm_2O_3	0.25	0.60	0.65	0.53	0.59	0.82	0.86	0.94	0.93	0.84	1.25	1.07	0.85	0.96	0.63	0.72	0.92	0.67
Gd_2O_3	0.00	0.02	0.00	0.05	0.25	0.00	0.05	0.13	0.11	0.14	0.12	0.34	0.08	0.20	0.09	0.00	0.18	0.17
ThO_2	0.00	0.26	0.02	0.40	0.03	0.21	0.00	0.00	0.00	0.02	0.00	0.00	0.00	0.02	0.01	0.00	0.00	0.00
SrO	3.92	4.17	3.75	5.41	3.76	4.69	2.43	2.64	2.07	2.57	1.98	2.02	2.12	1.78	3.66	3.41	1.84	3.03
FeO	0.20	0.79	0.39	0.42	0.58	1.00	0.05	0.23	1.51	0.60	0.32	1.47	3.64	0.07	0.71	0.52	0.29	3.03
SiO_2	1.32	0.26	0.09	0.21	0.30	0.00	0.21	0.15	0.38	0.26	0.21	1.09	0.12	0.00	0.39	1.13	0.00	0.41
Al_2O_3	31.33	30.98	31.29	31.08	30.13	30.76	29.56	30.82	29.51	29.54	29.32	30.05	29.19	30.55	30.01	29.66	30.09	29.32
P_2O_5	23.49	24.26	24.49	21.72	24.35	23.20	24.84	25.28	24.35	23.90	24.84	24.71	24.14	25.75	24.31	23.26	25.81	24.47
SO_3	3.58	2.82	2.86	4.06	2.71	3.47	2.06	2.14	1.84	2.40	1.54	1.69	1.88	1.82	2.87	2.75	1.59	2.36
F	0.63	1.15	0.79	0.34	0.31	0.40	0.30	0.50	0.41	0.64	0.63	0.18	0.50	0.49	0.54	0.82	0.67	0.16
Cl	0.01	0.08	0.05	0.11	0.05	0.03	0.06	0.03	0.02	0.06	0.05	0.04	0.10	0.07	0.03	0.06	0.05	0.03
Total	85.81	86.42	86.25	84.23	84.13	84.90	82.30	84.52	81.43	80.76	80.39	83.10	82.61	83.04	82.50	81.74	81.01	80.45
Ca	0.14	0.11	0.11	0.13	0.10	0.10	0.12	0.09	0.11	0.10	0.08	0.09	0.11	0.10	0.11	0.10	0.09	0.14
Y	0.00	0.00	0.00	0.00	0.00	0.00	0.00	0.00	0.00	0.00	0.00	0.00	0.00	0.00	0.00	0.00	0.00	0.00
La	0.15	0.11	0.13	0.11	0.12	0.13	0.13	0.11	0.11	0.12	0.08	0.10	0.10	0.11	0.11	0.14	0.10	0.09
Ce	0.30	0.27	0.29	0.29	0.30	0.28	0.31	0.30	0.29	0.26	0.25	0.26	0.28	0.30	0.27	0.25	0.26	0.22
Nd	0.12	0.19	0.19	0.17	0.17	0.17	0.18	0.19	0.17	0.19	0.25	0.20	0.17	0.18	0.15	0.16	0.19	0.13
Pr	0.04	0.04	0.05	0.03	0.05	0.04	0.05	0.05	0.05	0.05	0.05	0.05	0.05	0.06	0.05	0.05	0.05	0.05
Sm	0.01	0.02	0.02	0.02	0.02	0.02	0.03	0.03	0.03	0.03	0.04	0.03	0.03	0.03	0.02	0.02	0.03	0.02
Gd	0.00	0.00	0.00	0.00	0.01	0.00	0.00	0.00	0.00	0.00	0.00	0.01	0.00	0.01	0.00	0.00	0.01	0.00
Th	0.00	0.01	0.00	0.01	0.00	0.00	0.00	0.00	0.00	0.00	0.00	0.00	0.00	0.00	0.00	0.00	0.00	0.00
Sr	0.20	0.21	0.19	0.28	0.19	0.24	0.13	0.13	0.11	0.14	0.10	0.10	0.11	0.09	0.19	0.18	0.10	0.15
∑REE	0.96	0.96	0.98	1.04	0.96	0.98	0.95	0.90	0.87	0.89	0.85	0.84	0.85	0.88	0.90	0.90	0.83	0.80
Fe	0.01	0.06	0.03	0.03	0.04	0.07	0.00	0.02	0.11	0.05	0.02	0.11	0.27	0.01	0.05	0.04	0.02	0.22
Al	3.17	3.15	3.18	3.25	3.12	3.18	3.11	3.17	3.10	3.16	3.14	3.08	3.03	3.16	3.14	3.13	3.16	3.05
∑Al	3.18	3.21	3.21	3.28	3.16	3.25	3.11	3.19	3.21	3.21	3.16	3.19	3.30	3.17	3.19	3.17	3.18	3.27
Si	0.11	0.02	0.01	0.02	0.03	0.00	0.02	0.01	0.03	0.02	0.02	0.09	0.01	0.00	0.03	0.10	0.00	0.04
P	1.71	1.77	1.79	1.63	1.81	1.72	1.88	1.87	1.84	1.84	1.91	1.82	1.80	1.91	1.83	1.77	1.95	1.83
S	0.23	0.18	0.18	0.27	0.18	0.23	0.14	0.14	0.12	0.16	0.11	0.11	0.12	0.12	0.19	0.19	0.11	0.16
∑P	2.05	1.97	1.98	1.92	2.02	1.95	2.04	2.02	1.99	2.02	2.04	2.02	1.93	2.03	2.05	2.06	2.06	2.03
F	0.17	0.31	0.22	0.10	0.09	0.11	0.09	0.14	0.11	0.18	0.18	0.05	0.14	0.14	0.15	0.23	0.19	0.04
Cl	0.00	0.01	0.01	0.02	0.01	0.00	0.01	0.00	0.00	0.01	0.01	0.01	0.02	0.01	0.00	0.01	0.01	0.00
OH	5.83	5.68	5.78	5.89	5.91	5.89	5.91	5.86	5.88	5.81	5.81	5.95	5.84	5.85	5.84	5.76	5.80	5.95
∑OH	6.00	6.00	6.00	6.00	6.00	6.00	6.00	6.00	6.00	6.00	6.00	6.00	6.00	6.00	6.00	6.00	6.00	6.00
Flr	0.64	0.66	0.70	0.63	0.70	0.66	0.73	0.73	0.71	0.70	0.73	0.71	0.70	0.74	0.65	0.66	0.71	0.60
Wdh	0.16	0.14	0.13	0.14	0.13	0.12	0.15	0.14	0.17	0.15	0.14	0.15	0.18	0.15	0.16	0.14	0.16	0.23
Svb	0.13	0.10	0.11	0.24	0.09	0.18	0.01	0.04	0.00	0.05	0.00	0.01	0.00	0.00	0.06	0.10	0.00	0.00
Gyz	0.09	0.14	0.10	0.05	0.12	0.09	0.14	0.14	0.17	0.14	0.17	0.15	0.18	0.15	0.18	0.13	0.21	0.27
Hut	0.06	0.02	0.01	0.02	0.02	0.00	0.01	0.01	0.02	0.01	0.01	0.05	0.01	0.00	0.02	0.05	0.00	0.02

*Flr = Florencite, Wdh = Woodhouseite, Svb = Svanbergite, Gyz = Goyazite, Hut = Huttonite

**Formulae on basis of 14 atoms per formula unit (a.p.f.u.)

(Continued)

	W90	W92	W93	W94
	Wolverine (late)			
CaO	0.92	1.58	1.04	0.96
Y_2O_3	0.00	0.00	0.00	0.00
La_2O_3	3.49	2.91	3.20	3.52
Ce_2O_3	8.27	7.91	8.03	8.40
Nd_2O_3	4.19	3.08	3.86	4.16
Pr_2O_3	1.73	1.19	1.50	1.70
Sm_2O_3	0.78	0.78	0.78	0.78
Gd_2O_3	0.26	0.16	0.32	0.48
ThO_2	0.00	0.41	0.20	0.07
SrO	2.00	3.92	3.80	2.08
FeO	0.30	1.27	0.27	0.27
SiO_2	1.10	0.53	0.66	0.04
Al_2O_3	29.58	30.05	30.72	30.55
P_2O_5	25.72	23.55	24.83	25.82
SO_3	1.63	2.33	2.30	1.62
F	0.78	0.50	0.68	0.34
Cl	0.01	0.05	0.01	0.04
Total	80.77	80.22	82.19	80.82
Ca	0.09	0.15	0.10	0.09
Y	0.00	0.00	0.00	0.00
La	0.11	0.10	0.10	0.11
Ce	0.27	0.26	0.26	0.27
Nd	0.13	0.10	0.12	0.13
Pr	0.06	0.04	0.05	0.05
Sm	0.02	0.02	0.02	0.02
Gd	0.01	0.00	0.01	0.01
Th	0.00	0.01	0.00	0.00
Sr	0.10	0.20	0.19	0.11
∑REE	0.79	0.88	0.85	0.79
Fe	0.02	0.09	0.02	0.02
Al	3.09	3.15	3.15	3.18
∑Al	3.11	3.24	3.17	3.2
Si	0.10	0.05	0.06	0.00
P	1.93	1.78	1.83	1.93
S	0.11	0.16	0.15	0.11
∑P	2.14	1.99	2.04	2.04
F	0.22	0.14	0.19	0.09
Cl	0.00	0.01	0.00	0.01
OH	5.78	5.85	5.81	5.90
∑OH	6.00	6.00	6.00	6.00
Flr	0.68	0.58	0.62	0.67
Wdh	0.17	0.21	0.16	0.17
Svb	0.00	0.02	0.03	0.00
Gyz	0.23	0.24	0.22	0.23
Hut	0.05	0.03	0.03	0.00

*Flr = Florencite, Wdh = Woodhouseite, Svb = Svanbergite, Gyz = Goyazite, Hut = Huttonite

**Formulae on basis of 14 atoms per formula unit (a.p.f.u.)

Appendix 6

Chapter 6

Appendix 6-1: Grain scale map of the quartz grains analysed for fluid inclusion

Appendix 6-2: Composition of the standards for LA-ICP-MS analysis of fluid inclusions

Appendix 6-3: Microthermometry data of primary fluid inclusions in different quartz grains

Appendix 6-4: Fluid inclusion microthermometry dataset

Appendix 6-1: Grain scale map of the quartz grains analysed for fluid inclusion

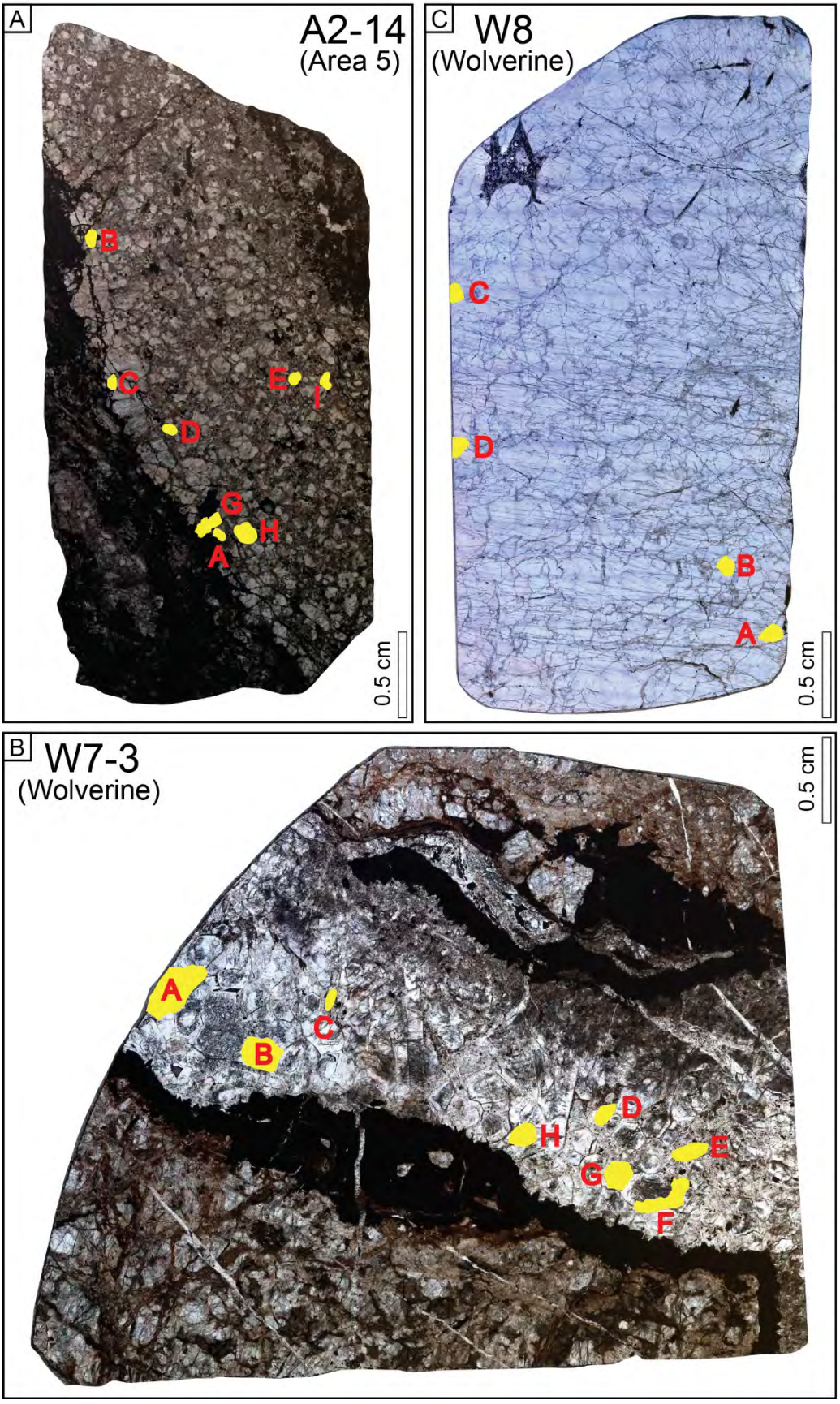

Fig. 1: Location of the quartz grains selected for fluid inclusion studies

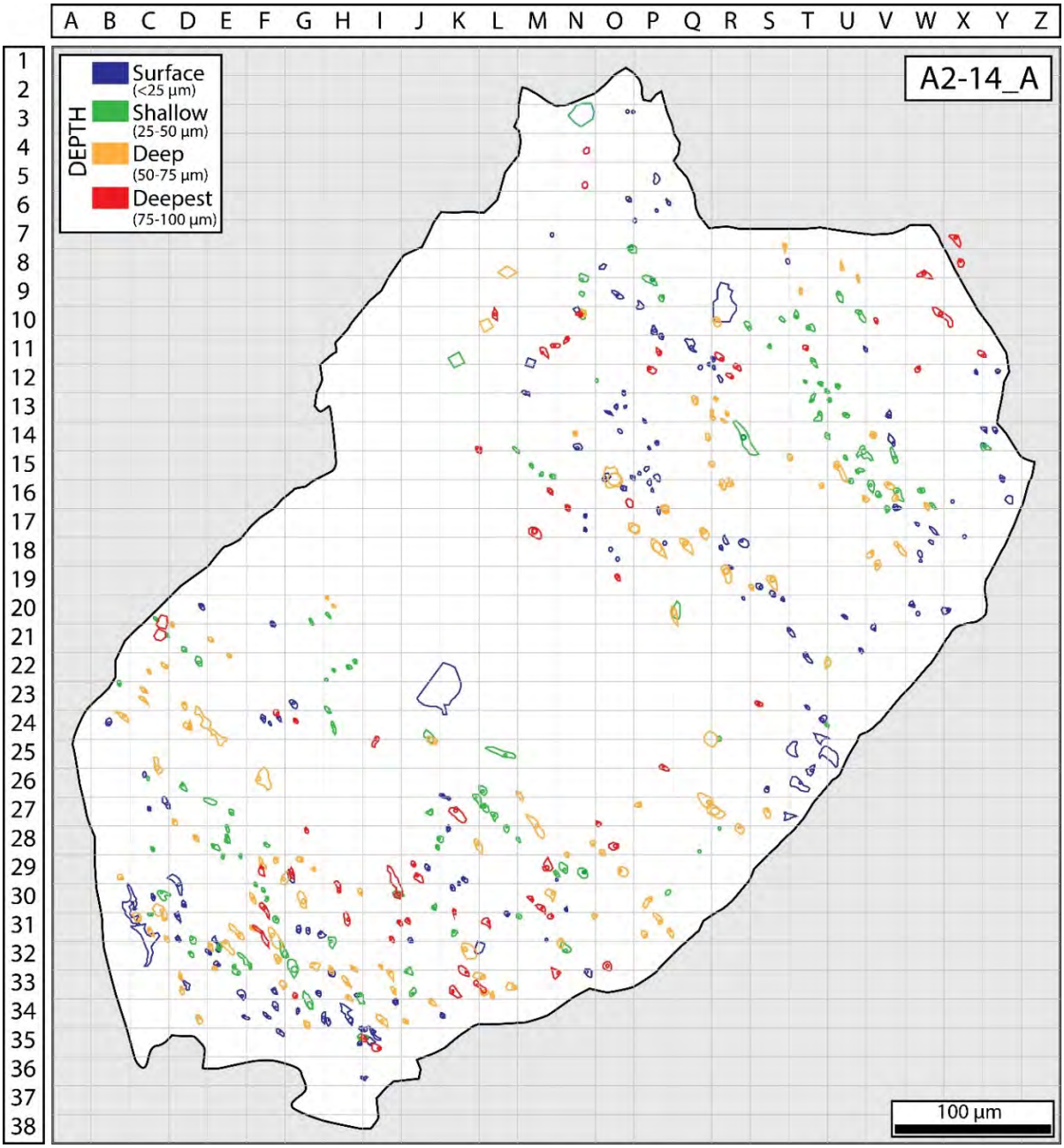

Fig. 2: Sample A2-14 (Area 5 deposit, mineralised), Grain A

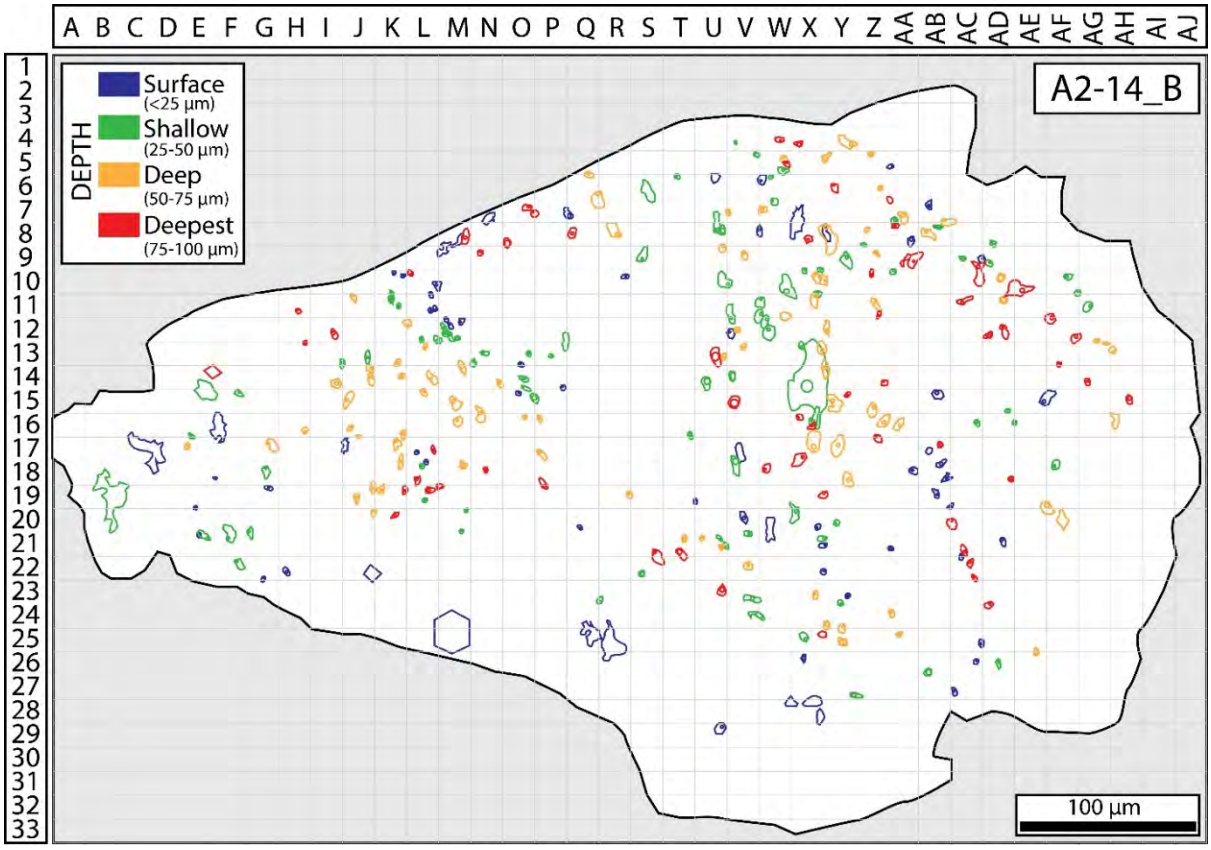

Fig. 3: Sample A2-14 (Area 5 deposit, mineralised), Grain B

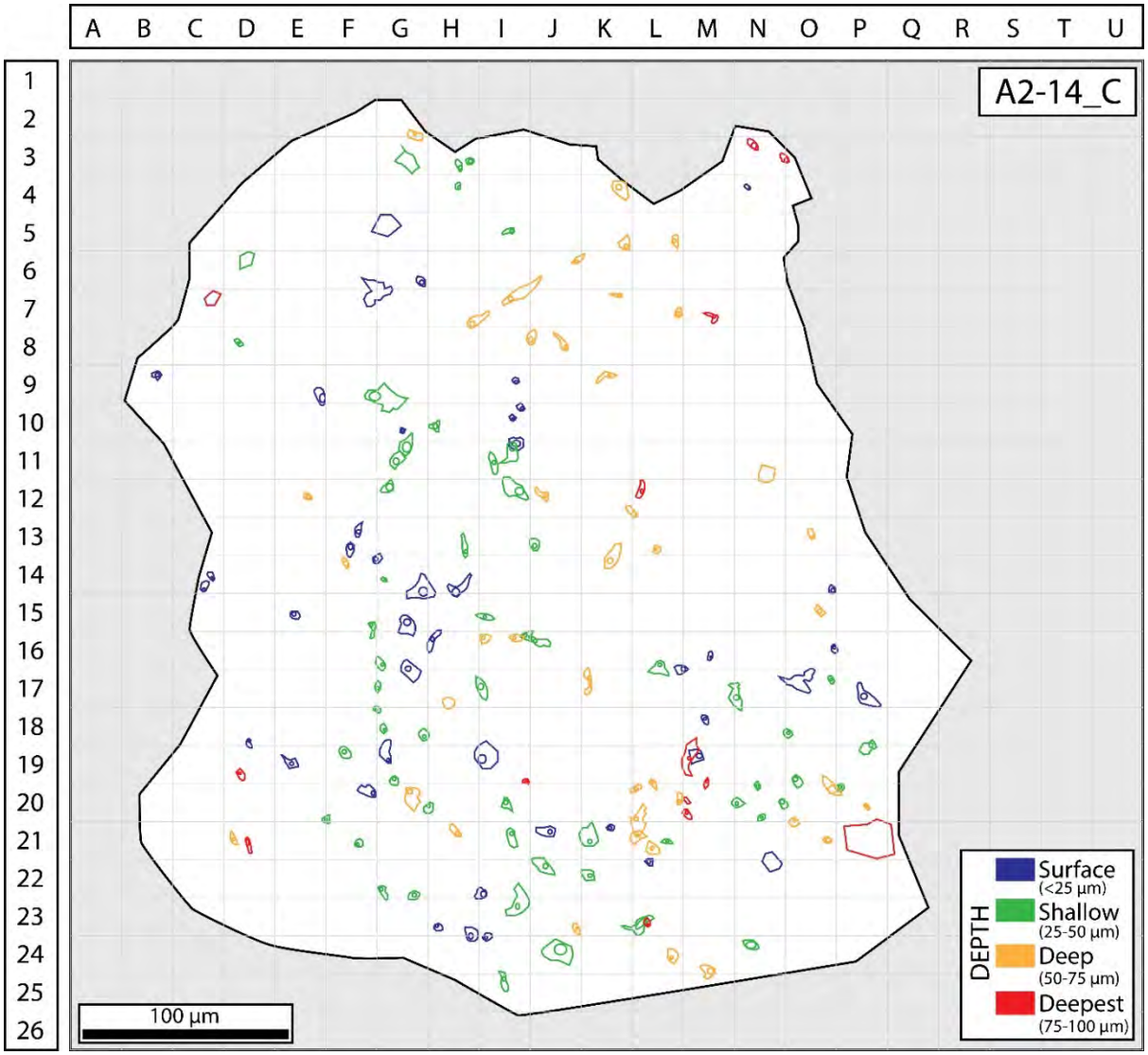

Fig. 4: Sample A2-14 (Area 5 deposit, mineralised), Grain C

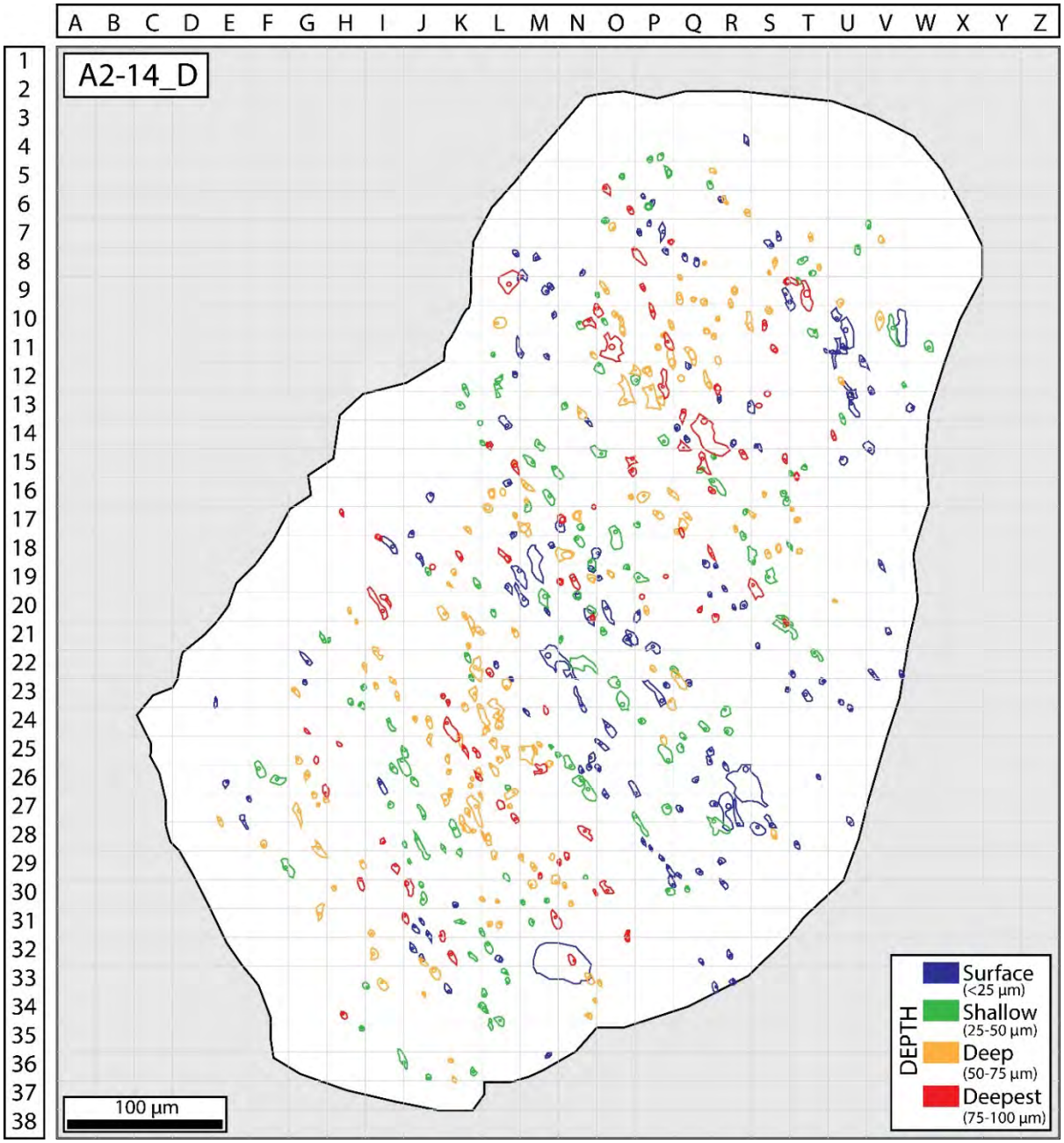

Fig. 5: Sample A2-14 (Area 5 deposit, mineralised), Grain D

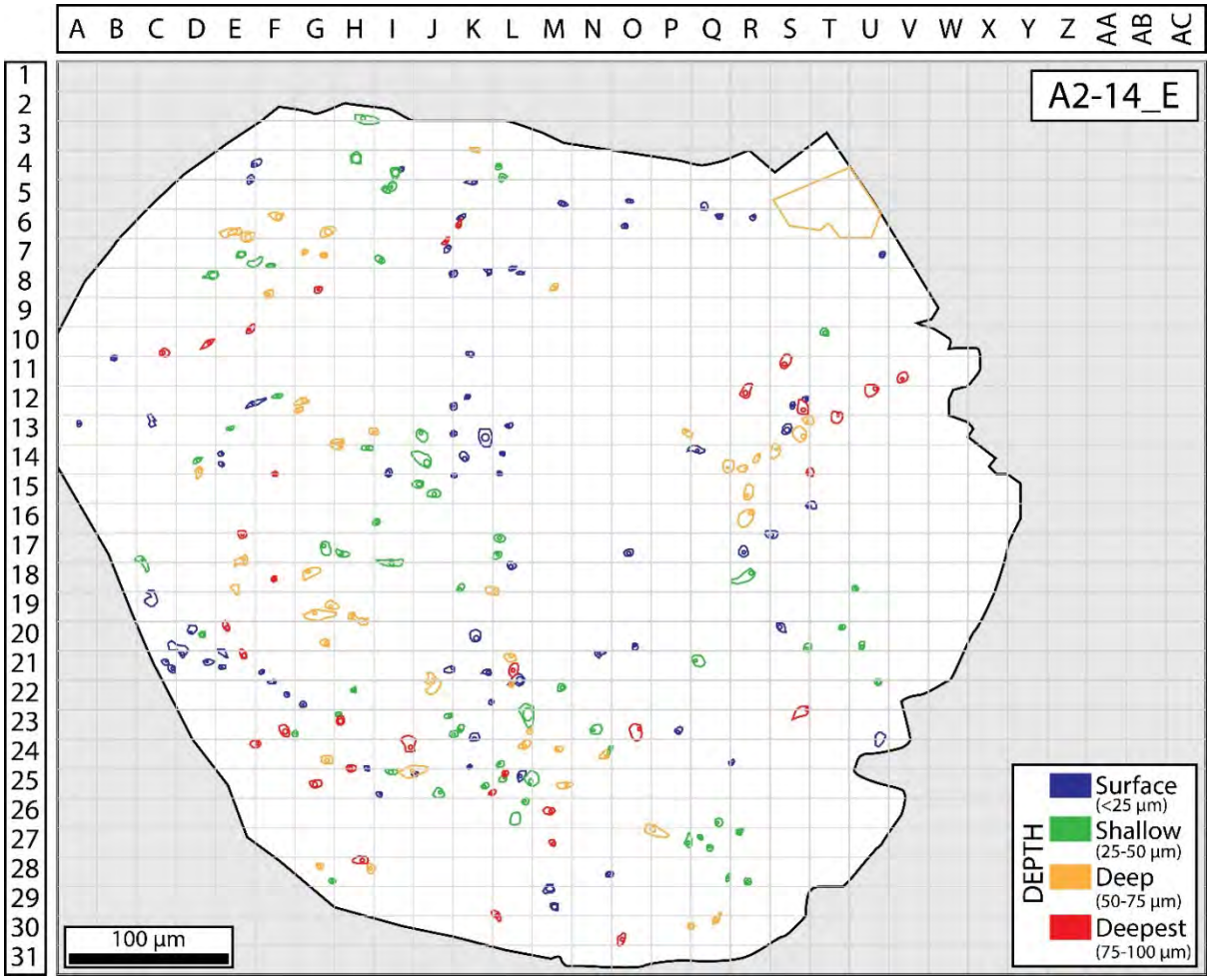

Fig. 6: Sample A2-14 (Area 5 deposit, mineralised), Grain E

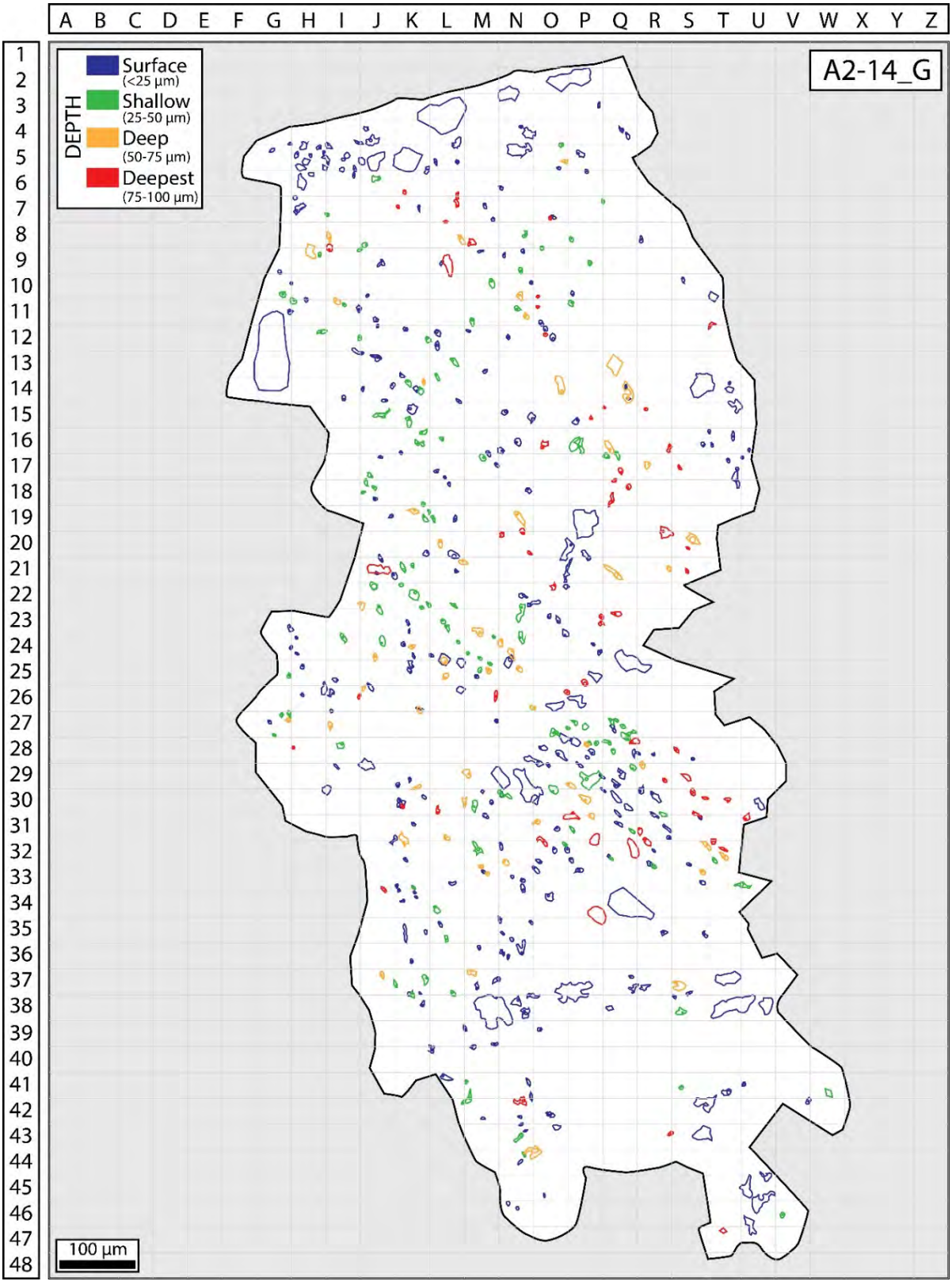

Fig. 7: Sample A2-14 (Area 5 deposit, mineralised), Grain G

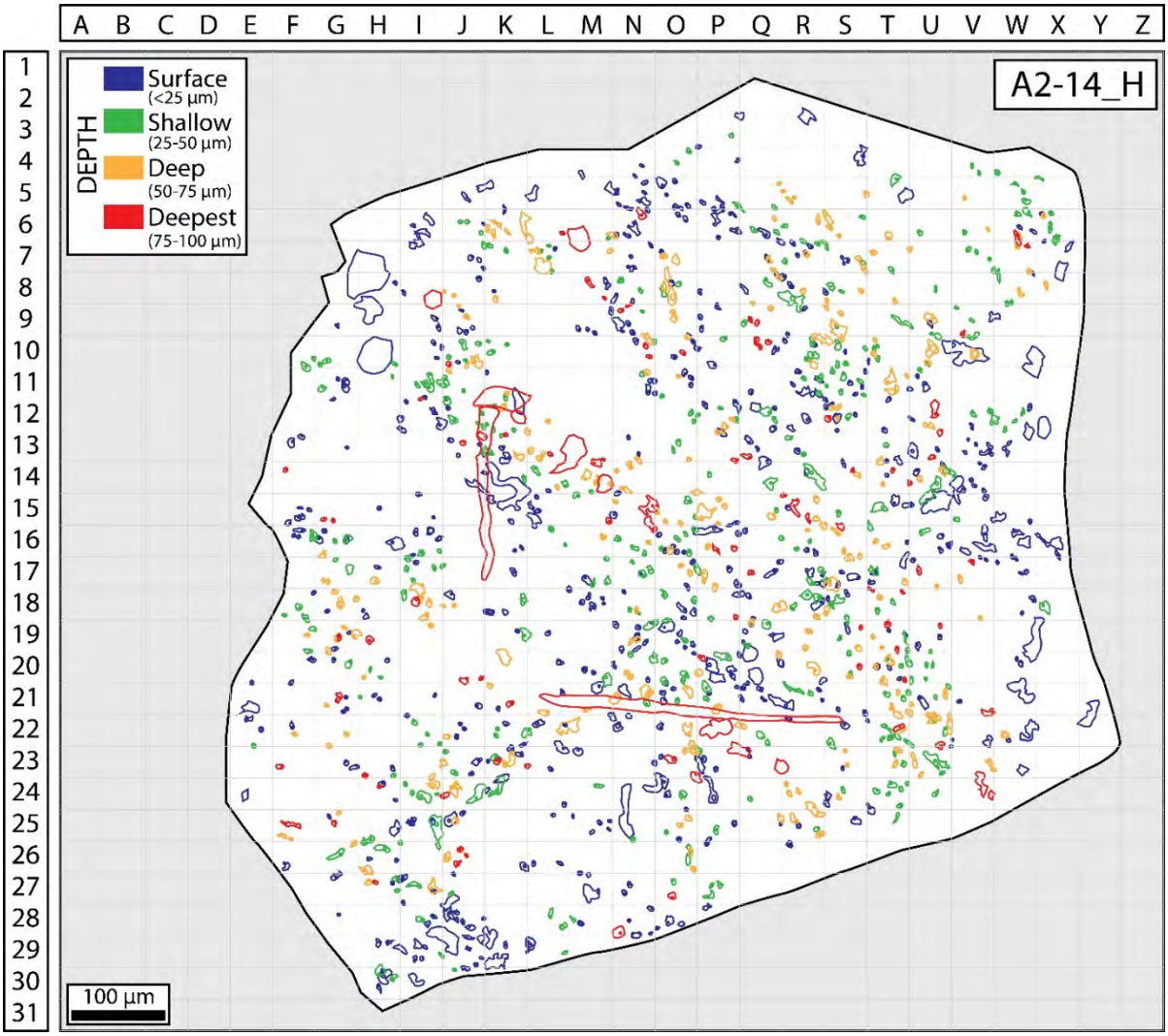

Fig. 8: Sample A2-14 (Area 5 deposit, mineralised), Grain H

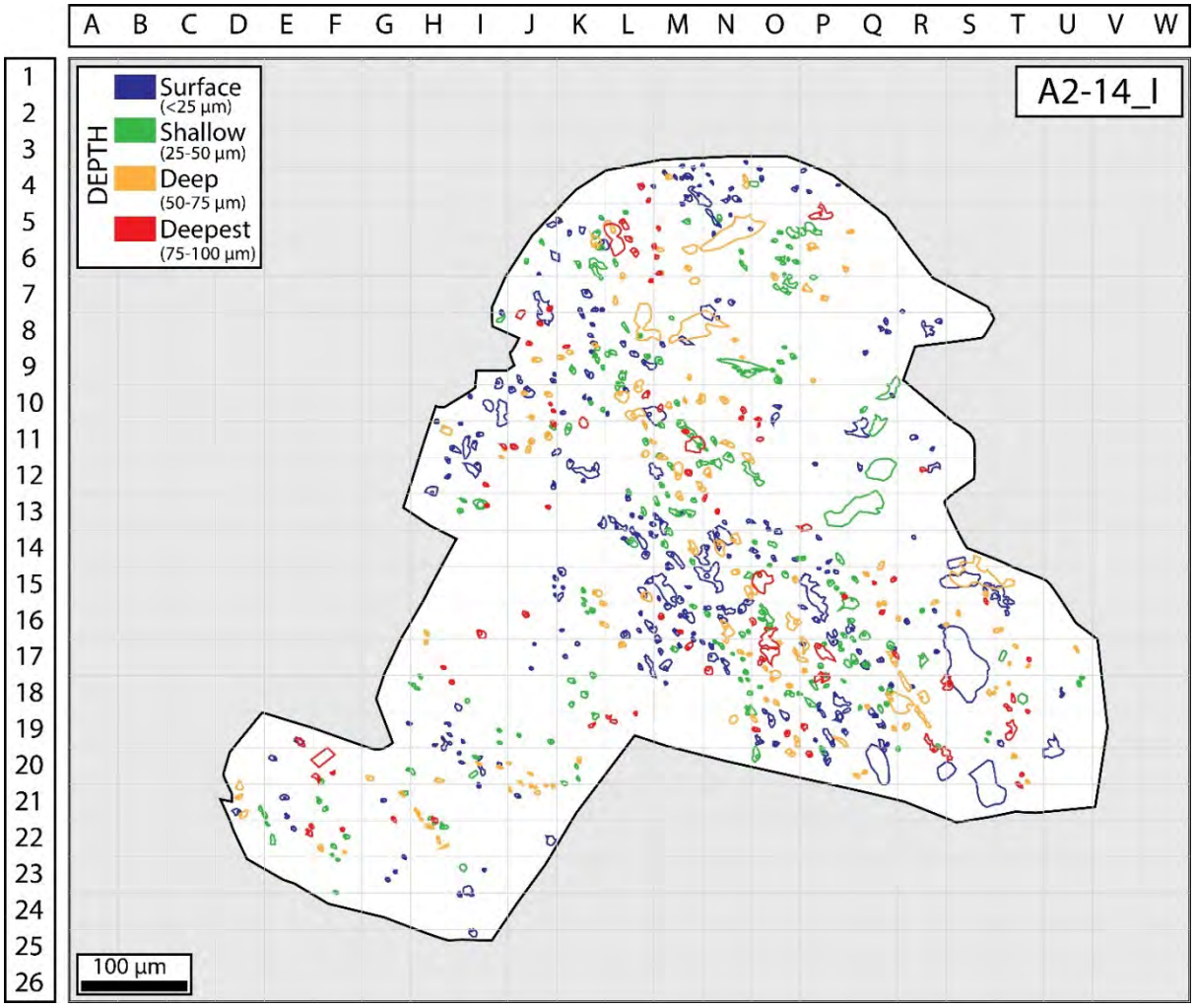

Fig. 9: Sample A2-14 (Area 5 deposit, mineralised), Grain I

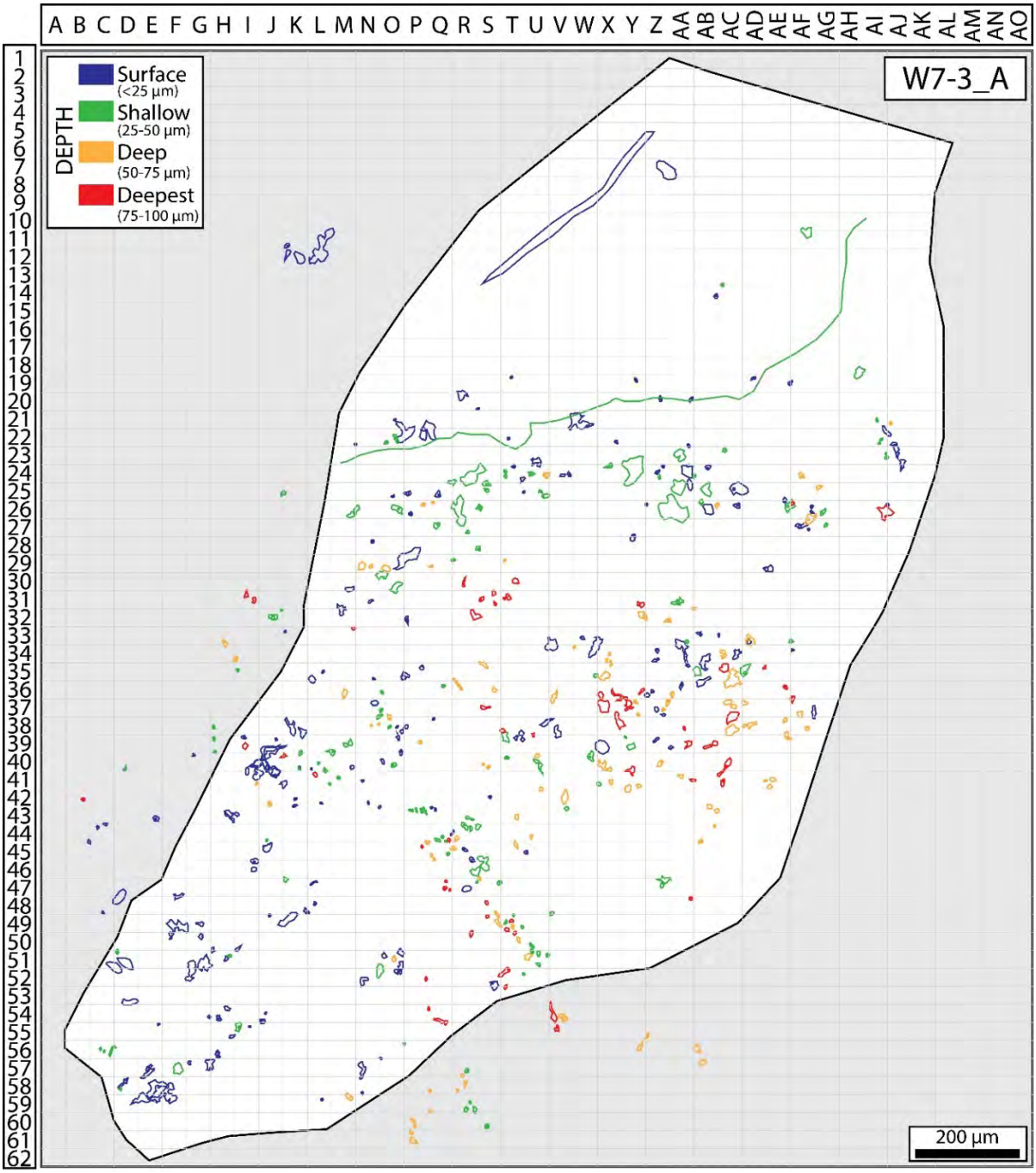

Fig. 10: Sample W7-3 (Wolverine deposit, mineralised), Grain A

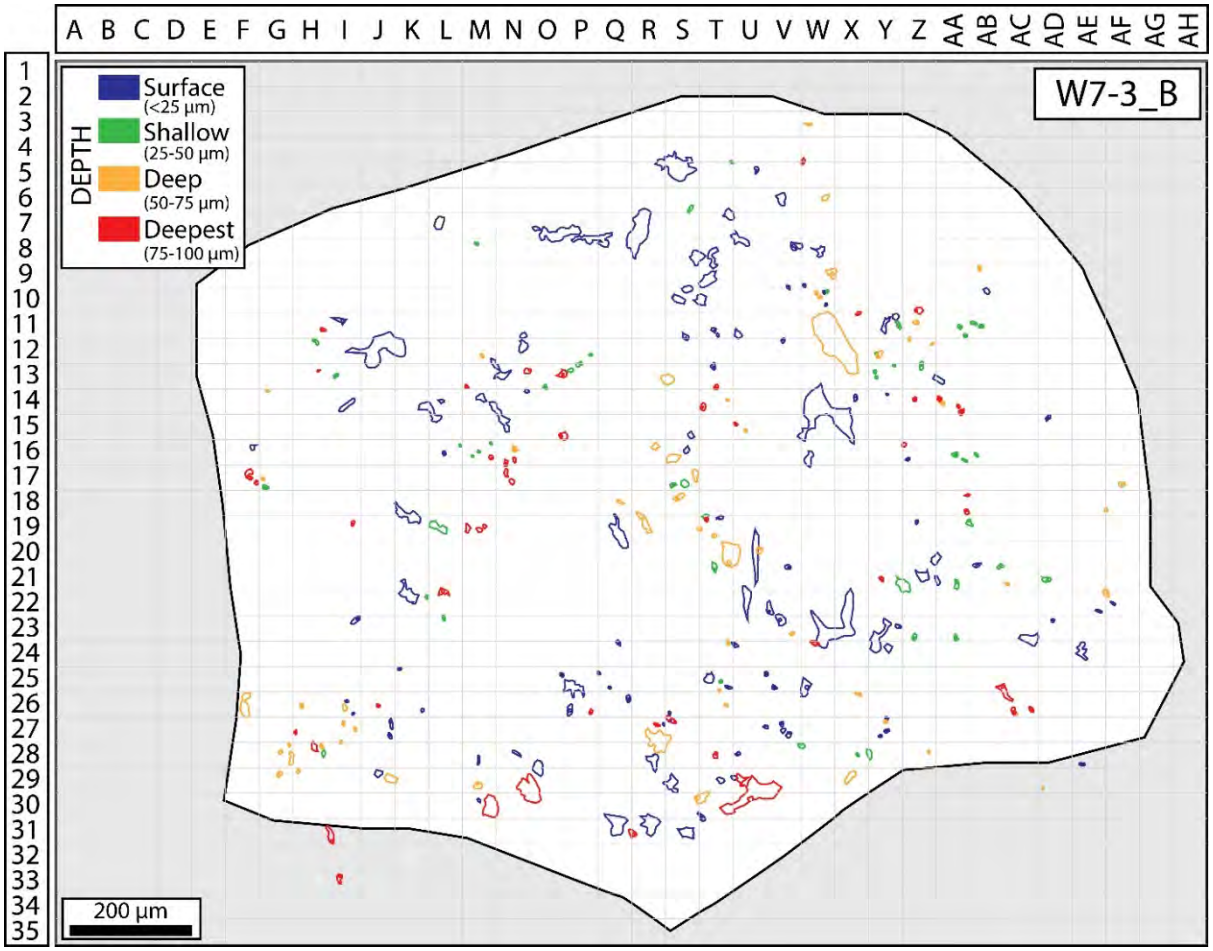

Fig. 11: Sample W7-3 (Wolverine deposit, mineralised), Grain B

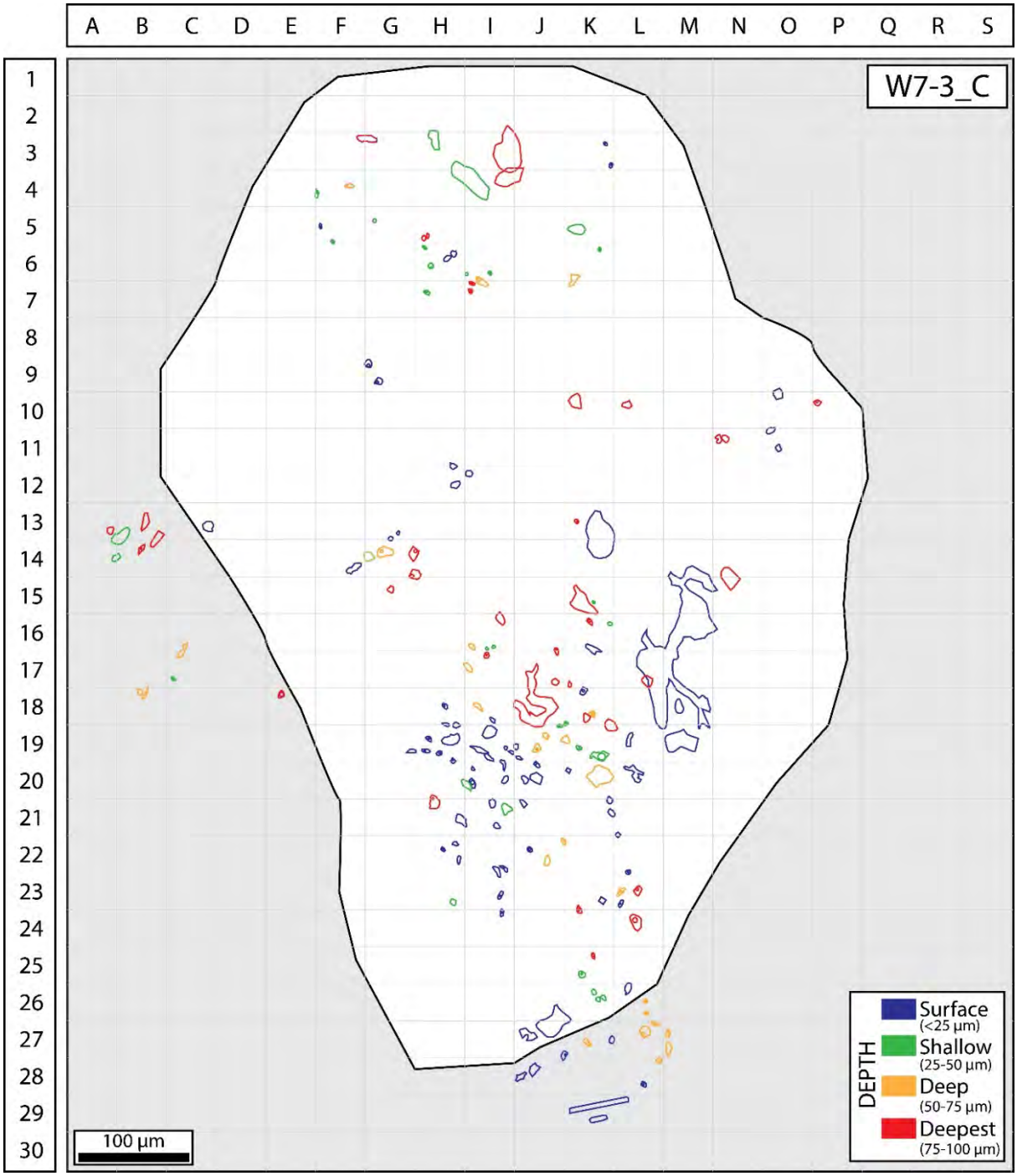

Fig. 12: Sample W7-3 (Wolverine deposit, mineralised), Grain C

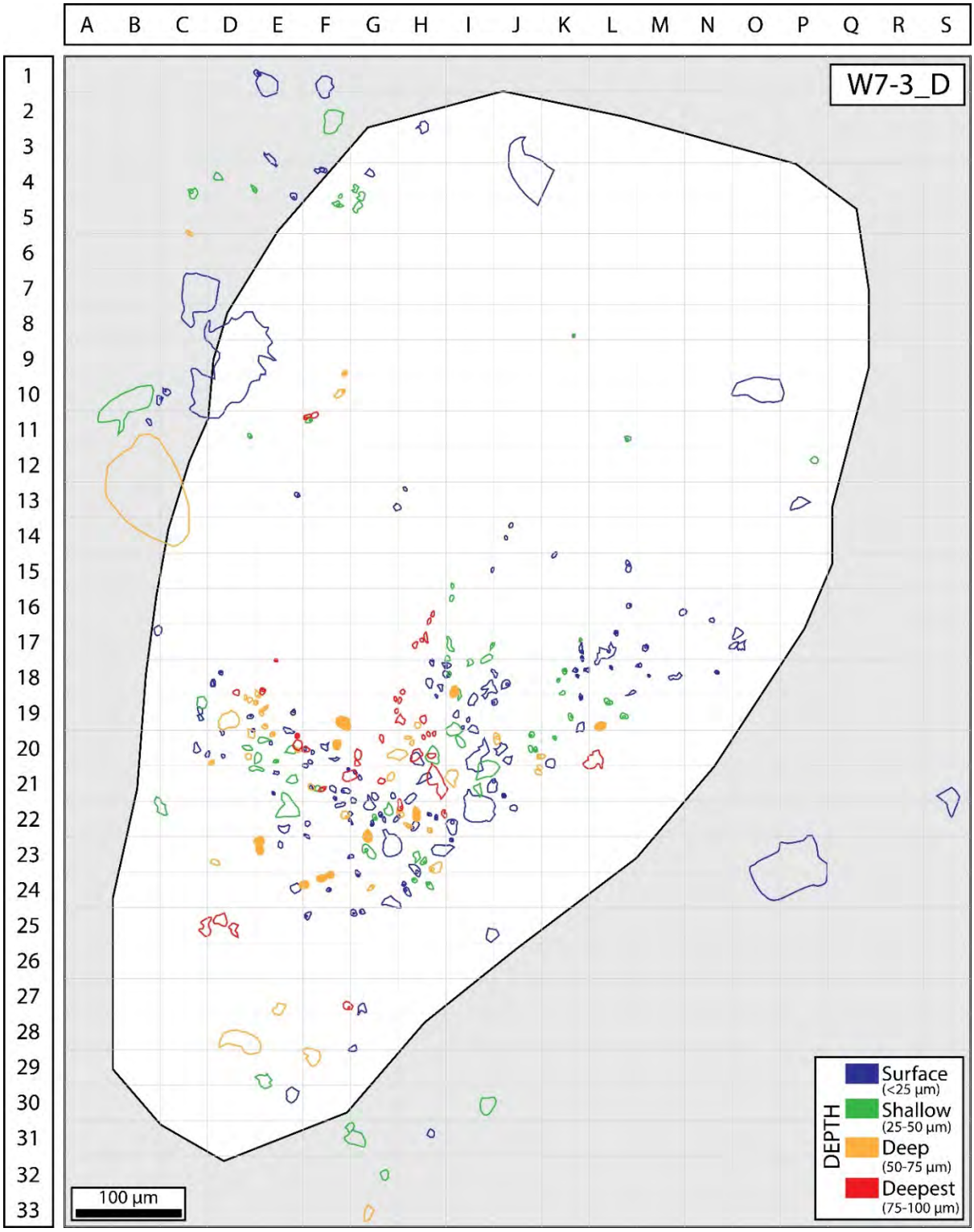

Fig. 13: Sample W7-3 (Wolverine deposit, mineralised), Grain D

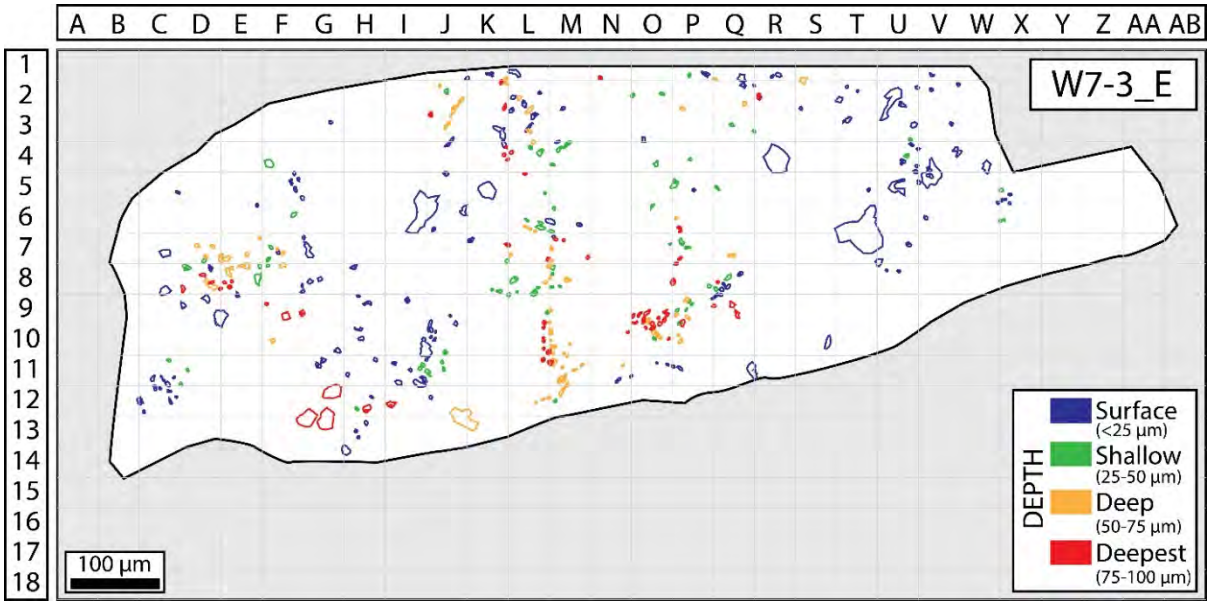

Fig. 14: Sample W7-3 (Wolverine deposit, mineralised), Grain E

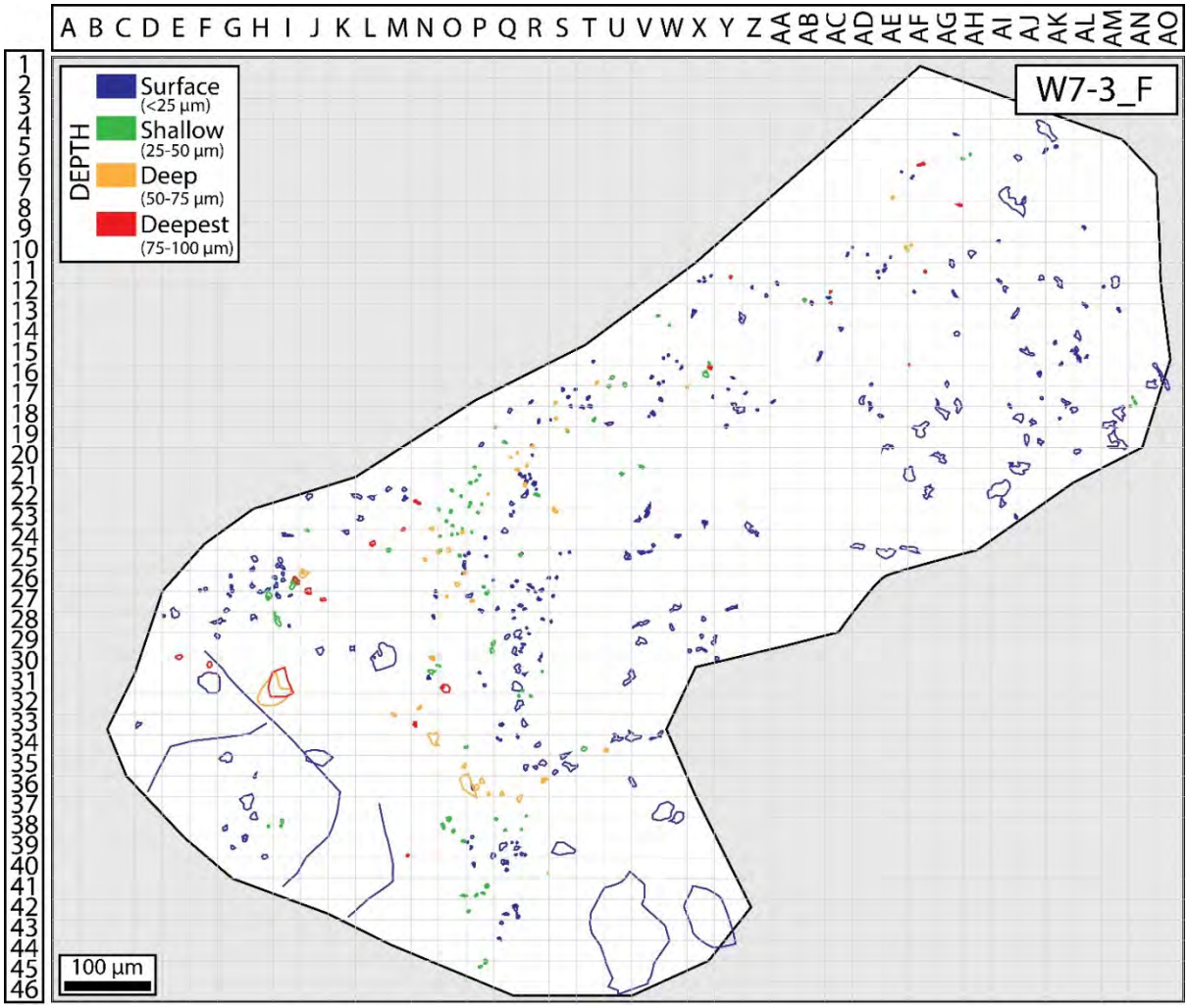

Fig. 15: Sample W7-3 (Wolverine deposit, mineralised), Grain F

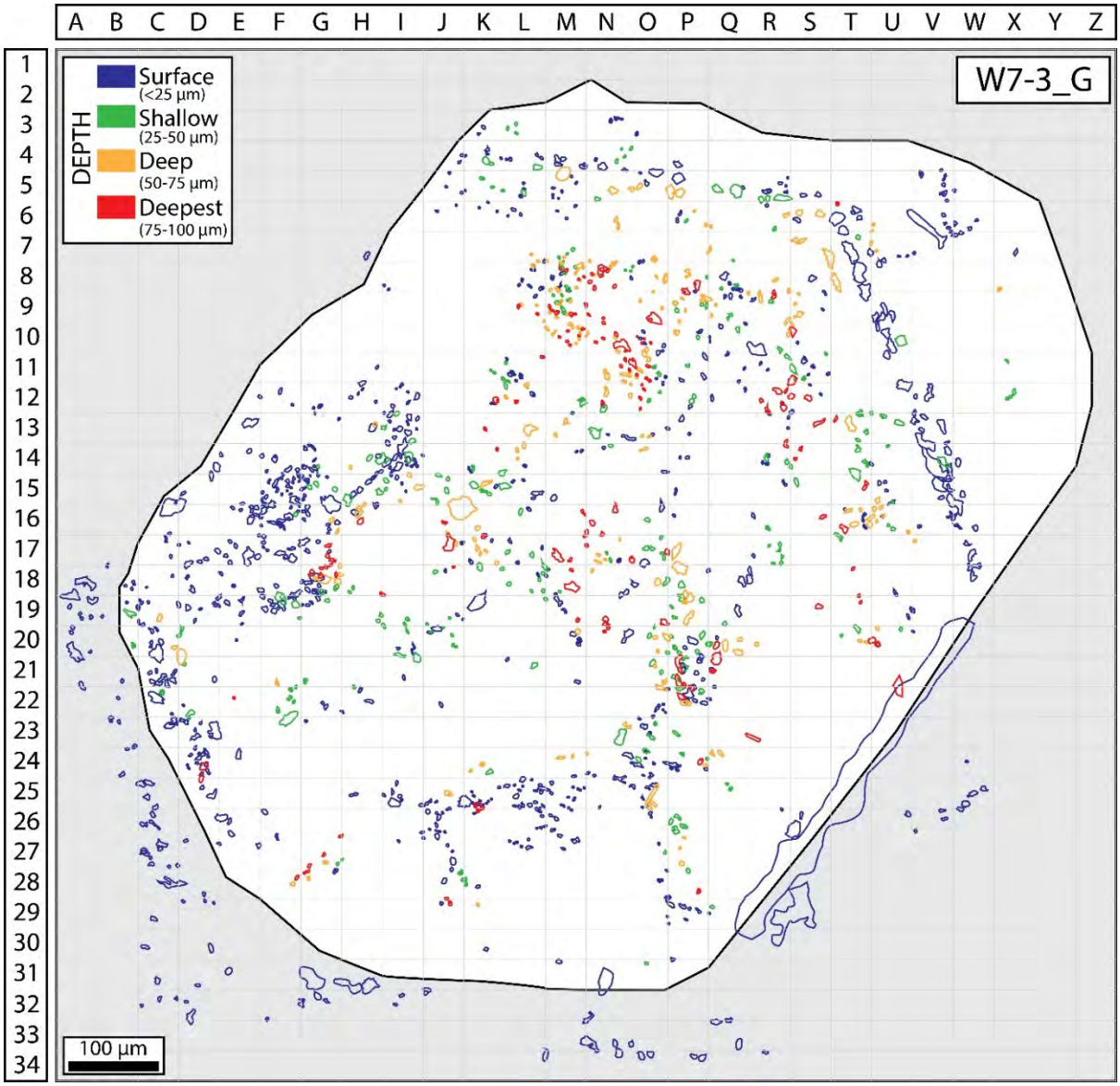

Fig. 16: Sample W7-3 (Wolverine deposit, mineralised), Grain G

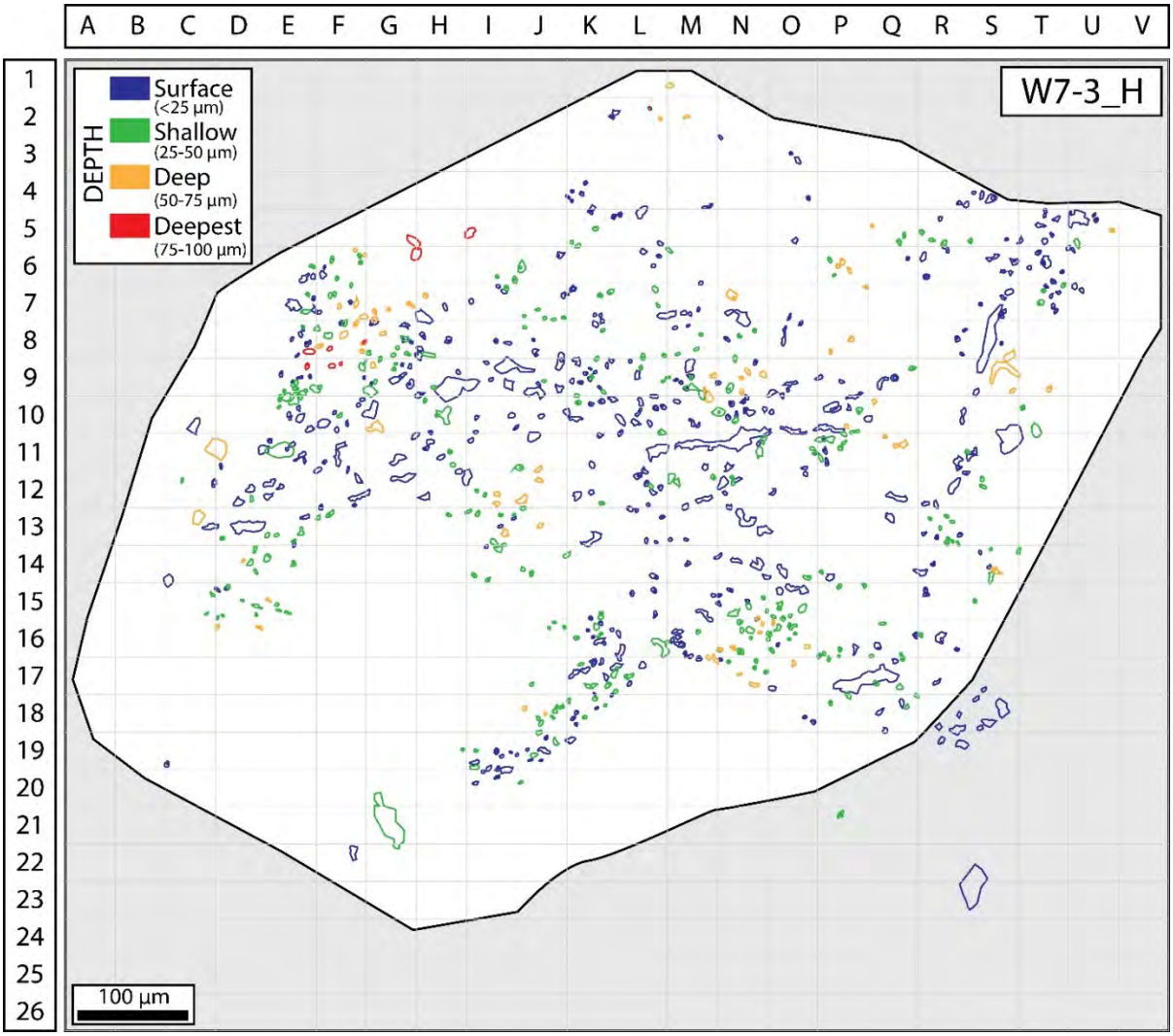

Fig. 17: Sample W7-3 (Wolverine deposit, mineralised), Grain H

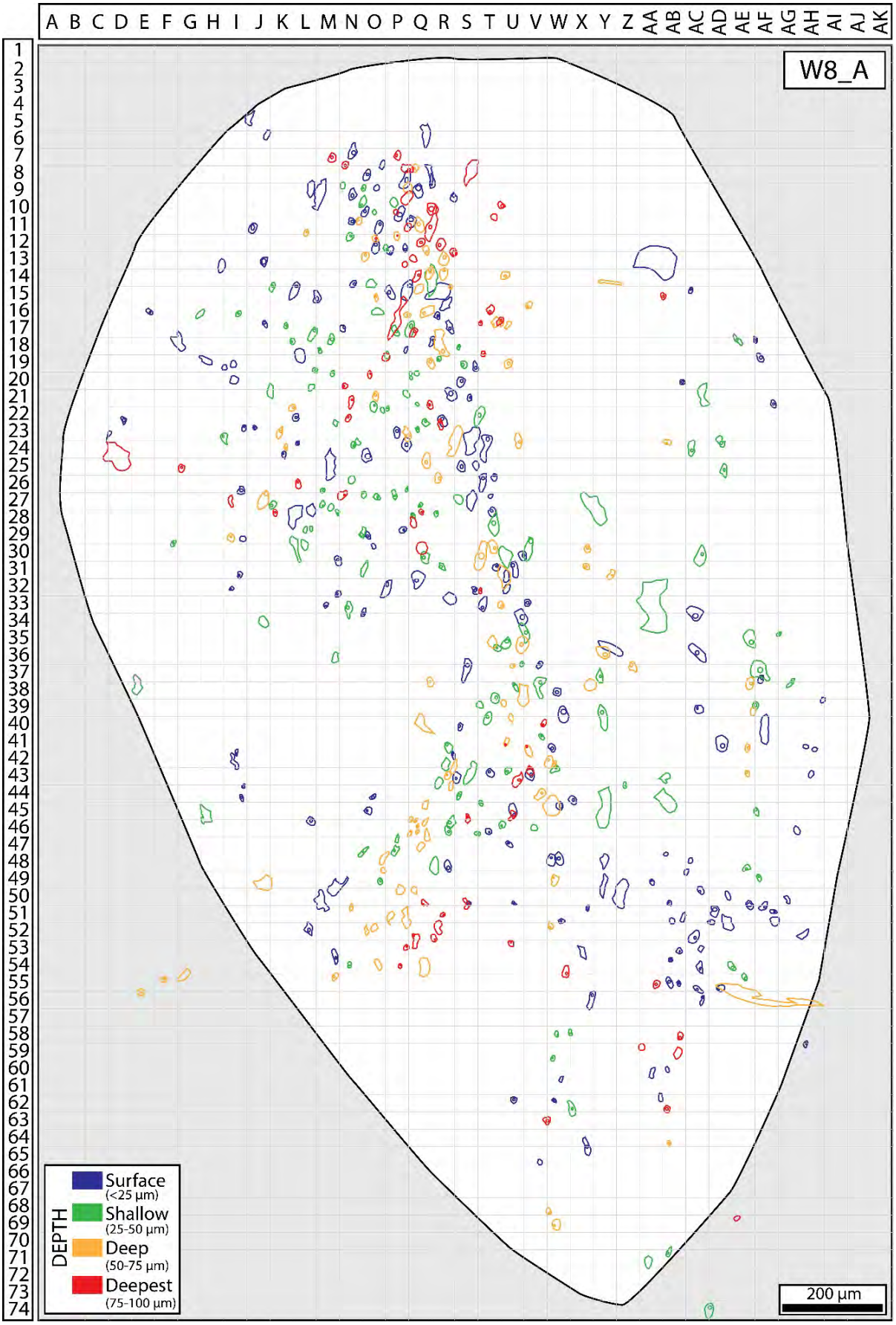

Fig. 18: Sample W8 (Wolverine deposit, non-mineralised), Grain A

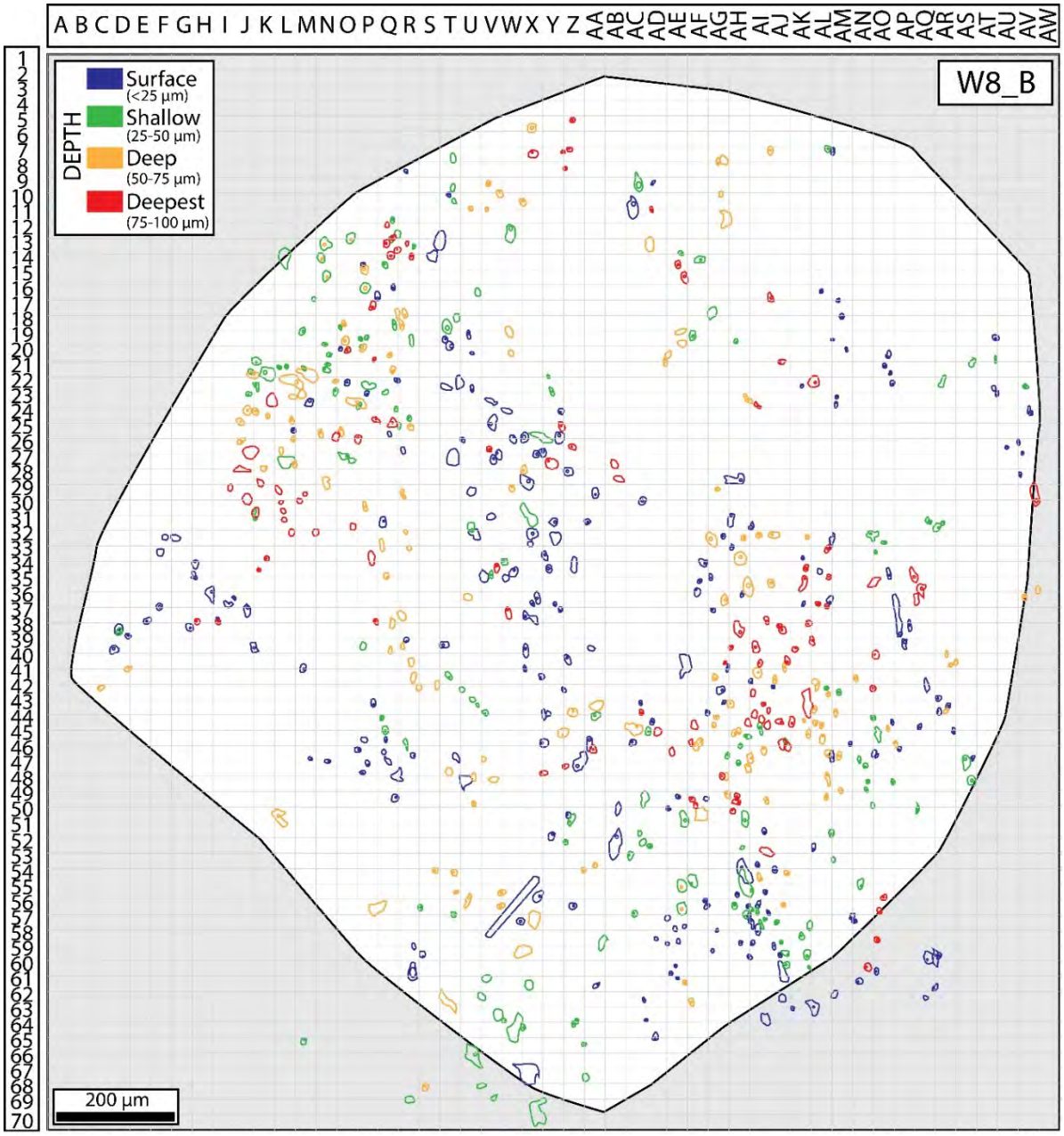

Fig. 19: Sample W8 (Wolverine deposit, non-mineralised), Grain B

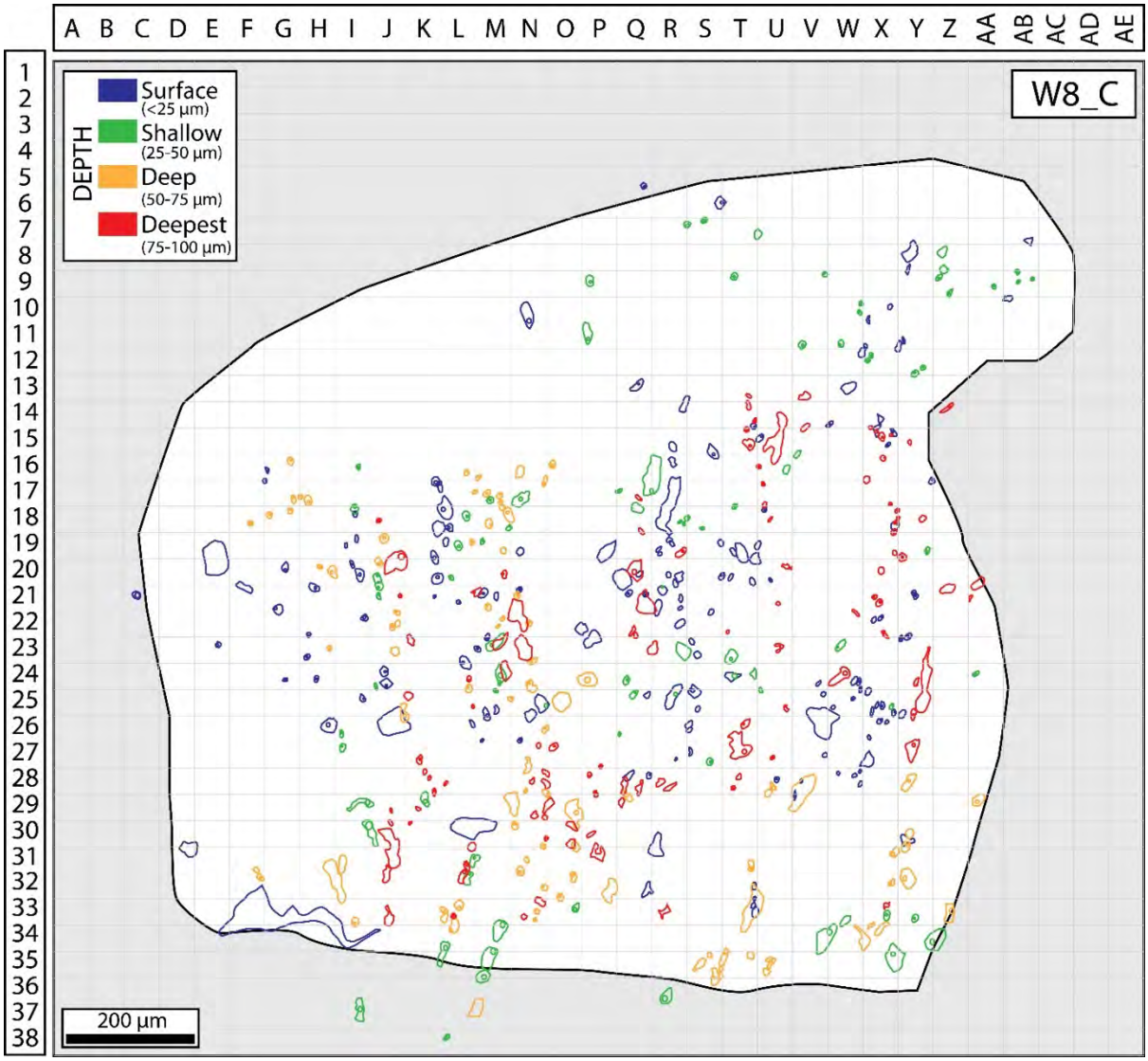

Fig. 20: Sample W8 (Wolverine deposit, non-mineralised), Grain C

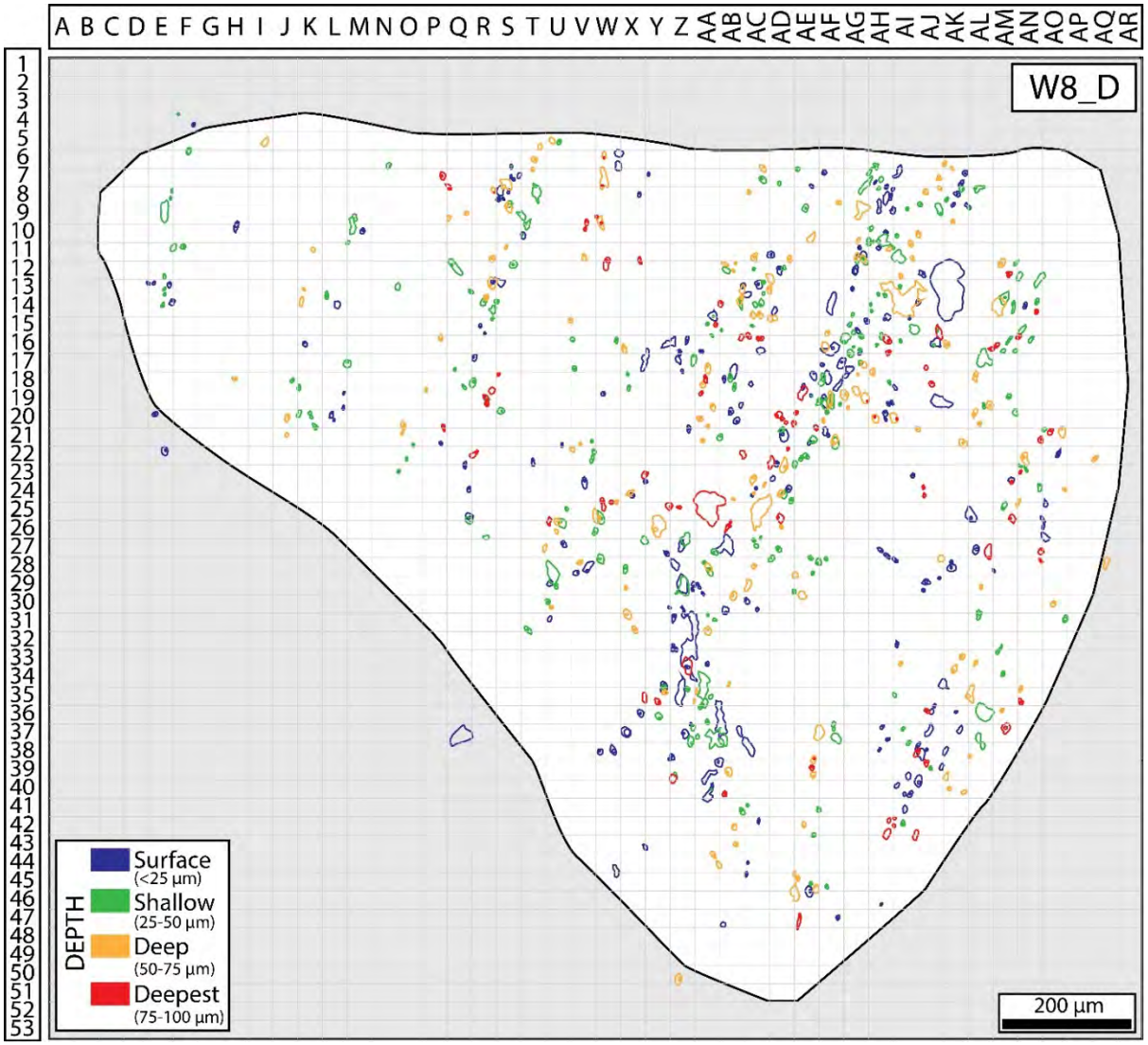

Fig. 21: Sample W8 (Wolverine deposit, non-mineralised), Grain D

Appendix 6-2: Composition of the standards for LA-ICP-MS analysis of fluid inclusions

Standard	Na (wt.%)	Si (wt.%)	P (wt.%)	Cl (wt.%)	K (wt.%)	Ca (wt.%)	Fe (wt.%)	Y (ppm)	Ce (ppm)	U (ppm)
T1G										
T1G-1	2.50	31.56	0.08	0.05	1.66	5.07	4.23	24.2	130.9	1.8
T1G-2	2.51	31.77	0.08	0.05	1.69	5.07	4.18	24.0	128.8	1.8
T1G-3	2.58	32.53	0.08	0.04	1.73	5.07	4.21	23.9	129.2	1.8
T1G-4	2.49	31.66	0.08	0.05	1.66	5.07	4.37	23.8	130.2	1.8
T1G-5	2.46	30.78	0.08	0.04	1.62	5.07	4.39	24.1	130.7	1.8
T1G-6	2.51	32.43	0.08	0.05	1.67	5.07	4.34	24.4	131.1	1.8
T1G-7	2.47	32.04	0.08	0.05	1.63	5.07	4.34	24.3	129.2	1.8
Average	2.50	31.83	0.08	0.05	1.66	5.07	4.29	24.1	130.0	1.8
SD	0.04	0.59	0.00	0.00	0.04	0.00	0.08	0.2	0.9	0.0
SD %	1.55	1.86	1.31	8.86	2.32	0.00	1.96	0.8	0.7	1.7
GSD										
GSD-1	2.86	28.42	0.10	0.05	2.55	5.15	8.26	8.26	41.0	41.6
GSD-2	2.84	28.46	0.10	0.05	2.56	5.15	8.27	8.27	40.5	41.5
GSD-3	2.85	27.96	0.09	0.05	2.54	5.15	8.23	8.23	40.8	41.7
GSD-4	2.83	28.32	0.10	0.05	2.49	5.15	8.62	8.62	40.9	41.9
GSD-5	2.88	28.62	0.10	0.04	2.54	5.15	8.62	8.62	41.0	41.8
GSD-6	2.81	29.33	0.10	0.05	2.46	5.15	8.64	8.64	41.6	41.9
GSD-7	2.74	28.36	0.10	0.05	2.40	5.15	8.45	8.45	41.5	41.7
Average	2.83	28.50	0.10	0.05	2.50	5.15	8.44	8.44	41.0	41.7
SD	0.05	0.42	0.00	0.00	0.06	0.00	0.19	0.19	0.4	0.2
SD %	1.65	1.47	1.48	7.52	2.40	0.00	2.23	2.23	0.9	0.4

Appendix 6-3: Microthermometry data of primary fluid inclusions in different quartz grains

Sample/Grain	Number of FI	Type	T_{mi}	T_m	T_h	Salinity (wt. %)
Sample W8						
Grain A	49	Type I	-7 – -17.7	-0.1 – -5.2	171.7 – 338.8	0.2 – 8.1
Grain B	50	Type I	-7.1 – -14.4	-0.1 – -5.5	170 – 340	0.2 – 8.5
Grain C	65	Type I	-7 – -13	-0.1 – -4.5	179.1 – 341.1	0.2 – 7.2
Grain D	62	Type I	-6 – -14	-0.1 – -3.8	170 – 350	0.2 – 6.2
Total	226	Type I	-6 – -17.7	-0.1 – -5.5	170 – 350	0.2 – 8.5
Sample A2-14						
Grain A	10	Type I	-9.7 – -15.5	-1.1 – -1.8	139.8 – 250	1.9 – 3.1
Grain A	2	Type II	-15 – -16	-9.8 – -10.1	155.6 – 166.5	13.7 – 14
Grain A	6	Type III	-33 – -50.3	-17.8 – -24.8	102.7 – 180	17.8 – 24.8
Grain B	23	Type I	-4.4 – -16.6	-0.1 — -4.6	99.1 – 269.5	0.2 – 7.3
Grain B	12	Type III	-23.3 – -51.1	-0.8 – -25.2	120.7 – 201.7	0.8 – 25.2
Grain C	15	Type I	-7 – -17.1	-0.1 – -6.5	128.6 – 243.9	0.2 – 9.9
Grain C	1	Type III	-37.7	-7.6	201	7.6
Grain D	3	Type I	-6.1 – -16	-0.1 – -6.5	123 – 236.6	0.2 – 9.9
Grain E	40	Type I	-5.2 – -17.7	-0.1 – -4.5	155.4 – 268.1	0.2 – 7.2
Grain E	1	Type II	-17	-12.1	198.1	16.1
Grain E	3	Type III	-24.4 – -49.1	-0.5 – -24.3	159.8 – 211.5	0.5 – 24.3
Grain G	12	Type I	-6 – -17	-0.1 – -6.1	119.9 – 220	0.2 – 9.3
Grain G	2	Type II	-16.6 – -16.7	-12.1 – -12.9	156.9 – 220.2	16.1 – 16.8
Grain G	13	Type III	-25.5 – -50.5	-3.5 – -24.6	115.1 – 241.2	3.5 – 24.6
Grain H	9	Type I	-7.7 – -19	-0.4 – -6.2	149.9 – 241.1	0.7 – 9.5
Grain H	3	Type II	-16	-14.4	213.3 – 200.1	18.1
Grain H	11	Type III	-22.9 – -51.3	-0.5 – -25.8	112.7 – 164.5	0.5 – 25.8
Grain I	22	Type I	-7 – -16.6	-0.1 – -3.6	140.5 – 272.3	0.2 – 5.9
Grain I	1	Type II	-21	-9.3	222.2	13.2
Grain I	3	Type III	-23.1 – -49.5	-0.6 – -24.6	143.2 – 207.7	0.6 – 24.6
Total	134	Type I	-4.4 – -17.1	-0.1 – -6.5	99.1 – 272.3	0.2 – 9.9
Total	9	Type II	-15 – -21	-9.3 – -12.9	155.6 – 222.2	13.2 – 18.1
Total	49	Type III	-22.9 – -51.3	-0.5 – -25.8	102.7 – 241.2	0.5 – 25.8
Sample W7-3						
Grain A	16	Type I	-6 – -16.7	-0.1 – -6.4	135 – 257	0.2 – 9.7
Grain A	6	Type III	-26.6 – -39.5	-2.1 – -15.1	132.5 – 210	2.1 – 15.1
Grain B	9	Type I	-8 – -17.7	-0.1 – -4.5	141.9 – 228.7	0.2 – 7.2
Grain B	2	Type III	-38.8 – -48.7	-19.4 – -21.4	116.7 – 174.5	19.4 – 21.4
Grain D	9	Type I	-7 – -11.1	-0.1 – -2.1	125.6 – 250.1	0.2 – 3.5
Grain D	1	Type II	-13	-8.8	200	12.6
Grain D	2	Type III	-33.3 – -37.2	-10.9 – -12.5	151.4 – 184.4	10.9 – 12.5
Grain E	6	Type I	-7 – -16.5	-0.1 – -3.5	120.9 – 224.7	0.2 – 5.7
Grain E	1	Type III	-31.1	-10.1	211.1	10.1
Grain F	17	Type I	-7 – -16	-0.1 – -6.2	131.9 – 241.7	0.2 – 9.5
Grain F	2	Type III	-29.5 – -48.8	-8.9 – -20.8	148.3 – 191.3	8.9 – 20.8
Grain G	7	Type I	-7 – -9	-0.1 – -0.5	167.6 – 220	0.2 – 0.9
Grain G	4	Type III	-23.3 – -27.6	-1.1 – -2.2	165 – 193.3	1.1 – 2.2
Grain H	34	Type I	-5 – -16.7	-0.1 – -4.5	121.9 – 255.5	0.2 – 7.2
Grain H	7	Type III	-28.5 – -47.6	-1.9 – -19.1	157.7 – 225.5	1.9 – 19.1
Total	98	Type I	-5 – -17.7	-0.1 – -6.4	120.9 – 257	0.2 – 9.7
Total	1	Type II	-13	-8.8	200	12.6
Total	24	Type III	-23.3 – -48.8	-1.1 – -21.4	116.7 – 22.5	1.1 – 21.4

*Type I: Low salinity H_2O-NaCl; Type II: medium salinity H_2O-NaCl; Type III: High salinity H_2O-$CaCl_2$-NaCl.

**Note that due to the lack of a next-to-last solid phase, accurate calculation of the salinity of the type III fluid inclusions was not possible. Instead, T_m was used as a rough estimation of the salinity.

Appendix 6-4: Fluid inclusion microthermometry dataset

Type	Composition	Deposit	Sample	Grain	FI No.	Bubble size	T_{mi}	T_m	T_h	Phases	Salinity	ρ (g/cm^3)
I	H_2O-NaCl	Wolverine	W8	A	AC34	S	-8	-0.1	217.7	L+V	0.2	0.84
I	H_2O-NaCl	Wolverine	W8	A	AC36	S	-8	-0.1	223.4	L+V	0.2	0.84
I	H_2O-NaCl	Wolverine	W8	A	AC39	S	-8	-0.1	205.5	L+V	0.2	0.86
I	H_2O-NaCl	Wolverine	W8	A	AD41	S	-7	-0.2	204.1	L+V	0.4	0.86
I	H_2O-NaCl	Wolverine	W8	A	AE35	S	-7	-0.5	210.3	L+V	0.9	0.86
I	H_2O-NaCl	Wolverine	W8	A	AF37	L	-10.5	-0.4	250.6	L+V	0.7	0.80
I	H_2O-NaCl	Wolverine	W8	A	AE39	S	-11.1	-0.7	238.1	L+V	1.2	0.82
I	H_2O-NaCl	Wolverine	W8	A	AF41	S	-10	-0.2	231.4	L+V	0.4	0.83
I	H_2O-NaCl	Wolverine	W8	A	AC30	S	-9	-0.1	202.7	L+V	0.2	0.86
I	H_2O-NaCl	Wolverine	W8	A	Y27	S	-10.5	-0.5	188.1	L+V	0.9	0.89
I	H_2O-NaCl	Wolverine	W8	A	AB24	S	-10.1	-0.7	210.3	L+V	1.2	0.86
I	H_2O-NaCl	Wolverine	W8	A	AC24	S	-10.1	-0.7	207.8	L+V	1.2	0.87
I	H_2O-NaCl	Wolverine	W8	A	AD24	S	-11	-0.9	190.3	L+V	1.6	0.89
I	H_2O-NaCl	Wolverine	W8	A	AD25	S	-11	-0.9	247.1	L+V	1.6	0.81
I	H_2O-NaCl	Wolverine	W8	A	AF19	S	-11	-0.3	283.5	L+V	0.5	0.74
I	H_2O-NaCl	Wolverine	W8	A	S20	S	-12	-0.8	282.7	L+V	1.4	0.75
I	H_2O-NaCl	Wolverine	W8	A	R21	S	-12	-0.8	290.1	L+V	1.4	0.74
I	H_2O-NaCl	Wolverine	W8	A	R22	S	-12	-1.1	200.4	L+V	1.9	0.88
I	H_2O-NaCl	Wolverine	W8	A	P23	S	-10	-0.7	216.2	L+V	1.2	0.85
I	H_2O-NaCl	Wolverine	W8	A	P24	S	-10	-0.7	236.6	L+V	1.2	0.83
I	H_2O-NaCl	Wolverine	W8	A	S25	S	-10	-0.9	301.1	L+V	1.6	0.72
I	H_2O-NaCl	Wolverine	W8	A	Q25	S	-16	-4.8	290.4	L+V	7.6	0.81
I	H_2O-NaCl	Wolverine	W8	A	R26	S	-16.1	-5.2	294.7	L+V	8.1	0.81
I	H_2O-NaCl	Wolverine	W8	A	U27	S	-9	-0.7	315.8	L+V	1.2	0.68
I	H_2O-NaCl	Wolverine	W8	A	M25	S	-14.4	-2.3	201.1	L+V	3.9	0.89
I	H_2O-NaCl	Wolverine	W8	A	O27	S	-12	-1.8	217.6	L+V	3.1	0.87
I	H_2O-NaCl	Wolverine	W8	A	M30	S	-12.5	-2.5	290.3	L+V	4.2	0.77
I	H_2O-NaCl	Wolverine	W8	A	Q30	S	-12.5	-2.8	290.7	L+V	4.6	0.77
I	H_2O-NaCl	Wolverine	W8	A	Q32	S	-12.5	-2.8	198.5	L+V	4.6	0.90
I	H_2O-NaCl	Wolverine	W8	A	R31	S	-14	-3.4	240.9	L+V	5.6	0.86
I	H_2O-NaCl	Wolverine	W8	A	N7	S	-10.1	-1.1	171.7	L+V	1.9	0.91
I	H_2O-NaCl	Wolverine	W8	A	O8	S	-10.1	-1.1	184.3	L+V	1.9	0.90
I	H_2O-NaCl	Wolverine	W8	A	O11	S	-7	-0.5	178	L+V	0.9	0.90
I	H_2O-NaCl	Wolverine	W8	A	O12	S	-7	-0.5	233.7	L+V	0.9	0.83
I	H_2O-NaCl	Wolverine	W8	A	P8	L	-7	-0.8	330.1	L+V	1.4	0.66
I	H_2O-NaCl	Wolverine	W8	A	Q9	L	-7	-0.8	325.2	L+V	1.4	0.67
I	H_2O-NaCl	Wolverine	W8	A	R10	S	-12.9	-2.9	338.8	L+V	4.8	0.69
I	H_2O-NaCl	Wolverine	W8	A	Q11	S	-12.9	-2.9	190.5	L+V	4.8	0.91
I	H_2O-NaCl	Wolverine	W8	A	R12	S	-17.7	-3.6	258.1	L+V	5.9	0.84
I	H_2O-NaCl	Wolverine	W8	A	R18	S	-15	-2.7	298.2	L+V	4.5	0.76
I	H_2O-NaCl	Wolverine	W8	A	R19	S	-15	-3.1	288.8	L+V	5.1	0.78
I	H_2O-NaCl	Wolverine	W8	A	Y36	S	-9	-0.7	217	L+V	1.2	0.85
I	H_2O-NaCl	Wolverine	W8	A	W38	S	-11.1	-1.2	221.5	L+V	2.1	0.85
I	H_2O-NaCl	Wolverine	W8	A	W39	S	-11.1	-1.3	203.7	L+V	2.2	0.88
I	H_2O-NaCl	Wolverine	W8	A	W41	S	-10	-0.7	257.7	L+V	1.2	0.79
I	H_2O-NaCl	Wolverine	W8	A	V43	S	-10	-0.9	248.2	L+V	1.6	0.81
I	H_2O-NaCl	Wolverine	W8	A	W45	S	-11	-1.3	205.8	L+V	2.2	0.88
I	H_2O-NaCl	Wolverine	W8	A	X44	S	-10	-0.3	214.3	L+V	0.5	0.85
I	H_2O-NaCl	Wolverine	W8	A	W48_1	S	-9	-0.1	189.1	L+V	0.2	0.88
I	H_2O-NaCl	Wolverine	W8	B	AA45	S	-9	-1.1	280.1	L+V	1.9	0.76
I	H_2O-NaCl	Wolverine	W8	B	X45	S	-11	-1.2	277	L+V	2.1	0.77
I	H_2O-NaCl	Wolverine	W8	B	AD44	S	-11.5	-1.6	260.4	L+V	2.7	0.80
I	H_2O-NaCl	Wolverine	W8	B	H36	S	-9.5	-0.3	180.9	L+V	0.5	0.89
I	H_2O-NaCl	Wolverine	W8	B	G38	S	-9.5	-0.7	235.4	L+V	1.2	0.83
I	H_2O-NaCl	Wolverine	W8	B	F36	L	-8	-0.1	201.1	L+V	0.2	0.87
I	H_2O-NaCl	Wolverine	W8	B	E37	S	-8	-0.5	205.5	L+V	0.9	0.87
I	H_2O-NaCl	Wolverine	W8	B	J37	S	-8.5	-0.1	230.1	L+V	0.2	0.83
I	H_2O-NaCl	Wolverine	W8	B	J39	S	-8.5	-0.9	200.7	L+V	1.6	0.88
I	H_2O-NaCl	Wolverine	W8	B	M41	S	-8.5	-0.8	209.1	L+V	1.4	0.87
I	H_2O-NaCl	Wolverine	W8	B	F32	S	-7.1	-0.3	195.3	L+V	0.5	0.88
I	H_2O-NaCl	Wolverine	W8	B	F33	S	-7.1	-0.3	188.7	L+V	0.5	0.88
I	H_2O-NaCl	Wolverine	W8	B	G32	S	-7.1	-0.3	190.8	L+V	0.5	0.88
I	H_2O-NaCl	Wolverine	W8	B	D38	S	-7.1	-0.6	210.7	L+V	1.1	0.86
I	H_2O-NaCl	Wolverine	W8	B	D39	S	-7.1	-0.6	207.3	L+V	1.1	0.87
I	H_2O-NaCl	Wolverine	W8	B	D40	S	-7.1	-0.9	193.3	L+V	1.6	0.89
I	H_2O-NaCl	Wolverine	W8	B	E41	S	-7.1	-0.9	190.1	L+V	1.6	0.89
I	H_2O-NaCl	Wolverine	W8	B	Y25_1	S	-14.4	-3.5	209.5	L+V	5.7	0.90
I	H_2O-NaCl	Wolverine	W8	B	Z26	S	-14.4	-4.9	244.7	L+V	7.7	0.87
I	H_2O-NaCl	Wolverine	W8	B	Y27	L	-14	-5.1	322.2	L+V	8.0	0.76
I	H_2O-NaCl	Wolverine	W8	B	V26	S	-14	-3.5	214.4	L+V	5.7	0.89
I	H_2O-NaCl	Wolverine	W8	B	Y24	S	-13	-5.5	280.9	L+V	8.5	0.83
I	H_2O-NaCl	Wolverine	W8	B	X25	S	-13	-4.5	254.7	L+V	7.2	0.85
I	H_2O-NaCl	Wolverine	W8	B	W29	S	-13.5	-4.3	290.3	L+V	6.9	0.80
I	H_2O-NaCl	Wolverine	W8	B	V31	S	-14	-5.2	250.9	L+V	8.1	0.87
I	H_2O-NaCl	Wolverine	W8	B	AA29	S	-13	-3.5	220.1	L+V	5.7	0.89

(Continued)

Type	Composition	Deposit	Sample	Grain	FI No.	Bubble size	T_{mi}	T_m	T_h	Phases	Salinity	ρ (g/cm^3)
I	H_2O-NaCl	Wolverine	W8	B	AA31	S	-13.5	-3.5	200.7	L+V	5.7	0.91
I	H_2O-NaCl	Wolverine	W8	B	AC30	S	-13	-3.8	214.8	L+V	6.2	0.90
I	H_2O-NaCl	Wolverine	W8	B	U32	S	-13	-2.2	270.8	L+V	3.7	0.80
I	H_2O-NaCl	Wolverine	W8	B	V35	S	-13	-2.8	330.1	L+V	4.6	0.70
I	H_2O-NaCl	Wolverine	W8	B	U29	S	-10	-1.6	291.3	L+V	2.7	0.75
I	H_2O-NaCl	Wolverine	W8	B	W34	S	-10.5	-1.8	170	L+V	3.1	0.92
I	H_2O-NaCl	Wolverine	W8	B	Y37	S	-10.5	-1.6	247.3	L+V	2.7	0.82
I	H_2O-NaCl	Wolverine	W8	B	Y36	S	-11	-1.7	240.1	L+V	2.9	0.84
I	H_2O-NaCl	Wolverine	W8	B	Y35	S	-11.3	-1.8	239.3	L+V	3.1	0.84
I	H_2O-NaCl	Wolverine	W8	B	Y34	S	-11.3	-1.9	240.1	L+V	3.2	0.84
I	H_2O-NaCl	Wolverine	W8	B	Y31	S	-11.4	-2.1	237.3	L+V	3.5	0.85
I	H_2O-NaCl	Wolverine	W8	B	AE40	S	-10.5	-1.4	240.1	L+V	2.4	0.83
I	H_2O-NaCl	Wolverine	W8	B	AF44	S	-10.2	-1.2	241	L+V	2.1	0.83
I	H_2O-NaCl	Wolverine	W8	B	AH31	S	-12.2	-1.8	197	L+V	3.1	0.89
I	H_2O-NaCl	Wolverine	W8	B	AI31	S	-12	-1.8	198.8	L+V	3.1	0.89
I	H_2O-NaCl	Wolverine	W8	B	AG32	S	-11.1	-1.3	217.7	L+V	2.2	0.86
I	H_2O-NaCl	Wolverine	W8	B	AL32	S	-10.1	-1.9	241.3	L+V	3.2	0.84
I	H_2O-NaCl	Wolverine	W8	B	AH35	L	-10	-1.1	259.9	L+V	1.9	0.80
I	H_2O-NaCl	Wolverine	W8	B	AG36	S	-10.2	-1.2	240.3	L+V	2.1	0.83
I	H_2O-NaCl	Wolverine	W8	B	AH38	S	-10	-1.5	248.1	L+V	2.6	0.82
I	H_2O-NaCl	Wolverine	W8	B	AJ35	S	-11	-0.9	237.7	L+V	1.6	0.83
I	H_2O-NaCl	Wolverine	W8	B	AK34	S	-12	-1.4	220.5	L+V	2.4	0.86
I	H_2O-NaCl	Wolverine	W8	B	AK35	S	-9	-0.8	231.1	L+V	1.4	0.84
I	H_2O-NaCl	Wolverine	W8	B	L14	L	-10	-2.1	340	L+V	3.5	0.67
I	H_2O-NaCl	Wolverine	W8	C	N10	S	-10.5	-1.5	187.7	L+V	2.6	0.90
I	H_2O-NaCl	Wolverine	W8	C	N8	S	-10.5	-2.2	205.7	L+V	3.7	0.89
I	H_2O-NaCl	Wolverine	W8	C	K13	S	-11	-1.5	198.7	L+V	2.6	0.89
I	H_2O-NaCl	Wolverine	W8	C	K14	S	-11.3	-1.8	182.2	L+V	3.1	0.91
I	H_2O-NaCl	Wolverine	W8	C	K15	S	-13	-3.4	179.1	L+V	5.6	0.93
I	H_2O-NaCl	Wolverine	W8	C	J11	S	-11.4	-1.2	201.3	L+V	2.1	0.88
I	H_2O-NaCl	Wolverine	W8	C	M11	S	-10.5	-0.7	199.3	L+V	1.2	0.88
I	H_2O-NaCl	Wolverine	W8	C	M8_1	S	-12	-2.5	210.3	L+V	4.2	0.89
I	H_2O-NaCl	Wolverine	W8	C	M8_2	S	-12	-2.5	200.3	L+V	4.2	0.90
I	H_2O-NaCl	Wolverine	W8	C	N9	S	-12	-2.8	191.1	L+V	4.6	0.91
I	H_2O-NaCl	Wolverine	W8	C	M7	S	-13	-4.5	183.2	L+V	7.2	0.94
I	H_2O-NaCl	Wolverine	W8	C	N5_1	S	-10.1	-2.2	202.2	L+V	3.7	0.89
I	H_2O-NaCl	Wolverine	W8	C	N5_2	S	-10	-2.5	203.8	L+V	4.2	0.89
I	H_2O-NaCl	Wolverine	W8	C	M6	S	-13	-3.1	180.3	L+V	5.1	0.93
I	H_2O-NaCl	Wolverine	W8	C	L7_1	S	-13	-3.3	179.7	L+V	5.4	0.93
I	H_2O-NaCl	Wolverine	W8	C	L7_2	S	-11	-2.3	181.1	L+V	3.9	0.92
I	H_2O-NaCl	Wolverine	W8	C	L6	L	-12	-0.3	311.5	L+V	0.5	0.68
I	H_2O-NaCl	Wolverine	W8	C	AA10	S	-9	-0.7	187.7	L+V	1.2	0.89
I	H_2O-NaCl	Wolverine	W8	C	AA9	S	-10	-0.9	201.3	L+V	1.6	0.88
I	H_2O-NaCl	Wolverine	W8	C	Z11	S	-7	-0.5	180	L+V	0.9	0.90
I	H_2O-NaCl	Wolverine	W8	C	Z7	L	-7	-0.4	193.3	L+V	0.7	0.88
I	H_2O-NaCl	Wolverine	W8	C	Z8	S	-8	-0.4	194.4	L+V	0.7	0.88
I	H_2O-NaCl	Wolverine	W8	C	Z9	S	-10.2	-0.2	201	L+V	0.4	0.87
I	H_2O-NaCl	Wolverine	W8	C	X5	L	-12	-2.6	341.1	L+V	4.3	0.68
I	H_2O-NaCl	Wolverine	W8	C	V3	S	-9	-0.3	191.1	L+V	0.5	0.88
I	H_2O-NaCl	Wolverine	W8	C	V5	S	-9	-0.3	180.6	L+V	0.5	0.89
I	H_2O-NaCl	Wolverine	W8	C	W6	S	-9	-1.3	186.6	L+V	2.2	0.90
I	H_2O-NaCl	Wolverine	W8	C	W7	S	-10	-1.3	213.9	L+V	2.2	0.87
I	H_2O-NaCl	Wolverine	W8	C	S6	S	-10.5	-1.5	190.9	L+V	2.6	0.90
I	H_2O-NaCl	Wolverine	W8	C	R6	S	-10.5	-1.5	199.6	L+V	2.6	0.89
I	H_2O-NaCl	Wolverine	W8	C	T9	S	-11	-1.1	188.7	L+V	1.9	0.89
I	H_2O-NaCl	Wolverine	W8	C	V9	S	-11.3	-1.1	207	L+V	1.9	0.87
I	H_2O-NaCl	Wolverine	W8	C	V11	S	-9	-1.7	225.5	L+V	2.9	0.86
I	H_2O-NaCl	Wolverine	W8	C	W11	S	-9	-1.7	218.8	L+V	2.9	0.86
I	H_2O-NaCl	Wolverine	W8	C	T14	S	-9	-1.5	231.3	L+V	2.6	0.84
I	H_2O-NaCl	Wolverine	W8	C	R16	L	-13	-2.1	300.7	L+V	3.5	0.74
I	H_2O-NaCl	Wolverine	W8	C	T20_1	S	-13	-2.4	273.3	L+V	4.0	0.80
I	H_2O-NaCl	Wolverine	W8	C	S19	S	-10.5	-1.4	187.7	L+V	2.4	0.90
I	H_2O-NaCl	Wolverine	W8	C	S20	S	-11	-1.4	182	L+V	2.4	0.91
I	H_2O-NaCl	Wolverine	W8	C	R23	S	-11.3	-0.5	221.4	L+V	0.9	0.84
I	H_2O-NaCl	Wolverine	W8	C	S23	S	-9	-0.4	253.4	L+V	0.7	0.79
I	H_2O-NaCl	Wolverine	W8	C	S24	S	-9	-0.4	248.7	L+V	0.7	0.80
I	H_2O-NaCl	Wolverine	W8	C	T23	S	-11	-2.2	196.6	L+V	3.7	0.90
I	H_2O-NaCl	Wolverine	W8	C	Y32	S	-10	-0.1	310	L+V	0.2	0.68
I	H_2O-NaCl	Wolverine	W8	C	X31	S	-10.5	-0.1	234.1	L+V	0.2	0.82
I	H_2O-NaCl	Wolverine	W8	C	Q24	S	-10.5	-0.8	312	L+V	1.4	0.69
I	H_2O-NaCl	Wolverine	W8	C	Q25	S	-11	-0.8	315	L+V	1.4	0.69
I	H_2O-NaCl	Wolverine	W8	C	P24	S	-11.3	-0.6	190	L+V	1.1	0.89
I	H_2O-NaCl	Wolverine	W8	C	N26	S	-9	-0.7	328.8	L+V	1.2	0.66
I	H_2O-NaCl	Wolverine	W8	C	L23	S	-9	-0.1	302.9	L+V	0.2	0.70
I	H_2O-NaCl	Wolverine	W8	C	L26	S	-9	-0.1	246	L+V	0.2	0.80

(Continued)

Type	Composition	Deposit	Sample	Grain	FI No.	Bubble size	T_{mi}	T_m	T_h	Phases	Salinity	ρ (g/cm^3)
I	H_2O-NaCl	Wolverine	W8	C	M26	S	-13	-0.1	198.7	L+V	0.2	0.87
I	H_2O-NaCl	Wolverine	W8	C	H26	S	-13	-1.7	196.2	L+V	2.9	0.89
I	H_2O-NaCl	Wolverine	W8	C	L18_1	S	-10	-1.3	341	L+V	2.2	0.65
I	H_2O-NaCl	Wolverine	W8	C	L18_2	S	-12	-1.3	325	L+V	2.2	0.68
I	H_2O-NaCl	Wolverine	W8	C	K19	S	-10	-0.2	185.5	L+V	0.4	0.89
I	H_2O-NaCl	Wolverine	W8	C	K20	S	-8	-0.2	181	L+V	0.4	0.89
I	H_2O-NaCl	Wolverine	W8	C	M21	S	-8	-0.5	275	L+V	0.9	0.76
I	H_2O-NaCl	Wolverine	W8	C	L16	S	-7	-0.1	192.9	L+V	0.2	0.88
I	H_2O-NaCl	Wolverine	W8	C	J20_1	S	-10	-1.3	180	L+V	2.2	0.91
I	H_2O-NaCl	Wolverine	W8	C	J20_2	S	-10.5	-2.5	246.6	L+V	4.2	0.84
I	H_2O-NaCl	Wolverine	W8	C	I20	S	-10.5	-2.6	195.3	L+V	4.3	0.90
I	H_2O-NaCl	Wolverine	W8	C	G20	S	-11	-2.6	196.1	L+V	4.3	0.90
I	H_2O-NaCl	Wolverine	W8	C	K29	S	-11.3	-1.5	230.7	L+V	2.6	0.85
I	H_2O-NaCl	Wolverine	W8	C	F12	S	-8	-0.1	194.4	L+V	0.2	0.88
I	H_2O-NaCl	Wolverine	W8	D	O13	S	-12	-2.1	202.7	L+V	3.5	0.89
I	H_2O-NaCl	Wolverine	W8	D	Q12	S	-14	-3.8	187.3	L+V	6.2	0.93
I	H_2O-NaCl	Wolverine	W8	D	R14_1	S	-7	-0.2	198	L+V	0.4	0.87
I	H_2O-NaCl	Wolverine	W8	D	R14_2	S	-7	-0.2	194.4	L+V	0.4	0.88
I	H_2O-NaCl	Wolverine	W8	D	S12	S	-6.5	-0.2	201.3	L+V	0.4	0.87
I	H_2O-NaCl	Wolverine	W8	D	P16	S	-6.5	-0.3	177.7	L+V	0.5	0.90
I	H_2O-NaCl	Wolverine	W8	D	S20	S	-6	-0.5	205.5	L+V	0.9	0.87
I	H_2O-NaCl	Wolverine	W8	D	O20	S	-10	-0.4	210.7	L+V	0.7	0.86
I	H_2O-NaCl	Wolverine	W8	D	J20	S	-10	-0.3	213.4	L+V	0.5	0.85
I	H_2O-NaCl	Wolverine	W8	D	R13_1	L	-10.5	-0.3	184	L+V	0.5	0.89
I	H_2O-NaCl	Wolverine	W8	D	R13_2	S	-10.5	-0.2	181	L+V	0.4	0.89
I	H_2O-NaCl	Wolverine	W8	D	R14_1	S	-11	-0.2	198	L+V	0.4	0.87
I	H_2O-NaCl	Wolverine	W8	D	R14_2	S	-11.8	-0.2	194.4	L+V	0.4	0.88
I	H_2O-NaCl	Wolverine	W8	D	P7	S	-9	-0.7	227.3	L+V	1.2	0.84
I	H_2O-NaCl	Wolverine	W8	D	Q8	S	-9	-0.7	218.3	L+V	1.2	0.85
I	H_2O-NaCl	Wolverine	W8	D	S7	L	-9	-2.3	240.4	L+V	3.9	0.84
I	H_2O-NaCl	Wolverine	W8	D	T10	L	-12	-0.8	197.7	L+V	1.4	0.88
I	H_2O-NaCl	Wolverine	W8	D	W9	S	-12.5	-0.7	210.2	L+V	1.2	0.86
I	H_2O-NaCl	Wolverine	W8	D	W12	S	-10	-1.1	225.5	L+V	1.9	0.85
I	H_2O-NaCl	Wolverine	W8	D	X12	S	-12	-0.9	183.7	L+V	1.6	0.90
I	H_2O-NaCl	Wolverine	W8	D	U27	S	-10	-0.9	203	L+V	1.6	0.87
I	H_2O-NaCl	Wolverine	W8	D	U28	S	-10.1	-1.8	250	L+V	3.1	0.82
I	H_2O-NaCl	Wolverine	W8	D	U29_1	S	-10.7	-1.1	244.1	L+V	1.9	0.82
I	H_2O-NaCl	Wolverine	W8	D	U29_2	S	-7	-1.1	210.7	L+V	1.9	0.87
I	H_2O-NaCl	Wolverine	W8	D	X28	S	-7	-0.8	198	L+V	1.4	0.88
I	H_2O-NaCl	Wolverine	W8	D	X29	S	-6.3	-0.8	201.1	L+V	1.4	0.88
I	H_2O-NaCl	Wolverine	W8	D	Q23	S	-6.3	-0.4	214.3	L+V	0.7	0.85
I	H_2O-NaCl	Wolverine	W8	D	Q24	S	-6	-0.4	219.9	L+V	0.7	0.85
I	H_2O-NaCl	Wolverine	W8	D	Q25	S	-10	-0.4	210.7	L+V	0.7	0.86
I	H_2O-NaCl	Wolverine	W8	D	T22	S	-10	-0.8	198	L+V	1.4	0.88
I	H_2O-NaCl	Wolverine	W8	D	V23	S	-9	-0.8	235.5	L+V	1.4	0.83
I	H_2O-NaCl	Wolverine	W8	D	AF38	L	-9	-1.4	350	L+V	2.4	0.63
I	H_2O-NaCl	Wolverine	W8	D	AK40	S	-13.1	-2.4	285.1	L+V	4.0	0.78
I	H_2O-NaCl	Wolverine	W8	D	AJ40	L	-13.2	-3.4	312	L+V	5.6	0.75
I	H_2O-NaCl	Wolverine	W8	D	AL27_2	S	-9	-1.2	267.2	L+V	2.1	0.79
I	H_2O-NaCl	Wolverine	W8	D	AK28	S	-11	-2.8	235.1	L+V	4.6	0.86
I	H_2O-NaCl	Wolverine	W8	D	AJ29_1	L	-13	-1.3	207.7	L+V	2.2	0.87
I	H_2O-NaCl	Wolverine	W8	D	AJ29_2	S	-12	-1.3	217.3	L+V	2.2	0.86
I	H_2O-NaCl	Wolverine	W8	D	AO21	S	-12.9	-1.9	340	L+V	3.2	0.66
I	H_2O-NaCl	Wolverine	W8	D	AP20	S	-6	-0.1	196.6	L+V	0.2	0.87
I	H_2O-NaCl	Wolverine	W8	D	AN21	S	-8.5	-0.4	176.8	L+V	0.7	0.90
I	H_2O-NaCl	Wolverine	W8	D	AN22	L	-10	-3.8	340	L+V	6.2	0.71
I	H_2O-NaCl	Wolverine	W8	D	AM12	L	-10.1	-1.1	188.8	L+V	1.9	0.89
I	H_2O-NaCl	Wolverine	W8	D	AI14	S	-10	-0.7	340	L+V	1.2	0.63
I	H_2O-NaCl	Wolverine	W8	D	AI15	L	-14	-1.3	277	L+V	2.2	0.77
I	H_2O-NaCl	Wolverine	W8	D	AJ16	L	-12	-2.3	311.3	L+V	3.9	0.73
I	H_2O-NaCl	Wolverine	W8	D	AG15	S	-9	-1.7	340	L+V	2.9	0.66
I	H_2O-NaCl	Wolverine	W8	D	AH16_2	S	-9	-1.3	193	L+V	2.2	0.89
I	H_2O-NaCl	Wolverine	W8	D	AG19_1	S	-13.1	-1.4	350	L+V	2.4	0.63
I	H_2O-NaCl	Wolverine	W8	D	AH20	S	-13	-1.1	210.2	L+V	1.9	0.87
I	H_2O-NaCl	Wolverine	W8	D	AI20	S	-9	-1.1	205.5	L+V	1.9	0.87
I	H_2O-NaCl	Wolverine	W8	D	AD20	S	-11	-1.8	225.6	L+V	3.1	0.86
I	H_2O-NaCl	Wolverine	W8	D	AF21	S	-13	-1.8	178.9	L+V	3.1	0.91
I	H_2O-NaCl	Wolverine	W8	D	AD29	S	-12	-0.2	170	L+V	0.4	0.90
I	H_2O-NaCl	Wolverine	W8	D	AA17	S	-11.1	-1.6	277.4	L+V	2.7	0.78
I	H_2O-NaCl	Wolverine	W8	D	AA19_1	S	-8	-0.7	281.1	L+V	1.2	0.75
I	H_2O-NaCl	Wolverine	W8	D	AA19_2	S	-8.5	-1.5	248	L+V	2.6	0.82
I	H_2O-NaCl	Wolverine	W8	D	Z17	S	-11	-1.6	267.7	L+V	2.7	0.79
I	H_2O-NaCl	Wolverine	W8	D	AB20_1	S	-10.1	-1.5	281	L+V	2.6	0.77
I	H_2O-NaCl	Wolverine	W8	D	AB20_2	S	-10	-1.5	278	L+V	2.6	0.77
I	H_2O-NaCl	Wolverine	W8	D	AB21	S	-12	-1.5	265	L+V	2.6	0.79
I	H_2O-NaCl	Wolverine	W8	D	Z21_2	S	-13	-0.8	335	L+V	1.4	0.65

(Continued)

Type	Composition	Deposit	Sample	Grain	FI No.	Bubble size	T_{mi}	T_m	T_h	Phases	Salinity	ρ (g/cm^3)
I	H_2O-NaCl	Area 5	A2-14	A	Q18	S	-10	-1.8	219.1	L+V	3.1	0.87
I	H_2O-NaCl	Area 5	A2-14	A	Q17	S	-11.7	-1.5	210.3	L+V	2.6	0.87
I	H_2O-NaCl	Area 5	A2-14	A	P17	S	-14.7	-1.3	199.7	L+V	2.2	0.88
I	H_2O-NaCl	Area 5	A2-14	A	R19	S	-15	-1.6	250	L+V	2.7	0.82
I	H_2O-NaCl	Area 5	A2-14	A	S19	S	-11.3	-1.3	219.1	L+V	2.2	0.86
I	H_2O-NaCl	Area 5	A2-14	A	R14	S	-9.7	-1.1	169.3	L+V	1.9	0.92
I	H_2O-NaCl	Area 5	A2-14	A	U15_1	S	-14.4	-1.6	174.1	L+V	2.7	0.92
I	H_2O-NaCl	Area 5	A2-14	A	V16	S	-15.5	-1.6	190.5	L+V	2.7	0.90
I	H_2O-NaCl	Area 5	A2-14	A	K32	S	-9.9	-1.3	139.8	L+V	2.2	0.95
I	H_2O-NaCl	Area 5	A2-14	A	M17	S	-10.1	-1.2	205.3	L+V	2.1	0.88
I	H_2O-NaCl	Area 5	A2-14	B	X14	L	-16.6	-2.4	230	L+V	4.0	0.86
I	H_2O-NaCl	Area 5	A2-14	B	W12	S	-16.6	-2.4	192.1	L+V	4.0	0.91
I	H_2O-NaCl	Area 5	A2-14	B	W11	S	-14.5	-1.5	164.5	L+V	2.6	0.92
I	H_2O-NaCl	Area 5	A2-14	B	U10	S	-14.4	-1.5	146.6	L+V	2.6	0.94
I	H_2O-NaCl	Area 5	A2-14	B	V11	S	-14.7	-1.5	115.5	L+V	2.6	0.97
I	H_2O-NaCl	Area 5	A2-14	B	Y13	S	-14.4	-2.8	250	L+V	4.6	0.84
I	H_2O-NaCl	Area 5	A2-14	B	AF11	L	-7.1	-0.3	205	L+V	0.5	0.86
I	H_2O-NaCl	Area 5	A2-14	B	W7_1	L	-9.3	-1.6	242.4	L+V	2.7	0.83
I	H_2O-NaCl	Area 5	A2-14	B	W7_2	S	-5.5	-0.3	99.1	L+V	0.5	0.97
I	H_2O-NaCl	Area 5	A2-14	B	Z10_2	S	-5.2	-0.3	128.3	L+V	0.5	0.94
I	H_2O-NaCl	Area 5	A2-14	B	AA8	S	-14.4	-4.6	185.4	L+V	7.3	0.94
I	H_2O-NaCl	Area 5	A2-14	B	AA10	S	-4.4	-0.1	185	L+V	0.2	0.89
I	H_2O-NaCl	Area 5	A2-14	B	Y9	L	-4.5	-0.1	247	L+V	0.2	0.80
I	H_2O-NaCl	Area 5	A2-14	B	U6	S	-4.8	-0.1	120.7	L+V	0.2	0.95
I	H_2O-NaCl	Area 5	A2-14	B	V8	S	-12.2	-1.7	152.4	L+V	2.9	0.94
I	H_2O-NaCl	Area 5	A2-14	B	U23	L	-6.6	-0.5	269.5	L+V	0.9	0.77
I	H_2O-NaCl	Area 5	A2-14	B	V22	S	-5.7	-0.3	250	L+V	0.5	0.80
I	H_2O-NaCl	Area 5	A2-14	B	U13	L	-8.1	-0.2	255	L+V	0.4	0.79
I	H_2O-NaCl	Area 5	A2-14	B	V15	L	-8.1	-0.2	250	L+V	0.4	0.80
I	H_2O-NaCl	Area 5	A2-14	B	U14	L	-8.1	-0.2	250	L+V	0.4	0.80
I	H_2O-NaCl	Area 5	A2-14	B	V12	S	-5.6	-0.1	250	L+V	0.2	0.79
I	H_2O-NaCl	Area 5	A2-14	B	Q8	S	-9.9	-0.1	222.2	L+V	0.2	0.84
I	H_2O-NaCl	Area 5	A2-14	B	O7	S	-11.4	-1.5	155.5	L+V	2.6	0.93
I	H_2O-NaCl	Area 5	A2-14	C	I7	S	-14.5	-4.1	171.4	L+V	6.6	0.95
I	H_2O-NaCl	Area 5	A2-14	C	H7	S	-15.5	-5.3	182.7	L+V	8.3	0.95
I	H_2O-NaCl	Area 5	A2-14	C	G14	L	-14.9	-4.4	208.3	L+V	7.0	0.91
I	H_2O-NaCl	Area 5	A2-14	C	I19	L	-14.1	-4.6	178.7	L+V	7.3	0.94
I	H_2O-NaCl	Area 5	A2-14	C	I17	S	-17	-4.6	220	L+V	7.3	0.90
I	H_2O-NaCl	Area 5	A2-14	C	J24	L	-7.1	-0.1	221.9	L+V	0.2	0.84
I	H_2O-NaCl	Area 5	A2-14	C	J22	S	-16.6	-2.9	151.9	L+V	4.8	0.95
I	H_2O-NaCl	Area 5	A2-14	C	P17	L	-10	-1.1	206.8	L+V	1.9	0.87
I	H_2O-NaCl	Area 5	A2-14	C	M19	S	-7	-0.1	243.9	L+V	0.2	0.80
I	H_2O-NaCl	Area 5	A2-14	C	G28	S	-16.6	-4.8	157.8	L+V	7.6	0.97
I	H_2O-NaCl	Area 5	A2-14	C	G17	L	-17.1	-5.8	239.1	L+V	8.9	0.89
I	H_2O-NaCl	Area 5	A2-14	C	E19	S	-17.1	-6.5	242.2	L+V	9.9	0.89
I	H_2O-NaCl	Area 5	A2-14	C	G20	S	-14.9	-2.4	128.6	L+V	4.0	0.97
I	H_2O-NaCl	Area 5	A2-14	C	H23	S	-9	-0.1	236.9	L+V	0.2	0.82
I	H_2O-NaCl	Area 5	A2-14	C	I24	S	-9	-0.1	236.9	L+V	0.2	0.82
I	H_2O-NaCl	Area 5	A2-14	D	T9_1	S	-16	-6.5	236.6	L+V	9.9	0.90
I	H_2O-NaCl	Area 5	A2-14	D	J33	S	-6.1	-0.1	123	L+V	0.2	0.95
I	H_2O-NaCl	Area 5	A2-14	D	K32	S	-6.2	-0.1	123	L+V	0.2	0.95
I	H_2O-NaCl	Area 5	A2-14	E	J13	S	-9.7	-0.6	231.8	L+V	1.1	0.83
I	H_2O-NaCl	Area 5	A2-14	E	J14	L	-9.7	-0.7	231.9	L+V	1.2	0.83
I	H_2O-NaCl	Area 5	A2-14	E	J15_1	S	-9.7	-0.7	250	L+V	1.2	0.80
I	H_2O-NaCl	Area 5	A2-14	E	J15_2	S	-6	-0.5	241.7	L+V	0.9	0.81
I	H_2O-NaCl	Area 5	A2-14	E	K13	L	-12.2	-1.2	250	L+V	2.1	0.81
I	H_2O-NaCl	Area 5	A2-14	E	K14	S	-6	-0.8	261.9	L+V	1.4	0.79
I	H_2O-NaCl	Area 5	A2-14	E	I14	S	-7	-0.2	220	L+V	0.4	0.84
I	H_2O-NaCl	Area 5	A2-14	E	I18	S	-7.1	-0.6	239.1	L+V	1.1	0.82
I	H_2O-NaCl	Area 5	A2-14	E	G19	S	-8.2	-0.1	179.8	L+V	0.2	0.89
I	H_2O-NaCl	Area 5	A2-14	E	G20	S	-8	-0.2	262.7	L+V	0.4	0.77
I	H_2O-NaCl	Area 5	A2-14	E	H24	L	-7.5	-0.5	250	L+V	0.9	0.80
I	H_2O-NaCl	Area 5	A2-14	E	I24	S	-5.2	-0.1	264.6	L+V	0.2	0.77
I	H_2O-NaCl	Area 5	A2-14	E	I25	S	-15	-4.5	166.6	L+V	7.2	0.95
I	H_2O-NaCl	Area 5	A2-14	E	L25_1	L	-8	-0.1	205.9	L+V	0.2	0.86
I	H_2O-NaCl	Area 5	A2-14	E	L25_2	S	-9	-0.7	264.6	L+V	1.2	0.78
I	H_2O-NaCl	Area 5	A2-14	E	L25_3	S	-11.1	-1.1	264.1	L+V	1.9	0.79
I	H_2O-NaCl	Area 5	A2-14	E	L23	L	-17.7	-2.5	245	L+V	4.2	0.84
I	H_2O-NaCl	Area 5	A2-14	E	K23	S	-14	-0.9	196.7	L+V	1.6	0.88
I	H_2O-NaCl	Area 5	A2-14	E	L24_1	S	-13.3	-0.8	232	L+V	1.4	0.83
I	H_2O-NaCl	Area 5	A2-14	E	L24_2	S	-12	-0.1	249.9	L+V	0.2	0.79
I	H_2O-NaCl	Area 5	A2-14	E	K25	S	-11.9	-0.8	230.8	L+V	1.4	0.84
I	H_2O-NaCl	Area 5	A2-14	E	M26	S	-14.4	-1.6	224.3	L+V	2.7	0.86
I	H_2O-NaCl	Area 5	A2-14	E	M27	S	-13	-1.2	268.1	L+V	2.1	0.78
I	H_2O-NaCl	Area 5	A2-14	E	L22	L	-13	-1.1	225	L+V	1.9	0.85

(Continued)

Type	Composition	Deposit	Sample	Grain	FI No.	Bubble size	T_{mi}	T_m	T_h	Phases	Salinity	ρ (g/cm^3)
I	H_2O-NaCl	Area 5	A2-14	E	K20	S	-9	-0.4	209.4	L+V	0.7	0.86
I	H_2O-NaCl	Area 5	A2-14	E	P27_1	S	-16.7	-3.5	241.1	L+V	5.7	0.86
I	H_2O-NaCl	Area 5	A2-14	E	Q27	S	-16	-3.1	169.9	L+V	5.1	0.94
I	H_2O-NaCl	Area 5	A2-14	E	Q26	S	-16	-3.1	172.2	L+V	5.1	0.93
I	H_2O-NaCl	Area 5	A2-14	E	S23	S	-7.7	-0.1	170.1	L+V	0.2	0.90
I	H_2O-NaCl	Area 5	A2-14	E	S20_1	S	-10	-0.2	247.3	L+V	0.4	0.80
I	H_2O-NaCl	Area 5	A2-14	E	S20_2	S	-10	-0.1	216.6	L+V	0.2	0.85
I	H_2O-NaCl	Area 5	A2-14	E	S20_3	S	-10	-0.1	234.1	L+V	0.2	0.82
I	H_2O-NaCl	Area 5	A2-14	E	R17	S	-10	-0.1	162.2	L+V	0.2	0.91
I	H_2O-NaCl	Area 5	A2-14	E	T16	S	-10	-0.1	255	L+V	0.2	0.79
I	H_2O-NaCl	Area 5	A2-14	E	R16	L	-12	-0.5	174.4	L+V	0.9	0.90
I	H_2O-NaCl	Area 5	A2-14	E	R15	S	-12	-0.5	174.5	L+V	0.9	0.90
I	H_2O-NaCl	Area 5	A2-14	E	S13_2	S	-17	-3.1	155.4	L+V	5.1	0.95
I	H_2O-NaCl	Area 5	A2-14	E	Q14_2	S	-11	-0.1	257.2	L+V	0.2	0.78
I	H_2O-NaCl	Area 5	A2-14	E	S11	S	-12	-0.6	182.5	L+V	1.1	0.90
I	H_2O-NaCl	Area 5	A2-14	E	O17	S	-11	-0.1	210	L+V	0.2	0.85
I	H_2O-NaCl	Area 5	A2-14	G	I11	S	-11	-0.1	158	L+V	0.2	0.92
I	H_2O-NaCl	Area 5	A2-14	G	L13	L	-11.3	-0.3	220	L+V	0.5	0.84
I	H_2O-NaCl	Area 5	A2-14	G	N10	L	-12.2	-1.9	149.6	L+V	3.2	0.94
I	H_2O-NaCl	Area 5	A2-14	G	K12	L	-17	-6.1	188.2	L+V	9.3	0.95
I	H_2O-NaCl	Area 5	A2-14	G	L12_1	S	-16.1	-6.1	133.6	L+V	9.3	1.00
I	H_2O-NaCl	Area 5	A2-14	G	O14	S	-15.9	-2.7	215	L+V	4.5	0.88
I	H_2O-NaCl	Area 5	A2-14	G	S20	L	-6	-0.6	215	L+V	1.1	0.85
I	H_2O-NaCl	Area 5	A2-14	G	R31_1	S	-10	-1.1	119.9	L+V	1.9	0.96
I	H_2O-NaCl	Area 5	A2-14	G	R31_2	S	-10	-1.1	148.7	L+V	1.9	0.94
I	H_2O-NaCl	Area 5	A2-14	G	P32_1	S	-13.3	-1.8	204.9	L+V	3.1	0.88
I	H_2O-NaCl	Area 5	A2-14	G	P32_2	S	-13.3	-1.8	205	L+V	3.1	0.88
I	H_2O-NaCl	Area 5	A2-14	G	P33	L	-8	-0.5	210.6	L+V	0.9	0.86
I	H_2O-NaCl	Area 5	A2-14	H	R13	S	-7.7	-0.5	215.2	L+V	0.9	0.85
I	H_2O-NaCl	Area 5	A2-14	H	Q6	S	-11	-1.5	213	L+V	2.6	0.87
I	H_2O-NaCl	Area 5	A2-14	H	M23	S	-9	-0.4	210	L+V	0.7	0.86
I	H_2O-NaCl	Area 5	A2-14	H	M22	S	-10	-0.6	198.6	L+V	1.1	0.88
I	H_2O-NaCl	Area 5	A2-14	H	N22	L	-10.1	-0.8	220	L+V	1.4	0.85
I	H_2O-NaCl	Area 5	A2-14	H	P22	S	-17.7	-6.2	241.1	L+V	9.5	0.89
I	H_2O-NaCl	Area 5	A2-14	H	S22_1	S	-13.3	-1.5	159.5	L+V	2.6	0.93
I	H_2O-NaCl	Area 5	A2-14	H	T24_2	S	-13.3	-1.5	149.9	L+V	2.6	0.94
I	H_2O-NaCl	Area 5	A2-14	H	V17	S	-19	-5.2	156.2	L+V	8.1	0.97
I	H_2O-NaCl	Area 5	A2-14	I	I16	L	-9	-0.3	214.6	L+V	0.5	0.85
I	H_2O-NaCl	Area 5	A2-14	I	J16	S	-9	-0.3	210	L+V	0.5	0.86
I	H_2O-NaCl	Area 5	A2-14	I	K18	S	-9	-0.2	152.7	L+V	0.4	0.92
I	H_2O-NaCl	Area 5	A2-14	I	L15	S	-12.2	-1.2	232.7	L+V	2.1	0.84
I	H_2O-NaCl	Area 5	A2-14	I	K15_2	S	-9	-0.8	171.5	L+V	1.4	0.91
I	H_2O-NaCl	Area 5	A2-14	I	L16_1	S	-9	-0.4	220	L+V	0.7	0.85
I	H_2O-NaCl	Area 5	A2-14	I	K13	S	-16.6	-3.6	157.4	L+V	5.9	0.95
I	H_2O-NaCl	Area 5	A2-14	I	N17	S	-10	-0.4	220	L+V	0.7	0.85
I	H_2O-NaCl	Area 5	A2-14	I	Q17	S	-12.5	-2.5	188.2	L+V	4.2	0.91
I	H_2O-NaCl	Area 5	A2-14	I	T20	S	-7	-0.3	258.6	L+V	0.5	0.78
I	H_2O-NaCl	Area 5	A2-14	I	L13	S	-7	-0.1	169.4	L+V	0.2	0.90
I	H_2O-NaCl	Area 5	A2-14	I	L11	S	-14.4	-2.5	140.5	L+V	4.2	0.96
I	H_2O-NaCl	Area 5	A2-14	I	I13	L	-8	-0.2	272.3	L+V	0.4	0.76
I	H_2O-NaCl	Area 5	A2-14	I	J11_1	S	-8	-0.2	202.4	L+V	0.4	0.87
I	H_2O-NaCl	Area 5	A2-14	I	J11_2	S	-8	-0.2	228.7	L+V	0.4	0.83
I	H_2O-NaCl	Area 5	A2-14	I	J11_3	S	-8	-0.2	216.2	L+V	0.4	0.85
I	H_2O-NaCl	Area 5	A2-14	I	J10	S	-7.5	-0.1	207.1	L+V	0.2	0.86
I	H_2O-NaCl	Area 5	A2-14	I	K9_1	S	-7.5	-0.1	173	L+V	0.2	0.90
I	H_2O-NaCl	Area 5	A2-14	I	O1	L	-8	-0.2	192.4	L+V	0.4	0.88
I	H_2O-NaCl	Area 5	A2-14	I	O2	L	-9.1	-0.3	218.1	L+V	0.5	0.85
I	H_2O-NaCl	Area 5	A2-14	I	P2	L	-10.1	-0.4	198.7	L+V	0.7	0.87
I	H_2O-NaCl	Area 5	A2-14	I	P1	S	-7.7	-0.1	209.9	L+V	0.2	0.85
II	H_2O-NaCl	Area 5	A2-14	A	X7	S	-15	-9.8	166.5	L+V	13.7	1.00
II	H_2O-NaCl	Area 5	A2-14	A	O29	S	-16	-10.1	155.6	L+V	14.0	1.01
II	H_2O-NaCl	Area 5	A2-14	E	N23	S	-17	-12.1	198.1	L+V	16.1	0.99
II	H_2O-NaCl	Area 5	A2-14	G	I8	S	-16.6	-12.1	220.2	L+V	16.1	0.97
II	H_2O-NaCl	Area 5	A2-14	G	J24_1	S	-16.7	-12.9	156.9	L+V	16.8	1.03
II	H_2O-NaCl	Area 5	A2-14	H	F11	S	-16	-14.4	200.1	L+V	18.1	1.01
II	H_2O-NaCl	Area 5	A2-14	H	G10	S	-16	-14.4	215.5	L+V	18.1	0.99
II	H_2O-NaCl	Area 5	A2-14	H	G11	S	-16	-14.4	213.3	L+V	18.1	0.99
II	H_2O-NaCl	Area 5	A2-14	I	Q16	S	-21	-9.3	222.2	L+V	13.2	0.94
III	H_2O-$CaCl_2$-NaCl	Area 5	A2-14	A	P9	S	-40	-17.8	180	L+V	19.6	1.05
III	H_2O-$CaCl_2$-NaCl	Area 5	A2-14	A	Q27	S	-50.1	-24.8	124.5	L+V	22.9	1.13
III	H_2O-$CaCl_2$-NaCl	Area 5	A2-14	A	N29	S	-50.3	-23.6	155	L+V	22.4	1.10
III	H_2O-$CaCl_2$-NaCl	Area 5	A2-14	A	W8	S	-37	-17.9	129.1	L+V	20.9	1.09
III	H_2O-$CaCl_2$-NaCl	Area 5	A2-14	A	W10	S	-33	-19.7	144	L+V	22.2	1.09
III	H_2O-$CaCl_2$-NaCl	Area 5	A2-14	A	O7	S	-35	-19.7	102.7	L+V	22.2	1.12
III	H_2O-$CaCl_2$-NaCl	Area 5	A2-14	B	W10	L	-48.7	-23.1	149.1	L+V	22.2	1.10

(Continued)

Type	Composition	Deposit	Sample	Grain	FI No.	Bubble size	T_{mi}	T_m	T_h	Phases	Salinity	ρ (g/cm^3)
III	H_2O-$CaCl_2$-NaCl	Area 5	A2-14	B	X11	S	-47.1	-23.2	171.5	L+V	22.2	1.08
III	H_2O-$CaCl_2$-NaCl	Area 5	A2-14	B	Y15	L	-45	-22.6	210.7	L+V	22.0	1.05
III	H_2O-$CaCl_2$-NaCl	Area 5	A2-14	B	Z15	L	-49.7	-24.1	146.6	L+V	22.6	1.11
III	H_2O-$CaCl_2$-NaCl	Area 5	A2-14	B	Y18	L	-51.1	-24.1	134.4	L+V	22.6	1.12
III	H_2O-$CaCl_2$-NaCl	Area 5	A2-14	B	X17	L	-50.6	-24.1	130.9	L+V	22.6	1.12
III	H_2O-$CaCl_2$-NaCl	Area 5	A2-14	B	Z10_1	S	-50	-25.2	181.1	L+V	23.1	1.09
III	H_2O-$CaCl_2$-NaCl	Area 5	A2-14	B	Z11	S	-47.7	-21.3	177.7	L+V	21.3	1.07
III	H_2O-$CaCl_2$-NaCl	Area 5	A2-14	B	AF19	L	-30.9	-2.7	187.8	L+V	5.1	0.91
III	H_2O-$CaCl_2$-NaCl	Area 5	A2-14	B	X20	S	-43.8	-21.1	145.5	L+V	21.3	1.09
III	H_2O-$CaCl_2$-NaCl	Area 5	A2-14	B	R8	S	-23.3	-0.8	168.8	L+V	1.4	0.91
III	H_2O-$CaCl_2$-NaCl	Area 5	A2-14	B	W6	S	-42	-20.8	120.7	L+V	22.9	1.11
III	H_2O-$CaCl_2$-NaCl	Area 5	A2-14	C	N17	S	-37.7	-7.6	201	L+V	11.8	0.95
III	H_2O-$CaCl_2$-NaCl	Area 5	A2-14	E	R18	S	-49.1	-24.3	177.7	L+V	22.7	1.08
III	H_2O-$CaCl_2$-NaCl	Area 5	A2-14	E	T12	S	-24.4	-0.5	159.8	L+V	0.9	0.92
III	H_2O-$CaCl_2$-NaCl	Area 5	A2-14	E	J25	S	-31	-16.1	211.5	L+V	19.5	1.01
III	H_2O-$CaCl_2$-NaCl	Area 5	A2-14	G	K14_1	S	-46.6	-24.2	125.2	L+V	22.7	1.13
III	H_2O-$CaCl_2$-NaCl	Area 5	A2-14	G	K14_2	S	-49.1	-23.2	120.5	L+V+S	22.2	1.12
III	H_2O-$CaCl_2$-NaCl	Area 5	A2-14	G	L12_2	L	-38.8	-6.9	241.2	L+V	11.0	0.90
III	H_2O-$CaCl_2$-NaCl	Area 5	A2-14	G	K13	S	-41.1	-14.8	128.2	L+V	17.8	1.07
III	H_2O-$CaCl_2$-NaCl	Area 5	A2-14	G	L20_1	L	-49.9	-24.5	174	L+V	22.8	1.09
III	H_2O-$CaCl_2$-NaCl	Area 5	A2-14	G	L20_2	S	-50.5	-24.6	115.1	L+V	22.8	1.13
III	H_2O-$CaCl_2$-NaCl	Area 5	A2-14	G	K22	S	-29.3	-9.2	185	L+V	13.3	0.98
III	H_2O-$CaCl_2$-NaCl	Area 5	A2-14	G	O12_1	S	-50.1	-24.1	178.5	L+V	22.6	1.08
III	H_2O-$CaCl_2$-NaCl	Area 5	A2-14	G	P21_2	S	-36.5	-11.6	124.2	L+V	15.5	1.05
III	H_2O-$CaCl_2$-NaCl	Area 5	A2-14	G	N25	S	-27.7	-7.2	210	L+V	11.2	0.94
III	H_2O-$CaCl_2$-NaCl	Area 5	A2-14	G	L41	S	-44.4	-21.2	158	L+V	21.3	1.08
III	H_2O-$CaCl_2$-NaCl	Area 5	A2-14	G	O34	S	-25.5	-3.5	130.9	L+V	6.2	0.98
III	H_2O-$CaCl_2$-NaCl	Area 5	A2-14	G	O33	S	-43.7	-20.8	134.6	L+V	21.1	1.10
III	H_2O-$CaCl_2$-NaCl	Area 5	A2-14	H	F13_2	S	-46.9	-22.5	142.4	L+V	21.9	1.10
III	H_2O-$CaCl_2$-NaCl	Area 5	A2-14	H	T15_1	L	-50.5	-24.7	135.3	L+V	22.9	1.12
III	H_2O-$CaCl_2$-NaCl	Area 5	A2-14	H	T15_2	L	-51.3	-25.8	119.5	L+V	23.3	1.14
III	H_2O-$CaCl_2$-NaCl	Area 5	A2-14	H	T15_3	S	-48.8	-25.1	153.6	L+V	23.1	1.11
III	H_2O-$CaCl_2$-NaCl	Area 5	A2-14	H	P17_3	S	-29.7	-2.5	144.9	L+V	4.8	0.95
III	H_2O-$CaCl_2$-NaCl	Area 5	A2-14	H	N19	S	-26.6	-0.6	123.7	L+V	1.2	0.95
III	H_2O-$CaCl_2$-NaCl	Area 5	A2-14	H	N13	S	-50	-25.2	150.1	L+V	23.1	1.11
III	H_2O-$CaCl_2$-NaCl	Area 5	A2-14	H	J26	S	-28.8	-3.2	149.9	L+V	5.8	0.96
III	H_2O-$CaCl_2$-NaCl	Area 5	A2-14	H	K26	S	-24.4	-2.5	112.7	L+V	4.5	0.98
III	H_2O-$CaCl_2$-NaCl	Area 5	A2-14	H	N21	L	-22.9	-0.5	155	L+V	0.7	0.92
III	H_2O-$CaCl_2$-NaCl	Area 5	A2-14	H	N15_1	S	-31	-18.2	164.5	L+V	21.1	1.06
III	H_2O-$CaCl_2$-NaCl	Area 5	A2-14	I	K16	S	-44.4	-23.5	143.2	L+V	22.4	1.11
III	H_2O-$CaCl_2$-NaCl	Area 5	A2-14	I	L16_2	L	-49.5	-24.6	207.7	L+V	22.8	1.06
III	H_2O-$CaCl_2$-NaCl	Area 5	A2-14	I	K7	S	-23.1	-0.6	173.1	L+V+S	1.0	0.91
I	H_2O-NaCl	Wolverine	W7-3	A	P20	L	-15.5	-3.4	210	L+V	5.6	0.90
I	H_2O-NaCl	Wolverine	W7-3	A	Q27	L	-16.7	-4.1	203.5	L+V	6.6	0.91
I	H_2O-NaCl	Wolverine	W7-3	A	S25_1	L	-11	-1.1	257	L+V	1.9	0.80
I	H_2O-NaCl	Wolverine	W7-3	A	S25_2	S	-16.6	-4.6	207.1	L+V	7.3	0.91
I	H_2O-NaCl	Wolverine	W7-3	A	U24	L	-16	-4.1	215	L+V	6.6	0.90
I	H_2O-NaCl	Wolverine	W7-3	A	T26	L	-6	-0.1	215	L+V	0.2	0.85
I	H_2O-NaCl	Wolverine	W7-3	A	Y23	L	-14.4	-2.8	220	L+V	4.6	0.88
I	H_2O-NaCl	Wolverine	W7-3	A	U45	S	-7	-0.3	135	L+V	0.5	0.94
I	H_2O-NaCl	Wolverine	W7-3	A	U51_1	S	-15	-5.6	144.5	L+V	8.7	0.98
I	H_2O-NaCl	Wolverine	W7-3	A	S47	S	-7	-0.8	224.3	L+V	1.4	0.84
I	H_2O-NaCl	Wolverine	W7-3	A	O35	L	-14.1	-6.4	210.7	L+V	9.7	0.93
I	H_2O-NaCl	Wolverine	W7-3	A	O37	L	-8	-0.1	175.7	L+V	0.2	0.90
I	H_2O-NaCl	Wolverine	W7-3	A	O39	L	-8	-0.1	180.1	L+V	0.2	0.89
I	H_2O-NaCl	Wolverine	W7-3	A	P62	L	-11.1	-1.3	210.1	L+V	2.2	0.87
I	H_2O-NaCl	Wolverine	W7-3	A	O63	S	-13.7	-6.1	194.4	L+V	9.3	0.94
I	H_2O-NaCl	Wolverine	W7-3	A	Y50	S	-8	-0.1	220.1	L+V	0.2	0.84
I	H_2O-NaCl	Wolverine	W7-3	B	W4	S	-8	-0.1	141.9	L+V	0.2	0.93
I	H_2O-NaCl	Wolverine	W7-3	B	M22_1	S	-8	-0.1	144.2	L+V	0.2	0.93
I	H_2O-NaCl	Wolverine	W7-3	B	M22_2	S	-8	-0.1	178.8	L+V	0.2	0.89
I	H_2O-NaCl	Wolverine	W7-3	B	M23	S	-8	-0.1	145.1	L+V	0.2	0.93
I	H_2O-NaCl	Wolverine	W7-3	B	P26_1	L	-17.7	-3.4	178.8	L+V	5.6	0.93
I	H_2O-NaCl	Wolverine	W7-3	B	P26_2	S	-8	-0.1	142.4	L+V	0.2	0.93
I	H_2O-NaCl	Wolverine	W7-3	B	P24	S	-13	-2.1	224.7	L+V	3.5	0.86
I	H_2O-NaCl	Wolverine	W7-3	B	T19	S	-13	-4.5	148.2	L+V	7.2	0.97
I	H_2O-NaCl	Wolverine	W7-3	B	O35	S	-13	-2.1	228.7	L+V	3.5	0.86
I	H_2O-NaCl	Wolverine	W7-3	D	J18	S	-11.1	-1.1	138.8	L+V	1.9	0.94
I	H_2O-NaCl	Wolverine	W7-3	D	I23	S	-7	-0.2	250.1	L+V	0.4	0.80
I	H_2O-NaCl	Wolverine	W7-3	D	H22_1	S	-7	-0.1	130.7	L+V	0.2	0.94
I	H_2O-NaCl	Wolverine	W7-3	D	H23_2	S	-7	-2.1	137.3	L+V	3.5	0.96
I	H_2O-NaCl	Wolverine	W7-3	D	H24_1	S	-8	-0.1	125.6	L+V	0.2	0.94
I	H_2O-NaCl	Wolverine	W7-3	D	H24_2	S	-8	-0.1	141.1	L+V	0.2	0.93
I	H_2O-NaCl	Wolverine	W7-3	D	G25_1	S	-8	-0.2	150.7	L+V	0.4	0.92
I	H_2O-NaCl	Wolverine	W7-3	D	E19	S	-8	-0.1	165.6	L+V	0.2	0.91

(Continued)

Type	Composition	Deposit	Sample	Grain	FI No.	Bubble size	T_{mi}	T_m	T_h	Phases	Salinity	ρ (g/cm^3)
I	H_2O-NaCl	Wolverine	W7-3	D	F19	S	-7	-0.1	142.2	L+V	0.2	0.93
I	H_2O-NaCl	Wolverine	W7-3	E	L8_1	L	-16.5	-3.5	224.7	L+V	5.7	0.88
I	H_2O-NaCl	Wolverine	W7-3	E	L9	S	-7	-0.1	180.6	L+V	0.2	0.89
I	H_2O-NaCl	Wolverine	W7-3	E	M4	L	-12.1	-1.2	146.8	L+V	2.1	0.94
I	H_2O-NaCl	Wolverine	W7-3	E	M6	S	-9	-0.1	152.2	L+V	0.2	0.92
I	H_2O-NaCl	Wolverine	W7-3	E	J10	S	-9	-0.2	120.9	L+V	0.4	0.95
I	H_2O-NaCl	Wolverine	W7-3	E	E8	S	-9	-0.1	212.7	L+V	0.2	0.85
I	H_2O-NaCl	Wolverine	W7-3	F	P41	L	-15.5	-4.4	221.9	L+V	7.0	0.89
I	H_2O-NaCl	Wolverine	W7-3	F	I27_2	S	-8.5	-0.2	131.9	L+V	0.4	0.94
I	H_2O-NaCl	Wolverine	W7-3	F	N23	S	-13	-5.5	160.8	L+V	8.5	0.97
I	H_2O-NaCl	Wolverine	W7-3	F	R18	L	-13.3	-1.8	215	L+V	3.1	0.87
I	H_2O-NaCl	Wolverine	W7-3	F	S17_1	L	-11	-1.5	210	L+V	2.6	0.87
I	H_2O-NaCl	Wolverine	W7-3	F	S17_2	L	-11	-1.1	220	L+V	1.9	0.85
I	H_2O-NaCl	Wolverine	W7-3	F	S17_3	L	-11	-1.2	215	L+V	2.1	0.86
I	H_2O-NaCl	Wolverine	W7-3	F	S17_4	L	-11	-1.7	215	L+V	2.9	0.87
I	H_2O-NaCl	Wolverine	W7-3	F	T17	L	-14.5	-2.1	210	L+V	3.5	0.88
I	H_2O-NaCl	Wolverine	W7-3	F	T16	L	-14.5	-2.7	215	L+V	4.5	0.88
I	H_2O-NaCl	Wolverine	W7-3	F	U16	L	-13.1	-6.2	157.5	L+V	9.5	0.98
I	H_2O-NaCl	Wolverine	W7-3	F	U17	L	-12.5	-2.5	210	L+V	4.2	0.89
I	H_2O-NaCl	Wolverine	W7-3	F	W15_1	S	-10	-0.5	204.8	L+V	0.9	0.87
I	H_2O-NaCl	Wolverine	W7-3	F	W15_2	S	-10	-0.5	241.7	L+V	0.9	0.81
I	H_2O-NaCl	Wolverine	W7-3	F	X16	S	-9	-0.2	225	L+V	0.4	0.84
I	H_2O-NaCl	Wolverine	W7-3	F	AC12	S	-16	-4.4	225.5	L+V	7.0	0.89
I	H_2O-NaCl	Wolverine	W7-3	F	AB12	L	-7	-0.1	170.7	L+V	0.2	0.90
I	H_2O-NaCl	Wolverine	W7-3	G	L21_1	L	-7	-0.1	185.7	L+V	0.2	0.89
I	H_2O-NaCl	Wolverine	W7-3	G	L21_2	S	-7	-0.2	180.3	L+V	0.4	0.89
I	H_2O-NaCl	Wolverine	W7-3	G	L21_3	S	-9	-0.5	175.1	L+V	0.9	0.90
I	H_2O-NaCl	Wolverine	W7-3	G	W23	S	-7	-0.1	205.5	L+V	0.2	0.86
I	H_2O-NaCl	Wolverine	W7-3	G	W24	S	-7	-0.1	190.7	L+V	0.2	0.88
I	H_2O-NaCl	Wolverine	W7-3	G	L1_2	L	-8	-0.2	220	L+V	0.4	0.84
I	H_2O-NaCl	Wolverine	W7-3	G	M1	S	-8	-0.3	167.6	L+V	0.5	0.91
I	H_2O-NaCl	Wolverine	W7-3	H	S5	S	-11.5	-1.3	228.7	L+V	2.2	0.85
I	H_2O-NaCl	Wolverine	W7-3	H	N4	S	-9.5	-0.8	178.1	L+V	1.4	0.90
I	H_2O-NaCl	Wolverine	W7-3	H	N9_1	S	-9.5	-0.5	220	L+V	0.9	0.85
I	H_2O-NaCl	Wolverine	W7-3	H	N9_2	S	-9.5	-0.5	255.5	L+V	0.9	0.79
I	H_2O-NaCl	Wolverine	W7-3	H	O10	L	-11.5	-1.5	250.5	L+V	2.6	0.82
I	H_2O-NaCl	Wolverine	W7-3	H	L10_1	S	-6	-0.4	152.2	L+V	0.7	0.92
I	H_2O-NaCl	Wolverine	W7-3	H	L10_2	S	-12.2	-1.5	148.9	L+V	2.6	0.94
I	H_2O-NaCl	Wolverine	W7-3	H	M9	S	-9.5	-0.2	138	L+V	0.4	0.94
I	H_2O-NaCl	Wolverine	W7-3	H	N8	S	-10	-1.1	225.1	L+V	1.9	0.85
I	H_2O-NaCl	Wolverine	W7-3	H	M8_1	S	-10.1	-2.1	226.6	L+V	3.5	0.86
I	H_2O-NaCl	Wolverine	W7-3	H	N10_1	S	-10.1	-2.1	254.3	L+V	3.5	0.82
I	H_2O-NaCl	Wolverine	W7-3	H	N10_2	S	-10.1	-2.3	249.1	L+V	3.9	0.83
I	H_2O-NaCl	Wolverine	W7-3	H	I19_1	S	-9	-0.8	193.7	L+V	1.4	0.88
I	H_2O-NaCl	Wolverine	W7-3	H	I19_2	S	-15.6	-3.1	195.5	L+V	5.1	0.91
I	H_2O-NaCl	Wolverine	W7-3	H	H19	S	-15.6	-3.5	147.7	L+V	5.7	0.96
I	H_2O-NaCl	Wolverine	W7-3	H	I13_1	S	-5	-0.3	140.9	L+V	0.5	0.93
I	H_2O-NaCl	Wolverine	W7-3	H	I13_2	S	-5.5	-0.2	155.5	L+V	0.4	0.92
I	H_2O-NaCl	Wolverine	W7-3	H	K7	S	-5.5	-0.4	162.6	L+V	0.7	0.91
I	H_2O-NaCl	Wolverine	W7-3	H	L5	L	-14.4	-3.7	245.1	L+V	6.0	0.86
I	H_2O-NaCl	Wolverine	W7-3	H	L6	S	-8	-0.5	237	L+V	0.9	0.82
I	H_2O-NaCl	Wolverine	W7-3	H	K4_1	S	-16.7	-4.5	200.5	L+V	7.2	0.92
I	H_2O-NaCl	Wolverine	W7-3	H	K4_2	S	-7	-0.5	235.1	L+V	0.9	0.82
I	H_2O-NaCl	Wolverine	W7-3	H	K4_3	S	-7	-0.8	220	L+V	1.4	0.85
I	H_2O-NaCl	Wolverine	W7-3	H	K4_4	S	-7	-0.4	136.8	L+V	0.7	0.94
I	H_2O-NaCl	Wolverine	W7-3	H	J6_2	S	-15.5	-2.9	149.3	L+V	4.8	0.95
I	H_2O-NaCl	Wolverine	W7-3	H	I6_1	S	-14.3	-1.8	121.9	L+V	3.1	0.97
I	H_2O-NaCl	Wolverine	W7-3	H	I6_2	S	-14.4	-2.5	215.2	L+V	4.2	0.88
I	H_2O-NaCl	Wolverine	W7-3	H	I7	S	-13	-3.5	250.5	L+V	5.7	0.85
I	H_2O-NaCl	Wolverine	W7-3	H	G8	S	-6	-0.1	211.3	L+V	0.2	0.85
I	H_2O-NaCl	Wolverine	W7-3	H	G9	S	-16.6	-3.1	215.5	L+V	5.1	0.89
I	H_2O-NaCl	Wolverine	W7-3	H	J14_1	S	-9	-1.1	220.2	L+V	1.9	0.85
I	H_2O-NaCl	Wolverine	W7-3	H	J14_2	L	-9	-1.2	245.5	L+V+S	2.1	0.82
I	H_2O-NaCl	Wolverine	W7-3	H	H25	L	-9	-0.1	228.8	L+V	0.2	0.83
I	H_2O-NaCl	Wolverine	W7-3	H	K9_1	L	-8	-0.5	158.9	L+V	0.9	0.92
I	H_2O-NaCl	Wolverine	W7-3	H	K9_2	L	-15	-4.1	245.7	L+V	6.6	0.86
II	H_2O-NaCl	Wolverine	W7-3	D	J19	S	-13	-8.8	200	L+V	12.6	0.96
III	H_2O-$CaCl_2$-NaCl	Wolverine	W7-3	A	P22	L	-26.6	-2.1	210	L+V	3.9	0.88
III	H_2O-$CaCl_2$-NaCl	Wolverine	W7-3	A	P25	L	-30.1	-7.5	198	L+V	11.5	0.95
III	H_2O-$CaCl_2$-NaCl	Wolverine	W7-3	A	Z24	S	-35.5	-6.1	171.9	L+V	10	0.97
III	H_2O-$CaCl_2$-NaCl	Wolverine	W7-3	A	V45	S	-39.5	-15.1	160.7	L+V	18	1.05
III	H_2O-$CaCl_2$-NaCl	Wolverine	W7-3	A	V54	L	-33.3	-6.3	198.8	L+V	10.2	0.94
III	H_2O-$CaCl_2$-NaCl	Wolverine	W7-3	A	U51_3	S	-29.7	-3.5	132.5	L+V	6.3	0.97
III	H_2O-$CaCl_2$-NaCl	Wolverine	W7-3	B	V11	S	-48.7	-21.4	116.7	L+V	21.4	1.12
III	H_2O-$CaCl_2$-NaCl	Wolverine	W7-3	B	M19	S	-38.8	-19.4	174.5	L+V	20.5	1.06

(Continued)

Type	Composition	Deposit	Sample	Grain	FI No.	Bubble size	T_{mi}	T_m	T_h	Phases	Salinity	ρ (g/cm^3)
III	H_2O-$CaCl_2$-NaCl	Wolverine	W7-3	D	H23_1	S	-33.3	-12.5	151.4	L+V	16.2	1.04
III	H_2O-$CaCl_2$-NaCl	Wolverine	W7-3	D	F21_1	S	-37.2	-10.9	184.4	L+V	14.9	1.00
III	H_2O-$CaCl_2$-NaCl	Wolverine	W7-3	E	M8	S	-31.1	-10.1	211.1	L+V	14.2	0.96
III	H_2O-$CaCl_2$-NaCl	Wolverine	W7-3	F	P25	S	-29.5	-8.9	191.3	L+V	13	0.97
III	H_2O-$CaCl_2$-NaCl	Wolverine	W7-3	F	L24	S	-48.8	-20.8	148.3	L+V	21.1	1.09
III	H_2O-$CaCl_2$-NaCl	Wolverine	W7-3	G	M20_1	S	-25.3	-2.2	170.7	L+V	4	0.93
III	H_2O-$CaCl_2$-NaCl	Wolverine	W7-3	G	M20_2	S	-27.6	-2.2	168.8	L+V	4.2	0.93
III	H_2O-$CaCl_2$-NaCl	Wolverine	W7-3	G	M20_3	S	-26.6	-2.2	165	L+V	4.1	0.93
III	H_2O-$CaCl_2$-NaCl	Wolverine	W7-3	G	L1_1	L	-23.3	-1.1	193.3	L+V+S	1.9	0.89
III	H_2O-$CaCl_2$-NaCl	Wolverine	W7-3	H	M8_2	S	-29.9	-4.5	218.6	L+V	7.8	0.90
III	H_2O-$CaCl_2$-NaCl	Wolverine	W7-3	H	L12	S	-28.5	-1.9	207.7	L+V	3.7	0.88
III	H_2O-$CaCl_2$-NaCl	Wolverine	W7-3	H	I19_3	L	-30	-2.9	225.5	L+V	5.4	0.87
III	H_2O-$CaCl_2$-NaCl	Wolverine	W7-3	H	L15	S	-47.6	-19.1	168.8	L+V	20.2	1.06
III	H_2O-$CaCl_2$-NaCl	Wolverine	W7-3	H	I11	S	-40	-15.7	157.7	L+V	18.3	1.05
III	H_2O-$CaCl_2$-NaCl	Wolverine	W7-3	H	I10_1	S	-41.1	-14.1	165.1	L+V	17.3	1.04
III	H_2O-$CaCl_2$-NaCl	Wolverine	W7-3	H	I10_2	S	-38.3	-13.7	170.7	L+V	17	1.03

*Type I: Low salinity H_2O-NaCl; Type II: medium salinity H_2O-NaCl; Type III: High salinity H_2O-$CaCl_2$-NaCl.